3-1995

Proceedings of the 1995 Annual Symposium on Engineering Geology and Geotechnical Engineering (No. 31)

Joseph A. Caliendo

Proceedings of the 1995 Annual Symposium on

Engineering Geology & Geotechnical Engineering

(No. 31)

Compiled and Edited by

Joseph A. Caliendo
Department of Civil and Environmental Engineering
Utah State University

Published March 1995

Copies of this and previous Proceedings volumes may be obtained from:
Lee Robinson
Idaho State University
P.O. Box 8371
Pocatello, ID 83209

Printed by
Publication Design & Production
Utah State University

SPONSORS

UTAH STATE UNIVERSITY	--Department of Geology
	--College of Engineering
IDAHO STATE UNIVERSITY	--Department of Geology
	--College of Engineering
BOISE STATE UNIVERSITY	--Department of Geology
	--Department of Physical Science and Engineering
UNIVERSITY OF IDAHO	--Department of Geology
	--Department of Civil Engineering
UNIVERSITY of NEVADA, RENO	--MacKay School of Mines
	--College of Engineering

ORGANIZING COMMITTEE - 1995 SYMPOSIUM

Joseph A. Caliendo, Loren R. Anderson, *Chairmen, Announcements, Abstract Review, Exhibitors*
Becky Hansen, *Compile Proceedings*
Les Youd, *Banquet Speaker*
John Franceski, Lance DiBernardi, *Field Trip*
Holly Johnson (Conference & Institute Division), *Registration, Banquet, Physical Arrangements*

SYMPOSIUM EXECUTIVE COMMITTEE

Utah State University	Joseph A. Caliendo, Loren R. Anderson
Idaho State University	Paul Link, Lee Robinson
University of Idaho	James H. Hardcastle, Terry R. Howard
Boise State University	Paul Donaldson, Charles Waag
University of Nevada-Reno	Gary Norris, Robert J. Watters
Executive Director/Treasurer:	Lee Robinson, Idaho State University

CONTENTS

I. Foundation Consideration

II. Soil Improvement

III. Slope Stability Considerations

IV. Seismic Issues & Dam Safety

V. Geomechanics

VI. Geotechnical Case Histories

VII. Testing & Investigation

VIII. Hydrogeology

CAPACITY EVALUATION METHODS OF DEEP FOUNDATIONS A CRITICAL REVIEW

George G. Goble[1]
and
Mohamad H. Hussein[2]

ABSTRACT

Determination of bearing capacity and behavior of deep foundations under applied load is one of the most important problems in foundation engineering. Several methods based on concepts ranging from purely theoretical to field testing are used to evaluate the load bearing capacity of deep foundation elements. This paper presents a critical review of a number of conventional methods and recently developed concepts for establishing pile load bearing capacity using field tests. For each method, theoretical principles, application considerations, and limitations will be discussed.

INTRODUCTION

The choice of foundation type is generally based on considerations of structural requirements, subsurface conditions, site characteristics and economics. Deep foundations are utilized when shallow type foundations do not provide adequate support. They are of two major categories: cast-in-place, or prefabricated and installed with a pile driving hammer. In some cases, a deep foundation element may incorporate both prefabricated and cast-in-place features. Driven elements usually having diameters less than about three feet are commonly referred to as piles while cast-in-place elements are known by a variety of names such as drilled shafts, bored piles, or caissons. The term "pile" will be used here to refer to a deep foundation element of any size or method of installation; distinction will, however, be made where necessary.

---

[1]Principal, Goble Rausche Likins and Associates, Boulder, Colorado

[2]Partner, Pile Dynamics, Inc., Cleveland, Ohio

Performance under applied load is a function of the pile strength and integrity as a structural element, supporting soil strength and deformation properties, pile-soil interaction characteristics, and the nature and magnitude of the applied load. In the case of pile foundations, it is possible and common to actually test single piles to determine their capacity. This paper presents a discussion of field testing methods for evaluation of axial compression load carrying capacity of single piles. Specifically, the following techniques are critically reviewed: conventional static loading tests, Osterberg Method, dynamic pile testing, and Statnamic.

There are many other considerations, in addition to strength, that place limitations on pile design. These considerations are handled using a variety of site assessment methods including subsurface investigation with borings, in-situ and laboratory tests for evaluation of soil and/or rock properties and ground water conditions. It is also necessary to evaluate the long term effects such as the potential for pile deterioration due to the chemical reaction between the soil and the pile, scour, downdrag, long term settlement, etc. For driven type piles, Wave Equation analysis is an integral part of the pile design, the selection of the installation equipment and the determination of driving criteria and procedures. Knowledge of the static load bearing capacity of single piles, the topic considered here, is essential for a proper evaluation of the foundation system but it is only one of several considerations.

STATIC LOADING TESTS

Traditionally, pile testing has meant a static loading test. The purpose of the test is to examine the response of a pile under load applied at the pile head. Several different procedures have been proposed for conducting this type of test. The main differences are in load application, instrumentation, and interpretation of results. Standards and procedures detailing arrangement, performance, and evaluation of results are available in the literature (ASTM D-1143; FHWA-SA-91-042, 1992; ISSMFE 1985; Canadian Foundation Engineering Manual, 1992). Pile testing may be performed during the design or construction phase of a project depending on whether foundation design parameters are desired or the pile adequacy is to be verified. For small projects, testing cost may be significant compared to the overall foundation cost. On projects involving a large number of piles, only a small percentage (typically one percent or less) of the piles are tested. In cases such as offshore construction and land construction in waterways or congested areas, static pile testing may be impractical or even impossible.

The number and location of the test piles is usually determined by the engineer after considerations of variability in subsurface conditions across the site, pile type and installation method, and loading type and magnitude. The physical setup for conducting the test is generally installed by the contractor. Testing is normally performed by the contractor under the supervision of the engineer.

Figure 1 presents "typical" arrangement for applying load and measuring movement at the pile head. A hydraulic jack acting against a reaction beam which is held by a system employing weights, piles, ground anchors, or a combination thereof is used for load application. Loads are measured with a load cell placed between the jack and the pile, by measuring the jack pressure, or by both methods. Pile head movement under

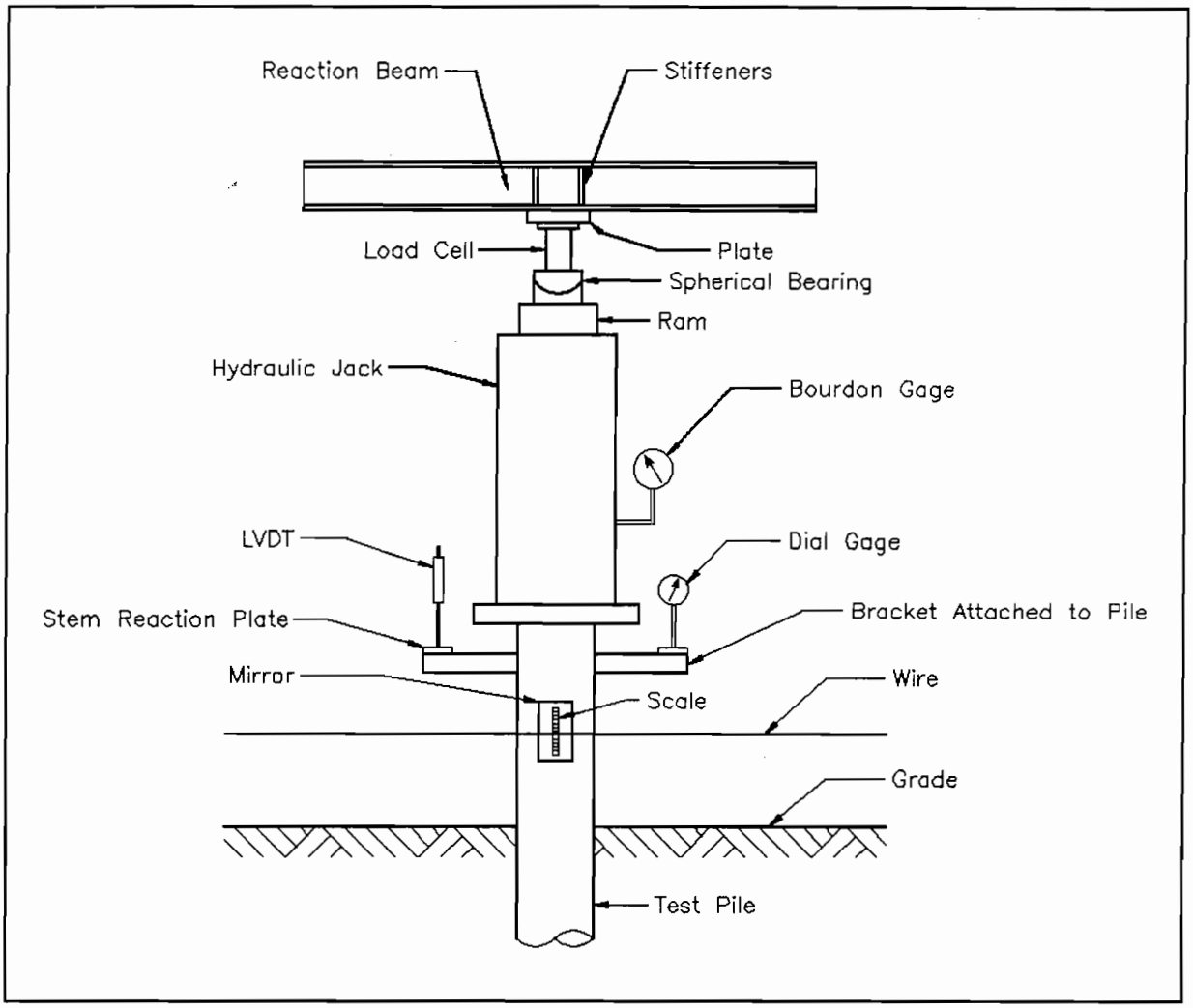

Figure 1: Typical Arrangement for Applying Load in and Axial Compression Test

applied load is measured with mechanical dial gages or electro-mechanical devices. Care must be taken to prevent apparent pile motion due to temperature effects on the dial gage supports. For redundancy, movement measurements are also taken with a wire-and-mirror system or with a surveyors level. Load and head movement measurements constitute the minimum measurements that are made during a static test. Measurements of movement along the pile shaft are sometimes obtained with telltales, rods that are supported at various levels along the pile and extended to the top where the measurements are made. Strain gages are occasionally used to measure internal forces at selected places along the pile length. For safety and proper evaluation of test results, movement of the reaction system should also monitored during the test.

The two most commonly used loading procedures are: the Maintained Load (ML) and the Constant Rate of Penetration (CRP) methods. According to the ML method, load is applied in increments that are large fractions of maximum anticipated load. Each increment is maintained until pile movement is less than a prescribed value (typically 0.01 inch per hour, or for two hours whichever occurs first). The final load is

maintained for 24 hours. The procedure is made into a "Quick Test" by applying fairly small load increments (25 to 40 increments of the maximum anticipated load) and holding each increment for a constant time interval (5 to 15 minutes). Pile movements are recorded before and after the application of each load increment. The CRP test method consists of continuously loading the pile such that its rate of pile head motion is constant (typically between 0.01 and 0.10 inches per minute). Readings of pile head movement are taken at least every 30 seconds. In some practices, the ML test is changed to the CRP procedure when the rate exceeds 0.8 inch per hour. Figure 2 presents plots of pile head load-movement relationships for the three loading procedures.

Commonly, test results are presented as a pile head load-movement plot. Other types of data may be obtained from the test, particularly with fully instrumented piles loaded to failure. Shapes of load-movement graphs vary considerably and so do the procedures used for evaluating the test result. Controversy arises in the interpretation of data due to the lack of a universally recognized definition of "failure". Practically, failure occurs when pile movement continues under sustained or slightly increased load.Studies have shown that it is possible to obtain a wide range of results from a single test depending on the method of interpretation (Fellenius 1980). The definition of failure is best based on rules that produce repeatable results independent of the engineers judgement.

The potential benefit of a static loading test should be carefully weighed against the cost and time required in performing a test. Although static load testing is an excellent procedure for evaluating pile load bearing capacity and insight into pile behavior under load, improperly performed or poorly executed load tests can produce results that do not reflect the conditions at the site.

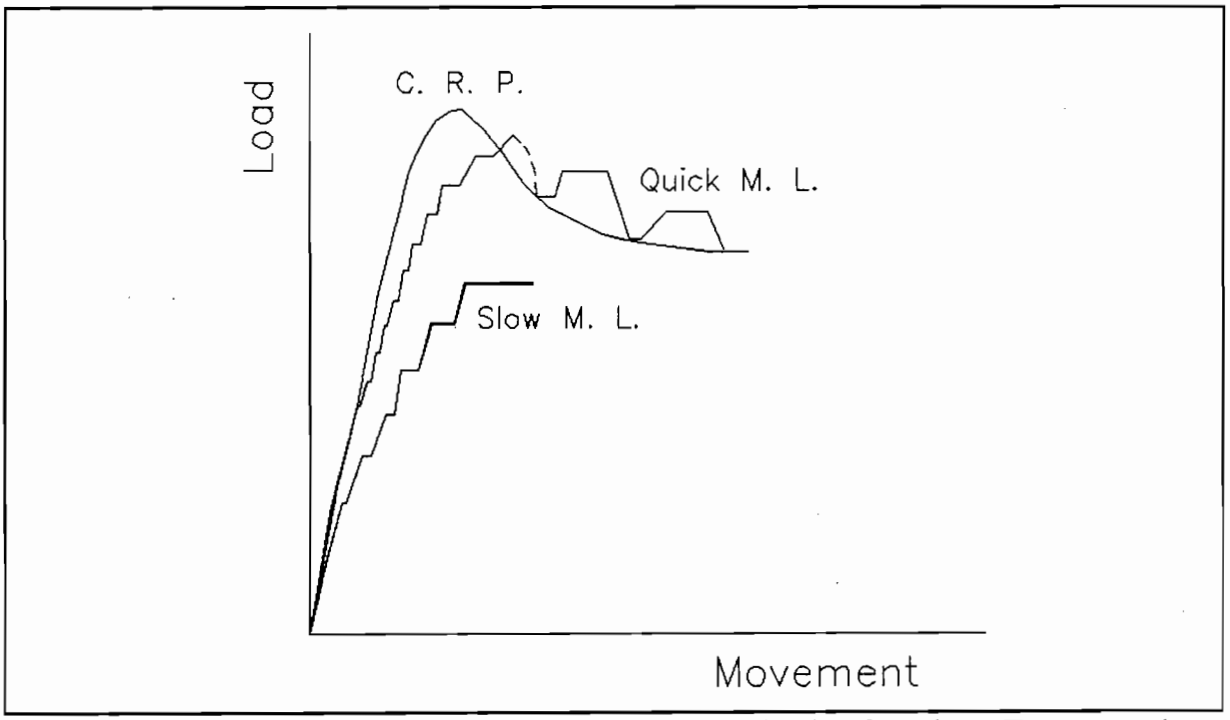

Figure 2: Comparison of Typical Load-Movement Behavior for Three Test Procedures

COMMENTS ON STATIC LOAD TEST ACCURACY AND RELIABILITY

The problems and limitations of the static load test fall into two categories; difficulties arising from incorrectly performed tests, and problems inherent in the static test itself. In the first category, static tests are limited by the cost and time required to perform the test. Furthermore, the cost will increase rapidly with the increased magnitude of the test load. Probably of all of the limitations this is the most serious.

Safety considerations present serious limitations. The large loads involved in a static test store large amounts of elastic energy. If something fails, serious injury of the testing personnel is possible. One hears frequently of failures in static load tests that cause injury and death of the testing staff.

Problems arise in the measurement of load and movement. Particularly load measurement can yield substantial error. The most common means of load measurement is to read the jack pressure. This can produce substantial error due to jack friction or simply a poor jack gage calibration. Fellenius (1980) has shown that an error of 15% may be typical due to jack friction. A poor calibration can lead to more serious errors. These problems become more serious when more than one jack is used in testing a high capacity pile. It is essential that an electronic load cell be used for measuring the applied load. In addition, the introduction of a spherical bearing in the load column will reduce the possibility of error in load measurement.

Probably the most serious problem with the performance of a successful static load test is the fact that most of the personnel that perform the test are inadequately trained. It seems that the test is looked upon as a relatively simple and routine task and ,therefore, special training is unnecessary. In fact, since the test must be performed correctly and carefully it is essential that the testing crew be well-trained.

Many, if not most, static tests are not carried to failure. They may not be carried to failure in order to limit expense and effort required to set up a suitable reaction system, or due to lack of a jack of sufficient size. In these cases the test result only represents a lower bound on the pile capacity. As such tests are normally performed they only represent proof tests and increased pile capacity cannot be justified. As the standard ML test is performed it often generates a failure load at the end of the load application. Since the load is rapidly applied failure only appears to occur when the load is held. In some cases if the load increments were smaller a lower failure load would occur.

Studies of data bases containing thousands of test results indicate that in most cases (certainly more than half) testing and test documentation were not done in a proper professional manner (i.e., in some cases pile type and dimensions, soil information, information on driving equipment, blow counts, etc.) (Dennis and Olson 1983) and (Wysockey and Long 1994).

In the second category, several basic problems inherent in the static test itself can be enumerated. The static test does not yield any information on pile driving stresses or hammer performance so a proper criteria cannot be set for production driving considering pile tension stresses and the possible need to vary the stroke during the driving of concrete piles. If a change is made in the hammer selection, then the absence of driving information severely reduces the reliability of the quality control for the production piles.

Most static load tests are impractical or impossible to perform offshore, in deep and strong river waters, or congested areas. In deep water, there is a danger that the test pile will buckle under load. Anchorage of the reaction system is also a difficult problem.

The static load test will not indicate pile structural damage in some cases. For cast-in-place piles where the concrete is totally lacking and all the load is taken by the steel reinforcement cage, if the steel can carry the test load this may mean trouble later if the steel corrodes. In general, the static test will not provide clear information on structural damage or integrity problems.

Even though the test is "static" it does not account for long term pile behavior (i.e., setup or relaxation, group effect, or long term settlement due to consolidation). There are even differences in results between ML and CRP results due to creep and loading rate effects (Walker 1972) and the lack of a uniform failure criteria is a further limitation.

In spite of the above limitations, the static test is still, appropriately, the standard by which pile capacity is evaluated. It is important that the test user understand that care must be used in performing the test. If the test is carefully executed and electronic load cells are used, it can be expected that the results will be good within the limitations listed in group two above. In the experience of the authors it is desirable that a rapid loading procedure be used so that over-night testing is not necessary. The long, maintained load test places larger demands on the testing crew and often lead to problems of test execution.

THE OSTERBERG LOAD CELL

The Osterberg test is a truly static load test that uses the shaft friction to react the toe force during the application of the toe load by hydraulic means (Osterberg 1984, Osterberg 1994). Using this method the cost of the static test must be reduced by eliminating the need for a reaction system. The test setup is shown in Figure 3. The Osterberg Test is performed using an Osterberg Load Cell (named for its inventor, Jorj Osterberg). Savings are achieved by utilizing the shaft soil resistance forces as the reaction load. The load cell (also known as the O-cell) is a calibrated high capacity hydraulic testing device of the flat jack type capable of exerting very large loads at high internal pressure. It is typically installed at the pile toe, but can also be located along the pile shaft. It is possible to utilize more than one O-cell in testing a single pile and, thus, determine more details of the resistance distribution. This testing method was originally developed for testing drilled shafts, but has been also applied to driven piles.

For typical applications, the O-cell is lowered to the bottom of the drilled shaft hole before concrete placement. A pipe, welded to the top of the device, extends to ground surface and serves as a conduit for applying fluid pressure to the cell. Inside this pipe is another smaller diameter pipe connected to the bottom of the device and extending to the top of the shaft for measurement of the downward movement of the bottom of the cell during the load application. Generally, the fluid used to apply pressure is water with a small percentage of water-miscible oil. When the test is completed the fluid can be replaced by grout.

Loading is achieved by internally pressurizing the cell, creating equal but opposite upward and downward forces. As the pressure in the cell increases, the inner pipe moves downward and toe resistance increases. The pile moves upward with load application and mobilizes the skin friction. The downward movement is measured with Dial Gage 2 (Figure 3) and pile top upward movement is measured with Dial Gage 1. Typically, three dial gages are used to measure the movement of the pile top in order to eliminate (by averaging) the effects of any pile bending. Tests are usually performed according to the ASTM D-1143 Quick Load Procedure. Load-downward movement for the bottom of the load cell in end bearing and load-upward movement plots are obtained from the test data. An example of the measured results is given in Figure 4. In this example the Minimum Capacity Curve will not really develop as the sum of the two curves since the pile toe will carry increasing load. With increased load, some failure condition will occur, either in end bearing or in shaft friction. At failure, no further increase in cell pressure can be obtained. The cell failure force can be considered to be a working load at the top of the shaft having a factor of safety of at least two against failure. Loads as high as 12,000 kips (6,000 kips each up and down) have been applied to shafts three feet or larger in diameter.

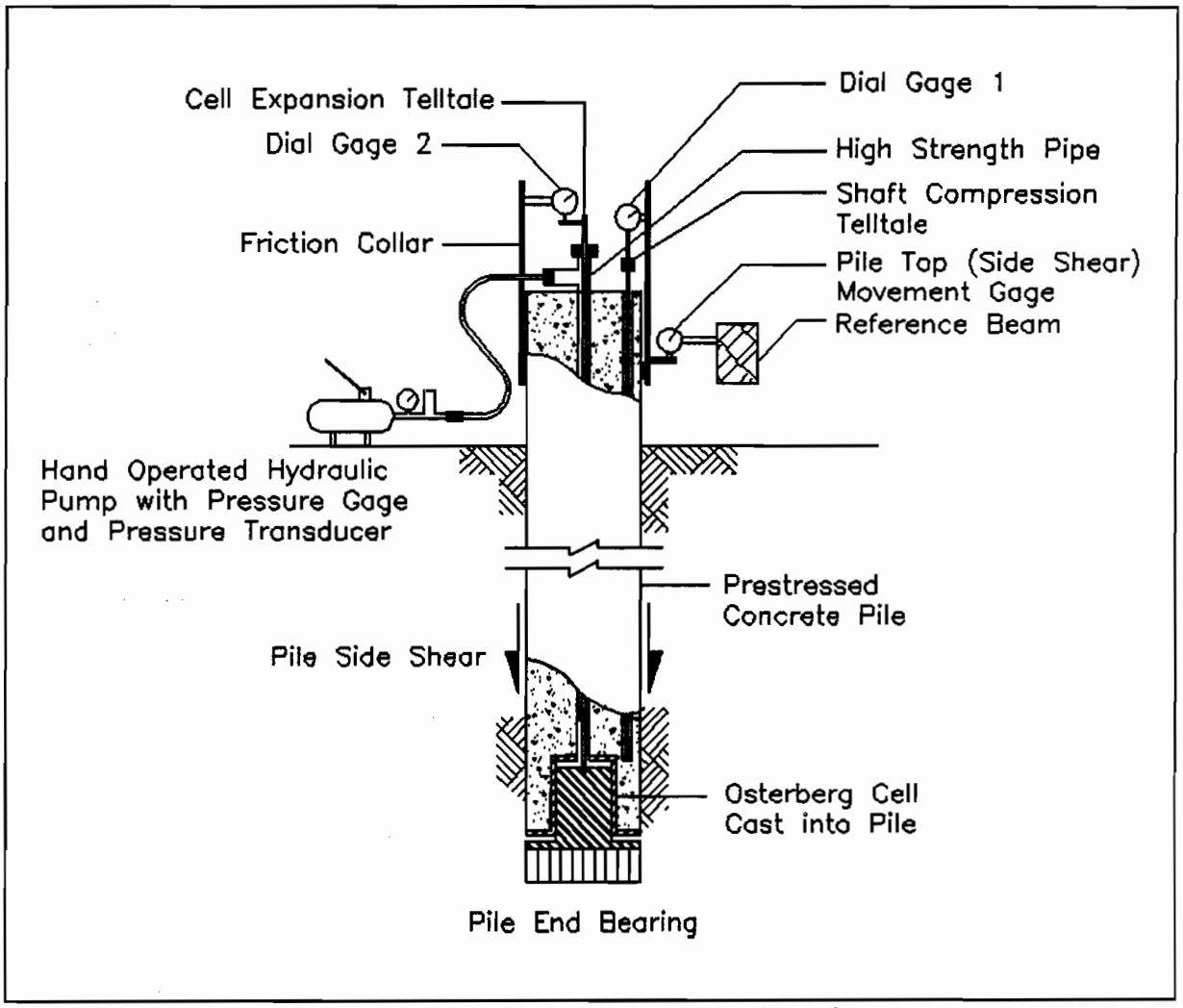

Figure 3: Osterberg Cell and Related Equipment

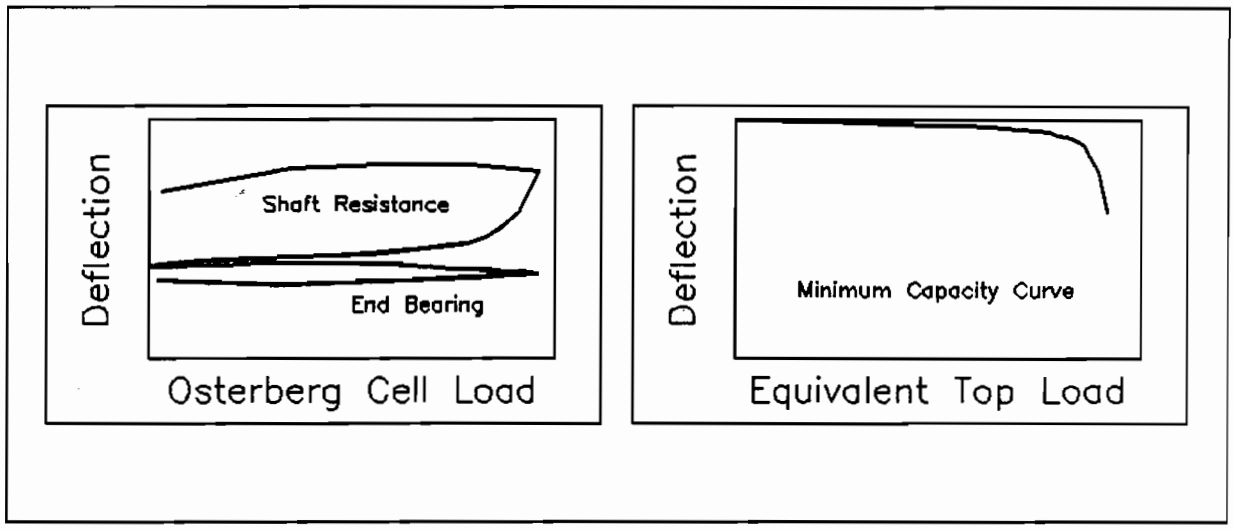

Figure 4: Equivalent Pile Head Load-Movement Curve

COMMENTS ON THE OSTERBERG LOAD TEST

The main advantage of the Osterberg test method over the conventional static test is the savings of time and cost in the test performance. In addition, the end bearing and skin friction are measured separately. Testing can be performed on piles over water, in congested areas, or on piles installed on a batter. Loading rates can be varied and it is possible to run several cycles of loading. Grouting the cell after the test takes advantage of the increased compression induced during the test and stiffens the end bearing resistance of the pile. The safety problems associated with the usual static load test are also greatly reduced.

Disadvantages of the Osterberg test method include most of the disadvantages of the second type listed above. In addition, the load cell must be installed prior to pile installation which eliminates the possibility of selecting the test pile on a random basis after the piles are installed. The load cell is expendable and cannot be retrieved. Total pile capacity in both friction and end bearing cannot be obtained since only one of the two fails. It may be more expensive than other testing methods for lightly loaded piles (perhaps up to about 400 kips). In addition, the test requires specialists for setup and performance and its applicability may be dependent on the soil conditions at the site.

DYNAMIC PILE TESTING

Modern dynamic pile testing methods are based on research initiated in 1964 at Case Institute of Technology (now Case Western Reserve University) with funding from the FHWA and the Ohio Department of Transportation. Additional funding was received from a number of state Highway Departments and private companies (Goble et al 1975, Goble et al 1980). Initially, the goal of the dynamic pile testing research was to develop methods for the evaluation of static pile capacity from measurements of pile force and acceleration under hammer impacts. The methods were later expanded to evaluate other

aspects of the hammer-pile-soil system. Today, these procedures are collectively called the Case Method and are routinely applied in the field using a dedicated computer based system called the Pile Driving Analyzer (PDA) (Rausche et al 1985). The Case Pile Wave Analysis Program (CAPWAP) was developed by the same investigators as an extension of the original research (Rausche 1970). Many organizations around the world have established standards and guidelines for dynamic pile testing (ASTM, FHWA, etc.). During the past fifteen years, the applicability of the method was expanded to test the various types of cast-in-place piles (Goble et al 1993).

The main objectives of dynamic pile testing now include: evaluation of pile driving resistance and static capacity, determination of pile driving stresses, assessment of pile structural integrity, and investigation of hammer and driving system performance.

Dynamic pile testing is performed by making measurements of pile force and motion under the hammer impact with reusable strain transducers and accelerometers attached near the pile top. The PDA is a field computer that acquires the data from the strain and acceleration transducers, provides signal conditioning, calibration and processing of those measured signals, integrates the acceleration to velocity, and displays the measurements for PDA operator evaluation. An example of a set of measured data is given in Figure 5. Using the measurements of force and velocity, the PDA applies the Case Method equations, derived from one dimensional wave mechanics, to compute, in real time, some 30 variables which fully describe the hammer-pile-soil system behavior. The Case Method capacity is calculated and displayed for each hammer blow.

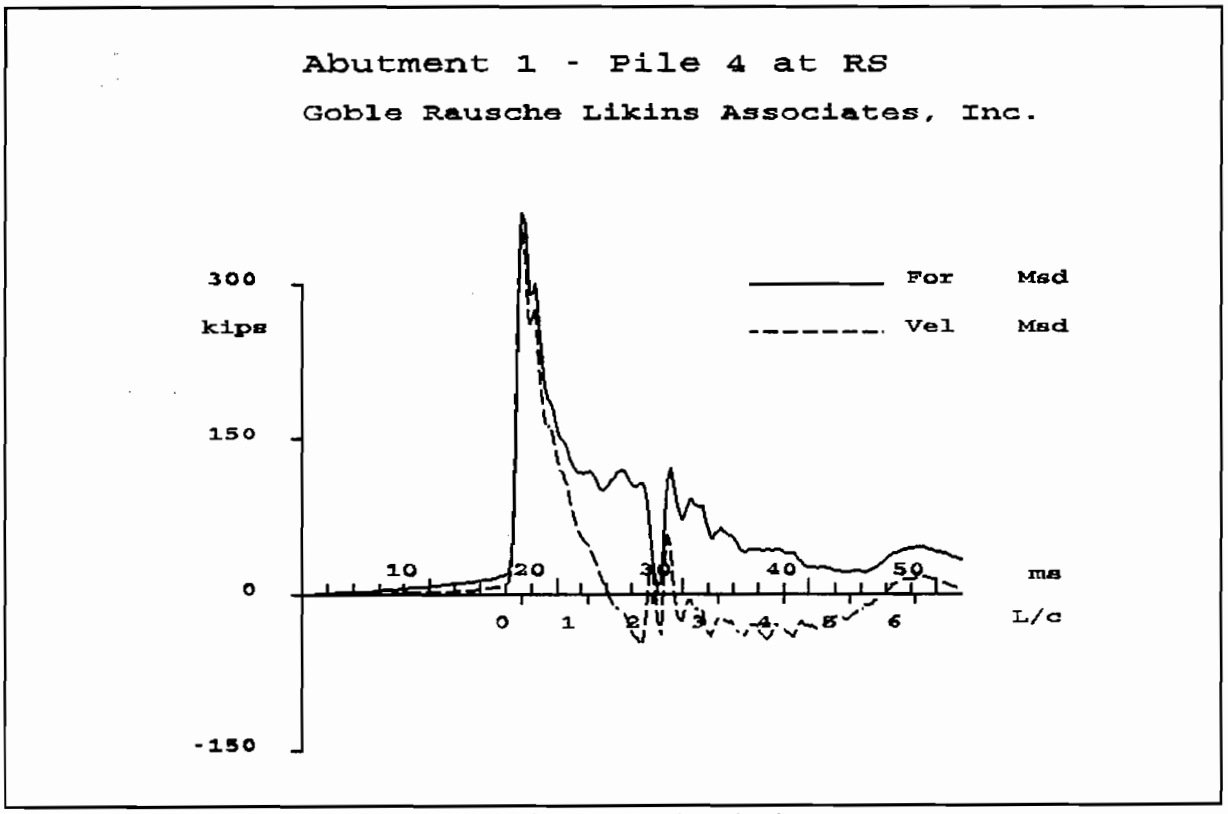

Figure 5: Example of Force and Velocity Measurement

The CAPWAP procedure is an analytical method that combines field measurements and a discrete wave equation type analysis to predict static pile capacity, soil resistance distribution, soil damping and stiffness values, pile load-movement and pile-soil interaction characteristics. The process is based on signal matching techniques utilizing system identification methods. Figure 6 shows a schematic description of the CAPWAP method. The result of the analysis gives not only the static capacity prediction but also the distribution of the static resistance forces and several other soil modeling parameters that give a more complete description of the soil.

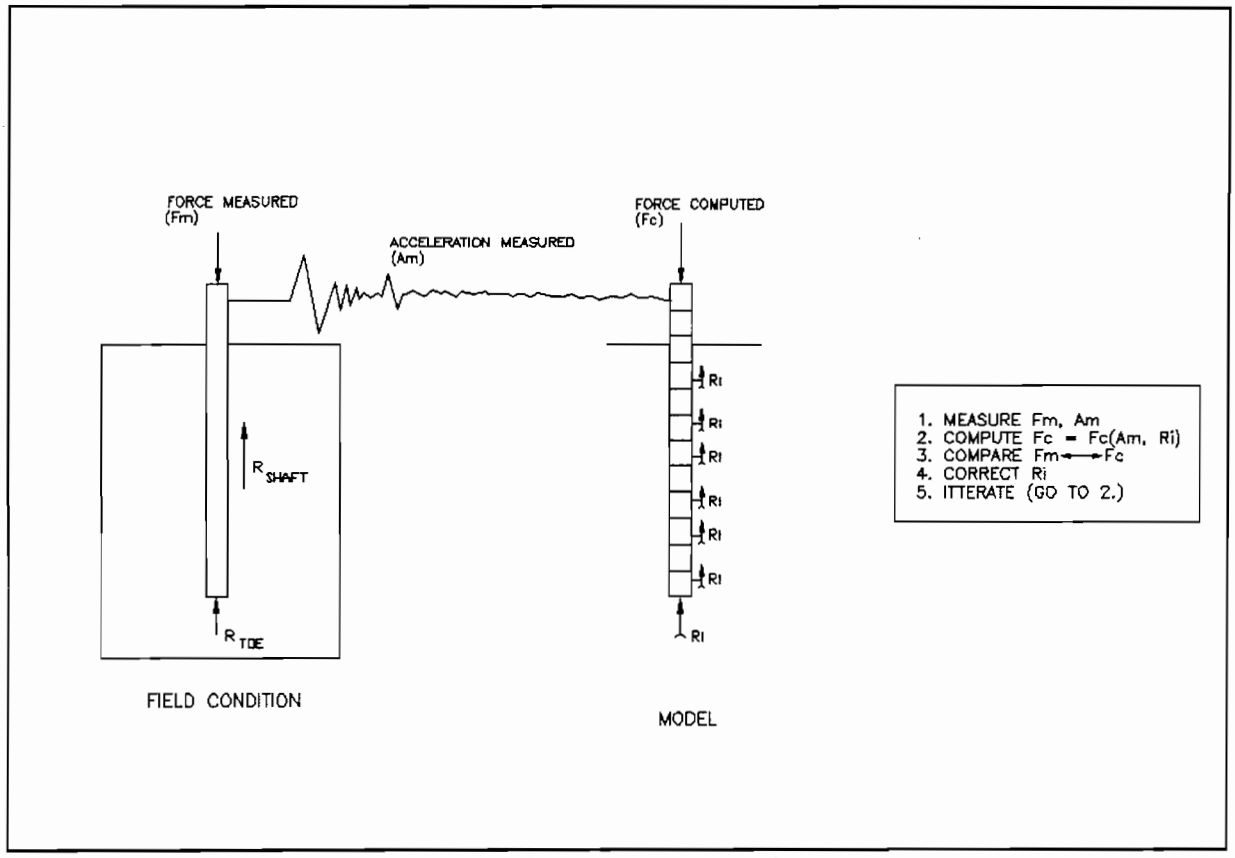

Figure 4: CAPWAP Method

An example of the results of the CAPWAP analysis is presented in Figure 7. Presented here are results of the analysis of a dynamic pile test. It includes plots of the force and velocity measurements, the match between measured and calculated impact force, soil resistance distribution at ultimate load, and pile top and toe load-movement relationships under a simulated static load test. The capacity obtained is the value existing at the time the test was conducted.

A dynamic pile test can be performed in a few minutes at a fraction of the cost of any other type of test. The technical literature contains numerous Class A prediction cases, assembled over the past 25 years, that compare results of dynamic testing and full scale load tests on the same pile. Also, pile damage predictions have been verified by inspection of extracted piles. Dynamic testing has been used routinely since 1972. In

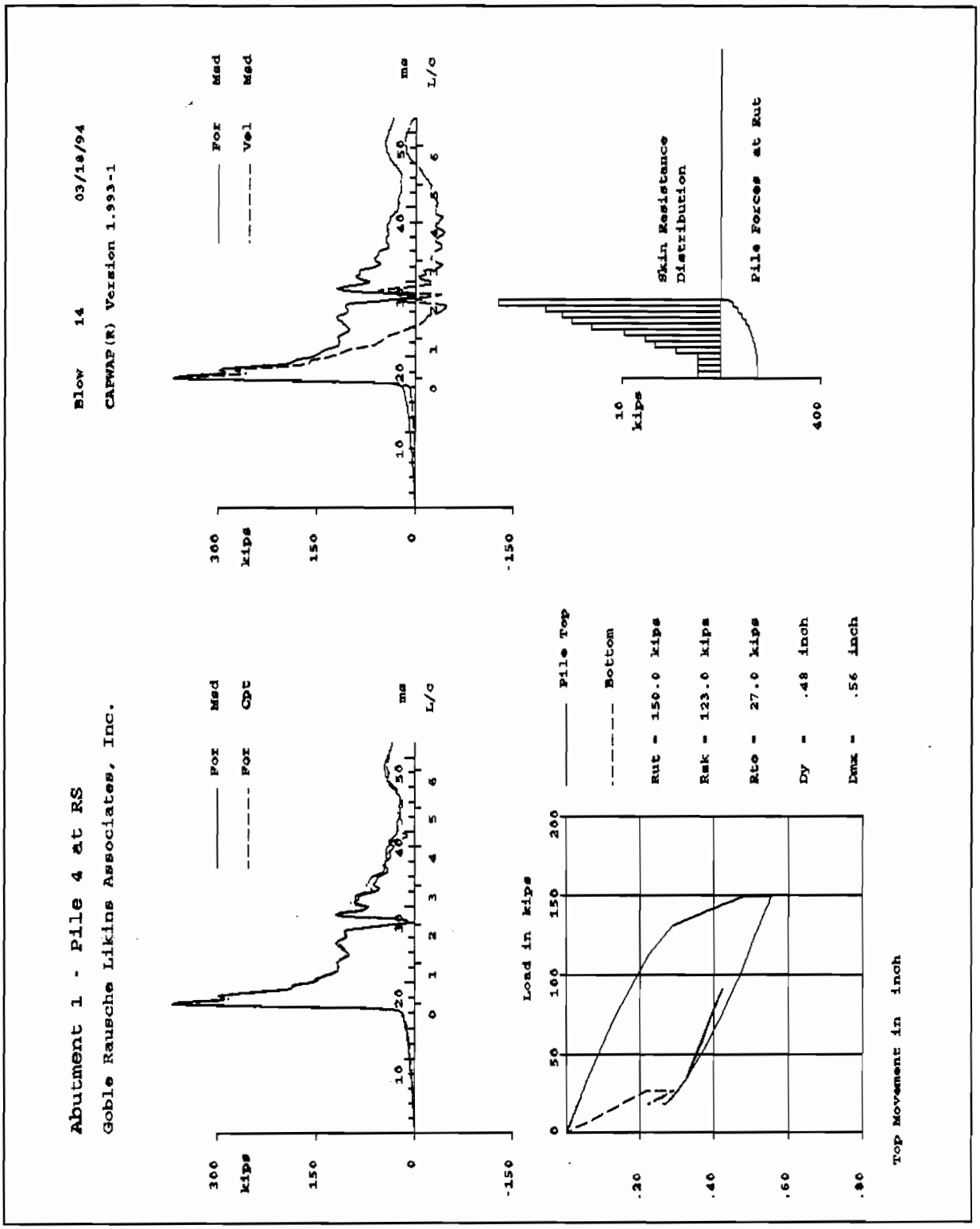

Figure 5: Sample of CAPWAP Result

locations where the method has been verified by static load tests it is often used to completely avoid the requirement of static testing. In other or areas, high foundation reliability can be achieved with dynamic testing combined with a calibrating static load test.

COMMENTS ON DYNAMIC TEST ACCURACY AND RELIABILITY

Like static tests dynamic tests do not consider group effect and long term settlement. Dynamically determined static capacity has been proven by correlation with static load tests conducted on the same piles. In fact, since the dynamic results were compared with a statically defined load it is natural that the capacities would be similar. A dynamic test can be used to assess setup and relaxation effects by performing the dynamic test at a variety of different wait periods.

The dynamic test can be performed using the pile driving hammer for driven piles, but requires a drop weight for drilled shafts. This drop weight must be about one percent of the capacity that must be predicted. The size of the ram for the dynamic test can be checked by Wave Equation analysis. Any pile that can be hit with a hammer can be dynamically tested.

The full pile capacity is not mobilized if displacement during the hammer impact is not sufficient. Depending on the soil type limiting blow counts will be in the range of 10 to 20 blows per inch. However, a capacity is determined and that value will be a lower bound on the total capacity. If it is sufficient, further testing is unnecessary. It is also possible to improve the capacity if dynamic measurements are available from the end of driving in addition to the restrike. Then the restrike shaft resistance can be added to the end of driving toe capacity to estimate the capacity gain from setup on the shaft.

Dynamic testing requires the use of specially trained personnel to perform the test and analyze the data. The training requirements are quite substantial and tests must be performed by an engineer.

STATNAMIC LOAD TESTING

The Statnamic test is a recently proposed testing procedure for determining static pile capacity. In this procedure, an explosive charge is set off on the top of the pile directly under a large mass. The force of the explosion is contained between the mass and the pile top. The inertia force of the mass, which is accelerated upward by the explosion, provides the reaction for the downward acting pile force. The system is shown in Figure 8. The rate of increase of the explosive force is controlled and is supposed to increase in an approximately linear fashion. The loading process is slow compared with an impact force. The time required to load the test pile will be on the order of 40 milliseconds compared with one or two milliseconds in a dynamic test. The total time of loading in a Statnamic test is about 0.1 seconds compared with about 0.02 seconds for a dynamic test.

When the test was initially suggested by the Bermingham Company, it was presented as being a static test. Subsequent work has caused researchers to conclude that

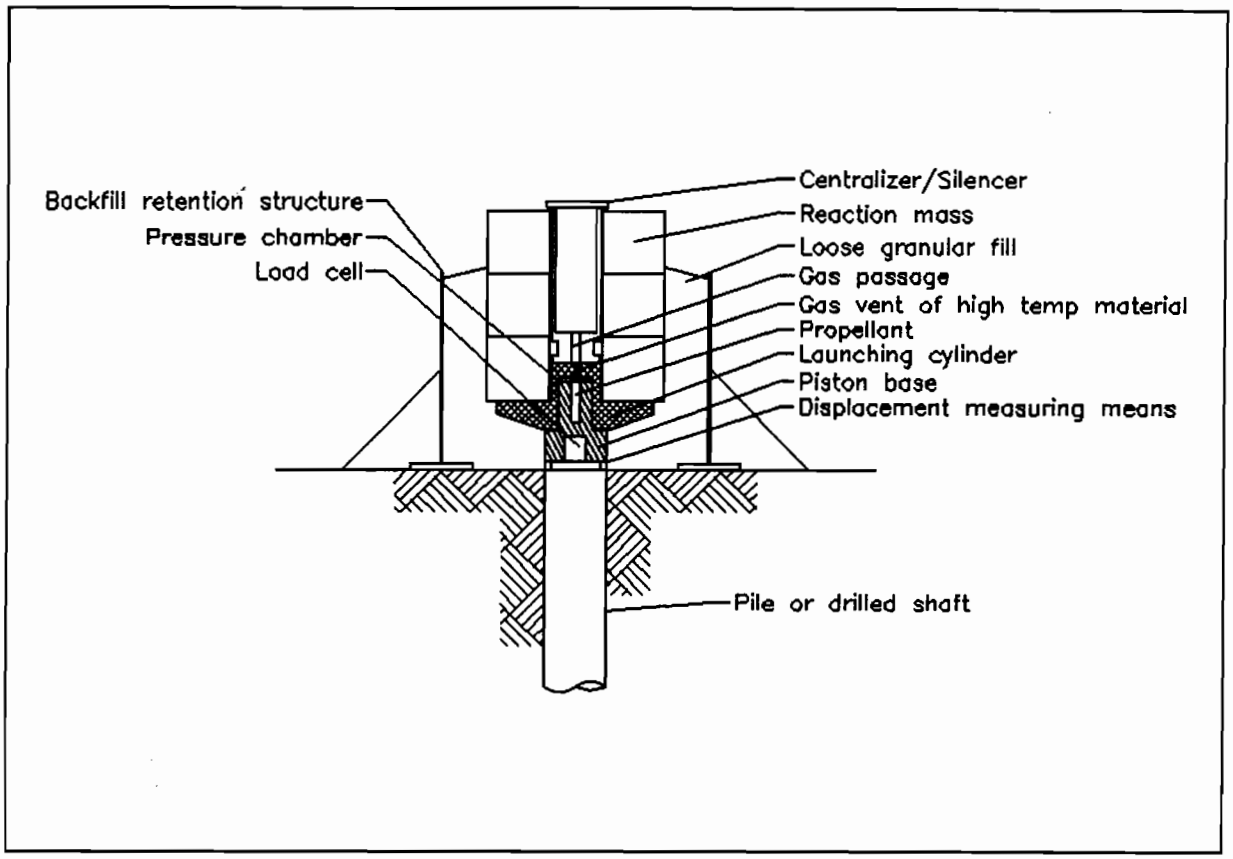

Figure 8: Statnamic System

the test is, in fact, "dynamic" (Middendorp et al 1992, Brown 1994). An analysis has been proposed by Middendorp (1992) that deals with the dynamic effects. During the application of the explosive force the pile moves into the ground, generating both static and dynamic resistance. Eventually, the pile downward movement stops and it rebounds upward to a final position. At the point of zero velocity the assumption is made that the dynamic resistance is zero and that all of the resistance is, therefore, static. This concept is based on the assumption that the pile is rigid.

The method is best described with an illustration. Consider the case shown in Figure 9. This shows the force-time record measured at the top of the pile during the explosion together with the pile top displacement. In Figure 9, the displacement is also plotted as a function of the force. The point of maximum displacement, point A, on these curves corresponds with the zero velocity condition and the load associated with this point is the predicted static capacity. The difference between the load at Point A and the maximum load is the dynamic component of the resistance. It is possible from this information to obtain a predicted load-displacement curve. The procedure was described in detail by Brown (1994).

The Statnamic test is a patented method and is promoted by the Bermingham Company of Hamilton, Ontario, Canada. Therefore, they are the only ones to perform the test. Until recently it was difficult to evaluate the results since the test evaluation

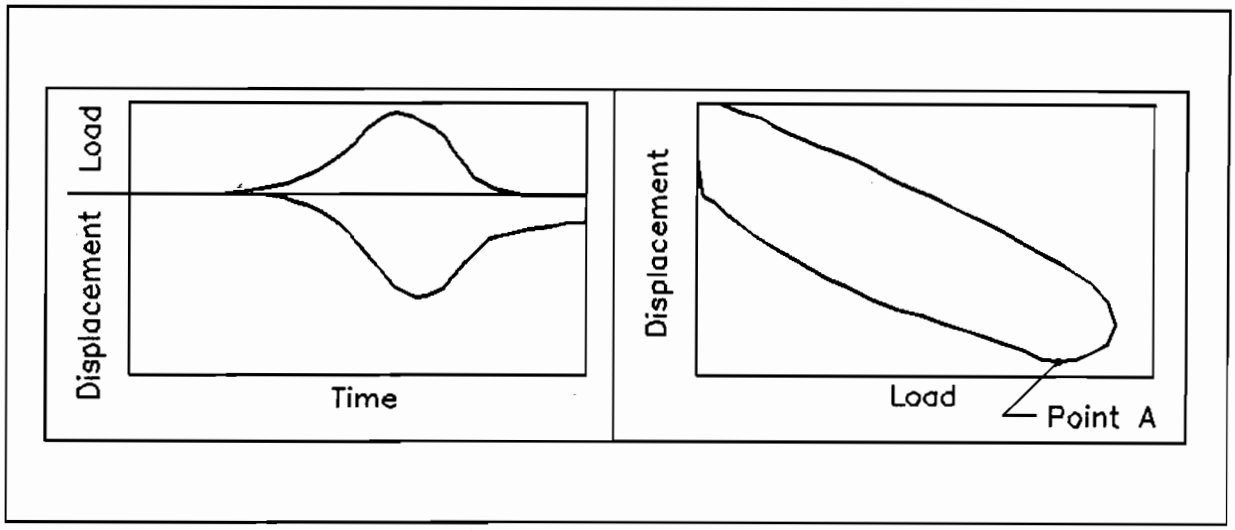

Figure 9: Force Time Measured at the Top of the Pile during the Explosion Together with the Pile Top Displacement

procedure was frequently changed. Thus, only very limited results of Class A predictions are available.

COMMENTS ON THE STATNAMIC TEST

The Statnamic test must be viewed as a dynamic test. Thus, some computational procedure must be used to evaluate the results. The currently used procedure assumes that the pile is rigid and that the soil resistance contains a portion that is a linear function of the pile velocity. The test has the advantage that it is less expensive than a static test. Costs on the order of half the cost of a static test have been mentioned. It does not require a load frame and it can be set up fairly quickly, probably in something less than one day. The test can be performed on batter piles as easily as on plumb piles.

The disadvantages include the fact that even though the test is dynamic the analysis procedure assumes that the pile is rigid and, therefore, the pile resistance distribution cannot be determined as in the case of the dynamic test or the Osterberg Test. The test is fundamentally different from other static tests in that it is performed by applying a force rather than a displacement.

SUMMARY COMMENTS

Over the past 30 years, the frequency of use of static pile tests has increased substantially with the reduced dependence on dynamic formula for pile capacity determination. Standards are available that govern the performance and evaluation of the test. However, the most commonly used standard, ASTM, does not describe a single method but, rather, multiple. This problem has inhibited the development of a set of orderly procedures. In addition, the test is often not performed as carefully as would be

desirable. Unless the engineer has specific reasons for doing otherwise, he should specify the Quick ML test with the load carried to failure or at least three times the design load, whichever is lower. Load measurement should be with an electronic load cell and evaluation should be by the Davisson Method.

As stated above the static load test remains the standard by which capacity is evaluated.

The Osterberg test offers the advantage that it is a static test. It can be performed on large diameter piles to very high capacity. It does load the soil surrounding the shaft in the opposite direction from the normal static test. However, the stress state at the toe of the pile is similar to the normal static test in that the toe is in compression and the influence of the toe compression on the lateral stresses on the shaft near the toe will be similar. This test will probably increase in popularity, particularly, for the very high capacity cast-in-piles. Since the test uses a patented system its general use will be somewhat limited.

The dynamic test has been in general use for about 20 years. A huge volume of experience has been generated, greatly expanding the usefulness of the test. Since the test is quite inexpensive it can be very effective in expanding the results of limited static testing. In many soils there is sufficient experience to make a static test unnecessary. The test does require that well-trained engineers perform the test and the measurement evaluation.

The Statnamic test has only recently appeared. During the early stages of its development it was presented as a static test. Now that it is treated as a dynamic method and procedures have been proposed for the test evaluation some time will elapse before sufficient Class A capacity predictions have been collected to evaluate the accuracy and reliability of the test. Due to its cost it must be proven to be an equivalent to the static test. It seems that it costs about the same as the Osterberg test. Like the Osterberg test it is limited by the fact that it uses a patented system.

REFERENCES

Brown, Dan A. (1994). "Evaluation of Static Capacity of Deep Foundations from Statnamic Testing." *Geotechnical Testing Journal*, ASTM, 17(4), 403-414.

Dennis, N. D. and Olson, R. E. (1983). "Axial Capacity of Steel Piles in Sand." *Proceedings of the Conference on Geotechnical Practice in Offshore Engineering*, Edited by Stephen G. Wright, ASCE, 389-402.

Fellenius, B. H. (1980). "The Analysis of Results from Routine Pile Load Tests." *Ground Engineering*, Foundation Publishing Ltd., London, United Kingdom, 13(5), 395-397.

Goble, G. G., Likins, G. E., and Rausche, F. (1975). "Bearing Capacity of Piles from Dynamic Measurements - Final Report." submitted to the Ohio Department of Transportation, Department of Civil Engineering, Case Western Reserve University, Cleveland Ohio.

Goble, G. G., Rausche, F., and Likins, G. E. (1980). "The Analysis of Pile Driving - A State-of-the-Art." *Proceedings of the Seminar on the Application of Stress Wave Theory on Piles*, Stockholm, Sweden.

Goble, G.G., Rausche, F., Likins, G.E. (1993). "Dynamic Capacity Testing of Drilled Shafts." *Foundation Drilling*, ADSC, Dallas, Texas, Sept. Oct.

Middendorp, P., Bermingham, P, and Kuiper, B. (1992). "Statnamic Load Testing of Foundation Piles." *Proceedings of the Fourth International Conference on the Application of Stress-Wave Theory to Piles*." A. A. Balkema Publishers, Rotterdam, 581-588.

Osterberg, J. O. (1984). "A New Simplified Method for Load Testing Drilled Shafts." *Foundation Drilling*, ADSC, Dallas, TX, 23(6), 9-11.

Osterberg, J. O. (1994). "Recent Advances in Load Testing Driven Piles and Drilled Shafts Using the Osterberg Load Cell Method." Geotechnical Lecture Series, Geotechnical Division of the Illinois Section, ASCE, Chicago, IL.

Rausche, F. (1970). "Soil Response from Dynamic Analysis and Measurements on Piles." Doctoral Thesis, Case Western Reserve University, Cleveland, Ohio.

Rausche, F., Goble, G. G., and Likins, G. E. (1985). "Dynamic Determination of Pile Capacity." *Journal of the Geotechnical Engineering Division*, ASCE, 111(3).

Walker, K. W. (1972). "Dependability of Pile Bearing Capacity Prediction Methods." Thesis Submitted in Partial Fulfillment of the Requirements for the Degree of Master of Science, School of Engineering, Case Western Reserve University, Cleveland, Ohio.

Wysockey, M. H. and Long, J. L. (1994). "Utility of Drilled Shaft Load Test Results." *Proceedings, International Conference on Design and Construction of Deep Foundations*, U. S. Federal Highway Administration, Orlando, Florida, 1789-1803.

USE OF POLYMER SLURRIES FOR DRILLED SHAFT CONSTRUCTION [1]

By: Barry C. Berkovitz, P.E.,
and Christopher S. Long,
Federal Highway Administration, Atlanta, GA, 30367

INTRODUCTION

Over the past few years there have been several problems regarding the routine use of polymer slurries for drilled shaft construction, primarily in the area of inconsistent construction performance. Many State DOTs have reported sidewall sloughing, excavation collapse, and bottom sedimentation when polymer slurries were utilized. Most of the problems were undetected during standard field slurry tests, sand content evaluations, and shaft bottom probing! Some were noticed only during or after concrete placement.

Research projects have not yet answered the outstanding questions that have been raised by DOTs. Several technical memos regarding this topic have been transmitted to FHWA State Division Offices and State DOTs, in an attempt to highlight the concerns and make arrangements for documentation and mitigation. Currently, The Federal Highway Administration (FHWA) and The International Association of Foundation Drilling (ADSC) both agree that polymers appear to show promise, but, more controlled research is needed before generic or product specific specifications and guidelines can be adopted for general use. ADSC has established a Task Force to study the problems and draft proposed guidelines.

Until there is more research, and specifications that facilitate consistent results, the Authors recommend using only mineral slurry (preferably bentonite, polymer-enhanced-bentonite, or bentonite enhanced with other additives) for routine production shafts, in accordance with FHWA guidelines and specifications. Any use of polymer slurries on Federal or State DOT projects is recommended to be under the criteria of FHWA's "Experimental" designation only. Under those guidelines, special Federal "experimental" funds are programmed and it is assumed that; environmental clearance is obtained from regulatory agencies; field and laboratory tests have been performed; slurry is used in accordance with site specific engineering guidelines and specifications; and a report is produced to document design, lab and field testing, construction procedures, and the finished foundation products.

In 1994, three ADSC workshops were held to define the problems, establish interim guidelines, and draft objectives. Additionally, four DOT/FHWA workshops were conducted to overview DOT concerns, to observe DOT and FHWA presentations and slurry

---

[1]Submitted for the 31st Symposium on Engineering Geology and Geotechnical Engineering, Logan, Utah, March 29, 1995.

demonstrations, to understand the level of DOT/FHWA experiences, and to observe construction demonstrations.

BACKGROUND

Drilled shafts have become a very popular foundation alternative due to their considerable load carrying capacities, substantial stiffness characteristics, and embedment capabilities. These characteristics are especially advantageous when designing high capacity foundations for vessel impact, scour, and seismic considerations.

Primary engineering objectives in successful drilled shaft excavations are to eliminate or minimize reductions in soil stress and prevent collapse of shaft excavations, thus, rendering the highest possible bearing capacity and most efficient foundation. This process essentially involves the removal of a cylindrical soil "plug" without disturbing the remaining adjacent materials. The different construction methods employed to accomplish this task usually require permanent or temporary casing, or drilling with a site appropriate slurry. It is important for a design engineer to identify and analyze which construction methods are most appropriate for a specific site, in order to evaluate cost efficiency and maximum ultimate bearing capacities. For example, a temporary or permanent vibratory installed casing will yield higher bearing capacities in loose to medium-dense sands than could be achieved with slurry drilling.

Soil arching, the phenomenon where soil is supported by adjacent and overlying interlocking materials, or mobilization of internal soil shear strength, may (depending on construction methods) have a tendency to minimize soil disturbance and horizontal and vertical stress reductions. These effects are more notable in smaller diameter shafts where excavations have been observed to remain stable for longer periods. However, when large diameter shafts are excavated, these effects are minimized. The reduction in horizontal soil stress effects shaft stability and ultimate load carrying capacity.

The main objectives of slurry drilling for shaft support are identical to the objectives for excavating any shaft: facilitate construction, and enhance excavation support. Slurries normally develop a "film" or a filter "cake" around the perimeter of the shaft which assists in minimizing fluid loss into the adjacent soil. The slurry fluid density helps to minimize soil stress reduction by providing internal horizontal stress and a counter balance against hydrostatic forces. The chemical and physical properties of both the subsurface environment and the type of slurry material effect its ability to form a cake or film, and to maintain the physical properties required for shaft stability. Current specifications for mineral slurries define the range of properties that control ideal slurry performance.

SLURRY MATERIALS

Materials currently being used for drilled shaft construction generally fall into categories of; natural, bentonite, attapulgite, and polymers. Current "generic" specifications for mineral slurries have been researched and refined over the past 20 years. FHWA and ADSC have

worked independently and collectively to advance the specifications to be applicable for any subsurface conditions where slurry drilling is appropriate. These specifications have been determined to not apply to the many types of polymer slurries available today. In jointly funded research (1), an attempt was made to draft generic specifications for polymer slurries, however, the ADSC, FHWA, researchers, and industry representatives did not feel that these draft guidelines were appropriate. Subsequent polymer slurry construction of full scale drilled shafts have reconfirmed the inappropriateness of these draft specifications.

Product specific manufacturer's specifications have been used on several state DOT's projects. This has resulted in what appears to be successful projects. However, in other cases where manufacturer's specifications were used, in conjunction with on-site supervision by a manufacturer's representative, the results were unsuccessful! This should serve as a caution to those who believe that an end product specification, and/or the requirement for on-site supervision by a manufacturer's representative, will render successful construction.

To comply with the Federal Clean Water Act and protect biologic life, disposal of all mineral slurries (and possibly polymers) is not allowed directly into streams, rivers, lakes or seawater.

Natural

Natural slurries consist of water and excavated soil particles that may be kept in suspension, depending on the drilling techniques and type of soil. Natural slurries normally do not form a filter cake, may produce a sidewall smear and/or facilitate soil swelling (and corresponding lower bearing capacity), are difficult to control, and may be very problematic. They do produce a fluid density that may balance hydrostatic and artesian forces, and may minimize horizontal and vertical stress reduction.

Bentonite

Bentonite slurry consists of water and sodium montmorillonite clay particles. Hydrated bentonite stays in suspension for a very long time, does an excellent job of holding spoils in suspension and maintaining hole stability during concrete placement. The clay particles may partially penetrate into permeable side wall materials and will create a filter cake. Its properties help to balance hydrostatic forces, minimize stress reductions and potential collapse. Bentonite use has been researched in laboratory and field applications for many years, and engineers are generally more comfortable with their foundation design assumptions. Some contractors, however, dislike the extensive mixing equipment, hydration periods, field processing, and an occasional project where off-site disposal may be required by local environmental agencies.

Attapulgite

Attapulgite slurry is similar to bentonite (4) as a weighted mineral, but does not stay in suspension without agitation, does not hold most spoils in suspension, and does not form a comparable filter cake. It has the advantages of not flocculating in the presence of ionized salts and has a shorter hydration period than bentonite.

Polymers

Concentrated dry or liquid polymers mix readily with water into large quantities of slurry, generally hydrate in less than one hour, and, in controlled environments, remain stable with the assistance of chemical stabilizers. For these reasons they are considered convenient by some contractors. They do not have the high density range associated with mineral slurries, and thus, have less ability to balance horizontal soil stresses and hydrostatic forces. They do not hold spoils in suspension and some case histories suggest that bottom sedimentation may occur after shaft bottom cleaning, thus having the effect of reducing the ultimate bearing capacity.

Polymers can be separated into the following types:

- Partially Hydrolyzed Polyacrylamide (PHPA)
- Dry Vinyls (Many Different Types)
- Biopolymer
- Chemical Modified Cellulose (CMC)
- Guar Gum

The scope of this Paper will focus primarily on the PHPAs and dry vinyls since they are the ones most frequently used by drilled shaft contractors.

Quality control of field operations is a major concern when polymer slurries are used. The appropriate properties that are required to provide proper support of the excavation; facilitate a clean, stable bottom, free of most sediment; and to render the highest possible ultimate bearing capacity, have yet to be thoroughly researched and developed. For instance, some slurry manufactures have recognized that thicker slurries (higher viscosities) are essential to excavation support as the soil particle sizes increase. Not all manufacturers have adopted this practice. Furthermore, the overall affects on bearing capacities has not been thoroughly researched for the higher viscosity slurries. Of additional concern is the fact that current manufacturers' specifications include use of Marsh Funnel readings for viscosity control. This should be eliminated and other appropriate methods used, because the polymer chains prohibit valid flow through the funnel.

PHPA

PHPA slurries tend to coat the shaft side walls in an apparent encapsulation process (5), (3), (6). PHPAs are only effective if the polymers are dispersed in a high pH environment, typically between 8 and 12. PHPAs are normally emulsified in water, but they can be obtained in a dry powder form. Unlike mineral slurries, PHPAs do not form a filter cake, are incapable of suspending granular particles (1), (6), and fluid loss into pervious side wall soils may be significant. The encapsulation ability of this slurry has been shown to prevent degradation of clay shale formations (2). PHPAs are not bio-degradable in the short term, but they are not considered by their vendors, to be toxic. Contractors consider this to be an advantage over mineral slurries when off-site disposal may be required. Further independent controlled research is considered necessary to evaluate environmental concerns.

Dry vinyl

Dry vinyl slurries have different chemical compositions which make up the several different types (3), (5). This Paper will not differentiate between the different types because

they generally perform alike. Similar to PHPA polymer slurries, dry vinyl slurries also do not form a filter cake and do not suspending granular particles at low viscosities (1). Contractors choose dry vinyls for the same reasons as PHPAs. They are also considered by their vendors to be non-toxic, however, further environmental research is also recommended for these products.

TECHNICAL ISSUES

Some marketing efforts by manufacturers and vendors of the various polymer slurry products have led to confusion regarding technical issues related to environmental and engineering concerns. These items should be researched by independent sources to clarify the confusion.

Principal factors in achieving a high capacity drilled shaft foundation, in a slurried excavation are: limit soil stress reductions, provide positive slurry pressure to counter-balance hydrostatic and soil forces, and limit fluid loss from the slurry into the adjacent soils.

The primary concern for design engineers is to develop the most cost-efficient drilled shaft foundation by utilizing construction techniques that render the highest possible ultimate bearing capacity, at the lowest corresponding deflection (settlement). This, however, usually conflicts with the contractor's main concerns of doing whatever it takes to keep the hole open long enough to place concrete, in the least amount of time, at the lowest possible cost. Unfortunately, current specifications are geared to just that, and quality assurance testing focuses on a void-free reinforced concrete shaft, not the quality of the soil-structure interface. The Authors are not aware of any specifications that focus on the quality of end product where a minimum value of ultimate bearing capacity is required to be proven by the contractor. Unless design-build contracts become common practice in the United States, it is likely that no such specifications will be seen in practice. More advanced specifications and construction techniques are considered essential to satisfy both the contractor's and engineer's interests.

In the design of drilled shaft foundations, engineers usually use parameters that include alpha (α), Beta (ß), N_c, N_δ, and N_q. The source of these are empirically derived, based on many years of research and development. When slurry drilling was used in the data base case histories, mineral slurries, primarily bentonite, were used.

Limited research (1) conducted at The University of Houston showed promise for polymers used in a cohesionless soil, inside laboratory model triaxial cells. However, in field conditions with full-sized shafts, through various soils, the results have been very inconsistent. The Authors believe that extensive, "controlled," full scale, slurry drilled shaft testing and research is essential, prior to any "routine" use of polymer slurries.

RECOMMENDATIONS

Subsequent to the above referenced 1994 meetings, the Authors, engineering community and many industry representatives believe that: substantial independent "controlled" research needs to be performed; industry needs to draft proposed interim construction guidelines and specifications that would be acceptable to engineers and geotechnical researchers; and all use of polymer slurries should involve detailed site specific engineering and field construction documentation. These efforts should also include:

1) Development of a generic specification (if possible) for all polymer slurries, in all types of soils and conditions;

2) Generic specifications should be field proven by performing full scale load tests in identical soil conditions;

3) All field testing should be entered into the FHWA deep foundation database;

4) All field construction should be fully documented to include: encountered soil conditions, pore water pressures, all construction operations, drilling tools and equipment, slurry properties, unusual construction conditions (fluid loss, bottom sedimentation, sidewall collapse), concrete properties, concrete placement and volume curves, and other items as may be appropriate;

5) Experimentation with polymer-bentonite blends to explore the best possible performance;

6) Resolution of all environmental issues; and,

7) Development of an "expert system."

REFERENCES

(1) Effect Of Mineral And Polymer Slurries On Perimeter Load Transfer In Drilled Shafts, M.W. O'Neill and E. Majano, University of Houston, January 1993.

(2) Polyacrylamide-Potassium Chloride Mud for Drilling Water-Sensitive Shales, R.N. Clarke, R.F. Scheuerman, H. Rath, and H. van Laar, J. Petrol. Technology, 261, No. June, pp. 719-727.

(3) The Merits of Polymeric Fluids as Support Slurries, J.J.Bresford, P.M. Cashman, and R.G. Hollambry, Proceedings International Conference on Piling and Deep Foundations, Vol. I, Loundon, May 15-18. pp 3-10.

(4) The Structural Scheme of Attapulgite, W.F. Bradley, Am. Mineralogist, 25, pp405-410.

(5) Composition and Properties of Drilling Completion Fluids, H.C. Darley, and G.R. Gray, Fifth Edition, Gulf Publishing Company, Houston TX., pp 643

(6) Adsorption Characteristics of PHPA on Formation Solids, W.A. Liao, D.R. Siems, Proceedings, IADC/SPE Drilling Conference, Houston TX., Feb. 27- March 2, pp. 297-308

PILE LENGTH DETERMINATION OF EXISTING PILES USING PDA

Juan M. Antorena[1] ,P.E. and
G.Thomas McDaniel[2], P.E.

Abstract: A dynamic testing program was performed to determine the ultimate capacities and approximate lengths of six existing 14-inch square precast prestressed piles installed twenty years ago. Five of the six piles were planned to be used as part of a new foundation for a 25-story condominium building in Naples, Florida. Pile installation records for the length and capacity of the existing piles were not available. In order to determine the approximate depths and compression capacities of the existing piles, we monitored the restriking of existing piles with the Pile Driving Analyzer (PDA). The depths of the piles are an important design factor to comply with the scour requirements. The subsurface profile generally consisted of sands and soft weathered limestones. One of the six piles was extracted to verify if the length obtained with the dynamic measurement agreed with the actual length and to calibrate the wave speed. **A close correlation was found between the PDA results and the actual pile length.** This paper presents descriptions of the pile restriking program along with findings regarding pile lengths and capacities from the Case Pile Wave Analysis Program (CAPWAP Analyses) and pile capacity correlations from dynamic and actual measurements.

INTRODUCTION

A new 25-story high rise condominium is being designed and will be located on Marco Island, Naples, Florida. The building structure will be supported by 750, 14-inch square precast prestressed concrete piles. The piles are design for a compression capacity of 60 tons and the minimum required pile tip elevation will be -40 feet (MSL). The subsurface soil conditions at the project site, as indicated by Standard Penetration Test (SPT) borings, can generally be described as loose to firm, clean to silty sand extending from ground surface to a depth of about 50 feet. This upper sand layer was underlying by a soft weathered limestone layer to the depth of 80 feet. The ground surface elevation was approximately +5 feet (MSL).

[1]Senior Geotechnical Engineer, Law Engineering,Inc., Miami Lakes, Florida.
[2]Chief Engineer, Law Engineering, Inc., Miami Lakes, Florida.

The intent of the dynamic testing program was to determine the length and capacities of six existing piles, driven at the site twenty years ago for the support of an antiaircraft missile base during the Cuban-Missile crisis in the early 60's. Five of these old piles coincided with the location of the new piles planned for the building. Existing records for the length and capacity of the existing piles were not available. In order to determine the approximate depths and compression capacities of the existing piles, we have monitored the restriking of existing piles with the PDA.

SUMMARY OF THE PILE TESTING PROGRAM

Field dynamic testing was accomplished with a Pile Driving Analyzer (PDA) and subsequent data analyses were performed according to the Case Pile Wave Analysis Program (CAPWAP) Method. The PDA provided signal conditioning, amplification, filtering calibration to measured signals and data quality assessment before applying Case Method equations to measured pile records of force and velocity following each hammer impact. This method was used to provide static pile capacity, structural pile integrity, and estimate pile lengths.

Dynamic measurements of strain and acceleration were taken approximately two feet below the head of each pile under hammer impacts during restrikes driving of the six piles. Since the lengths of the concrete piles were unknown, the wave speeds could not be determined with the normal routine. In order to determine the correct wave speed from the old piles, one "sacrificial" old pile was extracted to calibrate the wave speed for the rest of the pile. Even thought the concrete characteristic may vary from one pile to the other, we assumed that after twenty year the pile properties should be similar for the old piles.

Extraction and replacement of the old piles was also considered, but the jetting operation could loose the surrounding sands of the new piles already installed on the adjacent shear wall pile cap where the old piles were located.

Six, 14-inch square solid prestressed concrete piles were redriven on the same day with an ICE 640 double acting diesel pile hammer which had a maximum rated energy of 40,000 foot-pounds. The sacrificial pile was extracted the next day. The pile properties (compression wave velocity) were estimated at the time of the restrike driving and then were corrected for each pile after the compression wave velocity calibration. The calibration of the wave velocity was performed measuring the actual length from the extracted pile and reusing that data to recalculate the pile lengths and pile capacities using the PDA and CAPWAP. The actual dynamic pile measurements are summarized in Table 1.

The restrike driving was performed using only a 3-inch thick plywood pile top cushion, in order to maximize the transferred energy to the pile and ensure the mobilization of the pile. In addition,

the movement of the piles for every blow was accurate measured with a scale-wire system, which basically consisted of a horizontal wire attached to two fixed points. No overstresses on piles were measured with the PDA due to the pile cushion reduction.

The CAPWAP method was used to analyze field recorded dynamic pile records in an interactive environment using measured pile data and a wave equation type analysis in a system identification process using signal matching techniques. CAPWAP analysis results include mobilized static pile capacity, soil resistance distribution and dynamic behavior under hammer impacts, along with pile head and toe static load versus movement relationships. Numerically, for each pile segment, ultimate static soil resistance, soil quake, and soil damping factors are tabulated.

The following table summarizes the PDA and CAPWAP results:

TABLE 1

Old Pile No.	New Pile No.	Calculated* Pile Length (ft)	Measured Pile Length (ft)	Blows Per Inch	PDA** Ultimate Capacity (kips)	CAPWAP*** Ultimate Capacity (kips)	CAPWAP Ultimate Skin Resistance (kips)	Aver. Energy (kips-ft.)	Aver. Comp. Stresses (ksi)
72332	1093	47.5	-	44	312	317	222	7.1	2.73
72334	1148	64.5	-	46	370	364	253	7.6	2.65
72326	604	54.5	-	20	316	365	259	7.3	2.52
72320	547	56.5	-	20	372	362	269	7.5	2.4
N/A	336	49.5	-	30	330	323	231	10.8	3.42
Sacrificial	N/A	53.0	53.0	20	370	360	255	7.5	2.46

* Measured from top of existing pile.
** Assumed wave speed = 12500 feet/second at the time of the restrike.
*** Corrected wave speed.

CONCLUSIONS

The pile redriving program using dynamic pile measurements was used to determine the length and axial compression capacities of the existing piles. A close correlation was found between the PDA pile length determination and the actual extracted pile length. The piles were found to comply with the design pile capacity and scour requirements. It was therefore concluded that dynamic pile testing can be used to predict pile capacities and lengths with high degree of confidence.

LATERAL LOAD TESTING OF MODEL PILES IN CLAY

Steve D. Dapp[1], Joseph A. Caliendo[2], Loren R. Anderson[3]

I ABSTRACT

This Research project is underway at Utah State University on behalf of the Utah Department of Transportation (UDOT). Model piles will be subjected to static lateral loading in homogeneous, undisturbed clay with a known undrained shear strength (Su). Future efforts will include cyclic loading on pile groups. The model piles will have geometric dimensions of length (L), diameter (D), height from soil to applied load (H), and a stiffness parameter (EI) as determined by dimensional analysis to be consistent will full-scale steel pipe piles commonly used by UDOT . Deflection (d) vs. Lateral load (P), and a strain profile of the model pile will be obtained.

The results of these tests will be compared to predictions made by the design package LPGSTAN; a 3-D, non-linear, finite element analysis program written at the University of Florida. The Federal Highway Administration (FHWA) is looking to rely on LPGSTAN in the future as the standard design package for analysis of pile foundations. This interest in more sophisticated software has come about by the increased concern over extreme events such as earthquakes, ship impacts, and scour. LPGSTAN can model pile groups (including battered piles) and is capable of modeling a wide variety of loads and moments applied to the pile cap and / or super-structure.

II TEST FACILITY

The test facility consists of a ribbed steel tank 3 ft by 10 ft in plan, and 4 ft deep as shown in Figure 1. An impermeable liner retains the water to keep the soil saturated, while the geocomposite between the liner and the soil provides a drainage path to expedite the consolidation process. The clay soil is consolidated in the tank by means of ten cylinders, on five yokes, with each ram having a diameter of 4 inches. An effective overburden stress is simulated with hydraulic pressure according to the relationship:

$$\sigma' = \frac{P\ (10\ \text{cylinders})\ \pi\ (2\ \text{inches})^2}{(10\ \text{ft} * 3\ \text{ft})}$$

where: σ' = effective consolidating stress
P = hydraulic pressure (psi)
(10 ft * 3 ft) = soil area in plan view

The hydraulic system contains a pump and an accumulator to supply pressure to the cylinders. Any desired constant hydraulic consolidation pressure may be maintained within about $\pm$ 5 psi as the load plate "follows" the soil down while consolidation progresses. Figure 2 contains a simplified hydraulic schematic.

[1]M.S. Candidate, [2]Associate Professor, [3]Professor & Department Head
Utah State University, Department of Civil & Environmental Engineering, Logan, Utah 84322-4110

III TEST SOIL

Initial Procurement and Placement of Soil

The clay soil was dredged from a settling pond at a gravel washing operation in Hyrum, UT. Taking the soil from this pond ensured a homogeneous, uniform clay sample. The clay was then transported in a lined dump truck to the Utah Water Research Laboratory (UWRL) in a saturated slurry state.

The soil was loaded into the test cell in this loose slurry state, and a water level has been maintained above the soil surface at all times. This ensures that the soil remains saturated. A temporary wooden false work was constructed around the test bin to allow extra soil to be placed above the bin top. This was done so as to accommodate the anticipated consolidation. The soil is a type CL soil in accordance with the unified soil classification system.

Consolidation and Shear Strength of Soil

The soil slurry had to be given some initial strength before it could be loaded hydraulically to a higher consolidation pressure. This was accomplished by wrapping a geosynthetic drainage layer over the top surface of the soil, installing a drainage and load plate, and then systematically adding dead weight (concrete blocks) on top of the load plate. This was accomplished from 8 Sep. 94 to 23 Sep. 94, and stabilized at a final pressure of 180 lbf/ft^2. There was a total average settlement of about 0.23 inches during this dead load consolidation.

The hydraulic accumulator was pressurized to 300 psi (a simulated overburden of 1250 psf), and the soil consolidated from 14 Nov. 94 to 2 Jan. 95. Figure 3 shows this settlement curve. Shear strength profiles were tested on 23 Dec. 94 using a mini-vane shear. Figure 4 shows these shear strength profiles, with an average undrained shear strength of 452 psf. This profile proved useful in providing a loose correlation between our hydraulic consolidation pressure and the actual shear strength obtained.

The hydraulic accumulator pressure was then increased to 400 psi (a simulated overburden of 1675 psf), and the soil consolidated from 6 Jan. 95 to 16 Feb. 95. Figure 5 shows this settlement curve. Shear strength profiles were tested again on 26 Jan. 95 using a mini-vane shear. Figure 6 shows these shear strength profiles, with an average undrained shear strength of 657 psf.

A cone penetrometer test was made on 23 Feb. 95. Figure 7 shows the shear strength profile obtained, with an average undrained shear strength of 595 psf. This is in good general agreement with the mini-vane shear tests shown in Figure 6.

There may always be minor strength profile differences at within the test cell. This can be mitigated by taking strength profiles around the model piles after they have been tested and using an averaged strength profile as the input to the LPGSTAN computer program.

IV MODEL PILE

Dimensional Analysis

There are seven fundamental variables of interest, and these fundamental variables contain only the two basic dimensions of force (F) and length (L), as summarized below:

Fundamental Variables (F.V.'s):	Basic Dimensions (B.D.'s):
d (deflection of pile)	L
P (lateral load on pile)	F
D (outside diameter of pile)	L
L (length of pile)	L
EI (pile stiffness)	$F * L^2$
C (soil cohesion)	F / L^2
H (distance from ground level to load)	L

There are five required Pi terms (number of F.V.'s - number of B.D.'s). Since deflection (d) is the variable of interest, it is the non-repeating variable, and is a function of the other four Pi terms as shown below.

$$(d / D) = f [(PD^2 / EI) , (L / D) , (H/D) , (CD^4 / EI)]$$

It is sufficient to only model the pile prototype length to a depth where the pile is essentially fixed from lateral loads. The scale factors are established by equating the model Pi terms with the prototype Pi terms (ie. $(L/D)_m = (L/D)_p$ ..etc). Since the undrained shear strength is not a function of soil stress, the test soil can be established as the field prototype soil.

Any model diameter (D) may be chosen, which then fixes the length (L) and the height (H) of the applied load to the model pile by the Pi terms $(L/D)_m=(L/D)_p$ and $(H/D)_m=(H/D)_p$. However, the wall thickness, and subsequently the cross-sectional moment of inertia (I), is still independent at this point. This allows for the use of wall thickness to control model pile stiffness (EI) to yield a manageable model lateral load. The smaller the model pile stiffness, the smaller (and more manageable) the model lateral load needed to simulate a full-scale load according to the Pi term PD^2/EI. The length of the model pile must be limited such that it will not extend to within 3 pile diameters of the bottom of the test bin to discount boundary effects.

The second way of controlling model pile stiffness (EI), and thus the model lateral load needed (P), is through the model pile material (E). By using a model pile with a material with a lower modulus of elasticity (E), a smaller model load can simulate the given full-scale load. The danger of getting to low of a modulus of elasticity (E) is that its yield stress, and its stability against crimping failure are also reduced. The strain gages can be mounted equally easy on any metallic surface.

Model Pile Design

The model pile has been designed according to dimensionless Pi terms to approximate the pile type commonly specified by the Utah Department of Transportation (UDOT). The prototype pile is a 12-3/4" steel pipe pile with 5/16" wall thickness. It is not essential that a strict parallelism be maintained between model and prototype. This is because the results of these test will be compared to predictions made by the design package LPGSTAN. Once this design package is validated for characteristic Utah clay soils and piles it can be used with greater confidence for designs in this area.

Figure 8 contains the dimensional analysis data used to generate the design curves for the selected model material (6061 T6 Aluminum conforming to ATSM B 241). A 1 inch schedule 40 (1.315 inch OD, and 0.133 inch wall thickness) was chosen from the four possibilities according to the dimensional analysis, as shown in figure 9 (OD vs. T). Figure 10 (OD vs. L) shows the chosen size most effectively uses the four foot depth of test soil available by requiring an length of embedment of 44.6 inches. Figure 11 (OD vs. P) shows the lateral load required for this OD is 212.7 lbf.

Figure 12 contains the output from an analysis of the model pile run on COM624 (currently the most widely used software). This analysis shows that the point of fixity (critical length for a long, counter-flexured pile) is under 40 inches. The maximum stress is only about one third of the aluminum's yield stress, so a failure of this type is not expected. With a D/T ratio of only 8.5, a crimping failure is not expected.

Static, lateral loading of model pile groups may also be tested, and the results compared to predictions made by LPGSTAN. The test cell is large enough to allow the modeling of pile groups without having to account for boundary effects.

Instrumentation

Each pile tested will be instrumented with one LVDT, located at the point of lateral load application in order to determine the amount of lateral deflection that occurs each time the lateral load is incremented up. The amount of load will be known by simply the amount of weight that is being hung to produce this load. In this manner a load (P) vs. deflection (d) curve will be obtained.

Strain gages have been mounted in 14 diametric pairs on the inside length of the model pile, Figure 13 illustrates this. Strain gage readings will be taken after every increment of lateral load (P) applied to the model pile. In this manner a strain profile of the pile vs. applied lateral load will be obtained, and thus the soil reactions determined.

The gages are temperature compensated by wiring them in pairs with a three lead wire system. Lead wire lengths have been taken into account; they must be of the same length per gage pair (to maintain an impedance balance), and a small drop in the input voltage to the gages due to the long common wire accounted for. A multi-plexor and data-logger will process and transfer the test data obtained to a computer to be recorded on diskette.

V FUTURE TEST EFFORTS

Model Pile Installation

The model piles will be pushed into the clay soil rather than driven dynamically. The top of the pile will be slotted to accommodate the strain gage wires, and the end caped during installation to protect the strain gage wires from the installation load. The pile tip will be capped to prevent soil and water from entering and damaging the strain gages. The tip will be a 45° cone to aid in installation (ease and self-centering) and to least disturb the soil in contact with the model pile.

Two of the yolks, stripped of their hydraulics cylinders, have been installed at both ends of the test bin. Beams will be placed across these two yokes and serve as guides to ensure that the pile is driven straight, vertically down into the soil, and to protect the pile from buckling during the installation.

The model piles shall be placed no closer than 3 pile diameters from the bin wall, or 6 pile diameters from the next closest pile in the case of single piles. The bottom tip of the model pile will be sunk no closer that 3 pile diameters from the bottom of the containment bin. This will be done to eliminate boundary (edge) effects.

Model Pile Lateral Loading

Single model piles be subjected to a simple lateral load (allowed to pivot at the point of load application) at some specified height (H) above the soil surface. The pile top will be free to rotate. Testing of pile groups will include a pile cap which will fix the pile tops from rotation.

The static lateral loading will be applied to the pile by means of weights hanging from a cable and pulley system. Weights can be added incrementally to produce the desired lateral load. The load test will be performed in general accordance with ASTM D 3966.

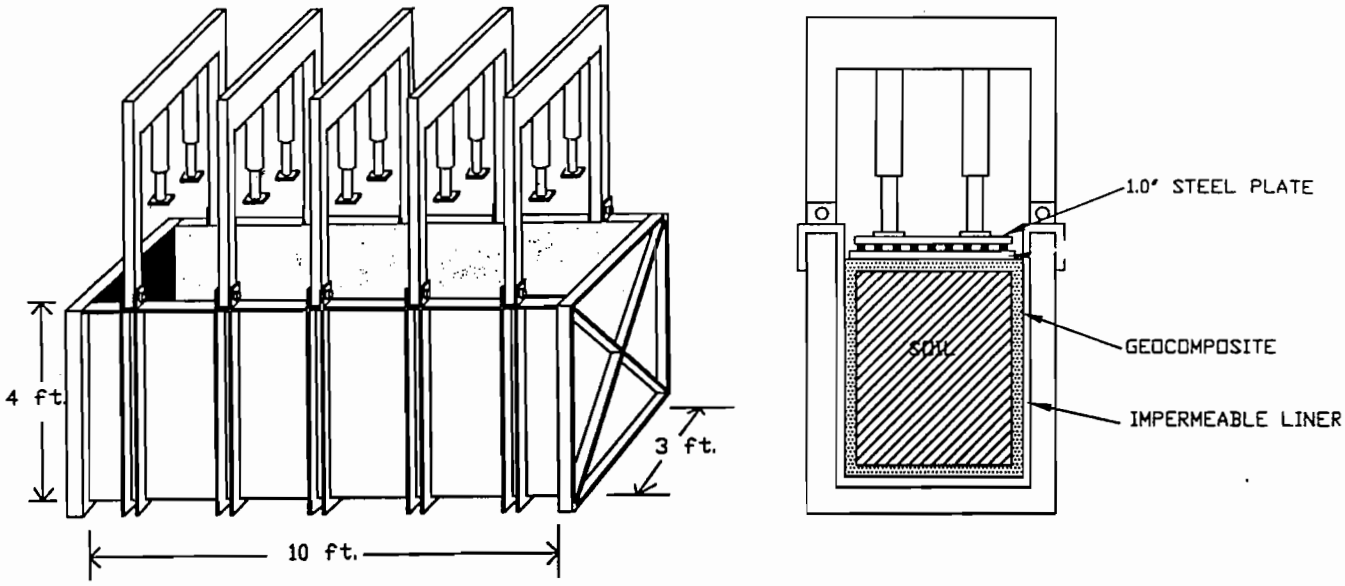

Figure 1: Test Facility

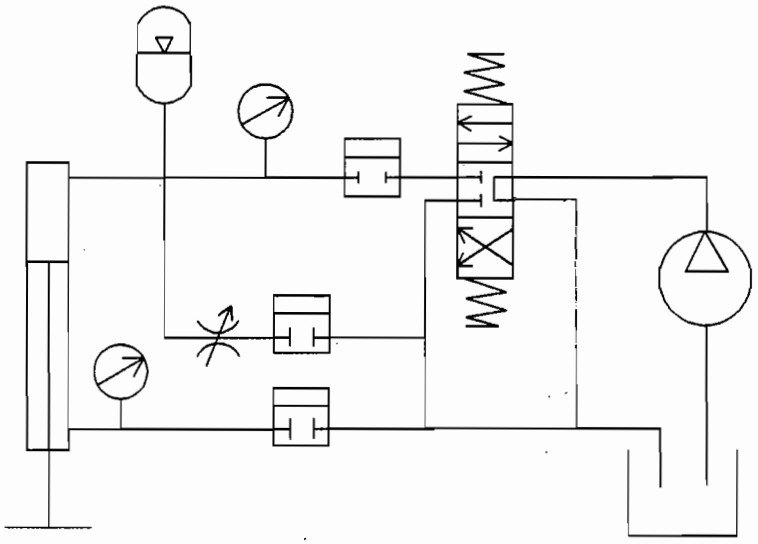

Figure 2: Simplified Hydraulic Schematic

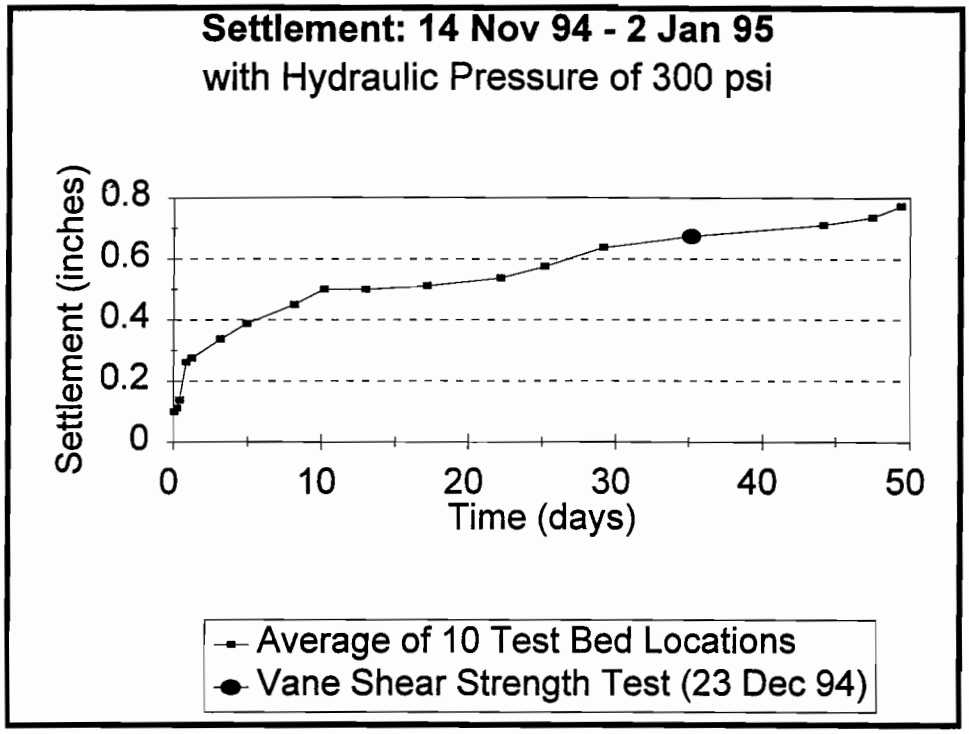

Figure 3: Settlement with Hydraulic Pressure of 300 psi (14 Nov 94 - 2 Jan 95)

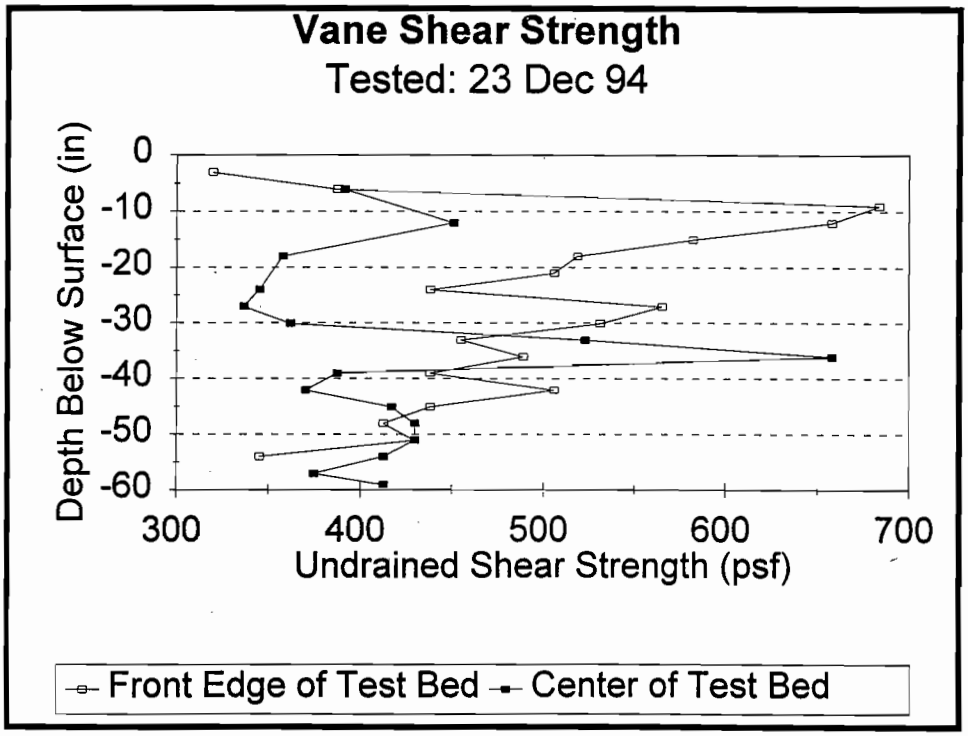

Figure 4: Vane Shear Strength Profile (23 Dec 94)

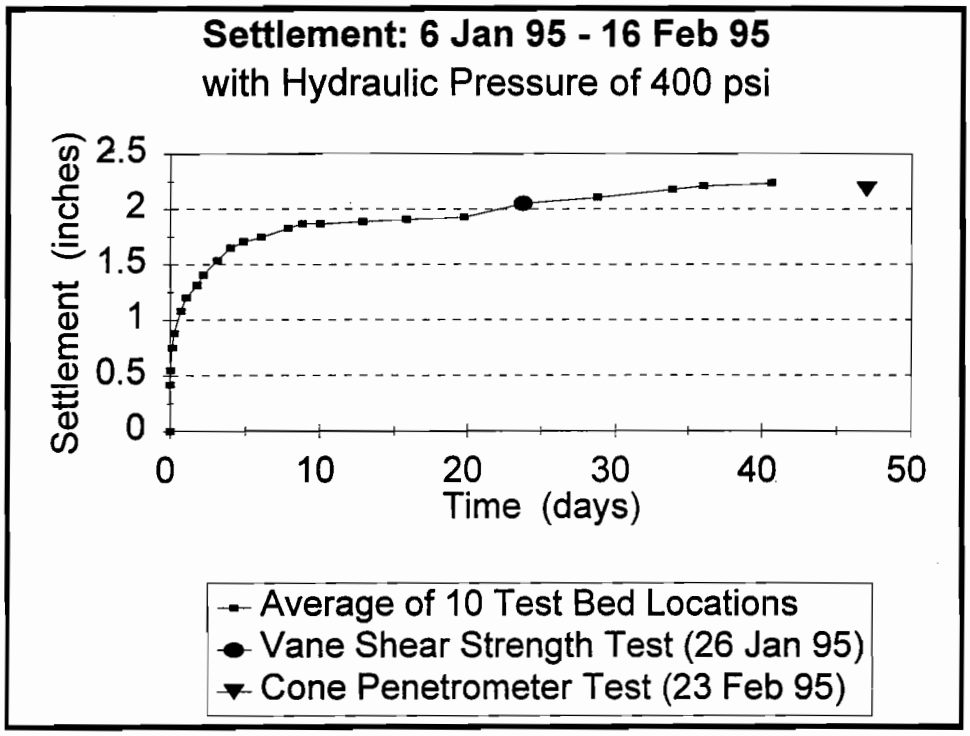

Figure 5: Settlement with Hydraulic Pressure of 400 psi (6 Jan 95 - 16 Feb 95)

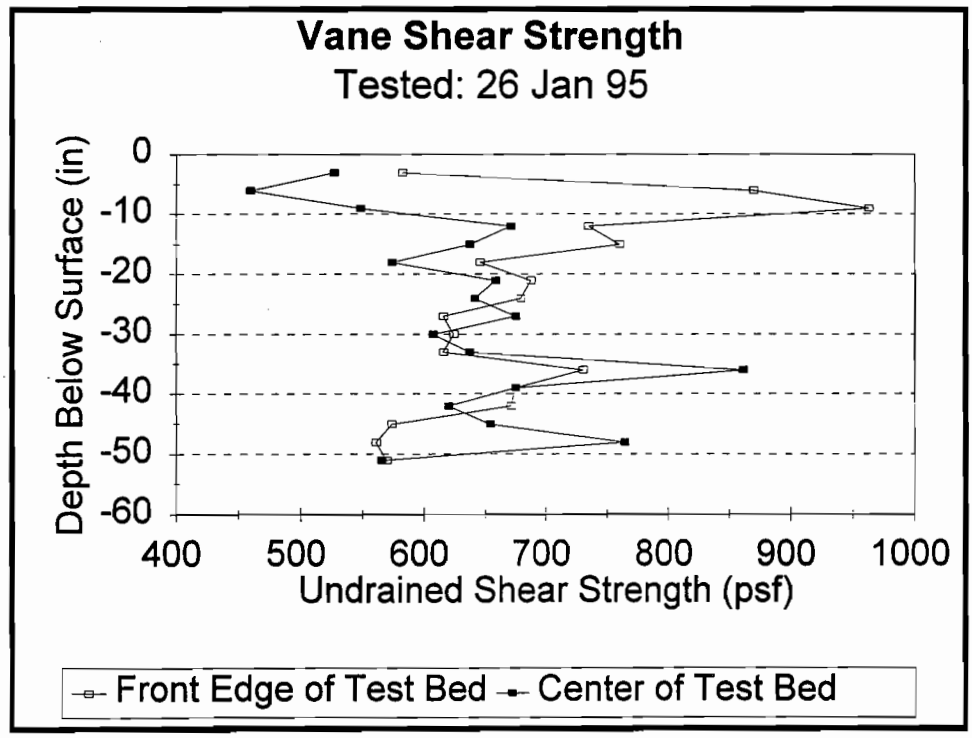

Figure 6: Vane Shear Strength Profile (26 Jan 94)

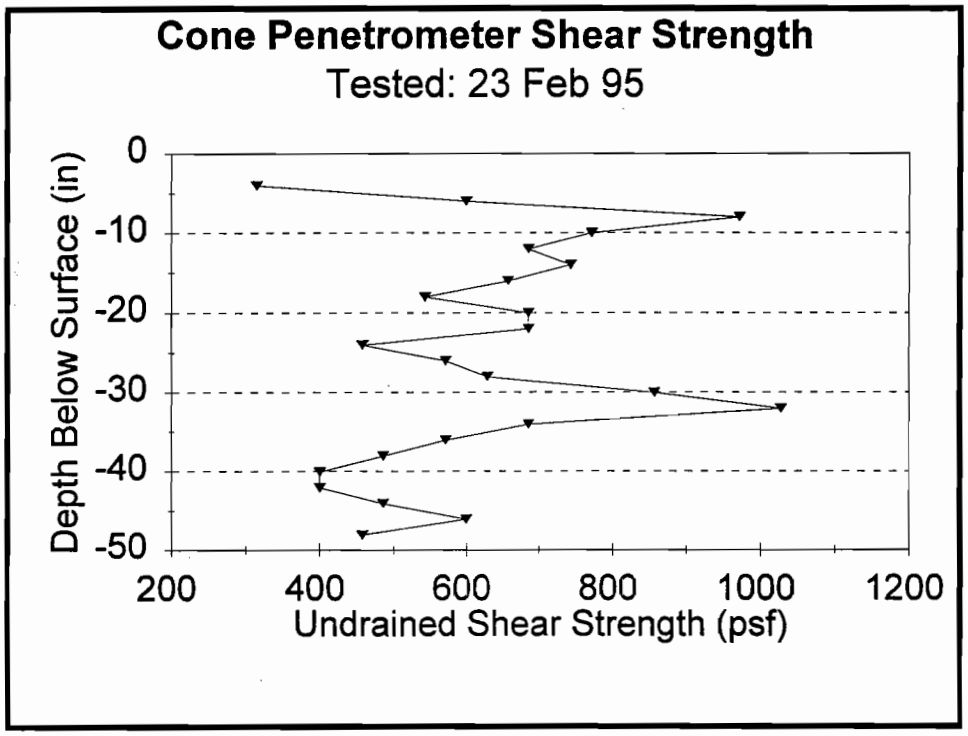

Figure 7: Cone Penetrometer Shear Strength Profile (23 Feb 95)

PROTOTYPE SPECIFICATIONS

P (lbf)	OD (in)	E (psi)	I (in^4)	L (in)	H (in)	Su (psi)	Delta (in)
20000	12.75	29000000	279	432	0	4.5	2.6

Dimentional Analysis is INDEPENDANT of Su, because it's SAME for PROTOTYPE and MODEL

6061 T6 ALUMINUM MODEL

(E = 1E+07 psi)

OD (inches)	ID (in)	T (in)	I (in^4)	P (lbf)	L (in)	H (in)	Delta (in)	Wall Thicknesses Readily Available (in)				
0.875	0.685307	0.094847	0.017947	94.19454	29.64706	0	0.178431	0.049	0.058	0.065		
1	0.783208	0.108396	0.030617	123.0296	33.88235	0	0.203922	0.035	0.049	0.058	0.065	0.083
1.125	0.881108	0.121946	0.049042	155.7093	38.11765	0	0.229412	0.035	0.058			
1.25	0.979009	0.135495	0.074748	192.2338	42.35294	0	0.254902	0.035	0.049	0.058	0.065	0.083
1.375	1.07691	0.149045	0.109439	232.6028	46.58824	0	0.280392	0.049	0.058			
1.5	1.174811	0.162594	0.154998	276.8166	50.82353	0	0.305882	0.035	0.049	0.058	0.065	0.083
1.625	1.272712	0.176144	0.213489	324.875	55.05882	0	0.331373	0.058				
1.75	1.370613	0.189693	0.287153	376.7782	59.29412	0	0.356863	0.058	0.083			
1.875	1.468514	0.203243	0.378413	432.526	63.52941	0	0.382353	0.058				
2	1.566415	0.216792	0.489871	492.1184	67.76471	0	0.407843	0.035	0.049	0.058	0.065	0.083
1.05	0.822368	0.113816	0.037215	135.6401	35.57647	0	0.214118	0.113	0.154			
1.315	1.029918	0.142541	0.091551	212.7459	44.55529	0	0.268157	0.133	0.179			
1.66	1.300124	0.179938	0.232484	339.0204	56.24471	0	0.33851	0.14	0.191			
1.9	1.488094	0.205953	0.399003	444.1369	64.37647	0	0.387451	0.145	0.2			

Figure 8: Model Design Spreadsheet (Dimensional Analysis)

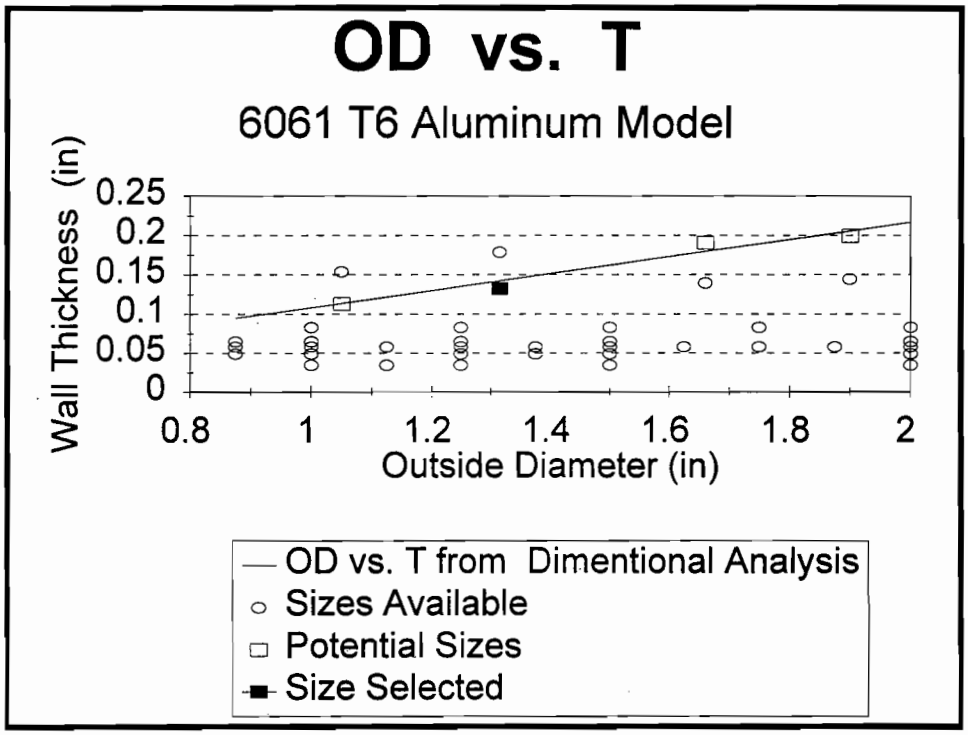

Figure 9: OD vs. T (Wall Thickness)

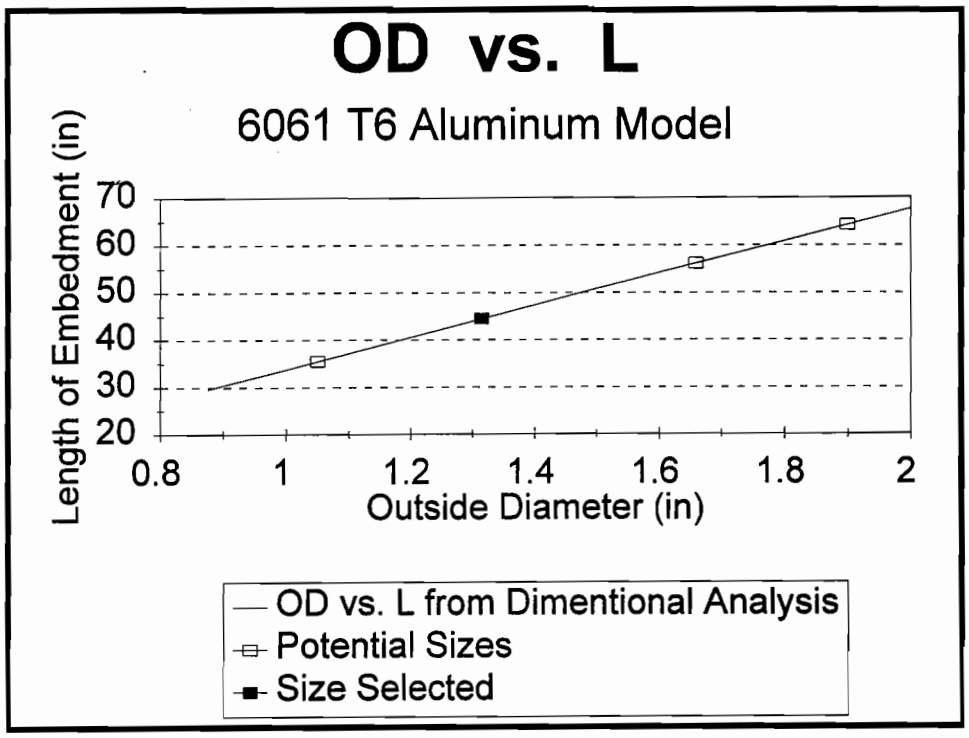

Figure 10: OD vs. L (Length)

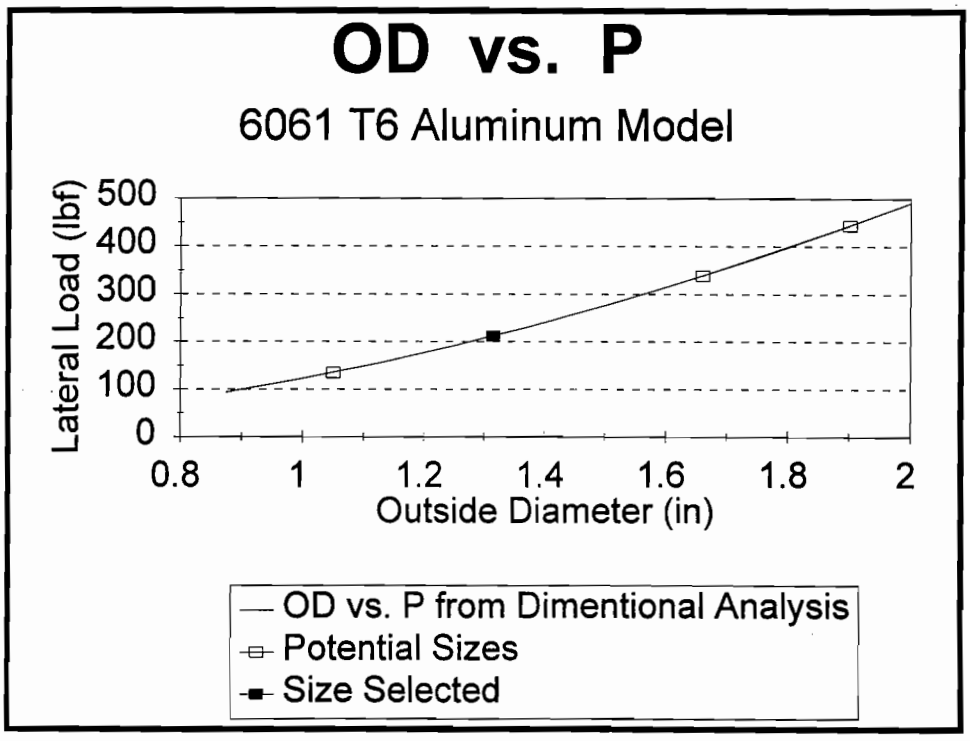

Figure 11: OD vs. P (Lateral Load)

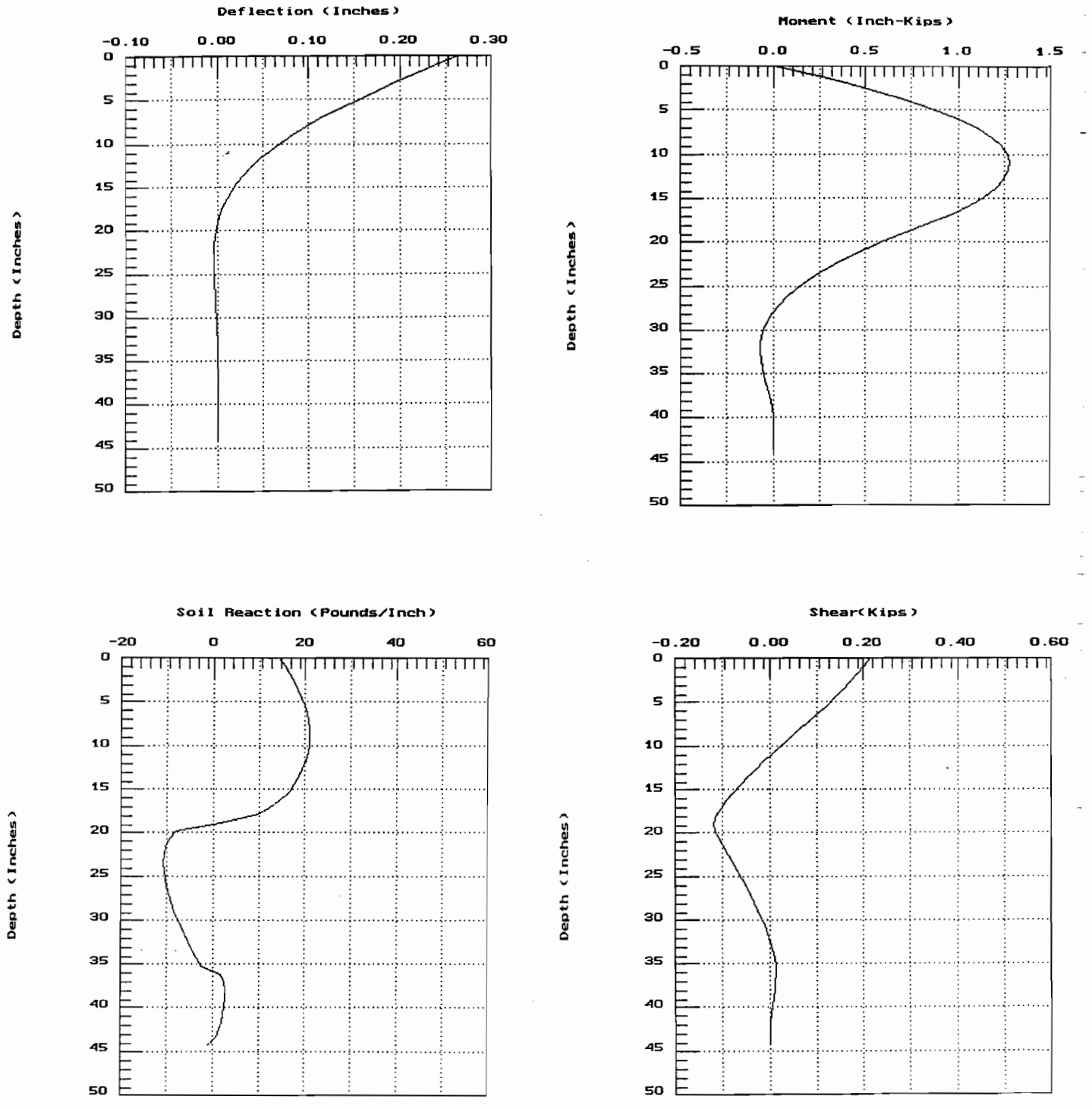

Figure 12: COM624 Results of Model Pile Analysis

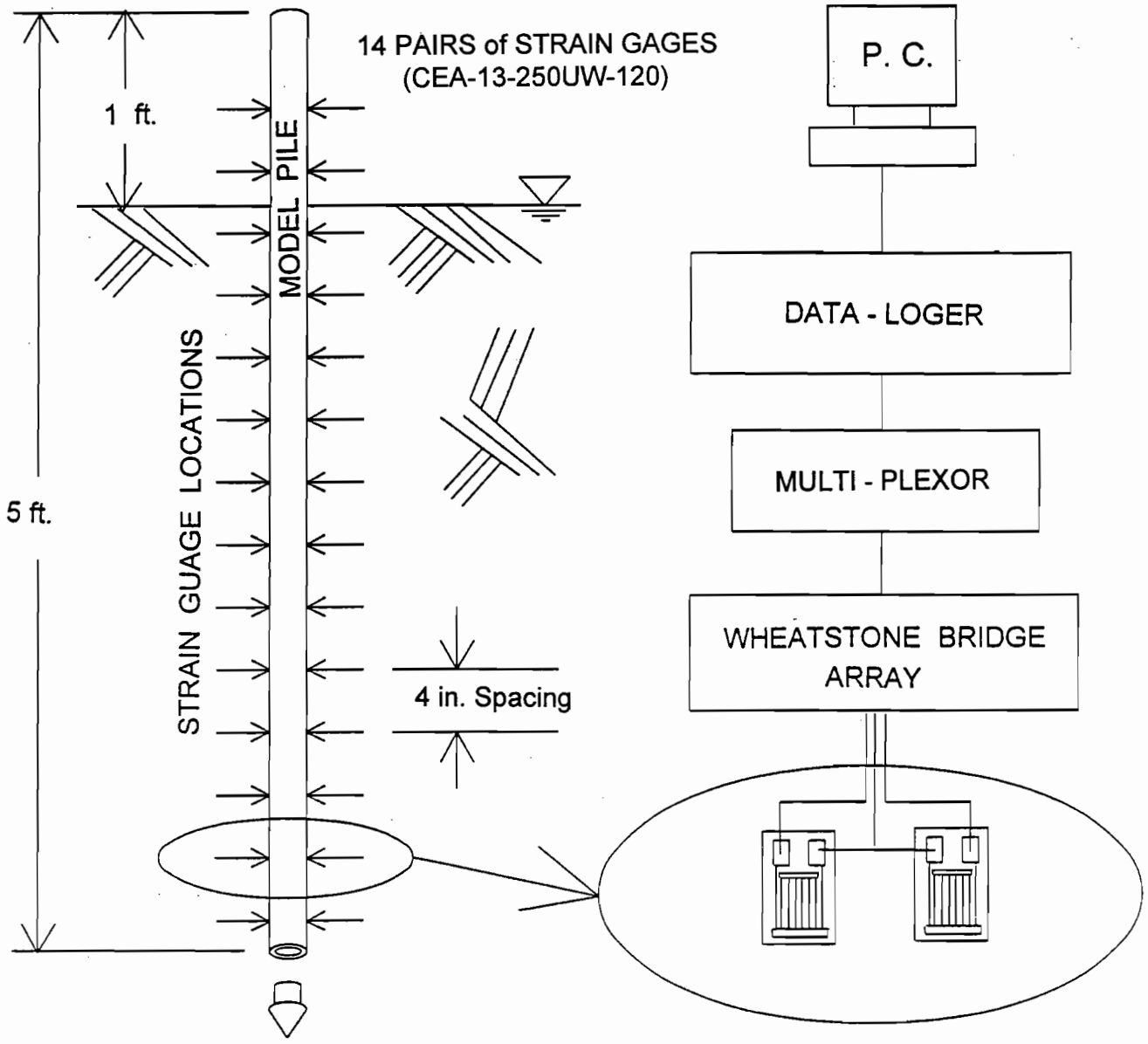

Figure 13: Instrumentation Diagram

THE NON-UNIQUENESS OF p-y CURVES FOR LATERALLY LOADED PILE ANALYSIS

G. Norris, M. Ashour, and P. Pilling

Department of Civil Engineering
University of Nevada, Reno
Reno, NV 89557

P. Gowda
Project Engineer
CalTrans
San Bernadino, CA 92402

ABSTRACT

The strain wedge (SW) model for laterally loaded pile behavior is a three-dimensional characterization that relates the stress-strain behavior of the soil in the developing passive wedge in front of the pile (denoted as the strain wedge) to the one-dimensional beam-on-elastic foundation (BEF) parameters commonly employed in so-called "p-y" curve analysis. As presented in the 26th Symposium papers, the SW model relates the developing horizontal stress change ($\Delta\sigma_h$) in the wedge at any depth to the line load force, p, of the p-y curve. Similarly, it relates the deflection pattern (y vs. depth, x) to the normal strain (ϵ) causing the variation in the stress change. Consequently, it relates the pattern of Young's modulus ($E = \Delta\sigma_h/\epsilon$) in the soil to the variation in the BEF subgrade modulus ($E_s = p/y$). The SW model does not specifically require the development of p-y curves; but, if p-y curves are desired, they can be assessed as a part of the SW solution.

This paper provides a demonstration that such theoretically based p-y curves are not unique. That is, they vary with the bending stiffness (EI) of the pile and the pile head fixity condition (fixed vs. free) as well as the soil properties (strength, compressibility, etc.). Further, the p-y curve for a given soil at a given depth will vary with a change in the soil immediately above or below it. The paper demonstrates the usefulness of the SW model in dealing with problems arising from nonunique p-y curve behavior.

OVERVIEW OF LATERALLY LOADED PILE BEHAVIOR AND OVERVIEW OF p-y CURVE EVALUATION BASED ON STRAIN WEDGE MODEL FORMULATION

The lateral response of an individual pile can be assessed based upon the so-called strain wedge model (see Norris and Abdollaholiaee, 1990 and Norris et al., 1991) which relates a) the lateral strain (ϵ) in the developing passive wedge in front of the pile to the resulting pile deflection pattern (y vs. x), b) the horizontal stress change ($\Delta\sigma_h$) to the beam on elastic foundation

(BEF) soil-pile reaction (p) and c) the Young's modulus of the soil ($E=\Delta\sigma_h/\epsilon$) to the BEF subgrade modulus ($E_s=p/y$). Thus, the strain wedge model is a means for relating the one-dimensional BEF model parameters to the (envisioned) three-dimensional soil-pile response. This is shown schematically in Fig. 1.

An interesting feature of such an approach is that the BEF p-y curves can be derived theoretically and have been shown (e.g., see Norris and Abdollaholiaee, 1990) to be in good agreement (for common one and two foot diameter piles) with the empirical curves that are a part of such programs as COM624 (Reese and Sullivan, 1980). However, strain wedge model formulation clearly shows that such p-y curves are a function of pile as well as soil properties. The pile properties that affect the p-y curves are the pile size, pile shape, its bending stiffness, EI, and the pile head fixity condition. It should be pointed out that the p-y curves are merely a by-product of this approach which solves for the Young's modulus profile for the soil for the specified value of horizontal strain. Knowing the pile and soil properties, the BEF subgrade modulus profile is obtained and traditional BEF analysis is invoked. In other words, there is an equivalent linear subgrade modulus profile that results for the horizontal strain assumed.

In three-dimensions it is assumed that the developing passive wedge opens up at a fan angle, ϕ_m, equal to the mobilized effective stress friction angle of the soil. This is shown in Fig. 2. With increasing lateral load, the base of the developing wedge moves down as does the depth of the first zero crossing of the pile (i.e., the first depth where lateral deflection, y, equals zero). As the wedge moves down it also opens up as strain, stress change and mobilized friction angle increase. Given this approach, it is easily understood that a stiff pile (high EI) will have a different zero crossing than a flexible pile under the same lateral pile head load and, therefore, will invoke a different depth of soil to provide the needed (mobilized) lateral passive pressure resistance (or horizontal stress change) required for equilibrium. This horizontal stress change (equivalent to the deviator stress in a triaxial test at a confining pressure equal to the effective overburden pressure, σ_{vo}), multiplied by the width of the front of the wedge at that depth plus side shear (τ) times the width (2B) from both sides of the pile (Fig. 2), is the corresponding BEF line load force, p, at that depth. In clay, the geometry of the wedge is a function of the mobilized effective stress friction angle but the stress change and strain are the deviator stress and axial strain from a consolidated undrained triaxial test (Norris et al., 1991). Line load, p, (as well as deflection, y, and, thereby, $E_s=p/y$) at any depth, x, will be a function of the pile bending stiffness, EI, and the pile head fixity condition. Likewise, the p-y curve at a given depth will vary depending upon the soil immediately above and below that in question.

The feature that makes the strain wedge model particularly useful in seismic application is that one knows the value of relative strain in the near-field soil region (i.e., within the wedge).

This allows a comparison with the free-field strain from the earthquake (as assessed from, say, a SHAKE analysis) over the same depth of soil. The Young's modulus (E), the subgrade modulus (E_s) and, therefore, the seismic pile head stiffness, k (= P_o/y_o, i.e., the pile head force, P_o, divided by the relative pile head displacement, y_o) are a function of the total strain (taken as the larger of the free-field versus the relative strain). Given the equivalent linear stiffness variation as a function of the relative strain (and, therefore, relative displacement of Fig. 3), one can then assess the pile head displacement, y_o, such that the relative strain equals the free-field value so that a horizontal cutoff can be superposed. This truncated stiffness variation represents the condition that, on the left, free-field strain is larger and a constant stiffness value (a function of the free-field strain) pertains. Only for a large relative pile head displacement, y_o (associated with relative strain, ϵ), does relative strain take over and the stiffness, on the right side, dip below this horizontal cutoff value. Of course, different magnitude earthquakes cause different magnitudes of free-field strain and, therefore, different heights of free-field cutoff. This, as well as additional discussion regarding the use of free-field versus near-field excess porewater pressure from developing liquefaction conditions in the strain wedge model, is presented by Norris (1994).

Note that the strain wedge model is good over the full range in soil strain, from $1x10^{-4}$% up to and beyond soil failure. The fact that the soil within the wedge reaches the failure strain means that the wedge angle cannot grow any further but does not mean that the wedge becomes locked at that depth; instead, it moves down adding on a greater volume of failed soil until a local flow-around failure, starting at ground surface, develops and propagates downward. (For clay, flow-around failure may initiate before failure stain develops.) Alternatively, a plastic hinge may develop in the pile, in which case, the wedge depth becomes fixed and soil resistance builds to its maximum for a fixed zero crossing.

At present, pile group interference effects similar to those noted by Brown et al. (1988) are being investigated via the strain wedge model. Due to the envisioned increase in the overlap of the developing wedges with increased load on or deflection of the pile group, the extent of interference between wedges and the redistribution of load to members of the group can be assessed in a straightforward manner. Different than elastic based solutions, the trend is that group interference increases with an increasing load or deflection level. Heretofore, the group effect was approximated for the strain wedge model evaluation of CalTrans' lateral pile group load tests on groups in Bay Mud and Merritt sand at Cypress (Norris et al., 1993) using the NAVFAC DM-7.2 (1982) reduction factor, R, given as a function of the center-to-center spacing of the piles. The fact that one determines the equivalent linear subgrade modulus (E_s) profile as part of the strain wedge model solution means that it is a simple matter to reduce the profile by factor R to account for pile group interference effects. However, after the completion of the current research, factor R

will no longer be used.

Research just starting includes the use of strain wedge model formulation to assess the p-y (and associated t-z) curves for the caissons of the Bay Bridge for CalTrans and p-y (and t-z) curves for large diameter drilled shafts in caliche laden soils for the U.S.-95 and I-15 Interchange in Las Vegas for the Nevada Department of Transportation (NDOT). This represents a departure from previous formulation for "infinitely" long piles.

While this section has summarized strain wedge model philosophy (based on the Norris and Abdolaholiaee 1990 presentation of strain wedge model formulation at this same conference) and past, present, and upcoming strain wedge model research, the intent in the following section is to show that, as Terzaghi (1955) stated, subgrade modulus, E_s (and, therefore, p-y curve), behavior is not soil but, rather, soil-pile related. Treating the bending stiffness, EI, of the pile in the governing BEF differential equation does not (a priori) allow the engineer to treat the soil-pile E_s or p-y response as purely soil behavior. Likewise, the p-y curve response at any depth will be a function of the soil at that depth but will vary depending upon a change in the soil layer immediately above or below it.

PARAMETRIC STUDIES OF THE EFFECT OF PILE PROPERTY, HEAD FIXITY, AND NEIGHBORING SOIL CHANGES ON p-y CURVE SHAPE

If strain wedge (SW) model characterization is considered realistic, then the following parametric SW studies regarding changes in pile property and head fixity conditions and in the over- or underlying soil on the resulting p-y curve shape suggest that p-y curves are, in some instances, reasonably unique whereas, in others, aren't at all.

Figures 4a and 4b show the effect of pile stiffness, EI, upon the resulting p-y curves at a 2- and 4-ft. depth in loose (ϕ = 30°, ϵ_{50} = 0.4%) and dense sand (ϕ = 40°, ϵ_{50} = 0.2%). (A common unit weight of 66 pcf was used corresponding to submerged conditions.) The stiff pile has an EI = 10.9 x 10^9 lb-in^2 corresponding to a 12-inch pipe pile backfilled with concrete. The flexible pile has an EI = 1.5 x 10^9 lb-in^2 corresponding to a 12-inch timber pile. As seen, the stiffer pile has a 30 to 50% stiffer p-y curve.

By contrast, the p-y curves for the same piles in soft clay (S_u = 500 psf, ϵ_{50} = 1.2%, ϕ' = 20°) and stiff clay (S_u = 1800 psf, ϵ_{50} = 0.5%, ϕ' = 20°) are, within reason, much the same regardless of pile stiffness and depth (the latter, provided S_u is constant), as shown in Figs. 5a and 5b. The p-y curves shown in Figs. 4 and 5 are for free- (i.e., pinned end) head conditions. Figure 6 shows the difference in p-y curves at a 2- and 4-ft. depth for the stiff pile in loose and dense sands for free- versus fixed-head conditions. (Here, fixed means free to translate but fixed against rotation.) Figure 7 makes the same comparison for the stiff pile in soft and stiff clay. Here, the difference due to fixity at larger deflections varies from 40 to 90% (fixed stiffer than the free-head curve).

Figure 8 shows the reason for the head fixity difference. As

indicated, the deflection, y, for the same strain, ϵ, or deflection angle, δ (= y_o/h, e.g., as shown in Fig. 2), for the fixed-head case must be greater than that for the free-head case because h (the depth of the wedge) is much greater for the fixed-head case. If ϵ is the same, then the Young's modulus and subgrade modulus profiles are the same for both cases. However, since y is greater at any depth, x, for the fixed case (see Fig. 8), then p (= $E_s y$ at the same secant slope, E_s) is greater and two points (p,y) on two separate p-y curves are generated for the fixed- and free-head cases. The same is true at other assumed values of strain, ϵ.

Figure 9 shows a situation (A versus B) that can, alternately, be considered a difference in head or embedment conditions. Whichever the reader chooses to call it, consider that the p-y curve at the same depth of 6 feet from ground surface is desired. But, in case A, the pile head load and deflection occur at a 4-ft. depth; while, in case B, they are at ground surface. Case A might be considered as the common situation where the pile top is at the base of an embedded pile cap. (Take the 4 feet from ground surface, in both cases A and B, to be fill at a unit weight of 120 pcf.) As can be judged from Fig. 10, there is some difference in the free-head p-y curve response at A vs. B for the stiff pile in both loose sand (Fig. 10a) and soft clay (Fig. 10b), though this difference is greater in sand.

Supposedly, p-y curves are independent of a change in neighboring soil material, i.e., changing the soil immediately above or below the soil for which the p-y curve is sought. Figures 11 and 12 show the effect of doing just that as established from strain wedge model analysis. As seen by the insert, the lower soil (from 6 feet down) in Fig. 11a has some effect on the p-y curves in loose sand at x = 2 and 4 feet (for free-head conditions of the stiff pile). The same is true of the sand at x = 8 feet where the upper 6-ft. layer is changed as shown in Fig. 12a. On the other hand, there is little effect on the p-y curves in soft clay at any depth for a change in either the lower (Fig. 11b) or upper soil layer (Fig. 12b).

DISCUSSION AND CONCLUSIONS

While most engineers prefer p-y curve BEF analysis as compared to elastic continuum or finite element analysis of laterally loaded pile behavior, the profession has reached a state where it is time that closer scrutiny be given the p-y curves used in the analysis. The p-y curves provided as part of COM624 were derived from a limited number of well-instrumented field tests that reflect a limited set of conditions. To consider that those p-y curves are unique is a fallacy. As shown here, there are conditions where they are far from unique, particularly when the soil is cohesionless. It is recommended that strain wedge model formulation be used to address this problem. Strain wedge model analysis has been shown to predict response in very good agreement with actual field test behavior from Mustang Island, Sabine, Lake Austin, and other field case studies. Its strength is that it is capable of taking into account the effect of changes in soil and pile properties, embedment and/or head conditions, etc., on the resulting p-y

curves. Further, it is applicable down into the small strain range (as required for seismic analysis) and should shortly be able to analyze the behavior of piles in a group with an attached embedded cap.

REFERENCES

Norris, G.M. and Abdollaholiaee, P., "BEF-Studies with the strain Wedge Model: part B," *Proceedings 26th Annual Symposium on Engineering Geology and Soils Engineering*, Pocatello, Idaho, April 1990, Paper 13.B, 13A and 13B.

Norris, G.M., Gowda, P.K., and Pilling, P.A., "Laterally Loaded Pile Analysis for Layered Soil Based on the Strain Wedge Model," CIS Report No. 91-11, October 1991.

Reese, L.C. and Sullivan, W.R., "Documentation of Computer Program COM624," Geotechnical Engineering Center, Bureau of Engineering Research Report, University of Texas, Austin, 1980.

Norris, G.M., "Seismic Bridge Pile Foundation Behavior," International Conference on Design and Construction of Deep Foundations, FHWA, Orlando, December 1994, Vol. I (keynote papers), pp. 27-136.

Brown, D.A., Morrison, C., and Reese, L.C., "Lateral Load Behavior of Pile Group in Sand," *Journal of Geotechnical Engineering*, ASCE, Vol. 114, No. 11, 1988, pp. 1261-1276.

Norris, G.M., Siddharthan, R., Zafir, Z., and Gowda, P., "Seismic Pile Foundation Stiffnesses at Cypress," *Transportation Research Record*, TRB, No. 1411, 1993, pp.70-80.

U.S. Navy, *Design Manual: Soil Mechanics, Foundations and Earth Structure*, NAVFAC DM 7.2, 1982, p. 241.

Terzaghi, K., "Evaluation of Coefficients of Subgrade Reaction," *Geotechnique*, Vol. V, No. 4, December 1955, pp. 297-326.

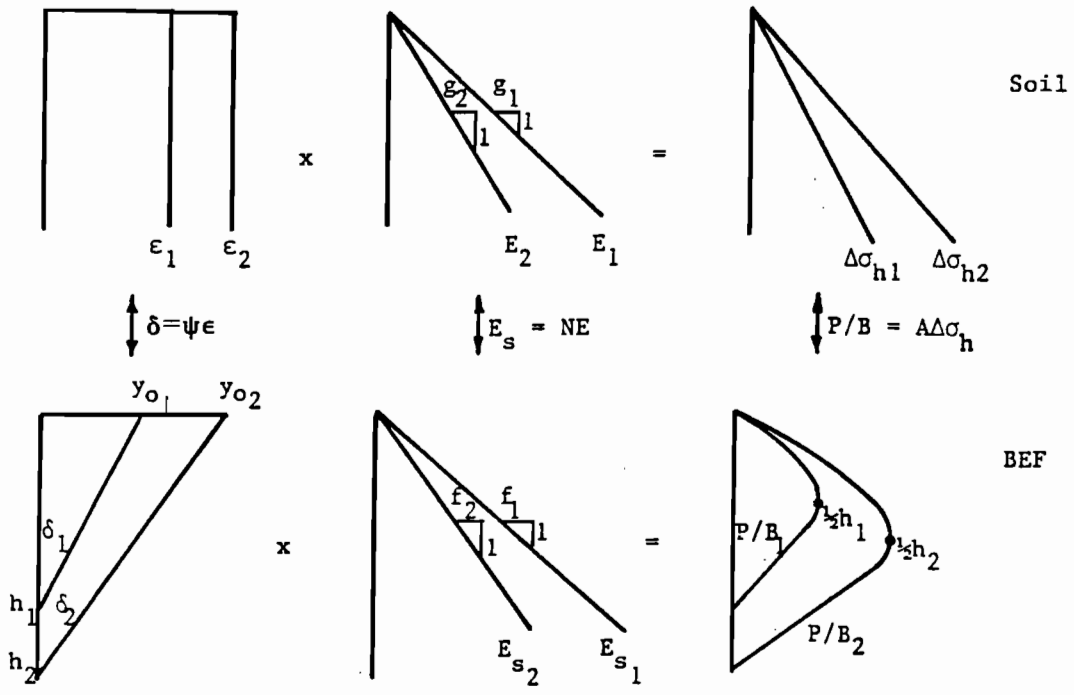

Fig. 1. Relationship between beam-on-elastic foundation (BEF) and soil parameters.

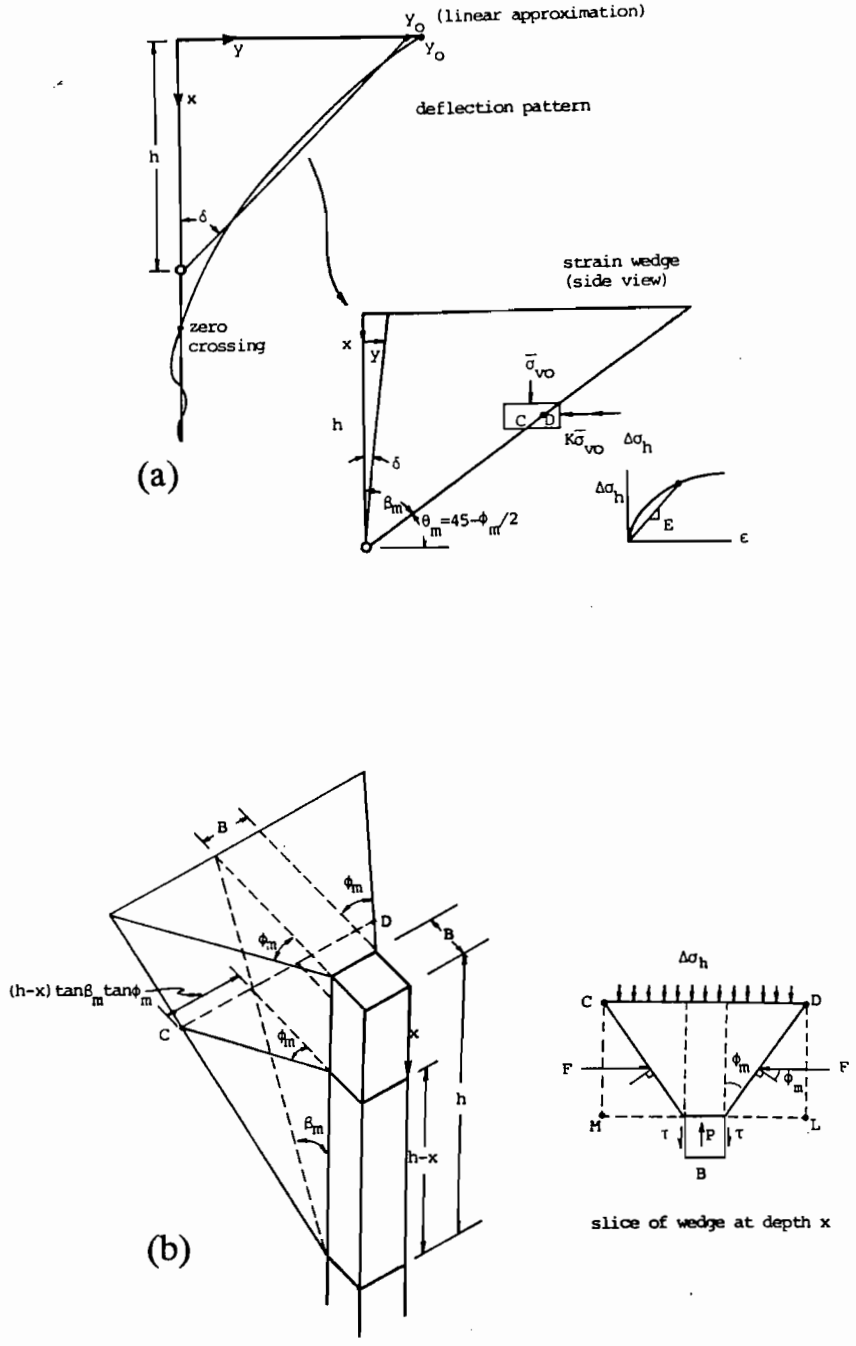

Fig. 2. Strain wedge a) side view and b) three-dimensional view.

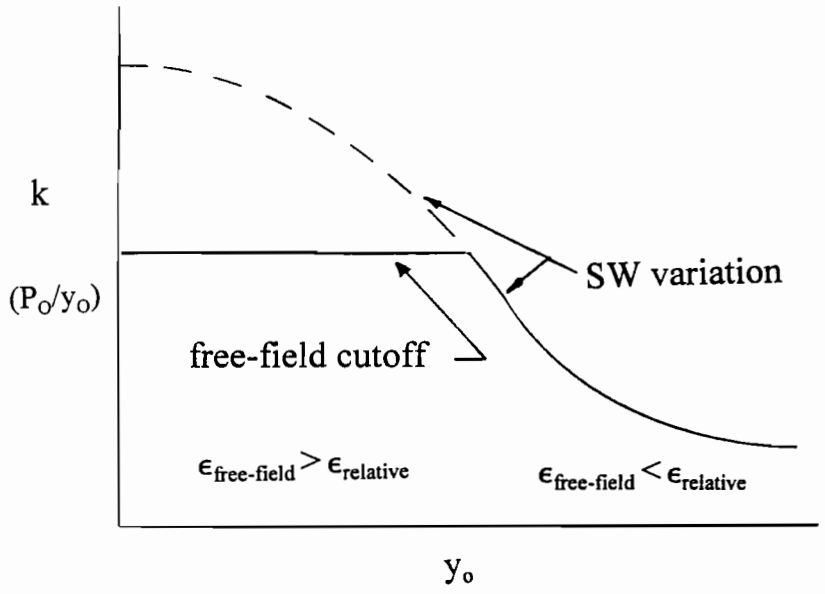

Fig. 3. Truncation of equivalent linear pile head stiffness (k) vs. relative pile top displacement (y_o) for free-field strain.

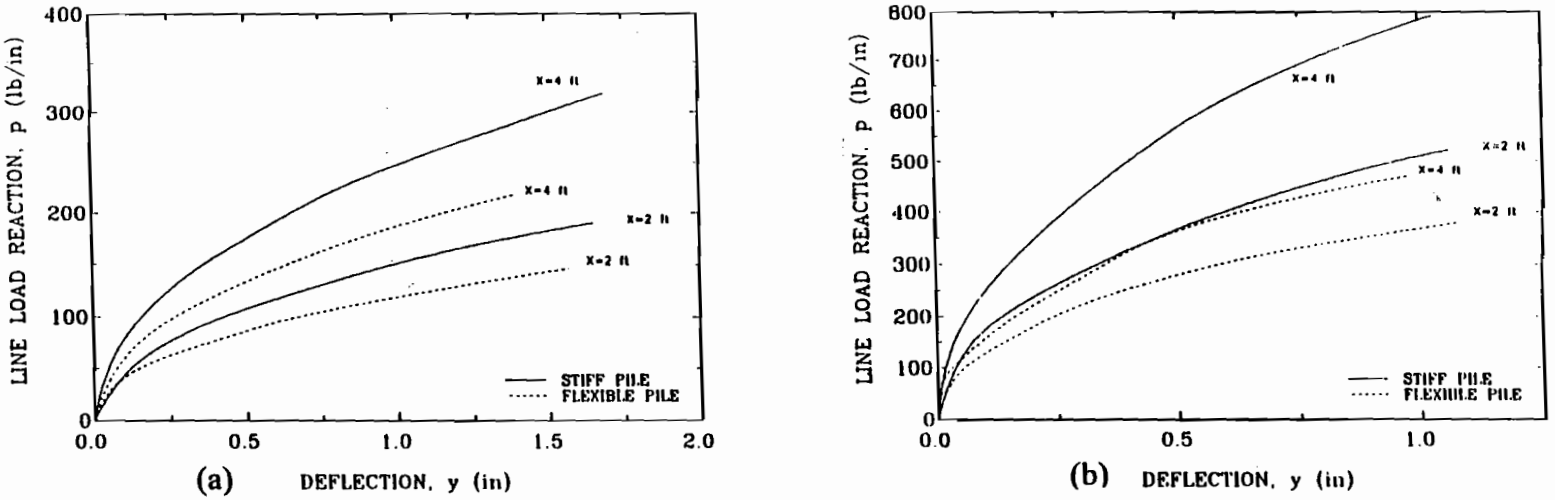

Fig. 4. Change in p-y curve in a) loose sand and b) dense sand for change in pile stiffness.

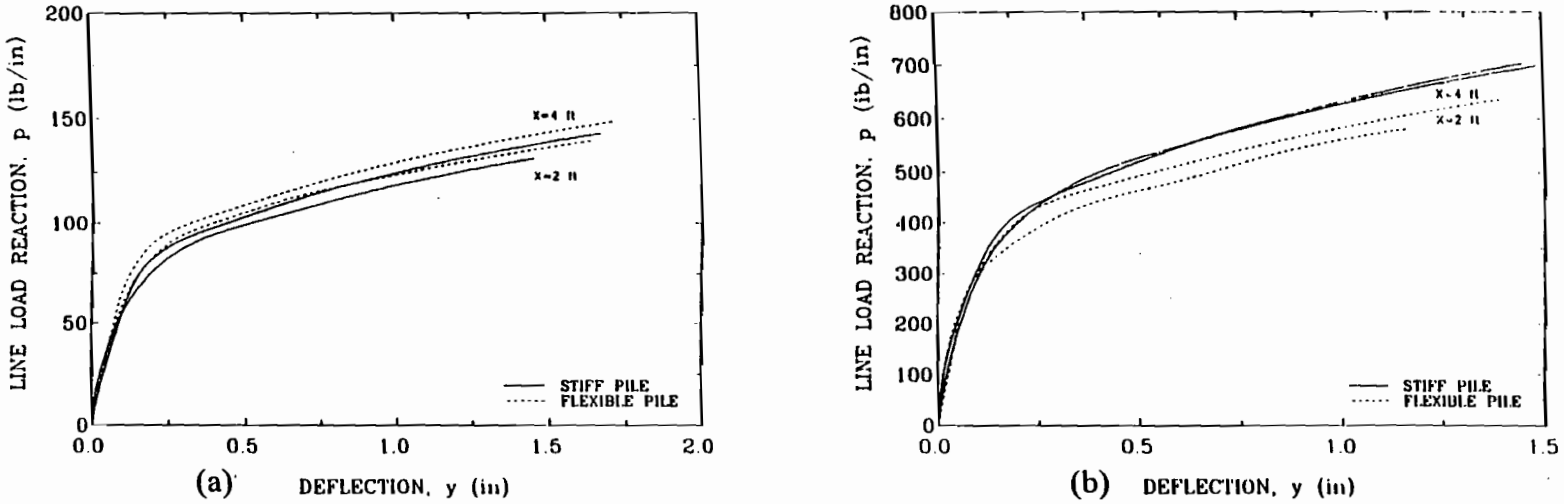

Fig. 5. Change in p-y curve in a) soft clay and b) stiff clay for change in pile stiffness.

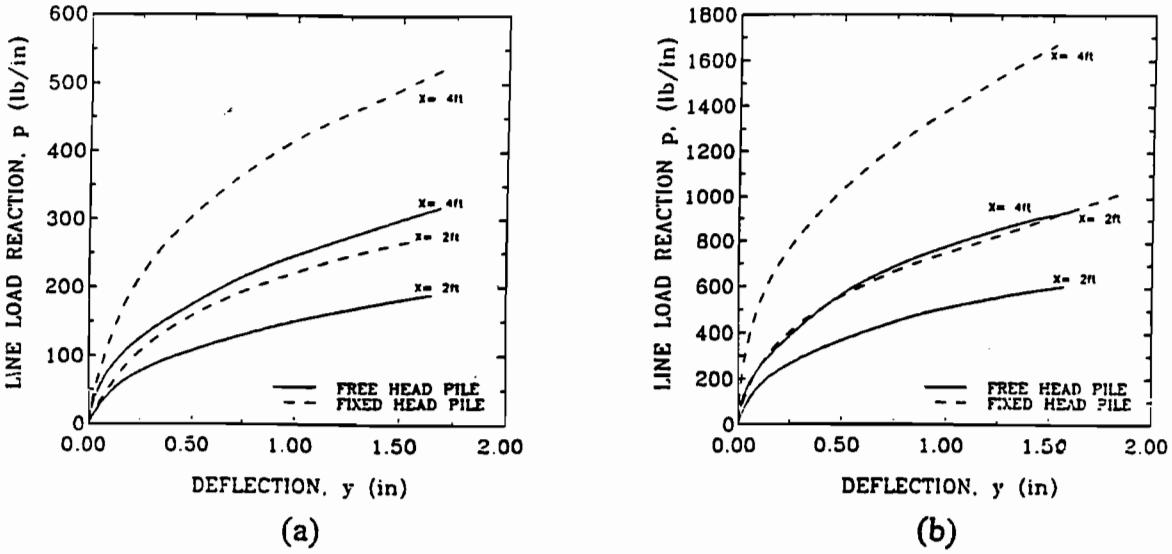

Fig. 6. Change in p-y curve in a) loose sand and b) dense sand for change in pile head fixity.

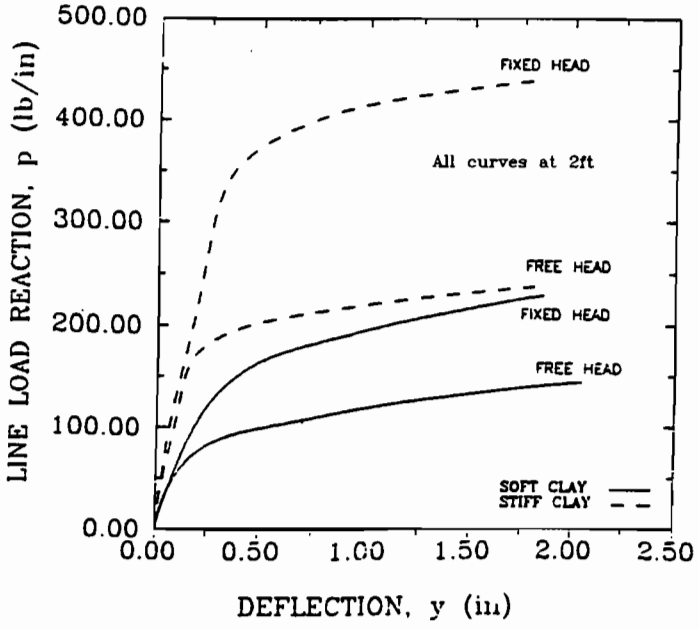

Fig. 7. Change in p-y curve in soft and stiff clay for change in pile head fixity.

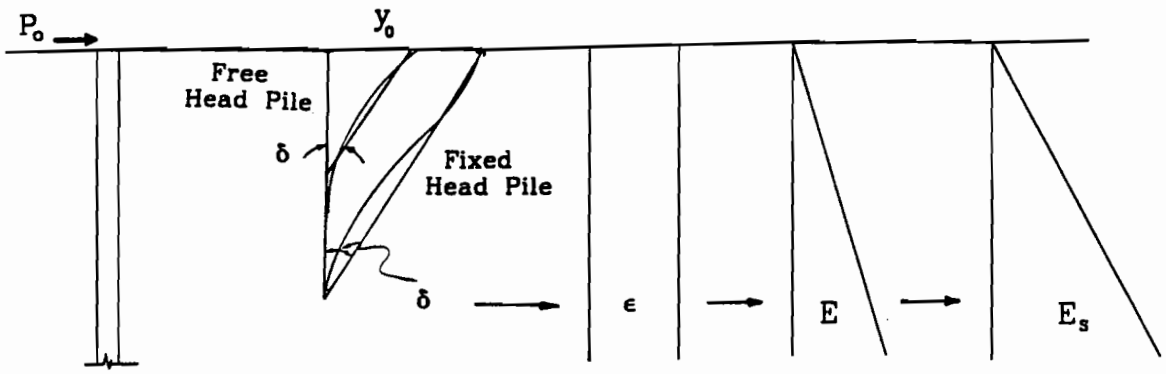

Fig. 8. Deflection pattern for fixed versus free head conditions for same strain.

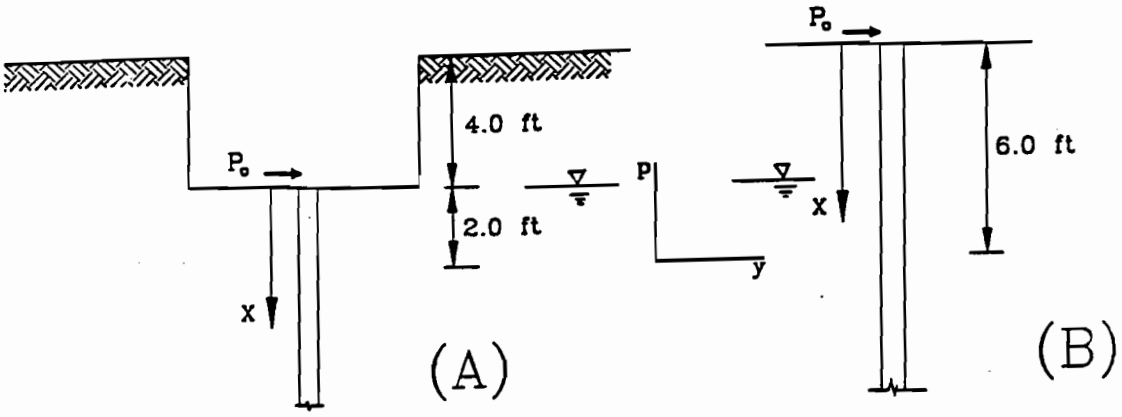

Fig. 9. Reference figure for p-y curve comparison for embedment conditions.

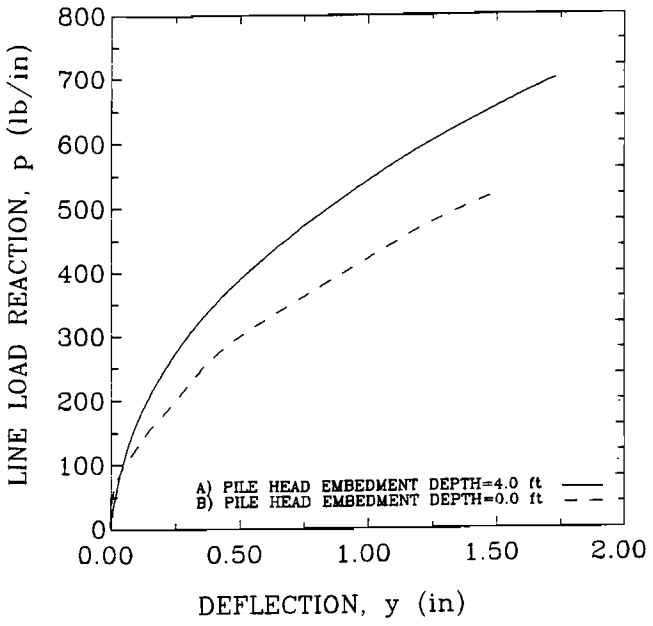

(a)

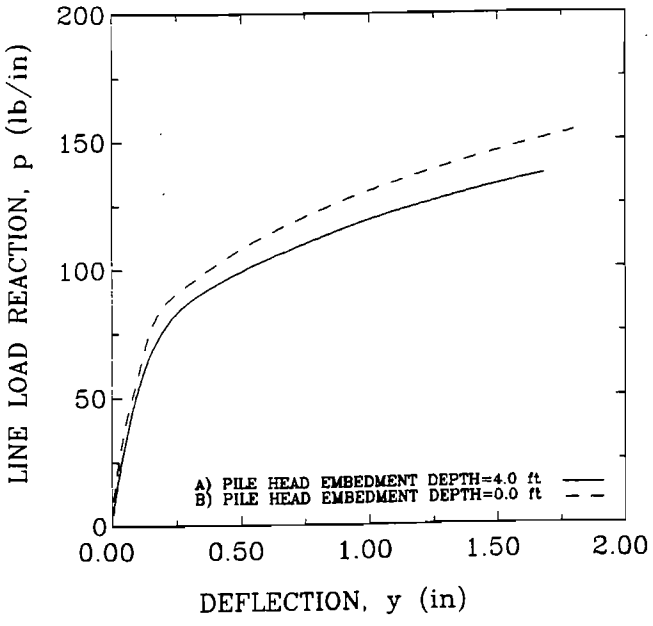

(b)

Fig. 10. Change in p-y curve in a) loose sand and b) soft clay for different pile head embedment conditions.

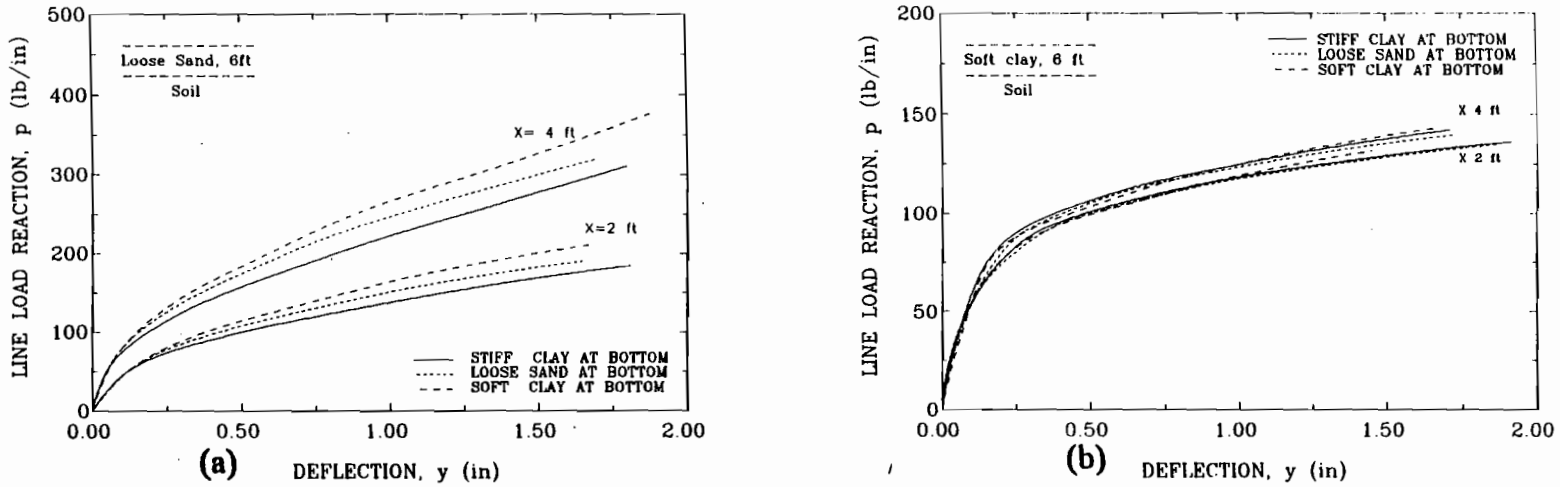

Fig. 11. Change in p-y curve for upper a) loose sand and b) soft clay for change in lower soil.

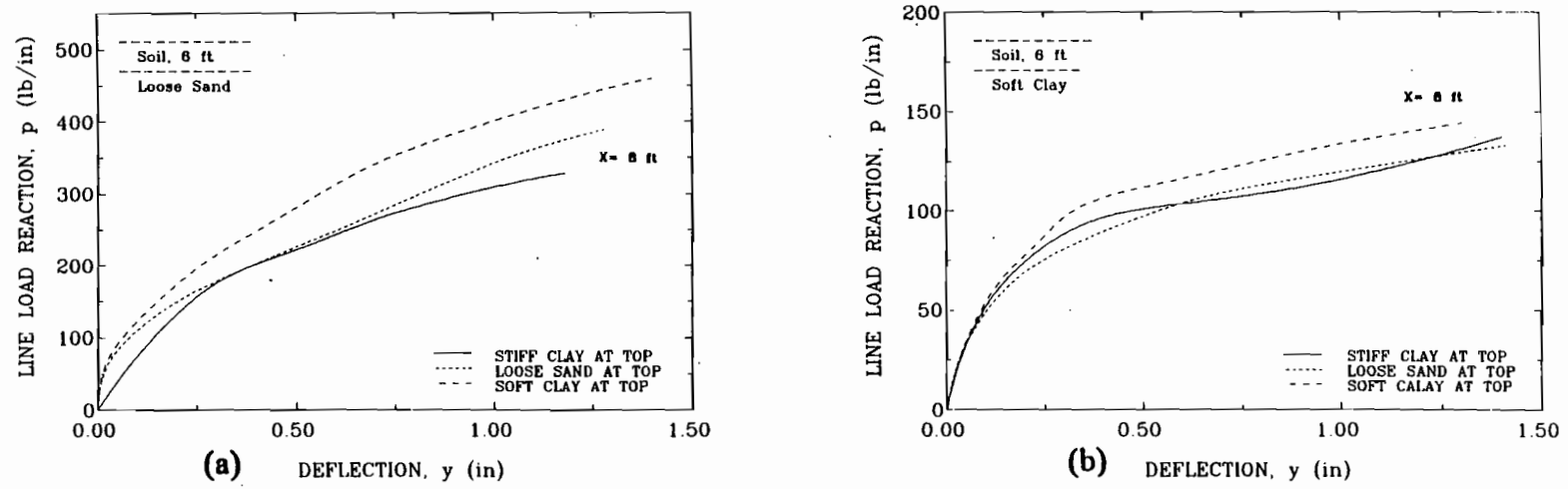

Fig. 12. Change in p-y curve for lower a) loose sand and b) soft clay for change in upper soil.

SETTLEMENT OF SHALLOW FOUNDATIONS ON DENSE, HIGHLY ANGULAR, SILTY SAND

Steven W. Perkins[1], Marsheila S. Rockwell[2] and Craig R. Madson[3]

ABSTRACT

Geotechnical centrifuge experiments have been performed on shallow foundations resting on or within a dense, highly angular silty sand for the purpose of establishing load versus settlement characteristics. The elastic modulus of the material used in the experiments is shown to be highly dependent on the mean normal stress confinement.

As a first attempt in predicting settlements observed in the experiments, a solution has been formulated within the framework of a strain influence method taking the soil to be linearly elastic. This method allows for the variation in elastic modulus to be taken into account by describing the level of mean normal stress within different material layers and assigning an elastic modulus appropriate to that stress level.

INTRODUCTION

Dense, angular sands commonly possess an elastic modulus which is dependent on the effective mean normal stress imposed on the sample prior to application of the shearing load. In practical terms, for the purpose of calculating foundation settlement within the context of elastic solutions, this observation implies the need to choose an elastic modulus appropriate to the average mean normal stress conditions present beneath a footing of some specified geometry and subject to some level of working load.

This observation also implies that any method used to determine the elastic modulus should be capable of replicating mean normal stress levels similar to those expected within the zone of soil influenced by the foundation. This last implication is easily accommodated for in the laboratory using conventional triaxial testing equipment. In practice, however, difficulties are encountered in sampling and testing

[1]Assistant Professor, Dept. of Civil Eng., Montana State University, Bozeman, MT, 59717
[2]Graduate Research Assistant, Dept. of Civil Eng., MSU
[3]Graduate Research Assistant, Dept. of Civil Eng., MSU

relatively clean sands, creating a need to rely on in situ tests to define elastic properties. This then creates the formidable problem of defining the dependence of the elastic modulus on mean normal stress from in situ test results.

Assuming that mean normal stress dependent elastic moduli are available, the problem then arises as to the manner in which an elastic modulus is chosen to represent conditions existing in the soil for the footing in question. As a first attempt, an approach to this problem is to use elastic solutions to define the level of effective mean normal stress within a particular layer of interest and to then assign an elastic modulus appropriate to that condition. This mean normal stress level will be dependent on the footing configuration and working load and on the position of the layer below the ground surface (i.e. stresses due to the footing load and self-weight stresses are accounted for). Conventional settlement calculations can then be performed for a layered elastic system, which is most easily accomplished through a conventional strain influence method (Schmertmann and Hartman, 1978).

MATERIAL

The material used in this study was a crushed basalt obtained from an abandoned quarry near Duluth, Minnesota. The material was chosen to match the properties of lunar soil for the purpose of examining geotechnical issues related to construction of facilities on the lunar surface. The main mineral chemical composition of the basalt consists of plagioclase, pyroxene, olivine and ilmenite. This chemical composition makes the bulk mineralogy quite comparable to the Apollo 11 lunar sample 10084 (Weiblen and Gordon, 1988). The basalt was collected, crushed, ground and sieved with the resulting material being classified as a highly angular silty sand. The specific gravity of the solid grains is 3.2. The grain size distribution of the soil is provided in Figure 1. This grain size distribution was created to match the mean grain size distribution curves available for lunar soil and is similar to soils found on earth. It is seen that approximately 43% passes the number 200 sieve while the coefficient of uniformity is 16 and the coefficient of curvature is 1.1, making the material well-graded. The fines are non-plastic.

The experiments used to classify the deformation characteristics of the material for the purposes of this study were conventional triaxial compression experiments performed on dry material. Standard sized cylindrical samples of 7 cm in diameter by 13.5 cm in height were used with fixed, non-lubricated ends. The samples were prepared in a rigid mold using a vibratory compactor. Samples were prepared to a density of 2.2 g/cm^3, representing a void ratio of 0.45.

Unloading and reloading loops were performed at a principal stress difference level approximately equal to 1/3 the peak value. Elastic moduli were determined both from the unloading-reloading loop and from a secant measure where the secant point was taken at a principal stress difference level equal to 1/2 the peak stress. An experiment illustrating the selection of these two elastic moduli is shown in Figure

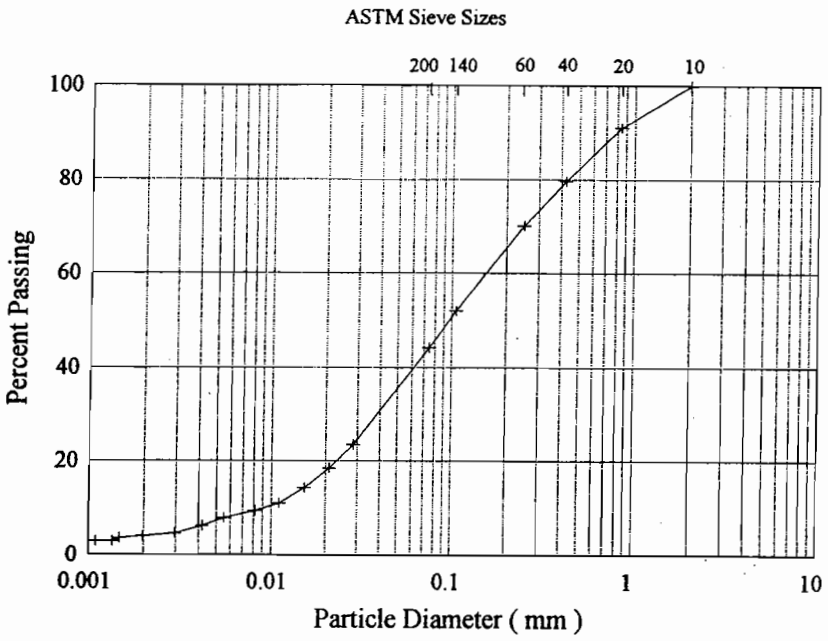

Figure 1: Grain Size Distribution of Silty Sand

2. Experiments were performed at confining pressures ranging from 3.4 to 750 kPa. Computed values of elastic modulus are given in Table 1.

In Figure 3 the computed values of unloading-reloading and secant elastic modulus have been plotted against the mean normal stress confinement present at the beginning of each test. Two curves have been fit to the experimental data. The equations for the curves take the functional form

$$F = E\left(1 + \frac{E}{E_a}\right)^m - \eta p = 0 \tag{1}$$

where m is a parameter describing the curvature of the function, η describes the slope of the curve, E_a is a reference modulus taken as 1 kPa and p is the normal stress invariant given as

$$p = \frac{\sigma_1 + \sigma_2 + \sigma_3}{3} \tag{2}$$

The values of m and η for the two different curves are given in Table 2.

CENTRIFUGE MODEL FOOTING EXPERIMENTS

Model footing experiments were performed using the 400 g-ton centrifuge located at the University of Colorado at Boulder. The centrifuge facility has been described in greater detail by Ko (1988). A total of 30 experiments were performed. The main variables included in the testing program were the acceleration level and

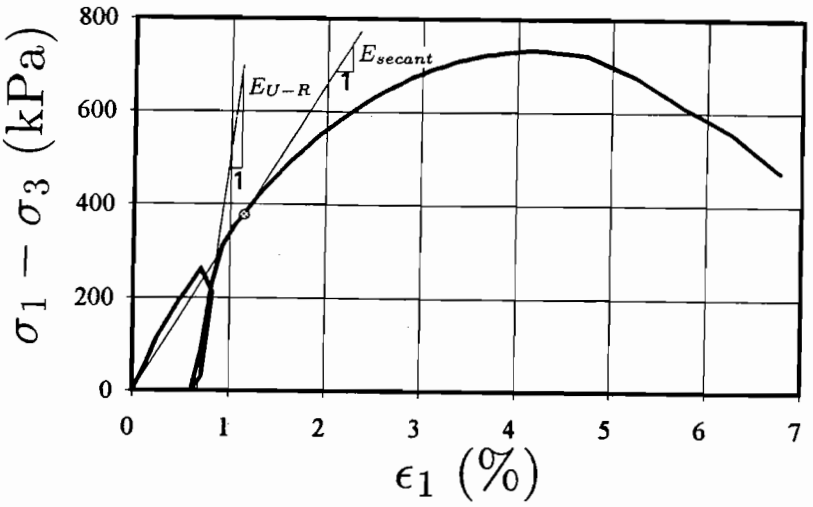

Figure 2: Typical Conventional Triaxial Compression Test Result at $\sigma_3 = 102$ kPa

Table 1: Computed Elastic Moduli From CTC Tests

Mean Normal Stress (kPa)	E_{U-R} (MPa)	E_{secant} (MPa)
3.44	10.9	5.00
6.89	24.9	4.71
13.8	50.6	15.8
34.4	86.0	18.7
68.9	134	33.3
102	160	35.0
204	263	48.4
502	417	92.3
649	500	83.8
750	545	116

Table 2: Curve Fit Parameters

	m	η
E_{U-R}	0.422	195,000
E_{secant}	0.720	611,000

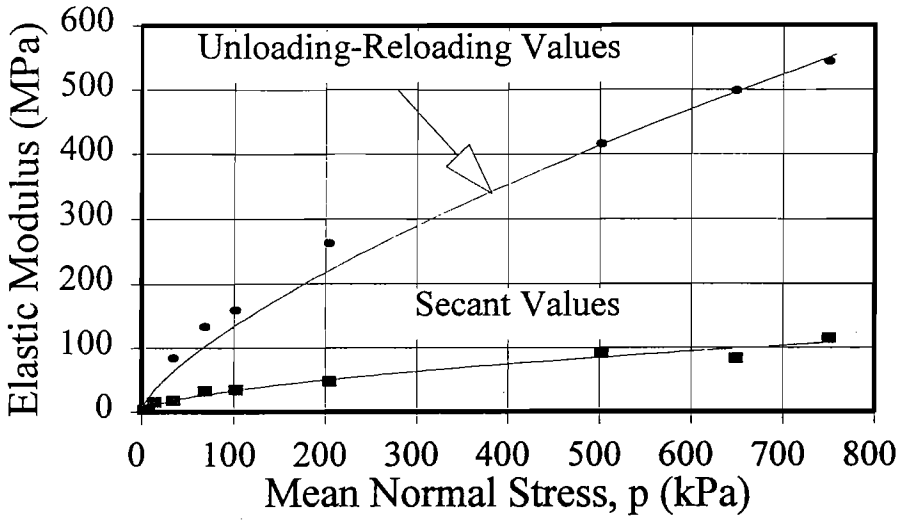

Figure 3: Variation of Elastic Modulus With Mean Normal Stress

the depth of footing embedment. Three acceleration levels of approximately 25-g, 17-g and 5-g were selected. A model footing with a width of 2 cm was used for all experiments. Experiments were performed at the previously stated g-levels and at three levels of footing burial, namely 0B, 0.5B, and 1B, where B is the footing width.

The experiments were performed in a rigid aluminum container. The container had an inside width and length of 1.09 m and 1.14 m, respectively and an inside height of 40 cm. The walls of the container were 3.8 cm in thickness. The container was reduced in size by inserting vertical walls supported by struts bearing against the aluminum container walls. These walls reduced the container width to 53 cm, while the length and height remained unchanged.

The footings were designed in a segmented fashion to allow independent measurement of load on each footing segment (Figure 4). The composite footing was constructed of five segments. The three interior segments each had a length equal to its width of 2 cm. The two end segments had a length equal to 6 cm (2B). These end segments had the same width as the interior segments. The segments were designed to have 0.5 mm of clearance between each other. The composite strip footing had a total length of 14 cm (7B).

The three interior segments were instrumented with load cells having a range of 0-8.9 kN. An uninstrumented steel rod was used to transmit load to the two end segments. The load to each segment was transmitted through an aluminum adapter which had a rounded tongue on its end. This tongue fit into a common size groove on top of the footing segment. The tongue and groove ran the length of the segment. This assembly allowed for rotation of the footing segments. Each loading adapter was connected to an aluminum cross-bar through the load cells or steel rods. These features, along with the loading system, are shown in Figure 4.

A 3.2 cm diameter, threaded, hardened steel rod was attached to the center

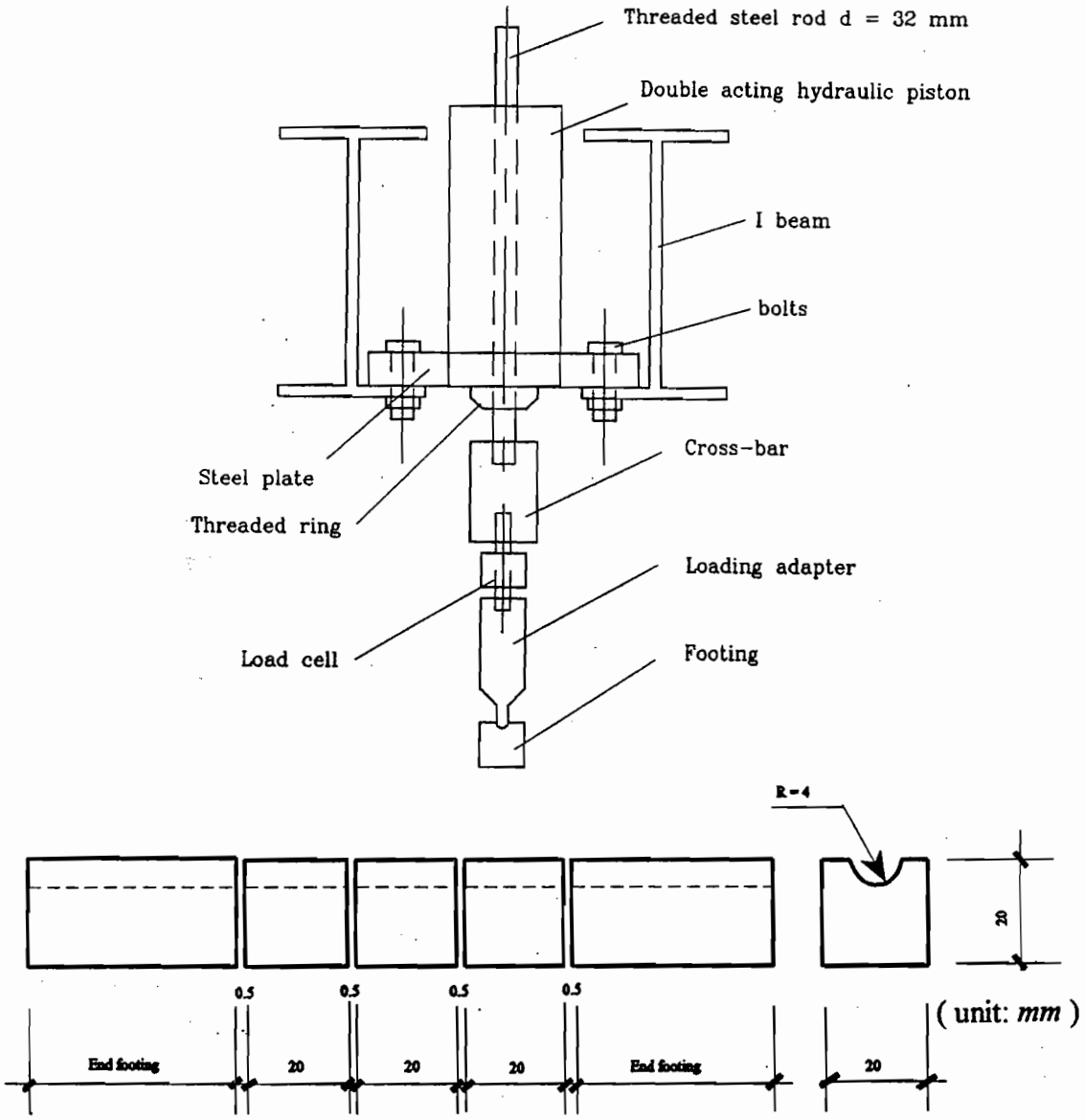

Figure 4: Segmented Footing Configuration

of the loading cross-bar. This rod was threaded through a ring which was threaded to the bottom of a hollow hydraulic piston. The threaded rod could then extend upwards through the hollow cavity of the piston. The double acting hydraulic piston was used to support the weight of the footing assembly during the initial spin-up stage of the test and then used to apply loads to the footing.

All test beds were prepared in equal lifts resulting in a final lift height of 4 cm. To ensure that the soil was deposited uniformly, a wire screen was placed over the container and segmented into 105 equal areas approximately 7.5 cm by 7.5 cm. Atop each area, an equal mass of soil was gently deposited. After all areas had received the prescribed mass of soil, the screen was gently vibrated to allow the soil to fall uniformly. The screen was then removed and the lift received additional compaction. This compaction was provided by a pneumatic ball vibrator attached to a 23 cm square steel plate. The plate was moved to different areas of the soil to compact the lift to a scribed lift height mark. The process was then repeated for the additional lifts. A more detailed description of the experimental set-up and sample preparation technique is given by Gui (1995).

The results of nine experiments at the three different acceleration levels and three different depths of embedment are shown in Figure 5. The footing widths denoted in Figure 5 have been scaled to the prototype dimension in 1-g. The footing pressure is the actual pressure observed in the experiments and scales one to one. The relative settlement, given as the ratio of the footing displacement to the footing width, also scales one to one.

Correction of the initial loading portion of the experimental curves has been achieved by extending the initial slope of the curves backwards to the zero load line. This necessitated shifting the displacements slightly to account for seating of the footings as load was applied. The footing relative settlement corresponding to a footing pressure equal to 1/2 the peak pressure is given in Table 3.

SOLUTION FOR SETTLEMENT

Calculation of footing settlements within the context of elastic solutions depends directly on the selection of the elastic modulus for the material. The selection of an elastic modulus becomes difficult for a material whose modulus exhibits a strong dependence on the mean normal stress confinement. The principal problem addressed in this paper is the guidance used to choose an elastic modulus for a particular footing configuration and loading for such materials. As a first attempt in addressing this problem, the mean normal stress is determined for various material layers beneath the base of the foundation. This normal stress is due to the pressure from the foundation and from self-weight stresses. The level of mean normal stress is then used to determine an elastic modulus appropriate for the layer. Settlements are then calculated within the framework of a strain influence method.

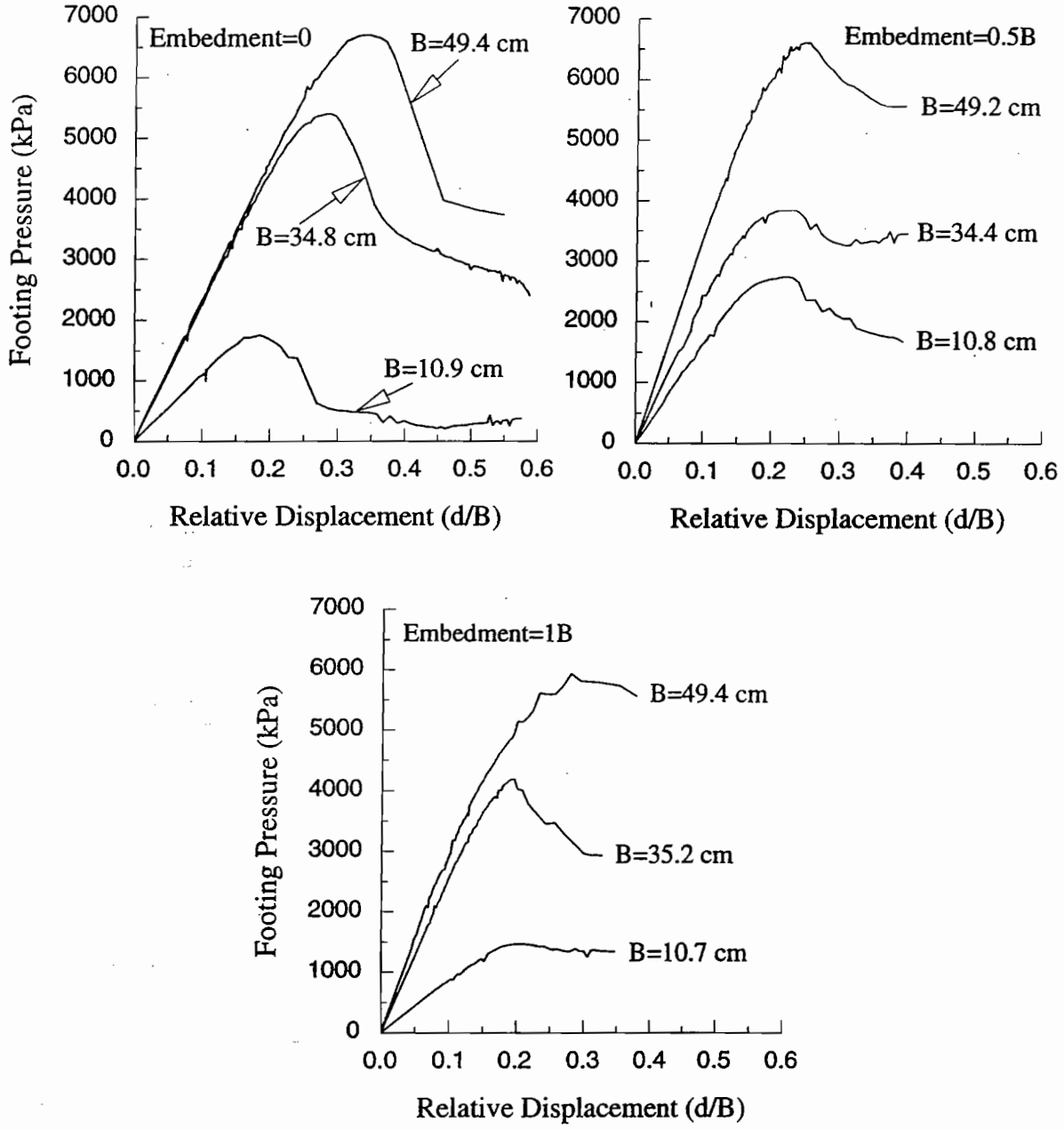

Figure 5: Centrifuge Footing Penetration Results

Table 3: Relative Settlement and Footing Pressure at 1/2 Peak Pressure

Footing Embedment (*B)	Footing Width (cm)	Relative Settlement (d/B)	Footing Pressure (kPa)
0	49.4	0.145	3350
0	34.8	0.118	2700
0	10.9	0.0798	875
0.5	49.2	0.0981	3310
0.5	34.9	0.0831	1925
0.5	10.8	0.0860	1370
1	49.4	0.0996	2905
1	35.2	0.0785	2095
1	10.7	0.0841	735

The mean normal stress within a delineated material layer is calculated by using elastic solutions for a linear elastic, isotropic half-space. The foundation is assumed to be flexible and infinite in length. Consider a thin material layer beneath the footing whose mid-point is denoted by a distance z from the bottom of the foundation base, as shown in Figure 6. The stresses σ_z, σ_y and σ_x are given as

$$\sigma_z = \sigma_1 = \frac{q}{\pi}(\alpha + \sin\alpha) \tag{3}$$

$$\sigma_y = \sigma_2 = \frac{q}{\pi}(\alpha - \sin\alpha) \tag{4}$$

$$\sigma_x = \sigma_3 = \frac{q}{\pi} 2\nu\alpha \tag{5}$$

where ν is Poission's ratio and α is given as

$$\alpha = 2\arctan\left(\frac{B}{2z}\right) \tag{6}$$

The mean normal stress due to q is then 1/3 the sum of the above 3 principal stresses, or

$$p = \frac{2q\alpha}{3\pi}(1+\nu) \tag{7}$$

The mean normal stress due to the material self-weight is calculated by assuming that the two lateral principal stresses can be calculated from the earth pressure coefficient at rest such that

$$p = \frac{\sigma_v}{3}(1+2k_o) \tag{8}$$

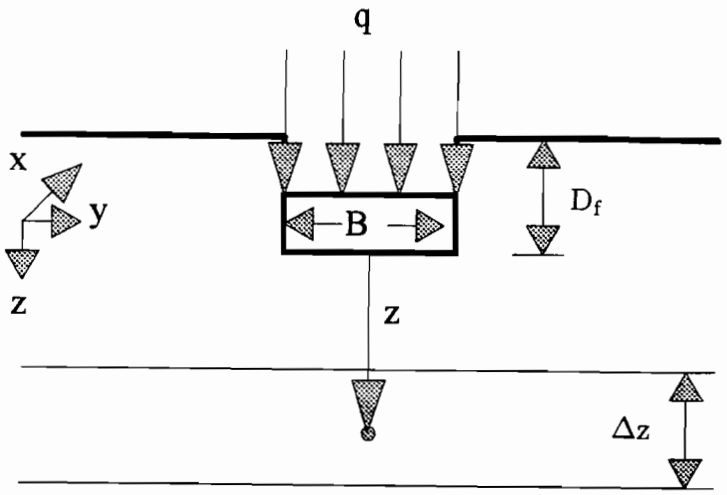

Figure 6: Mean Normal Stress At A Point

where σ_v can be calculated from the overburden material giving

$$p = \frac{\rho g z}{3}(1 + 2k_o) \tag{9}$$

The total mean normal stress due to self-weight and footing pressure is then equal to the sum of equations 7 and 9 giving

$$p = \frac{1}{3}\left[\rho g z(1 + 2k_o) + \frac{2q\alpha}{\pi}(1 + \nu)\right] \tag{10}$$

With the mean normal stress calculated for a particular layer, equation 1 is then used to calculate the elastic modulus for that layer. As will be demonstrated in the following section, elastic moduli have been calculated according to unloading-reloading and secant values. A strain influence value, Iz, is then calculated from the following equations

$$\begin{aligned} I_z &= 0.2 + \frac{0.3z}{B} \qquad 0 \leq z \leq B \\ I_z &= \frac{2}{3} - \frac{z}{6B} \qquad B < z \leq 4B \end{aligned} \tag{11}$$

where z is the depth below the footing base to the layer mid-height. These equations are approximations of exact solutions and apply to long continuous footings. Settlement of the footing is then calculated from the equation (Schmertmann and Hartman, 1978)

$$S = \left(q - \frac{3}{2}q_o\right)\sum_{i=1}^{n}\frac{I_z \Delta z}{E_i} \tag{12}$$

Table 4: Relative Settlement Predictions At 1/2 Peak Footing Pressure

Footing Embedment (*B)	Footing Width (cm)	Experiment Relative Settlement	U-R Relative Settlement	Secant Relative Settlement
0	49.4	0.145	0.00775	0.0365
0	34.8	0.118	0.00727	0.0345
0	10.9	0.0798	0.00520	0.0216
0.5	49.2	0.0981	0.00772	0.0376
0.5	34.9	0.0831	0.00656	0.0301
0.5	10.8	0.0860	0.00594	0.0259
1	49.4	0.0996	0.00741	0.0356
1	35.2	0.0785	0.00673	0.0310
1	10.7	0.0841	0.00493	0.0199

where q_o is the surcharge at the base of the foundation, Δz is the layer thickness and n represents the number of layers in the system.

SETTLEMENT PREDICTIONS

The solution formulated above was used to calculate settlement for the footing configurations given in Table 3. The soil beneath the footing was divided into 5 layers. Additional analyses demonstrated that breaking the soil into as many as 30 layers resulted in a 1% increase in the computed settlement. Earlier work indicated that k_o is as high as 2. From the CTC tests Poission's ratio was seen to be approximately equal to 0.35. For purposes of comparison, settlement was calculated at a footing pressure equal to 1/2 the peak pressure seen in the experiments. Settlements were calculated using unloading-reloading moduli and secant moduli, where the secant measures were determined from points on the CTC stress-strain curves corresponding to a principal stress difference level equal to 1/2 the peak value. For all the predictions made, the maximum and minimum elastic modulus corresponding to the unloading-reloading and secant measures was 91, 990 and 25, 176 MPa, respectively. Results from these predictions, expressed as a relative settlement defined as the settlement divided by the footing width, are given in Table 4.

These results have been plotted in Figure 7 by dividing the relative settlement seen in the experiments by the predicted values and plotting this ratio against the respective footing width for each experiment. Using the unloading-reloading elastic moduli, it is seen that the settlement seen in the experiments ranges from approximately 12-18 times the predicted values. Using the secant measures this range decreases to 2.5-4. It is clear that the secant values offer much better predictions than the unloading-reloading measures, yet even the secant measures are unconservative by a factor as great as 4. The large value of the underprediction ratio using the

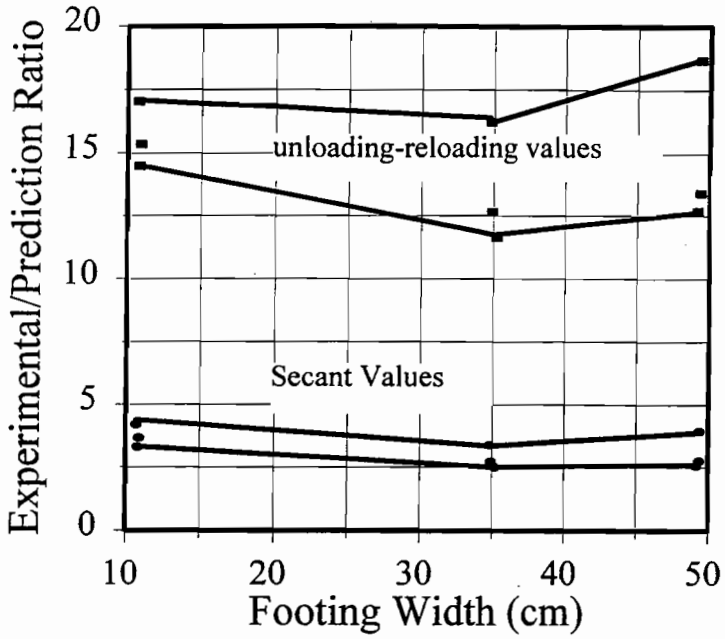

Figure 7: Comparison of Experimental and Predicted Settlements

unloading-reloading values is an indication that appreciable plastic deformations are occuring at footing load levels equal to 1/2 the peak load.

CONCLUSIONS

The problem of predicting settlements for shallow, continuous foundations resting on a material exhibiting a significant variation in elastic modulus with mean normal stress confinement has been addressed within the framework of a conventional strain influence method by assigning an elastic modulus to various material layers experiencing differing levels of mean normal stress confinement. This approach has indicated that using a secant measure for the elastic modulus from CTC experiments produces predictions which underpredict the experimentally observed settlement by a factor ranging from 2.5-4.

Earlier work (Perkins and Gui, 1994) using a strain-softening, non-associated, elastic-plastic finite element program indicated that underprediction factors no greater than 1.5 are observed. While improvements can be made by adopting more sophisticated approaches which account for plastic deformations, this study has shown that reasonable predictions can be made considering the relative simplicity of the approach taken. This study has also pointed to the importance, and ensuing problems, associated with defining the variation of elastic modulus with confinement for certain materials. Commercially available in situ tests used to define elastic properties are presently unable to predict these variations and may well be defining elastic properties for a mean stress level inappropriate for the intended application.

ACKNOWLEDGEMENT

The author gratefully acknowledges support provided by the Montana State University Engineering Experiment Station under grant 162253.

REFERENCES

Gui, D. (1995), "Bearing Capacity of a Simulated Lunar Soil", M.S. Thesis, Montana State University, 220p.

Ko, H.-Y. (1988), "The Colorado Centrifuge Facility", *Centrifuge 88*, Balkema, Rotterdam, pp. 73-75.

Perkins, S.W. and Gui, D. (1994), "Mechanical Properties of Lunar Regolith and Their Effect On Bearing Capacity", *Proc. 8th Int. Conf. on Computer Methods and Advances in Geomechanics*, V.2, pp.1521-1526.

Schmertmann, J.H and Hartman, J.P. (1978), "Improved Strain Influence Factor Diagrams", *Journal of the Geotechnical Engineering Division*, ASCE, V.104, No. GT8, pp.1131-1135.

Weiblen, P.W., and Gordon, K.L. (1988) "Characteristics of a Simulant for Lunar Surface Materials", *Symposium on Lunar Bases and Space Activities in the 21st Century*, Paper No.LBS-88-213, Houston.

PILE LOAD TEST DATABASE AND AN EVALUATION OF SPT91 AND SPILE COMPUTER PROGRAMS

by

Hogan H. Chang[1], Joseph A. Caliendo[2]

ABSTRACT

Full-scale pile load tests give the most reliable information for establishing pile capacity. Since pile load tests are expensive and time consuming, various analytical methods have been developed for pile capacity and design. The computer program SPT91, as well as the SPILE program, is used to predict the static axial capacity of driven piles and is used widely in Florida and the southeastern USA. This methodology has not been extensively used in the Intermountain region. In order to evaluate the effectiveness of SPT91 and SPILE, a new pile load test database was established, with pile load test results provided by Utah Department of Transportation and Pennsylvania Department of Transportation, by employing the template sheet of the latest University of Florida pile load test database. The predicted computer results are compared with the measured capacity to establish the validity of SPT91 and SPILE programs.

INTRODUCTION

General

Design and behavior of pile foundations are always the concern of geotechnical engineers. In most cases, the design of pile foundations is achieved by means of theoretical equations or empirical formulas. A number of papers that present empirical static formulas to predict ultimate resistances of piles have been published. These empirical formulas were based on data obtained from in situ tests such as Standard Penetration Tests (SPT) and Cone Penetration Tests (CPT). Pile load tests are the most reliable methods of determining the ultimate loads supported by test piles. Because pile load tests are expensive and time consuming, many computer programs have been developed employing these empirical formulas to predict the ultimate capacities of piles.

The SPT91 computer program was based on empirical formulas for typical Florida soil types. Application of this method to the soils encountered in the Utah region may require certain modifications between measured and predicted pile capacity. The SPILE program can be used to calculate ultimate capacity of any pile type and is presently upgraded by Utah State University for the FHWA to run under a window environment. The latest University of Florida pile load test database including Macros was developed by Pedro F. Ruesta. This database consisted only of concrete piles which were mostly from Florida.

---

1. Graduate student, Utah State University
2. Associate Professor of Department of Civil Engineering, Utah State University

Objectives and Scope

The first objective of this research was to evaluate the accuracy of two computer programs, SPT91 and SPILE. Both of these computer programs were designed to predict static axial pile capacity based on in situ test data of various subsoil conditions. By comparing predicted ultimate capacities of two computer programs, with measured ultimate capacities from pile load tests, it is possible to determine the accuracy of the predicted results.

The second objective was to update an existing pile load test database by adding the actual results of pile load tests. The existing database was compiled by the University of Florida (UF) on behalf of the Florida Department of Transportation and the Federal Highway Administration (Davidson and Townsend, 1993).

The scope of this research was limited to individual driven piles including prestressed concrete piles, H-shape steel piles, and plugged steel pipe piles. All piles were subjected to static axial compressive loads.

Procedures

First, load test information was obtained from the Utah Department of Transportation (Dixon et al., 1992), the Pennsylvania Department of Transportation (1989), and the existing pile load test database of the Federal Highway Administration (Davidson and Townsend, 1993). This information included boring-log data, SPT blow counts, final driving resistances, and load-settlement results. Also, pile installation records, pile-driving equipment and procedures, pile material, dimensions, and specifications were collected.

Secondly, predicted static capacities were calculated from two computer programs. Also, employing the Davisson failure criterion, measured ultimate pile capacities from load test results were determined.

Finally, predicted and measured pile capacities were summarized in tables. According to different pile groups, the predicted capacities were compared with the measured capacities. In order to clearly evaluate the accuracy of these two computer programs, figures were plotted showing predicted capacities versus measured capacities.

SPT91 PROGRAM

Introduction

The SPT91 computer program was designed to estimate the static vertical capacity of driven piles (Bartholomew et al., 1991). The methodology was based on Research Bulletin 121 (RB-121), *Guidelines for use in the soils Investigation and Design of Foundations for Bridge Structures in the State of Florida* (Schmertmann, 1967). Since 1987 several modifications of the program have been made. The current program was last improved in 1991 and was given the designation SPT91. The program is used primarily for the estimation of the static axial capacity of driven concrete piles, although plugged steel pipe piles can also be accommodated. The recent version is available on IBM or compatible microcomputers running under MS-DOS version 3.3 or above.

Method of analysis

Schmertmann (1967) reported that more than half of the State Road Departments in the U.S. used Standard Penetration Tests as the basis for their preliminary design of pile depths and capacities. Bulletin 121 provided empirical equations and design charts related to SPT91 N-values. The methodology of the SPT91 computer program is based on empirical

formulas from Standard Penetration Tests for typical Florida soil types. Table 1 shows five soil types which can be recognized by the program.

Table 1. Soil types recognized by SPT91

Soil type	Description
1	Plastic clay
2	Clay-silt-sand mixtures, very silty sand, silts and marls
3	Clean sands
4	Soft limestone, very shelly sands
5	Voids (no capacity)

In order to define the soil profile, the user inputs soil types, depths, and the SPT N-values corresponding to the depths. The program establishes a layer change at the elevation where a new soil type has been inputed. The program accepts any SPT N-values. Calculation procedures truncate SPT N-values which are less than 5 to 0, and those which are greater than 60 to 60 automatically.

Research at the University of Florida and the Florida Department of Transportation suggested that in order to have the calculated ultimate capacities, as predicted by the RB-121 methods, better match the measured ultimate capacities as determined by the Davisson criterion, the "mobilized end-bearing capacities" must be set equal to 1/3 of the RB-121 ultimate end-bearing capacities (Bartholomew et al., 1991). The SPT Davisson capacities are the sum of the ultimate skin capacities and the mobilized end-bearing capacities. The ultimate capacities of SPT91 are equal to 3 times the mobilized end-bearing capacities plus the ultimate skin capacities.

Mobilized end-bearing capacity

The ultimate unit end-bearing capacity at a given depth is influenced by the SPT N-values and soil types. Figure 1 shows the curves of the mobilized unit end-bearing capacities versus SPT N-values for the four typical soil types. The SPT91 program assumes that the soils between 3.5 B below the pile tip and 8.0 B above the pile tip contribute to the end-bearing capacity. B indicates the pile width or diameter. When the bearing layer is weaker than the overlying layer, the upper limit terminates at the layer change rather than 8.0 B. This termination is to prevent a "punching" failure. Correction factors based on the critical depth ratios are used to obtain the corrected unit end-bearing capacity in the bearing layer.

Ultimate side friction capacity

Figure 2 shows the curves of the ultimate unit side capacities versus SPT N-values for the four soil types. The ultimate unit side capacities above the bearing layer and in the bearing layer are calculated separately and then summed. In the bearing layer, the correction factors are required to calculate the corrected ultimate side capacity.

Critical depth corrections

The method of critical depth corrections is used for both end-bearing capacities and

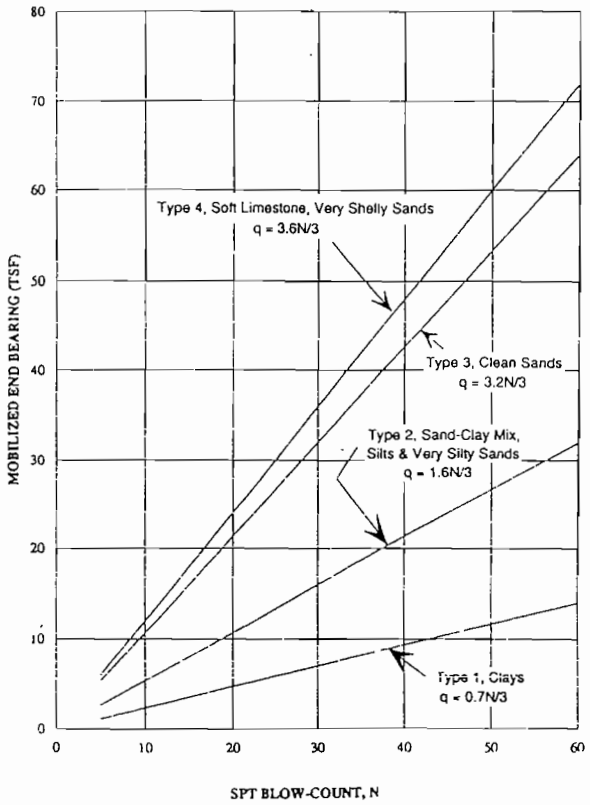

Figure 1. Design chart for mobilized end-bearing capacities (after Bartholomew et al., 1991).

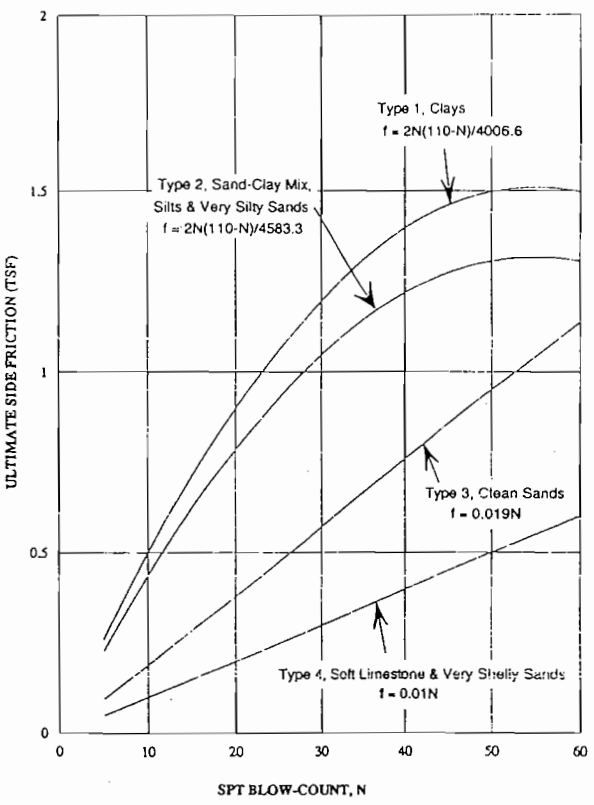

Figure 2. Design chart for ultimate unit side capacities (after Bartholomew et al., 1991).

side friction capacities in the bearing layer. At a critical depth/width ratio (D/B), the end-bearing capacity reaches a maximum value. Beyond the critical D/B ratio, the value of the end-bearing capacity remains constant. The D is the depth of embedment in the bearing layer and B is the pile width. Table 2 gives the critical depth ratios used in the SPT91 program.

Table 2. Critical depth ratios of soil types

Soil type	Description	Critical depth ratio (D/B)
1	Plastic clay	2
2	Clay-silt-sand mixtures, very silty sand, silts, and marls	4
	Clean sands	
	(N=12 or less)	6
	(N=30 or less)	9
3	(N greater than 30)	12
4	Soft limestone and very shelly sands	6

For the end-bearing capacity, when the critical depth is greater than the actual depth of embedment, and when the overlying layer is weaker than the bearing layer, a correction factor (reduction) is applied to the unit end-bearing capacity. The corrected unit bearing capacity is calculated as shown below.

$$q = q_{LC} + \frac{D_A}{D_C}(q_T - q_{LC}) \qquad (1)$$

where q = corrected unit end-bearing capacity at pile tip
q_{LC} = unit end-bearing capacity at layer change
q_T = uncorrected unit end-bearing capacity at pile tip
D_A = actual embedment in bearing layer
D_C = critical depth of embedment

For the side friction capacity, when the critical depth is greater than the actual depth of embedment in the bearing layer, and if the bearing layer is stronger than the overlying layer, the side friction in the bearing layer is corrected (reduced) as follows:

$$CSFBL = \frac{SFBL}{q_T}\left[q_{LC} + \frac{D_A}{2D_C}(q_T - q_{LC})\right] \qquad (2)$$

where CSFBL = corrected side friction in the bearing layer
SFBL = uncorrected side friction in the bearing layer

If the critical depth is less than the actual embedment in the bearing layer, and if the bearing layer is stronger than the overlying layer, the side friction capacity between the top of the bearing layer and the critical depth is reduced as following equation.

$$CSFACD=\frac{USFACD}{q_{CD}}[q_{LC}+0.5(q_{CD}-q_{LC})] \quad (3)$$

where CSFACD = corrected side friction in the bearing layer from the top of the bearing layer to the critical depth
USFACD = uncorrected side friction from the top of the bearing layer to the critical depth
q_{CD} = unit end bearing capacity at critical depth

SPILE PROGRAM

Introduction

The SPILE microcomputer program is used for determination of the ultimate vertical static pile capacity (Urzua, 1993). The methodology of the SPILE program is based on Cheney and Chassie (1982), Meyerhof (1976), Nordlund (1963, 1979), Thurman (1964), and Tomlinson (1979, 1985). The program was coded in Turbo Pascal 5.0 and was available on IBM or compatible microcomputers. Presently the program is upgraded by Utah State University for the FHWA to run under a window environment. The code implements portions of the microcomputer program SAF-TR and SAF-I developed by PROTOTYPE Engineering, Inc., Winchester, MA. SPILE can be used to calculate the ultimate capacities of pipe piles (closed end), timber piles, precast concrete piles, Raymond step-taper piles, Raymond uniform taper piles, H piles, and monotube piles.

Shaft resistance

The ultimate shaft resistance is calculated as follows:

$$Q_f=\int_{length} f_s C_d * dz \quad (4)$$

where f_s= ultimate skin resistance per unit area of shaft
C_d= effective perimeter of pile
l= length of pile embedded below ground surface
z= depth coordinate

The unit skin resistance, f_s, is variable along the pile shaft and is a function of adhesion, friction angle, and the status of stress at the pile-soil interface. For cohesive soil, because the internal friction angle is zero, f_s is expressed as follows:

$$f_s=C_a=\alpha * C_u \quad (5)$$

The pile-soil adhesion, C_a, is related to the undrained shear strength, C_u, where α = empirical adhesion factor. α depends on the nature and strength of soils, pile types, methods of installation, and soil strata. SPILE uses the α values suggested by Tomlinson (1979, 1985). Because the program contains the digitized versions of the Tomlinson's curves, the user can select the appropriate curve.

For cohesionless soils, the SPILE program uses Nordlund's (1963, 1979) equations to calculate the unit skin frictional resistance.

$$f_s=K_\delta C_f * P_d \frac{\sin(w+\delta)}{\cos w} \quad (6)$$

where K_δ = coefficient of lateral stress at depth z
C_f = correction factor for K_δ when $\delta \neq \phi$
P_d = effective overburden pressure
w = angle of pile taper
δ = pile-soil friction angle

End-bearing resistance

The ultimate end-bearing capacity per area of pile tip, q_p, is expressed as

$$q_p = CN_c + qN_q + \frac{\gamma B}{2} N_\gamma \qquad (7)$$

where C=cohesion of the soil
q= vertical stress at pile tip level
B= pile diameter or width
γ= unit weight of the soil
N_c, N_q and N_γ = dimensionless parameters

The dimensionless parameters are the functions of the soil friction angle ϕ. For cohesive soil, because the friction angle is zero, N_q=1 and N_γ=0. The values of N_c lie between 7 and 16. A value of N_c=9 is usually recommended. C is the undrained shear strength, C_u. Considering the pile weight, the ultimate end-bearing capacity of clay can be expressed as follows:

$$Q_p = C_u N_c A_p \qquad (8)$$

For cohesionless soil, the SPILE program uses Thurman's (1964) equations to calculate the ultimate end-bearing capacity.

$$Q_{pnet} = q' \alpha N_q' A_p \qquad (9)$$

where N'_q = bearing capacity factor
α = dimensionless factor

The dimensionless factor, α, is influenced by the depth-width relationship of the pile. When the computed unit point resistances exceed the limiting values suggested by Meyerhof (1976), the program selects the limiting values as the ultimate end-bearing capacities of piles.

The program accepts a maximum of 20 layers of soil. The division of soil layers is dependent on the judgement of the boring log data. The depth of the top layer is required to be 0.0 ft. SPILE assumes that the depth of the bottom of the last soil layer is the depth of the pile tip. The program allows values of the unit weight of the soil between 62.4 and 250 lb/ft^3. One unit weight value is used in each soil layer. The program provides the correction factors of the SPT N-values due to the influence of the effective overburden pressure.

DATABASE

General Information

Many deep foundation load test databases have been developed at the University of Florida (UF) on behalf of the Florida Department of Transportation and the Federal Highway

Administration. The latest UF pile load test database including Macros was developed by Pedro F. Ruesta employing Lotus 123 Version 3.1 (Avasarala, 1993). This database consisted only of concrete piles that are mostly from Florida. One objective of this research was to establish a new database with load test results from other geographic areas. In order to update the database, more pile load test results, which included 10 plugged steel pipe piles and 38 H-piles, were added. The new database consisted of 104 pile load test results including the original UF database. The current database was divided into three sub-database files: prestressed concrete pile file (PCPILES.WK3), steel pipe pile file (SPPFILES.WK3), and H-pile file (H-PPILES.WK3). Table 3 summarizes the number of piles with different pile types and sources.

Table 3. Number of piles in different groups of piles

Pile types	Number of piles	Sources
PCP	56	UF
SPP	10	UDOT
H-P	38	PDOT
Total	104	

The first sheet (Sheet A) of each sub-database file is a directory of all the piles in the corresponding files. The directory contains a table of contents and a summary table. Sheet B is the macro sheet including macros designed to complete a number of Lotus commands with only a few steps. The third sheet is the template sheet, which is the standard format for every pile sheet.

Individual Pile Data Sheet

An individual pile data sheet is to accept pertinent information such as pile data, load test results, and in situ test results. The individual pile sheet was designed to include all the information required by the computer programs. Additional information, such as cone penetration test results and pile-driving data, were retained for possible future use.

The load-settlement data were very important to this research. Based on the load-settlement curves, the Davisson ultimate capacities were determined and compared with the predicted ultimate capacities as calculated from the SPT91 and SPILE programs. The Davisson criterion is a graphical method to define the ultimate pile capacity from the load-settlement curves. The Davisson ultimate capacity is the load corresponding to the movement, which is the total amount of the elastic compression of the pile and a value of 0.15 inches plus the factor equal to 0.1 times the pile diameter in feet.

EVALUATION OF PREDICTED CAPACITIES

General

This section compares the measured ultimate capacities, according to the Davisson criterion from the load-settlement curves, with the predicted ultimate capacities, calculated from two computer programs (SPT91 and SPILE) that use in situ test results. For different groups of piles, comparisons were presented in plots. Since the University of Florida has

addressed the comparisons of prestressed concrete piles, this research focused on the steel pipe pile results of the UDOT and the H-pile results of the PDOT.

Comparisons According to Pile Types

For 10 steel pipe piles, Figure 3 shows that the average of the ratios of the predicted SPT91 capacities to the measured Davisson capacities is 0.50. Observation of the data reveals that the SPT91 determination is conservative. Figure 4 illustrates the comparison of SPILE capacities with Davisson capacities, and the average ratio is 0.77. The results of H-pile comparisons are shown in Figures 5 and 6. For H-piles, the average of the ratios indicates both SPT91 and SPILE are overpredicted.

Comparisons According to Soil Types

Consideration of the load transfer mechanism shows that the skin friction resistance is fully developed before much of the load gets to the pile tip at the bearing layer. Referring to bearing piles, which were driven to bearing layers with potential ultimate bearing capacities, Schmertmann (1967) mentioned that the bearing piles might be bearing piles in theory, but they were friction piles in practice. The comparisons according to soil types were essentially based on the types of friction soils supporting the major part of the applied load.

Figures 7 and 8 show the plots of H-piles in sand, although the number of H-piles is not adequate to support the average ratio. For silt, Figures 9 and 10 show the comparisons of H-piles. In Figure 9, most points lie above the 45-degree line. Also with an average ratio of 1.88, the SPT91 capacities are unconservative. Figure 10 shows the SPILE computer to be very unconservative. For clayey soil, Figures 11 and 12 present the graphic forms of comparison of 10 steel pipe piles. The 10 pipe piles are not adequate to obtain any meaningful statistical results, but all the points of Figure 11 lie below the 45-degree line, indicating that the SPT91 method is conservative in clay.

DISCUSSION AND SUMMARY

Discussion

The calculated or predicted ultimate capacities are not the actual ultimate capacities. Based on the load transfer mechanism, the calculated ultimate capacities are higher than the real ultimate capacities. The real ultimate capacity of a single pile should be the failure load applied on this single pile. Generally, the failure load was obtained from the load-settlement curves of pile load test results.

Fellenius (1975) defined the peak point of the load-settlement curves, from the Constant-Rate of Penetration method (CRP), as the ultimate capacity of a pile. However, such a peak could only be clearly defined from friction piles in soft or loose soils. For load-settlement curves without the "clear peak," some simple approaches were proposed to find the failure load. Fellenius summarized several methods of determination of the failure load. In Fellenius's report, the value of the Davisson method was the lowest one of six methods. The Davisson method is proposed for application on load test results from Quick Maintain Load Tests only. Peck, Hanson, and Thornburn (1974) believed that the Davisson capacity was conservative because both the Davisson method and Quick ML Tests did not take into account the consolidation settlements and creep effects.

For SPT91, depths, N-values, and soil types are enough to perform the calculations. For SPILE, the unit weight of soils, the depth of ground- water, and the undrained shear

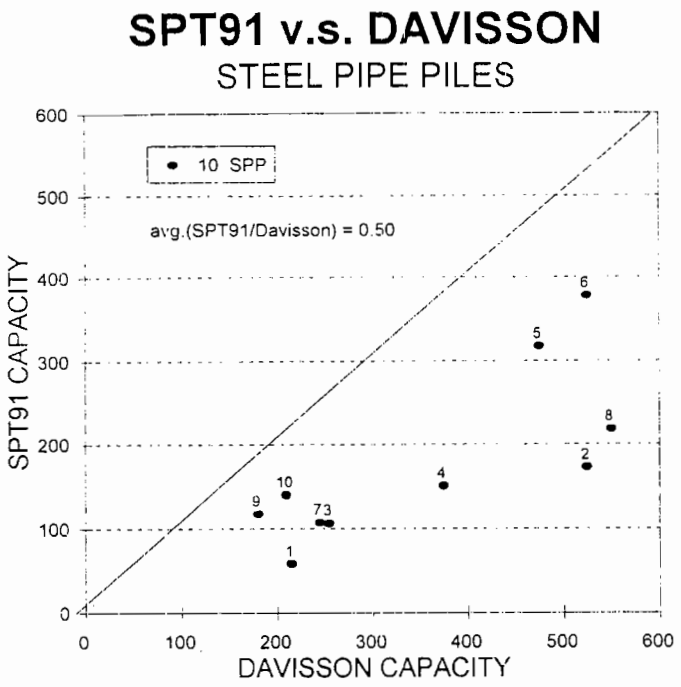

Figure 3. Graphic comparison of SPT91 predicted vs. Davisson measured ultimate capacities for steel piles.

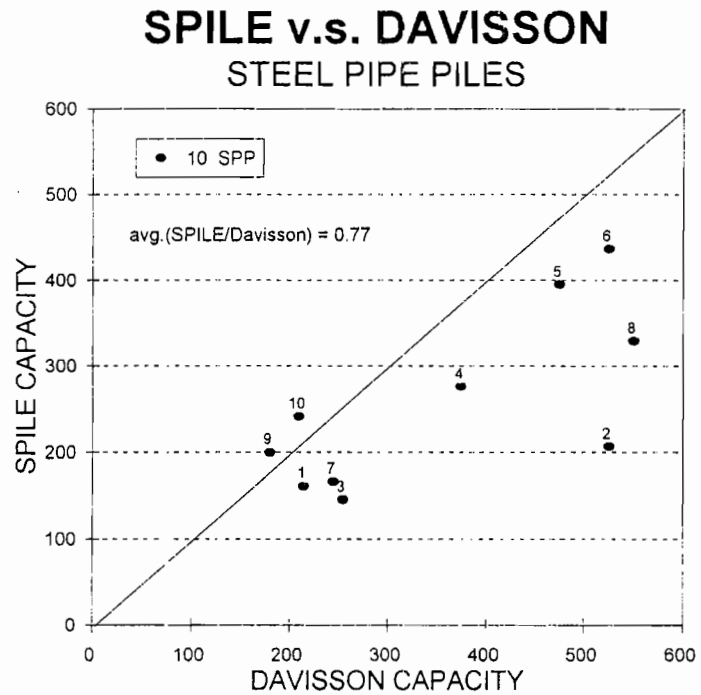

Figure 4. Graphic comparison of SPILE predicted vs. Davisson measured ultimate capacities for steel piles.

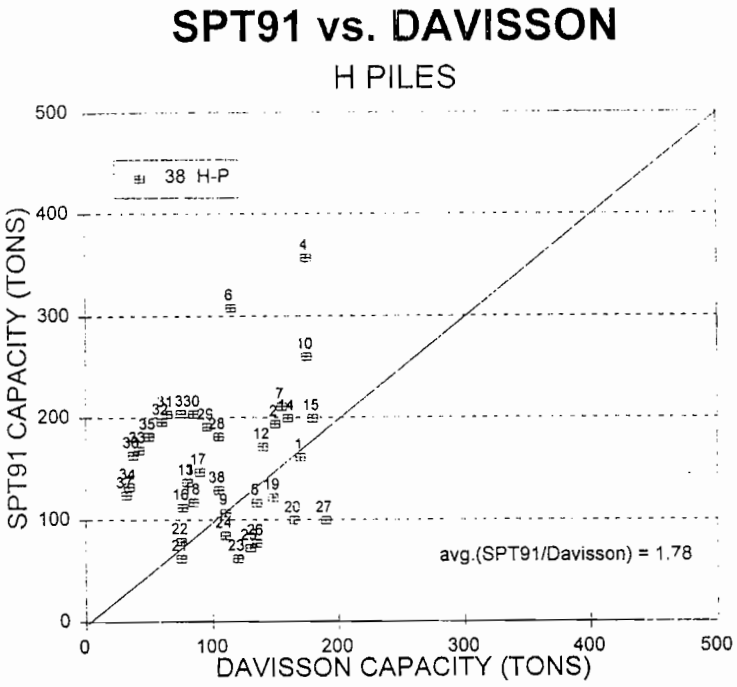

Figure 5. Graphic comparison of SPT91 predicted vs. Davisson measured ultimate capacities for H-piles.

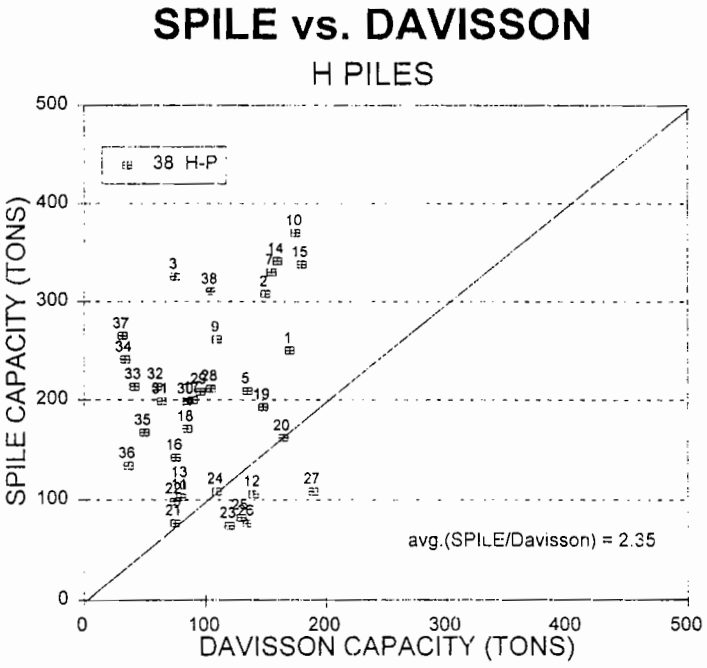

Figure 6. Graphic comparison of SPILE predicted vs. Davisson measured ultimate capacities for H-piles.

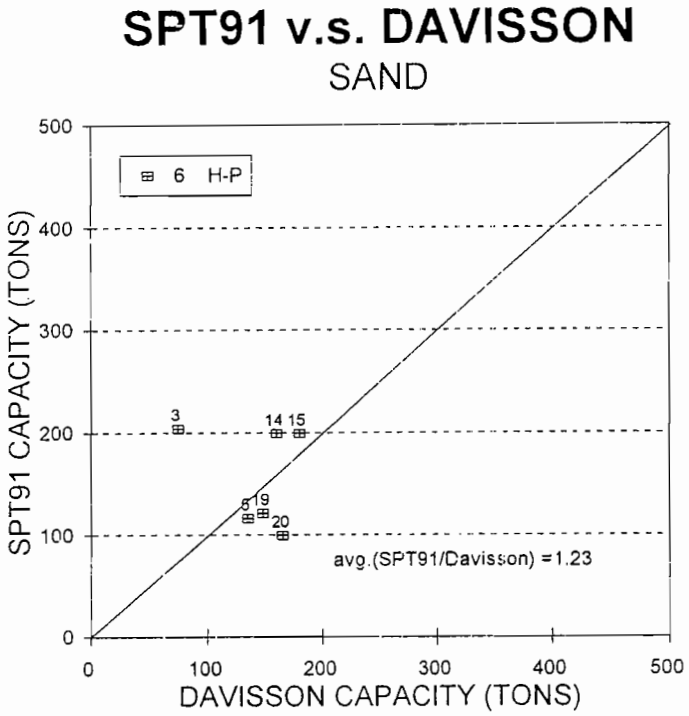

Figure 7. Graphic comparison of SPT91 predicted vs. Davisson measured ultimate capacities for H-piles in sand.

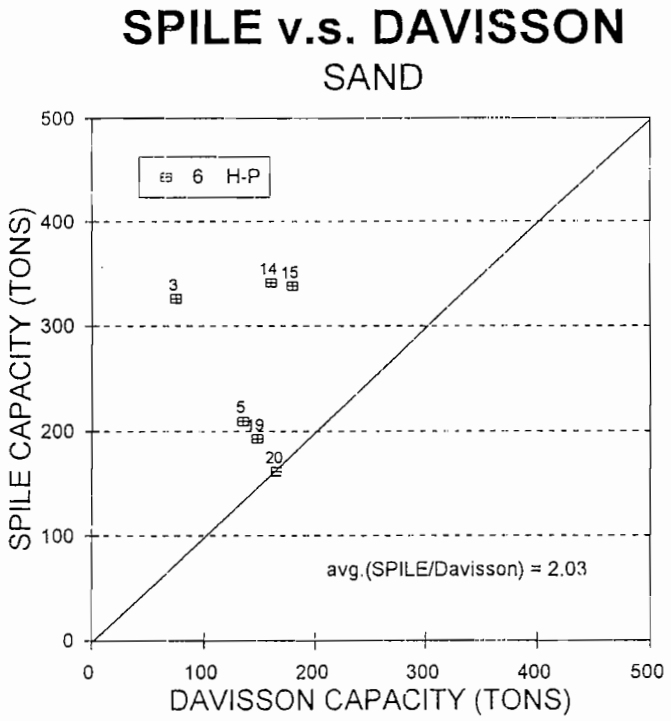

Figure 8. Graphic comparison of SPILE predicted vs. Davisson measured ultimate capacities for H-piles in sand.

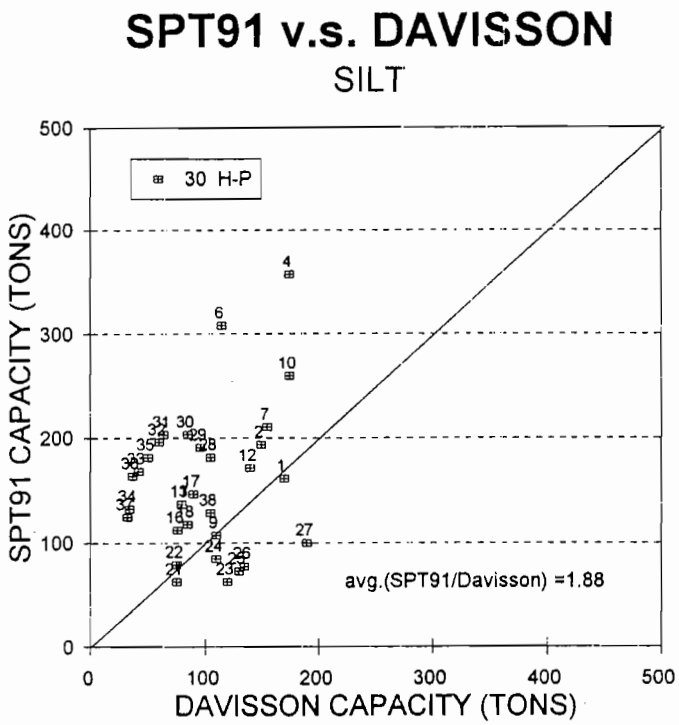

Figure 9. Graphic comparison of SPT91 predicted vs. Davisson measured ultimate capacities for H-piles in silty soil.

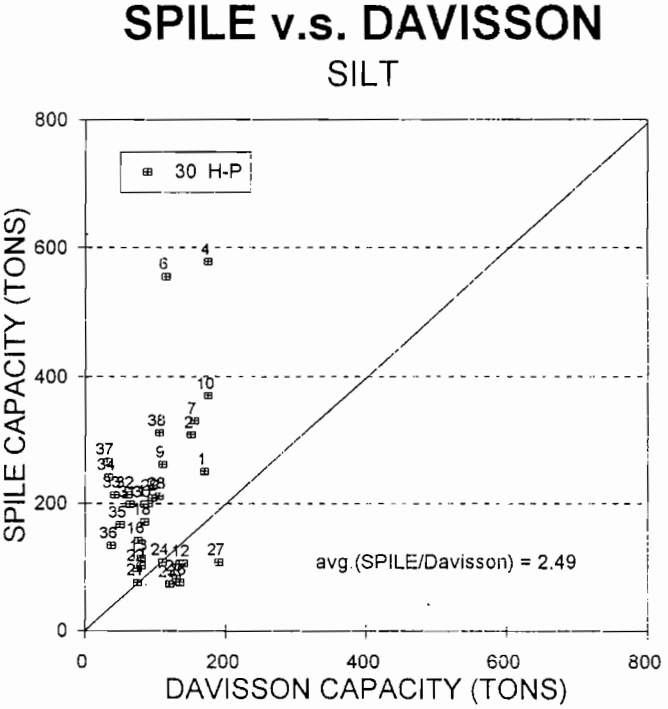

Figure 10. Graphic comparison of SPILE predicted vs. Davisson measured ultimate capacities for H-piles in silty soil.

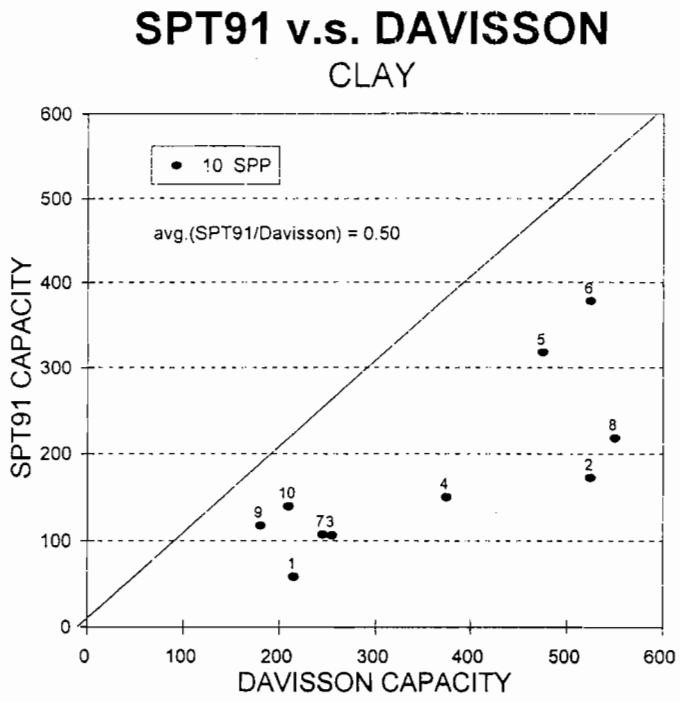

Figure 11. Graphic comparison of SPT91 predicted vs. Davisson measured ultimate capacities for pipe piles in clay.

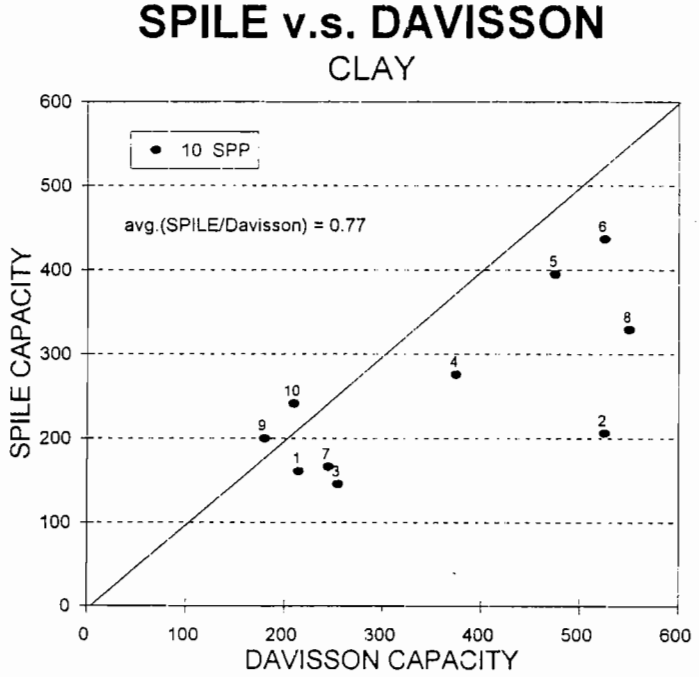

Figure 12. Graphic comparison of SPILE predicted vs. Davisson measured ultimate capacities for pipe piles in clay.

strength of clay or the internal friction angles of sand are necessary for the calculations of capacities. Due to the lack of those parameters, judgment was used to choose reasonable values according to the correlation of N-values and soil parameters. The N-values were strongly influenced by operation and equipment. Human error and inappropriate test procedures will result in some look-alike anomalous N-values. Based on these "representive" N-values, the soil parameters are very vulnerable and uncertain.

Summary

The pile database established at the University of Florida has been updated by adding 48 pile load test results. The current database consists of a total 104 pile records. During research, the database has been used to evaluate two computer programs, SPT91 and SPILE. The load-settlement data were stored in the database, and were used to determine the measured ultimate capacities employing the Davisson criterion.

The SPT91 program gives a conservative estimation of the ultimate capacities of steel pipe piles in clay. The average of the ratios of SPT91 capacities to Davisson capacities is 0.5. The SPT91 program shows unconservative predictions of the ultimate capacities of H-piles in silt. The average of the SPT91/Davisson ratios is 1.78.

The SPILE program shows overpredicted results in H-piles in silt. The average of the ratios of SPILE/Davisson is 2.49. On the other hand, the SPILE program underpredicted the steel pipe piles, as the average ratio is 0.77.

The Tomlinson's adhesion factor method used in the SPILE program for clay is very unconservative, especially in the soil profile containing thin, stiff clay with overburden sand layers. The corrections used to determine the undrained shear strength, according to the SPT N-values, are too wide to approximate. This factor may affect the accuracy of SPILE predictions in stiff layers.

REFERENCES

Avasarala, Swamy Kumar V. 1993. Pile load test database and an evaluation of the SPILE and UNIPILE programs. Unpublished MS thesis. University of Florida.

Bartholomew, M., Joseph A. Caliendo, P Lai, and K Graham. 1991. Static pile bearing analysis program SPT91 - User's Manual. Structure Design Office, FDOT.

Cheney, R. S., and R. G. Chassie. 1982. "Pile capacity - static analysis." Soils and Foundations Workshop Manual. U.S. Department of Transportation, FHWA.

Davidson, John L. and Frank C. Townsend. 1993. Maintenance of load test bases. Department of Civil Engineering, University of Florida.

Dixon, B. G., L. R. Anderson, R. Rahman, and E. Keane. 1992. "Estimation of ultimate capacity of piles in the utah region by dynamic methods." The 28th Symposium on Engineering Geology and Geotechnical Engineering. Boise, Idaho.

Fellenius, B. H. 1975. "Test loading of piles and new proof testing procedure." Journal of the Geotechnical Engineering Division. ASCE.

Meyerhof, G. G. 1976. "Bearing capacity and settlement of pile foundation." Journal of the Geotechnical Engineering Division. ASCE.

Nordlund, R. L. 1963. "Bearing capacity of piles in cohesionless soils." Soil Mechanics & Foundations Journal. ASCE.

Nordlund, R. L. 1979. "Point bearing and shaft friction of piles in sand." 5th Annual Fundamentals of Deep Foundation Design. University of Missouri-Rolla.

Peck, R. B., W. E. Hanson., and T. H. Thornburn. 1974. Foundation engineering. 2nd ed., John Wiley & Sons, Inc., New York.

Pennsylvania Department of Transportation. 1989. Compilation of pile load test and wave equation information. PUB 15A. Harrisburg, PA.

Schmertmann, J. H. 1967. Guidelines for use in the soils investigation and design of foundations for bridge structures in the state of florida. RB-121. FDOT.

Thurman, A. G. 1964. Computed load capacity and movement of friction and end-bearing piles embedded in uniform and stratified soil. Ph.D. Dissertation. Carnegie Institute of Technology.

Tomlinson, M. J. 1979. Pile design and construction practice. Viewpoint Publications, Cement and Concrete Association, London.

Tomlinson, M. J. 1985. Foundation design and construction. Longman Scientific and Technical, Essex, England.

Urzua, Alfredo. 1993. SPILE: A microcomputer program for determining ultimate vertical static pile capacity. FHWA-SA-92-044. U.S. Department of Transportation, FHWA.

Performance of Shallow Spread Footings on Geogrid Reinforced Sand

Michael Adams, Federal Highway Administration
Washington, D.C.

Recently, a series of experiments were performed to evaluate the performance of shallow spread footings on sand reinforced with geogrids. These experiments, which were performed in the foundation test pit at the Federal Highway Administration's Turner-Fairbanks Highway Research Center, were undertaken to evaluate the benefits and to optimize the design of simple geogrid reinforced sand-spread footing systems.

Load tests were performed in a 5.5 m x 7.0 m x 6.0 m deep test pit. To date, four geogrid reinforcement test series have been performed. In each series the sand was excavated and replaced in 0.3 m lifts. Each lift was compacted with a vibratory plate tamper to a specified target density. Sand density was tested with a nuclear density gauge.

Four spread footings models ranging from 0.3 m x 0.3 m to 1.0 m x 1.0 m in size were used for the experiments. In each test series, approximately five load tests were performed. All spread footings were tested on surface of the sand with zero embedment. In three of the test series, a control spread footing was loaded without reinforcement. Results from the control test were used to correlate results between test series and to evaluate overall performance. Data collected for each test included load and settlement at each corner of the spread footing and reinforcement configuration beneath each spread footing. Numerous load tests were performed with variations in the area and spacing of the grid layers. A maximum number of three geogrid layers were used to remain within economic limits and to be competitive with other ground improvements techniques.

Results indicate that soils reinforced with geogrids can significantly increase the bearing capacity and reduce the differential settlement of axially loaded spread footings on low relative density fine grained soils. Additionally, some reduction in elastic deformation was noted in the experiments. Although more experiments are planned, it is reasonable to conclude that geogrid reinforced soil should be considered as an economic solution for poor foundation support in fine grained low relative density sands, or at least as a safety net to prevent structure collapses due to bearing capacity failure.

FIELD APPLICATION AND INSTRUMENTATION OF EXPANDED POLYSTYRENE BLOCKS AS BRIDGE BACKFILL

Terje Preber, Associate Professor
Sangchul Bang, Professor
South Dakota School of Mines & Technology
Rapid City, South Dakota

ABSTRACT

Expanded Polystyrene (EPS) blocks were installed as bridge abutment backfill on I-90 in Wyoming as part of a full scale instrumented field test. The purpose of the study was to evaluate the behavior of EPS Blocks as bridge abutment backfill under high traffic loads.

Two layers (four feet) of 1.5 pcf type EPS blocks were placed across the entire roadway on both abutments, and to a distance of 35 feet from the abutments. The blocks were placed on a level surface of gravel. After installation, a polyethylene membrane and one foot of sand backfill were placed above the blocks. A concrete apron was then poured above the sand to a distance of 25 feet from the abutment, with asphalt pavement butting up against the slab. Settlement plates were placed on the gravel at the bottom of the blocks, in between the two EPS layers, and at the top of the EPS blocks. In addition, devices for measuring lateral displacements were placed near the abutments, and were connected with readout stations on the inside of the bridge abutments.

Lateral displacements and settlements were measured for a period of one year, and showed settlements on the order of 2 mm or less. Virtually all settlements appeared to originate from seating of the EPS blocks on the gravel and from settlement of the sand fill above the blocks. Lateral displacements (relative movement between the abutment and the EPS blocks) were 5 mm or less away from the abutment. Thus, virtually no lateral stresses were transferred to the abutment.

INTRODUCTION

The geotechnical engineering and construction industry have been seeking inexpensive light weight construction materials for backfill against retaining structures (such as bridge abutments), fill for embankments on soft grounds and/or beneath pavements, and material for slope stabilization. The use of light weight materials has been considered as a technically acceptable and economical solution to many instability and settlement problems related to weak soils.

Super light "Expanded Polystyrene Blocks (EPS Blocks)" was introduced in the road construction industry as a light weight material in 1972. A literature search indicates that the Norwegian Road Research Laboratory has constructed more than 100 projects with this material with great success. It has been reported that EPS Blocks

produce almost "zero" lateral pressure on the bridge abutment walls. EPS Blocks have also been used extensively as frost proofing layer in highways in Europe.
The first application of EPS Blocks in the United States was by the Colorado Department of Highways for the reconstruction of a 200 foot failed section of US. Highway 160 near Durango in 1987. EPS Blocks were selected mainly because the fragile slope could not support any more weight than the highway itself.

EPS is typically used as insulation and packaging material. Its density is approximately 0.196 kN/m^3 (about 1 lb/ft^3), equivalent to 1/50 of the water density. It is therefore extremely light, producing almost no gravity-induced stress, and easy to handle. It is stable chemically and not subject to decay. It is also safe against frost, has an extremely low thermal conductivity, and is therefore well suited for use as insulation material in regions with frost problems.

Because of the extremely light weight, the cost of conventional earthwork can be dramatically decreased if EPS is used. Engineering structures constructed with EPS Blocks are expected to experience less stresses than the ones constructed with conventional techniques, resulting in substantial savings in construction industry.

PROJECT DESCRIPTION

The purpose of this project was to provide pertinent technical information related to the field application of EPS Blocks, so that the material can be used with confidence among geotechnical and construction engineers. The research consisted of three different tasks. Task 1 was to perform a laboratory testing program to determine the basic engineering properties, while Task 2 was to perform an analytical study. Task 3 was to install a full scale instrumentation backfill and to perform long term monitoring of it's performance.

Task 1 provided information on material compressive, tensile, flexural and shear strengths, and Young's modulus and Poisson's ratio for different density EPS materials. Also, constitutive relationships (stress -strain relationship) and long term stress - strain behavior (creep) were determined. The creep testing has been going on for a year and is still in progress. To date, the results show that the creep deformation, under the estimated working stress, is approaching a linear relationship with the logarithm of time, and that the creep deformation is on the order of 0.6 percent over one log cycle of time in years. Thus, for the next 20 years, total creep deformation is estimated at 0.8 percent. Behavior under repeated loads was also observed and found to be virtually negligible under working stress conditions. From the strength testing it was found that, depending on the unit weight of the EPS material, the compressive strengths ranged from 14.4 to 168 kN/m^2 (300 to 3,500 psf.) Deformation characteristics were also found to be similar to those of soil, with Young's modulus in the range of 958 to 7660 kN/m^2 (20,000 to 160,000 psf) in the initial range (up to 1.2 to 2.0 percent axial deformation), and from 168 to 600 kN/m^2 (3,500 psf to 12,500 psf) for the plastic range. Thus the material possesses a distinct bilinear stress-strain relationship, with the compression modulus decreasing to approximately one tenth of the initial modulus after approximately 2.0

percent deformation. The volume change characteristics indicate that Poisson's ratio varies from 0.2 for low stresses to less than -0.3 at high stress levels. Any vertical loading will therefore result in small to negligible, or even negative lateral deformation, thereby essentially negating any lateral pressure against walls.

Under Task 2 the proposed approach slab was analyzed with EPS blocks directly underneath the concrete pavement. The details of the finite element analysis are described in a companion paper entitled, "Evaluation of Expanded Polystyrene Block Bridge Backfill by Finite Element Method of Analysis."

The results of the analysis showed that maximum downward displacement of pavement was calculated to be 10 mm (.39 in.), of which 5 mm (.22 in.) was contributed by the EPS material. Maximum compressive stress within the EPS blocks was 24.5 kN/m^2 (511 psf.)

The analysis showed that the lateral stress developed against the abutment at the top was 30 psf, while the bottom section showed separation between the wall and the EPS blocks.

APPROACH

As a follow-up to the analytical study (Task 2), a full scale instrumented field test was made at the two bridge abutments on the eastbound lane of Moorcroft-Sundance Road at Milepost 157.62 (Project IM-90-4(98)155) in the State of Wyoming. The project consisted of installing EPS blocks in lieu of backfill with reinforcing fabrics behind the bridge abutments and under the approach slabs.

Two layers of 0.236 kN/m^3(1.5 lb/cu. ft.) EPS blocks were placed across the entire roadway. The bottom layer was placed to a distance of 10.4 m (34 feet) from the abutment, while the top layer was placed to a distance of 10.7 m (35 feet) from the abutment. Thus EPS blocks were placed under the entire approach slab, and extended a distance of 10 feet beyond the approach slab. In order to minimize stress concentration arising in the event of cracking of the approach slab, 30.5 cm (12 inch layer) of sand was placed between the concrete approach slab and EPS blocks. An impermeable plastic membrane was also installed between the EPS blocks and the sand to prevent loss of fines into openings between the blocks, to minimize puncturing of the EPS blocks by the sand, and to possibly keep deleterious substances away from the EPS. The membrane was wrapped up against and tacked to the abutment wall, such that sand would not fall in between the EPS blocks and the abutment. In order to provide adequate friction between the EPS blocks, timber fasteners were to be placed between adjoining surfaces. However, the timber fasteners did not arrive in time, hence 4 inch diameter rings made from barbed wire were used and appeared to function satisfactorily. One ring was placed for every four square feet of contact area. The proposed construction layout used is shown in Figures 1 and 2.

Special consideration was to be given to the bedding surface for the EPS Blocks. The original plan called for a thin bedding layer of fine to medium sand. The surface of the bedding layer was to be sufficiently level such as neither to induce additional stresses due to bending of the EPS Blocks, nor areas of concentrated contact stress.

However, the Wyoming Department of Transportation decided to use 25 to 50 mm (1 to 2 inch) size crushed rock at the east abutment and pea gravel at the west abutment.

Field measurements included 1) deformations within the EPS Blocks at three levels behind the abutment wall one inch from the wall, 2) movements behind the abutment wall five inches from the wall, and 3) short and long term vertical deflections of the approach slab. The proposed instrumentation is shown schematically in Figures 3 and 4.

There were no problems related to installation. As stated previously, the bedding material provided for the EPS blocks were not as specified, and it was feared that settlements caused by the gravel penetrating the blocks upon loading would lead to excessive settlements. Installation of the anchor plates for the horizontal measurement devices posed some problems, as a snug fit within the EPS blocks proved difficult. Originally, a groove was cut for the measurement rods, then the plates were heated and forced into the EPS block. As the EPS melted around the plate, a snug fit of the plate was not fully obtained. On the west abutment, groves for the plates were cut using an electric chain saw, resulting in a good seating.

Due to the roughness of the abutment surface, the EPS blocks could not be placed level with the abutment wall surface. Overall, a gap of approximately 10 mm was left between the wall and the EPS blocks.

FIELD MEASUREMENTS

After completion of the construction, initial readings of all instrumentation were taken. However, base readings for the vertical movements (settlements) could not be taken until paving was completed.

Initially, readings were to be taken at weekly intervals for the first month and monthly thereafter. However, the rate of movement proved to be slow, and the surveying time interval was increased to biweekly after the first set of readings for a period of three months, and were then planned for monthly thereafter. However, heavy snowfall and icy roads resulted in cancellation of several readings over the winter for safety reasons. Settlement measurements were also prevented due to freezing of water in the cups around the settlement monuments.

DISCUSSION

East Abutment

Lateral Movements

The lateral movements at the east abutment are shown in Figures 5 and 6. The results show a relative movement away from the abutment for the first four months, followed by an apparent movement towards the abutment. The trend is the same for both monuments located one inch from the abutment wall as five inches from the wall. Maximum relative movement was measured to be approximately 5 mm away from the wall and 3 mm towards the wall. Thus, based on the movements, contact between the EPS blocks and the

abutment wall has not taken place. The initial trend of movements away from the wall is in accordance with the predictions, as the blocks would cave laterally upon vertical loading since Poisson's ratio may reach a negative value. However, the continuing trend of movements towards the abutment through the following spring and summer cannot be explained this way. It is felt that the observed relative movements were the result of thermal effects, as the culvert deck underwent shrinkage as the temperature decreased towards the winter, and then expanded as the temperature increased during the spring and summer. Based on calculations for temperature expansion and contraction, a variation in culvert deck length could easily approach 5 to 10 mm. Such movements are well within the range of those measured. The measurements on the east abutment also show considerable scatter. It is felt that the scatter in part may have originated from the seating problems experienced with the anchor plates. Due to the problem with anchor plate seating, the plates may have been susceptible to shifting as caused by traffic induced vibrations.

Vertical Movements

The records of the vertical movements are shown in Figure 7. The settlements at the east abutment were on the order of 2 mm, which were well below those predicted. Transient movements, as measured by dial gage fluctuation under traffic was on the order of 1 mm. The permanent settlements represent compression of the full depth of EPS and the base material under the pavement for the bottom monument, and compression of the upper two feet of EPS and the base material for the middle monument, and compression of the base material for the upper monument. The upper monument indicates that the base material has compressed a total of one millimeter, while the upper two feet of EPS have compressed only fraction of a millimeter. However, the lower two feet of the EPS appears to have compressed an additional millimeter. This movement appears to have taken place between the initial and the first sets of measurements, indicating that the lower EPS seated quickly into the gravel following loading. Compression of the granular base under the pavement also took place early. Thus, except for the deformation caused by seating of the EPS in the gravel, only negligible compression of the EPS blocks appear to have occurred.

West Abutment

Lateral Movements

The lateral movements at the west abutment are shown in Figures 8 and 9. The overall movements recorded indicates a negligible movement away from the wall, while 5 mm movement was recorded towards the wall during the summer of 1994. The records show that the same trend in movement as observed at the east abutment is also evident at the west abutment, with an initial apparent separation between the abutment and the EPS blocks followed by a narrowing of the gap between the wall and the EPS.

Vertical Movements

The vertical movements at the west abutment are show in Figure 10. The maximum settlement recorded was on the order of 1 mm, and was again recorded for the relative movement between the pavement and the bottom layer of EPS blocks. At this location, the EPS blocks were placed on pea gravel, which is felt to have resulted in less seating movement. Also, no compression of the upper two feet of EPS appear to have taken place, as the difference in movement between the top monument seated on top of the upper EPS blocks and in between the blocks was less than 1/4 mm. Also, most movements appeared to occur within the first 100 days, hence long term movements appear to be negligible.

CONCLUSIONS

The EPS block backfill appear to be functioning satisfactorily, with no pressures building up against the abutment, as the gap between the EPS blocks and the abutment wall has not closed sufficiently to make contact. Settlements of the approach slab has been less on the order of 2 mm or less, with half of the settlement resulting from compression of the granular base.

Based on the results of the monitoring, it appears that the compression of the EPS blocks have been negligible, and that the major contribution to the settlement of the pavement is seating of the EPS blocks against the gravel bedding material and compression of the granular base material under the concrete apron. Lateral movements appear to be overshadowed by the movements of the abutment resulting from thermal expansion and shrinkage of the culvert deck.

ACKNOWLEDGMENT

The authors wish to express their gratitude to the South Dakota Governors Office of Economic Development for sponsoring the project, and to Benchmark Foam, Inc. and Mr. John Devine for the ideas regarding the project and for sharing the cost of the project. The authors also wish to thank the Wyoming Department of Transportation for being receptive to the project and for their outstanding assistance and support during the execution of the monitoring phase of the project.

REFERENCES

1. H. Skuggedal and R. Aaboe. *Temporary Overpass Bridge on Expanded Polystyrene.* Seminar on the Use of EPS in Road Construction, Oslo, Norway, June, 1991.
2. T. A. Coleman. Polystyrene Foan is Competitive, Lightweight Fill. *Civil Engineering*, ASCE, February 1974.

3. T. E. Frydenlund. *Expanded Polystyrene - A Lighter Way Across Soft Ground.* Internal Report, Norwegian Road Research Laboratory, May, 1991.
4. O. Myhre. *Regarding Possible Standardization of Polystyrene blocks.* Seminar on the Use of EPS in Road Construction, Oslo, Norway, June, 1991.
5. BASF Corporation. Technical Bulletin E-3, Chemicals Division, Parsippani, NJ, 1993.
6. L. Rutz. *Expanded Polystyrene as an Embankment Alternative for Highway Slope Failures.* A Report by Colorado State Department of Transportation, Project No. MP20-0160-30, 1987.

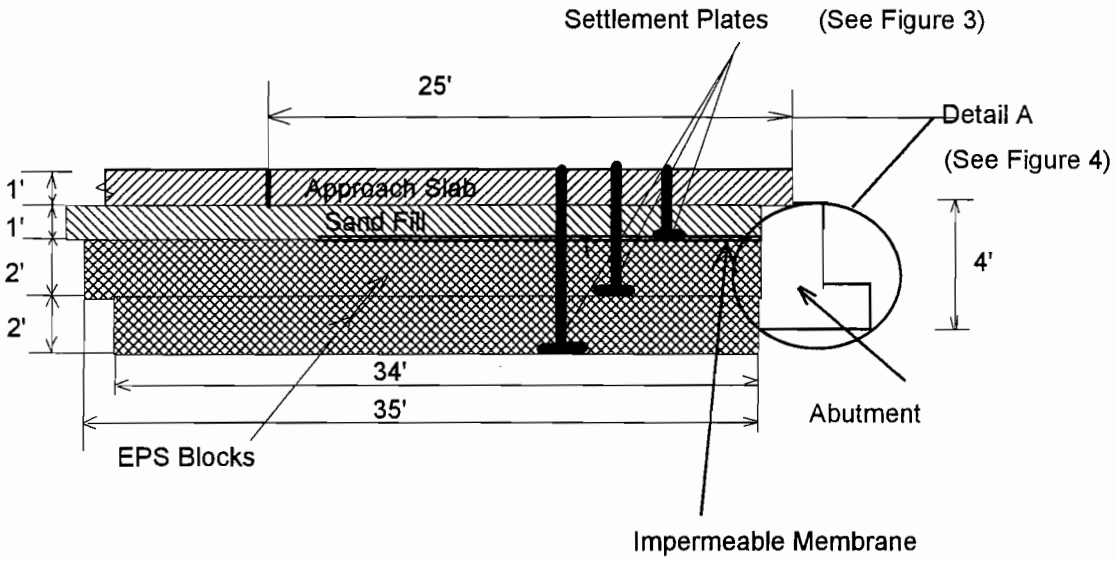

FIGURE 1. VIEW THROUGH CENTERLINE SECTION

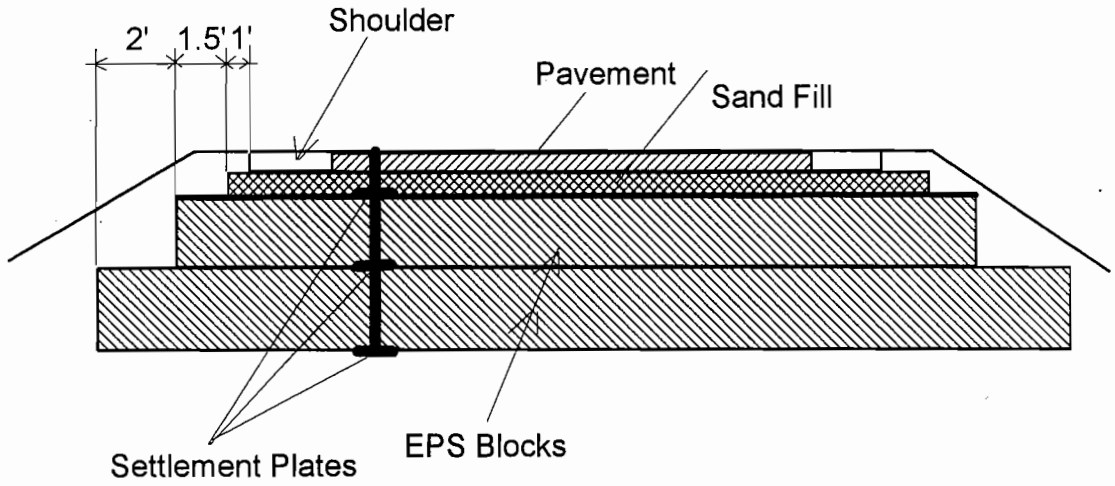

FIGURE 2. CROSS SECTION

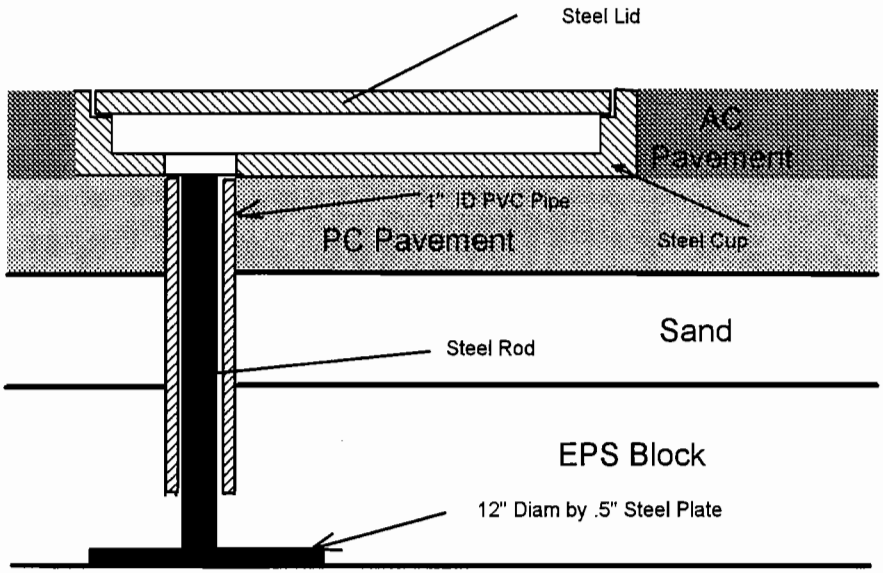

FIGURE 3. DETAIL OF SETTLEMENT PLATE

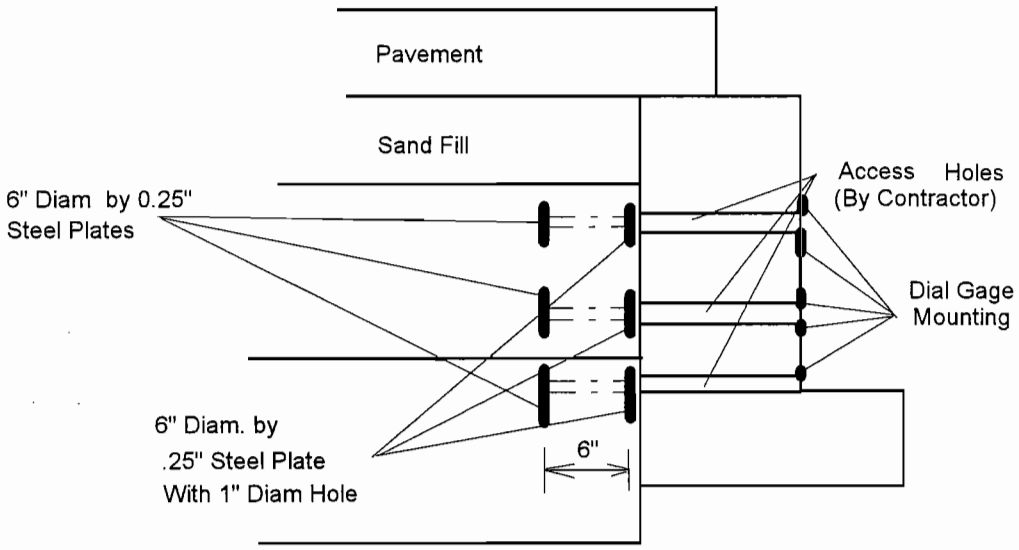

FIGURE 4. DETAIL OF ABUTMENT INSTRUMENTATION

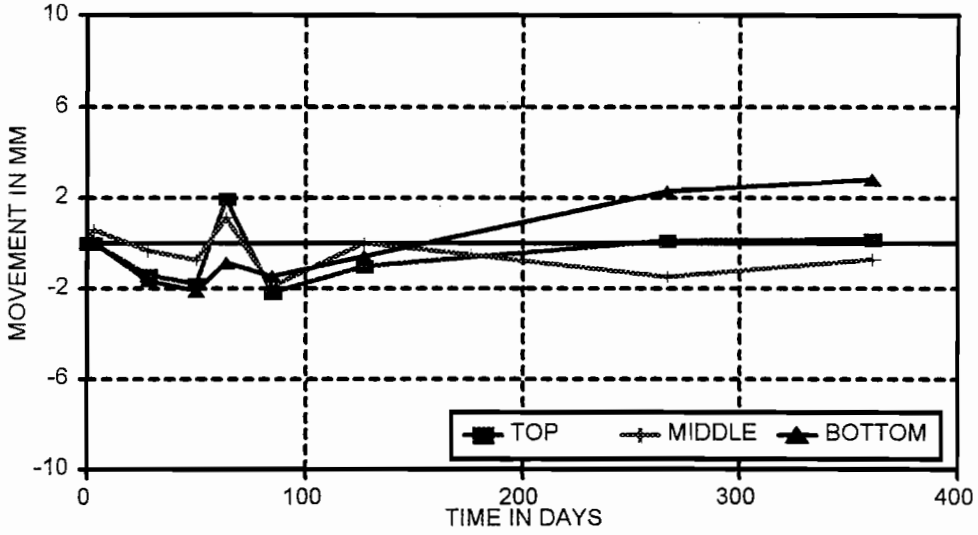

FIGURE 5. LATERAL MOVEMENTS AT EAST ABUTMENT - 1" FROM WALL

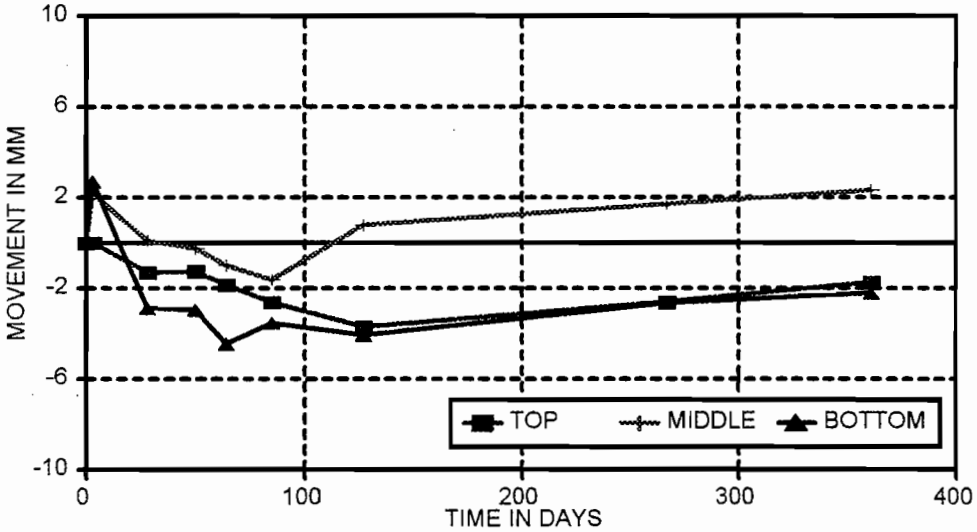

FIGURE 6. LATERAL MOVEMENTS AT EAST ABUTMENT - 5" FROM WALL

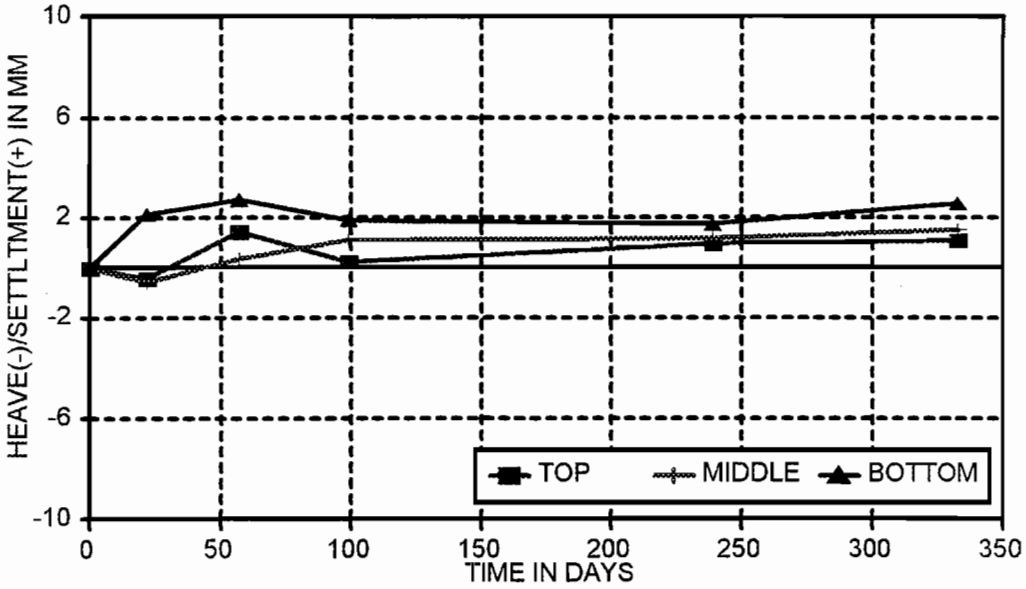

FIGURE 7. SETTLEMENTS AT EAST ABUTMENT

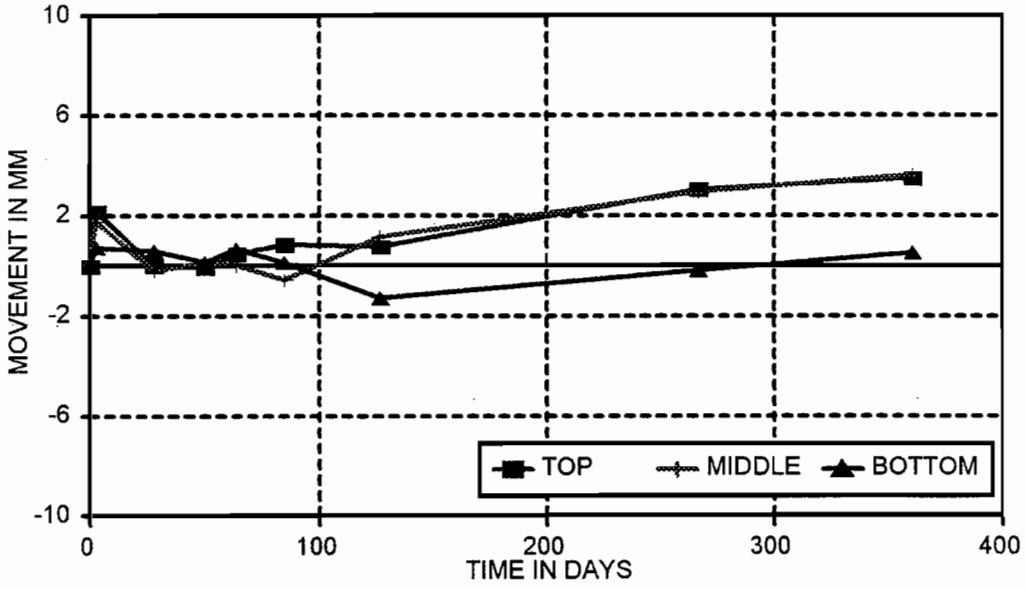

FIGURE 8. LATERAL MOVEMENTS AT WEST ABUTMENT - 1" FROM WALL

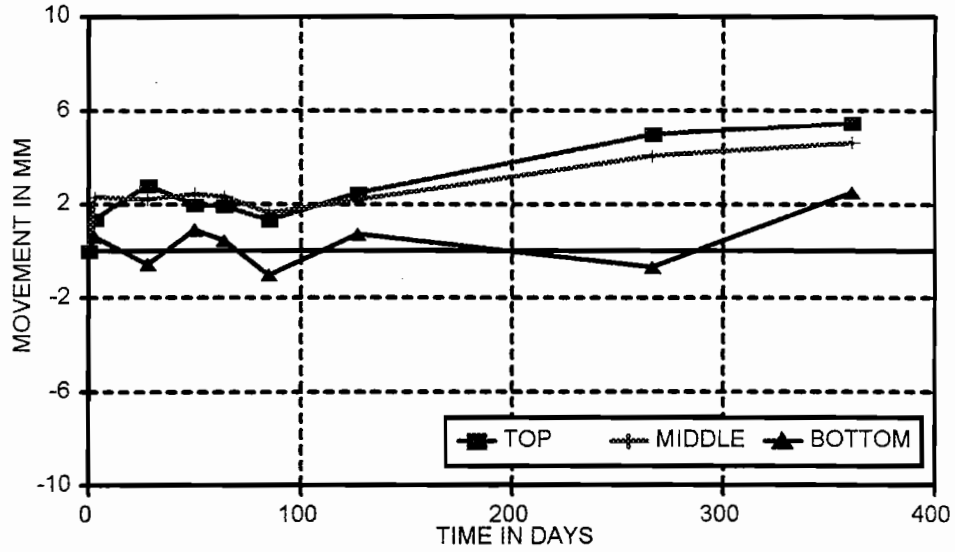

FIGURE 9. LATERAL MOVEMENTS AT WEST ABUTMENT5" FROM WALL

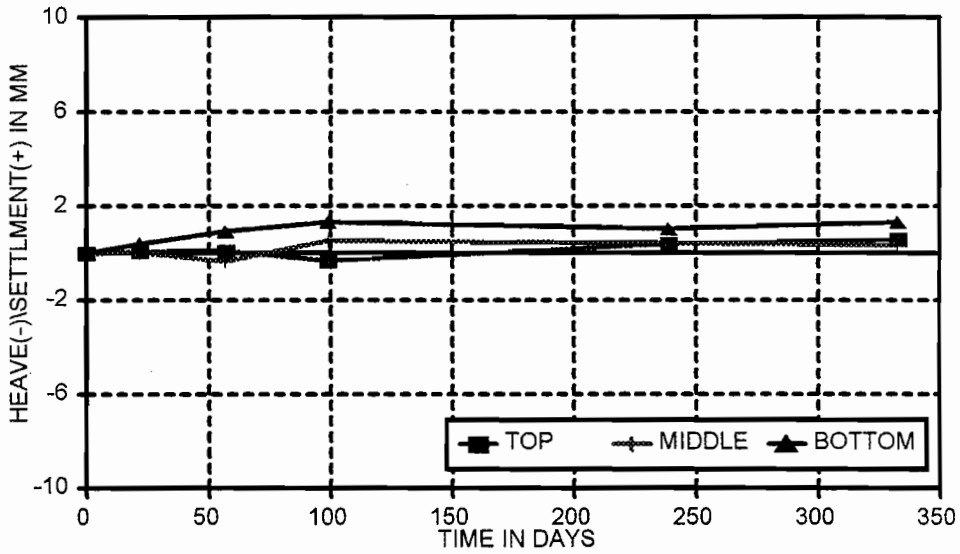

FIGURE 10. SETTLEMENTS AT WEST ABUTMENT

EVALUATION OF EXPANDED POLYSTYRENE BLOCK BRIDGE BACKFILL BY FINITE ELEMENT METHOD OF ANALYSIS

S. Bang, T. Preber and Y. Cho
Department of Civil and Environmental Engineering
South Dakota School of Mines and Technology
Rapid City, SD

ABSTRACT

Expanded Polystyrene (EPS) Blocks were installed as bridge abutment backfill on I-90 in Wyoming as part of a full scale field instrumentaion study. This paper describes the details of an analytical study that compares the results of field measurements with the predictions made from a finite element analysis.

The results of the finite element analysis compared reasonably well with the field measurements of both the vertical settlements of the approach slab and the lateral movements of the retaining wall. The finite element analysis was also found to be able to model the separation behavior of the EPS Blocks from the abutment wall.

INTRODUCTION

A field demonstration project utilizing Expanded Polystyrene (EPS) Blocks, commonly known as Styrofoam blocks, as bridge abutment backfill was initiated by the writers in cooperation with the Wyoming Department of Transportation in June, 1993. It included a full scale field instrumentation to monitor the short and long term performance of the EPS Blocks as backfill material behind bridge abutment retaining walls under heavy traffic loads. The project was located along the east bound I-90 at mileage post 157.62, near Moorcroft, Wyoming. The field instrumentation started right after the construction was completed and continued for a period of 12 months. The details of the field instrumentation results are not included in this paper, but are presented in a companion paper entitled, "Field Application and Instrumentation of Expanded Polystyrene Blocks as Bridge Backfill."

This paper describes the details of an analytical study that compared the results of field measurements with the predictions made from the analytical solution method.

METHOD OF ANALYSIS

A finite element method of analysis was adopted to analyze the detailed response of the bridge abutment system with EPS Blocks as backfill. The finite element method of analysis incorporated the detailed material behavior of EPS Blocks with various unit

weights, which typically vary from 1 to 2 pcf. They were obtained from unconsolidated undrained laboratory triaxial tests under various confining pressures. However, because of the impermeable nature of the EPS samples, the conventional triaxial test method could not be applied. The triaxial apparatus was therefore modified to measure the volume change characteristics of the EPS samples during the triaxial tests as shown in Fig - 1 (2).

The laboratory triaxial tests indicated that the stress-strain relationship of the EPS Blocks generally follow a bi-linear curve with a distinctive yield strength as shown in Fig - 2 (1, 2, 3). To characterize this observed bilinear stress-strain relationship under a given confining pressure, four parameters as shown in Fig - 3, were introduced. The definitions of these parameters, Ei, Ep, I, and Yo, are

Ei = Initial modulus
Ep = Plastic modulus
I = Intersection of axial stress axis and plastic tangent line
Xo = Strain value at the intersection of initial tangent line and plastic tangent line, which can be determined from Ei, Ep, and I.
Yo = Stress value corresponding to strain Xo.

The volume change measurements from the triaxial tests both at yield and failure strengths indicated that the Poisson's ratio starts at a positive value of approximately 0.2 and decreases as the applied stress increases and eventually becomes less than zero as shown in Fig - 4 (1, 2, 3). The negative Poisson's ratio indicates that total volume decrease may occur as the applied compressional stress increases, indicating that the EPS Blocks may separate from the adjacent material under certain loading conditions.

Because of this reason, the finite element method of analysis utilized special interface elements to model the possible separation of the EPS Blocks from the abutment stem. The interface elements possess orthotropic material properties with resistance against compressive stresses only.

The finite element grid prepared for the analysis included a 2 ft. thick bridge abutment with a 1 ft. thick concrete approach slab sitting on top of two layers of EPS block backfill with each layer being 2 ft. thick. They rested on top of a foundation soil. The analysis included the following assumptions.

1. One HS 20-44 truck load was used to simulate the traffic loading. It has three axles with 14 ft. spacing between them. Front axle load was 4 tons with the other two axle loads being 16 tons each. These axle loads were assumed to be uniformly distributed over 6 ft., which was the distance between the wheels. The final configuration in the analysis did not include the front axle load, since the length of the approach slab was not long enough to include all three axles - the length of the approach slab was 25 ft. Therefore, with a factor of safety of 1.275, two line loads with a magnitude of 6,800 lbs/ft were applied on top of the approach slab to simulate the traffic loading.

2. The foundation soil was modeled by a hyperbolic soil constitutive relationship proposed by Duncan and Chang (4) with the following parameters

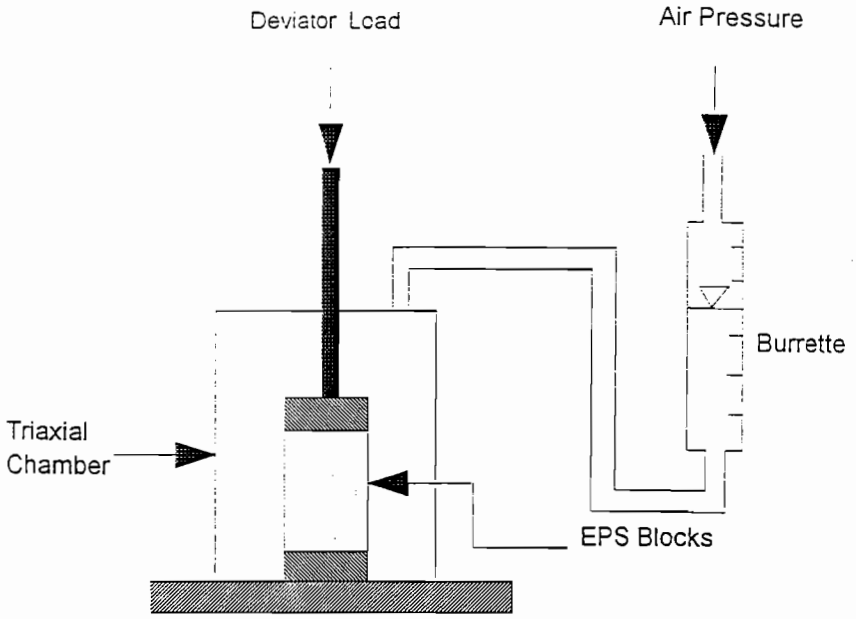

Fig - 1 Schematics of Volume Change Measurement

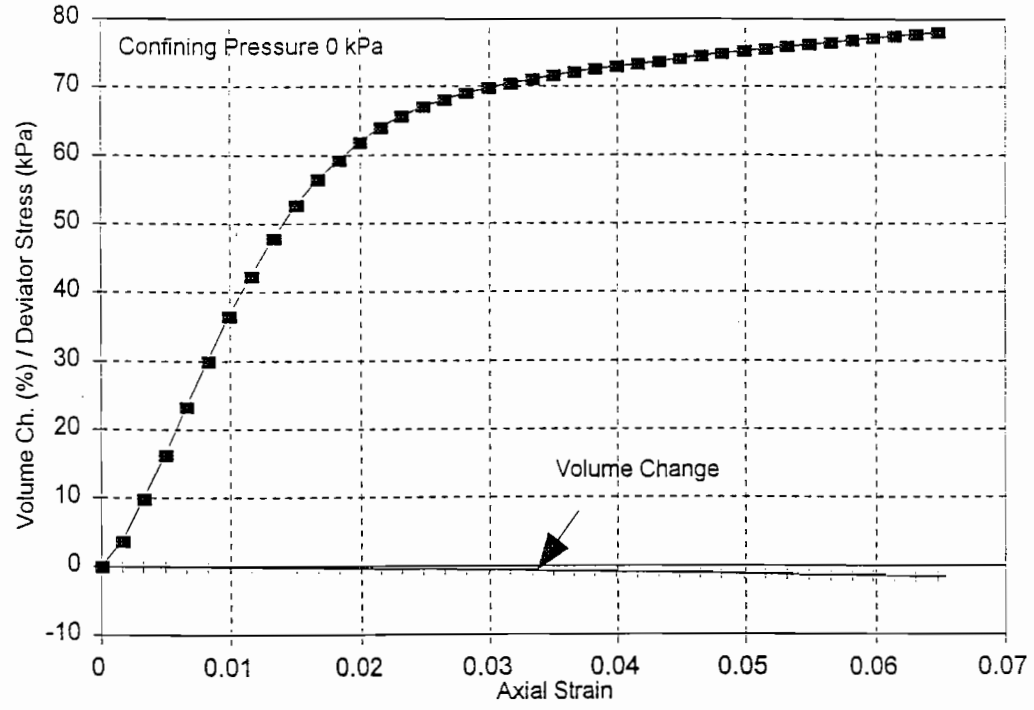

Fig - 2 Undrained Triaxial Test Results

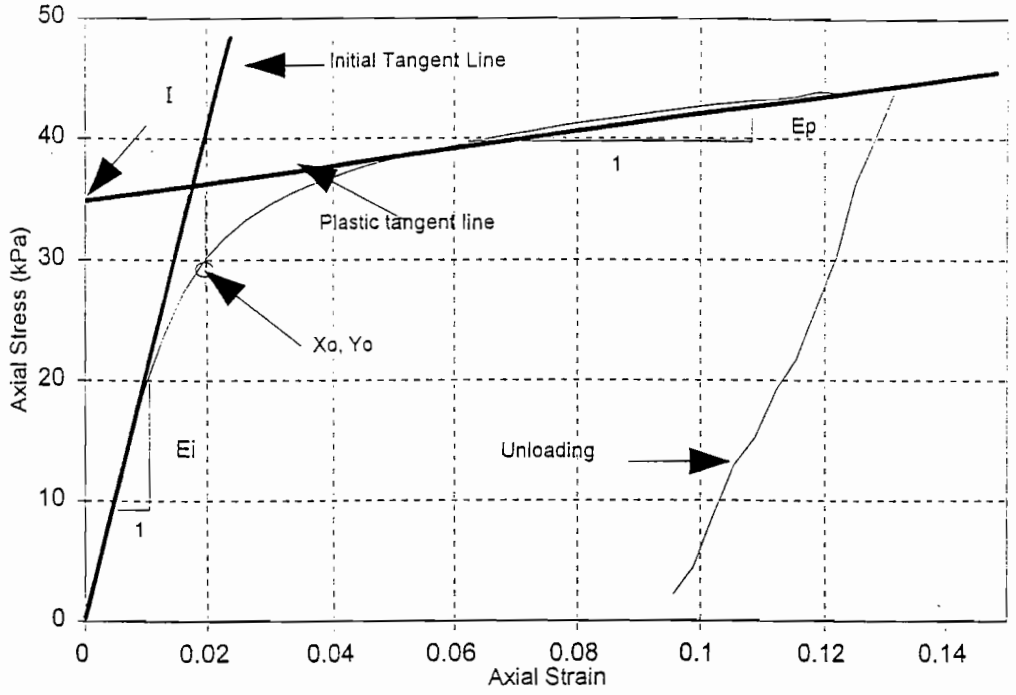

Fig - 3 Proposed Stress-Strain Relationship of EPS Blocks

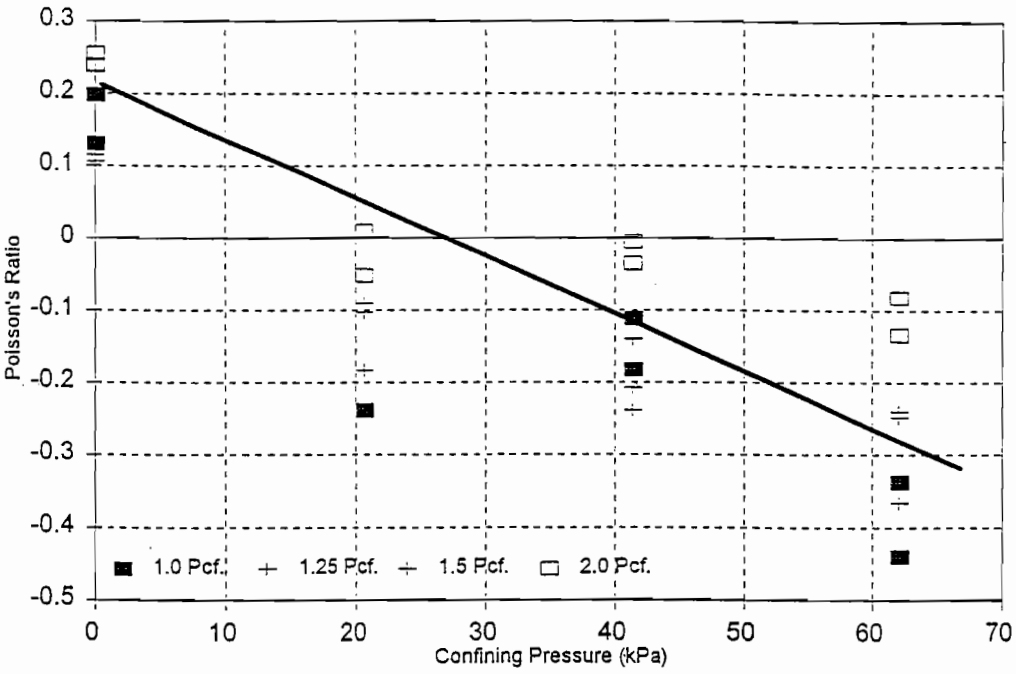

Fig - 4 Variation of Poisson's Ratio

Loading modulus =	320
Modulus exponent =	0.38
Failure ratio =	0.53
Soil Cohesion =	1,200 psf
Soil angle of internal friction =	24 degrees
Soil Unit weight =	100 pcf
Poisson's ratio =	0.25.

3. The behavior of the EPS Blocks was modeled by a bilinear stress-strain relationship with a variable Poisson's ratio. According to the laboratory tests (2), they have an initial elastic modulus of 80,00 to 105,000 psf and plastic modulus of 4,300 to 8,800 psf, depending on the confining pressure applied. The Poisson's ratio varies from 0.2 at zero confining pressure to -0.3 at confining pressure of 9 psi for all EPS material unit weights. The EPS Blocks used for the construction have a unit weight of 1.5 pcf.

4. The concrete retaining wall was modeled by linear elastic frame elements that could resist against axial forces, shear forces, and bending moments. The elastic modulus was 30,000,000 psi.

5. The approach slab concrete pavement was modeled by linear elastic continuum elements. The material properties included the modulus of 30,000,000 psi, Poisson's ratio of 0.25, unit weight of 150 pcf, and a thickness of 1 ft.

RESULTS AND COMPARISONS

The results of the finite element analysis indicated that the shape of the vertical displacements of the approach slab was concave with the maximum displacement occurring between the two line loads. The maximum downward displacement was calculated to be 0.39 inches, of which 0.22 inches and 0.17 inches were attributed to the EPS Blocks and the foundation soil compressions, respectively. At both ends of the approach slabs, the downward movements were calculated to be 0.36 inches, of which 0.18 inches was due to the compression of the EPS Blocks.

The maximum compressive stress within the EPS Blocks occurred right below the approach slab half way between the applied line loads. The magnitudes were 511 psf and 198 psf for vertical and horizontal stresses, respectively. This vertical stress resulted in a factor of safety of 3.4 - 4.8, based on the compressive strength of 1,728 - 2,448 psf for the EPS samples with a unit weight of 1.5 pcf at 5 % deformation (5). The vertical stress developed within the EPS Blocks adjacent to the retaining wall was calculated to be 198 psf. It is interesting to note that the developed horizontal stress within the lower EPS block layer located right next to the retaining wall was 16 psf in tension, indicating a possible separation between the retaining wall and the lower EPS block layer occurred. The upper EPS block layer adjacent to the retaining wall however still experienced horizontal compressive stress of 52 psf. The lateral movement calculations showed that

the top of the retaining wall moved outward with a magnitude of average of 0.05 inches. However, a tensile separation of 0.0001 inch was observed at the bottom of the retaining wall, which supported the tensile stress developed within the lower EPS block layer.

To compare the finite element predictions with the field measurements, field measurements of 50 days after the completion of the retaining wall construction was chosen. The reasons were that the measurements generally peaked at this date, that the finite element analysis was solely based on the elastic response of the system, and that beyond this date the effect of temperature became rather significant. The field measurements indicated that the top of the upper EPS block layer of the east abutment experienced a maximum settlement of 0.1 inches at 50 days after the completion of the retaining wall. The predicted vertical compression of the EPS Blocks was 0.22 inches, resulting in a ratio of approximately 1:2. The measured lateral movements of the EPS Blocks adjacent to the retaining wall was approximately 0.08 inches in separation both at the top and the bottom of the east retaining wall. They gradually started to move toward the retaining wall with time, possibly due to the creep and/or internal self-adjustment of the EPS Blocks. The predicted lateral movement of the EPS Blocks relative to the retaining wall was 0.0001 inches in separation near the bottom of the retaining wall. Even though the predicted and measured magnitudes of the EPS block lateral movement did not agree well each other, they agreed in the direction of the movement. The magnitudes of the movements were however very small and could be considered well within the variation resulting from the temperature changes.

CONCLUSIONS

This paper describes an analytical study that compares the predicted displacements and stresses of the bridge abutment retaining wall system with EPS Blocks as backfill from the finite element method of analysis with the field measurements. The details of the field instrumentation are described in a companion paper included in this proceeding. The finite element analysis included detailed EPS material characterization obtained from the laboratory triaxial tests. The comparison indicated that the field behavior of the system, including the vertical settlements of the approach slab and the lateral movements of the EPS Blocks, may be simulated with a reasonable accuracy by the finite element method of analysis, if correct material characterizations are used.

It has been observed from both the analytical study and the field instrumentation that the EPS Blocks may separate from the retaining wall upon application of the vertical compressive loading due to its special material properties. This behavior could be simulated in the finite element analysis by utilizing non-linear, confining pressure - dependent Poisson's ratio description of the EPS Blocks and special interface elements between the EPS Blocks and the retaining wall.

ACKNOWLEDGMENT

This research was performed under the sponsorship of the South Dakota Governor's Office of Economic Development and the Benchmark Foam Inc., Watertown, South Dakota. The authors are extremely grateful to their financial supports.

REFERENCES

1. Preber, T. and S. Bang, "Geotechnical Engineering Application of Expanded Polystyrene Blocks," Final report to the South Dakota Governor's Office of Economic Development and to the Wyoming Department of Transportation, Dec., 1994.
2. Cho, Y., "Behavior of Retaining Wall with EPS Blocks as Backfill," M.S. thesis, South Dakota School of Mines and Technology, 1992.
3. Preber, T., S. Bang, Y. Chung, and Y. Cho, "Behavior of Expanded Polystyrene Blocks," In Press, Transportation Research Record.
4. Duncan, J. M. and C. Y. Chang, "Nonlinear Analysis of Stress and Strain in Soils," Journal of the Soil Mechanics and Foundation Division, ASCE, Vol. 96, No. SM5, 1970.
5. BSAF Corporation, "Strength Characteristic of EPS Thermal Insulation," Technical Bulletin E-3, Chemicals Division, Parsippani, NJ, 1993.

INCREASE IN SUBGRADE MODULUS OF BEARING SOILS FOR PAVEMENTS BY THE INSTALLATION OF SHORT, STABILIZED, GRANULAR COLUMNS

By Kimberley S. Robinson[1], Evert C. Lawton[2], and Nathaniel S. Fox[3]

ABSTRACT

A method is proposed whereby subsoils for support of roadway, airfield, and parking area pavements will be improved and reinforced by the incorporation of a grid of small diameter, short, stabilized, vertical, granular columns. To estimate the potential improvement in subgrade modulus that might be obtained using this method, a series of one-dimensional compression tests were performed at approximately one-half scale using a sandy-silt/sandy-clay matrix soil. The soil was compacted at a water content of 20% to a dry unit weight of 12.75 kN/m^3 (81.2 pcf) to simulate a poor in-situ bearing soil. Columnar material, columnar length to diameter ratio, reinforcement area ratio (columnar area to total area), and shape of columnar compactor head were all varied. A column of crushed granitic gneiss compacted to 25.13 kN/m^3 (160 pcf) placed at a surface area ratio of 2.8% and a columnar length to diameter ratio of 5 increased the secant subgrade modulus at a deformation of 5.1 mm (0.2 in) by over four times. Expanding the surface area ratio to 11.1% and using the same column length caused an increase in the secant subgrade modulus of over thirteen times the modulus of the unreinforced matrix soil.

From this study the following trends were determined:

1. The type of columnar material used had a significant effect; chemically stabilized soils were particularly effective in stiffening the soil.
2. An increase in areal ratio produced an increase in stiffness.
3. For the same areal ratio, subgrade modulus increased as length to diameter ratio increased.
4. The shape of the compactor head has an influence on the resultant subgrade modulus.
5. Columns installed in stiffer soils using vertical and lateral displacement of matrix soil were not particularly effective in increasing the subgrade modulus of the soil. Augering holes is being considered as an alternate to reduce problems related to displacement of soil during penetration.

INTRODUCTION

Soil stabilization of subgrades for support of pavements typically involves one of the following approaches: (a) in-situ compaction with moisture control., (b) excavation, chemical stabilization or modification of excavated material with moisture control, or excavation of

[1] Undergraduate Student, Department of Civil Engineering, University of Utah, 3220 Merrill Engineering Building, Salt Lake City, Utah 84112.

[2] Associate Professor, Department of Civil Engineering, University of Utah, 3220 Merrill Engineering Building, Salt Lake City, Utah 84112.

[3] President, Geopier Foundation Company, Inc., 769 Lake Drive, Lithonia, Georgia 30058

substandard soils and replacement with select borrow materials which are compacted with moisture control. At the completion of these procedures, sufficiently rigid subbase and base courses are typically applied before the pavement surface can be installed. The difficulty in controlling moisture content in the field complicates the achievement of the desired as-compacted properties in the soil, and the entire process is generally time consuming and costly. In addition, adequate supplies of quality base and subbase materials may be lacking in some regions.

It is proposed that subsoils may be improved and reinforced by the installation of a grid of small diameter, short, vertical, stabilized, granular columns. To construct these small diameter columns, the use of a mobile apparatus which is capable of creating a grid of columns simultaneously will be used. A conceptual drawing of one possible apparatus with these capabilities is illustrated in Figure 1, which would likely be economical for large projects.

It is anticipated that at field scale the columns will be approximately 76 mm (3 in.) in diameter by 305 mm (12 in.) deep and will be spaced approximately 305 mm (12 in.) apart. A similar method, on a larger scale, is currently being used to reinforce bearing soils beneath building foundations (Lawton et al. 1994; Lawton and Fox 1994). The use of short, small diameter columns appears to be a viable method for improvement of soft, loose, or otherwise inadequate subgrade soils to support traditional subbase and base courses. The use of the method to improve moderate to good subgrade soils may also be possible, thus enabling the subbase or base courses to be reduced in thickness or eliminated, or the pavement thickness to be reduced.

To determine the increase in subgrade modulus that can be expected from using this method and to provide the basis for subsequent field tests, a series of laboratory one-dimensional compression tests were conducted at approximately one-half scale. This paper presents the results of these experiments and examines the effects of the following parameters on specimen stiffness: columnar material, reinforcement area ratio (columnar surface area to total surface area), columnar length to diameter ratio, compaction method, and shape of columnar compactor head.

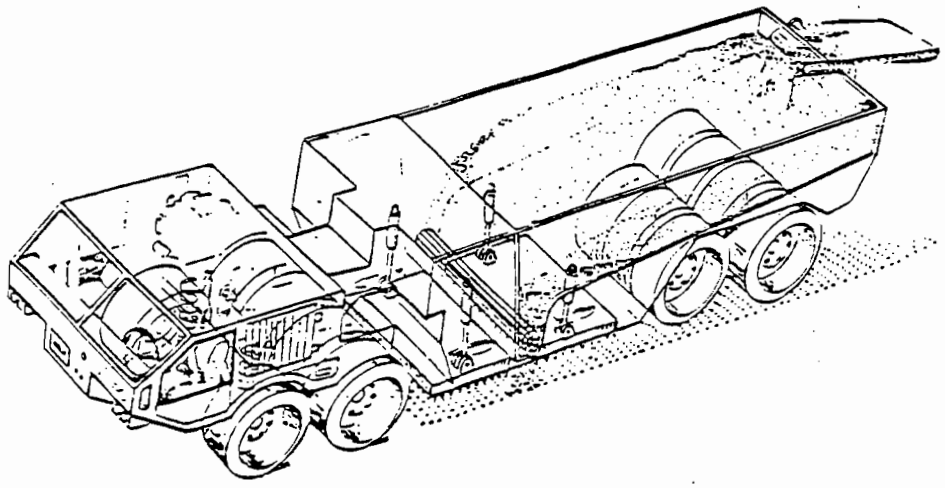

Figure 1. Conceptual Drawing of Proposed Apparatus for Major Projects

BACKGROUND

There are generally two types of pavement used for the creation of roads, parking lots, and airways: Portland cement concrete (PCC) and asphaltic cement (AC). Because PCC is sufficiently rigid to distribute traffic loads over a larger area, it is generally not cost effective to use a base/subbase course for the sole purpose of increasing the stiffness of the bearing soil. Any excessive stresses that may be encountered due to poor bearing soils can be alleviated by adding a small increase to the depth of the concrete. Base or subbase courses are generally used for other purposes in PCC design, such as preventing soil pumping; minimizing damage due to frost susceptible, shrinking, and swelling soils; and improving drainage around the concrete to increase the life of the pavement. It is clear from the facts outlined above that short, granular columns of small diameter may not be economical for use in rigid pavements.

Alternately, flexible pavement design has problems to which granular columns may provide excellent solutions. Failure of flexible pavements is generally caused by two types of strain, the horizontal tensile strain induced at the bottom of the AC layer and the vertical compressive strain at the subgrade/subbase interface (rutting). When a wheel load is applied to the surface of a flexible pavement, a zone of compression is created at the interface of the subgrade soil. If the soil's subgrade modulus is low and the applied stress is high, the subgrade may deflect sufficiently to induce a tensile strain at the base of the asphaltic concrete. High capacity vehicular traffic creates a cyclic loading in the pavement that generally leads to failure by fatigue fracture in the tensile strain zone. It is expected that the installation of granular columns into the subgrade will increase the subgrade modulus of the bearing soil, thereby minimizing subgrade deflection and, consequently reducing tensile strains in the pavement.

MATERIALS AND TEST METHODS

The matrix soil used in this investigation was a sandy-silt, sandy-clay material, SM-SC as classified by the United Soil Classification System. This soil was compacted at a water content of 20% to a dry unit weight of 12.75 kN/m^3 (81.2 pcf) to simulate a poor in-situ subgrade soil. Four columnar materials were used: crushed granitic gneiss, coarse sand, crushed glass, and the matrix soil stabilized with cement. The granitic gneiss, sand, and glass were all well graded.

Tests were performed in a conventional CBR mold 17.78 cm (7 in.) in height and 15.24 cm (6 in.) in diameter. The matrix soil was compacted to a height of 15.24 cm (6 in.) and allowed to age for 1 day prior to testing. Each columnar cavity was formed by pushing a piston with a conical head into the soil at a constant rate of 6.35 mm/min (0.25 in./min). Two conical heads were used: one with a 2.54 cm (1 in.) diameter corresponding to an areal reinforcement ratio of 2.8%, and one with a 5.08 cm (2 in.) diameter corresponding to an areal reinforcement ratio of 11.1%. The columnar material was compacted at 6% water content (10% for the cement stabilized columns) into the cavity in 1 inch lifts using either a semi-spherical, cylindrical, or frustro-conical compaction head. Static compaction of the columnar material was accomplished by lowering the compaction head into the soil at a constant rate of 6.35 mm/min (0.25 in./min). Columns were dynamically compacted by releasing a 4,723.5 g (10.41 lb) weight along a vertical slider from a pre-determined height. Unless otherwise noted, all columns were statically compacted to a nominal dry density of 25.13 kN/m^3 (160 pcf) based on the volume of the hole

Figure 2. Schematic of Reinforced Specimen

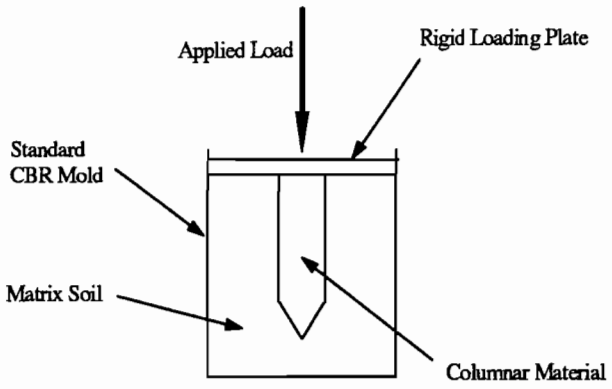

using a frustro-conical compaction head. The resulting reinforced specimen is depicted schematically in Figure 2.

All specimens were loaded in one-dimensional compression at a constant deflection rate of 0.254 mm/min (0.01 in./min) using a standard loading frame.

Values of subgrade moduli reported in this paper are for a 15.24 cm (6 in.) diameter circularly loaded area and were determined by dividing the measured stress at 5 mm (0.2 in.) deflection by that deflection, thus all are secant values of subgrade modulus for 5.1 mm (0.2 in.) deflection. It is important to recognize that subgrade modulus is a function of loaded area and that subgrade moduli for pavement design are typically determined using 76.2 cm (30 in.) diameter plate bearing tests. Thus, these values of subgrade modulus are presented to enable comparisons between unreinforced and reinforced specimens, and between differing reinforced samples, but the values are not necessarily representative of the field values that would be obtained from 76.2 (30 in.) diameter plate bearing tests.

RESULTS

Typical test results are depicted in Figure 3. The installation of short, small-diameter columns was found to have a significant impact when placed in poor bearing soils. The resulting secant subgrade moduli are summarized in Table 1. The stiffness of the reinforced soil was found to be a function of columnar material, areal ratio, columnar length or columnar length to diameter ratio, columnar compaction technique, and the shape of the compactor head.

Effect of Columnar Material

The type of columnar material used to reinforce the matrix soil was found to have a considerable influence on the resulting specimen stiffness. The most significant improvement was observed when the matrix soil was stabilized with 10% cement, mixed at a 10% water content to initiate hydration, and compacted into the columnar cavity. As listed in Table 1, the use of an 11.1% areal ratio and a length to diameter ratio of 2.5 improved the subgrade modulus by 22.5 times over the unreinforced matrix soil. Cement stabilized columns outperformed all other columnar materials throughout the range of deformations that were studied.

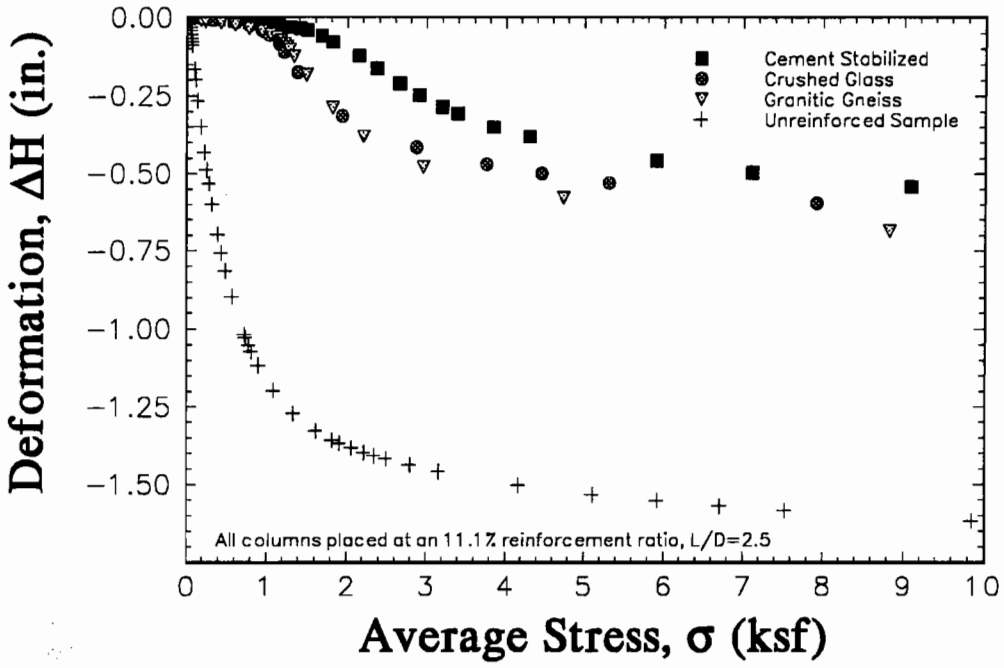

Figure 3. Columnar Material Comparison, 127 mm (5.0 in.) Columns

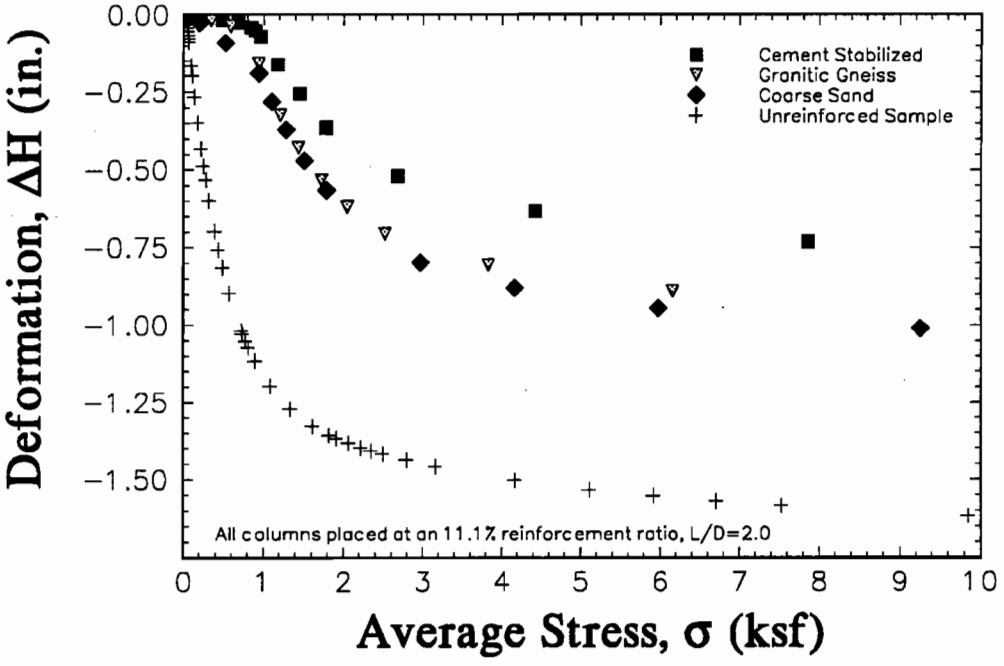

Figure 4. Columnar Material Comparison, 102 mm (4.0 in.) Columns

TABLE 1. Subgrade Moduli for Reinforced and Unreinforced Specimens

Columnar Material	Areal Ratio	Columnar Dimensions		Length to Diameter Ratio	k at 5.1 mm (0.2 in) Deflection		Improvement Ratio
		Length mm (in)	Diameter mm (in)		kN/m^3	pci	(k_r/k_u)*
Unreinforced	——	——		——	1,086	4.0	——
Cement Stabilized Sandy-Silt/Sandy-Clay	11.1%	127 (5.0)	51 (2.0)	2.5	24,430	90	22.5
		102 (4.0)	51 (2.0)	2.0	11,944	44	11.0
		76 (3.0)	51 (2.0)	1.5	8,143	30	7.5
Crushed Granitic Gneiss	2.8%	127 (5.0)	25 (1.0)	5.0	4,807	18	4.2
		102 (4.0)	25 (1.0)	4.0	4,524	17	4.4
	11.1%	127 (5.0)	51 (2.0)	2.5	14,325	53	13.2
		102 (4.0)	51 (2.0)	2.0	9,330	34	8.6
		76 (3.0)	51 (2.0)	1.5	6,880	25	6.3
Semi-Spherical Compactor Head	11.1%	127 (5.0)	51 (2.0)	2.5	9,840	36	9.1
		102 (4.0)	51 (2.0)	2.0	8,765	32	8.1
		76 (3.0)	51 (2.0)	1.5	5,843	22	5.4
Cylindrical Compactor Head	11.1%	102 (4.0)	51 (2.0)	2.0	7,003	26	6.4
Dynamically Compacted	11.1%	127 (5.0)	51 (2.0)	2.5	9,519	35	8.8
		102 (4.0)	51 (2.0)	2.0	6,786	25	6.2
		76 (3.0)	51 (2.0)	1.5	3,663	13	3.4
Course, Sub-Rounded Sand	11.1%	102 (4.0)	51 (2.0)	2.0	9,613	35	8.9
Crushed Glass *(Dynamically Compacted)*	11.1%	127 (5.0)	51 (2.0)	2.5	13,854	51	12.8

* k_r/k_u=Reinforced subgrade modulus / unreinforced subgrade modulus

The granular materials that were studied performed similarly at deflections of 5.1 mm (0.2 in.). At higher deformations, the use of crushed glass produced a stiffer composite soil compared to the other granular materials (see Figure 3.) The use of the coarse sand produced the smallest improvement in stiffness, yet the subgrade modulus was still increased significantly by installing this material at a reinforcement area ratio of 11.1% and a length to diameter ratio of 2.0 (see Figure 4.)

The selection of columnar material for use on a specific project would involve an analysis of the stiffness and type of soil to be reinforced and would take into account the cost of construction and the availability of the required materials.

Effect of Reinforcement Area Ratio

The reinforcement area ratio is defined as the ratio of the cross-sectional area of the column to the total cross-sectional area (A_{Column}/A_{Total}). Short, aggregate piers installed to stiffen

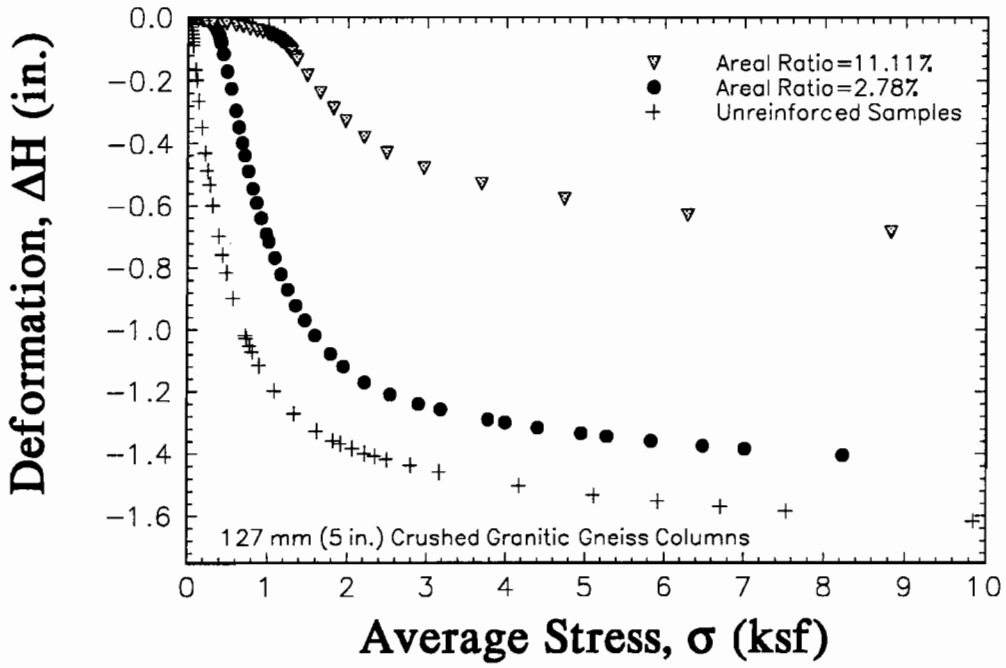

Figure 5. Influence of Areal Ratio

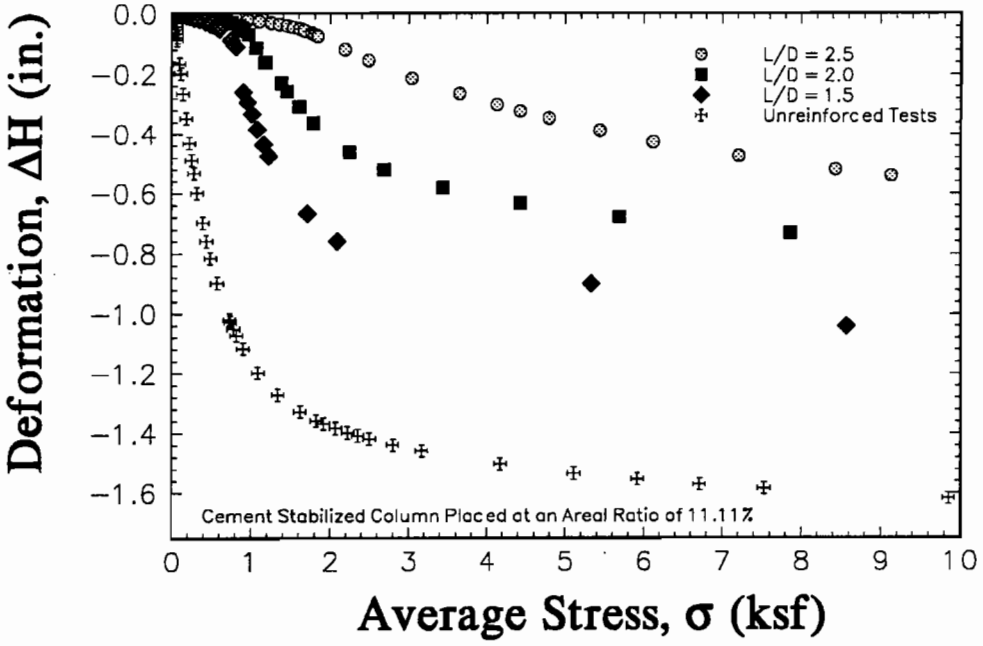

Figure 6. Effect of Length to Diameter Ratio (L/D)

bearing soils for support of foundations for structures are generally placed at areal ratios between 20 to 40% (Lawton and Fox 1994). Two diameters of columns were tested: 1 in. and 2 in., with corresponding areal ratios of 2.8% and 11.1%. Lower areal ratios were considered in an effort to create an economically feasible solution to subsoil stabilization and reinforcement for pavement support.

Crushed granitic gneiss was selected as the columnar material for comparison of areal ratio. Despite the small amount of columnar material used, the 2.8% areal ratio specimens increased the soil's subgrade modulus by a factor of more than four. The columns installed at an 11.1% areal ratio produced a specimen that was nearly twice as stiff as those installed at a 2.8% areal ratio when constructed to the same length. Overall, the stiffness of the composite soil was shown to increase with an increase in areal ratio. (See Figure 5.)

Effects of Length to Diameter Ratio, Compaction Method, and Compactor Head Shape

Results of the columnar length to diameter variation are depicted in Figures 6 and 7 and summarized in Table 1. These findings show an unequivocal increase in subgrade modulus as the length to diameter ratio is increased. Though there is likely a length to diameter ratio at which a greater increase in length produces only negligible increase in stiffness, the geometry of the specimen container used in this series of experiments restricted the determination of that ratio.

To create an effective column, the length of the column should be equivalent or greater than its diameter, (length to diameter ratio greater than 1.0.) At smaller areal ratios, the length of the column should be greater than twice its diameter to produce any significant increase in stiffness.

The effects of compaction method are depicted in Figure 8. The use of dynamic compaction results in a lower subgrade modulus than static compaction at smaller deformations. Larger deformations, however, show that the stiffness of the composite soil is nearly independent of method of compaction.

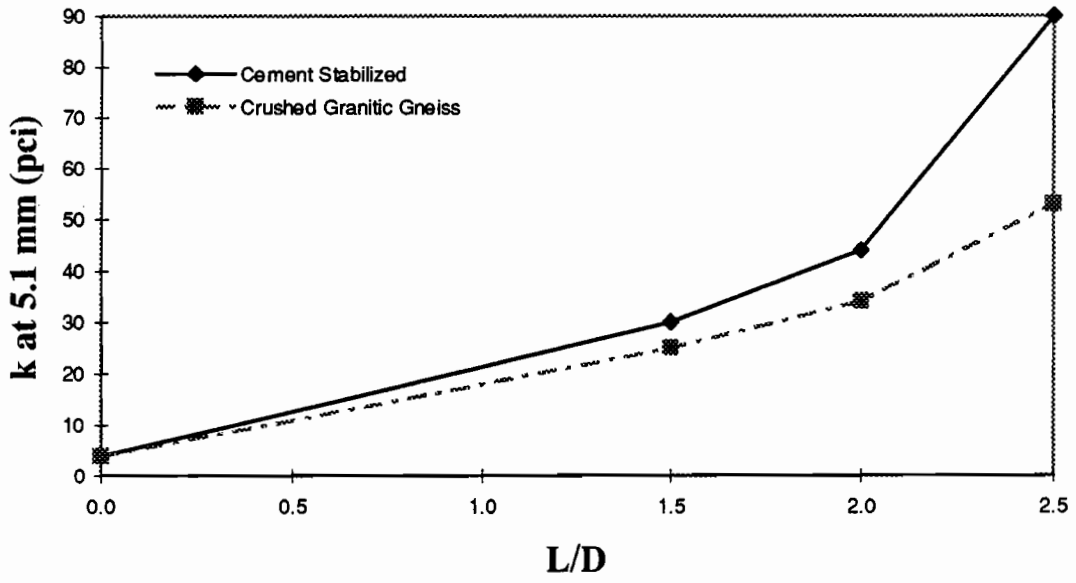

Figure 7. Subgrade Moduli vs. L/D Ratio for 11.1% Areal Ratio Samples

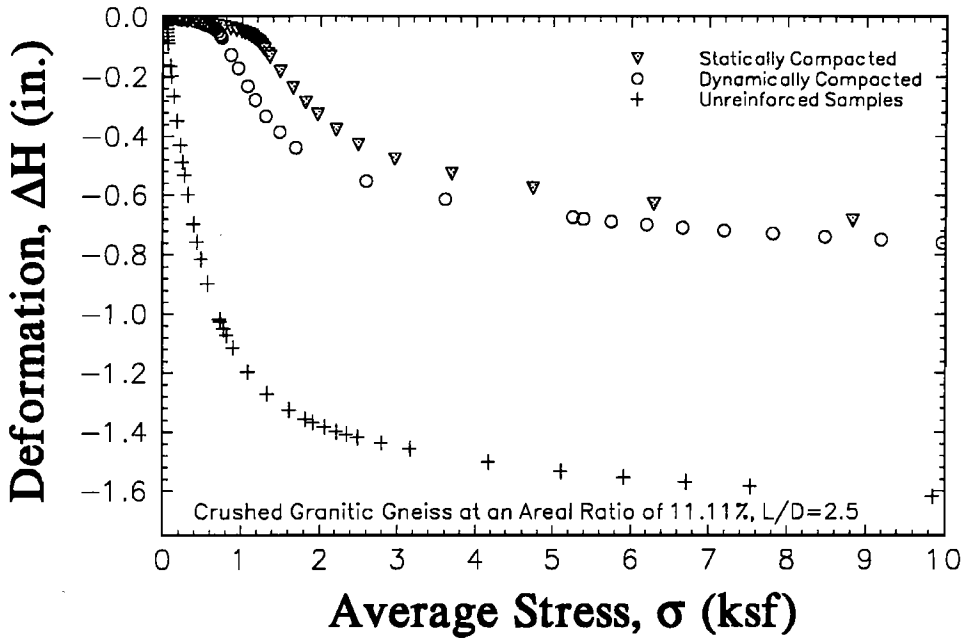

Figure 8. Comparison of Compaction Method

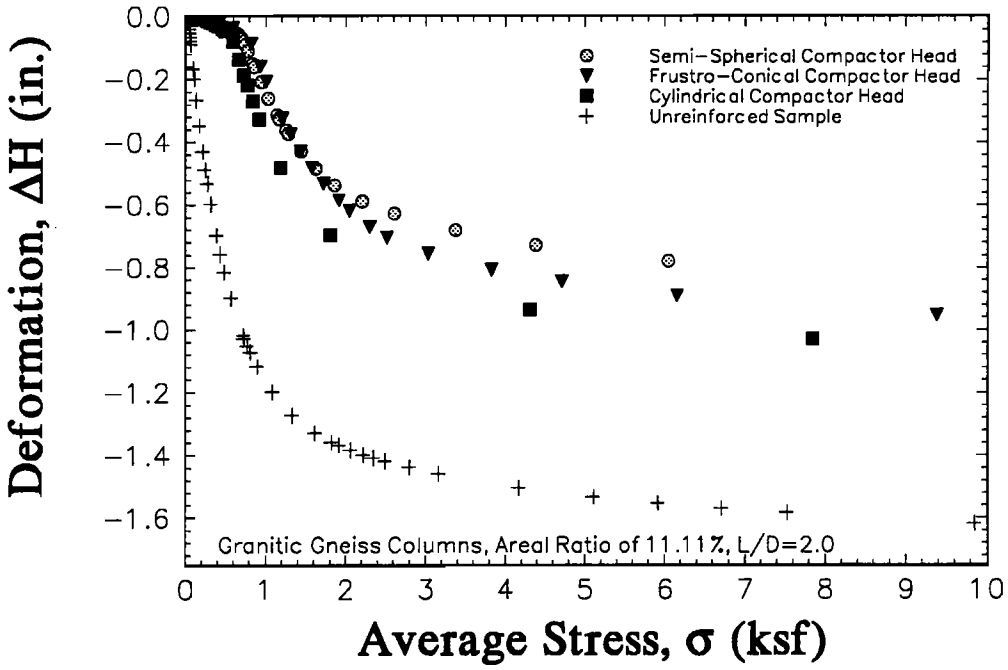

Figure 9. Comparison of Compactor Head Shape

Figure 9 shows the resulting stress/displacement curves from the various compactor head shapes. The frustro-conical compaction head produced a more rigid specimen in the lower displacement ranges. At higher displacement ranges, the semi-spherical compactor head produced specimens with greater stiffness than the frustro-conical compactor head. The cylindrical compactor head produced the specimen with the least stiffness because this shape does not generate the degree of lateral pressures during compaction that the semi-spherical and frustro-conical heads do. Because these columns are generally formed from non-cohesive materials, the stiffness of the columns is dependent on the lateral confining pressure obtained from the matrix soil.

LOAD DISTRIBUTION

To examine the distribution of the load being carried by the column, a device was designed and manufactured to measure separately the loads on the columnar and matrix materials. A schematic of this device is depicted in Figure 10. Using this system, the matrix soil and columnar material are loaded using separate pistons. An internal load cell is mounted on the columnar piston and a rigid plate with an external load cell is used to load both pistons simultaneously.

The resulting subgrade moduli of the matrix soil, columnar material, and specimen are summarized in Table 2 and depicted in Figure 11. Although the matrix soil is improved somewhat by the installation of the column, the majority of the increase in subgrade modulus is in the stiffness of the column. The crushed glass column was shown to improve the matrix soil to the greatest extent of those tested in this manner.

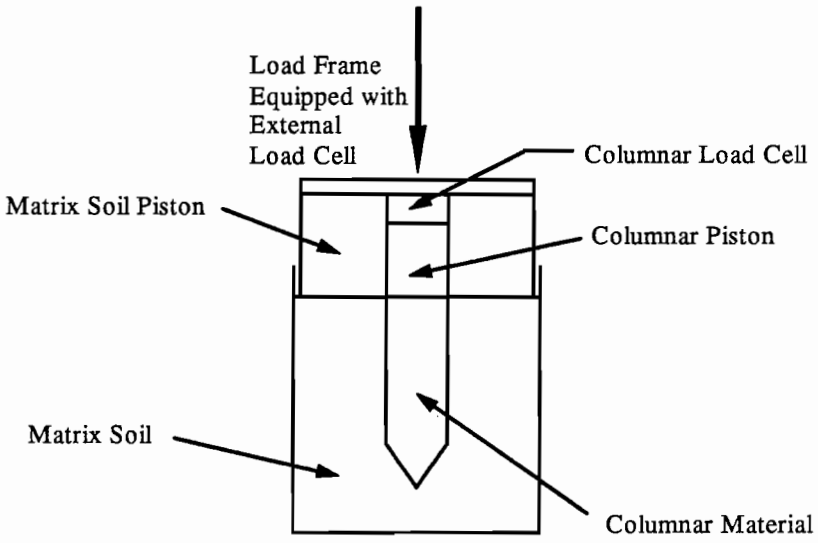

Figure 10. Load Separation Device

TABLE 2. Columnar and Matrix Subgrade Moduli for Columns Compacted Dynamically with a Areal Ratio of 11.1%

Columnar Material	Columnar Dimensions		Length to Diameter Ratio	Subgrade Modulus kN/m3 (pci)			Improvement Ratio (k_r/k_u)		
	Length mm (in.)	Diameter mm (in.)		Matrix	Column	Total	Matrix	Column	Total
Crushed Granitic Gneiss	127 (5.0)	51 (2.0)	2.5	4,618 (17)	48,537 (178)	9,519 (35)	4.3	44.7	8.8
	102 (4.0)	51 (2.0)	2.0	4,335 (16)	26,295 (97)	6,786 (25)	4.0	24.2	6.2
	76 (3.0)	51 (2.0)	1.5	1,885 (7)	18,001 (66)	3,663 (13)	1.7	16.6	3.4
Crushed Glass	127 (5.0)	51 (2.0)	2.5	8,859 (33)	53,815 (198)	13,854 (51)	8.2	49.6	12.8

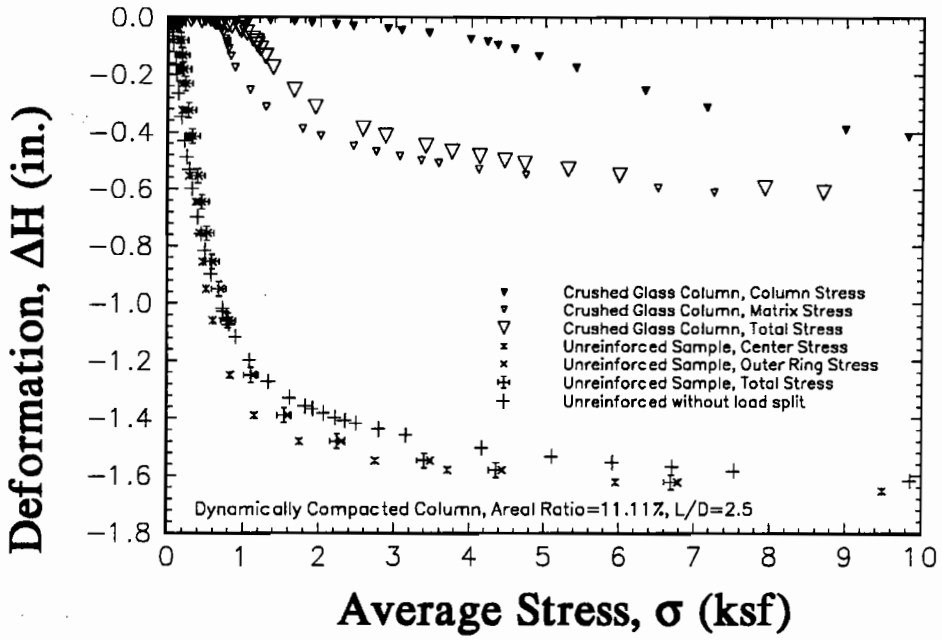

Figure 11. Load Separation Results from Dynamically Compacted Glass Column

RESULTS OF TESTS CONDUCTED IN STIFFER SOILS

Preliminary results from tests on columns installed in stiffer soils indicate that the inclusion of a column produces a composite material that is less stiff than the unreinforced matrix soil. The use of vertical and lateral displacement techniques to form a cavity in which to place the columnar material disrupts the natural cementation and fabric of the soil and has the tendency of loosening it. Tests performed with the load separation device show that although the column is rigid, the stiffness of the matrix soil is greatly reduced. Future testing is planned to examine the effects of other columnar forming techniques on subgrade modulus.

SUMMARY AND CONCLUSIONS

Short, small diameter, granular columns have been shown to increase the subgrade modulus of a poor bearing soil. The degree of improvement that can be expected in a soil using this method is a function of columnar material, columnar geometry, and the subgrade soil. From this study the following trends were determined:

1. The type of columnar material used had a significant effect; chemically stabilized soils were particularly effective in stiffening the soil.
2. An increase in areal ratio produced a significant increase in stiffness.
3. For the same areal ratio, subgrade modulus increased as length to diameter ratio increased.
4. The shape of the compactor head has an influence on the resultant subgrade modulus. A frustro-conical or semi-spherical compaction head induces higher lateral pressures in the matrix soil to produce a stiffer composite material.

These results confirm the applicability of this method to stabilize poor bearing soils for support of pavements. Although the use of vertical and lateral displacement techniques used to install these short, granular columns serve to densify and improve poor or loose soils, this method appears not to be appropriate for column installation in good soils. An alternate procedure of opening holes by augering rather than penetration and displacement is being evaluated for use in good soils.

ACKNOWLEDGMENTS

This research was funded by Phase I Small Business Innovative Research grant number DMI-9360798 from the National Science Foundation.

REFERENCES

Huang, Yang H. (1993). *Pavement Analysis and Design*, Prentice-Hall, Englewood Cliffs, New Jersey.

Yoder, E. J., and Witczak, M. W. (1975) *Principles of Pavement Design*, 2nd ed., John Wiley & Sons, New York, New York.

Lawton, E. C., and Fox, N. S. (1994). "Settlement of Structures Supported on Marginal or Inadequate Soils Stiffened with Short Aggregate Piers." *Geotechnical Special Publication No. 40: Vertical and Horizontal Deformations of Foundations and Embankments,* ASCE, 2, 962-974.

Lawton, E. C., Fox, N. S., and Handy, R. L. (1994). "Control of Settlement and Uplift of Structures Using Short Aggregate Piers." *Geotechnical Special Publication No. 45: In-Situ Deep Soil Improvement,* ASCE, 2, 962-974.

USES OF WASTE FOUNDRY SANDS IN CIVIL ENGINEERING

C. W. Lovell, Research Engineer
School of Civil Engineering
Purdue University, West Lafayette, IN 47907

and

Sayeed Javed
Geotest Engineering, Inc.
5600 Bintliff Drive, Houston TX 77036

ABSTRACT

Molds and cores for metal castings are normally sands with chemical or clay binders and other additives. After the casting is complete, the sand is disaggregated, and a judgment made about reuse. However, after several uses the sand is no longer suitable and is designated as a waste (WFS). Such waste has been disposed in a landfill, public or private.

While some WFSs may contain excessive amounts of harmful heavy metals, those discarded after ferrous castings, contain only iron, and this concentration is controlled by magnetic extraction from the waste. At this point, only WFSs from ferrous castings are perceived to have a high probability of being environmentally acceptable.

Through laboratory study of the mechanical/physical properties of WFSs from the greensand, shell, and chemically bonded processes for ferrous castings, a number of Civil Engineering uses have been identified. These are: structural fill, subgrade, flowable fill, and fine aggregate replacement in asphaltic concrete.

The paper briefly describes the index properties of the WFSs, and the appropriate test parameters for the various uses listed above. The next step in the process is to build demonstration/implementation projects to prove the practicality of the use, and to provide long-term evidence of the absence of significant environmental effects.

Introduction

Recent legislation in Indiana has intensified study of the use of industrial/domestic waste products in Civil Engineering, particularly in highways. The wastes given primary attention are: scrap tires, coal combustion byproducts, destructed pavement materials and building demolition products, and spent foundry sands. This paper summarizes properties and potential uses of this spent (waste) foundry sand.

The desire of Indiana foundries to reduce disposal costs, led to the sponsorship of a 2-year study of waste foundry sand (WFS) in the School of Civil Engineering at Purdue University. Funding was by an association of Indiana foundries. The Indiana Cast Metals Association (INCMA) represents 38 Indiana foundries.

The research report resulting from the study is authored by the authors of this paper (Javed and Lovell, 1994). The potential uses given greatest attention were WFS as: embankment and subgrade material; fine aggregate in controlled low strength material (CLSM)...also called flowable fill; and fine aggregate in asphaltic concrete. The last named use was the subject of a previous paper (Javed et al., 1994), and will not be repeated here.

Background

Sands have long been used for metal casting. They are chosen for several important reasons (Parkes et al., 1970): readily available; inexpensive; highly refractory; and readily bonded by clays or other inorganic and organic material.

There are three types of molding processes: greensand; chemically bonded; and shell molded. In Indiana, the most commonly used process is greensand molding. The greensand mixture contains clay, combustible additives like seacoal, and water. The predominant metal cast is gray iron. After a number of uses, the molding sands lose the desired qualities and are discarded. The foundry may operate a monofill for these wastes, or may transport them to a municipal solid waste landfill. In either case, the disposal costs are significant, and the foundries are anxious to reduce them.

The grain size distribution of WFS is quite uniform, with a majority of the sizes within a narrow range between the No. 50 and No. 100 sieves. This means that they are finer than the materials generally specified for fine aggregates.

The greensands, with their additives of clay, demonstrate cohesive type behavior, while the chemically bonded and shell molded sands show cohesionless response. Consequently, greensand compaction curves show a definite dependence on compaction moisture content, while the compacted unit weights of others is almost independent of that moisture content.

The results of standard heavy metal leaching tests, like the EPTOX and the TCLP, depend on the metals cast, since the WFSs are commonly contaminated by these metals. Much of the metal cast in Indiana is ferrous, and while limits are seldom exceeded, iron is occasionally present in concentrations above those stated. Chemically bonded and shell molded WFSs contain chemicals and organics which may require special environmental assessment, prior to routine use.

Characterization of WFSs

Experimental work on WFSs in the School of Civil Engineering, Purdue University involved 7 samples from greensand processes, two from chemically bonded processes, and one from a shell molding process. All of these involved ferrous castings.

Compactability of these sands is of considerable interest for embankment and subgrade applications. The WFSs from chemically bonded and shell molded processes are cohesionless and respond best to vibratory compaction. The waste greensands are best compacted by impact (Proctor) type processes. Figure 1 shows the moisture-unit weight and moisture-California Bearing Ratio (CBR) relations for the raw sand (R1) which comprises the casting sands. As is common for such materials, unit weight varies little with compaction water content, although it is somewhat higher for a "flushed" condition. The soaked CBR is also maximized at this higher water content.

The WFSs from greensand casting are illustrated in response by Figure 2 for sample G1. Unit weight is strongly dependent on moisture content, and soaked CBR is maximized at about the optimum moisture content. Note that swell upon soaking is small, and that the soaked CBR values compare very favorably with compacted natural soils.

Shear strength parameters were determined by performing direct shear tests on dry samples at various unit weights. The data are summarizing in Table 1, along with typical values for natural sands. The G symbol represents greensand; the C is for chemically bonded; the S for shell molded; and R is for the raw sand. The ϕ values represent peak strengths for dense samples and ultimate strengths for loose samples; (D_r) is relative density.

To determine the suitability of WFSs for subgrade, resilient modulus (M_r) tests were run. These are reported in detail in Javed and Lovell (1994). It was found that the laboratory compacted greensands had values comparable or higher than soils typically used for subgrades in Indiana (Lee, 1993).

Use of WFS as a fine aggregate supplement in asphalt concrete has been previously reported (Javed et al., 1994). Based upon simple testing, it was determined that as much as 15% of the conventional sand content of asphalt concrete could be replaced by WFS.

One of the more promising new engineering materials is a mixture called Controlled Low Strength Material (CLSM). These mixtures of cementitious materials, fly ash, sand and water are able to flow into hard-to-access locations, and to set up to produce strengths comparable to compacted soils within a few hours. Since it often desirable to be able to remove/replace these materials, e.g., in utility cuts, their strengths should be relatively low.

The CLSM mix will then have parameters of flow, rate of strength gain, and final strength which vary with mix constituents and percentages. In this study the constituents were: Type 1 cement, class F fly ash, water, and WFSs. The use of WFS in CLSM mixes is relatively new, and therefore comparisons with mixes using conventional sand seemed appropriate. Table 2 shows these comparisons.

The WFSs are assumed to be free of charge, and within a short distance of source, produce CLSMs which are economical. Mix 3 is the preferred one within this set, but the use of WFS raises questions of porosity and permeability, as well as setting rate. These are being addressed in current research (Bhat et al., 1995).

Environmental Concerns

All of the WFSs tested in this study were from ferrous castings. Therefore, one would expect that the only elements present in the waste sand would be the additives and a small amount of iron. Since the principal additives in greensand are clay and seacoal, these materials would be expected to pass all reasonable environmental tests.

The greensands do pass the various leaching tests. Bio-assay testing (a waste water technique) is also planned for these materials, but they are expected to pass.

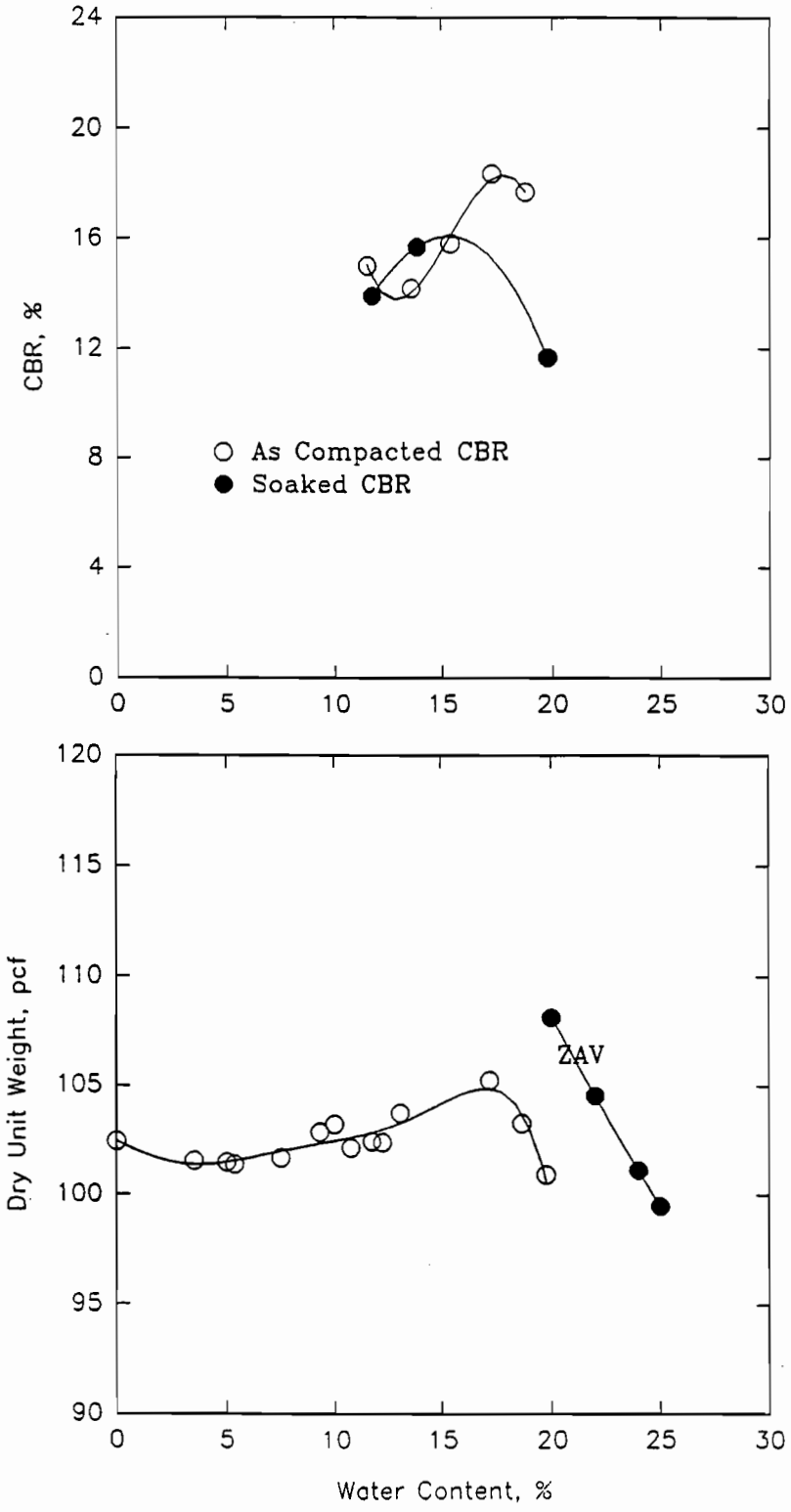

Figure 1 Moisture-unit weight-CBR relationship of R1

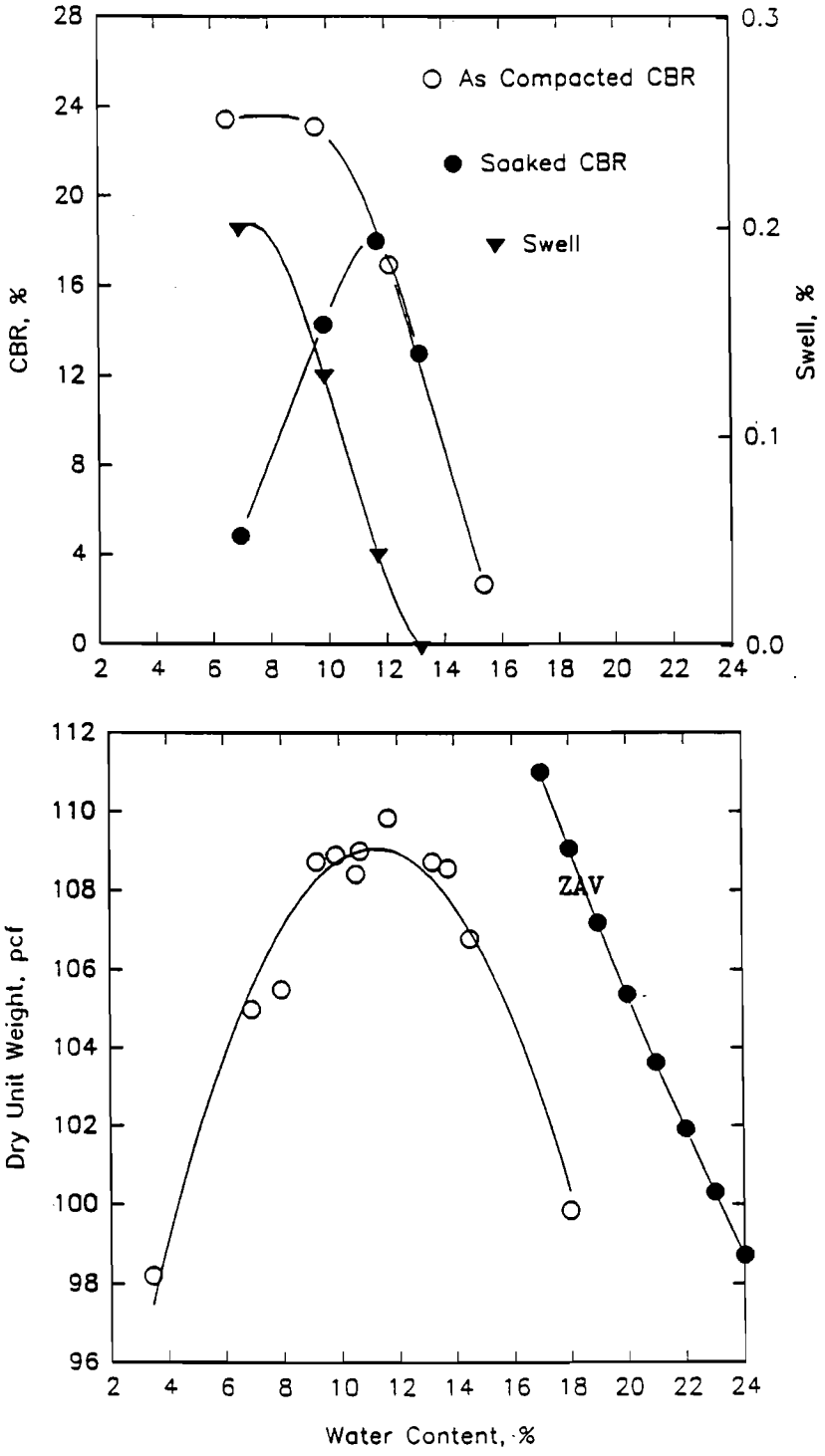

Figure 2 Moisture-unit weight-CBR relationship of G1

Table 1 Results of Direct Shear Tests

Sample #	Dr	Loose		Dr	Dense	
		c (psi)	ø (deg)		c (psi)	ø (deg)
G1	29	0.60	32.4	90	1.44	36.6
G3	34	0.75	34.2	98	1.82	40.9
C2	22	0.06	30.4	94	1.04	34.9
S1	31	0.06	30.8	94	0.69	36.5
R1	32	0.03	30.4	88	0.17	33.8
Uniform	Moderately			Very		
medium sand[a]	dense		32-34	dense		35-38
Sand[b]	Loose		29-30	Dense		36-41

[a] From Terzaghi and Peck, 1948

[b] From Peck, Hanson and Thornburn, 1974

Table 2 Spread, Unit Weight and Compressive Strength for Different Mixes

Mix No.	1	2	3	4	5	1A[1]	ES-1[2]
Cement (pcy)	131	124	99	55	76	80	63
Fly ash (pcy)	436	414	158	183	139	420	321
Water (pcy)	698	745	741	738	765	561	494
WFS or Sand (pcy)	1922	1822	2134	2128	2126	2535	2774
Spread (in.)	7.5	9.0	8.2	8.1	8.2	-	5-6
Unit weight (pcf)	118	115	116	115	115	-	134
Compressive strength (psi)							
3 - Day	43	41	36	8.5	24	-	20
7 - Day	67	54	44	9	31	45	30
28 - Day	103	80	70	8	55	120	80

[1] From Amon (1990)
[2] From Nantung (1993)

There is no specific environmental testing for the chemicals and other inorganic/organic substances used in chemically bonded and shell molded WFSs, therefore more potential risk is involved. One also expects that greensand casting of other metals, e.g., aluminum, will yield a non hazardous waste. Conversely, other castings, like brass, would be highly suspect.

Two usage scenarios seem well suited for demonstration usage of greensand from ferrous casting.

(1) Well drained situations like subgrades and embankments. Leachate in such situations is small, and is further minimized by clay encasing layers on the sides. Some sort of growing layer would need to be placed at the sides, even without the encasement requirement.

(2) Stabilized mixtures like CLSMs. While these are wet and poorly drained situations, viz., trenches, around pipes and tanks, the WFSs are reasonably well "fixed" in the mix. Porosity and permeability of the CLSM need to be given greater attention to increase confidence in this usage.

Conclusions

1. The WFSs of this study passed all environmental tests and demonstrated good physical/mechanical properties.
2. Greensands from ferrous castings seem likely to pose very low environmental risk.
3. Shell molded and chemically bonded WFSs pass all existing leaching tests, but warrant further study with respect to chemical/organic additives, prior to use.
4. Uses most favored for demonstration projects are: (1) well drained embankments and subgrades; and (2) as a fine aggregate in CLSMs.
5. The WFSs are likely to be economically competitive when the project is close to a disposal source.

Acknowledgements

The research reported herein was funded by the Indiana Cast Metals Association (ICMA) with headquarters in Indianapolis, Indiana.

References Cited

1. Amon, J. A. (1990), " Controlled Low-Strength Material", Construction Specifier, Vol. 43, No. 12, December, pp. 98-101.

2. Bhat, S. T., Lovell, C. W., Scholer, C. F. and Nantung, T. E. (1995), "Flowable Fill Using Waste Foundry Sand", Proceedings, 11th International Symposium on Use and Management of Coal Combustion By-Products, Vol. 2, (CCBs), EPRI TR-104657-V2, Project 3176, Orlando, FL, January, pp. 39-1 to 39-14.

3. Javed, S., Lovell, C. W. and Wood, L. E. (1994), "Waste Foundry Sand in Asphalt Concrete", TRR 1437, TRB, Washington, D. C., Oct., pp. 27-34.

4. Javed, S. and Lovell, C. W. (1994), "Use of Waste Foundry Sand in Highway Construction", JHRP/INDOT/FHWA-94/2, School of Civil Engineering, Purdue University, W. Lafayette, IN, July, 276 pp.

5. Lee W. (1993), "Evaluation of In-Service Subgrade Resilient Modulus with Considerations of Seasonal Effects", Ph.D. Thesis, Purdue University, West Lafayette, IN 272 pp.

6. Nantung, T. (1993), "Design Criteria of Controlled Low Strength Materials", Ph.D. Thesis, Purdue University, West Lafayette, IN, August.

7. Parkes, E., Westwood, G. and Grigg, R. (1970), "Molding and Core Sands", Applied Science in the Casting of Metals, K. Strauss (Editor), Foesco International Limited, Permagon Press, Birmingham, Great Britain, pp. 313-360.

8. Peck, R. B., Hanson, W. E. and Thornburn, T. H. (1974), Foundation Engineering, John Wiley and Sons, Inc., New York, 514 pp.

9. Terzaghi, K. and Peck, R. B. (1948), Soil Mechanics in Engineering Practice, John Wiley and Sons, Inc., New York, 566 pp.

A NEW LOOK AT SLOPE STABILITY METHODS

Lee Robinson, Professor of Engineering
Idaho State University, Box 8371
Pocatello, ID 83201, (208)236-3273

ABSTRACT

Commonly used limit equilibrium methods for slope stability were developed when hand computations were usual and digital computers were large and cumbersome mainframes. With today's powerful personal computers, most of us now have tremendous computational capability right at our desk. We have the capability to readily use the most sophisticated software. Does this mean we should?

One basic "rule" of numerical analysis is that the more sophisticated or higher-order the method, the more potential for instability and the more difficult it is to use. Is the additional power of methods such as Morganstern-Price or Spencer method worth the extra effort and user expertise required?

This study takes a practical look at various methods. "Real" analysis and design problems from the author's case files and from the literature have been reanalyzed by a variety of methods. The cases include design of highway cut slopes and fill slopes, analysis and remediation of landslides, and design of a simple pond embankment. Based on these analyses a comparison of the "usual" accuracy and the potential for instability of various methods has been made.

The results indicate little difference in accuracy between common methods. Simpler methods are often as good for every-day engineering problems. Other factors such as the ease of use, general acceptance and completeness of testing should be considered as important as analysis method in selection of a software package.

SOFTWARE AND METHODS

The methods most widely incorporated into computer software include Fellenius, Simplified Bishop, Simplified Janbu, Spencer, and Morganstern-Price.

All these methods divide a potential failure mass into vertical slices or strips for analysis as finite elements as shown in Fig. 1. To determine the safety of the slope, a

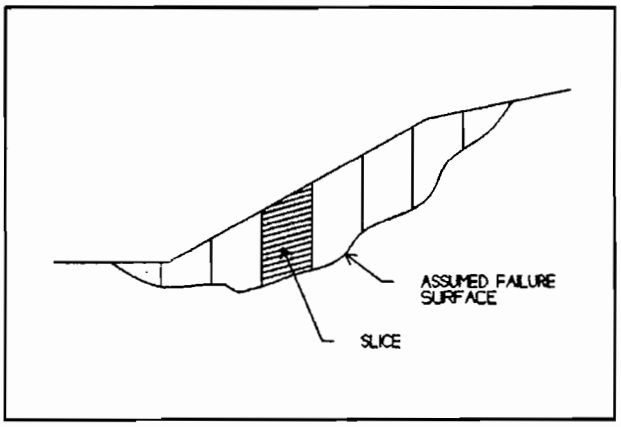

Fig. 1--Method of slices.

variety of failure surfaces are assumed in a search to find the critical surface with the minimum factor of safety.

This approach requires a relationship to describe the force acting on the sides of the slices as shown in Fig. 2. The actual physical relationship defining this force would be obtained by integrating the internal stress on each vertical face. This relationship depends on the geometry, soil types and strengths, groundwater conditions, earthquake considerations, etc. and cannot be represented by a simple function or even a single relationship. Since the physical relationship cannot be readily determined, a simplified assumption is ordinarily made. The major difference between the above listed methods lies in the different assumptions adopted.

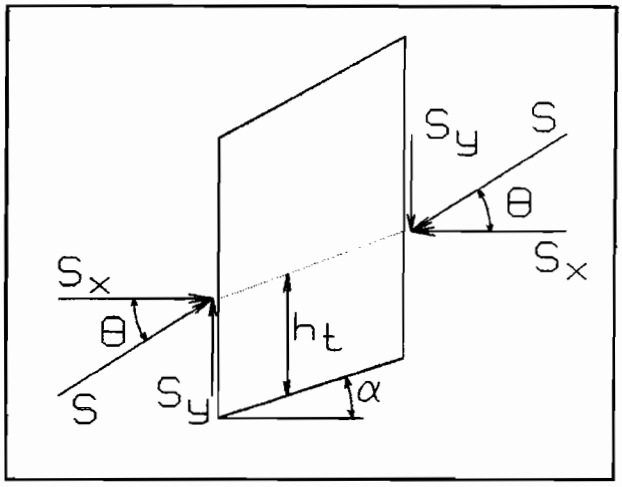

Fig. 2--Definitions of quantities for side force assumptions.

The effects of various side friction functions can be illustrated using an example for which all the above methods perform well (adapted from Janbu ,1973). The earth slope shown in Fig. 3 is homogeneous with soil density = 125 pcf, cohesion = 205 psf and friction angle = 33.8°. The effect of water flow is accounted for by an assumed pore pressure ratio of 0.4. Stability for the circular arc failure surface illustrated has been analyzed using Bishop, Janbu and Spencer methods, utilizing the programs STABR (Duncan and Wong, 1985) and STABL5M (Achilleos, 1988), supplemented by spreadsheet computations using Lotus 123. For comparison, an elastic solution using the finite element program ANSYS (DeSalvo and Gorman, 1990) was also computed.

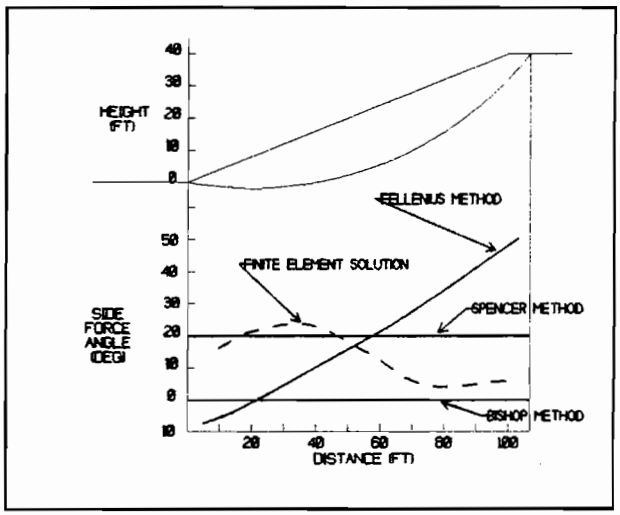

Fig. 3--Example showing side force angles by various methods compared with elastic finite element solution.

In the literature, much has been made of the fact that some side force assumptions mathematically allow computation of "slice equilibrium" while others do not. In actuality, any assumption can only produce slice equilibrium when that assumption accurately models the correct

physical relationship, which generally does not happen. A more important limitation of those methods which do not compute slice equilibrium is that they must use overall moment equilibrium to compute a factor of safety. This requirement limits their application to circular surfaces, which have a defined center of moments.

Fellenius Method

Fellenius developed the first slices method (often termed the "ordinary" or "conventional" method) in the 1930's. This method can be readily computed by hand, but sometimes produces seriously erroneous results and is limited to circular failure surfaces. The ordinary method of slices assumes that the forces acting on the side of each slice is parallel to the base of the slice, i.e. $\theta = \alpha$. Other methods have almost completely supplanted the Fellenius method for computer use. However, students are often taught the ordinary method of slices for hand solution, so comparison with other methods is of some use.

The Fellenius side force assumption is not at all realistic--the angle continuously increases from the downhill to uphill end of the failure surface as illustrated in Fig. 3, whereas the correct angle (qualitatively indicated by the finite element solution) increases from a small angle to near constant, then decreases again at the uphill end. The effect on the computed factor of safety is erratic.

Bishop's Simplified Method

Bishop's simplified method, introduced in 1955, assumes the slice side forces act horizontally ($\theta = 0$). This assumption is not compatible with slice moment equilibrium which requires limitation of the method to circular failure surfaces. Bishop's method can be computed by hand, but is better adapted to computer solution. A number of computer programs incorporate Bishop's method.

Bishop's side force assumption is reasonable at the uphill and downhill ends of the failure mass, but inaccurate in the central portion of the slope (see Fig. 3). Bishop method computes the factor of safety for force equilibrium. As shown in Fig. 4, the force equilibrium relation (represented by the

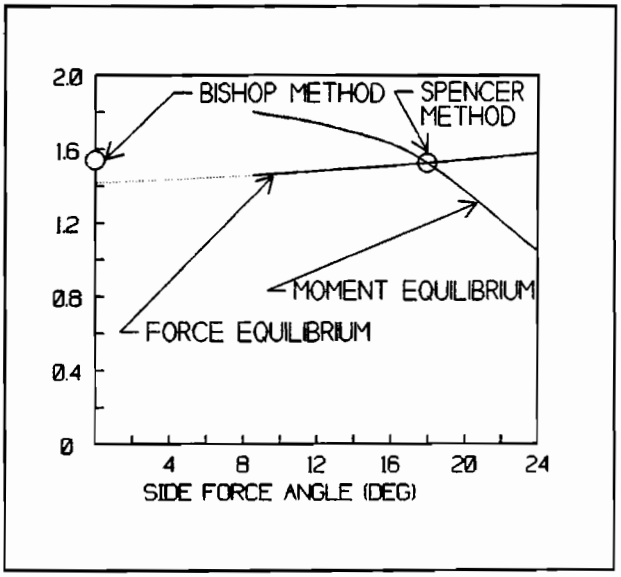

Fig. 4--Comparison of force and moment equilibrium (Spencer) with Bishop method for the example.

Spencer solution) is insensitive to side force angle, which tends to compensate for Bishop's deficient side force assumption.

Janbu Method

Janbu introduced his method in 1954. His method can be computed by hand but is better adapted to computer solution. Janbu's method can be applied to circular or non-circular failure surfaces. His solution method requires iteration to solve for the normal and friction components of the side force. If the procedure is stopped after the first iteration, the method is termed the "Simplified Janbu Method." An empirical correction can be applied to Simplified Janbu results to approximate the results from a completely iterated solution. The widely circulated STABL series of computer programs (Achilleos, 1988) utilizes the Simplified Janbu Method. The empirical correction is available in current versions of the program.

The Janbu method assumes the line of thrust, h_t, is known. Typically, computer programs assume h_t is one-third the slice height. This assumption is valid for usual conditions which produce triangular pressure distributions. For materials which behave elastically (e.g., the finite element line of thrust in Fig. 5), or when "arching" occurs the point of action would be expected to be near mid-height, whereas the point of action would be below the third point when tensile cracks are present.

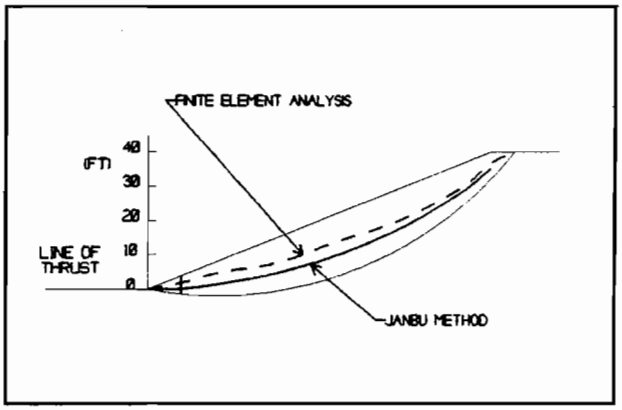

Fig. 5--Line of thrust by Modified Janbu and Elastic Analysis for the example..

Morganstern-Price and Spencer Methods

Morganstern Price method introduced in 1965 and Spencer's method introduced in 1967 are very similar in that two equations are solved for a factor of safety. Both can be applied to circular and non-circular failures and are only amenable to computer solution. The Morganstern-Price approach requires selection of an arbitrary relation between the normal and friction force components on the sides of the slices. Spencer's method can be viewed as a special case of Morganstern-Price, with the normal and frictional forces proportional (i.e., θ is constant). Moganstern-Price and Spencer's methods are utilized by several software packages. Only Spencer's method is included in this study.

Spencer's side force assumption is reasonable for interior slices (see Fig. 3), but not at the

uphill and downhill ends of the failure mass. Sometimes this causes Spencer method to produce an unrealistic line of thrust near the top of the slope (Sharma and Moudud, 1991). Typically, an unrealistic line of thrust has little effect on the computed factor of safety .

BASIS OF COMPARISON

Since the physically correct safety factor is never known, most comparative studies simply compare methods with one another, without addressing which is best. Such comparisons are not of much practical use. For this study, we have attempted to choose a reasonable estimate of the physically correct result as the basis of comparison.

From the above discussion, it is evident that no single side force assumption will be "best" for all cases and conditions. Bishop's method generally will produce realistic results for most cases, but not be as accurate as Janbu or Spencer for particular cases. Spencer's method allows iteration to achieve a more realistic line of thrust than assumed by Janbu for certain cases. However, Janbu never gives a wildly unrealistic line of thrust which Spencer's method may do in other cases. In short, Bishop will be consistently close, but either Janbu or Spencer may be more accurate for a particular problem. An average of the factors of safety from these three methods would be expected to balance these effects to produce a reasonable estimate of the physically correct value.

Based on this reasoning, the average factor of safety from Bishop, Spencer and corrected Janbu analyses computed by STABL5M were used as a basis to compare the methods.

CASES FOR ANALYSIS

Often in the literature, mathematically "worst cases" have been used to compare methods. For example, one study (Thomaz, et. al., 1988) compares methods for a slope with a factor of safety of about 0.5 or less. In the real world, such a slope could never be created or exist--it would fail before ever becoming so steep. In software development, such analyses are certainly valid, as a part of testing, but have little meaning for practical application. On the other end of the spectrum, for real world analysis we do not care if the analysis produces an error of, say 30 percent, for a case with a computed factor of safety of 2.8. The correct conclusion that the slope is extremely stable is unaffected by the error. Error bounds suggested for various methods from such studies are unrealistic and may be misleading.

For this study, we attempted to choose realistic cases for comparison. Eleven cases were chosen from actual slope designs performed by the author. Most of the cases were from highway projects. Two cases of back-computation of landslides were included. One of these landslide cases was from a well documented case in the literature (McKinnell and Mock, 1977) and the other, from the files of the Idaho Highway Department (Jones, 1972) was observed by and is well

known to the author.

Each case selected met the following criteria:

1. The reasoning used in selection of strength values and groundwater conditions for analysis are well known to the author.

2. Each case was used to make a design decision and generally gave the minimum factor of safety from a search.

3. Each landslide analysis had a well defined failure surface ascertained by observations and borings.

4. A broad range of conditions and geometries needed to be represented: shallow and deep failure surfaces, cut slopes, fill slopes, natural slopes, undrained and drained conditions, earthquake and non-earthquake conditions.

5. Both cut and fill slope conditions needed to be included.

Table 1 describes the characteristics of the chosen cases. For the two landslide analysis cases, best engineering strength estimates were used for computation, rather than back calculated strengths to give a factor of safety of 1.0.

COMPARISONS

Factors of safety for the test cases were computed using three programs: STABR (Duncan and Wong, 1985) for Simplified Bishop and Fellenius methods and STABL5M for Bishop, Simplified Janbu (with and without correction) and Spencer methods. These computations allowed us to compare the various methods, the algorithmic differences between two well-tested programs for the same method (Simplified Bishop), and the relative importance of soil property selection to selection of method.

To be useful, a method should be more accurate than the soil properties used in the computation. As a rule of thumb, the coefficient of variation of the factor of safety for the method should be at most half the coefficient of variation due to variation in soil strength. According to Singh and Lee (1970) a coefficient of variation for direct shear testing produces a minimum coefficient of variation of about 15 and 20 percent for friction angle and cohesion, respectively, for favorable test conditions on samples from the same depth and location. For less favorable conditions, they report two to 3 times this minimum variation. Variability within the soil layer would add at least several percent to these values. From the author's experience in

stochastic analysis using BISTAT (Felio, 1987), the coefficient of variation in the factor of safety is typically about half the coefficient of variation in soil strength. (Examples in Christian, et. al., 1994, show similar effects). Based on these assumptions, the coefficient of variation in

Table 1-- Chosen cases and their characteristics.

CASE	DESCRIPTION
1	Highway cut slope, Effective stress analysis of cohesive soils, high groundwater, moderately shallow cutting arc.
2	Surface water detention dam for municipal landfill, cohesionless dam over undrained clay base soil, moderately deep cutting arc.
3	Highway cut slope, Effective stress analysis of cohesive soil, spring isolated to seam near center of slope, moderately deep cutting arc.
4	Approach fill for highway bridge, cohesionless fill over undrained clay base soil, groundwater at base of slope, earthquake case, moderately deep cutting arc.
5	Highway fill with berm, cohesionless rockfill over undrained cohesive base soil, shallow groundwater, very deep cutting arc.
6	Same as Case 5, but earthquake case.
7	Highway fill, cohesionless rockfill over undrained cohesive base soil, shallow groundwater, very deep cutting arc.
8	Same as Case 7, but with cohesionless granular borrow instead of rockfill.
9	Highway fill, cohesionless lightweight fill over undrained cohesive base soil, shallow groundwater, very deep cutting arc.
10	Same as Case 7, but with rockfill instead of lightweight fill.
11	Highway cut slope, effective stress analysis of cohesive soil, moderately shallow cutting arc.
12	Landslide on highway fill slope, granular fill over cohesive base soil, effective stress analysis, high groundwater, moderately deep cutting arc.
13	Landslide on ski hill, cohesionless soil over cohesionless weathered bedrock, effective stress analysis, very shallow arc to model infinite slope failure.

the factor of safety due to soil strength would be expected to range from about 10 percent for near ideal sampling and testing conditions to about 30 percent for less favorable conditions.

Correspondingly, as a rule an acceptable stability analysis should produce a coefficient of variation due to the method assumptions of about 5 percent.

Table 2 lists the computed factors of safety for all of the analyses. These results were normalized by dividing by the average of factors of safety from Bishop, Corrected Janbu, and Spencer method computed using STABL. The mean and the standard error of the normalized results (coefficient of variation of the factors of safety) was then computed for the various methods and software as summarized in Tables 3 and 4.

Table 2-- Factors of safety computed for practical cases using various algorithms and methods.

CASE	BISHOP (STABL)	CORRECTED JANBU (STABL)	SPENCER (STABL)	FELLENIUS (STABR)	BISHOP (STABR)	UNCORRECTED JANBU (STABL)
1	1.27	1.34	1.21[a]	1.31	1.30	1.25
2	1.57	1.40	1.49	1.23	1.56	1.33
3	1.97	1.93	2.13	1.75	1.88	1.86
4	0.93	0.90	0.91	0.95	0.93	0.83
5	1.98	2.06	1.98	1.87	1.97	1.97
6	1.04	1.11	0.96[a]	1.07	1.03	1.01
7	1.64	1.81	1.63[a]	1.60	1.60	1.63
8	1.15	1.26	1.06[a]	1.13	1.13	1.13
9	1.29	1.30	1.29	1.12	1.15	1.19
10	0.91	0.93	0.90	0.89	0.90	0.84
11	1.45	1.45	1.44	1.38	1.43	1.37
12	0.88	0.95	0.88[a]	0.96	1.00	0.88
13	0.81	0.81	0.75[a]	0.79	0.81	0.79

[a] Spencer assumption produced unrealistic line of thrust.

EXPLANATION OF RESULTS

The normalized mean in Table 3 and 4 is expected to be 1.00 for a method which, on the average correctly models the physically correct solution (assuming the three-method average described above is valid). A method is expected, on the average, to produce conservative results if the normalized mean is less than one, and nonconservative if the normalized mean is greater than one. A normalized mean of 1.05, for example, would indicate that the method is on average 5 percent non-conservative.

The tabulated coefficient of variation describes the variability of each method about its

normalized mean. A coefficient of variation of 5 percent, for example, would mean that about 2/3 of the time the method will compute a factor of safety within 5 percent of the normalized mean. From the above discussion, a "good" method ought to produce a coefficient of variation of 5 percent or less.

Table 3: Comparison of Slope Stability Methods.

METHOD	NORMALIZED MEAN	COEFFICIENT OF VARIATION (%)
FELLENIUS (STABR)	0.96	7.04
BISHOP (STABL)	1.00	2.22
UNCORRECTED JANBU (STABL)	0.95	3.25
CORRECTED JANBU (STABL)	1.02	4.26
SPENCER (STABL)	1.00[a] 0.98	2.37[a] 3.59

[a] With cases which produce unrealistic lines of thrust removed from statistic.

The results listed in Tables 3 and 4 lead to the following observations:

1. As expected, the Fellenius Method produces a coefficient of variation much greater than the suggested 5 percent limit. For this reason, the Fellenius Method should not be used for serious design or analysis computations. The remaining methods all produce acceptable coefficients of variation and are acceptable.

2. The Simplified Bishop Method and Spencer's Method for cases for which it produces a realistic safety factor are the most accurate and least variable of the methods compared. Both predict the correct factor of safety almost exactly on average with a normalized mean of 1.00. Both have a very small coefficient of variation of just slightly more than 2 percent, less than half the suggested limit of 5 percent.

3. The Corrected Janbu and Spencer Method when unrealistic lines of thrust are allowed are slightly less accurate than those of Item 2 above. Both predict the correct factor of safety within about 2 percent on average, and have about the same coefficient of variation (about 4 percent), still less that the suggested 5 percent limit. Often revising a Spencer analysis for unrealistic line of thrust is impractical (see Sharma and Moudud). These results suggest that accepting results from such Spencer analyses will achieve acceptable accuracy for practical purposes. Alternately, using the corrected Janbu approach will achieve similar accuracy with a realistic line of thrust.

4. The uncorrected Janbu Method produces very acceptable accuracy with a coefficient of variation of about 3 percent. The method is about 5 percent conservative on average. Users of the uncorrected Janbu method should recognize this conservatism in evaluating results. If this effect is recognized, the Janbu Method without correction is an excellent choice.

5. From Table 4, it appears that differences between algorithms used by different software packages to compute geometry, forces, neutral stresses, etc. can have as large an effect on the variability of results as the difference between methods. Both STABR and STABL are well designed programs with long track records of use, yet coefficients of variation of abut 2 and 5 percent, span the range of those among the methods from Table 3, except for the unacceptable Fellenius method. However, the two values are at or within the suggested 5 percent maximum. Two conclusions may be drawn from these results: First, well designed and tested software should produce acceptable accuracy, and second, choosing a software package is probably as important than choosing a method of analysis.

Table 4 -- Comparison of Simplified Bishop Method for three algorithms.

COMPUTER PROGRAM	NORMALIZED MEAN	COEFFICIENT OF VARIATION (%)
STABR	0.99	5.23
STABL	1.00	2.22

SELECTION OF ANALYSIS METHODS AND SOFTWARE

The choice between Bishop, Janbu (with or without correction) and Spencer method is largely a matter of the personal preference of the user. All will produce acceptable results. Factors such as ease of data entry, ability to handle a variety of groundwater conditions, availability of pre- or post processing with graphical capability, general acceptance and completeness of testing should be as important to the user than the analysis method(s) used by the software.

Bishop method is limited to circular arc analysis. This limitation is probably not significant for design of cut and fill slopes, since according to Sanderson et. al (1970) arc surfaces generally produce minimum factors of safety equal to or slightly less than those produced by combined arc and planar surfaces. For landslide analysis, it is often important to model an actual failure surface which is not arc-shaped. Janbu or Spencer would be needed for such analyses.

LITERATURE CITED

Achilleos, E. (1988) "User Guide for PC STABL 5," Joint Highway Research Project JHRP-88/19, Purdue University.

Christian, J.T., et. al. (1994) "Reliability Applied to Slope Stability Analysis," Journal of Geotechnical Engineering, Vol. 120, No. 12, pp. 2180-2207.

DeSalvo, G.J. and R.W. Gorman (1990) "ANSYS Engineering Analysis System," Revision 4.4A, Swanson Analysis Systems, Inc., Houston, PA.

Duncan, J.M. and K.S. Wong (1985) "STABR: A Computer Program for Slope Stability Analysis with Circular Slip Surfaces (Microcomputer Version)," Department of Civil Engineering, Virginia Polytechnic Institute and State University, Blacksburg.

Felio, G.F. (1987) "User's Manual for BISTAT," Civil Engineering Department, University of California, Los Angeles.

Janbu, N (1973) "Slope Stability Computations," in Embankment Dam Engineering, R.C. Hirschfield and S.J. Poulos, ed., Casagrande Volume, John Wiley and Sons, New York, pp. 47-86.

Jones, W.V. (1972) "Landslide Investigation and Corrective Treatment - Evans Property," Project: I-15-1(38)21, Internal Memo, Idaho Department of Highways.

McKinnell, W.P. and R.G. Mock (1977) "Analysis of a Landslide During Construction of the Howelson Hill Ski Jump Complex, Steamboat Springs, Colorado," Proceedings, Fifteenth Symposium on Engineering and Soils Engineering, Pocatello, ID, pp.57-72.

Sanderson, R.L., et. al., (1970) "Parametric Effects on Slope Stability Analysis," Proceedings, 8th Symposium on Engineering Geology and Soils Engineering, Pocatello, ID, pp. 109-122.

Sharma, S. and Moudud, A., (1991) "A Review of Spencer's Method for Slope Analysis," Proceedings, 27th Symposium on Engineering Geology and Geotechnical Engineering, Logan, UT, Paper No. 22.

Singh, A. and K.L. Lee (1970) "Variability in Soil Parameters," Proceedings, 8th Symposium on Engineering Geology and Soils Engineering, Pocatello, ID, pp. 159-186.

Thomaz, J.E., et. al. (1988) "PCSTABL5M, An Improved Slope Stability Program," Proceedings, 24th Symposium on Engineering Geology and Soils Engineering, Coeur D'Alene, ID, pp. 299-318.

Van Aller, H.W. (1992) "STED: Smart Editor for PCSTABL," Version 6.13, (Shareware) 1440 Foxwood Court, Annapolis, MD.

LANDSLIDE-CAUSING FACTORS: CLASSIFICATION AND NUMERICAL ASSESSMENT

Vadim I. Khazin, Ph.D.
Center for Water Resources and Environmental Research,
City College, City University of New York
Convent Ave. at 140th St., Room T-107, New York, NY 10031

ABSTRACT

To prevent landslides in time, as well as to ensure efficient landslide control, one must assign measures of landslide control according to the landslide-causing factors (LCFs) at the site in question. The LCFs may be either already acting or just potential, but in any case the approach should be as much site-related as possible (though a regional approach is needed too to comprehend some geologic factors) and include indications as to the LCFs' relative importance. Otherwise, there would be no certainty concerning the factors accounted for and the capital investments made: some particular LCFs may be either not identified or overestimated, and as a result the measures taken would be inappropriate or fall beyond the necessary limits.

It is highly desirable to be able to express the significance of each particular LCF in quantitative parameters, and the best option would be if we could range all the LCFs according to their relative importance. Unfortunately, this ultimate goal is unrealistic because many LCFs are not liable to numerical assessment, but one should try to come as close to it as possible.

With this aim in mind, the Author first presents a practice-oriented three-step classification of the factors mentioned: they are divided into two categories — natural and anthropogenic, or manmade ones, and then into 12 groups, the total number of LCFs exceeding 30. Then some recommendations as to simple numerical methods to be used for their eventual assessment are given, with examples based on the Author's experience in Ukraine. The methods include using correlation and slope stability analyses, the latter allowing for calculating criteria characterizing the relative role of particular LCFs.

INTRODUCTION

To cope with the hazard of landslides, especially in urbanized areas, it is essential to assign measures of landslide control according to the landslide-causing factors (LCFs) at the site in question. These LCFs may be either already acting or just potential, but in any case the approach should be as much site-related as possible (though a regional approach is needed too to comprehend some geologic factors) and include indications as to the LCFs' relative importance. Otherwise, there would be no certainty concerning the factors accounted for and the capital investments made: some particular LCFs may be either not identified or overestimated, and as a result the measures taken would be inappropriate or fall beyond the necessary limits.

Since specifying landslide control measures should correspond to the LCFs at the particular site, the estimate of the LCFs' significance is highly desirable. The best option would be if we could range all the LCFs according to their relative importance. Unfortunately, this ultimate goal is unrealistic because not all the LCFs are liable to numerical assessment, but one should try to come as close to it as possible.

BACKGROUND

Dozens of classifications of landslide-causing factors have been proposed. Most of the authors classify them into two groups, with further subdivisions. In his classical work *Mechanism of Landslides,* Terzaghi (1950) divided all the LCFs into (i) external (causing increase of shear stresses in soils at their shear resistance unchanged), and (ii) internal (causing decrease of shear resistance at the shear stresses unchanged.) Drannikov (1964) also suggested their two-group division into (i) passive, i.e. conditions determining proneness to landsliding, and (ii) active, i.e. directly causing or triggering landslides. Alexander (1992) separates (i) exogenic and (ii) endogenic factors. Some researchers just give a list of possible LCFs without classifying them, like Záruba and Mencl (1982) who present a list of "the most important" factors, some of them apparently intermingled (like "weathering" and "frost effects".) Crozier (1986), also giving just a list of LCFs which he names "causes of instability", stresses on their attitude toward the landslide event by indicating that they may serve as "preparatory", "triggering" or "controlling" (that is, determining the character of the event in progress.) Thomson and Tiedemann (1982) give a rather limited classification scheme dividing all the LCFs (or rather "processes" as they put it) into two categories: natural and man-induced, and then each of these categories into long-term and short-term ones.

Not attempting to analyze these classifications in detail, we can denote that one of their common features is that they all seem to be designated for the use of landslide specialists only, not "landslide causers," so to say. Meanwhile, landslide phenomena have already passed from the category of purely natural events to that of combined natural-manmade origin, and in urbanized areas their occurrence is becoming predominantly anthropogenic ever more. That is why such a classification of LCFs is needed which could render due representation to this relatively new class of factors. Moreover, since those who cause such manmade landslides do this inadvertently, through the lack of understanding, the classification should better be expressed in plain language clear to nonspecialists.

CLASSIFICATION OF LANDSLIDE-CAUSING FACTORS

It is clear that landslides may be caused by quite a number of factors, rarely by just one of them, and a suitable classification of these factors, or LCFs, could help us not only comprehend their nature but determine correct and efficient countermeasures. And since the overall number of LCFs is several dozens, it should be — for the sake of convenience at least — a more-than-one-step classification. What the Author proposes is a three-step classification where each LCF is meant not just as a possible cause of a

landslide but rather as a factor to be accounted for as contributing to the probability of landslide occurrence at the site considered. The classification is based on the genetic principle, and the major division is proposed to lie between the two categories: natural and anthropogenic (artificial, manmade) LCFs.

This can be justified by their different character and manageability. As to the character, natural factors more often than not represent conditions or background for landslides to occur, triggering them relatively seldom, while anthropogenic factors, on the contrary, represent human actions affecting the existing natural conditions and quite often leading to (or triggering) landslides. As to their manageability, the natural LCFs are either not manageable at all or manageable to a certain extent but with great expenses involved; meanwhile, the anthropogenic LCFs are mostly quite manageable and/or even avoidable.

The groups of factors falling into these two categories include LCFs designated here by letters and numbers as follows:

NATURAL (N)

N-1. *Topographic:*

- **N-1.1.** Presence and nearness of natural slope(s)
- **N-1.2.** Steepness of the slope(s)
- **N-1.3.** Exposure of the slope(s)

N-2. *Geologic:*

- **N-2.1.** Presence (above the slope toe) of relatively weak (usually clayey) layers or material filling discontinuities in rocks
- **N-2.2.** Dipping of strata or discontinuities with respect to the slope

N-3. *Hydrogeologic:*

- **N-3.1.** Presence of aquifer(s) whose phreatic or piezometric level is above the slope toe
- **N-3.2.** Hydraulic properties of the aquifer(s)
- **N-3.3.** Preconditions for temporary aquifer(s) to form

N-4. *Hydrologic:*

- **N-4.1.** Presence of a water body like sea, lake or river at the slope toe
- **N-4.2.** Intensity of erosion or abrasion produced by this water body

N-5. *Meteorological:*

- **N-5.1.** Peculiarities of precipitation (quantity, intensity, distribution by time and state of matter)
- **N-5.2.** Pattern of water balance (infiltration, evapotranspiration, surface runoff)

N-6. *Vegetational:*

- **N-6.1.** Presence and density pattern of trees and/or bushes on the slope(s)
- **N-6.2.** Characteristic features of this vegetation like depth of the root system and water absorbing ability

N-7. *Endogenic:*

- **N-7.1.** Regional neotectonic activity
- **N-7.2.** Seismicity (in terms of anticipated earthquake intensity)

ANTHROPOGENIC (A)

A-1. *Actions affecting topography:*

A-1.1. Creation of new slopes (fills or cutoffs)

A-1.2. Undercutting of the existing slopes

A-1.3. Overloading of the existing slopes by fills, spoil heaps, etc.

A-2. *Actions initiating or activating bank erosion or abrasion:*

A-2.1. Creation of a reservoir at the slope toe

A-2.2. Intensity of reservoir bank erosion

A-2.3. Removal of beach or bottom material from below the slope

A-2.4. Adverse interference into the longshore drift of sediments by improper placement or maintenance of coast-protection structures

A-2.5. Waves produced by vessels

A-3. *Actions affecting hydraulic regime:*

A-3.1. Saturation of slope(s) by leakages from water-conveying conduits

A-3.2. Uplift of groundwater level due to the filling of reservoirs or to the construction of lengthwise (e.g. retaining) structures on the slope without proper drainage

A-3.3. Rapid drawdown in the reservoir at the slope toe

A-4. *Actions affecting surface runoff:*

A-4.1. Improper maintenance of surface drainage causing local increases of infiltration into the slope

A-4.2. Irrigation, ploughing, etc. on or near the slope, facilitating infiltration

A-4.3. Deforestation

A-4.4. Snow dumping on or near the slope

A-5. *Additional static and/or dynamic loads:*

A-5.1. Erection of buildings or other structures on or near the upper part of a potential landslide

A-5.2. Vibration caused by blasting, pile driving, percussion drilling, railway or other vehicles, etc. on or near the slope.

So we have 12 groups of LCFs, their total number exceeding 30 but easily expandable if further detailing is needed. One of the main goals of such a classification, as to the Author, is to help (or rather to alert) those who, not being landslide specialists, are however authorized to make decisions which may lead to a landslide, so that they could consider this hazard in advance. But just indicating the LCFs at the site in question is not enough to assign necessary measures of landslide control; moreover, this could be misleading: not knowing the relative importance of every LCF, one may strive for eliminating all of them, which in most cases would lead to considerable overspendings. Unfortunately, this task is not completely soluble since not all the LCFs can be expressed numerically; but this should be the goal, and certain attempts in this direction have been made and are briefly described below.

NUMERICAL ASSESSMENT OF LANDSLIDE-CAUSING FACTORS

When dealing with landslides, a typical numerical approach is to use methods of slope stability analysis, and for the aims of this paper they can be used too; but first let us suggest another approach. If we are trying to make a judgment about the role of a certain LCF on a regional or local scale, and possess information on landslide activity (regional or local) on a long-term time scale, we may search for a correlation between these two variables. A necessary prerequisite for this however is that the LCF being estimated could also be expressed numerically on the same time scale. As for the landslide activity, it can be expressed either in numbers (volumes) of landslides — on a regional scale, or in some movement characteristics of a slope (bank) or even one large landslide — on a local scale. Here is an example.

It is well known that atmospheric precipitation may directly cause or trigger superficial landslides; there have been proposed various parameters to characterize it in this respect. The simplest and always available one is just the quantity of precipitation per any period of time. We used this parameter to find a seemingly obvious correlation between it and the landslide activity in Kiev, Ukraine, expressed by the annual number of such events (mainly shallow flowslides). The information available for both sides of the equation covered a 18-year period. By trial and error method we found that the best correlation is encountered when taking total precipitation in millimeters during 1.5 years preceding the year for which the number of landslide events (LE) is considered. This amount of precipitation being designated PR, the linear correlation found is as follows:

$$LE = -21.013 + 0.03276\,PR \qquad (1)$$

This relationship can be interpreted in such a manner that every 100 mm increase of PR leads to 3-4 more of LEs in the year to come.

Likewise, a correlational approach can be used to assess numerically the role of some other LCFs fluctuating in time, e.g. those designated above as N-4.2, N-7.2, A-3.2. Such relationships, if found, can serve as a justification of implementing measures of landslide control aimed directly against the corresponding LCF.

Unfortunately, this method can rarely serve for a certain slope or landslide; it reflects relationships more or less statistically. Much more exact and specific could be using for this aim (numerical assessment of the LCFs) methods of slope stability analysis. But first some preliminary remarks regarding these methods. A lot of them has been developed but neither can be considered completely reliable in terms of the result obtained (safety factor, F): a landslide may well occur on a slope found to be quite stable by calculations, and not occur on a slope labeled "unstable". This observation, particularly impressive when making "back analysis" of slopes after actual failure (when, by definition, the stability had to correspond to the equality $F = 1$), can be explained by (i) uncertainties as to the soil shear strength characteristics mobilized against failure; (ii) uncertainties as to the mechanism and failure surface of a would-be landslide; (iii) multiplicity of methods and approaches both determining the soil strength and analyzing the slope stability.

However, fortunately enough, we can avoid this frequent inadequacy of the results of slope stability analysis when using these results to determine the role of certain LCFs. In such occasions the accuracy of F is of minor importance because what we need to know is not its absolute value but the difference between the two values, $F_0 - F_f$, where F_f corresponds to the situation when the estimated factor is acting and F_0 when it is extinct. So, the numerical criterion C_{lf} characterizing the role of an LCF will be expressed as:

$$C_{lf} = \frac{F_0 - F_f}{F_0} \cdot 100\% \qquad (2)$$

The problem exists however of how to account for the action of various LCFs. Here we see three possible ways, i.e. three different approaches to different factors: (i) to consider this action regardless of its duration (e.g. N-3.1); (ii) to consider it for a certain (say, 10-year) duration (N-4.2, A-2.2); (iii) to consider certain grades of this action whenever they can be expressed numerically (N-1.2, N-2.2, N-3.2, N-7.2, A-1, A-2.3, A-3.2, A-3.3, A-5.1). Some examples can illustrate all these approaches.

First. It has long been considered a fact beyond doubt that in Kiev one of a few major LCFs is groundwater; accordingly, major efforts and investments have been directed toward subsurface drainage. Indeed, there are two aquifers above the slope toes, and failure surfaces often initiate in two respective aquifuges below them. However, to check the unspoken assumption that this factor (N-3.1) contributes to the instability of slopes more or less uniformly, we tried to estimate its role expressed by C_{lf} (2) for 14 slopes using parallelly two methods of slope stability analysis. The results fell within a rather wide range — from 6% to 39%, suggesting that, when designing subsurface drainage in the city, a differentiation of slopes is needed instead of a regional, universal approach .

Second. Abrasion, or bank erosion (factor N-4.2) is a major LCF in various Black Sea Coast regions. Knowing by observation the average annual rate of this process (in terms of either volume of eroded soil or advance of the shoreline), we can use slope stability analyses to estimate the corresponding C_{lf} (2) for, say, a 10-year period. Such an analysis performed for a certain slope in the city of Odessa, Ukraine, gave us $C_{lf} = 13\%$. This and similar results can be used for the sake of predicting decrease of slope stability and assigning correspondent measures of control.

Third. When a multistory building was designed to be built near the upper edge of a slope in the city of Lvov, Ukraine, we studied the dynamics of F changing in time as a result of two oppositely influencing consecutive procedures: excavation which increased F, and erection of the building which decreased it (factor A-5.1). The result appeared to be surprisingly high and unacceptable: $C_{lf} = 40\%$, but it was late to change the whole project, since the excavation had already been accomplished, so the only realistic solution was to diminish the load produced by the designed building by lowering its height (the number of stories).

DISCUSSION

The classification of landslide-causing factors presented above is far from being final: some factors may have been omitted (especially within the anthropogenic category) while others perhaps not subdivided enough or not sounding as belonging to the same classification level. But, even as such, it proved useful, particularly when dealing with nonprofessional decision-makers able to cause landslides by taking improper actions or failing to take proper ones.

While the principle of numerical assessment of the LCFs' role by calculating the C_{lf} as suggested in (2) seems quite logical, its practical realization is not as clear. Not only different approaches to different LCFs are needed (accounting or not for their duration and/or grading), but even for a particular LCF it may be difficult to prefer one of several approaches possible. Subsurface water is an example. Its presence and action may be considered, when doing slope stability analyses, at least as follows: (i) by accounting for the soil(s) weight changes; (ii) by accounting for the decreases in soil(s) shear strength — either through moisture or pore pressure mechanism; (iii) by accounting for the hydrodynamic forces exerted by the water flow or eventual artesian head; (iv) by accounting for internal erosion, scouring, etc.

Since most of the landslide control measures or structures are directed toward the elimination (or reduction) of certain LCFs, a similar approach is possible when evaluating the efficiency of such measures or structures. Using slope stability analyses for this goal would provide (again, not for all the scope of these measures or structures, unfortunately) answers to the following question: how much greater (in relative units) will the safety factor become after accomplishing the measures or structures designed. However, this problem is associated with another one: the efficiency mentioned above can and should be expressed not only in terms of increasing the safety factor but otherwise as well. Some suggestions in this regard have already been developed (Khazin, 1979, 1983.)

REFERENCES

1. Alexander, D. , 1992, On the Causes of Landslides: Human Activities, Perception, and Natural Processes. Environ. Geol. Water Sci., vol. 20, No.3, p.165-179.

2. Crozier, M.J., 1986, Landslides: Causes, Consequences and Environment. London, Sydney, Dover, NH: Croom Helm, 252 pp.

3. Drannikov, A.M., 1964, Engineering Geology (in Russian). Kiev: Gosstroyizdat, 255 pp.

4. Khazin, V., 1979, Classification of the Types of Effectiveness of Landslide-Control Measures (in Russian). In: Engineering-Geological Properties of Soils and Characteristics of Geodynamical Processes. Kiev: Naukova Dumka, p.123-129.

5. Khazin, V., 1983, Principles of Assessment of the Effectiveness of Landslide-Control Measures (in Russian). In: Landslides of Moldavia and Environmental Protection. Kishinev: Shtiintsa, p.137-138.

6. Terzaghi, K, 1950, Mechanism of Landslides. Geol. Soc. of America, Application of Geology to Engineering Practice, Berkey Volume, p.83-123.

7. Thomson, S., Tiedemann, C.E., 1982, A Review of Factors Affecting Landslides in Urban Areas. Bull. of the Assoc. of Engng. Geologists, vol. XIX, No.1, p.55-65.

8. Záruba, Q., Mencl, V., 1982, Landslides and their Control (Developments in Geotechnical Engineering; 31; 2nd Ed.). Amsterdam, Oxford, New York: Elsevier Publ. Co., 324 pp.

SLOPE STABILITY EVALUATION USING DISCONTINUOUS DEFORMATION ANALYSIS

Mary M. MacLaughlin, Nicholas Sitar, and Tracy S. Dobson
Department of Civil Engineering, University of California, Berkeley, CA 94720

ABSTRACT

Traditional limit equilibrium analysis methods used in the evaluation of rock slope stability do not fully account for the kinematics of motion. In contrast, the Discontinuous Deformation Analysis (DDA) reproduces the actual displacements along discontinuities: joint sets within the sliding mass, as well as the failure surface. DDA is a fully dynamic model which allows these displacements to develop with time. Consequently, DDA can be used to predict the initiation of failure *and* to study the subsequent kinematics of the failed mass. In this study we tested the DDA method by analyzing three simple block sliding problems for which we could obtain simple analytical solutions. The results show not only that the DDA method is accurate, but that it also applicable to the analysis of complicated slope stability problems. While circular-shaped failure surfaces do not display much sensitivity to kinematic constraints, failures on non-circular surfaces show that the presence of discontinuities at critical locations may have a major effect on slope stability, independent of shear strength characteristics of the failure plane.

INTRODUCTION

Discontinuous Deformation Analysis, DDA, is a numerical method developed to model the behavior of discontinuous media (Shi, 1993). Its formulation is based on a dynamic equilibrium which considers the kinematics of individual blocks. The penalty method is used to prevent penetration between blocks, and the solution is obtained by minimizing the potential energy. Thus, the minimum energy solution has no penetration and equilibrium is satisfied at every time step. The energy consumption/dissipation occurs as a result of interblock friction which is modelled using the Mohr-Coulomb criterion.

The current computer implementation of DDA is a suite of programs originally written and recently updated by Shi (1988, 1994). In this implementation, each discontinuity (joint) may have a different friction angle, cohesion, and tensile strength. The blocks are deformable, with the deformability governed by the Young's modulus and Poisson's ratio. A brief outline of the algorithm of the main DDA program is shown in Figure 1. DDA has been applied to a wide variety of problems, from tunneling to toppling (Yeung, 1991), as illustrated in Figure 2.

Our interest has been to develop DDA as an engineering analysis tool with a specific emphasis on slope stability. In particular, the stability of discontinuous rock masses still presents a major challenge to analysts and practitioners alike, and the principal features of DDA make it an obvious candidate as an analysis tool. However, before applying such a sophisticated numerical tool to complicated problems, it is prudent to study a few simple problems to make sure that the method is applicable and the results are accurate. Since slope stability problems involve sliding and interacting blocks, we chose three problems that allow the verification of both motion and interaction, as described next.

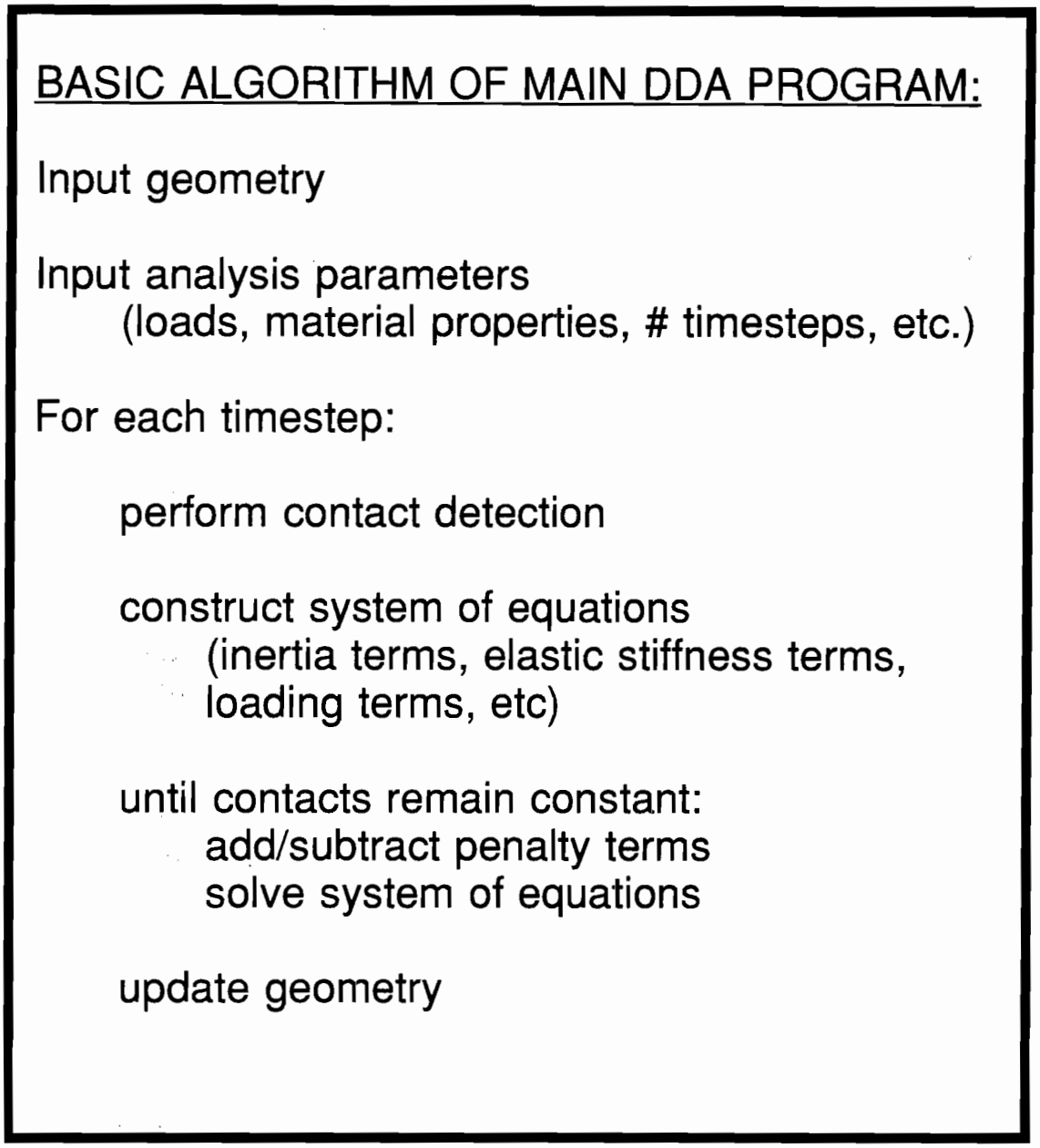

Figure 1. Algorithm showing the structure of the main analysis program.

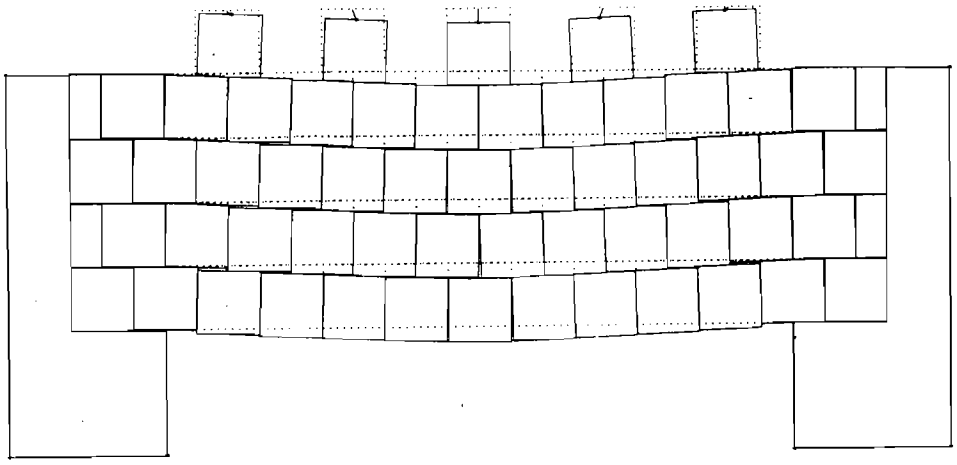

(a)

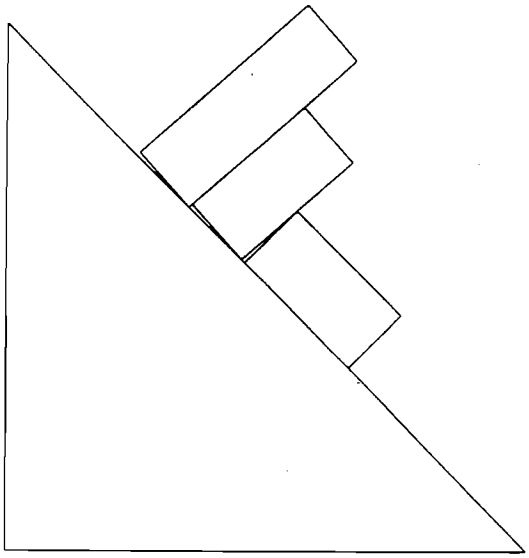

(b)

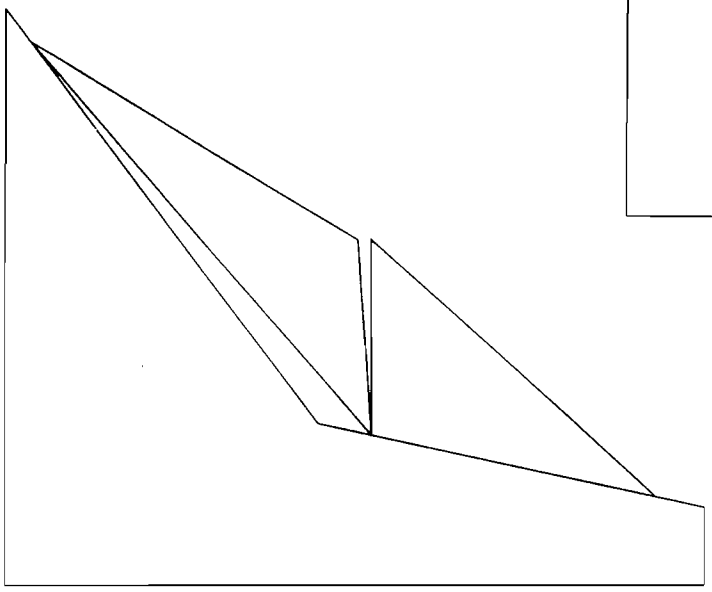

(c)

Figure 2. Examples illustrating the capabilities of the DDA program: (a) tunneling (from Yeung, 1991), (b) toppling, (c) rock slope stability.

VALIDATION

The three problems chosen for the validation study all involve block sliding, as follows: single block on an inclined plane, single block on a double incline, and two blocks on a double incline. These geometries are sufficiently simple to be solved analytically, yet complex enough to test the accuracy and capability of the numerical scheme. The material parameters used in the analyses were unit weight of 161 pcf, Young's modulus between 10^5 to 10^6 psf, and Poisson's ratio of 0.49.

Single Block / Single Incline

The simplest problem is a single block sliding down an inclined plane (Figure 3a). For a plane inclined at an angle α, with friction along the surface ϕ, and the acceleration of gravity g, the analytical solution for displacement d as a function of time t is:

$$d=\frac{1}{2}at^2=\frac{1}{2}(g\sin\alpha-g\cos\alpha\tan\phi)t^2$$

Figure 3b shows a plot of this analytical solution compared to the results of DDA for a case of a 2.3 feet long and 1.15 feet high rectangular block, sliding on a slope inclined at 30°, for three values of ϕ equal to 0°, 20°, and 30°, respectively. The plot shows that the displacements computed using DDA exactly match the analytically computed displacements over the whole range examined in this problem, from zero to six feet.

Single Block / Double Incline

The second problem is slightly more complex. The geometry and symbols used are shown in Figure 4(a). Assuming that the block is a point mass which starts at a height of h on the upper incline, where the slope angle is greater than the friction angle, it slides down the first incline and transfers, instantaneously, onto the second incline. The velocity at the base of the first incline is v_1 and the velocity at the top of the second incline is v_2 are given by:

$$v_1=\sqrt{2gh(1-\tan\phi_1/\tan\alpha_1)} \qquad v_2=v_1\cos(\alpha_1-\alpha_2)$$

and the energy equilibrium equation on the second incline is:

$$\frac{1}{2}mv_2^2+mgd(\sin\alpha_2)-mgd(\cos\alpha_2)(\tan\phi_2)=0$$

If the inclination of the second incline is less than the friction angle, the block will decelerate. The energy equation can then be solved for the distance that the block will slide before it comes to a stop, as follows:

$$d=\frac{v_2^2}{2g(\cos\alpha_2\tan\phi_2-\sin\alpha_2)}$$

Figure 4(a) shows one of the test cases with incline #1 = 30° and incline #2 = 15°. A "target distance" was calculated from the analytical solution assuming that the block could be represented

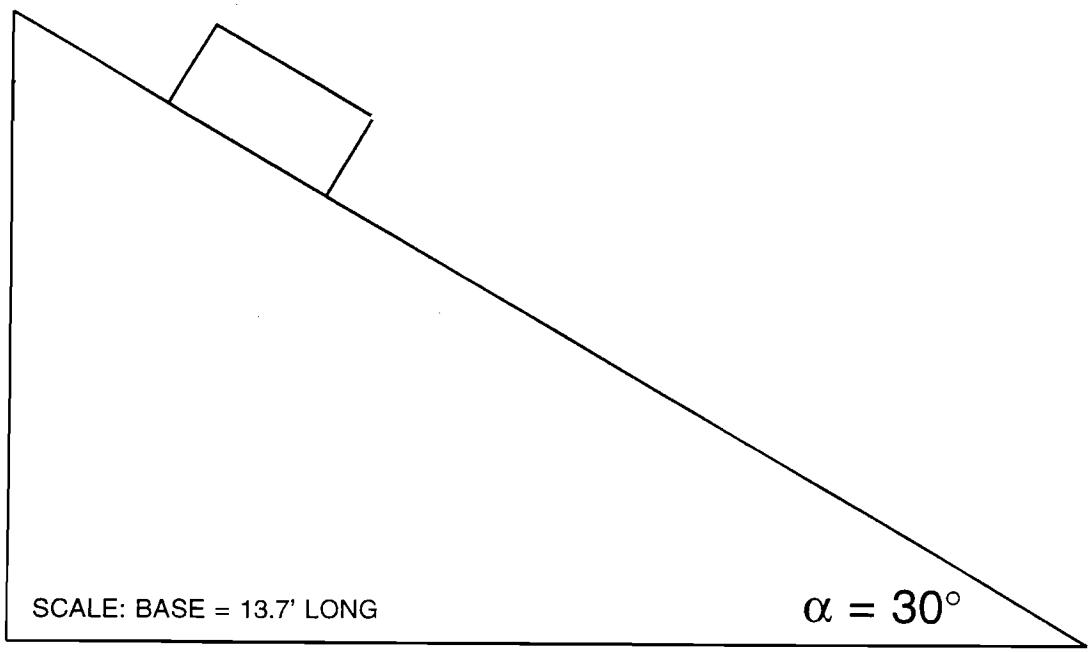

(a)

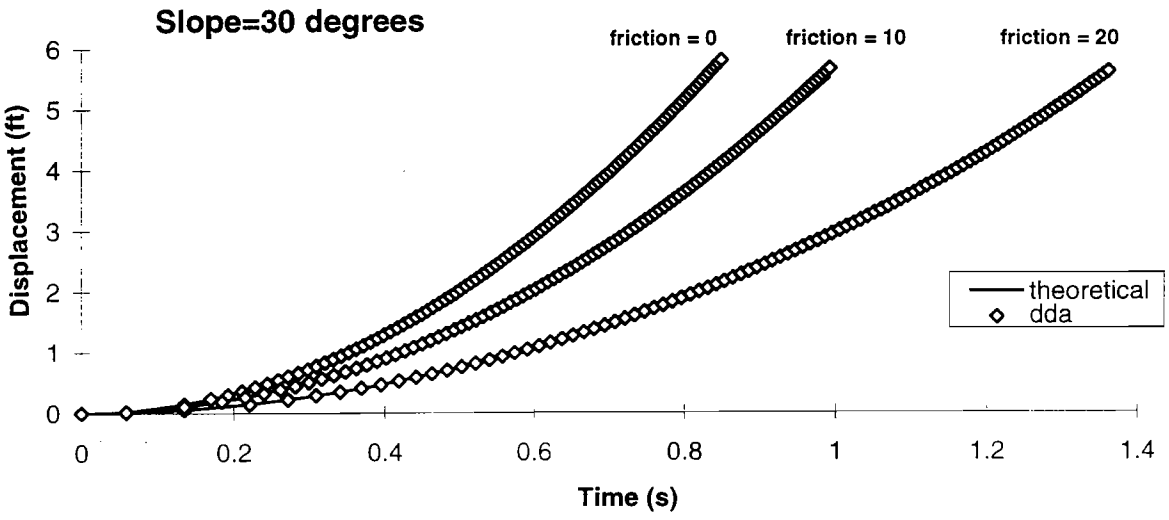

(b)

Figure 3. Single block on an incline. (a) Problem geometry. (b) Comparison of computed displacements versus time for different values of interface friction.

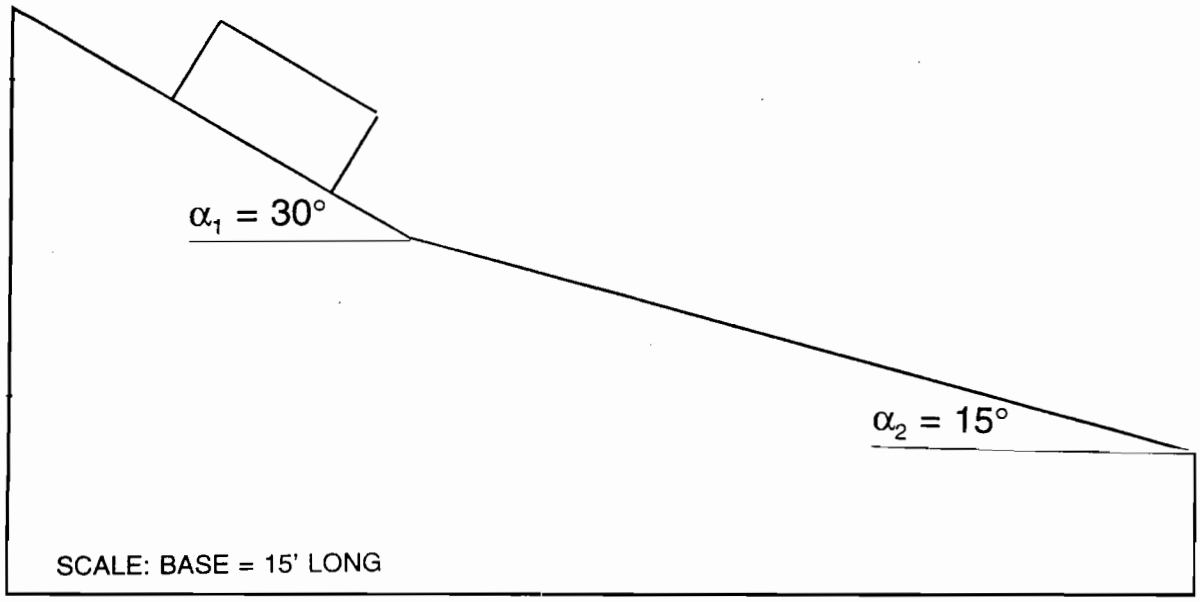

(a)

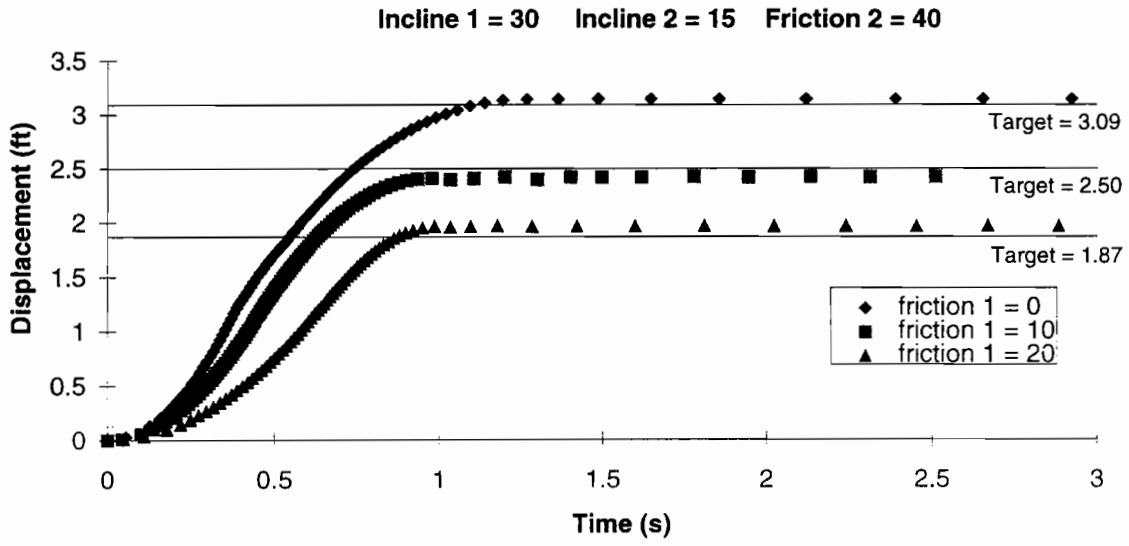

(b)

Figure 4. Single block on a double incline. (a) Problem geometry. (b) Computed displacements versus time compared to analytically predicted target distance for different values of interface friction on the upper incline (ϕ_1 = 0°, 10°, and 20°) and a fixed value friction on the lower incline ϕ_2 = 40°.

by a point mass located at the midpoint of the base of the block. Figure 4(b) shows a plot of the displacement of the block as a function of time, as calculated by the DDA program, for several different cases (ϕ_1 = 0°, 10°, and 20°). The results show that the DDA stopping distance is within 5% of the "target distance" computed using the analytical solution. This is a very satisfactory result, considering that the assumptions present in the analytical solution do not match the DDA model exactly.

Two Blocks / Double Incline

The third test case was patterned after case solved analytically by Goodman (1989). An upper "active" block and a lower "passive" block are separated by a vertical discontinuity. Figure 5(a) shows the configuration of the problem and the symbols used. W_1 and W_2 are the weights of the upper and lower blocks, α_1 and α_2 are the upper and lower slope angles (30° and 5° in this case), and ϕ_1, ϕ_2, and ϕ_3 are the friction angles on the upper and lower slopes and the vertical discontinuity, respectively. The resultant force between the blocks is given by:

$$F_1 = \frac{W_1 \tan(\alpha_1 - \phi_1)}{\cos\phi_3 + \sin\phi_3 \tan(\alpha_1 - \phi_1)}$$

and the corresponding equilibrium equation for a restoring force F_2 (e.g. rock bolt), inclined at θ below horizontal, is given by:

$$F_2\cos(\alpha_2 - \phi_2 - \theta) - F_1\cos(\alpha_2 - \phi_2 - \phi_3) - W_2\sin(\alpha_2 - \phi_2) = 0$$

If the friction angle along the base of the passive block is high enough, the configuration may be in equilibrium without any restoring force at all. With the restoring force F_2= 0, the equation reduces to (after rearranging and solving for ϕ_2):

$$\phi_2 = \alpha_2 - \tan^{-1}\left(\frac{-F_1\cos\phi_3}{F_1\sin\phi_3 + W_2}\right)$$

In order to model the situation with no kinematic constraints as described by this equation, a small "hole" is created at the base of the active block to allow the active block to slide along the upper slope without immediately moving onto the lower slope. Figure 5(b) shows the configuration with the hole and Table 1 and Figure 6 display the analytical solution and the DDA results for the case with slope angles α_1 = 30° and α_2 = 5°.

The DDA results are displayed in pairs. The lower number of the pair is the lowest value of ϕ_2 for which the blocks do not smoothly and directly accelerate to failure. Instead the blocks creep slowly down the slope until they accumulate enough momentum to accelerate. The higher number of the pair indicates the lowest value of ϕ_2 for which the blocks come to a complete halt after a tiny amount of initial displacement due to elastic deformation. The upper number, which can be obtained with nothing more that visual observations during the analysis, is within 5° of the analytical solution, and is on the conservative side. The lower number matches the analytical solution very well, but must be obtained by plotting the computed block displacements.

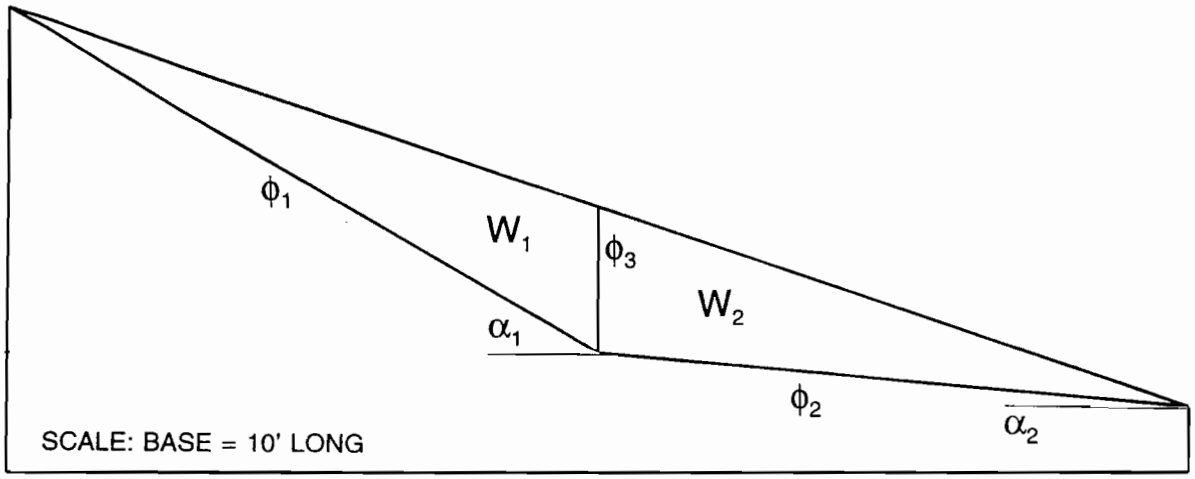

(a)

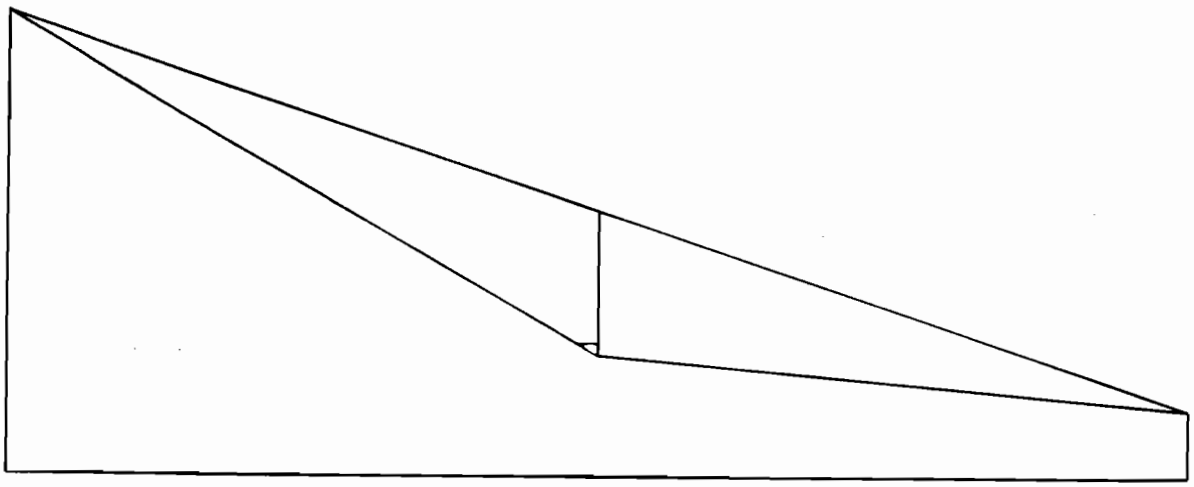

(b)

Figure 5. Two sliding blocks on a double incline. (a) Two blocks separated by a vertical discontinuity (after Goodman, 1989). (b) Two blocks separated by a vertical discontinuity with a small opening at the base of the upper block.

Table 1: The analytical solution and DDA results for the "Two Blocks / Double Incline" validation problem, for the case $\alpha_1 = 30°$ and $\alpha_2 = 5°$. (All values are degrees.)

ϕ_1	ϕ_3	ϕ_2-Analytical	ϕ2-DDA (no kinematic constraints)	ϕ2-DDA (with kinematic constraints)
0	0	35.0	35-38	10-12
0	10	30.6	31-34	10-12
0	20	27.1	27-31	10-12
0	30	24.1	24-31	10-12
10	0	25.0	25-30	9-11
10	10	22.9	23-28	9-11
10	20	21.1	21-25	9-11
10	30	19.4	20-23	9-11
20	0	15.0	16-19	7-9
20	10	14.4	15-19	7-9
20	20	13.9	15-18	7-9
20	30	13.3	14-17	7-9

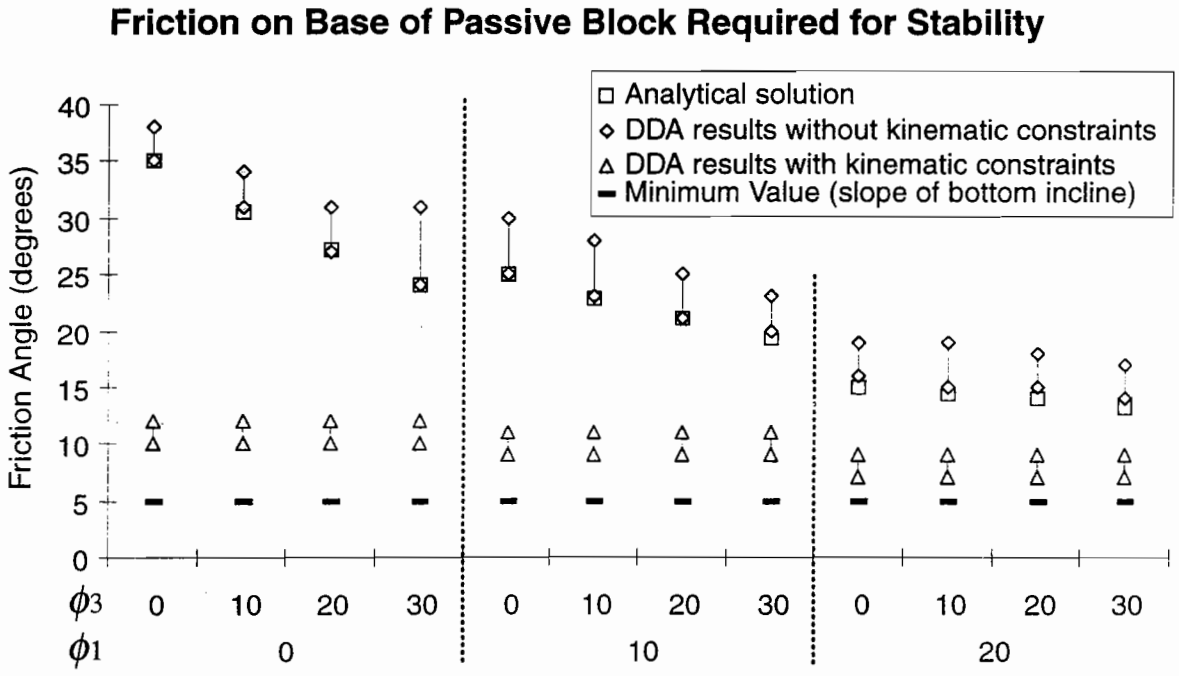

Figure 6: A graphical representation of the data in Table 1.

When kinematic constraints are enforced by analyzing the configuration without the hole, the results are quite different, as shown in the last column of Table 1. The friction along the base of the passive block required for stability is now much lower (approaching the lower limit of $\alpha_2 = 5°$) because the active block is actually sliding along the shallower lower slope instead of the steeper upper slope (note that the lower corner of the active block is in contact with the lower sliding plane right at the start). This suggests that the analytical solution, which is based totally on static equilibrium, may be over-conservative. Provided there is enough friction along the lower slope to absorb the energy due to momentum, allowing the upper block to displace a small amount and thus transfer its load to the lower slope will result in a drastic reduction in the required stabilizing force. Also note that the strength of the vertical discontinuity is irrelevant in this case, since the two blocks are both sliding down the same slope and therefore no displacement is occurring along that discontinuity.

APPLICATION TO SLOPE STABILITY PROBLEMS

We performed DDA analyses on several more complicated slope stability-type problems, both circular and non-circular configurations. The main objectives were to study the influence of number, location, and strength of internal discontinuities on the stability of the slope, as well as the behavior of the sliding mass after the initiation of failure.

Circular Failure Surfaces

Figure 7a shows one of the circular failure configurations. If the sliding mass is analyzed as a single block, a friction angle of 38° is required to prevent failure. A single discontinuity was added in different locations throughout the sliding block to determine whether the location of a discontinuity is important. The sliding mass was then further broken up into 4, 8, and 16 blocks. All of these cases were analyzed for three different values of friction: 0°, 20°, and 40°, along the vertical discontinuities. The results of the analyses show that increasing the number of vertical blocks has little effect on the slope stability, independent of the interface friction, as long as the main mode of failure is rotation. This certainly not surprising. However, as the number of slices increases to more than 16, toppling becomes a possible mode of failure when the friction angle between the vertical slices is sufficiently low. The significance of this result is that traditional limit equilibrium analyses would not show this possibility, and thus might severely overestimate the friction required for stability.

Using DDA, we were also able to study the behavior of the slope after it began to move. We found that for friction angles higher than 15°, the sliding mass would come to rest after a certain amount of movement. A plot of this "ultimate displacement" as a function of friction angle along the sliding surface for the single block case is shown in Figure 7b. This type of plot could potentially be useful in estimating the amount of displacement a slope may undergo, which in turn would influence the mitigation measures. The optimum mitigation philosophy for a slope that is expected to move 1 foot or less may be very different from that for a slope that is expected to move more than 10 feet.

Non-Circular Failure Surfaces

The cross-section of the Vaiont Slide is shown in Figure 8 (after Hendron and Patton, 1986), and as can be seen the failure surface is quite non-circular in shape. The DDA analysis of the configuration used by Hendron and Patton in their limit equilibrium analyses matches their

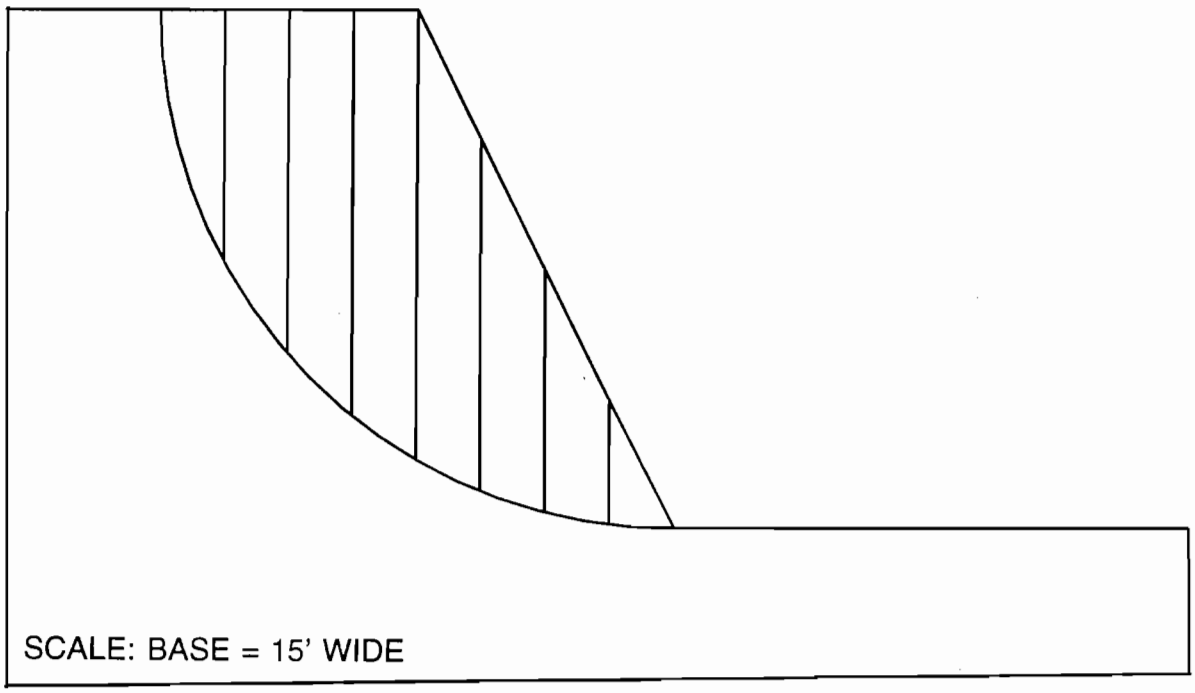

(a)

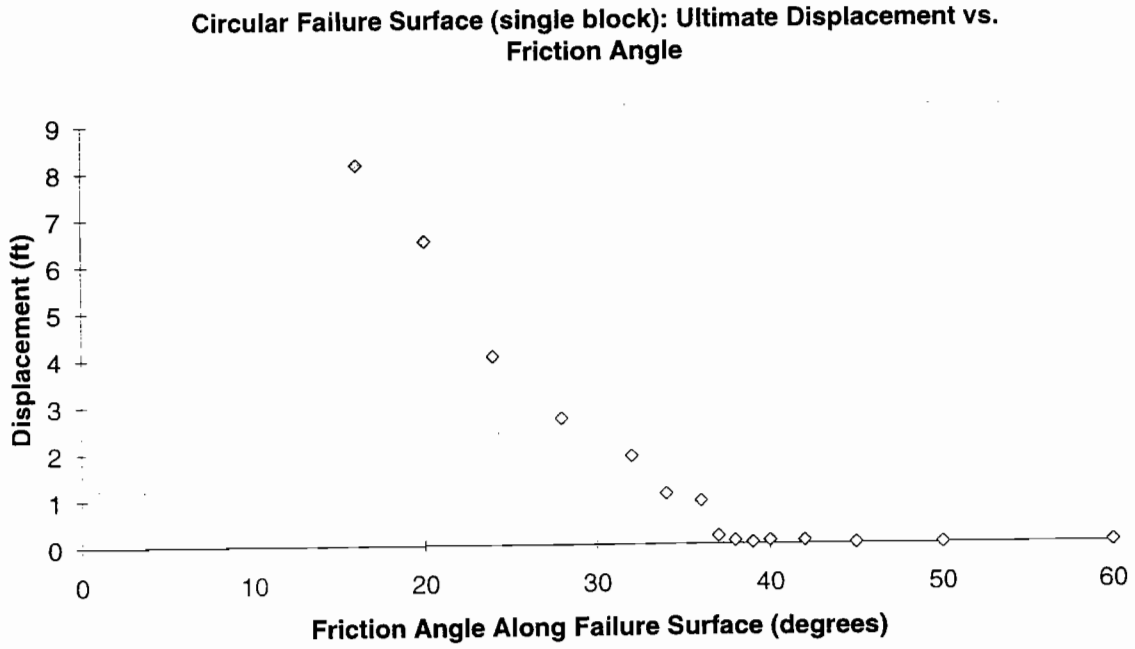

(b)

Figure 7. DDA analysis of a circular-shaped failure surface with vertical discontinuities. (a) Problem geometry. (b) Ultimate displacement as a function of friction angle for a single sliding block.

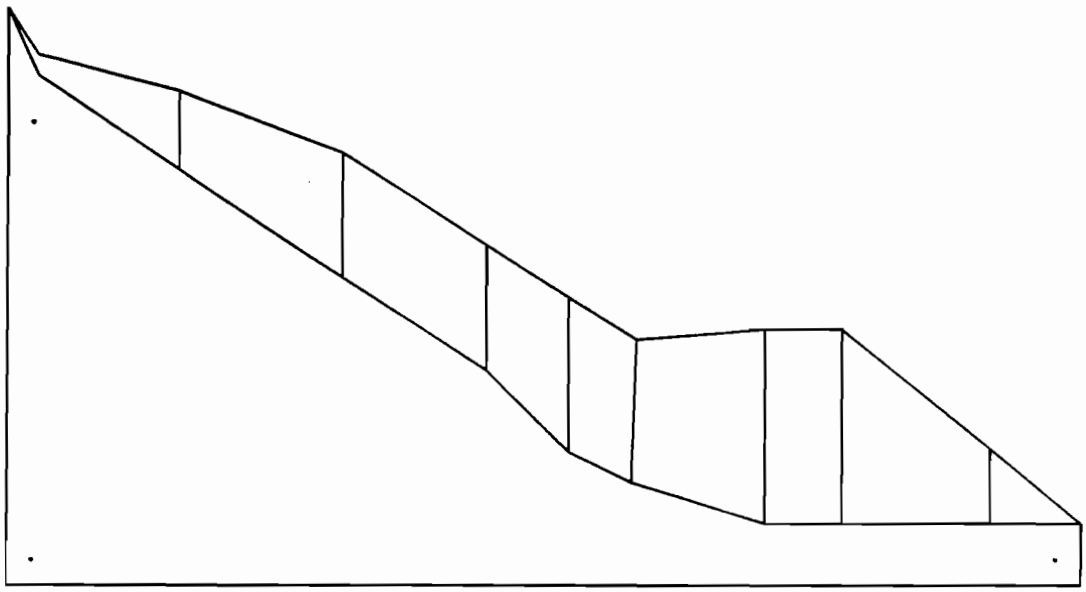

Figure 8. Cross section of the Vaiont slide used for DDA analysis.

results almost exactly: H&P = 14.9°, DDA = 15°. However, DDA analyses of different configurations have drastically different results. The sliding mass analyzed as a single block requires 7° for stability, while a 2-block sliding mass with a single vertical discontinuity near the center requires 14°. Considering that the friction angle along the failure surface was estimated to be around 12°, this is a significant difference. Thus, it is apparent that kinematic constraints have a great deal of influence on the stability of slopes with non-circular failure surfaces.

CONCLUSIONS

The validation studies showed that DDA provides accurate results, and make it possible to model situations where a block starts to move and then reaches equilibrium and comes to a halt. Additionally, the DDA results show that "two block / double incline" analytical solution based on statics alone may be overconservative because the kinematics of the problem changes after some initial displacement.

While kinematic constraints are not necessarily important for circular failure surfaces, they do appear to be a major factor for non-circular shaped surfaces. More importantly, DDA makes it possible to account for kinematics during slope stability analyses without making assumptions regarding the mode of failure.

ACKNOWLEDGMENT

The research presented in this paper was supported in part by a grant from the U.S. Army Engineer, Waterways Experiment Station, Vicksburg, MS, and an undergraduate research development grant from the College of Engineering, UC Berkeley.

REFERENCES

Goodman, Richard E. (1989). *Introduction to Rock Mechanics, Second Edition*, John Wiley & Sons, New York, 562 pp.

Hendron, A.J. and Patton, F.D. (1986). *The Vaiont Slide, a Geotechnical Analysis Based on New Geologic Observations of the Failure Surface*, U.S. Army Engineer Waterways Experiment Station Technical Report GL-85-5, 324 p.

Shi, Gen-hua (1988). *Discontinuous Deformation Analysis: A New Numerical Model for the Statics and Dynamics of Block Systems*, Ph.D. Thesis, Department of Civil Engineering, University of California, Berkeley, 378 pp.

Shi, Gen-hua (1993). *Block System Modelling by Discontinuous Deformation Analysis*, Computational Mechanics Publications, London, England, 209 pp.

Shi, Gen-hua (1994). Personal communication.

Yeung, Man-chu R. (1991). *Application of Shi's Discontinuous Deformation Analysis to the Study of Rock Behavior*, Ph.D. Thesis, Department of Civil Engineering, University of California, Berkeley, 341 pp.

TESTS OF SELECTED EROSION CONTROL MATERIALS ON HILLSLOPES UNDER SIMULATED RAIN AND SUNLIGHT

Gilberto E. Urroz and C. Earl Israelsen
Utah Water Research Laboratory
Utah State University
Logan, Utah 84322-8200

ABSTRACT

The Utah Water Research Laboratory's Rainfall Simulator Facility consists of a 6.09 m x 6.09 m (20 ft x 20 ft) rainfall simulator that produces rainfall intensities from 25.4 mm/hr (1 in/hr) up to 787.4 mm (31 in/hr), a tilting flume where soil 0.30-m (1-foot) deep can be tilted up to 45° to simulate hillslopes, and a sunlight simulator used for plant growth studies. A wind generator is also available that produces wind velocities of up to 60 mph over the Erosion Basin.

Tests performed at the Utah Water Research Laboratory's Rainfall Simulator Facility for a set of twenty different erosion control applications were used to evaluate the effectiveness of those products in controlling erosion in a sandy-loam soil. Results include not only values of soil erosion and water runoff from test plots for each of the products tested, but also evaluation of the plant germination rates and dry weight after a week of growth under a Sunlight Simulator. All tests were performed at a rainfall intensity of 127 mm/hr (5 in/hr) for a total of thirty minutes and at a 2-1/2: 1 slope. Products tested included hydromulches and erosion control blankets.

INTRODUCTION

The results presented in this paper are based on a erosion control testing study performed by the Utah Water Research Laboratory (UWRL) for the Mountain-Plains Consortium (MPC), a University Transportation Centers Program for Transportation Research, Public Service and Education. The purpose of the study was to compare the performance of selected erosion control products under simulated rainfall and sunlight conditions in terms of soil loss reduction and vegetation growth. The Mountain-Plains Consortium involves universities in the states of Colorado, North Dakota, Utah and Wyoming, therefore, input was requested from the Departments of Transportation of these four states on which materials to test. A total of 19 materials, 11 mulches and 8 erosion control blankets were selected and are listed in Table 1. A code has been given to each material to facilitate the graphic representation of test results. Tests were performed in the UWRL rainfall simulator facility in which the variables of soil, slope, and rainfall rate and duration can be controlled.

Table 1. List of products tested.

Hydromulches		Erosion Control Blankets	
Code	Brand	Code	Brand
M1	Climatizer Mulch (*)	B1	High-velocity Curlex
M2	Cellumulch (*)	B2	Conwed Futerra
M3	Verdyol Mulch (*)	B3	North-American Green S-150 BN
M4	Nature's Own Mulch (*)	B4	North-American Green SC-150 BN
M5	Silva Fiber Mulch (*)	B5	Anti-Wash GeoJute
M6	Conwed Mulch (*)	B6	Dekowe 400 Coir
M7	Re-Fiber Mulch (*)	B7	Bonterra S-1
M8	Re-Fiber Mix Mulch (*)	B8	Bonterra S-2
M9	Grass Fiber Mulch (*)		
M10	Conwed 2000 Mulch (*)		
M11	Conwed 2000 Mulch (**)		
M12	Soil Guard (†)		

(*) Applied at 2246 kg/ha (2000 lb/Ac).
(**) Applied at 3370 kg/ha (3000 lb/Ac).
(†) Applied at 3931 kg/ha (3500 lb/Ac).

RAINFALL SIMULATOR FACILITY

The UWRL rainfall simulator facility consists of a rainfall simulator, a tilting flume, a sunlight simulator, and a wind generator. The rainfall simulator and the tilting flume allow for the measurement of erosion and water runoff rates. The sunlight simulator enables us to grow vegetation in the test plots, and the wind generator produces unidirectional wind up to about 60 mph for checking on wind effects on mulches. No wind was applied to the present tests, however, as wind tests are used mainly with straw mulches and none was tested in this program.

Rainfall Simulator

The rainfall simulator is a drip-type device in which individual raindrops are formed by water emitting from small-diameter brass tubes. The simulator consists of one hundred modules arranged and supported to form a square horizontal area containing 37.16 m^2 (400 ft^2). Each module has separate manually-operated controls. The rate of flow is controlled by admitting water into a manifold chamber through fixed orifice plates under constant hydraulic pressure. Five separate inlet orifices are used in each chamber or module. The ratios of the areas of these orifices are 1:2:4:8:16. By controlling the flow of water to the orifices with electrically operated solenoid

valves, it is possible to vary flow in on-off increments with 31 equal steps up to a maximum rainfall rate of 787.4 mm/hr (31 in/hr). Outlet from the chambers or modules is through uniform equally-spaced brass tubes. Each module is 609.6 mm (2 ft) x (2 ft) 609.6 mm x (1 in) 25.4 mm deep enclosed box oriented so that the tubes or needles form a horizontal level plane from which the water drips. Each module contains more than 600 brass tubes spaced in a 25.4-mm (1 in) square pattern. A schematic of the rainfall simulator is shown in Figure 1.

Raindrops have diameters of approximately 4 mm (0.16 in), and their velocities of impact represent the energy of typical high-intensity storms. The spatial distribution of rainfall is essentially uniform and the control of application rates is within the accuracy requirements of most experiments. The simulator has been extensively tested and used in research since its construction in 1973. The original plexiglass modules were replaced with aluminum panels in 1992.

Tilting Flume

The tilting flume is square and measures 6.10 m (20 ft) on each side. The flume is designed so that a vacuum can be maintained beneath the soil, when desired, to aid infiltration, and water sheet flow can be maintained over the top of the soil when this is necessary. The rainfall simulator is supported over the flume so that rain falls directly onto the soil.

Approximately 304.8 mm (1 ft) depth of soil is supported in the tilting flume by a metal grating covered with filter cloth through which water can drain. For the tests performed in this study the flume was divided into six test plots, each measuring approximately 0.609 m (2 ft) by 5.94 m (19.5 ft). Three blocks of two plots are separated from each other and from the side walls by 0.609-m (2-ft) wide walkways as presented schematically in Figure 2. Runoff from each plot is collected in large plastic tubs, then dried and weighed for determining the amount of soil and water runoff leaving the plot. The flume can be tilted hydraulically to any angle up to 43° from horizontal for simulating hill slopes.

Sunlight Simulator

A balance of radiant energy needed for good plant growth is provided to the test plots by a sunlight simulator which utilizes several incandescent lamps as well as an array of flourescent lamps. The simulator is the same size as the tilting flume, square, measuring 6.10 m (20 ft) on each side. The sunlight simulator is rolled on and off the test plots on horizontal rails mounted on top of the side walls of the tilting flume. When in position, it is about 0.91 m (3 ft) above the test plot surfaces, and provides enough illumination to facilitate plant growth on seeded plots after the rainfall events.

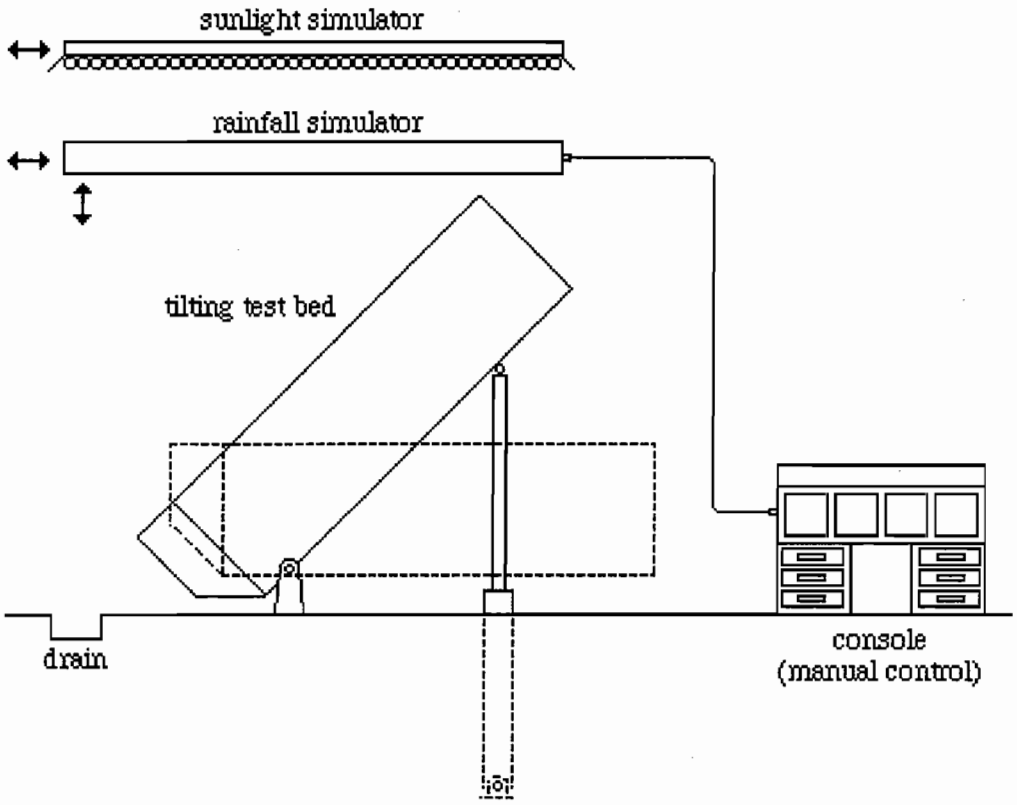

Figure 1. Schematic of Rainfall Simulator Facility.

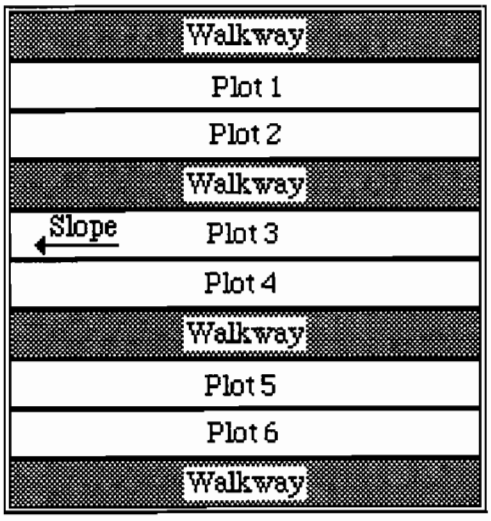

Figure 2. Layout of test plots.

TEST PROCEDURE

Test Parameters

In order to compare the performance of all the materials tested a single set of test conditions were selected as follows:

soil type: sandy - loam (56% sand, 29% silt, 15% clay)
soil slope: 2.5:1
rainfall intensity: 127 mm/hr (5 in/hr)
rainfall duration: 30 minutes (60 minutes for materials M11 and M12)
seed: barley
plant growth time: 6 days.

After reviewing the results of the tests it is obvious that the slope and rainfall intensity used are relatively high for mulch covers allowing them to produce excessive amounts of soil erosion as compared to erosion control blankets. These results point out the need to select appropriate testing conditions for different type of erosion control materials when developing test standards.

Plot Preparation

The selected soil was originally placed in the six plots to a depth of approximately 304.8 mm (1 ft), and cultivated with a garden tiller to a depth of approximately 152.4 mm (6 in). Each plot was then leveled, uniformly compacted with a lawn roller and raked to produce a rough surface. After every test run the top layer of soil, up to the maximum depth of erosion, was removed and discarded and new soil added. The soil in each plot was then spaded to the full 304.8 mm (1 ft) depth, and the entire process of tilling, leveling, compacting and raking repeated to prepare the plots for the next test run. After the plots were prepared, the erosion control material (mulch or erosion control blanket) was applied and the test flume was tilted to the desired slope in preparation for rain application.

Mulch and Seed Application

Three replications of two mulches were applied in each mulch test at a rate of 2246 kg/ha (2000 lb/Ac), except for materials M11 and M12 that were applied at a different rate (see Table 1). Barley seed was applied at a rate of 225 kg/ha (200 lb/Ac). The mulch and seed were mixed together in a water slurry in a laboratory-sized hydromulcher and then applied under pressure through a hose to the plots while the test bed was in a horizontal position. Afterwards the plots were allowed to drain overnight before the rain was applied.

The laboratory-sized hydromulcher consists of a barrel 0.36 m (14 inch) in diameter and 0.53 m (21 inch)-high provided with a rigid axis to which rubber flaps are attached. A small electric motor drives the axis allowing the flaps to mix the hydromulch and seed with water before application to the plots. The barrel is connected through a funnel to a small centrifugal pump. A hose ending in a spreader allows for the application of the mulch-seed mixture to the plot surface.

Tests on Erosion Control Blankets

Three samples of two erosion control blankets were laid in the plots in each blanket test. Each sample was secured by rows of 152.4 mm- (6 in-) long, steel staples driven through the soil at both edges along the slope. Staples on these rows were separated 0.91 m (3 ft) between each other. A third row of staples, with the same 0.91 m (3 ft) separation but staggered by 0.45 m (1.5 ft), was used along the centerline. In addition, rows of three staples were used to secure the both the upstream and downstream edges of the blankets. The staple pattern just described is shown schematically in Figure 3. For tests on erosion control blankets, seed was applied by hand before lying the blanket on each plot. The application rate of seed in these tests was the same as in mulch applications.

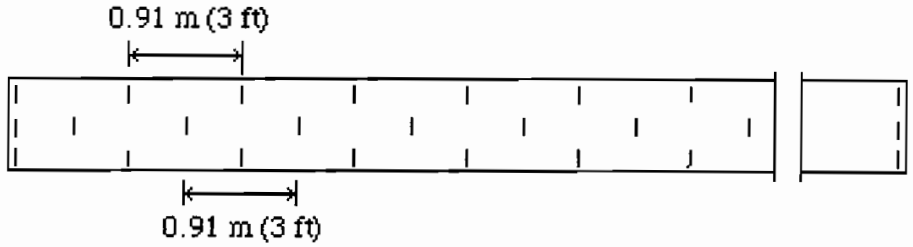

Figure 3. Staple pattern for erosion control blankets.

Rainfall Application

The test flume containing the selected erosion control materials was tilted to the prescribed slope and covered with a plastic sheet. The rainfall simulator was turned on at full capacity to purge the air from the system. During the purging the rain fell onto the plastic and into a drain without wetting the plots. When the purging was completed, the rain was adjusted to the desired rate and allowed to stabilize. The plastic cover was then quickly removed so the rain fell onto the plots and the time clock was started. Rain was applied for 30 minutes in all tests.

Runoff Measurements

All of the runoff (water and sediment) leaving each plot during a test was collected in large plastic tubs. The runoff was subsequently filtered through fabric clothes that retained the solid materials for drying and weighing. The sediment-laden fiber clothes were then placed on top of metal grids and left to dry at air temperature for periods ranging from a few days up to two weeks.

Sunlight Application

When rainfall ended in each test, the sunlight simulator was rolled into position over the plots, and the entire assembly was tilted to the prescribed slope. Sunlight was applied for six days, 24 hours a day, with the plots still in the tilted position, after which the vegetation was

harvested. The barley seed used produced plants after two or three days that could grow up to approximately 200 mm (7.9 in).

Harvesting of Plant Samples

When the predetermined time for the test had elapsed, the test bed was returned to a horizontal position and the sunlight simulator was removed. Using a template prepared for the purpose, six 0.092 m^2 (1 ft^2) sample areas were randomly selected on each plot, two at the lower end of the slope, two towards the center, and two other near the top. Samples were gathered from each plot and the plants counted, measured, dried, and weighed. Counts were made also of seeds that did not germinate.

RESULTS

Results obtained from each test include water runoff rate, soil erosion rate, average plant height, dry weight of plants and percentages of lost and germinating seed. Water runoff and soil erosion rates for the nineteen materials tested are presented in Table 2 and Figures 4 and 5, while plant data is given in Table 3 and Figures 6 through 9.

It follows from the data of Table 2 and Figure 4 that, for the test conditions used, hydromulches, in general, allowed more soil loss than erosion control blankets. It should be pointed out that the slope and rainfall intensity used in these tests may have been too extreme for most of the hydromulches tested to effectively protect the soil against excessive erosion. The numbers from Table 3 and Figure 4 may give the impression that hydromulches are always at a disadvantage with respect to erosion control blankets. It may be the case, however, that for flatter hillslopes and lower rainfall intensities the performance of hydromulches and of the erosion control blankets is comparable. Additional testing is necessary, therefore, to determine the appropriate range of slopes and rainfall intensities for the controlled testing of hydromulches and erosion control blankets.

The hydromulches tested, with the exceptions of those identified as M10, M11 and M12, did not include tackifiers. The addition of a tackifier or other additives may in most cases improve the erosion control performance of a hydromulch, particularly under the extreme test conditions used in this program. The effect of adding tackifiers to a hydromulch cover is evident when comparing the performance of mulch M6 with than of M10 or M11 in Figure 4, the two latter being essentially the same as M6, but with a tackifier added.

Data from Table 2 and Figure 5 suggest that, in general, blankets also retained more water than did hydromulch covers. This is a beneficial aspect of an erosion control product for it helps in the growth of a vegetative cover. The effects of water retention will be more apparent when plant data is discussed below.

The vegetative cover characteristics are related to the amount of soil and water retained by a given erosion control material. It is not surprising then to find from the data in Table 3 that, in general, the vegetation in plots with erosion control blankets performed better, in terms of plant characteristics and germinations rates, than the plants in most hydromulch plots.

While the data from Figure 6 indicates that the average plant height was about the same for all blankets and for mulch M12, there are differences in terms of the dry weight of plants for those materials as indicated in Figure 7. These differences can be attributed to the different seed

germination rates (Figure 8) as well as to the amount of water retained by each material (Figure 5). (Plant weight may also be influenced by the chemical composition of the erosion control cover, although such parameters were not under scrutiny in these tests.) For hydromulches, both plant height and dry weight of plants show more variation than for erosion control blankets as depicted in Figures 6 and 7. Again, such variation is related to the amount of water and soil retained, which, in turn, affects the germination rates (compare Figures 5, 7 and 8). Although the relationships between runoff and plant characteristics are not easily quantifiable, a good qualitative picture can be inferred from the data in Figures 5 through 8. Namely, that the more soil and water retained the better the germination rates and the taller the plants, which translate into higher plant weight.

Figures 8 and 9 present for each material the percentage of seed germinating and seed lost from the plots, respectively. The percentage of seed germinating (Figure 8) was calculated from the known seed application rates and the measured plant population. From the data shown in that Figure it follows that the erosion control blankets had the best germination rates (50 percent or more). The rates of seed lost in Figure 9 were estimated from the count of plants and of seeds left in the samples collected from each plot. The data from Figure 9 indicate that hydromulches, which allowed the largest amount of runoff, also allowed the largest percentage of seed lost. This result is not surprising as the seed was laid on top of the soil or of the hydromulch cover and was easily carried off the plots by the flowing water.

Table 2. Water runoff and soil erosion data. Averages of three replications of tests.

Material Code	Brand Name	Water runoff rate lt/hr	(gal/hr)	Soil erosion rate kg/hr	(lb/hr)
M1	Climatizer Mulch (*)	351.33	(92.68)	52.55	(115.60)
M2	Cellumulch (*)	344.09	(90.77)	46.58	(102.47)
M3	Verdyol Mulch (*)	296.24	(78.15)	32.67	(71.87)
M4	Nature's Own Mulch (*)	321.76	(84.88)	48.97	(107.73)
M5	Silva Fiber Mulch (*)	332.30	(87.66)	32.00	(70.40)
M6	Conwed Mulch (*)	328.55	(86.67)	31.64	(69.60)
M7	Re-Fiber Mulch (*)	324.36	(85.56)	46.18	(101.60)
M8	Re-Fiber Mix Mulch (*)	307.03	(80.99)	51.30	(112.87)
M9	Grass Fiber Mulch (*)	346.76	(91.47)	62.09	(136.60)
M10	Conwed 2000 Mulch(*)	213.12	(56.22)	10.03	(22.07)
M11	Conwed 2000 Mulch (**)	144.45	(38.11)	3.714	(8.171)
M12	Soil Guard (†)	34.68	(9.15)	0.054	(0.119)
B1	High-velocity Curlex	37.06	(9.78)	0.427	(0.939)
B2	Conwed Futerra	64.91	(17.12)	0.021	(0.045)
B3	NAG S-150 BN	8.55	(2.25)	0.006	(0.013)
B4	NAG SC-150 BN	4.30	(1.14)	0.004	(0.008)
B5	Anti-wash Geojute	180.97	(47.74)	5.030	(11.067)
B6	Dekowe 400 Coir	288.42	(76.08)	9.879	(21.733)
B7	Bonterra S-1	70.21	(18.52)	1.183	(2.603)
B8	Bonterra S-2	25.48	(6.72)	0.077	(0.170)

(*) Applied at 2246 kg/ha (2000 lb/Ac).
(**) Applied at 3370 kg/ha (3000 lb/Ac).
(†) Applied at 3931 kg/ha (3500 lb/Ac).

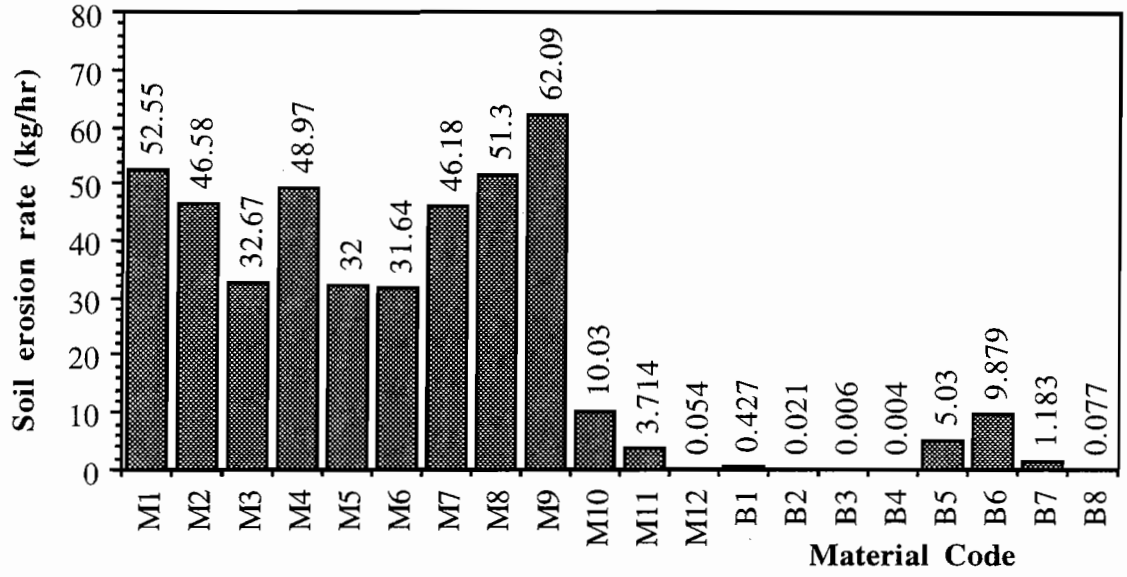

Figure 4. Soil erosion rates.

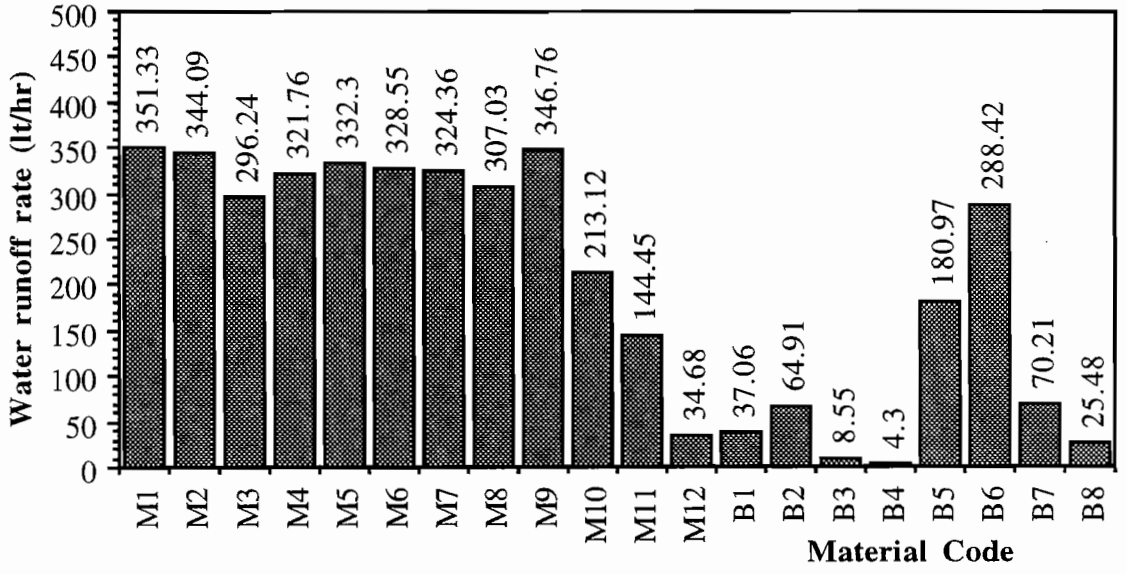

Figure 5. Water runoff rates.

Table 3. Plant height, weight and germination data. Averages of three replications of tests.

Material Code	Brand	Plant height mm	(in)	Dry weight kg/ha	(lb/Ac)	Percentage of seed lost	germ.	non-g.
M1	Climatizer Mulch (*)	87.3	(3.44)	11.73	(10.44)	71.01	14.95	14.04
M2	Cellumulch (*)	110.7	(4.36)	22.16	(19.73)	71.01	20.00	8.99
M3	Verdyol Mulch (*)	125.0	(4.92)	26.97	(24.01)	65.76	22.42	11.82
M4	Nature's Own Mulch (*)	123.9	(4.88)	38.06	(33.89)	66.67	26.06	7.27
M5	Silva Fiber Mulch (*)	132.7	(5.22)	58.18	(51.80)	44.65	40.61	14.74
M6	Conwed Mulch (*)	135.5	(5.33)	61.69	(54.92)	42.02	43.84	14.14
M7	Re-Fiber Mulch (*)	117.6	(4.63)	30.53	(27.18)	58.08	24.65	17.27
M8	Re-Fiber Mix Mulch (*)	115.9	(4.56)	29.53	(26.29)	64.85	24.44	10.71
M9	Grass Fiber Mulch (*)	129.2	(5.09)	26.03	(23.17)	63.94	18.69	17.37
M10	Conwed 2000 Mulch (*)	134.5	(5.30)	44.38	(39.51)	49.29	33.44	17.27
M11	Conwed 2000 Mulch (**)	169.9	(6.69)	104.91	(93.41)	34.04	49.19	16.77
M12	Soil Guard (†)	165.3	(6.51)	128.90	(114.76)	26.57	62.93	10.50
B1	High-velocity Curlex	165.3	(6.51)	104.25	(92.82)	13.43	73.52	13.05
B2	Conwed Futerra	167.2	(6.58)	120.92	(107.66)	12.02	84.51	3.47
B3	NAG S-150 BN	166.5	(6.56)	147.72	(131.52)	11.92	68.59	19.49
B4	NAG SC-150 BN	163.6	(6.44)	135.22	(120.39)	16.87	55.66	27.47
B5	Anti-wash Geojute	146.2	(5.76)	101.19	(90.09)	22.93	55.15	21.92
B6	Dekowe 400 Coir	152.6	(6.01)	130.97	(116.60)	25.56	50.50	23.94
B7	Bonterra S-1	152.4	(6.00)	110.19	(98.10)	9.05	70.76	20.19
B8	Bonterra S-2	151.0	(5.94)	89.93	(80.06)	8.86	68.57	22.57

(*) Applied at 2246 kg/ha (2000 lb/Ac).
(**) Applied at 3370 kg/ha (3000 lb/Ac).
(†) Applied at 3931 kg/ha (3500 lb/Ac).

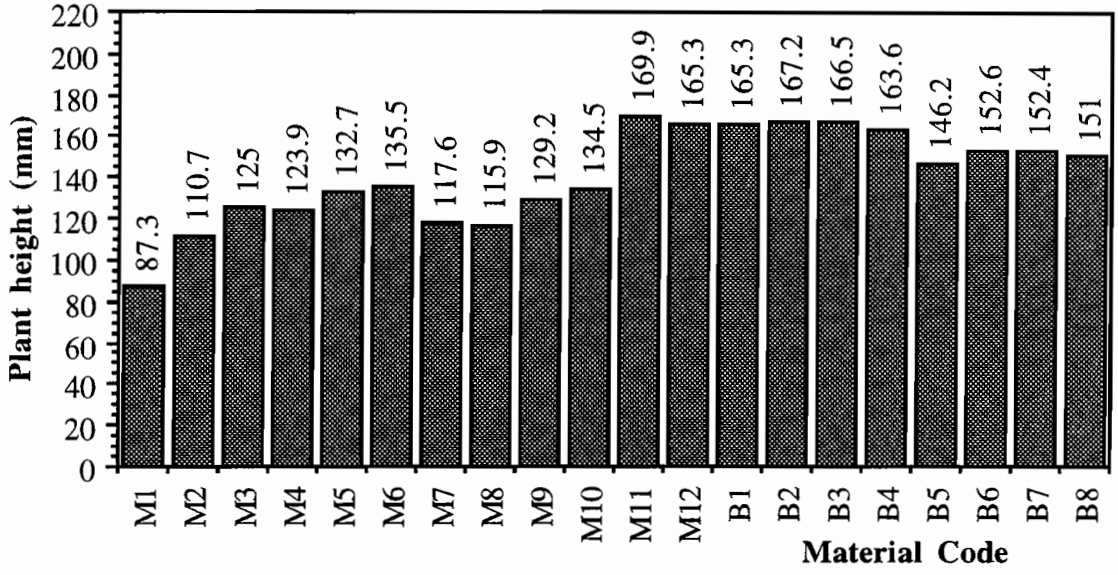

Figure 6. Average plant height.

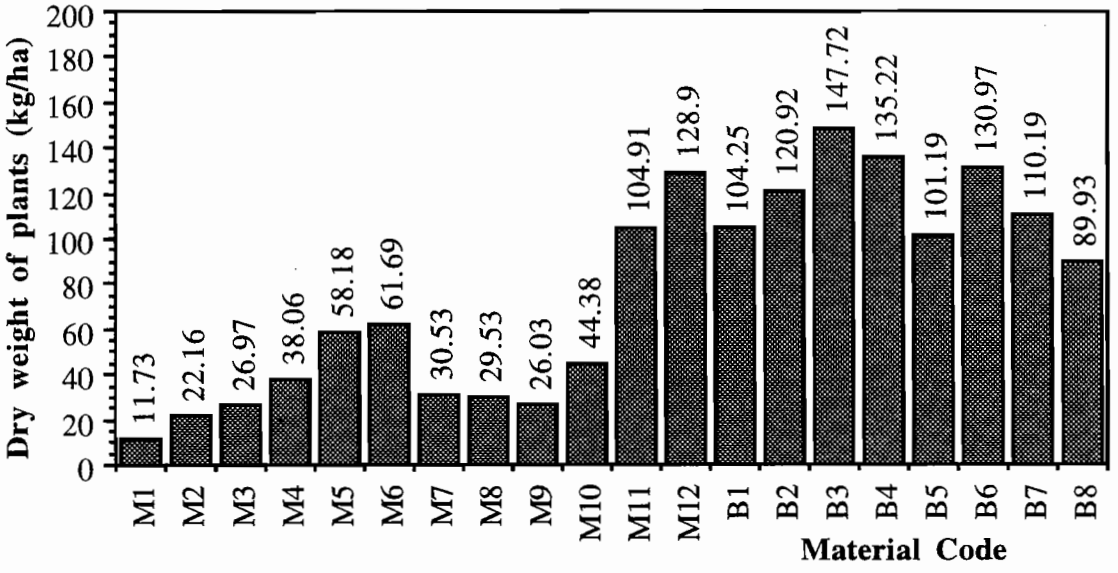

Figure 7. Dry weight of plants.

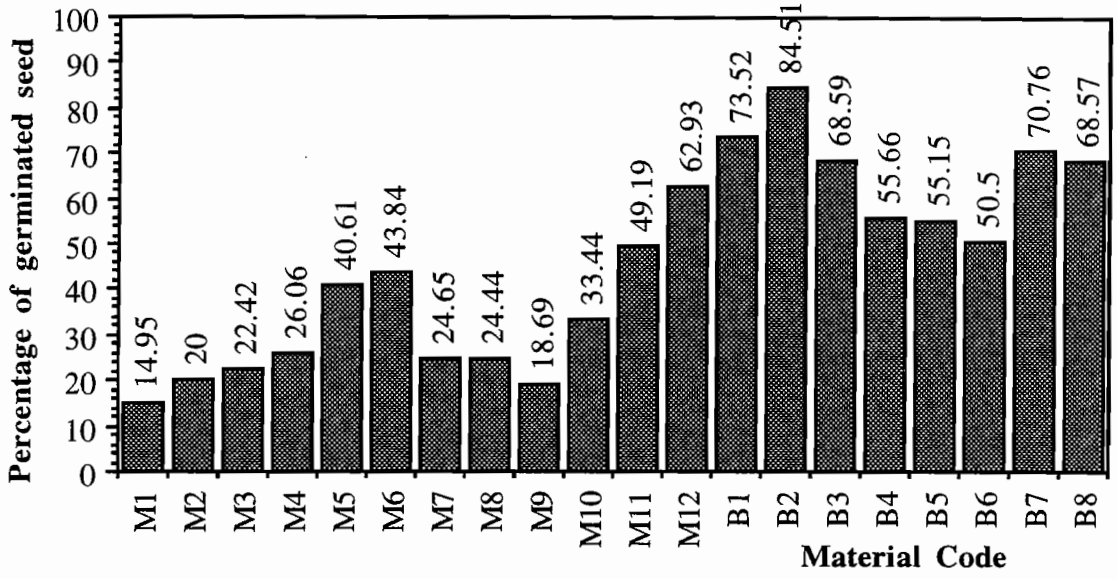

Figure 8. Percentage of germinating seed.

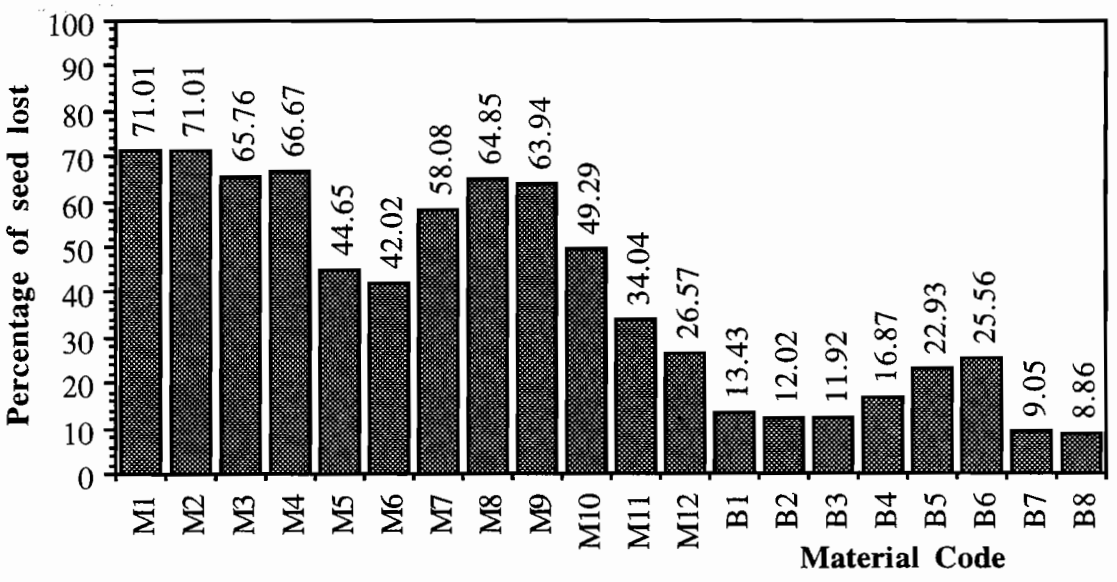

Figure 9. Percentage of seed lost.

SUMMARY

The present tests on hydromulches and erosion control blankets under controlled slope and rainfall conditions were of a exploratory nature and their results should not be taken as the definitive criteria in the selection of erosion control systems. Only a single set of soil type, soil slope, rainfall intensity and duration was used, therefore placing hydromulches at a disadvantage with respect to erosion control blankets as the soil slope (2.5:1) and the rainfall intensity (127 mm/hr or 5 in/hr) were relatively high. The results of these test point out, however, the need for sustained program of testing on hydromulches, blankets and other erosion control systems, under a varied set of conditions, in order to determine not only their relative performance, but also the range of conditions (soil types, slopes and rainfall intensities and durations) for which each system is more appropriate.

Observations from this series of tests do point out the advantage of using hydromulches with tackifiers to better protect soil slopes from rainfall erosion.

REFERENCES

1. Israelsen, C.E., C.G. Clyde, J.E. Fletcher, E.K. Israelsen and F.W. Haws, 1980, "Erosion Control During Highway Construction - Manual of Principles and Practices," National Cooperative Highway Research Program Report 221, Transportation Research Board, National Research Council, Washington, D.C., April.

2. Israelsen, C.E. and G.E. Urroz, 1990, "Erosion Control Products Testing Facility," Proceedings of Conference XXI "Erosion Control: Technology in Transition," International Erosion Control Association, Washington, D.C., February.

3. Meyer, L.D., 1994, "Rainfall Simulators for Soil Erosion Research," Chapter 4 in "Soil Erosion Research Methods," R. Lal (ed.), Soil and Water Conservation Society, St. Lucie Press, Delray Beach, Florida.

4. Urroz, G.E. and C.E. Israelsen, 1993, "Erosion control testing under simulated rainfall and in high-velocity flows," 48th Annual Meeting of the Rocky Mountain Hydrologic Research Center, Allens Park, Colorado, September.

5. Urroz, G.E. and C.E. Israelsen, 1994, "Erosion Control Product Test Facilities of the Utah Water Research Laboratory", Proceedings of the 30th Symposium on Engineering Geology and Geotechnical Engineering 1994: "Hydrogeology: Waste Disposal, Science and Politics," Boise, Idaho, March.

EVALUATION OF DEEP FOUNDATIONS BENEATH BUILDINGS DAMAGED DURING THE 1994 NORTHRIDGE EARTHQUAKE

Allen G. Davis, Ph.D., D.Sc.
STS Consultants, Ltd., 431 S 300 E Salt Lake City, UT 84111

ABSTRACT

Two 16-story reinforced concrete apartment blocks founded on drilled shafts (CIP piles) were damaged in the 1994 Northridge earthquake. In order to assess the viability of the buildings for retrofit, it was considered necessary to evaluate the integrity of the existing drilled shafts. This paper describes the use of various nondestructive testing methods for this evaluation, including ground penetrating radar, parallel seismic and impulse response tests.

1. INTRODUCTION

The reinforced concrete shear walls of two 16-story apartment buildings in the Los Angeles area were damaged by the 1994 Northridge earthquake. Because the existing piles were known to be reinforced to only 12 feet (3.65 m) below the pile cap bases, it was considered propitious to evaluate the integrity of the foundations beneath the buildings. The two towers are founded on 20-inch (500 mm) and 24-inch (600 mm) diameter drilled cast-in-place (CIP) concrete piles. The north west tower is founded on a mixture of older CIP piles, constructed in 1966 and left over from an abandoned project, and newer CIP piles of the same diameters, cast in 1971/2. The older piles were thought to be approximately 50 feet (15.25 m) long. The newer piles were specified on the original foundation plan to have a minimum length of 40 feet (12.2 m). The same plan gives the position of the pile caps for both towers, as well as the projected pile locations. The pile caps have a nominal thickness of 6.5 feet (2 m). The parking garage basement at pile cap level has a concrete floor slab, approximately 10 inches (250 mm) thick.

The soil profile at the site comprised a varying thickness of sand and gravel fill under the floor slabs (from 2 to 7 feet (0.6 to 2.1 m)), followed by medium dense silty sands to approximately 40 feet (12.2 m), with dense sands with cobbles below. The water table at the time of pile construction was at 30 feet (9.1 m) below slab level.

2. PROJECT APPROACH

The investigation program included three nondestructive testing methods to evaluate the integrity of the existing piles:

a) ground penetrating radar (GPR) to map the borders of the pile caps to be tested below the existing basement floor slab,
b) Parallel Seismic (PS) testing of selected pile pairs beneath critical pile caps to ascertain pile integrity and stress wave velocity, and

c) Impulse Response tests (also known as Transient Dynamic Response, or TDR) through the pile caps at selected positions above pile centers to check pile shaft lengths and integrity.

The total program required 5 days on site with a two-person testing team. The test methods and their applications are fully described below.

2.1 Ground Penetrating Radar

GPR uses a high-frequency electromagnetic pulse which penetrates the subsurface and consequently provides a form of cross sectional image of subsurface features [1]. The GPR signal reflections occur at the interfaces between subsurface materials with differing dielectric properties; in this case, the interface between the base of the concrete slab or pile cap and the subgrade below. GPR data is obtained by dragging a suitable radar antenna across the floor and displaying the resultant data on either a strip chart or on a color video monitor. The vertical interfaces between the 10-inch (250 mm) thick floor slab and the pile caps were located in this manner, in order to position the vertical borings for the PS testing as close as possible to the edge of the pile caps. An example of the GPR image from the floor slab/pile cap interface is given in Figure 1. The mesh reinforcement in the slab can be seen, as well as the more substantial reinforcement in the pile cap.

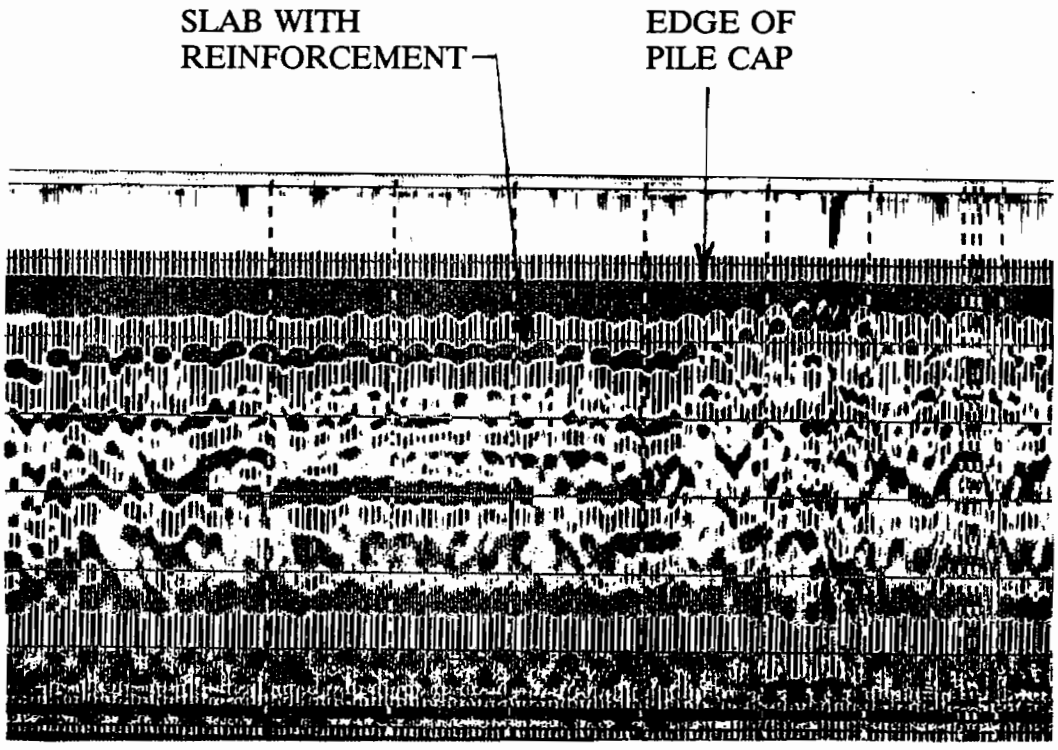

Figure 1. Typical Ground Penetrating Radar Profile

2.2 Parallel Seismic

This test was first developed in France for checking the integrity and length of piles in situations where the pile top is not accessible [2,3]. It consists of measuring the propagation velocity of an acoustic wave transmitted through the pile cap of the structure being investigated, and received at a number of uniformly spaced points down the side of the pile shaft. The test equipment includes a hydrophone and an instrumented hammer, both connected to a data acquisition system. The hydrophone can be placed either in a coring drilled in the structure under test, or in a boring drilled in the adjacent soil, close to and parallel with the structure. The principle of the method is illustrated in Figure 2.

The hydrophone is placed in the boring at a fixed position, and the selected test point on the structure is struck with the hammer. The transit time for the stress wave to reach the hydrophone is recorded. The hydrophone position is then changed in equal increments, and the test repeated. The cumulated results are plotted as a graph of depth against transit time. A change in the rate of time increase with depth indicates either the base of the element being tested, or a discontinuity in the element. Six different pile caps were examined here, with a boring at each cap down to a depth of more than 40 feet (12.2 m). Refusal of the drilling tool was reached at the bottom of each boring in dense sandy gravel with large cobbles.

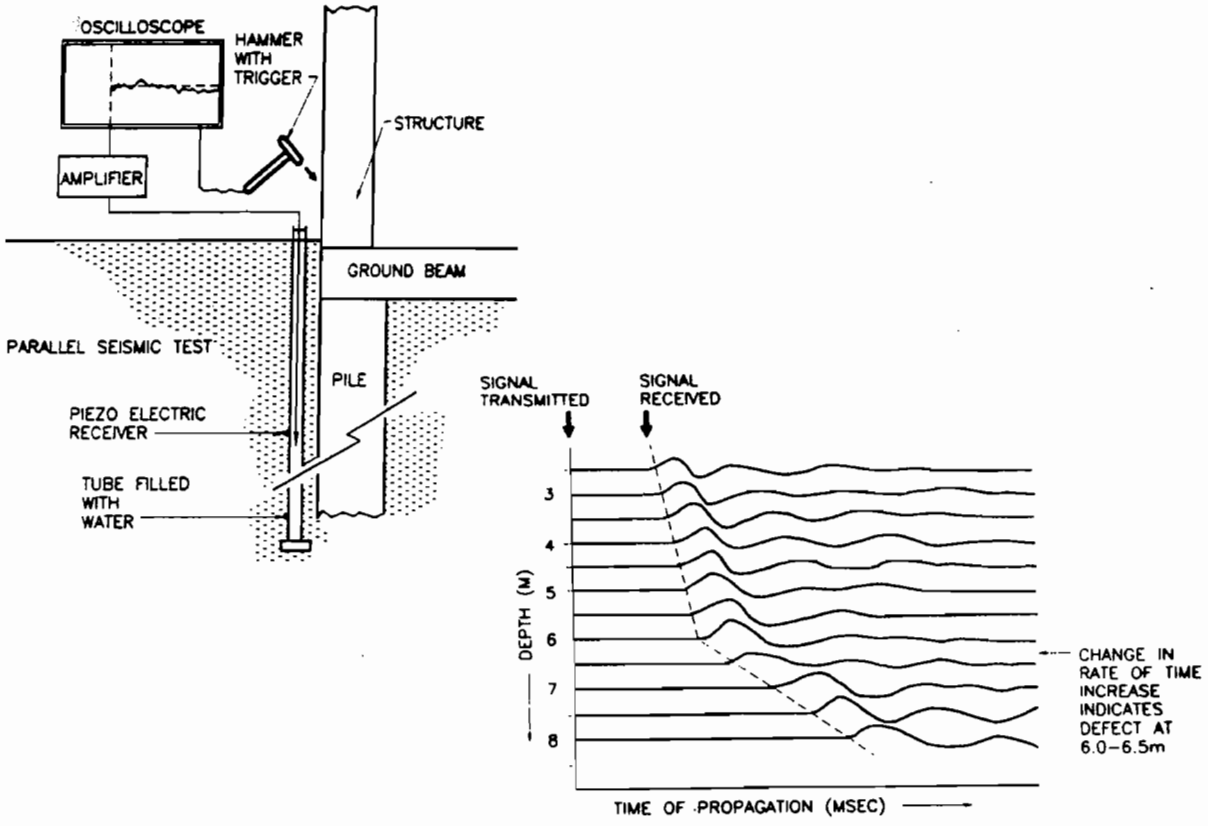

Figure 2. Principle of Parallel Seismic Test

The borings for the PS test were fully lined with a PVC casing, 2-inch (50 mm) I.D., sealed at the tube base and well grouted in the surrounding soil. Each boring was vertical and flush against the existing pile cap, spaced equidistantly from the two adjacent piles under test. The restricted headroom and access to the basement area required low headroom drilling, and the casing had to be assembled and installed in 3-foot (0.9 m) segments.

The velocity of the signal, hence the transit time, varies when the wave path includes materials of differing elastic modulus, such as poor quality concrete, or the soil or rock below the base of the structure. When the signal is diverted by voids or discontinuities the path length is effectively increased, and the transit time increases accordingly. These variations in transit time are visible as deflections on the time-distance graph, and so the depth of the structure, the uniformity of the concrete and the presence of any defects can be confirmed.

2.3 Impulse Response (TDR)

TDR is a nondestructive test which has been successfully applied to problems where pile integrity is in question [2,3]. The test equipment consists of a hammer equipped with a load cell and a geophone, both of which are linked to a data acquisition unit in a portable computer. Each test is performed by striking the pile head (or pile cap) over the pile axis with the hammer, and measuring the response of the pile to the hammer blow with the geophone, placed approximately 3 to 6 inches (75 to 150 mm) inside the pile perimeter.

The velocity measured by the geophone divided by the hammer force (v/F) is the mobility of the tested unit (in this case, the pile cap and the pile). The depth to reflectors of the downwards-travelling shock wave can be calculated from the mobility plotted as a function of the frequency of the blow, usually over the range 0-2000 Hz.

In this case, the relatively thick pile cap provided a limited damping effect on the return signal from the pile, thereby allowing useful information on the pile shaft length and continuity to be obtained. A total of 57 piles were tested by this method, and pile tip length measurements were possible in 49 cases. Calibration of pile lengths was ensured by using the pile stress wave velocities obtained with the Parallel Seismic tests.

3. TEST RESULTS

3.1 Parallel Seismic

A typical result from the PS testing at this site is given in Figure 3. The purpose of the PS testing was to measure the average concrete stress wave velocity, to be used in calculating pile lengths from the TDR test results. The PS tests gave an average stress wave velocity of 10,700 ft/s (3,260 m/s).

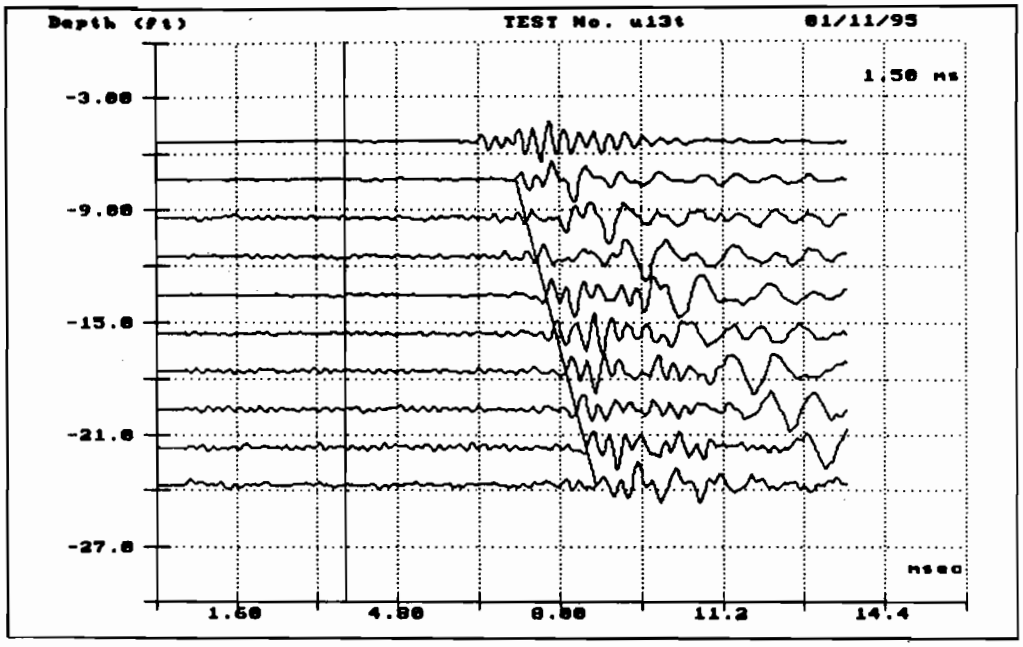

Figure 3. Parallel Seismic Test Profile - Pile Stress Wave

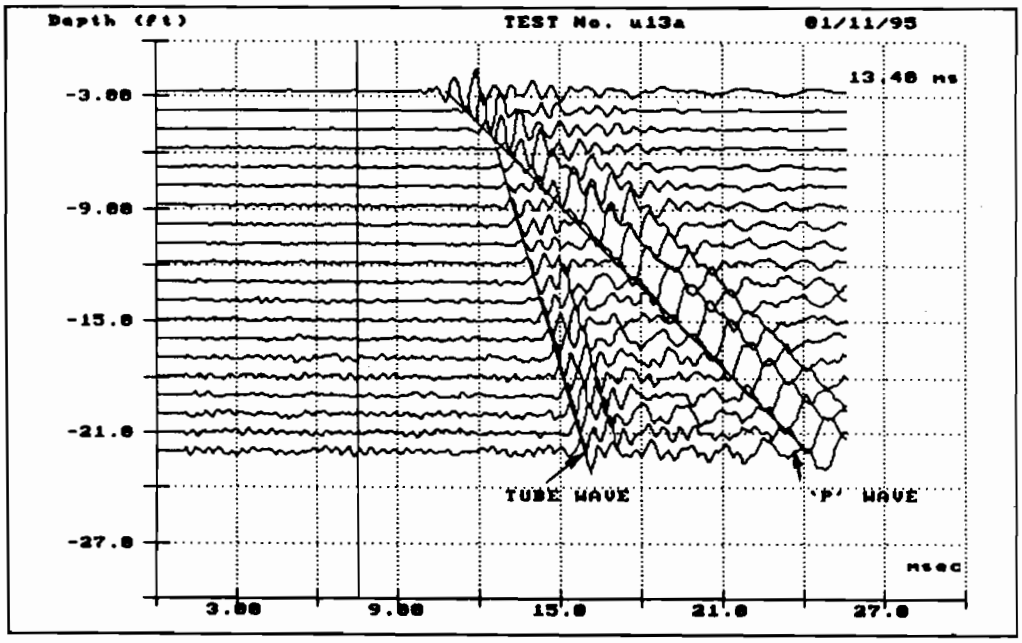

Figure 4. Parallel Seismic Test Profile - Ground 'P' Wave

The very low water table and the sandy soil conditions resulted in two cases of poor bond between the PVC tube and the surrounding soil. The stress wave down the pile was too weak to be transmitted through the soil to the receiver; in these cases, the predominant wave form received was that of the seismic compression, or 'P' wave through the soil profile immediately surrounding the tube. An example of this soil P wave is given in Figure 4, and the average compression wave velocity for the medium-dense sandy soil at this site was 1,420 ft/s (430 m/s).

3.2 Impulse Response (TDR)

Forty nine piles tested by the TDR method gave definite pile tip responses. The TDR test collects raw time-base data for both the hammer force and pile velocity. This data can be analyzed in several ways[3,4]:

1) using the velocity-time response to measure the time taken for the stress wave to travel to the pile tip and back (Sonic Echo),
2) taking the transfer function of the velocity and force readings to compute the pile mobility spectrum (Mobility),
3) using a double Fast Fourier Transform (FFT) on the velocity time-base data to calculate velocity reflectors, and
4) calculating the pile profile by the Impedance Log method.

With the substantial pile cap in place, the frequency spectrum obtained by (2) (the Mobility technique) is usually marred by the preponderant effect of the pile cap itself. This was the case here, and very few pile lengths could be verified by this method.

Some pile lengths were obtained by method (1) (Sonic Echo), with the velocity-time trace exponentially amplified. An example is given in Figure 5.

The most successful approach was by method (3), where the velocity-time trace is transformed twice by the FFT calculation to produce a plot of the most significant stress wave velocity reflectors encountered down the pile shaft. Figure 6 shows an example of such a plot.

The Impedance Log normally does not yield a satisfactory result with such a deep pile cap. For this site, the early part of the velocity-time trace (corresponding to signal reflections down to the pile cap base) was suppressed, in an effort to eliminate the effect of the cap. In most cases, the simulated pile shape was obtained from the Impedance Log.

Figures 7 and 8 show examples of two impedance profiles obtained. Figure 7 indicates a straight-sided shaft of the correct diameter, with the tip reflection at 38 ft (11.6 m). Figure 8 shows the presence of bulbs on the shaft at 14 ft (4.25 m) and at 28 ft (8.5 m), with the pile tip at 42 ft (12.8 m). Of the 49 piles successfully tested, 23 had bulbs at depths varying from 14 to 28 ft (4.25 to 9.5 m), and four had slight neck-ins at between 12 and 14 ft (3.65 and 4.25 m). The pile tip depths varied from pile cap to pile cap, with pile lengths ranging between 37 and 56 ft (11.25 and 17.05 m) below the pile caps tops. No test showed any evidence of possible pile shaft breaks at the level of the base of the reinforcing steel.

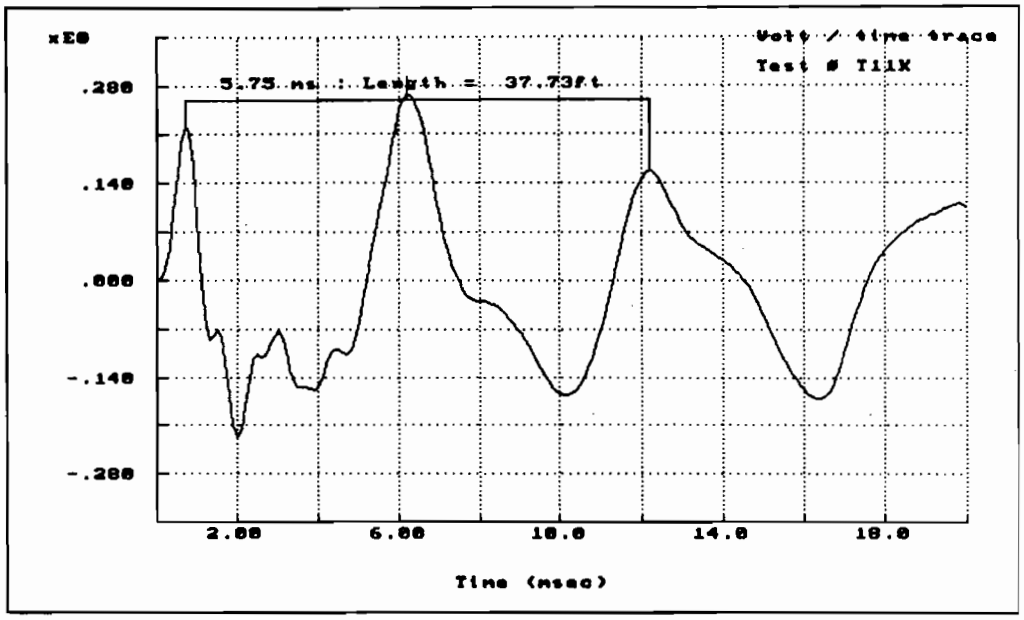

Figure 5. Amplified Sonic Echo velocity-time Trace

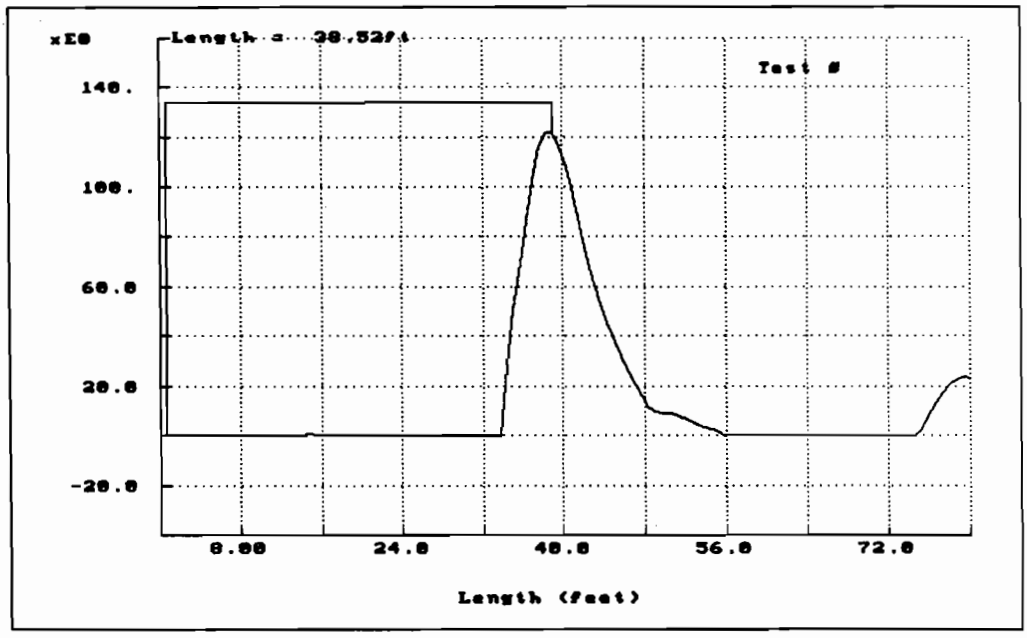

Figure 6. Velocity Reflector Trace

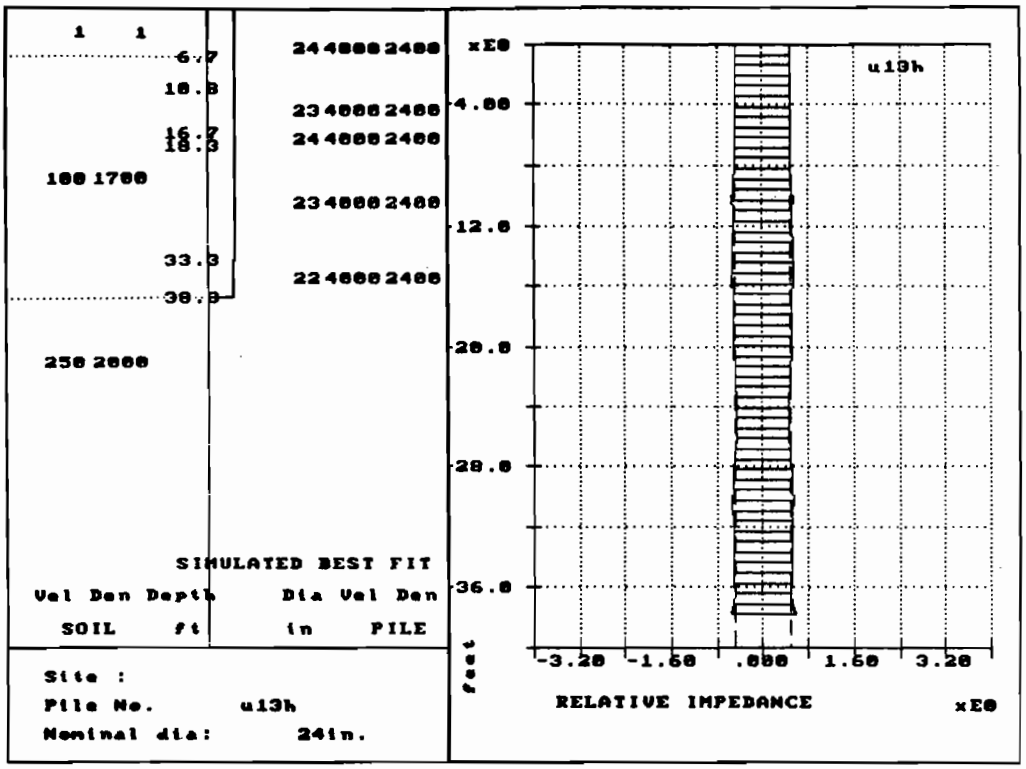

Figure 7. Impedance Log Profile - Straight-sided Shaft

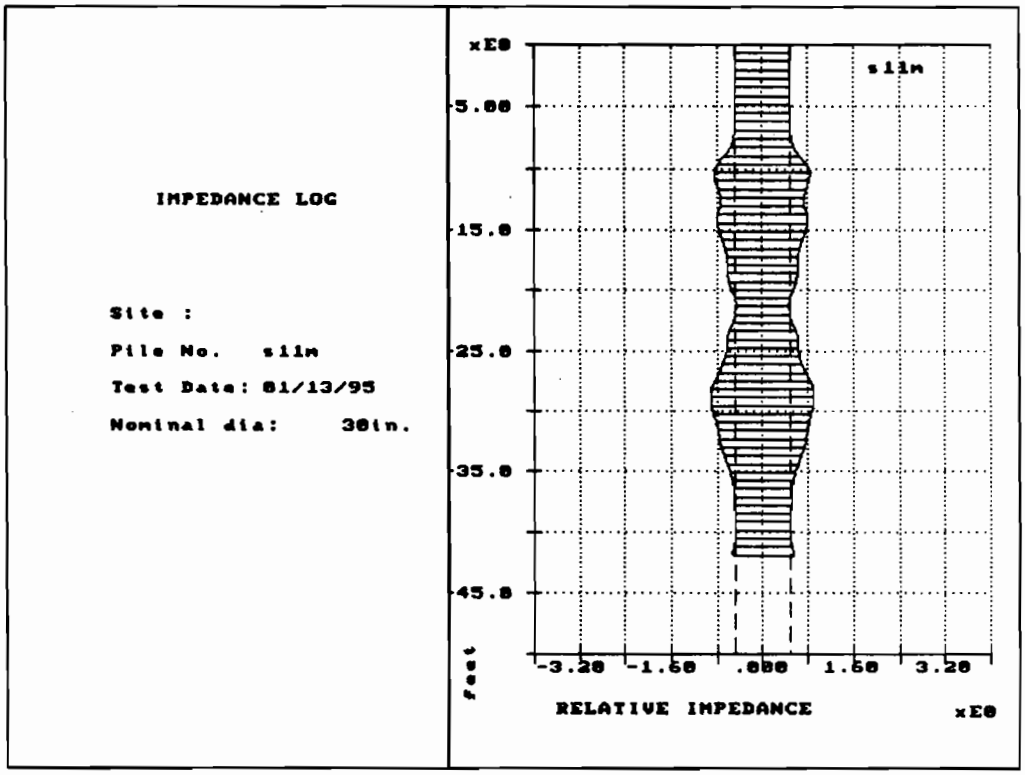

Figure 8. Impedance Log Profile - Shaft with Bulbs

These measured pile tip depths corresponded to the depth of the layer of dense sand with cobbles encountered during drilling for the installation of the Parallel Seismic tubes.

4. CONCLUSIONS

The nondestructive testing program described in this paper was the only feasible approach for the evaluation of the integrity and the length of critical piles under the two buildings, with a minimum amount of disruption and cost. The basement parking garage remained in service throughout the field testing.

5. REFERENCES

1. Clemena, G.G. (1991). "Short-pulse radar methods." *Handbook on nondestructive testing of concrete,* Malhotra and Carino, eds., CRC Press, Boca Raton, Fla., 11, 253-274.

2. Stain, R.T. (1982). "Integrity testing." *Civ. Engrg.,* United Kingdom (Apr.), 55-59 and (May), 77-87.

3. Davis, A.G. (1995). "Nondestructive evaluation of existing deep foundations." *J. Perf. Constr. Fac.,* ASCE 9(1), 57-74.

4. Baker, C.N. Jr., Drumwright, E.E., Briaud, J.-L., Mensah-Dumwah, F. and Parikh, G. (1993). "Drilled shafts for Bridge Foundations." *FHwA Publi. No. FHWA-RD-92-004.* Federal Hwy. Administration (FHWA), Washington, D.C.

Seismic Evaluation of Earth-Fill Dams

David K. Marble, P.E.
Utah Division of Water Rights
Dam Safety Section

Introduction

The historical performance of dams during earthquakes has generally been quite good. There are several conditions, however, which warrant detailed seismic evaluation of a dam. Typical analyses in a seismic evaluation include stability and deformation evaluations. There are several additional areas, including fault displacement, cracking, drainage, and possible overtopping due to seiches or slides, which need to be evaluated but are not conducive to analytical techniques.

Requirements for seismic evaluations in Utah are reviewed. The seismic design process is discussed and several methods of conducting deformation analyses are outlined. Based on evaluations submitted to the Utah State Engineer's Office for review, several areas where additional effort is commonly needed are presented.

Historic Performance of Dams During Earthquakes

In order to adequately address the seismic evaluation of dams, is it helpful to understand the historical performance of earth-fill dams. This perspective provides critical assistance in defining where time and effort should be spent. Historically, earth-fill dams have performed quite well during earthquakes. The United States Committee on Large Dams (USCOLD) has documented the performance of numerous dams world-wide beginning with the 1906 San Francisco Earthquake through the 1989 Loma Prieta Earthquake. During this period of time 19 cases of total dam failure and another 13 cases of serious to severe damage have been documented (1). The dams that have failed have consisted primarily of tailings or hydraulic fill dams, or relatively small and older dams that may have had an inadequate design.

Dams that experienced serious to severe damage include the Austrian Dam (2) with 2.8 feet of settlement and major cracking, and the Lower San Fernando Dam with a major upstream slope failure. The dam avoided total failure only because the reservoir was relatively low (3). Three of the total failures and three of the serious damage cases were located in the United States. Considering that in the U.S. alone there are in excess of 5200 dams higher than 50 feet (1), this is an outstanding safety record.

A legitimate question can be raised considering the safety record. Why should seismic stability be a worthwhile topic of discussion? There are several reasons. First, except for a few

cases, most dams have never experienced ground motion equivalent to the Maximum Credible Earthquake (MCE). Second, some of the cases where dams have experienced serious damage were under shaking conditions much less than the MCE (1,2). Third, albeit the above referenced safety record is admirable, nonetheless, it shows that there are dams with the potential to fail during a seismic event and there are lives and property at risk below these structures.

Engineers and those responsible for public policy should recognize that seismic considerations need to be included in the design of new dams. In addition, Engineers and those responsible for public policy should recognize that there are existing dams which pose a real downstream seismic related hazard which need remediation.

Areas of Impact

Given the above discussion, it might be surmised that there may be documented conditions where seismic concerns are more critical than other conditions. The most reasonable approach to seismic evaluation of earth dams, then, is to identify these respective conditions. Efforts can be directed to those areas with a potential for impact and avoid wasting time and resources (i.e. money) in those areas that will not increase the safety of dams. H. Bolton Seed addressed this issue in his 1979 Rankine Lecture (3). A summary of his conclusions in this area are as follows:

1. Dams constructed of clayey soils on clay or rock foundations have performed very well with strong shaking in excess of 0.35g.

2. Dams which have suffered complete failure or slope failures as a result of earthquake shaking have generally been associated with liquefaction of saturated sandy shells or foundation soils.

3. Virtually any well-built dam on a firm foundation can withstand moderate earthquake shaking with peak accelerations of about 0.2g or higher.

4. In order to avoid wasting time and money, efforts should only be expended on dams where strong shaking in excess of 0.2g is expected or where potentially liquefiable soils are incorporated in the dam or foundation.

Experience from seismic events and the dynamic analysis of new and existing dams since the time of Seed's Rankine Lecture have reinforced the above conclusions. In order to direct appropriate efforts, design standards from the Bureau of Reclamation (4) and the Utah State Engineer's Office (5) require minimal seismic analysis under conditions conducive to good dam performance. These conditions, consistent with above discussion, are when the dam meets static stability criteria, the embankment and foundation are not subject to liquefaction, adequate freeboard is available (i.e.

2 to 3 percent of the embankment height but not less than 3 feet), and the site is not subject to strong motion (greater than 0.2g or 0.35g if clayey). It is the experience author that even if the ground motion is greater than 0.2g to 0.35g, if the other criteria are meet, dam performance is often acceptable.

Evaluation Considerations

Careful consideration must be applied to areas where analytical methods are insufficient for a complete seismic evaluation. The following are some possible ways in which earthquake may case failure of an earth dam (3):

1. Disruption of dam by major fault movement in foundation,
2. Loss of freeboard due to differential tectonic ground movements,
3. Slope failures induced by ground motion,
4. Loss of freeboard due to slope failure or soil compaction,
5. Sliding of dam on weak foundation materials,
6. Piping failure through cracks induced by ground motions,
7. Overtopping of dam due to seiches in reservoir,
8. Overtopping of dam due to slides or rockfalls into reservoir,
9. Failure of spillway or outlet works.

As indicated, many of these potential failure modes do not lend themselves to analytical treatment, but can be adequately addressed by adopting defensive design measures such as the following (3):

1. Allow ample freeboard to allow for settlement, slumping or fault movement.
2. Use wide transition zones of material not vulnerable to cracking.
3. Use chimney drains near the central portion of the embankment.
4. Provide ample drainage zones to allow for possible flow of water through cracks.
5. Use wide core zones of plastic material not vulnerable to cracking.
6. Use a well-graded filter zone upstream of the core to serve as a crack-stopper.
7. Provide crest details which will prevent erosion in the event of overtopping.
8. Flare the embankment core at abutment contacts.
9. Locate the core to minimize the degree of saturation of materials.
10. Stabilize slopes around the reservoir rim to prevent slides into the reservoir.
11. Provide special details if danger of fault movement in foundation.

The consideration of these potential failure modes and the installation of defensive design measures is a relatively simple matter in the design of a new dam, but can be difficult and subjective in the evaluation of an existing dam. An example is the

necessity for a chimney drain and filters. These features would be difficult to add to an existing structure, and yet a thorough seismic evaluation must consider their need. A case in point is the Austrian Dam previously referred to. While the dam experienced 2.8 feet of deformation during the 1989 Loma Prieta Earthquake, transverse cracks near the left and right abutments required excavation and replacement of material to depths of 30 and 25 feet respectively to repair the damage (2).

Utah Dam Safety Requirements for Dynamic Analysis

Dam performance criteria is based on issues of predicted stability and deformation. Consistent with the recommendations of the Committee on Safety Criteria for Dams (6), the analysis of dams should be completed for the following two conditions:

The Maximum Credible Earthquake (MCE) defined as: "All active sources of seismicity with the potential to impact the stability of a dam should be assigned a maximum credible seismic event. The event which has the greatest potential to cause damage at the site will be defined as the Maximum Credible Earthquake." (5) In essence this is the worst, but credible, case condition.

The Operating Basis Earthquake (OBE) defined as: "All active sources of seismicity with the potential to impact the stability of a dam should be assigned an operating basis seismic event. This event is considered to have a return interval of at least 200 years. The event which has the greatest potential to cause damage at the site will be defined as the Operating Basis Earthquake." (5) In essence this is the largest seismic event that the dam is likely to experience during its lifetime.

The philosophy of design for the above referenced design earthquakes is that under MCE conditions the dam may sustain significant damage that may require repair and possibly even breaching, but there should be no uncontrolled release of reservoir water. Under OBE conditions, the dam should not sustain any significant damage and should be able to resume operation with a minimum of delay after the earthquake.

The type of dynamic analysis performed for an embankment falls into the following categories (5):

Category 1: Dam and Foundation NOT subject to Liquefaction

Subcategory: Low to moderate ground shaking potential
Subcategory: High ground shaking potential

Category 2: Dam and/or Foundation subject to Liquefaction

In Category 1, low to moderate ground shaking potential is considered to be a peak acceleration of 0.2g or less, or if the dam is constructed of clay soils and is on a clay or bedrock foundation, a peak acceleration of 0.35g or less. High ground

shaking potential are sites with peak accelerations anticipated to be greater than those described above.

The analysis for a site considered to be in Category 1, subcategory, low to moderate ground shaking potential, should consist of a pseudo-static analysis using a coefficient equal to at least 50 percent of the peak site acceleration with a minimum factor of safety equal to 1.0.

The analysis for a site considered to be in Category 1, subcategory, high ground shaking potential, should consist of a deformation analysis. Generally a pseudo-static analysis will also be required to determine the yield acceleration (i.e. where the calculated factor of safety is unity). The sophistication of the deformation analysis is a site specific issue based on site conditions and the consequence of failure. Further discussion of various methods will be presented later in this paper.

The ground motion predictions used in these analyses are usually based on mean attenuation relationship values leaving a high possibility that actual ground motion, and consequently actual deformation, will be greater than predicted. In addition, the analyses techniques used are not exact and therefore have an associated amount of uncertainty. For these reasons it is required that the ratio of initial freeboard to predicted deformation be in the range of 2.5 to 3 for MCE conditions. In some cases if the ground motion predictions and the analysis are conservative, this ratio may be reduced to 2.

For category 2, a post-earthquake stability analysis should be performed to show that following the cessation of ground motion the embankment is stable. This requires a minimum factor of safety of 1.2. If stability criteria is met, then deformation estimates during shaking should be made to verify that sufficient freeboard is available. The post-earthquake stability analysis is a static analysis considering shear strength loss in non-liquefied zones due to pore pressure build up, and residual undrained shear strength in liquefied zones. This strength is also referred to in the literature as either undrained critical strength or steady-state strength. A relationship between blow counts and Residual Undrained Shear Strength as proposed by Seed and Harder (7) is included as Figure 1. Any borderline cases should be included in category 2.

Seismic Design Process

The seismic design process, or "dynamic analysis," consists of four basic steps. Others (3,8), have suggested a greater number of steps with which the serious designer should be familiar, but these suggestions are in greater detail and can be grouped into these four:

1. Identification of potential seismic activity that would affect the site.

2. Achieve a frame-work of understanding of pre-existing field conditions.

3. Estimate the effects of ground motions on site conditions (Dynamic response computations).

4. Evaluate the performance of the dam.

The first step involves the assignment of design earthquakes and ground motion parameters needed for design. The design values will consist of those identified that have the greatest potential for damage at the site. Input from the seismologic and geologic community is indispensable in this step.

The second step consists of identifying all of the existing field conditions necessary to complete the analysis. The amount of data required to be obtained in this step will depend on the sophistication of the analyses to be performed in the succeeding steps. As previously discussed, where the seismic concerns are not great, and simplified procedures are used, the required data may not be significantly more than that needed for a static evaluation. Where conditions require a more complex approach, greater data is needed. The required information may include site geometrics, subsurface profile, initial stress conditions, and static and dynamic material properties. Since material characteristics are non-linear, it is also necessary to determine how they vary with strain.

The third step involves the dynamic response computations, or simply the evaluation of the site response to the input seismic motion. These evaluations may include several phases to estimate liquefaction potential, induced shear stresses, variations of ground motion through the foundation and embankment, natural period of vibration of the embankment, yield acceleration of the embankment, etc. The computations completed and the information identified in this step will vary widely depending on the type of analysis to be performed in final step.

At the most basic level, this step will involve an evaluation of the site potential for liquefaction and the identification of an appropriate pseudo-static coefficient. When stability analyses are used in any dynamic evaluation, the potential of the dynamic motion to cause a loss of strength or pore pressure build up needs to be evaluated. The resulting loss of shear resistance due to this cause can be modeled as pore pressure increases or as reduced undrained strengths (4).

Analyses with increasing degrees of sophistication that may be required in preparation of deformation estimates are the simplified procedures recommended by Makdisi and Seed (9), 1-dimensional computer programs such as Shake (10), or 2-dimensional computer programs (i.e. dynamic finite elements like QUAD4). Computations with increasing sophistication generally required and produce greater information, and, theoretically, greater accuracy. For

example, Makdisi and Seed's method provides estimates of the embankment natural period of vibration and peak crest acceleration required for their deformation estimation. That method does not give estimates of induced shear-stress, calculation of response spectrum, or alterations of the time-history of ground motion. that may be required in more complex evaluations. These types of information can be obtained through the 1 or 2 dimensional computer programs, although caution should be used in using 1 dimensional programs since the resulting data can be miss leading and/or inaccurate.

The final step is prediction of the dam performance and involves considerations of stability and deformation. Stability calculations in this phase usually consist of a pseudo-static analysis. Where there is a low to moderate potential for ground shaking, this analysis may be all that is required. Where high ground shaking is a concern, a pseudo-static analysis may be required to estimate the yield acceleration to be used in a deformation calculation.

Methods to evaluate deformation vary widely. The most basic techniques consist of empirical correlations. Methods with increasing sophistication include simplified procedures proposed by Makdisi and Seed, Newmark Method, and dynamic numerical. In general, it is most appropriate to begin these analyses using simpler techniques and progress to the more sophisticated methods as the project needs require.

Discussion Deformation Analysis Techniques

Empirical methods based on historical data are considered useful as screening tools and reasonability checks for more sophisticated methods. For cases were deformation is obviously not a concern or for situations of low to moderate downstream hazard, these methods may be sufficient by themselves.

One such method was proposed by Jim Swaisgood (11) of the consulting firm ATC Engineer Consultants Inc. (ECI). ECI plotted historically available data of the dam crest settlement, or deformation, during earthquakes. This settlement data was plotted as a percent of dam height and alluvial thickness verses the estimated peak ground acceleration at the base of the dam. Enveloping curves have been plotted through the data to represent "Average Performance" and "Estimated Maximum Limit." A copy of this recent plot is included as Figure 2.

Makdisi and Seed (3) conducted numerous dynamic response analyses of embankment dams to estimate the deformation for varying conditions. They found that the results of their studies could be normalized to provide a relationship between the amount of deformation, yield acceleration, embankment acceleration, natural period of the embankment and earthquake magnitude. Makdisi and Seed's method is an acceptable method of analysis by the Utah State Engineer's Office where deformations are shown to be of minor

concern (i.e. less than about 1 foot).

The Newmark Method (12) is based on the concept of a sliding block on a sloping surface (Figure 3). Accelerations higher than the yield acceleration initiate movement of the block. An earthquake time-history is used in the analysis. Where the accelerations in the time-history exceed the yield acceleration the deformation is calculated through a double integration of the area under the curve. The total deformation is obtained by summing the deformation experienced during each period during which the yield acceleration was exceeded.

This method is considered to be of sufficient sophistication for most conditions. Computer programs are available (13) which implement this method or the method can also be programmed in a spread-sheet program. The complexity of this analysis is in the dynamic response calculations where reasonable estimates of earthquake motion within the embankment need to be made. These estimates need to consider that actual motions vary not only in time but also in location. Generally, the earthquake motion amplifies significantly through the height of the dam. Yield acceleration calculations and the application of a time history to a sliding block both assume that acceleration is constant throughout the failure mass at any given instant.

Conservative estimates of deformation are calculated by using a maximum record acceleration equal to the peak crest acceleration. In the experience of the writer, reasonable estimates of deformations can be obtained by using a maximum record acceleration equal to the average of the peak crest and peak toe accelerations. This is an area where research and back calculation of known cases histories could provide more rational and dependable ways to model predicted deformation.

The most sophisticated methods of analysis available are dynamic numerical models such as finite elements or finite difference techniques. These methods would only be required under the most hazardous and critical conditions.

Makdisi and Seed, Newmark, and numerical methods can all be used to estimate deformation where liquefaction is an issue (8). They must be used very cautiously and with the appropriate soil parameters such as residual strengths for liquefied soils (7). Deformation resulting from liquefaction is highly variable and not accurately predicted with currently available methods (14).

Comparison of Methods

The calculated deformation for Chabot dam by Makdisi and Seed (3), ranges from 0.47 feet to 1.5 feet. They anticipated a more realistic estimate of between 0.47 feet and 0.58 feet. The Swaisgood chart would suggest that the anticipated deformation would vary from (average to maximum) 0.38 feet to 1.69 feet. Deformation as estimated by the Newmark Method is 0.49 feet for an

acceleration equal to the average of the peak crest and toe accelerations. Using the peak crest acceleration, which is likely conservative, 1.43 feet was calculated. These methods correlate well and are close to values observed in the dam following the 1906 San Francisco Earthquake (3).

Problem Areas

The following is a list of areas in many engineers have not adequately addressed in submissions to the Utah State Engineer's Office.

1. It may be worthwhile to spend more money on investigations of site conditions than in increased sophistication of computer analysis. The analysis is only as good as the input data.

2. Shear strength testing needs to be of high quality and have appropriate drainage conditions. Multi-stage testing may not adequately depict strain incompatibilities. The use of cohesion should be used with discrimination and sound rational judgement. Judgements made about cohesion are more critical in smaller structures where effective stresses are lower.

3. Earthquake records used in the analyses need to be appropriate. Records should approximate the design event as closely as possible in such characteristics as fault type, magnitude, and peak acceleration.

4. Calculations of yield acceleration should account for the loss of shear resistance in both liquefied and non-liquefied soil, as applicable. The loss of shear resistance can be modeled as either pore pressure build-up or in reduced undrained shear strength.

5. Deformations can occur on both the upstream and downstream faces of a dam. Depending on the configuration of the critical failure surfaces these deformations may be cumulative.

Conclusions

Efforts to evaluate the seismic response of dams should be concentrated in cases where liquefaction can occur in the foundation and/or embankment, where reasonable static stability of a dam may be questionable, or in cases of very strong ground motion. In other conditions, dam performance is generally very good and does not warrant the commitment of time and resources to perform a very refined analysis.

Careful attention should be applied to all potential failure modes and where ever possible defensive design measures should be included. Not all areas of seismic evaluation of dams is conducive to analytical evaluation.

The dynamic analysis of a dam includes 4 steps; first, identification of seismic parameters; second, identification of pre-existing conditions; third, conduct a dynamic response analysis; and forth, evaluation of the embankment performance.

References

1. "Observed Performance of Dams During Earthquakes," USCOLD (1992).

2. "Seismic Rehabilitation of Earth Dams," W.F. Marcuson, P.F. Hadala, R.H. Ledbetter, Proceedings Geotechnical Practice in Dam Rehabilitation, ASCE specialty conference, 1993.

3. "Considerations in the Earthquake-Resistant Design of Earth and Rockfill Dams," H.B. Seed, Rankine Lecture 1979, Geotechnique 29, No. 3, 215-263.

4. "Design Standards Embankment Dams, Chapter 13, Seismic Design and Analysis," Bureau of Reclamation, 7610-00-907-1120 R, December 1989.

5. "Administrative Rules for Dam Safety," Utah Division of Water Rights, Robert L. Morgan and Richard B. Hall, Revised January, 1993.

6. "Safety of Dams, Flood and Earthquake Criteria," Committee on Safety Criteria for Dams, National Research Council, 1985, pp 107-108.

7. "SPT-Based Analysis of Cyclic Pore Pressure Generation and Undrained Residual Strength," Raymond B. Seed and Leslie F. Harder, Jr., H. Bolton Seed Memorial Symposium, Volume 2, BiTech Publishers, May 1990.

8. "Evaluation and Use of Residual Strength in Seismic Safety Analysis of Embankments," W.F. Marcuson, M.E. Hynes, A.G. Franklin, Earthquake Spectra, Vol. 6, No. 3, 1990.

9. "A Simplified Procedure for Estimating Earthquake-Induced Deformations in Dams and Embankments," F.I. Makdisi and H.B. Seed, Report No. UCB/EERC-77/19, University of California, Berkeley, August 1977.

10. "Shake," P.B. Schnabel, J. Lysmer, and H.B. Seed, A computer program for earthquake response analysis of horizontally layered soils, Report No. EERC 72-12, University of California, Berkeley, December 1972.

11. "Embankment Dam Behavior During Earthquakes," James R. Swaisgood, ATC Engineering Consultants Inc., State of Utah Dam Safety Workshop, March 1992.

12. "Effects of Earthquakes on Dams and Embankments," N.M. Newmark, Geotechnique 15(2):139-160, 1965.

13. "Microcomputer-Aided Evaluation of Earthquake-Induced Permanent Slope displacements," Sandra L. Houston, William N. Houston, and J. Manuel Padilla, Arizona State University, Microcomputers in Civil Engineering, Elsevier Science Publishing Co., 1987.

14. "Design Problems in Soil Liquefaction," H. Bolton Seed, ASCE Journal of Geotechnical Engineering, Vol. 113, No. 8, August 1987.

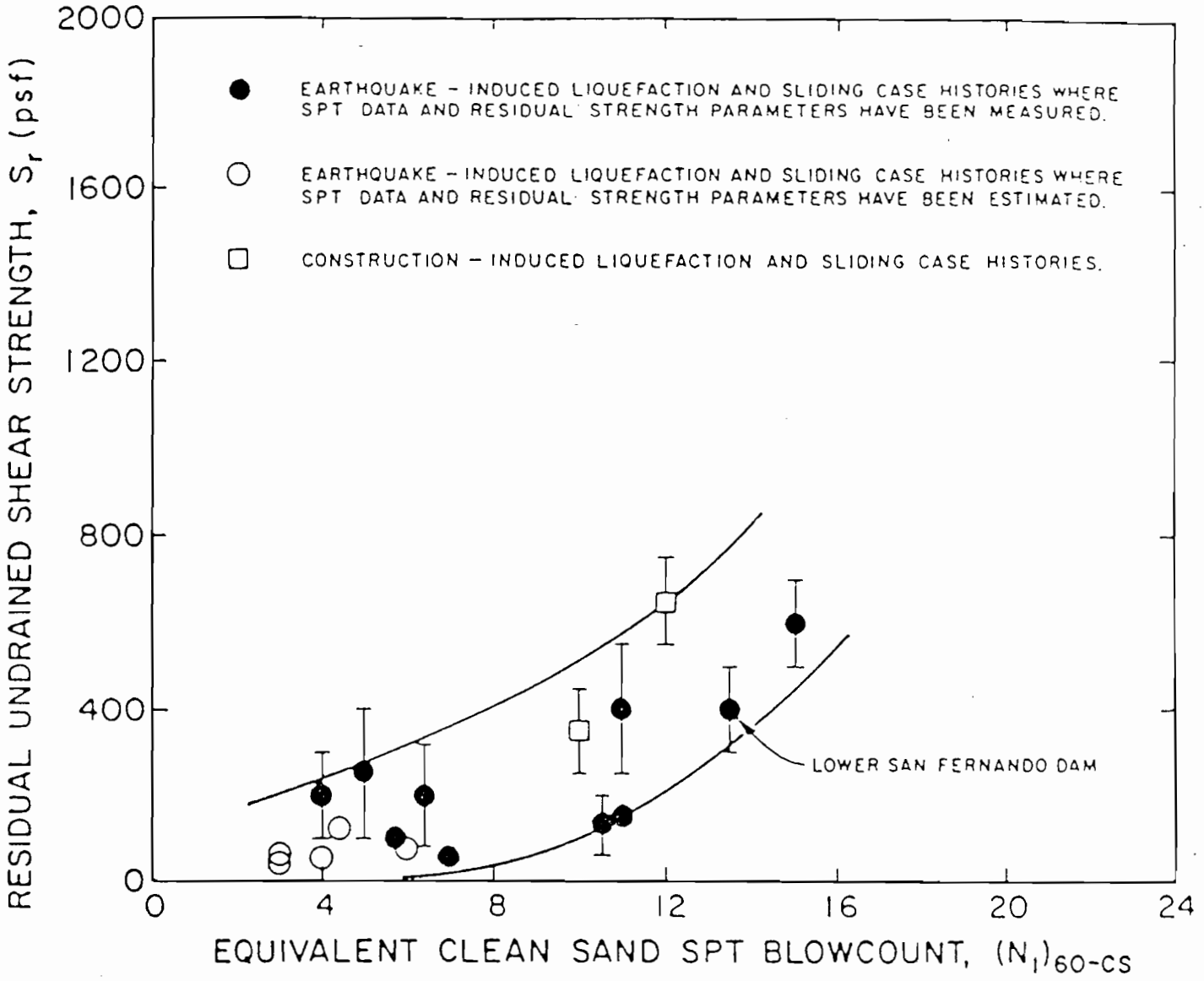

Relationship Between Corrected "Clean Sand" Blowcount $(N_1)_{60\text{-}cs}$ and Undrained Residual Strength (S_r) from Case Studies

Figure 1

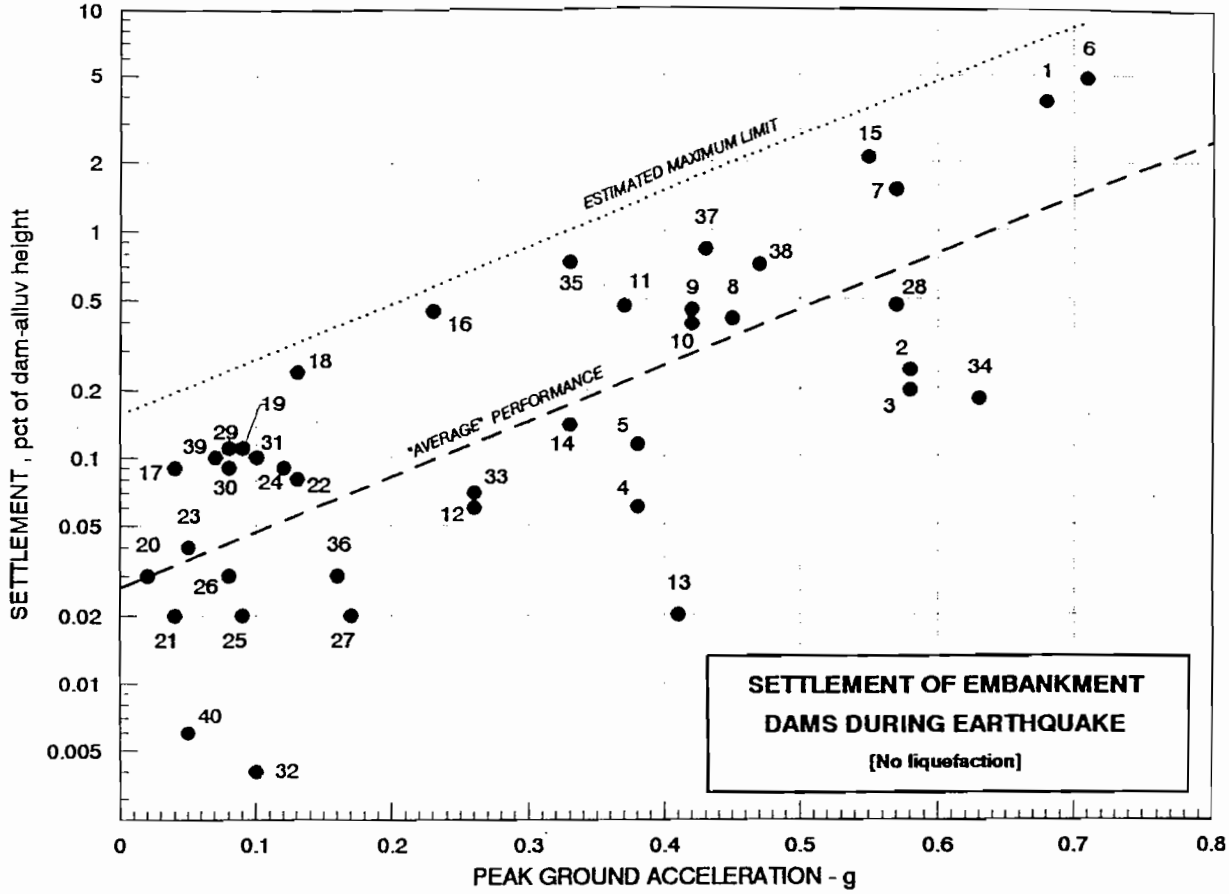

ID No	NAME OF DAM	LOCATION	DAM TYPE	DH feet	AT feet	EARTHQUAKE NAME	DATE	M	D, mi	PGA, g,	CREST SETTLEMENT in ft.(a)	in % (b)	REFERENCES
1	MASIWAY	Philippines	E	82	10	Philippines	16Jul90	7.7	1.7	0.68 E	3.49	3.79	6, 12
2	PANTABANGAN	Philippines	ECRD	375	0	Philippines	16Jul90	7.7	3.5	0.58 E	0.91	0.243	6, 12
3	AYA	Philippines	ECRD	335	0	Philippines	16Jul90	7.7	3.7	0.58 E	0.66	0.197	6, 12
4	CANILI	Philippines	ECRD	230	0	Philippines	16Jul90	7.7	10.9	0.38 E	0.14	0.06	6, 12
5	DIAYO	Philippines	ECRD	197	0	Philippines	16Jul90	7.7	10.9	0.38 E	0.22	0.114	6, 12
6	HEBGEN	Montana	E	82	33	W. Yellowstone	17Aug59	7.6	0.13	0.71 E	5.54	4.82	10, 11, 14, 17
7	AUSTRIAN	California	E	186	0	Loma Prieta	17Oct89	7.1	1	0.67 E	2.79	1.51	2, 4, 9
8	LEXINGTON	California	E	205	0	Loma Prieta	17Oct89	7.1	2	0.46 R	0.84	0.41	2, 4
9	GUADALUPE	California	E	142	? (c)	Loma Prieta	17Oct89	7.1	6	0.42 E	0.64	0.45	2, 4
10	ELMER J. CHESBRO	California	E	95	?	Loma Prieta	17Oct89	7.1	8	0.42 E	0.37	0.39	2, 4
11	VASONA	California	E	34	?	Loma Prieta	17Oct89	7.1	6.5	0.37 E	0.16	0.47	2, 4
12	LEROY ANDERSON	California	ECRD	235	0	Loma Prieta	17Oct89	7.1	13	0.26 R	0.14	0.06	2, 4
13	LEROY ANDERSON	California	ECRD	235	0	Morgan Hill	24Apr84	6.2	1.5	0.41 R	0.05	0.02	13, 17
14	MATAHINA	New Zealand	ECRD	282	?	Edgecumbe	02Mar87	6.3	5.3	0.33 R	0.39	0.14	5, 3, 8
15	U. SAN FERNANDO	California	HF	82	60	San Fernando	09Feb71	6.6	1	0.55 E	3.00	2.11	1, 11
16	COGOTI	Chile	CFRD	275	?	Illapel	06Apr43	7.9	10	0.23 E	1.24	0.45	11,17
17	LA VILLITA	Mexico	ECRD	197	247		21Sep85	7.5	38	0.04 R	0.4	0.09	5, 16, 17
18	LA VILLITA	Mexico	ECRD	197	247	Mich.-Guerrero	19Sep85	8.1	27	0.13 R	1.08	0.24	5, 16, 17
19	LA VILLITA	Mexico	ECRD	197	247	Playa Azul	25Oct81	7.3	19	0.09 R	0.47	0.11	16
20	LA VILLITA	Mexico	ECRD	197	247	n/a	14Mar79	7.6	67	0.02 R	0.15	0.03	16
21	LA VILLITA	Mexico	ECRD	197	247	n/a	15Nov75	7.2	12.4	0.04 R	0.08	0.02	5, 16, 17
22	EL INFIERNILLO	Mexico	ECRD	479	0	Mich.-Guerrero	19Sep85	8.1	6.2	0.13 R	0.36	0.08	5, 16, 17
23	EL INFIERNILLO	Mexico	ECRD	479	0	Playa Azul	25Oct81	7.3	34	0.05 E	0.21	0.04	16
24	EL INFIERNILLO	Mexico	ECRD	479	0	n/a	14Mar79	7.6	59	0.12 R	0.43	0.09	16
25	EL INFIERNILLO	Mexico	ECRD	479	0	n/a	15Nov75	7.2	14.2	0.09 R	0.08	0.02	16
26	EL INFIERNILLO	Mexico	ECRD	479	0	n/a	11Oct75	6.9	49	0.08 R	0.12	0.03	16
27	MIBORO	Japan	ECRD	430	0	Kita-muto	19Aug61	7.0	12.4	0.17 E	0.09	0.02	5, 7, 11
28	MAKIO	Japan	ECRD	254	94	Naganoken	14Sep84	6.8	3.2	0.57 E	1.64	0.47	5, 7
29	NAMIOKA	Japan	ECRD	171	0	Nihonkai-Chubu	26May83	7.7	90	0.08 R	0.19	0.11	5
30	MINASE	Japan	CFRD	220	?	Nigata	16Jun64	7.5	90	0.08 E	0.20	0.09	15, 17
31	MALPASSO	Peru	ECRD	255	?		10Oct38	VI+		0.10 E	0.25	0.10	15, 17
32	OROVILLE	California	ECRD	770	?	Oroville	01Aug75	5.9	4.3	0.10 R	0.03	0.004	16
33	SAN JUSTO	California	ECRD	131	46	Loma Prieta	17Oct89	7.1	17	0.26 R	0.12	0.07	4, 17
34	COYOTE	California	E	140	0	Morgan Hill	24Apr84	6.2	0.01	0.63 E[d]	0.25	0.18	13, 17
35	ONO	Japan	E	124	10	Kanto	01Sep23	8.2	61	0.33 E	0.98	0.73	7, 14
36	TSENGWEN	Taiwan	ECRD	431	?	n/a	14Apr76	6.3	5.0	0.16 E	0.13	0.03	5
37	UPPER MURAYAMA	Japan	E	79	0	Kanto	01Sep23	8.2	11.2	0.43 E	0.66	0.83	7, 14
38	CHATSWORTH NO.2	California	HF	35	?	n/a	30Aug30	5.3	0.62	0.47 E	0.25	0.71	14, 17
39	SOUTH HAYWEE	California	HF	81	0	Kern County	21Jul52	7.7	94	0.07 E	0.08	0.10	14, 17
40	MAGAT	Philippines	ECRD	328	0	Philippines	16Jul90	7.7	60	0.05 E	0.02	0.006	6

NOTES:

DH = dam height
AT = alluvium thickness
M = earthquake magnitude, Richter scale
D = distance from nearest ground rupture or epicenter, whichever is reported closest
PGA = peak ground acceleration
E = estimated
R = recorded

DAM TYPES
HF - Hydraulic Fill
E - Earthfill
ECRD - Earth Core Rockfill Dam
CFRD - Concrete Faced Rockfill Dam

(a) - Settlement shown is the single maximum reported or is an average from upstream, downstream and centerline readings
(b) - Determined as a percentage of combined dam height and alluvium thickness
(c) - If alluvium thickness unknown, it is considered to be 0 for % settlement calculations
(d) - Recorded nearby at 1.29g; estimated value from attenuation curves for mag 6.2 eq at 0.1m. distance.

Figure 2

References for Figure 2

1. ASCE/USCOLD (1975), "Upper San Fernando Dam", Lessons from Dam Incidents, U.S.A., pp. 364-365.

2. Bureau, Gilles, Babbitt, Donald H., Bischoff, John A., Volpe, Richard L., and Tepel, Robert E. (1989), "Effects on Dams of the Loma Prieta Earthquake of October 17, 1989", USCOLD Newsletter, Issue No. 90, November, pp. 1-4.

3. Gillon, M.D. (1988), "The Observed Seismic Behavior of the Matahina Dam", Proceedings of Second International Conference of Case Histories in Geotechnical Engineering, St. Louis, Missouri, June 1-5, Paper 4.29, pp. 841-848.

4. Harder, L.F. (1991), "Performance of Earth Dams During the Loma Prieta Earthquake", in Proceedings, Second International Conference on Recent Advances in Geotechnical Earthquake Engineering and Soil Dynamics, Paper No. LP05, March 1991.

5. Ishihara, K., Kuwano, J., and Lee, H.C. (1990), "Permanent Earthquake Deformation of Embankment Dams", in Dam Engineering, Volume 1, Issue 3, July 1990.

6. National Irrigation Administration of the Philippines - Dam Safety Group (1990), "Pantabangan Dam Complex, July 16, 1990 Earthquake Post Event Inspection Report".

7. Okamoto, S. (1973), "Introduction to Earthquake Engineering", Halsted Press, 571 pp.

8. Pender, M.J. and Robertson, T.W. (1987), "Edgecumbe Earthquake: Reconnaissance Report", in Earthquake Spectra, Volume 3, No. 4, EERI, November 1987.

9. Rodda, K.V., Harlan, R.D. and Pardini, R.J. (1990), "Performance of Austrian Dam During the October 17, 1989 Loma Prieta Earthquake", in USCOLD Newsletter, Issue No. 91, March 1990.

10. Seed, H.B. (1972), "Stability of Earth and Rockfill Dams During Earthquakes", in Embankment Dam Engineering - Casagrande Volume, edited by R.C. Hirschfield and S.J. Poulos, John Wiley & Sons.

11. Seed, H.B., Makdisi, F.I., and DeAlba, P. (1978), "The Performance of Earthquake Dams During Earthquakes", Journal of the Geotechnical Engineering Division, ASCE, Volume 104, No. GT7, pp. 967-994.

12. Swaisgood, J.R. and Au-Yeung, Y. (1991), "Behavior of Dams During the 1990 Philippines Earthquake", Presented at the ASDSO 1991 Annual Conference, San Diego, California, September 29 to October 2.

13. Tepel, R.E., Volpe, R.L. and Bureau, G. (1984), "Performance of Anderson and Coyote Dams During the Morgan Hill Earthquake of 24 April 1984", California Division of Mines and Geology, Special Publication 68, pp. 53-70.

14. Sherard, J.L. et al (1963), "Earth and Earth-Rock Dams", John Wiley and Sons, Inc., Publisher, New York, 3rd printing, 1975, 725 pp.

15. Bureau, G., Volpe, R.L., Roth, W.H. and Udaka, T., "Seismic Analysis of Concrete Face Rockfill Dams", International Symposium, Detroit, October 21, Concrete Face Rockfill Dams - Design, Construction and Performance, J. Barry Cooke and J.L. Sherard, Editors, ASCE Publisher, pp. 479-508, 1985.

16. Bureau, G., Volpe, R.L., Roth, W.H., and Udaka, T., "Seismic Analysis of Concrete Face Rockfill Dams", Closure, ASCE Journal of the Geotechnical Division, Volume 113, No. GT10, October, pp. 1255-1264, 1987.

17. USCOLD (1992), Observed Performance of Dams during Earthquakes.

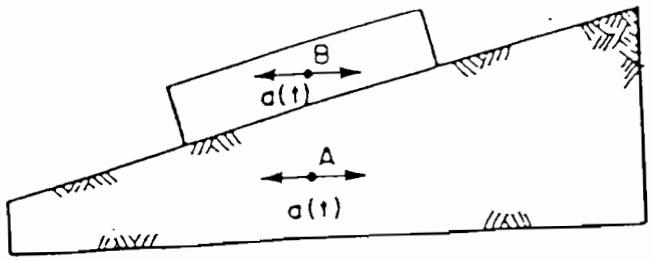

The sliding block analogy.

Typical slope failure to which block analogy is applied.

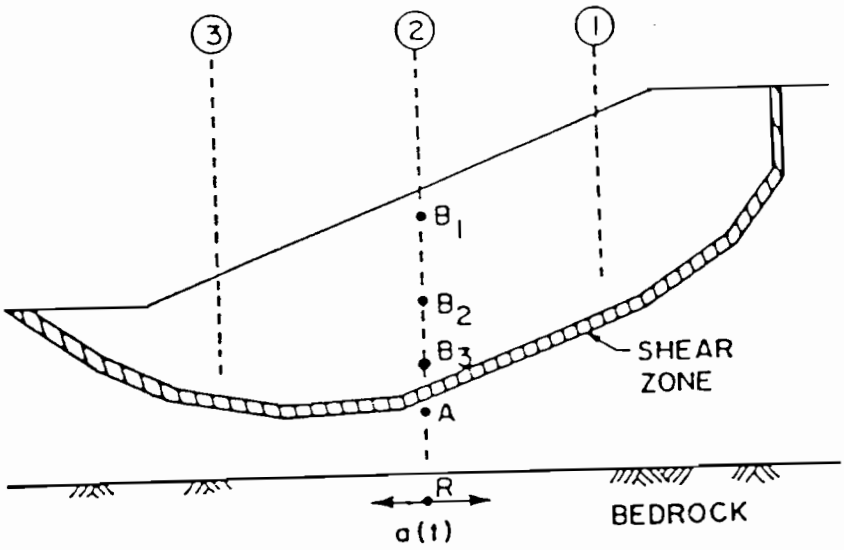

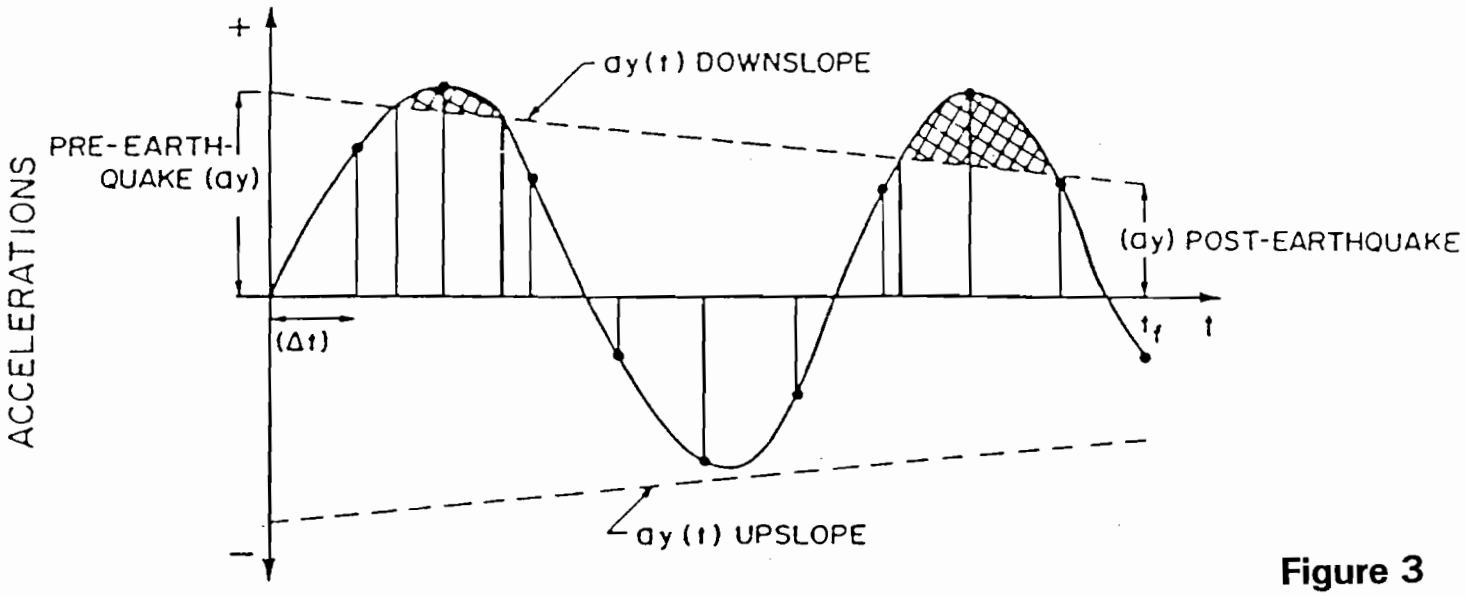

Figure 3

Numerical integration of the acceleration–time history.

Dam Safety - How Safe is Safe Enough?

David S. Bowles[1], Loren R. Anderson[2] and Terry F. Glover[3]

ABSTRACT

Engineers, State and Federal Agencies and Elected Public Officials continue to be faced with making decisions regarding the safety of existing dams. Current dam safety criteria have been developed largely from the view point of design criteria for new dams. These criteria have changed over the years for both hydrologic and "sunny day" events such as earthquakes and various static conditions, and upgrading existing dams to meet a more stringent criteria can be much more difficult and costly that for new construction. More than 50% of existing dams probably do not meet current dam safety design criteria and in many cases this criteria exceeds the criteria that is acceptable for the design of nuclear power plants and other hazardous industrial facilities. Since the owners of many of these "unsafe dams" dams do not have the financial base to upgrade the dams, public officials are faced with the question of "How Safe is Safe Enough?". Incremental flood analysis and risk assessment are helping to answer this important question but there is still not a clear policy on what constitutes acceptable risk. Risk assessment can provide policy owners with valuable information for making a dam safety decision, including probability of failure, cost to save a life, economic risk costs and factors that contribute to the probability of life loss. This presentation describes the risk assessment procedure and suggests a method for evaluating risk of life loss so that it can be compared with acceptable standards use in the nuclear power and other industries dealing with hazardous materials.

[1] Director, Utah Water Research Laboratory and Professor of Civil and Environmental Engineering, Utah State University, [2] Professor and Head, Department of Civil and Environmental Engineering, Utah State University, [3] Professor of Economics, Utah State University, Logan, Utah 84322

ANALYSIS OF SUBSIDENCE AND EARTH FISSURES FOR DESIGN OF A PROPOSED ASH AND SLUDGE IMPOUNDMENT IN SOUTHEASTERN ARIZONA

Jeffrey R. Keaton[1], **George H. Beckwith**[2], **Michael L. Rucker**[2], and **Suang S. Cheng**[2]
AGRA Earth & Environmental, Inc.
[1]4137 South 500 West, Salt Lake City, Utah 84123; [2]3232 West Virginia, Phoenix, Arizona 85009

ABSTRACT

An earth fissure was discovered at the site of a proposed ash and sludge storage pond system after a design by others had been submitted to the Arizona Department of Environmental Quality (ADEQ) in support of an Aquifer Protection Permit. The authors conducted an independent evaluation of the cause of the fissure and its significance to the design, operation, and closure of the proposed pond system. The proposed pond design included a liner system consisting of a high density polyethylene (HDPE) geomembrane liner over a minimum of 8 inches of compacted clayey soils. The main issues raised by discovery of the fissure are its potential effects on the liner system, seepage from the facility, and stability of the dikes.

Logs of wells from a comprehensive ground-water investigation, and surface survey results allowed detailed analysis of subsurface geologic conditions, ground-water levels, and subsidence. A SOILSTRUCT finite element model was calibrated to the measured settlement profile. The profiles of settlements, horizontal movements, and horizontal strains were computed for various times during the history of subsidence and over the project life. Tensile strains computed at the fissure location were similar to the threshold of failure (earth fissuring) estimated by other investigations for similar basin-fill deposits. The zone of differential settlement and higher tensile strains was related to a transition between medial alluvial-fan and distal alluvial-fan and lake-bed deposits.

The capacity of 60-mil HDPE liner to span the predicted opening of the earth fissure was investigated by laboratory pullout tests and theoretical analyses, and a double liner was provided over the fissure zone. A comprehensive program of monitoring settlements and horizontal movements was initiated to confirm movements predicted with the SOILSTRUCT model.

INTRODUCTION

An earth fissure was discovered in March 1993 at the site of a proposed ash and sludge storage pond system located 0.5 to 1.5 miles northwest of the existing Arizona Electric Power Cooperative, Inc. (AEPCO) Apache Generating Station in Cochise County, Arizona (Figure 1). Design of the proposed storage ponds was completed in 1992 by others and submitted to the Arizona Department of Environmental Quality (ADEQ) in support of an Aquifer Protection Permit application prior to discovery of the earth fissure. In April 1993, AEPCO retained AGRA Earth & Environmental to provide an independent evaluation of the cause of the fissure and its significance to the design, operation, and closure of the proposed pond system. The proposed pond design includes a liner system consisting of a high density polyethylene (HDPE) geomembrane liner over a minimum of 8 inches of compacted clayey soils. The main issues raised by discovery of the fissure are its potential effects on the liner system,

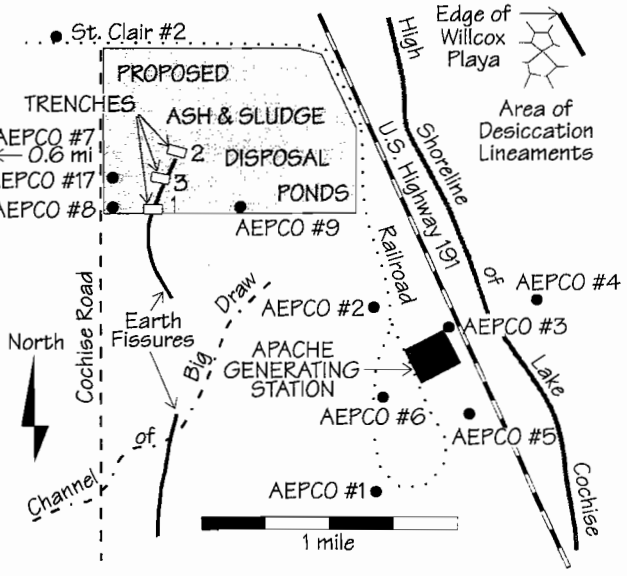

Figure 1. Location map showing Apache Generating Station and proposed pond site. Solid circles are water wells. The site is approximately 75 miles east of Tucson.

seepage from the facility, and stability of the dikes.

Review of available geologic, hydrologic, and engineering data revealed a physical setting in which withdrawal of ground water from an unconsolidated aquifer system has resulted in differential subsidence of the land surface. The differential subsidence occurred because of lateral variability of the aquifer formation and, to a lesser extent, differences in bedrock depth and ground-water decline. Differential subsidence resulted in horizontal tensile strain which caused a tension crack; surface processes of precipitation, ponding, and infiltration eroded the tension crack into a series of elongated, steep-sided depressions. These depressions are the surface expression of the earth fissure.

FISSURE INVESTIGATION

A linear series of discontinuous depressions and sink holes was discovered on the site in March, 1993. Heavy precipitation in January, 1993, probably caused most of the noticeable depressions on the site. The most prominent surface expression consisted of three aligned depressions ranging from 6 to 8 feet long, 3 to 5 feet wide, and 1 to 5 feet deep (Figure 2). These depressions were located in an area where surface water collected adjacent to a north-trending concrete-lined irrigation ditch. South of the site in an area of natural vegetation, the fissure was expressed as an older-looking series of linear, discontinuous depressions (Figure 3).

Figure 2. Sink hole on pond site adjacent to concrete-lined irrigation ditch as it appeared in April, 1993.

Figure 3. Fissure south of pond site.

The stratigraphy of the site was investigated by excavating three trenches 65 to 80 feet long at positions across surface features of the fissure or projections of it. The stratigraphy exposed in the trenches is similar (Figure 4), and indicates a distal alluvial-fan environment. Five basic units were mapped in the trenches. The upper most unit is historical and consists of fill and disturbed soil caused by levelling the site for agriculture and irrigation.

The second unit is brown to pale reddish brown sandy and silty clay. It contains soft masses of light gray carbonate which appear to have been eroded from a calcic soil horizon and redeposited at the site. The original depositional structure of Unit 2 materials has been completely disturbed by burrowing animals and plant roots (bioturbation). A zone of coarse sand in Trench 2 (Figure 4) appears to have been a minor channel. The upper part of Unit 2 has a weak argillic (Bt) horizon, and the lower part has carbonate accumulation consistent with a K horizon. The environment of deposition appears to have been distal alluvial fan or floodplain adjacent to a channel. Unit 2 is interpreted to be Holocene in age.

The third unit consists of an upper reddish brown

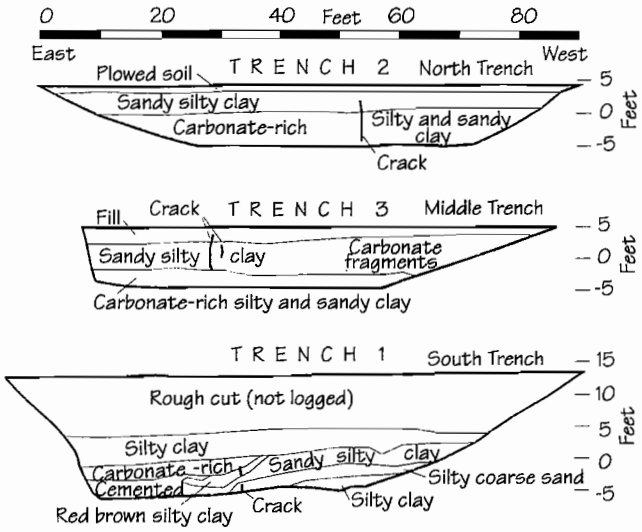

Figure 4. Generalized logs of trenches excavated across earth fissure on pond site. Trench locations on Figure 1.

silty clay with sand and occasional gravel, overlying a carbonate-rich light gray to mottled light gray and reddish brown silty and sandy clay. The upper part is interpreted to be a buried Bt horizon; it has fine, angular blocky structure with clay skins on ped faces and root tubes. The lower part is locally cemented and interpreted to be a Km horizon that is late Pleistocene in age.

The fourth unit is similar to the third, with an upper reddish brown with light gray mottling sandy and silty clay. It has fine, angular blocky structure and is a second buried Bt horizon. The lower part is light gray to pinkish gray with reddish brown mottling sandy and silty clay to clayey gravel with a variable degree of cementation (Km). The environment of deposition is interpreted to be channel and overbank or distal alluvial fan of older late Pleistocene age.

The fifth unit is different from the others. The upper part of Unit 5 is light brown silty coarse sand with variable carbonate cementation. The lower part is chiefly mottled reddish brown and light gray silty clay. One small area was observed to be mottled gray green and light gray in color. The environment of deposition appears to have been sheet wash on the distal part of an alluvial fan. It is interpreted to be older late Pleistocene.

Features exposed in the trenches apparently related to the earth fissure consist of open voids, soil-filled cracks, and hairline cracks. The base of the fill in Trench 3 (Figure 5) is uniform across the soil-filled crack and open void, indicating that no surface depression existed at the time of fill placement. Coarse sand was observed on the fracture surfaces in Trench 2, but the crack does not appear to have been filled. It is unclear if the coarse sand accumulated in a narrow open crack, or if silt and clay from around the coarse sand particles fell into a narrow crack leaving the coarse sand behind. In either case, the crack appears to be relatively young.

A void occurs at the base of Trench 1 in the coarse sand of Unit 5; a prominent fracture occurs in silty sand of Unit 4 approximately above the void, but not connected with it. The coarse sand and silty clay of Unit 5 dips to the east and the contact with the overlying Unit 4 sediments appears to steepen somewhat within two feet of the void. Within Unit 4, a marked change in the character of the carbonate-rich zone exists in the vicinity of the void. It appears that surface water intercepted by the surface expression of the fissure infiltrated, selectively leaching the carbonate cement in Unit 4 in Trench 1. Similar leaching with resulting local changes in

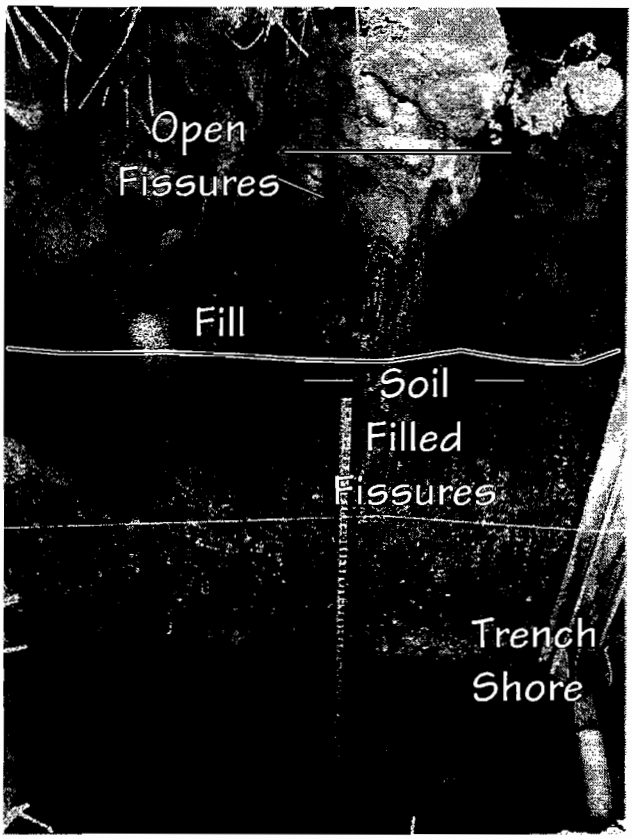

Figure 5. View of south wall of Trench 3 showing open and soil filled fissures. Ruler is 2 m long.

character was also observed in Unit 3 sediments in Trench 3.

Detailed examination of stereoscopic aerial photographs of the site area taken on April 15, 1993, at a scale of 1 inch equals 400 feet, revealed numerous lineaments. Examination of the ground surface resulted in the conclusion that, with the exception of the earth fissure on the site and its continuation to the south, all air photo lineaments were caused by vegetation contrasts related to animal trails, vehicle tracks, and/or sandy stream channels on the alluvial fan of Big Draw. Desiccation polygons exist within a limited area near the margin of Willcox Playa east of the site. It was thus determined with a high degree of assurance that the earth fissure discovered on the site between AEPCO Wells. 8 and 9 is the only earth fissure on the site.

Many earth fissures have been documented in the region of Sulphur Springs Valley north and west of the town of Willcox (Holzer, 1984). Ground-water development resulting in water-table decline in the Willcox area apparently began in the mid-1940s, and subsidence northwest of Willcox reached 5.35 feet over the period 1937 to 1974 (Holzer, 1980). Protruding well casings indicate shallow aquifer compaction in the area.

Alternative explanations for the cause of the fissure at the site must be considered even though ground-water decline and associated land subsidence has been documented in the Sulphur Springs Valley. Bell (1981) lists eight possible origins for earth fissures in Las Vegas Valley, and Keaton and Shlemon (1991) list nine possibilities for fissures in west Texas; the combined list of possibilities is:

1. Aseismic fault slip.
2. Neotectonic folding.
3. Earthquake shaking (or nuclear detonations near Las Vegas).
4. Subsurface dissolution of soluble deposits.
5. Differential compaction.
6. Desiccation of expansive soils.
7. Pedogenesis (soil formation).
8. Strain release from nearby buried channel incision
9. Hydrocompaction.
10. Differential subsidence induced by ground-water withdrawal owing to differences in bedrock depth, soil lithology, and ground-water decline.

The weight of geologic evidence indicates that differential subsidence of subsurface material due to ground-water withdrawal is the cause of the fissure on the site, even though the area has been shaken by several earthquakes, most notably the 1887 San Bernardino, Sonora, event (DuBois and Smith, 1980). Holzer (1984) notes that earth fissures form when differential subsidence is distributed over a narrow zone and causes the overburden to bend.

SETTLEMENT SURVEYS

Three surveys provide elevation data for U.S. Highway 191 (formerly U.S. 666 and originally State Route 114) for the years 1992, 1962, and 1949 (Figure 6). Ground surface subsidence of up to several feet has occurred along U.S. 191 in the project area. The average settlement between 1949 and 1992 is 2.3 times the average settlement between 1949 and 1962. Elevation changes along the south, west, and north edges of the plant site in Section 10 between 1962 and 1992 are shown on Figure 7. Approximate elevation changes along the railroad spur between 1976 and 1993 are shown on Figure 8. Settlements across the north edge of the site increase from 0.3 feet to about 1.9 feet from west to east

ENGINEERING GEOLOGY AND HYDROLOGY

Geologic Setting

The site area is characterized by northwest-trending linear mountain ranges separated by broad valleys typical of the Basin and Range Physiographic

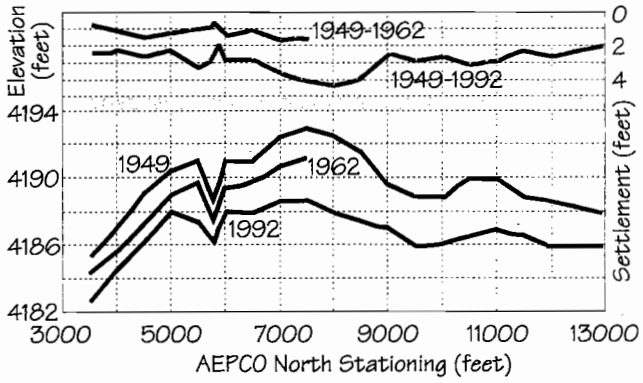

Figure 6. Elevation and settlement profiles along U.S. Highway 191.

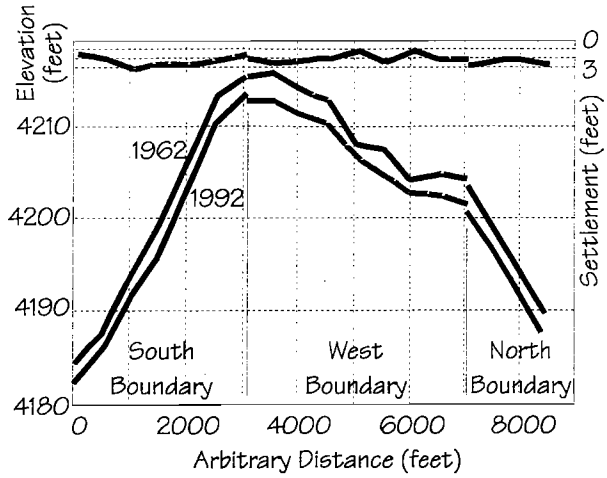

Figure 7. Elevation and settlement profiles along south, west, and north boundaries of the pond site.

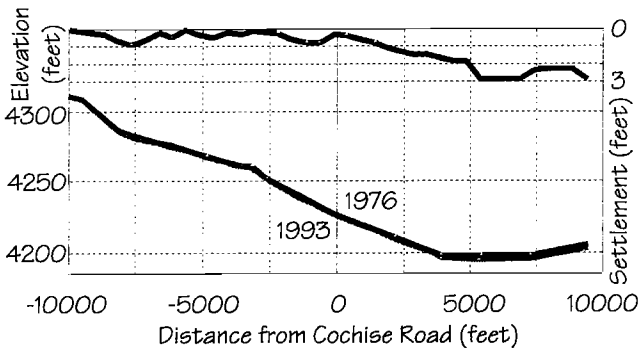

Figure 8. Elevation and settlement profiles along the plant railroad grade.

Province. The site is located on the west side of the internally drained Willcox Basin which is the northern part of the Sulphur Springs Valley (Brown and Schumann, 1969). Alluvial sediments eroded from the surrounding mountains form coalescing alluvial fans leading to the flat surface of Willcox Playa (Figure 9). The geology of the site region is discussed by Drewes et al. (1985), Drewes (1980), and Cooper (1960). Elevations across the site range from about 4190 feet at the northeast corner to about 4235 feet in the southwest corner. The Gunnison Hills are located approximately four miles southwest of the site, and the Red Bird Hills are located approximately four miles to the northwest.

Big Draw, with a 29-square-mile drainage basin, has created a large, gently sloping alluvial fan which has coalesced with alluvial fans created by adjacent, unnamed drainages. The line on the U.S. Geological Survey provisional 7.5' Cochise Quadrangle (1985) indicating the Big Draw channel ends approximately one-quarter mile south of the site. Big Draw in the vicinity of the site is a broad, moderately well defined channel dominated by coarse sand and occasional gravel and cobbles. The site is located on the distal part of the bajada on the east side of the Gunnison Hills. The site has been leveled for agriculture with flood irrigation. Adjacent unmodified land is covered with a moderate growth of mesquite trees and associated shrubs and grasses.

The size and shape of the playa in the Willcox Basin has changed throughout geologic time as the

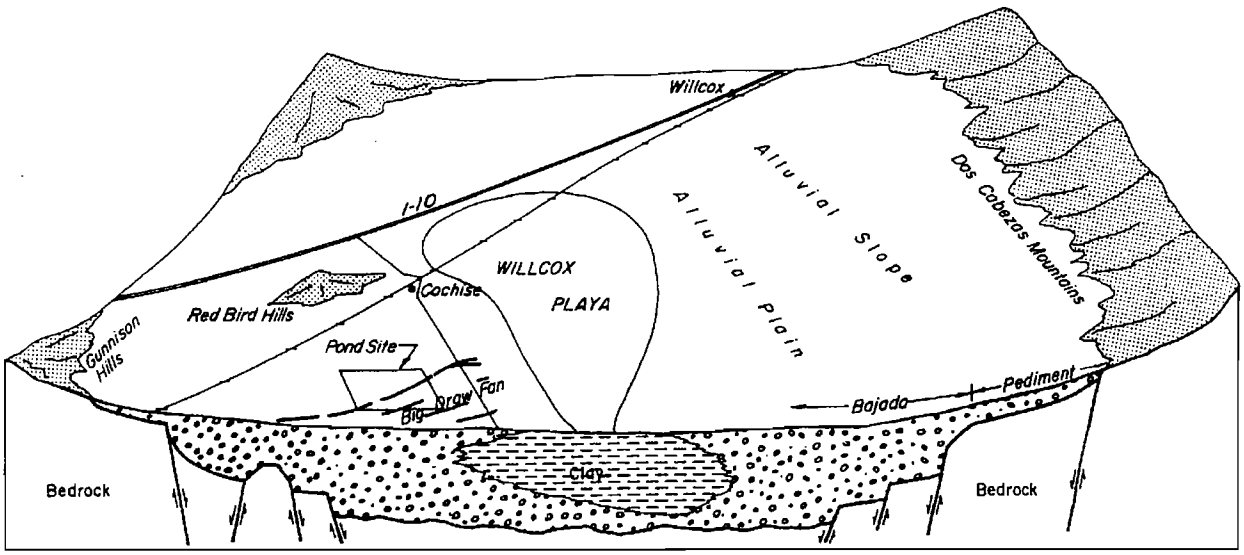

Figure 9. Geomorphic setting of the site.

basin became filled with sediment. Willcox Playa is farther from the Dos Cabezas and Chiricahua Mountains than it is from the Gunnison Hills and Dragoon Mountains. This asymmetric character indicates that more sediment was produced from the east than the west (Martin, 1963). The clayey sediments of the quiet-water playa environment are interbedded with the distal alluvial-fan deposits. At those times when a substantial depth of water existed in Lake Cochise, beaches formed around the margin of the lake. The highest shoreline is located approximately 1,000 feet east of the site. Water wells in the site area show interbedded sandy layers in predominantly clayey soils typical of a distal alluvial-fan environment on the west side of the site and more clayey lakebed deposits on the east side of the site near the playa.

Hydrologic Setting

Ground-water levels in the vicinity of the proposed pond site by 1992 had declined about 120 feet from their levels in 1910 (Figure 10). The ground-water decline in the site area has been 2.5 to 5.0 feet per year since about 1979. A shallow perched water table is present in the vicinity of the Willcox Playa. The piezometric surface of this perched zone is about the same elevation of the playa near the playa, and gradually falls with increasing distance. Thus, the playa appears now to be the recharge area for the shallow aquifer which is perched on clay horizons with an elevation range of 4050 to 4130 feet.

An intermediate-depth aquifer is indicated by geophysical logs at about elevation 3860 to 4000 feet in the area north and west of the site. The intermediate-depth aquifer does not appear to be significant in the site area east of the fissure. Water levels in 1992 were at about 4070 feet in AEPCO Wells 7 and 8 and about 4053 feet in AEPCO Well 9 (see Figure 1 for well locations). Pump test data shown on Figure 11 demonstrates that three days of pumping on AEPCO Well 8 west of the fissure does not result in measurable decline in the water level in AEPCO Well 9 east of the fissure. The lack of response indicates that the hydraulic connection between these two wells is very limited. Transmissivities for Well 8 were calculated in the range of 33,000 to 79,000 gpd/ft, while those for Well 9 were in the range of 5,000 to 10,000 gpd/ft. Total pumpage from 1979 through 1992 from Wells 7, 8, and 9 was 20,200, 13,600, and 11,900 acre-feet, respectively. Ground-water elevations in these wells in March 1992 were 4068, 4070, and 4052, respectively. It is important to note that the water level in Well 9 is nearly 20 feet lower than the level in Well 8.

AEPCO well pumping records for 1979 through 1992 show an annual average pumping rate of 4200 acre-feet per year, and a total withdrawal of 59,000 acre-feet for that period. Pumping in the past 4 years has ranged from 5600 to 6600 acre-feet per year. Plans for the facility in 1993 called for pumping about 6500 acre-feet per year from 1992 to 2014, and 4875 acre-feet per year from 2015 to 2025.

The probable extent of the principal permeable aquifer being pumped by AEPCO is reflected in the Big Draw alluvial fan, and has an area of perhaps 10 square miles. Up to about 70 feet of decline has

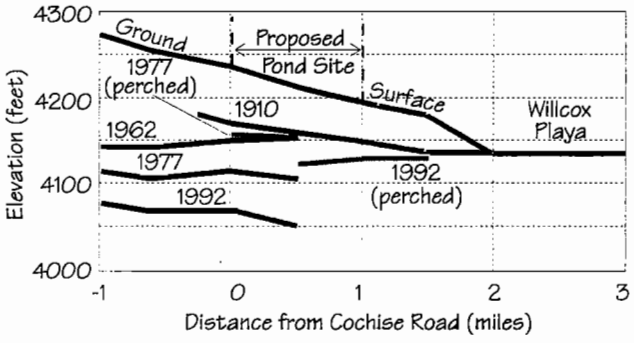

Figure 10. Ground-water elevation history.

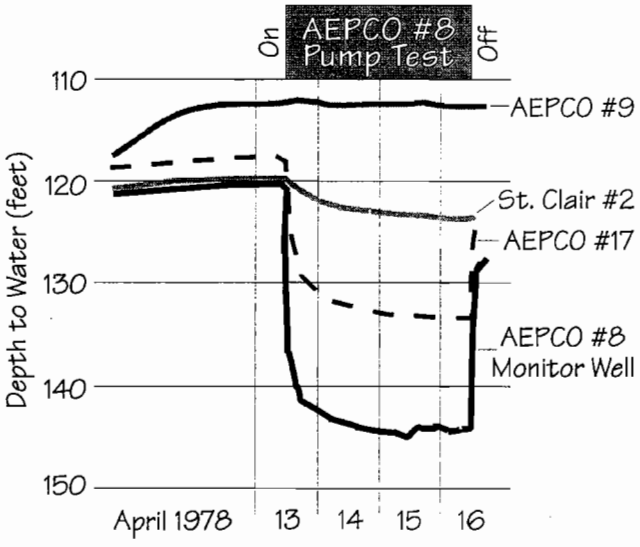

Figure 11. Results of pump test of well AEPCO #8.

occurred in this aquifer between 1979 and 1992 (Figure 12), corresponding to a rate of decline of about five feet per year. The ground-water decline between 1981 and 1992 was 10 to 30 feet, for an average annual rate of about 2.5 feet. For the planned pumping rates, ground-water decline is estimated to occur at four to five feet per year. The more regional ground-water decline rate in Well 21ccc (Arizona system) is a relatively constant 2 feet per year between 1962 and 1992 as shown on Figure 12. It is appropriate to note that agricultural pumping is taking place in the site area as well as pumping for the power plant.

Bell (1981) notes that tension cracks commonly are open at depth, but are not initially well expressed in softer Holocene deposits. They later become opened as fissures by erosion processes. Brown and Schumann (1969) do not mention earth fissures in their geohydrology study of the Willcox Basin; however, Holzer (1980) reports that fissure in the basin began to form between 1935 and 1958, the dates of the earliest two sets of aerial photographs. Major pumping in the Willcox Basin began in the mid-1940s (Holzer, 1980), so it is reasonable to assume that fissure formation began about this time. By 1962, up to 20 feet of ground-water decline had occurred in the vicinity of the site. By 1979, 40 feet of decline had occurred. A rapid ground-water decline occurred in the site area between 1979 and 1981 It is reasonable to assume that the tension crack between AEPCO Wells 8 and 9 occurred after the beginning of this rapid ground-water decline.

Apparent average annual ground-water decline during the period 1979 to 1992 was 2.5 to 5.0 feet. During this same period, average annual subsidence was about 0.1 feet. Thus, the subsidence per unit water level decline was about 0.02 to 0.04. Holzer

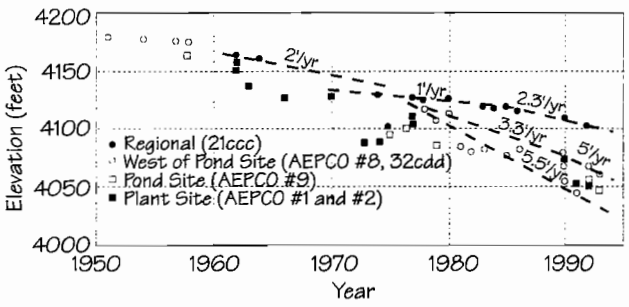

Figure 12. Water level trends and rates of water level decline in the vicinity of the proposed pond site.

(1981) calculated values of subsidence per unit water level decline for six areas, including the Eloy-Picacho area in Arizona. He found subsidence per unit water level decline to be 0.037 to 0.053 for ground-water declines that exceeded the preconsolidation stress of the aquifer formations. The internally drained Willcox Basin is a geologic setting that would be expected to create normally consolidated deposits.

ENGINEERING ANALYSIS

It has long been recognized that earth fissures in areas of large ground-water withdrawal are caused by differential settlements due to irregularities in the thickness and character of the alluvium above bedrock and development of tensile strains in convex portions of the settlement profiles (Anderson, 1973; Jennings, 1977; Pankratz et al., 1978; Raymond et al., 1979; U.S. Bureau of Reclamation, 1979; Holzer and Pampeyan, 1981; Holzer, 1984; Jachens and Holzer, 1979, 1982; Raymond, 1986, 1987; Pewe et al., 1987). The geomechanics of this type of process has been widely studied for a variety of settlement problems. The processes which lead to subsidence-induced earth fissures are essentially the same as those involved in settlement of embankment dams on compressible foundations (Sherard, 1973) and mining subsidence induced by long-wall coal mining (National Coal Board, 1975).

Settlement, horizontal deformation, and horizontal strain analysis was first performed by simplified methods (Helm, 1984; Lee and Shen, 1969). Measured settlements at the site were compared with settlements computed with moduli of deformation back-figured from measured settlements in response to ground-water withdrawal in similar basins. Values of Young's modulus of 6 ksi was estimated by Bell (1981) for clay layers in Las Vegas Valley, while 24 ksi was estimated for granular layers. Based on the relative amounts of clay and silt, and sand and gravel, Young's modulus values of 10 ksi were used for the distal fan facies and 20 ksi were used for the medial fan facies.

Horizontal movements and strains due to subsidence based on a beam analogy were developed by Lee and Shen (1969) and applied to the south boundary of the site. The soil above the water table was assumed to act as a rigid beam over a

compressible foundation. Peak horizontal strains of 1.0 percent and differential horizontal movements of 4 inches across the fissure were obtained - values that seemed high. Jachens and Holzer (1982) compared measurements of settlement and horizontal strain created by ground-water decline in the Eloy-Casa Grande basin with analysis by the Lee and Shen method and a finite element method. They found that the Lee and Shen method gave horizontal strains larger and more erratic than the finite element method.

Detailed analysis was then performed with the SOILSTRUCT finite element program (Filz et al., 1990) for cross sections along the north edge and the south edge of the site. The mesh had 401 elements and 448 nodes. Bulk modulus parameters representing the compressibility of the soils in the model were established according to Duncan et al. (1980). The bulk modulus values were varied interactively until estimated settlements along the north edge of the site matched measured settlements along the railroad spur on the north edge of the site for the period 1976 to 1992. The calculated settlement of 3.0 feet at the southeast corner of the site using these parameters closely approximates the settlement measured for the railroad and U.S. Highway 191 for this period.

Based on this model calibration, settlements, horizontal movements, and horizontal strains were estimated for profiles along the north and south sides of the site from the beginning of ground-water pumping to 1977, 1993, 2000, and 2020 (Figure 13).

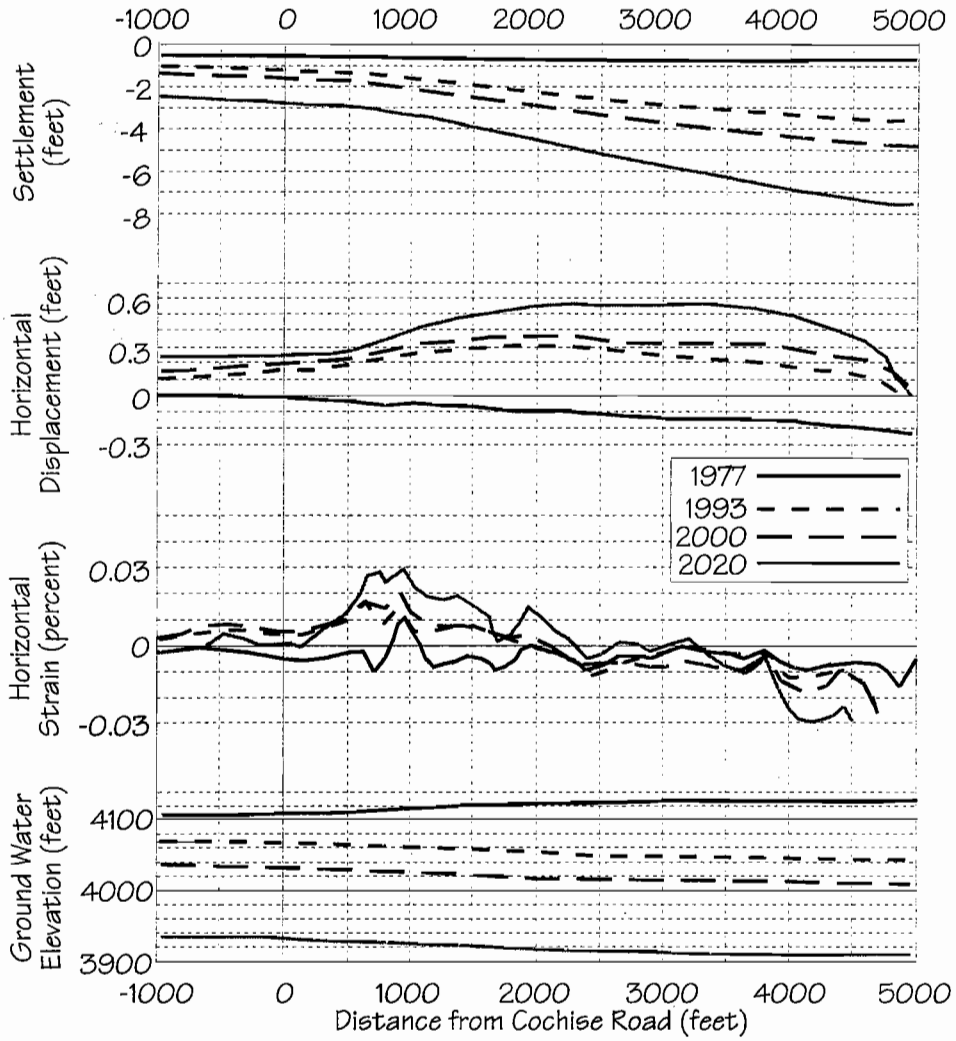

Figure 13. Results of the finite-element analysis along the south side of the site.

The reported ground-water decline was used for the 1977 and 1993 analyses, while an estimated rate of ground-water decline of 5 feet per year was used for the future analyses. Settlement analyses were performed for the south side profile for the cases of Well 9 being used and not being used (Figure 14).

As shown on Figure 13, peak horizontal tensile strain of 0.019 percent was estimated in the area of the fissure for 1993. Jachens and Holzer (1979, 1982) evaluated threshold tensile strains for fissuring in the Eloy-Casa Grande area, and concluded that most fissuring occurred in the range of 0.02 to 0.06 percent horizontal strain. The estimated peak horizontal strain for 1993 (Figure 13) is at the lower range of Jachens and Holzer's threshold, suggesting that the fissure on the site formed recently.

The peak horizontal strain on the north side of the site for 1993 was 0.012 percent. By the year 2020, the peak horizontal strain is estimated to be 0.025 percent, indicating that the fissure should be expected to migrate northward across the site during the life of the ponds.

Differential horizontal extensional movements in the area of the fissure for 1993 are estimated at 1.6 inches. This agrees closely with the maximum opening of 1.5 inches observed in the trenches. The estimated differential horizontal movement in the area of estimated peak horizontal strain along the north side of the site for 1993 is about 1.0 inch, and a recommendation was made that pumping Well 9 be terminated to minimize future opening of the existing fissure and strain accumulation to the north. With this provision, the fissure was estimated to open as much as 1.5 inches by 2020, and the fissure will migrate to some point north of the site by that time.

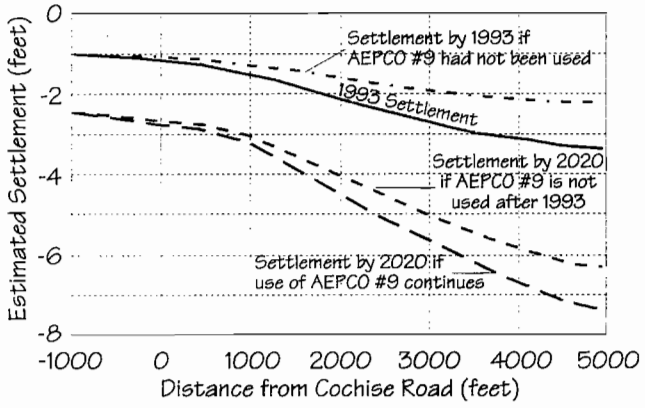

Figure 14. Estimated settlements showing the effects of well AEPCO #9.

Pullout tests of 60 mil HDPE under simulated worst-case field conditions showed maximum tensile strain in the liner of 5 to 13 percent, or less than to about equal to the yield strain, or about 1 or 2 percent of failure strain.

CONCLUSIONS

Detailed examination of subsurface sediments in three trenches excavated across the fissure to depths of 10 to 20 feet revealed that cracking has occurred once in sediments of late Pleistocene age which are estimated to be as old as 130,000 years. In most places, the tension crack had been filled with soil eroded from the surface and transported downward in the crack. The maximum observed width of the crack opening was 1.5 inches; in most places, where the crack was observed it ranged from a hairline crack to a soil-filled crack less than 1.0 inch wide. The maximum observed crack width compares closely with about 2 inches of predicted horizontal differential movement in the region of the fissure obtained in finite-element analysis. Based on projected plant water demand, an additional 67 to 135 feet of ground-water decline is estimated to occur beneath the site by 2020. Differential settlements will be minimized if Well No. 9 is removed from service (Figure 15). For the estimated water-table decline without Well No. 9 pumping, total settlements at the site will increase to about 1.5 to 3.0

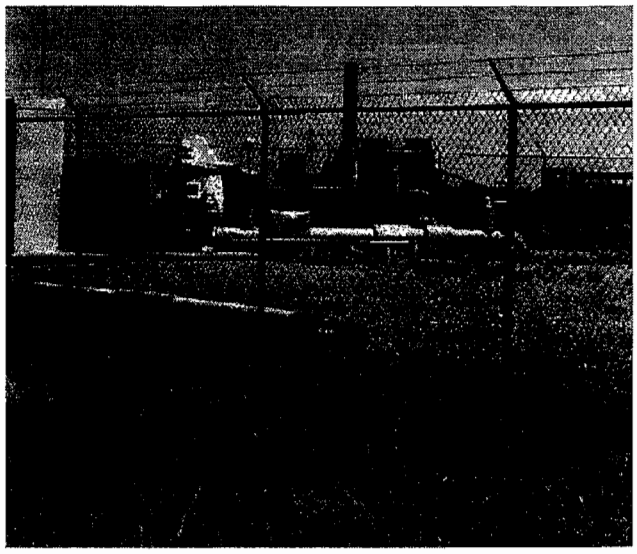

Figure 15. Well AEPCO #9 with Apache Generating Station in background. View to southeast.

feet at the northwest and southwest corners and 5.5 to 8.0 feet at the northeast and southeast corners. Based on computer modeling, it is estimated that without Well No. 9 operating, the existing fissure will open an additional 1.5 inches by 2020. However, the model also indicates that horizontal strains will increase along the center of the transition zone north of the existing fissure. It is probably that will cause the fissure to extend northward beyond the north boundary of the site. The fissure is projected to be open about 1.5 inches at failure and will open to a total of about 3.0 inches by 2020. No other zones of high tensile strain with the potential for formation of fissures were identified on the site.

Both level surveys and finite-element analyses indicate that relatively abrupt differential subsidence has occurred between the east and west sides of the site in response to the ground-water decline. Surveys in 1977 and 1993 along a railroad at the north edge of the site indicate about 0.4 feet of settlement at the northwest corner and about 2.0 feet at the northeast corner of the site. The ground surface along U.S. Highway 191 southeast of the site had subsided as much as 1.8 feet between 1949 and 1962, and as much as 4.5 feet between 1949 and 1992. Ground surface subsidence has been about 0.1 foot per year. Approximate 0.02 to 0.04 feet of subsidence occurs in response to each foot of ground-water level decline. Based on the computer simulations, it is estimated that the settlement since beginning of pumping of wells to 1992 range from about 1.0 foot at the northwest corner of the site to 2.5 feet at the northeast corner. Because of a localized cone of depression caused by pumping of Well No. 9 in the center of the south side of the site, greater differential settlements are estimated along the south edge of the site through the fissure. Total settlements from the beginning of well pumping to 1992 are estimated to be 1.0 foot at the southwest corner of the site to 4.2 feet at the southeast corner.

Driller's logs of wells in the area and the response of adjacent wells to pumping of wells on the site closely define the transition between coarser alluvial-fan deposits on the west side of the site and finer lakebed deposits near the east boundary. The transition appears to be roughly parallel to the margin of Willcox Playa. The western edge of the transition is located between AEPCO Well Nos. 8 and 9. The location of the earth fissure coincides with the distal alluvial-fan facies between the coarser medial alluvial-fan facies and finer lakebed facies. Measured ground-water level decline and surface subsidence, combined with the subsurface information from the wells, clearly indicates that the earth fissure at the site was caused by this well documented process of differential settlements between materials of varying compressibility. This is confirmed by computer simulation of settlements, horizontal movements and horizontal strains. Other possible causes of the fissure were considered and ruled out. These included earthquake shaking, desiccation of clays, solution of deep salt deposits, and movements due to tectonic stresses in the earth.

Generally accepted practice based on the concept of a standard leak per acre developed by the U.S. Environmental Protection Agency was employed in the design of the geomembrane liner. Seepage through a standard leak was analyzed to evaluate the potential for erosion and widening of the fissure. It was found that seepage below the liner will occur as unsaturated flow in which pore-water pressures are negative and seepage velocities are very small unless the standard defect were directly over the fissure. The probability of a defect directly over or immediately adjacent to the fissure is estimated to be grater than 1 in 100. The presence of a defect directly over the fissure could cause fully saturated flow and erosion of the fissure. To further reduce this possibility, a 22.5-foot-wide strip of 60-mil HDPE geomembrane liner was recommended to be placed on top of the primary geomembrane liner centered over the existing fissure. This additional liner should be extended north of the existing fissure under lined pond areas over the zone in which the fissure is expected to migrate before 2020. With double geomembrane liner over the fissure, the probability of standard defects in the two liners lining up over the fissure is negligible. With the recommended treatment and the provision of and maintenance of positive exterior drainage, virtually no potential exists for erosion of the fissure below the liner. Because an unsaturated flow system will be involved, the presence of a fissure beneath the liner will not create a preferential seepage pathway or increase the volume of seepage from the condition analyzed in the 1992 application for an Aquifer Protection Permit.

Laboratory tests simulating soil-geomembrane liner interaction during fissure formation and

theoretical analysis indicates the HDPE primary liner will span fissures well in excess of 3 inches with a large margin of safety. Based on the use of geomembrane liners in important earth dams subject to fissures and for containments which undergo large horizontal deformations, the modified liner design was determined to meet the requirements of Best Available Demonstrated Control Technology (BADCT) as required by ADEQ. Accordingly, it was concluded that the liner system as presently designed with the recommended second 60-mil HDPE liner over the fissure will provide a safe design for both dike stability and ground-water protection.

A monitoring program of frequent inspection of the perimeter of the dike and precise measurements of a system of survey monuments was recommended. This will allow confirmation of the analysis, obtain precise measurements of any movement of the existing fissure and its extension, and allow identification of any pattern of deformations and horizontal strains that might lead to formation of additional fissures.

ACKNOWLEDGMENTS

Publication of the information in this paper was authorized by Mr. Charles S. Reece, IV, of Arizona Electric Power Cooperative, Benson, Arizona. The assistance of Mr. Reece and other AEPCO personnel is gratefully acknowledged.

REFERENCES

Anderson, S.L., 1973, Investigation of Mesa Earth-Crack, Arizona, Attributed to Differential Subsidence Due to Groundwater Withdrawal: Department of Geology, Arizona State University, Master's Thesis.

Bell, J.W., 1981, Subsidence in Las Vegas Valley, Nevada: Nevada Bureau of Mines and Geology Bulletin 95.

Brown, S.G., and Schumann, H.H., 1969, Geohydrology and water utilization in the Willcox Basin, Graham and Cochise Counties, Arizona: U.S. Geological Survey Water Supply Paper 1859-F.

Drewes, H., 1980, Tectonic map of southeast Arizona: U.S. Geological Survey Map I-1109.

Drewes, H., Houser, B.B., Hedlund, D.C., Richter, D.H., Thorman, C.H., and Finnel, T.L., 1985, Geologic map of the Silver City 1° x 2° Quadrangle: U.S. Geological Survey Map I-1310-C.

DuBois, S.M., and Smith, A.W., 1980, The 1887 Earthquake in San Bernardino Valley, Sonora: Historic Accounts and Intensity Patterns in Arizona: Arizona Bureau of Geology and Mineral Technology, Special Paper No. 3.

Duncan, J.M., Byrne, P., Wong, K.S., and Mabry, P., 1980, Strength and Bulk Modulus Parameters for Finite Element Analysis of Stresses and Movements in Soil Masses: Department of Civil Engineering, Virginia Polytechnic Institute and State University, Blacksburg, VA.

Filz, G., Clough, G.W., and Duncan, J.M., 1990, Draft Users' Manual for Program SOILSTRUCT, (Isotropic) Plain Strain with Beam Element: Department of Civil Engineering, Virginia Polytecnic Institute and State University, Blacksburg, VA.

Helm, D.C., 1984, Field-Based Computational Techniques for Predicting Subsidence Due to Fluid Withdrawal, in Reviews in Engineering Geology: v. 6, Geological Society of America, Boulder, CO.

Holzer, T.L., 1980, Earth Fissures and Land Response, Bowie and Willcox Areas, Arizona: U.S. Geological Survey Map MF-1156.

Holzer, T.L., 1981, Preconsolidation Stress of Aquifer Systems in Areas of Induced Land Subsidence: Water Resources Research, v. 17, n. 3.

Holzer, T.L., 1984, Ground Failure Induced by Ground-Water Withdrawal from Unconsolidated Sediment, in Reviews in Engineering Geology: v. 6, Geological Society of America, Boulder, CO

Holzer, T.L., and Pampeyan, E.H., 1981, Earth Fissures and Localized Differential Subsidence: Water Resources Research, v. 17, n. 1.

Jachens, R.C., and Holzer, T.L., 1979, Geophysical Investigations of Ground Failure Related to Groundwater Withdrawal - Picacho Basin, Arizona: Groundwater, v. 17, n. 6.

Jachens, R.C., and Holzer, T.L., 1982, Differential Compaction Mechanism for Earth Fissures Near Casa Grande, Arizona: Geological Society of America Bulletin, v. 93, n. 10.

Jennings, M.D., 1977, Geophysical Investigations Near Subsidence Fissures in Northern Pinal and Southern Maricopa Counties, Arizona: Department of Geology, Arizona State University, Master's Thesis.

Keaton, J.R., and Shlemon, R.J., 1991, The Fort Hancock Earth Fissure System, Hudspeth County, Texas, Uncertainties and Implications, in Land Subsidence: Proceedings of the Fourth International Conference on Land Subsidence, IAHS Publication No. 200.

Lee, K.L., and Shen, C.K., 1969, Horizontal Movements Related to Subsidence: American Society of Civil Engineers, Journal of the Soil Mechanics and Foundations Divisions, v. 95, n. SM1.

Martin, P.S., 1963, Geochronology of Pluvial Lake Cochise, Southern Arizona, II, Pollen Analysis of a 42-Meter Core: Ecology, v. 44, n. 3.

Motts, W.S., 1970, Introduction to Playa Studies, in Motts, W.S., ed., Geology and Hydrology of Selected Playas in the Western United States: U.S. Air Force, Cambridge Research Laboratories, Bedford, Massachusetts.

National Coal Board, 1975, Subsidence Engineers Handbook: National Coal Board, Mining Department, London.

Pankratz, L.W., Hassemer, J.H., and Ackermann, H.D., 1978, Geophysical Studies Relating to Earth Fissures in Central Arizona (abstract): Geophysics, v. 44, n. 3.

Pewe, T.L., Raymond, R.H., and Schumann, H.H., 1987, Land Subsidence and Earth-Fissure Formation in Eastern Phoenix Metropolitan Area, Arizona, in Geologic Diversity of Arizona and its Margins: Excursions to Choice Areas: Arizona Bureau of Geology and Mineral Technology, Special Paper 5.

Raymond, R.H., Laney, R.L., Pankratz, L.W., Riley, F.S., and Carpenter, M.C., 1979, Relationship of Earth Fissures in Alluvial Basins in Southcentral Arizona to Irregularities in the Underlying Formations (abstract): Geological Society of America Abstracts with Programs, v. 11, n. 7.

Raymond, R.H., 1986. Seven Geologic Settings for Earth Fissures in Southcentral Arizona (abstract): Arizona-Nevada Academy of Science Proceedings, v. 21.

Raymond, R.H., 1987, Land Subsidence and Earth Fissures, in The Urbanized Desert: A Challenge for the Geosciences: Geological Society of America Report of the Committee on Geology and Public Policy, Phoenix, Arizona.

Sherard, J.L., 1973, Embankment Dam Cracking, in Embankment Dam Engineering: John Wiley & Sons, New York.

U.S. Bureau of Reclamation, 1979, Final Environmental Impact Statement, Salt-Gila Aqueduct, Central Arizona Project, Arizona: U.S. Bureau of Reclamation, Lower Colorado Region, Boulder City, Nevada.

USING THE BIOT-GEERTSMA-GASSMANN EQUATIONS TO ESTIMATE (A)POROUS ROCK COMPRESSIBILITIES AND (B) SEISMIC VELOCITIES FOR POROUS, FLUID-FILLED ROCKS

Alvin K. Benson and Jie Wu
Department of Geology, Brigham Young University
Provo, UT 84602

ABSTRACT

The velocity of sound in porous, fluid-saturated rocks can be estimated using the Biot-Geertsma-Gassmann (BGG) equations. However, the bulk compressibility and shear modulus of the empty, porous rock are very difficult to obtain in situ. Therefore, the BGG equations are inverted to generate values for these parameters using available velocity and porosity data obtained from well logs and/or cores for water/brine- saturated rocks. These values of the bulk compressibility and shear modulus of the empty, porous rock, along with reasonable estimates of rock-matrix and fluid parameters, are then used to estimate compressional- and shear-wave velocities, compressional-shear-wave ratios, and reflection coefficients at the interfaces between host rocks and fluid-saturated rocks, either fully or partially saturated.

A computer algorithm has been developed to carry out all these calculations and to plot the velocity inforamtion as a function of depth, porosity, and water saturation. The resulting relationships are useful in interpreting seismic data and well log data and in developing reasonable models of the corresponding subsurface geology. Examples will illustrate some of the applications.

INTRODUCTION

The velocities of compressional and shear waves are very important parameters for understanding and classifying porous, fluid-saturated rocks. Much theoretical and experimental work has been done over the past forty-two years to obtain accurate velocity values in these media. This includes (1) theoretical studies to estimate seismic velocity as a function of fluid saturation (Gassmann, 1951; Brandt, 1955; Biot, 1956; Geertsma, 1961; Geertsma and Smit, 1961; Toksöz et al., 1974, 1976), (2) laboratory studies to measure compressional- and shear-wave velocity and elastic properties in dry, fully or partially-saturated rocks as a function of porosity, clay content, and depth (Faust, 1951; Wyllie et al., 1956, 1958; Mann and Fatt, 1960; Domenico, 1974, 1976, 1977, 1984; Gregory, 1976, 1977; Kowallis et al., 1984; Winkler, 1985; Castagna et al., 1985; Marion et al., 1992), (3) model calculations (Klimentos, 1991; Benson, 1992a, 1992b, 1993b), and (4) the study of pore fluid properties (Clark, 1992; Batzle and Wang, 1992).

Compressional- and shear-wave velocities are predictable functions of mineralogy,

porosity, and pore fluids. In the Biot-Geertsma-Gassmann equation, the compressional velocity depends on the following parameters: (a) the compressibility of the matrix material, C_s; (b) the compressibility of the empty reservoir bulk material, C_b; (c) the shear modulus of the reservoir bulk material, μ_b; (d) the compressibility of the fluid, C_f; (e) the bulk density, ρ_b; and (f) the rock porosity, ϕ. Among these parameters, the most difficult parameters to obtain reasonable in-situ values for are the compressibility of the empty porous rock, C_b, and shear modulus of the empty porous rock, μ_b. In the past, this equation has typically been used in a forward modeling mode by specifying values of C_b and μ_b a priori (Domenico 1974, 1976, 1977, 1984, for example). However, this limits the practical applications of the BGG equation for many exploration problems. This research develops a new approach for using the BGG equation to estimate compressional and shear-wave velocities for in-situ porous rock systems.

EQUATIONS FOR COMPRESSIONAL AND SHEAR-WAVE VELOCITIES

Sound waves travel through different media with different velocities. If the medium is a fluid-saturated, porous rock, then the type and amount of the fluid, as well as numerous other parameters, affect the velocity. One of the most useful expressions relating the relevant parameters for determination of compressional velocities in porous media is the Biot-Geertsma-Gassmann (BGG) equation, which is given by

$$V_p = \sqrt{\left(\frac{1}{\rho_b}\right)\left[\frac{r\beta}{C_s} + \frac{(1-\beta)^2}{(1-\phi-\beta)C_s + \phi C_f}\right]}\ , \qquad (1.1)$$

where

$$\beta = \frac{C_s}{C_b}\ , \qquad (1.2)$$

$$r = 3\left(\frac{1-\sigma_b}{1+\sigma_b}\right)\ , \qquad (1.3)$$

$$\rho_b = \rho_f\phi + \rho_s(1-\phi)\ , \qquad (1.4)$$

$$C_f = S_w C_w + (1-S_w)C_h\ , \qquad (1.5)$$

and

$$\rho_f = \rho_w S_w + (1-S_w)\rho_h\ . \qquad (1.6)$$

The parameters in equations (1.1) to (1.6) represent the following physical quantities:

V_p: velocity of the compressional wave,
C_s: compressibility of the matrix material,
C_b: compressibility of the bulk rock free from fluid (dry),
C_f: compressibility of the fluid,
C_w: compressibility of water/brine,
C_h: compressibility of hydrocarbons,
σ_b: Poisson's ratio of the empty reservoir bulk material,
ϕ: rock porosity (typically expressed as a decimal in this thesis),
ρ_b: density of the reservoir bulk material,
ρ_s: density of the matrix grains,
ρ_f: density of the fluid,
ρ_w: density of water/brine,
ρ_h: density of hydrocarbons, and
S_w: water/brine saturation

(Gassmann, 1951; Biot, 1955, 1956; Geertsma, 1961).

The BGG equation was derived for a macrohomogeneous, macroisotropic, linearly-elastic medium with pore sizes concentrated about an average value and probing wavelengths greater than the largest pore size. Since the wavelengths of sound are typically much greater than the pore dimensions, the latter assumption is usually valid for seismic exploration. Transmission of a compressional wave through a rock is assumed to produce small elastic variations from the initial state, and these variations are assumed to be small enough to allow the application of Hooke's Law. If there are different matrix components, each must carry its share of the load and have compressional moduli which don't differ too greatly from each other. The equation doesn't account for chemical interactions, surface tension effects, nor the effects of attenuation or dispersion (Biot, 1956; Geertsma, 1961; Geertsma and Smit, 1961). Relative to the first-order effects that are properly described by the BGG equation, these latter effects can be viewed as being of secondary importance (Murphy, 1984; Winkler, 1985). In summary, the BGG equation governs to first-order the fluid-saturation effects on compressional velocities in granular, geological materials as a function of mineralogy and porosity.

The equation used to determine shear-wave velocities, V_s, is

$$V_s = \sqrt{\frac{\mu_b}{\rho_b}}, \qquad (2)$$

where

μ_b: shear modulus of the reservoir bulk material, and
ρ_b: density of the reservoir bulk material.

This equation is often included as one of the BGG equations, and we will do so in this paper. Using the Toksöz-Kuster scattering model (1974), a reasonable estimate for μ_b for rocks with spherically-shaped pores is given by

$$\mu_b = \mu_s \left\{ \frac{1-\phi}{1+\phi\left(\frac{6+12\mu_s C_s}{9+8\mu_s C_s}\right)} \right\}, \qquad (3)$$

where

μ_s : shear modulus of the matrix material,

ϕ : rock porosity, and

C_s : compressibility of the matrix material.

Approximating the bracketed term in the denominator by one, an estimate for the bulk shear modulus is given by the expression

$$\mu_b = \mu_s\left(\frac{1-\phi}{1+\phi}\right) . \qquad (4)$$

This equation appeals to common sense since it suggests that the shear stiffness of a rock is simply weakened by the holes. However, since it does depend upon other factors, it can yield nonphysical results at high porosities. A more general, useful expression for the relationship between C_b and μ_b can be derived from the definition of Poisson's ratio,

$$\sigma_b = \frac{1-2(V_s/V_p)^2}{2(1-(V_s/V_p)^2)} . \qquad (5)$$

Combining equation (1.1), (2), and (5), along with some extensive algebra, it is found that

$$\mu_b = \frac{3(1-2\sigma_b)}{2C_b(1+\sigma_b)} . \qquad (6.1)$$

For clean sandstones, σ_b has an average value of about 0.1 (Castagna et al., 1985). Putting this value into equation (6.1),

$$\mu_b = \frac{1.091}{C_b} \qquad (6.2)$$

for clean sandstones, which is in agreement with results recently reported by Murphy, et al. (1993). Equations (1.1), (2), (4), and (6.1) will be used in the computer algorithm developed in this paper to estimate in-situ values for C_b and μ_b, and then V_p and V_s will be predicted for in-situ, porous rocks fully or partially saturated with oil and/or gas.

With the velocity values generated from this algorithm, rock impedances (the product of velocity and bulk density) will be estimated. From these impedances, the reflection coefficients, R, at each impedance boundary can be predicted from

$$R = \frac{\rho_b V - \rho_b' V'}{\rho_b V + \rho_b' V'}, \qquad (7)$$

where

ρ_b: bulk density of the reservoir material below the boundary,
ρ_b': bulk density of the reservoir material above the boundary,
V: compressional or shear-wave velocity of the reservoir material below the boundary, and
V′: compressional or shear-wave velocity of the reservoir material above the boundary.

These reflection coefficients can then be compared with acquired seismic data in the area of interest. Subsequently, using the input and output parameters from the BGG equation, subsurface models can be developed which are self consistent with the seismic data. These models should be reasonable estimates of the in-situ geology and will be valuable in making engineering and exploration decisions.

COMPUTER ALGORITHM BASED UPON THE BGG EQUATION

The BGG equations (1.1) and (2) can be inverted to estimate values of C_b and μ_b from available field data for water/brine-saturated rocks, such as the well-log data compiled by Gregory (1977), Bird (1986) and Benson (1993a) for Gulf Coast sands. The choice of beginning with equation (1.1) or equation (2) depends on the available velocity data for water-saturated rocks in the study area. If available, shear-wave velocities are the first choice since they are less sensitive to the effects of fluid saturation. Because C_b and μ_b are dry rock parameters, their values for a given depth should not change when the rock is saturated with different amounts and/or types of fluid. Thus, once C_b is determined for a porous rock at a given depth, compressional-wave velocities can be generated from equation (1.1) for a reservoir containing different types of fluid.

Inverting equation (1.1), using some extensive algebra, we obtain

$$(C_f/C_b) = X(1-\sqrt{1-Y}), \qquad (8.1)$$

where,

$$X = \frac{r(1-\phi+\phi(C_f/C_s))+\rho_b C_s V_p^2 - 2}{2(r-1)}, \qquad (8.2)$$

$$Y = \frac{(1-\phi+\phi(C_f/C_s))*\rho_b C_s V_p^2 - 1}{(r-1)*X^2}, \qquad (8.3)$$

and the other parameters are defined following equation (1.1) above.

From equation (2), μ_b is given by

$$\mu_b = \rho_b (V_s)^2 , \tag{9}$$

and the other parameters are defined as in equation (2).

Fluid densities and compressibilities are important input parameters for the BGG equation. Values for fluid densities and compressibilities as a function of composition, pressure and temperature can be determined from some approximate equations discussed by Batzle and Wang (1992). Densities and compressibilities vary substantially, but approximate analytical expressions can be determined for the pressure and temperature conditions typical for subsurface exploration. With reasonable estimates of in-situ pressure and temperature, more realistic values can be calculated.

At typical pressures and temperatures encountered in the subsurface, the approximate equations for gas density and compressibility, respectively, are given by

$$\rho_g \cong \frac{28.8GP}{ZRT_a} , \tag{10.1}$$

$$C_g = \frac{1}{K_s}, \tag{10.2}$$

where

$$T_a = T+273.15 , \tag{10.3}$$

$$Z = [0.03+0.00527(3.5-T_{pr})^3]P_{pr}+(0.642T_{pr} -0.007T_{pr}^4-0.52)+E , \tag{10.4}$$

$$P_{pr} = \frac{P}{(4.892-0.4048G)} , \tag{10.5}$$

$$T_{pr} = \frac{T_a}{(94.72+170.75G)} , \tag{10.6}$$

$$E = \frac{0.109(3.85-T_{pr})^2}{\exp[P_{pr}^{1.2}(0.45+8(0.56-1/T_{pr})^2)/T_{pr}]}, \tag{10.7}$$

$$K_s = \frac{P\gamma_0}{\left(1-\frac{P_{pr}}{Z}\frac{\partial Z}{\partial P_{pr}}\right)_T}, \tag{10.8}$$

$$\frac{\partial Z}{\partial P_{pr}} = 0.03+0.00527(3.5-T_{pr})^3 - \left\{\frac{0.1308P_{pr}^{0.2}(0.45+8(0.56-1/T_{pr})^2)(3.85-T_{pr})^2}{\exp[P_{pr}^{1.2}(0.45+8(0.56-1/T_{pr})^2)/T_{pr}]T_{pr}}\right\}, \tag{10.9}$$

$$\gamma_0 = 0.85+\frac{5.6}{(P_{pr}+2)}+\frac{27.1}{(P_{pr}+3.5)^2} - \frac{8.7}{\exp(0.65(P_{pr}+1))}. \tag{10.10}$$

The parameters in the equations (10.1) to (10.10) are defined as follows:

ρ_g: gas density,
C_g: gas compressibility,
G: gas specific gravity,
P: reservoir pressure in MPa,
T: reservoir temperature in °C,
P_{pr}: reduced pressure,
T_{pr}: reduced temperature, and
R: gas constant, which is 8.3118 MPa per °K per gram-mole in this unit system.

These approximate equations work well as long as P_{pr} and T_{pr} are not both within about 0.1 of unity (Batzle and Wang, 1992).

The compressibilities for oil, water and/or brine are determined from the expression (Batzle and Wang, 1992)

$$C_f = \frac{1}{\rho_f V_f^2}, \tag{11}$$

where

C_f: fluid compressibility
ρ_f: fluid density, and
V_f: fluid velocity.

Knowing the American Petroleum Institute oil gravity (API) number, reasonable estimates can be made for the gas-oil-ratio (GOR) and solution-gas specific gravity (G_s), from which the density and velocity of crude oil under in-situ conditions can be determined by the following procedures:

a. Determine the bubble point pressure, BBP, at reservoir conditions using the following equation:

$$BBP = \frac{\left(47.103\frac{GOR}{G_s}\right)^{\frac{1}{1.205}}}{\exp\left[\frac{4.072}{\rho_s}-0.00377T\right]}, \qquad (12.1)$$

where

$$\rho_s = \frac{141.5}{API+131.5}. \qquad (12.2)$$

and G_s is the solution gas density.

b. Compare this bubble point pressure with reservoir pressure.

c. If reservoir pressure is below the bubble point pressure, the oil is saturated, and the equations for density and pseudo-density of oil are given by

$$\rho_o = \frac{(\rho_s+0.0012G_sR_G)}{B_o}, \qquad (13.1)$$

$$\rho' = \frac{\rho_s}{B_o(1+0.001R_G)}, \qquad (13.2)$$

where

$$R_G = 0.02123G(P\exp[4.072/\rho_s-0.00377T])^{1.205}, \qquad (13.3)$$

$$B_o = 0.972+0.00038[2.4R_G(G/\rho_s)^{1/2}+T+17.8]^{1.175}, \qquad (13.4)$$

and

R_G: gas-oil-ratio,

B_o: oil-formation volume factor, which is the volume at reservoir conditions occupied by one stock tank barrel of oil plus gas in solution.

ρ': pseudo-density, which is an estimated density including the expansion caused by gas intake.

d. If reservoir pressure is above bubble point pressure, the oil is undersaturated, and the density and pseudo-density can be determined from

$$\rho_o = \rho_G + [0.00277(P-BBP) - 1.71\times10^{-7}(P-BBP)^3] + (\rho_G - 1.15)^2 + 3.49\times10^{-4}(P-BBP) \quad (14.1)$$

$$\rho' = \frac{\rho_a}{B_o(1+0.001GOR)} , \quad (14.2)$$

where

$$\rho_G = \frac{\rho_a + 0.0012(G_g)GOR}{0.972+0.00038[2.4GOR(G_g/\rho_a)^{1/2}+T+17.8]^{1.175}} , \quad (14.3)$$

$$B_o = \frac{\rho_a + 0.0012(G_g)GOR}{\rho_o} , \quad (14.4)$$

e. Determine the oil velocity from

$$V_o = 2096[\rho'/(2.6-\rho')]^{1/2} - 3.7T + 4.64P + 0.0115[4.12(1.08/\rho'-1)^{1/2}-1]TP , \quad (15)$$

where

ρ': pseudo-density of oil, and

V_o: oil velocity in meters per second.

Using existing data (Rowe and Chou, 1970; Zarembo and Fedorov, 1975; Potter and Brown, 1977), a polynomial fit in temperature, pressure, and salinity can be determined to calculate the density of water and/or brine (Batzle and Wang, 1992):

$$\rho_w = 1+1\times10^{-6}(-80T-3.3T^2+0.00175T^3+489P-2TP$$
$$+0.016T^2P-1.3\times10^{-5}T^3P-0.333P^2-0.002TP^2)\ , \qquad (16.1)$$

$$\rho_b = \rho_w+S\{0.668+0.44S+1\times10^{-6}[300P-2400PS$$
$$+T(80+3T-3300S-13P+47PS)]\}\ , \qquad (16.2)$$

where

ρ_w: water density,

ρ_b: brine density, and

S: brine salinity in ppm.

Using the data of Wyllie et al.(1956), Chen et al. (1978) developed the following equation for the velocity of water and/or brine:

$$V_w = \sum_{i=0}^{4}\sum_{j=0}^{3} w_{ij}T^iP^j\ , \qquad (17.1)$$

$$V_b = V_w+S(1170-9.6T+0.055T^2-8.5\times10^{-5}T^3+2.6P-0.0029TP$$
$$-0.0476P^2)+S^{1.5}(780-10P+0.16P^2)-820S^2, \qquad (17.2)$$

where

V_w: water velocity,

V_b: brine velocity,

and the constants w_{ij} are given in Chen et al. (1976).

A computer algorithm has been developed to determine (a) C_b from equation (8.1) and μ_b from equation (6.1) or μ_b from equation (9) and C_b from equation (6.1) based upon the available data for brine-saturated rocks, and then calculate (b) V_p from equation (1.1) for rocks partially saturated with oil and/or gas, and V_s from equation (2).

The major procedures in the algorithm are the following:

1. Input rock matrix parameters and fluid parameters .

The physical parameters of the rock matrix and fluids required for the algorithm are (1) density of the matrix, (2) compressibility of the matrix, (3) poisson's ratio of the dry bulk rock, (4) salinity of brine, (5) API gravity of oil, (6) gas-oil-ratio, (7) solution- gas specific gravity, and (8) gas specific gravity. The user can easily adjust these parameters to fit the particular formation and typical oil, gas, water and/or brine for a given region.

Since pore fluids strongly influence the seismic properties of rocks, it is necessary

to understand their properties. Using our computer algorithm and equations (10.1) through (17.2), densities and compressibilities were calculated as a function of depth for gases, oils, and brines. The depth dependence is directly related to the in-situ pressure and temperature. In general, an increase in pressure will increase the fluid density and decrease the fluid compressibility, whereas an increase in temperature will decrease the fluid density and increase the fluid compressibility.

For the calculations in this paper, the oil is assumed to have an API gravity of 32, a gas-oil-ratio (GOR) of 350 scf/stb, and a solution gas gravity of 0.7, which are typical values for south Louisiana wells (Bird, 1986). We also assume that the gas has a specific gravity of 0.7, and the brine salinity is 100,000 parts per million (ppm). All of these parameters can be adjusted to the region and depths of interest.

Representative values of densities and compressibilities for a pure sandstone matrix (Simmons, 1965) and a pure limestone matrix (Humbert and Pheque, 1972) are given in Table 1. The matrix density and compressibility remain essentially constant as a function of depth (Domenico, 1974). Average values of Poisson's ratio for sandstone and limestone are also given in Table 1 (see Toksoz and Kuster, 1974). Based upon well log data for a given area, such as that compiled by Gregory (1977) for the Gulf Coast, a polynomial fit of porosity versus depth can be made for sandstone and other rocks. The average differential pressure gradient is taken as 1.74 psi/m, and the temperature is assumed to increase an average rate of 0.03281°F/m. These are typical values for the Gulf Coast (Domenico, 1974), and they can be adjusted to the area of interest.

Table 1. Matrix Properties of Rocks used for Calculation.

Rock	Density (g/cm^3)	compressibility (cm^2/dyne)	Dry Poisson's Ratio
sandstone	2.65	2.63158E-12	0.1
limestone	2.71	1.30378E-12	0.29
shale	2.68	1.98413E-12	0.25

2. Input compressional- or shear-wave velocities of water/brine-saturated porous rocks.

Existing velocity data for water/brine-saturated rocks, such as from well log data, are needed in our algorithm in order to calculate the dry reservoir bulk compressibility, C_b, and shear modulus, μ_b. The well log data compiled by Gregory (1977) for average Gulf Coast sandstones, and by Kithas (1976) for Lea County (New Mexico) limestones are used in our calculations.

3. The algorithm calculates the following parameters:

(a) The dry reservoir bulk compressibility C_b, or the bulk modulus, K_b (reciprocal of C_b), and the bulk shear modulus, μ_b, are estimated using equations (8.1), (6.1), and (9).

(b) Using equation (1.1) and values determined in the algorithm for C_b, the compressional-wave velocity, V_p, is calculated for oil- or gas-saturated rocks, or partially-saturated rocks, as a function of depth or porosity for a given water saturation, and as a function of water saturation for a given porosity.

(c) Using equation (2) and values determined in the algorithm for μ_b, the shear-wave velocity, V_s, is calculated for oil- or gas-saturated rocks, or partially-saturated rocks, as a function of depth or porosity for a given water saturation, and as a function of water saturation for a given porosity.

(d) The ratio of compressional-wave velocity to shear-wave velocity (V_p/V_s) is calculated as a function of depth and/or water saturation by using the results from (b) and (c). This parameter is a useful indicator of subsurface lithology and foundation conditions (Tatham and Stoffa, 1976; Tatham, 1982; Benson, 1991).

(e) Using results from (b) and (c), compressional and shear-wave impedances and reflection coefficients are estimated from equation (7) as a function of depth and/or water saturation for interfaces, such as the following: (1) gas-saturated rock over oil-saturated rock; (2) oil-saturated rock over brine-saturated rock; (3) gas-saturated rock over brine-saturated rock; (4) shale over gas-saturated rock; and (5) shale over oil-saturated rock. Reflection coefficients at these boundaries are indicative of foundation conditions, such as depth to bedrock, fault delineation, fluid contacts, etc.

4. Using the output parameters described in (3) above, the following output data are available from the algorithm:

(a) Tables of velocities, impedances, V_s/V_p ratios, and reflection coefficients can be generated as a function of depth, porosity, and/or water saturation. Tables of densities and compressibilities of pore fluids as a function of depths can also be generated.

(b) Plots of important relationships, such as V_p and V_s vs. water saturation, V_p and V_s vs. porosity, and V_p and V_s vs. depth can be produced. These relationships are the basis for building models to estimate the subsurface geology and lithology.

VELOCITY ESTIMATES FOR IN-SITU CONDITIONS

Our computer algorithm calculates the compressibility and shear modulus of dry reservoir rocks. Using this data, it calculates the velocities, V_p/V_s ratios, and reflection coefficients for both sandstone and limestone reservoir rocks saturated with different amounts and types of fluid. As an example, consider Gulf Coast sandstones and take brine-saturated compressional-wave velocities and porosities as a function of depth (Gregory, 1976,1977) as the input into our algorithm to generate the compressibilities and shear moduli of empty reservoir rocks.

Estimates of the bulk modulus and shear modulus computed by our algorithm as a function of depth for average Gulf Coast sandstones are shown in Figure 1. The moduli increase nonlinearly as the depth increases, with the shear modulus curve slightly above the bulk modulus curve. The moduli appear to be an exponential-type function of porosity at depths below 1700 m, and quasi-linear functions of porosity at depths above 1700 m.

Velocities as a function of depth or porosity

Using the values of the moduli shown in Figure 1, compressional- and shear-wave

velocities are calculated for a variety of reservoir conditions. Figure 2 shows the calculated results as a function of depth for average Gulf Coast sandstones. As expected, the compressional-wave velocities in brine-saturated rocks are higher than in oil-saturated rocks, and the velocities in gas-saturated rocks are the lowest. However, for the case of shear waves, the gas-saturated rocks have the highest velocities and the brine-saturated rocks have the lowest velocities.

Velocity as a function of brine saturation

Compressional-wave and shear-wave velocities as a function of changing brine saturation are plotted in Figure 3 for average Gulf Coast sandstones. The compressional-wave velocities in rocks containing oil and brine increase monotonically from zero brine saturation to 100% brine saturation (at each porosity), and the total change decreases as the porosity decreases. In contrast, when these rocks contain gas and brine, compressional-wave velocities decrease as brine saturation increases from zero to around 70% - 80%, and then increase up to the compressional velocity of a 100% brine-saturated rock. The largest change occurs as the last 5 to 10 percent of the pore space is filled with brine. The brine-saturation value at which the velocity starts to rise depends upon the porosity of the reservoir rock. For lower porosities, this transition occurs at a lower saturation because the fluid effects are smaller in lower porosity rocks.

According to equation (8.1), as brine saturation increases, the compressional-wave velocity decreases with increasing bulk density and increases with decreasing fluid compressibility. For an oil-brine saturated rock, as the brine percentage increases, the decrease in velocity caused by increasing bulk density is more than compensated for by the increase in velocity due to decreasing fluid compressibility. In contrast, for a gas-brine saturated rock, the decrease in velocity caused by the very high compressibility of gas compared to that of brine is the dominating factor until the brine saturation reaches a transition point where the increasing density becomes the dominant factor. At this point, the compressional-wave velocity rises dramatically.

The shear-wave velocities (Figure 3b) decrease with increasing brine saturation for both partially oil-saturated and partially gas-saturated rocks, with the largest changes occurring for the sands containing gas. Since the bulk shear modulus of the reservoir rock remains unchanged (Gassmann, 1951), this is primarily due to the effect of the increasing fluid density as brine saturation increases. As can be seen from Figure 3, as the brine saturation increases, the changes in the compressional-wave velocity are much larger than in the shear-wave velocities. Thus, V_p/V_s ratios may be useful indicators of the fluid content in porous, sedimentary rocks.

Significance of V_p/V_s ratio

The ratio of compressional-wave velocity to shear-wave velocity is plotted in Figure 4 as a function of depth for sandstones. For average Gulf Coast sandstones, gas-saturated rocks have the lowest (nearly constant) V_p/V_s ratio of about 1.5. The curves for oil- and brine-saturated sandstones have similar shapes, with the V_p/V_s ratios of brine sands about 0.05 higher than those for oil sands. The V_p/V_s ratios of brine- and oil-sands decrease rapidly as depth increases (or porosity decreases), after which both gradually decrease. The

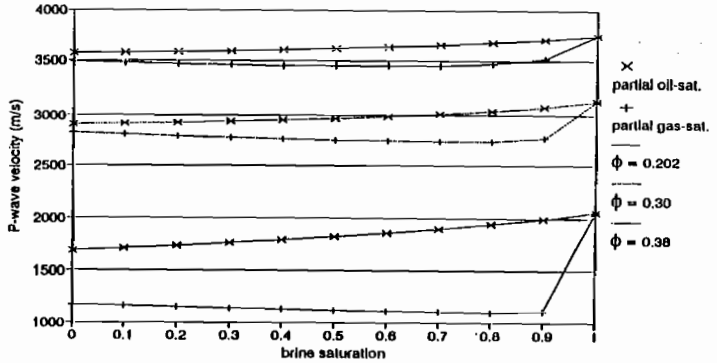

Figure 3a. Predicted P-wave velocities as a function of water saturation for average Gulf Coast sandstones with porosity ranging from 0.202 to 0.38, and changing partial saturations of gas, oil, and water. All input parameters are the same as those used in Figure 2.

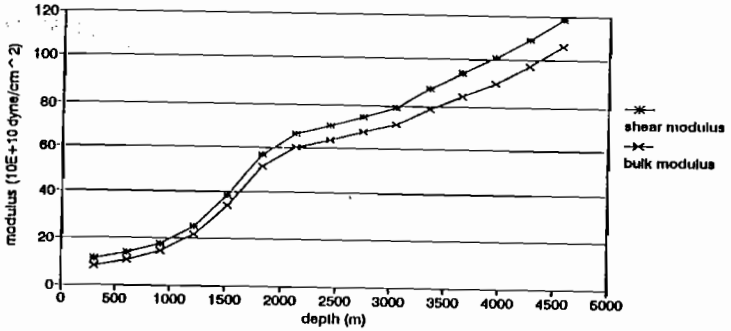

Figure 1. Using our inversion equation (8.1), the bulk and shear moduli of the empty reservoir rock as a function of depth are generated for average Gulf Coast sandstones. The matrix parameters are in Table 1. The brine parameters are determined using equations (16.1) through (17.2) adapted from Batzle and Wang (1992). The brine-saturated P-wave velocities for average Gulf Coast sandstones used as input into our algorithm are from well log data compiled by Gregory (1976, 1977).

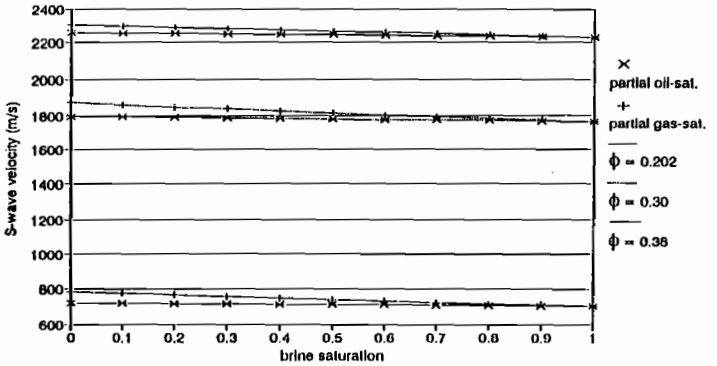

Figure 3b. Predicted S-wave velocities as a function of water saturation for average Gulf Coast sandstones with porosity ranging from 0.202 to 0.38, and changing partial saturations of gas, oil, and water. All input parameters are the same as those used in Figure 2.

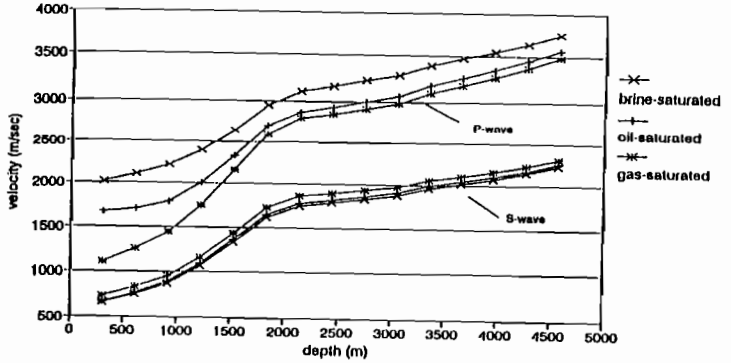

Figure 2. Predicted P-wave and S-wave velocities as a function of depth for average Gulf Coast sandstones saturated with oil or gas. The fluid parameters are calculated using equations (10.1) through (17.2) adapted from Batzle and Wang (1992). All other input parameters are the same as those used in Figure 1.

values of V_p/V_s for brine-saturated sandstones with porosities lower than 0.31 are below 1.8 and decrease toward 1.6, or even lower, as porosity decreases, which is in agreement with Pickett's crossplot (1963) for a variety of core samples for Gulf Coast rocks.

V_p/V_s ratios as a function of brine saturation are plotted in Figure 5 for the Gulf coast sandstones. The V_p/V_s ratio of gas-brine reservoir rocks decreases slightly from the V_p/V_s of the pure gas-saturated rocks as brine saturation increases from zero to 90%. As the last 10% of the gas is replaced by brine, V_p/V_s increase abruptly to the values of the pure brine-saturated rocks. The V_p/V_s ratios of oil-brine saturated rocks behave similarly to the compressional-wave velocities of oil-brine saturated rocks as brine saturation increases, with the ratios increasing as brine saturation increases. As the porosity increases, the V_p/V_s ratios become larger than for lower porosity rocks. In summary, it appears that V_p/V_s ratios may help indicate whether a rock is porous or nonporous, what fluids are present, and what kind of rock is in situ, all of which are vital concerns to many engineering and exploration decisions.

Reflection coefficients

Using the velocity and density data from the algorithm, reflection coefficients are calculated for both sandstones and limestones at different fluid-saturated boundaries. For average Gulf Coast sandstones, the results from the algorithm as a function of depth are shown in Figure 6.

For compressional waves, the reflection coefficients at a gas over brine boundary decrease rapidly at shallow depth and then taper off slowly at depths greater than 1700 m. The reflection coefficients at a gas over oil boundary are similar to those at a gas-brine boundary, but this reflection coefficient is somewhat idealized. Since gas would dissolve in oil if the oil were undersaturated, this boundary would not exist until there is enough gas to make the oil become saturated. Figure 7 shows the reflection coefficients at boundaries between (a) a gas and a brine, (b) a gas and a saturated oil, (c) a saturated oil and brine, (d) a shale and a saturated oil, and (e) a shale and a gas. Comparing Figures 6 and 7, it can be seen that the reflection coefficients at a gas, saturated-oil interface decrease more rapidly than those at a gas, undersaturated oil interface as depth increases. Also,the reflection coefficients at a saturated-oil, brine interface are larger than those at a gas, saturated-oil interface at depths greater than about 1700 m.

Using the velocities and porosities as a function of depth for average Gulf Coast shales (Gregory, 1976, 1977), the reflection coefficients for the boundaries between shale overlying a gas-saturated sand and shale overlying an oil-saturated sand are calculated and shown in Figure 6. The values for the reflection coefficients at these boundaries are negative because sound waves travel from higher impedance materials to lower impedance materials. The two curves are similar in shape, but the magnitudes of the reflection coefficients are higher at a shale-gas interface. The "ladle" shape of these curves is probably due to the abrupt change of shale velocities and porosities at shallow depths (Gregory, 1976, 1977).

The velocity and reflection coefficient data from Figures 2 thru 7 should be helpful in building realisitic subsurface models of the geology, aiding in the direct detection of subsurface fluids, imaging seismic data through self-consistent modeling, inverting seismic

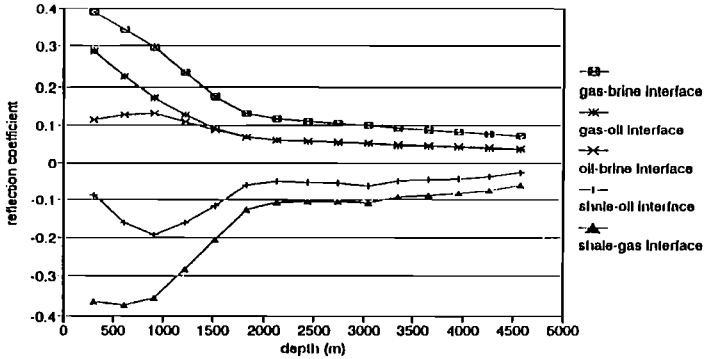

Figure 6a. Predicted P-wave reflection coefficients for different interfaces as a function of depth for average Gulf Coast sandstones saturated with either gas, oil, or water, overlain by water-saturated shales. The velocities and densities of shale are from Gregory (1976, 1977). All other input parameters are the same as those used in Figure 2.

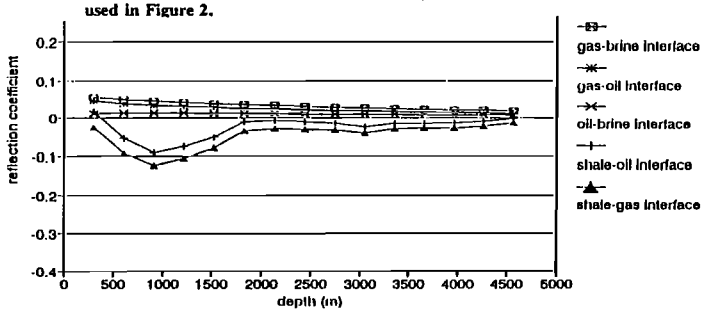

Figure 6b. Predicted S-wave reflection coefficients for different interfaces as a function of depth for average Gulf Coast sandstones saturated with either gas, oil, or water, overlain by water-saturated shales. All input parameters are the same as those used in Figure 6a.

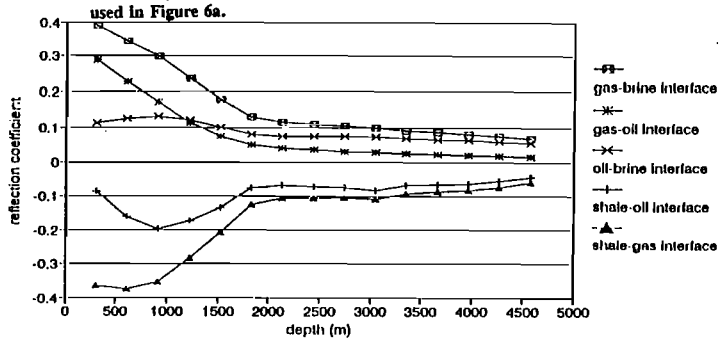

Figure 7. Predicted P-wave reflection coefficients for different interfaces as a function of depth for average Gulf Coast sandstones saturated with either gas, oil, or water, overlain by water-saturated shales. However, in this case, the oil is gas-saturated. All other parameters are the same as those used in Figure 6a.

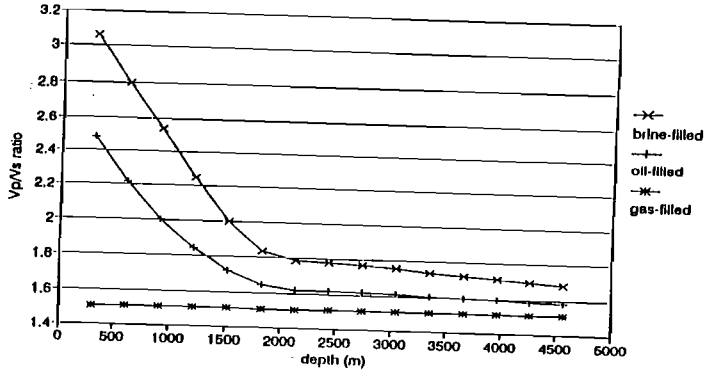

Figure 4. Predicted Vp/Vs ratios versus depth for average Gulf Coast sandstones saturated with either water, oil, or gas. All input fluid and matrix parameters are the same as those used in Figure 2.

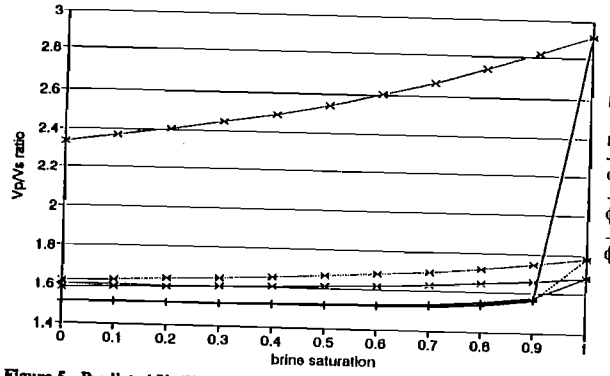

Figure 5. Predicted Vp/Vs ratios as a function of water saturation for average Gulf Coast sandstones with porosity ranging from 0.202 to 0.38, and changing partial saturations of gas, oil, and water. All input parameters are the same as those used in Figure 2.

data to help recover the lithology, and in making corrections to predict the sonic log velocities in the uninvaded formation from those measured in the invaded formation.

CONCLUSIONS

A computer algorithm based upon the BGG equations has been developed to predict the following in-situ parameters:

a. the bulk and shear moduli of dry reservoir rocks based upon available velocity and porosity data for water/brine-saturated rocks. In the past, these values were chosen a priori and input in a forward modeling mode. However, in this algorithm, these parameters are estimated in situ by inverting the BGG equations;
b. compressional- and shear-wave velocities and V_p/V_s ratios for rocks fully or partially saturated with fluids, such as oil and/or gas, and;
c. the reflection coefficients at the interfaces between hydrocarbon-saturated rocks and brine-saturated rocks, or between overlying rocks, such as shales, and fluid-saturated rocks.

The applicability of our algorithm has been tested using laboratory velocity data for water-saturated rocks under controlled conditions. The percentage error between shear velocities predicted by the algorithm and values measured in the laboratory are usually less than 10% for both sandstone and limestone samples, which is typically good enough to accurately image seismic data in depth.

Using the compressional-wave velocities of brine-saturated rocks and the porosities from well logs for average Gulf Coast sandstones, we used our computer algorithm to calculate the bulk and shear moduli, then the compressional and shear velocities, the V_p/V_s ratios, and the reflection coefficients for fully or partially gas- and/or oil-saturated rocks as a function of depth and/or porosity. The predicted bulk and shear moduli of dry rocks decrease linearly with increasing porosities for well-consolidated sandstones and limestones. For high-porosity sandstones, the moduli appear to be an exponential function of porosity. The predicted V_p/V_s ratios are useful for identifying gas-saturated rocks and rock types in-situ, and these ratios may also help indicate whether a rock is consolidated or unconsolidated.

Since the in-situ seismic velocities for porous, multiphase, fully or partially, fluid-saturated rocks as a function of depth, porosity, and brine saturation can be reasonably predicted using our computer algorithm, more accurate seismic modeling and interpretation of the subsurface geology and foundation conditions can be made using seismic and well log data.

REFERENCES

Batzle, M. and Wang, Z., 1992, Seismic properties of pore fluids: Geophysics, v. 57, p. 1396-1408.

Benson, A.K., 1993a, Personal communication.

_____1993b, Determination of depth models through self-consistent structural modeling to help delineate potential hydrocarbon traps: American Association of Petroleum

Geologists Bulletin, in Press.

_____1992a, Depth images of complex geology, such as the overthrust belt, through self-consistent modeling: Geological Society of America Abstracts, Rocky Mountain Section, vol. 24, p. 41.

_____1992b, Determination of depth models through self-consistent modeling to help delineate hydrocarbon traps in the Uinta Basin, Utah: in Mineral and Hydrocarbon Resources of the Uinta Basin, Utah and Colorado, Utah geological Association Guidebook, vol. 20, p. 219-226.

_____1991, Applications of shear, compressional, and V_s/V_p data to evaluate subsurface geology and associated conditions and hazards: Proceedings of the 27th Symposium on Engineering Geology and Geotechnical Engineering, v. 27, 39.1-39.18.

Biot, M.A., 1955, Theory of elasticity and consolidation for a porous anisotropic solid: Journal of Applied Physics, v. 26, p. 182-185.

_____1956, Theory of propagation of elastic waves in a fluid-saturated porous solid, 1. lower frequency range, 2. higher frequency range: Journal of Acoustical Society of America, v. 28, 168-191.

Bird, W.E., 1986, Conoco, Inc., Unpublished data, Personal Communication.

Brandt, H., 1955, A study of the speed of sound in porous granular materials: Journal of Applied Mechanics, v. 22, p. 479-486.

Castagna, J.P., Batzle, M.L., and Eastwood, R.L., 1985, Relationships between compressional-wave and shear-wave velocities in clastic silicate rocks: Geophysics, v. 50, p. 571-581.

Chen, C.T., Chen, L.S., and Millero, F.J., 1978, Speed of sound in NaCl, $MgCl_2$, Na_2So_4, and $MgSO_4$ aqueous solutions as functions of concentration, temperature, and pressure: Journal of Acoustic Society, America, v. 63, p. 1795-1800.

Clark, V.A., 1992, The effect of oil under in-situ conditions on the seismic properties of rocks: Geophysics, v. 57, p.894-901.

Domenico, S. N., 1974, Effect of water saturation on seismic reflectivity of sand reservoir encased in shale: Geophysics, v. 39, p. 759-769.

____1976, Effect of brine-gas mixture on velocity in an unconsolidated sand reservoir: Geophysics, v. 41, p. 882-894.

_____1977, Elastic properties of unconsolidated porous sand reservoirs: Geophysics, v. 42, p. 1339-1368.

_____1984, Rock lithology and porosity determination from shear and compressional wave velocity: Geophysics, v. 49, p. 1188-1195.

Faust, L.Y., 1951, Seismic velocity as a function of depth and geological time: Geophysics, v. 16, p. 192-206.

Gassmann, F., 1951, Elastic waves through a packing of spheres: Geophysics, v. 15, p. 673-685.

Geertsma, J., 1961, Velocity-log interpretation: The effect of rock bulk compressibility: Society Petroleum Engineering Journal, v. 1, p. 235-248.

Geertsma, J., and Smit, D.C., 1961, Some aspects of elastic wave propagation in fluid-saturated porous solids: Geophysics, v. 26, 169-181.

Gregory A. R., 1976, Fluid saturation effects on dynamic elastic properties of sedimentary

rock: Geophysics, v. 41, p.895-921.

_____1977, Aspects of rock physics from Laboratory and log data that are important to seismic interpretation, in Payton, C.E., Ed. Seismic-stratigraphy-application to hydrocarbon exploration: American Association of Petroleum Geologists Memoir 26, p. 15-46.

Humbert, P., and Pheque, F., 1972, "Elastic Constants for Carbonates," Computational Rendus, B275, 391.

Kithas, B.A., 1976, Lithology, gas detection, and rock properties from acoustic logging systems: Society of Professional Well Log Analysts 17th Annual Logging Symposium, R1-R10.

Klimentos, T., 1991, The effects of porosity-permeability-clay content on the velocity of compressional waves: Geophysics, v. 56, p. 1930-1939.

Kowallis, B. J., Jones, L. E. A., and Wang, H. F., 1984, Velocity-porosity-clay content systematics of poorly consolidated sandstone: Journal of Geophysics Research, v. 89, p. 10355-10364.

Mann, R.L., and Fatt, I., 1960, Effect of pore fluids on the elastic properties of sandstone: Geophysics, v. 25, p. 433-443.

Marion, D., Nur, A., Yin, H., and Han, D., 1992, Compressional velocity and porosity in sand-clay mixture: Geophysics, v. 57, p. 554-563.

Murphy, W. F., 1984, Seismic to ultrasonic velocity drift: Intrinsic absorption and dispersion in crystalline rock: Geophysical Research Letters, v. 11, p. 1239-1242.

Murphy, W.F., Reischer, A., and Hsu, K., 1993, Modulus decomposition of compressional and shear velocities in sand bodies: Geophysics, v. 58, p. 227-239.

Pickett, G.R., 1963, Acoustic character log and their application in formation evaluation: Journal of Petroleum Technology, v. 15, p. 659-667.

Potter, R.W., II, and Brown, D.L., 1977, The volumetric properties of sodium chloride solution from 0 to 500°C at pressures up to 2000 bars based on a regression of available data in the literature: U.S. Geological Survey Bulletin 121-C.

Rowe, A.M., and Chou, J.C.S., 1970, Pressure-volume-temperature-concentration relation of aqueous NaCl solutions: Journal of Chemistry Engineering Data, v. 15, p. 61-66.

Simmons, G., 1965, "Elastic Constants Measured in the Laboratory For Various Minerals," Journal of the Graduate Research Center, Southern Methodist University Press, v. 39, 3.

Tatham, R.H., and Stoffa, P.L., 1976, V_s/V_p--potential hydrocarbon indicator: Geophysics, v. 41, p. 837-849.

Tatham, R.H., 1982, V_p/V_s and lithology: Geophysics, v. 47, p.336.

Toksöz, M. N., Cheng, C. H., and Timur, A., 1976, Velocities of seismic waves in porous rocks: Geophysics, v. 41, p. 621-645.

Toksöz, M.N., and Kuster, G.T., 1974, Velocity and attenuation of seismic waves in tow-phase media: Part I. Theoretical formulations: Geophysics, v. 39, p. 587-606.

Winkler, K. W., 1985, Dispersion analysis of velocity and attenuation in Berea sandstone: Journal of Geophysics Research, v. 90, p. 6793-6800.

Wyllie, M.R.J., Gregory, A. R., and Gardner, G. H. F., 1958, An experimental investigation of factors affecting elastic wave velocity in porous media: Geophysics,

v. 23, p. 459-493.
Wyllie, M.R.J., Gregory, A.R., and Gardner, L.W., 1956, Elastic wave velocities in heterogeneous and porous media: Geophysics, v. 21, p. 41-70.
Zarembo, V.I., and Fedorov, M.K., 1975, Density of sodium chloride solution in the temperature range 25-350°C at pressures up to 1000kg/cm^2: Journal of Applied Chemistry USSR, v. 48, p. 1949-1953, (English trans).

CLOSED FORM STRESS ANALYSES OF A SUPPORTED CIRCULAR TUNNEL IN A BIAXIAL STRESS FIELD IN ELASTIC AND LINEAR VISCOELASTIC ROCK MEDIA

by
J Scott Leech, P.E.
U.S. Army Corps of Engineers, Jacksonville, Florida

ABSTRACT

Of major importance to mining and civil engineering applications in rock tunneling is the analysis of underground openings subjected to applied stresses. Of particular practical significance is the circular cross sectional opening subjected to a biaxial stress field. Elastic analysis predictions of rock behavior can provide instantaneous values for deformations and stresses for a constant applied load but do not take into account the time-dependant behavior exhibited by the rock mass under those same loading conditions.

Time-dependant behavior can be described by a stress-relaxation relationship where stress is dependant on a given strain history or by a creep relationship where strain is dependant on a given stress history. A creep relational approach will be used in this presentation.

The phenomenon of "squeezing" or the slow accumulation of load on support systems with time has been well documented in laboratory creep experiments as well as in field observations in boreholes, tunnels and other underground openings. Squeezing may be caused by a number of factors such as localized fracturing, increases in effective stresses due to drainage of openings, swelling due to temperature or by humidity changes. Some rocks are inherently viscoelastic in their stress-strain response. Rocks which exhibit both instananeous and delayed deformation when loaded are referred to as being viscoelastic. Soft rocks such as salt, shales and tar sands exhibit creep behavior at low service loads within the elastic range. Harder rocks such as granite can also exhibit creep behavior but at much higher service loads which induce cracking as the rock transitions from the elastic range into the plastic range. In real life, stresses do not remain constant with time, especially where fracturing is occuring and stresses are redistributed and therefore, probably no rocks are ideally linearly viscoelastic, however, linear viscoelastic theory may be applied at different stress increments to approach problems where stress is subject to redistribution.

INTRODUCTION

The purpose of this investigation is to provide first approximations of stresses and displacements within the rock mass and supports subjected to a biaxial stress field in a linear viscoelastic media. The following paragraphs present a compilation of accepted models used to predict viscoelastic behavior as well as present the techniques used to develop the models. The formulations presented herein will utilize polar coordinates and stress notation as shown in Figure 1. The biaxial stress field is represented by the principal stresses p_1 and p_2 in a state of compression.

ELASTIC SOLUTION OF AN UNLINED CIRCULAR TUNNEL

If the rock surrounding the tunnel is considered massive with widely spaced and tightly closed joints, the rock may then be considered to be a homogeneous isotropic body. In addition, if the applied stresses fall below the elastic limit of the rock, solutions using the theory of elasticity are often used in practice as a tool to evaluate and predict the stress and deformation characteristics of the opening. To simplify the problem at hand, if one considers the circular tunnel as being significantly longer than the dimension of the opening, a state of plane strain can be assumed. In 1898, Kirsch considered the problem of a circular opening subjected to a biaxial stress field and derived the expressions for stress and displacements provided in equations (1) - (5) below:

$$\sigma_r = \frac{p_1+p_2}{2}\left(1-\frac{a^2}{r^2}\right) + \frac{p_1-p_2}{2}\left(1-4\frac{a^2}{r^2}+3\frac{a^4}{r^4}\right)\cos 2\theta \quad \ldots\ldots (1)$$

$$\sigma_\theta = \frac{p_1+p_2}{2}\left(1+\frac{a^2}{r^2}\right) - \frac{p_1-p_2}{2}\left(1+3\frac{a^4}{r^4}\right)\cos 2\theta \quad \ldots\ldots (2)$$

$$\tau_{r\theta} = -\frac{p_1-p_2}{2}\left(1+2\frac{a^2}{r^2}-3\frac{a^4}{r^4}\right)\sin 2\theta \quad \ldots\ldots (3)$$

$$u_r = \frac{p_1+p_2}{4G}\frac{a^2}{r} + \frac{p_1-p_2}{4G}\frac{a^2}{r}\left(4(1-\nu)-\frac{a^2}{r^2}\right)\sin 2\theta \quad \ldots\ldots (4)$$

$$v_\theta = -\frac{p_1-p_2}{4G}\frac{a^2}{r}\left(2(1-2\nu)+\frac{a^2}{r^2}\right)\sin 2\theta \quad \ldots\ldots (5)$$

Derivations of these equations are provided in Obert and Duval (1967) using a real Airy stress function and in Jaeger and Cook (1979) using complex stress functions. It should be stated that the Kirsch solution models an existing opening being subjected to an applied biaxial stress field. In reality, initial displacements within the rock have already occured under the stress field prior to the excavation of the opening. Therefore, the displacements given in equations (4) and (5) are relative displacements of the tunnel after the initial diplacements have taken place.

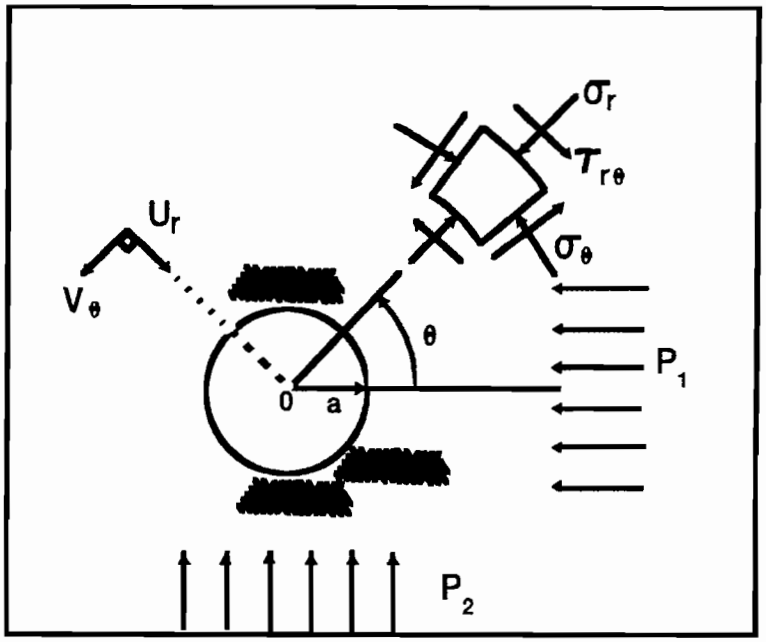

Figure 1. Polar Coordinate Notation

The expressions for these initial displacements for the plane strain problem in the unaltered rock mass are provided in equations (6) and (7):

$$u_{r_i} = \frac{(1-2\nu)(p_1+p_2)r + (p_1-p_2)r\cos 2\theta}{4G} \quad \ldots\ldots (6)$$

$$v_{\theta_i} = -\frac{(p_1-p_2)r\sin 2\theta}{4G} \quad \ldots\ldots (7)$$

Combining equations (4) and (5) with equations (6) and (7), respectively, one can readily obtain the total displacement as presented by Kirsch. The relative displacements, applicable to field measurements, are those contained in equations (4) and (5).

Figure 2. shows the stress distribution of σ_r and σ_θ for p_1/p_2 ratios of one

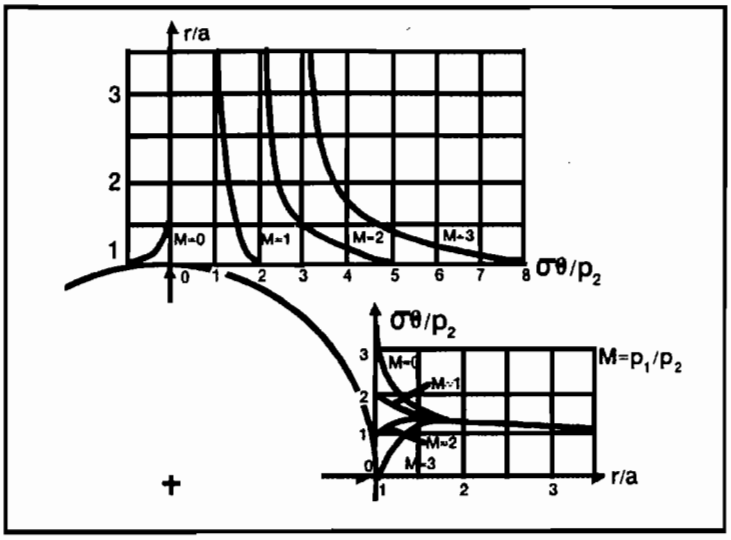

Figure 2. Elastic Principal Stresses

and two at the springline and crown of the tunnel. As can be seen the tangential stresses, σ_θ , are highest at the tunnel surface and diminish rapidly approaching the principal stress values at the springline and crown θ = 0° and θ = 90°) . The radial stresses, however, are zero at the opening face and increase until they too approach the principal stresses of p_1 and p_2 at the springline and crown. It should also be noted that the tangential stress also reaches its maximum of $3p_2 - p_1$ at θ = 90° and a minimum of $3p_1 - p_2$ at θ = 0° as θ is varied.

RHEOLOGIC MODELS FOR A LINEAR VISCOELASTIC MATERIAL

When samples are subjected to creep tests a creep curve similar to that shown in Figure 3. is generated. As indicated, there are three distinct areas or regions labeled as primary, secondary and tertiary creep. In the primary area there is an immediate strain at time equal zero which increases nonlinearly to the threshhold of secondary creep. During the secondary creep stage, the strain increases linearly with time until a critical time where the strain experiences a rapid nonlinear increase in strain rate which ultimately ends in creep rupture. In this area, termed tertiary creep, intact specimens

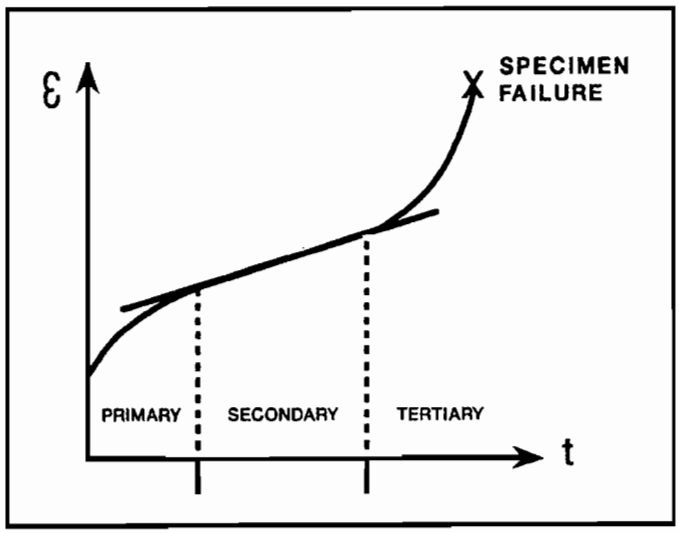

Figure 3. Primary, Secondary and Tertiary Creep

fracture and become plastic. When the rock mass has been allowed to strain within this region, support efforts become extremely difficult if impossible. Therefore it is important to apply support systems as expeditiously as possible to limit accumulation of strain.

It has been observed that the increase of strain with time is highly dependant on the stress level. As seen in Figure 4., rocks subjected to stresses below a critical stress level are stable without support.

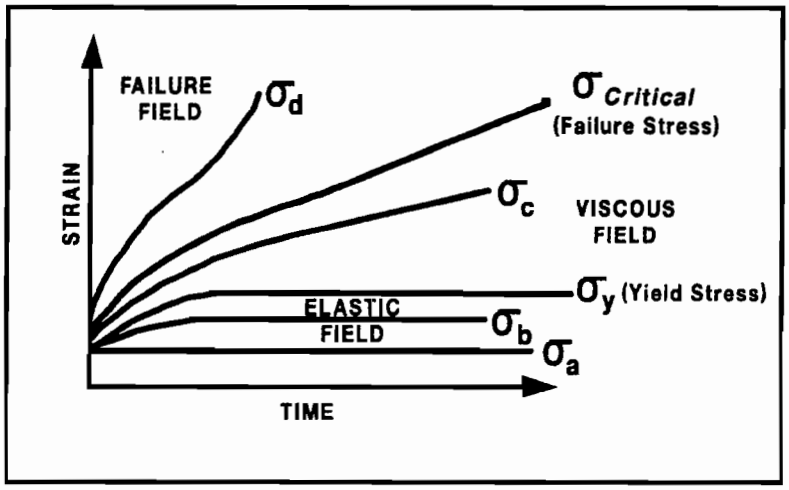

Figure 4. Strain Versus Time Curves at Various Stress Levels

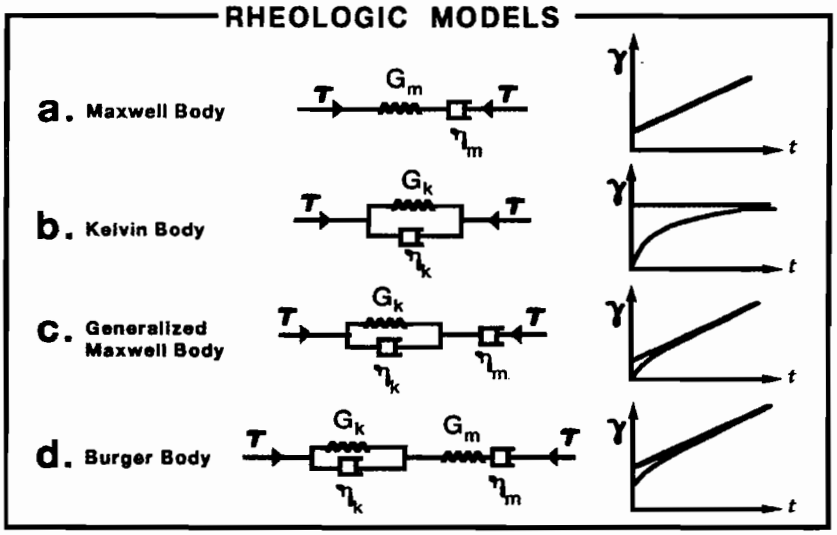

Figure 5. Rheologic Models Used to Predict Creep Behavior

Empirical curve fitting techniques are often used to make creep test data match a power curve, however the use of a rheologic model to predict the creep response mathematically is of greater utility. Several rheologic models have

been developed over the years to model time-dependant behavior of materials. Delayed deformation in rocks or viscoelasticity can be expressed as follows:

$$\tau = \eta \frac{d\gamma}{dt} = \eta\dot{\gamma} \quad \ldots\ldots (8)$$

In the above expression, τ, the shear stress, is proportional to the shear strain rate, $d\gamma/dt$, by a constant dynamic viscosity, η. In rheologic models, η is depicted as a dashpot as shown in Figure 5(a). Elastic or intantaneous deformation can be modeled using the expression

$$\tau = G\gamma \quad \ldots\ldots (9)$$

where the shear stress is proportional to the shear strain by a constant, G, the shear modulus. Instantaneous deformation is modeled using a spring element as shown in Figure 5(a).

Deformational behavior for different materials can be modeled using combinations of such elements either fixed in series or parallel units. Some of the basic model combinations used in this presentation are shown in Figure 5. Of the various models available, the Burger model has been found to be preferable for most purposes for rock. Comparisons made by Alfrouz and Harvey (1974) between various rheologic models and creep test data affirm the superiority of the Burger model over less complex models.

The constants G_k, η_k, G_m and η_m depicted in Figure 5. for the Burger model are determined from the creep test data as described by Goodman (1989). These deformability constants have physical meaning with G_m being the elastic shear modulus, G_k controlling the amount of delayed elasticity, η_k describing the rate of delayed elasticity and η_m describing the rate of viscous flow. Of special interest is the fact that the slope of the asymptote to the strain versus time curve in Figure 5(d). is inversely proportional to η_m and therefore as η_m approaches ∞, the strain becomes constant and the potential for creep rupture is greatly diminished.

LINEAR VISCOELASTIC SOLUTION OF AN UNSUPPORTED CIRCULAR TUNNEL

Solutions for the unsupported circular tunnel displacements in a linear viscoelastic Burger material have been presented by Gnirk and Johnson (1964) for the hydrostatic stress field applicable to shafts and by Goodman (1989) for the biaxial stress field. The following describes the method used in the derivation of the radial deformation as a function of time in a Burger material up to the threshhold of tertiary creep.

Deviatoric and Dilatational Stress and Strain

It is convenient in an isotropic elastic material to divide the state of stress and corresponding strains into two components known as the deviatoric stress (σ_{dev}) and the non-deviatoric (σ_{mean}) or dilatational stress. The dilational stresses are compressive stresses applied equally in each direction or the equivalent of a hydrostatic state of stress applied to the body and is equated as the average of the three principal stresses as follows:

$$\sigma_{mean} = \frac{(\sigma_1+\sigma_2+\sigma_3)}{3} \quad \ldots\ldots (10)$$

The deviator stresses are the normal and shear stresses that remain on the body after the dilatational stresses are subtracted from each total normal stress component

$$\sigma_{dev_i} = \sigma_i - \sigma_{mean} \quad \ldots\ldots (11)$$

There are deviatoric and dilatational strains that corresponded to their respective deviatoric and dilational stresses and are given as follows:

$$e_{mean} = \frac{(e_1+e_2+e_3)}{3} \quad \ldots\ldots (12)$$

$$\epsilon_{dev_i} = \epsilon_i - \epsilon_{mean} \quad (13)$$

The deformational character of rock is such that a body under a dilational state of stress does not in general become distorted. However, under a deviatoric state of stress distortion of the body is produced which may eventually lead to the destruction of the rock. The triaxial test illustrates this principal in that the specimen will not fail under the uniform confining pressure but can fail in shear once a critical deviator stress is applied.

An important property of the shear modulus, G, is that not only does it relate the shear strain to the shear stress but it also relates the deviatoric stress and the deviatoric strain

$$\sigma_{dev_i} = 2G\epsilon_{dev_i} \quad (14)$$

Similarly the dilational strain is related to the dilational stress by the bulk modulus

$$\sigma_{mean} = 3K\epsilon_{mean} \quad (15)$$

where the bulk modulus, K, is related to the elastic modulus, E, and Poisson's ratio, ν, by

$$K = \frac{E}{3(1-2\nu)} \quad (16)$$

Operator Notation

Given the Burger rheological model shown in Figure 5(d)., the constitutive equation relating shear stress and shear strain as a function of time can be readily established.

If the Burger model is subjected to a constant shear stress, τ, the total shear strain, γ, can be described as the summation of the Kelvin model and the spring and dashpot elements of the Maxwell model

$$\gamma = \gamma_G + \gamma_\eta + \gamma_{Kelvin} \quad (17)$$

By differentiating equation (17) with respect to time, it could also be stated that

$$\dot{\gamma} = \dot{\gamma}_G + \dot{\gamma}_\eta + \dot{\gamma}_{Kelvin} \quad (18)$$

It can be further stated after differentiating equation (18) that

$$\ddot{\gamma} = \ddot{\gamma}_G + \ddot{\gamma}_\eta + \ddot{\gamma}_{Kelvin} \quad (19)$$

Using equation (9) with the identity of $\tau = \eta d\gamma/dt$ and inspection of Figure 5(b)., one can deduce the following:

$$\tau(t) = G_m \gamma_G(t) \quad (20)$$

$$\tau(t) = \eta_m \dot{\gamma}_\eta(t) \quad (21)$$

$$\tau(t) = \eta_k \dot{\gamma}_{Kelvin}(t) \quad (22)$$

Differentiating equation (20) and inserting values for $d\gamma_i/dt$ into equation (18), $d\gamma/dt$ becomes

$$\dot{\gamma} = \frac{\dot{\tau}}{G_m} + \frac{\tau}{\eta_m} + \left(\frac{\tau - G_k \gamma_{Kelvin}}{\eta_k} \right) \quad (23)$$

Differentiating equation (23) it follows that

$$\dot{\gamma} = \frac{\dot{\tau}}{G_m} + \frac{\tau}{\eta_m} + \left(\frac{\tau - G_k \dot{\gamma}_{Kelvin}}{\eta_k} \right) \quad (24)$$

Rearranging equation (18) and substituting appropriate values of γ_G and γ_η,

$$\dot{\gamma}_{Kelvin} = \dot{\gamma} - \frac{\dot{\tau}}{G_m} - \frac{\tau}{\eta_m} \quad (25)$$

By substituting equation (25) into equation (24) it follows that

$$\frac{\ddot{\tau}(t)}{G_m} + \left(\frac{G_m}{G_k \eta_m} + \frac{1}{\eta_m} + \frac{1}{\eta_k} \right) \dot{\tau}(t) + \frac{G_k}{2\eta_m \eta_k} \tau(t) = \ddot{\gamma}(t) + \frac{G_k}{\eta_k} \dot{\gamma}(t) \quad (26)$$

Equation (26) is the constitutive equation for a Burger material. Similar constitutive equations for the other models shown in Figure 5. can be established by the same procedure given above. This second order non-homogeneous differential equation can be integrated directly but it is more convenient to evaluate the Burger model seperately as Kelvin and Maxwell models.

Equation (26) can be written in its operational form as

$$P\tau = Q\gamma \quad (27)$$

where **P** and **Q** are linear differential time operators with constant coefficients and are equal to $c_2 d_2/dt^2 + c_1 d/dt + c_0$ and $d^2/dt^2 + d_1 d/dt$ respectively. A detailed discussion of differential operators is contained in Churchhill (1958).

The Correspondence Principle

Under certain conditions, stress analysis of linear viscoelastic bodies can be evaluated using the Laplace transformation technique described by Bland (1960) and Gnirk and Johnson (1964). The technique has been used for the circular loaded shaft in a hydrostatic stress field by Gnirk and Johnson (1964). The conditions are that at all material points, the conditions demanded by the system do not change during load application, a point on the boundary must not change from a point of prescribed traction to one of a prescribed displacement or vice versa and the body shape must not change during loading. With these conditions assumed to be satisfied, one must also assume that the loading is not applied until the tunnel is excavated. The applied loads of interest are only activated after time equals zero and remain constant. In such a case, the limits of integration of the Laplace transform, $t = -\infty$ and $t = +\infty$, are replaced by $t = 0$ and $t = +\infty$.

$$f(s) = \mathcal{L}[f(t)] = \int_0^{+\infty} e^{-st} f(t)\,dt \quad (28)$$

The correspondence principle presented by Bland (1960) states that if Laplace transforms exist for the dependant variables of governing equations and boundary conditions exist for the initially static viscoelastic material, the visocelastic solution can be obtained by replacing the elastic moduli with the corresponding s-varying moduli and inverting the resulting expressions for the transforms of the dependant variables.

Using the Laplace transform technique, elastic moduli such as the shear modulus, G, and Poisson's ratio, ν, become time-dependant. Applied loads become time-dependant through the use of the unit step function commonly known as the Heaviside unit function. This loading case, the most simplistic loading pattern, is applicable to most excavation cases. The Heaviside unit function has the property that it is equal to zero when $t \leq 0$ and equal to one when $t > 0$. Furthermore its Laplace transform is given as:

$$\mathcal{L}[H(t)] = f(s) = \frac{1}{s} \quad (29)$$

Stresses and Displacements in the Biaxial Stress Field

If the tunnel is unlined resulting in zero or constant pressures on the boundaries, the stresses in the Kirsch solution of equations (1) - (3) are applicable for a linear viscoelastic material. However, with time the viscoelastic material will creep or strain and equation (4) needs to be modified to account for the viscoelastic displacement. A state of plane strain is assumed. It is also assumed that the bulk modulus, K, is independent of time.

In practice, the radial displacement of the wall is used to measure tunnel performance. To determine the radial displacement with time, the elastic solution contained in equation (4) must be modified to account for instananeous loading after an at rest condition by multiplying the applied loads p_1 and p_2 by H(t). It is also convenient to eliminate Poisson's ratio from the equation by replacing $1 - \nu$ with the equivalent statement of (3K+4G)/(6K+2G) in equation (4) or

$$u_r = \left(\frac{p_1+p_2}{4G}\frac{a^2}{r}+\frac{p_1-p_2}{4G}\frac{a^2}{r}\left[4\left(\frac{3K+4G}{6K+2G}\right)-\frac{a^2}{r^2}\right]\cos 2\theta\right)H(t) \quad (30)$$

By the correspondence principle, we must now find G and H(t) as a function of the variable s using the Laplace transform.

To evaluate G(s) it is convenient to consider the Burger model as a combination of the Maxwell model and the Kelvin model or in terms of their respective radial strains

$$\epsilon_{Burger} = \epsilon_{Maxwell} + \epsilon_{Kelvin} \quad (31)$$

And since the radial strain is the differential of the radial displacement, it could also be stated that

$$u_{r\ Burger} = u_{r\ Maxwell} + u_{r\ Kelvin} \quad (32)$$

Time-Dependant Shear Modulus of a Kelvin Body

The relationship for the Kelvin body shown in Figure 5(b). can be described by

$$\tau = \left(\eta_k\frac{d}{dt}+G_k\right)\gamma \quad (33)$$

Comparing equations (9) and (33) results in

$$G = \frac{Q(t)}{P(t)} = \frac{\tau}{\gamma} = \left(\eta_k\frac{d}{dt}+G_k\right) \quad (34)$$

where **P(t)** =1 and **Q(t)** = $n_k d/dt + G_k$ or **Q(t)** = G(t). Taking the Laplace transform of **Q(t)**, G(s) is determined as follows:

$$G(s) = \mathcal{L}[Q] = \eta_k\int_0^\infty\frac{de^{-st}}{dt}dt+G_k\int_0^\infty e^{-st}dt = \eta_k s+G_k \quad (35)$$

Substituting equations (35) and (29) into equation (30) becomes

$$u_{r\ Kelvin} = \left[\frac{A}{\eta_k s+G_k}+\frac{B}{4(\eta_k s+G_k)}\left(4\left[\frac{3K+4(\eta_k s+G_k)}{6K+2(\eta_k s+G_k)}\right]-\frac{a^2}{r^2}\right)\right]\frac{1}{s} \quad (36)$$

where $A = \frac{p_1+p_2}{4}\frac{a^2}{r}$, $B = \frac{p_1-p_2}{4}\frac{a^2}{r}\cos 2\theta$, $C = \frac{p_1-p_2}{4}\frac{a^4}{r^3}\cos 2\theta$.

Equation (36) has three terms as functions of s that must be evaluated using the method of partial fractions. Term 1 is defined as follows excluding the constant A:

$$f_1(s) = \frac{1}{s(\eta_k s+G_k)} = \frac{A_1}{s}+\frac{B_1}{\eta_k\left(s+\frac{G_k}{\eta_k}\right)} \quad (37)$$

Solving for the constants A_1 and B_1, we find $A_1 = 1/G_1$ and $B_1 = -n_1/G_1$. To find

$f_1(s)$ as a function of time, we take the inverse Laplace transform of equation (37) using the standard inverse Laplace transforms given as

$$\mathcal{L}^{-1}\left[\frac{1}{s}\right] = 1,\ \mathcal{L}^{-1}\left[\frac{1}{(s-a)}\right] = e^{at},\ \mathcal{L}^{-1}\left[\frac{1}{s^2}\right] = t \quad \ldots\ldots(38)$$

Applying the inverse Laplace transform, equation (37) becomes

$$\mathcal{L}^{-1}[f_1(s)] = \mathcal{L}^{-1}\left[\frac{1}{G_k s}\right] + \mathcal{L}^{-1}\left[-\frac{1}{G_k\left(s+\frac{G_k}{\eta_k}\right)}\right] = \left[\frac{1}{G_k} - \frac{1}{G_k}e^{-\frac{G_k}{\eta_k}t}\right] \quad \ldots\ldots(39)$$

Multiplying the result of equation (39) by the constant A, term 1 is given as

$$A\mathcal{L}^{-1}[f_1(s)] = A\left[\frac{1}{G_k} - \frac{1}{G_k}e^{-\frac{G_k}{\eta_k}t}\right] \quad \ldots\ldots(40)$$

Using the same process we define term 2, excluding the constant B as

$$f_2(s) = \frac{3K+4(\eta_k s+G_k)}{2\eta_k^2\left(s+\frac{G_k}{\eta_k}\right)\left(s+3\frac{K}{\eta_k}+\frac{G_k}{\eta_k}\right)s} \quad \ldots\ldots(41)$$

Using the method of partial fractions as before, $f_2(s)$ becomes

$$f_2(s) = \frac{-\left(1+\frac{G_k}{3}K\right)\left(\frac{3K+4G_k}{6KG_k+2G_k^2}\right)+\frac{2}{3K}}{\left(s+\frac{G_k}{\eta_k}\right)} + \frac{\frac{1}{3K}\left(\frac{3K+4G_k}{6K+2G_k}\right)-\frac{2}{3K}}{\left(s+\frac{3K}{\eta_k}+\frac{G_k}{\eta_k}\right)} + \frac{\left(\frac{3K+4G_k}{6KG_k+2G_k^2}\right)}{s} \quad \ldots\ldots(42)$$

Applying the inverse transforms of equation (38) to equation (42) and multiplying the result by the constant B, we obtain

$$B\mathcal{L}^{-1}[f_2(s)] = B\left[\begin{array}{l}\left(-\left(1+\frac{G_k}{3K}\right)\left(\frac{3K+4G_k}{6KG_k+2G_k^2}\right)+\frac{2}{2K}\right)e^{-\frac{G_k}{\eta_k}t} \\ +\left(\frac{1}{3K}\left(\frac{3K+4G_k}{6K+2G_k}\right)-\frac{2}{3K}\right)e^{-\left(\frac{3K+G_k}{\eta_k}\right)t}+\frac{3K+4G_k}{6KG_k+2G_k^2}\end{array}\right] \quad \ldots\ldots(43)$$

Using the same process as used in term 1, term 3 is determined as follows:

$$-C\mathcal{L}^{-1}[f_3(s)] = -C\left(\frac{1}{G_k} - \frac{1}{G_k}e^{-\frac{G_k}{\eta_k}t}\right) \quad \ldots\ldots(44)$$

Time-Dependant Shear Modulus of a Maxwell Body

By inspection of Figure 5(a)., the shear stress-strain relationship for the Maxwell body is given as

$$\left(\frac{1}{\eta_m}+\frac{1}{G_m}\frac{d}{dt}\right)\tau = \frac{d}{dt}\gamma \quad \ldots\ldots(45)$$

where **P(t)** = $1/n_2 + 1/G_2 * d/dt$ and **Q(t)** = d/dt. Comparing equation (9) with equation (45) and applying the Laplace transform to **P(t)** and **Q(t)** as done on the Kelvin model, we find that

$$G(s) = \frac{\mathcal{L}[Q(t)]}{\mathcal{L}[P(t)]} = \frac{s}{\frac{1}{\eta_m}+\frac{s}{G_m}} = \frac{s\eta_m G_m}{G_m+\eta_m s} \quad \ldots\ldots(46)$$

Substituting the values of G(s) and $\mathcal{L}\{H(t)\}$ into equation (30) as before, there result three terms as a funtion of s. Using the same process as determining the three terms using the method of partial fractions and inverting the terms in s to t using the inverse Laplace transform, the three Maxwell body terms are

$$A\mathcal{L}^{-1}[f_1(s)] = \frac{At}{\eta_m}+\frac{A}{G_m} = A\left[\frac{t}{\eta_m}+\frac{1}{G_m}\right] \quad (47)$$

$$B\mathcal{L}^{-1}[f_2(s)] = B\left[\frac{K+G_m}{2G_mK}-\frac{G_m}{K(6K+2G_m)}e^{-\left(\frac{3KG_m}{3K\eta_m+G_m\eta_m}\right)t}+\frac{t}{2\eta_m}\right] \quad (48)$$

$$-C\mathcal{L}^{-1}[f_3(s)] = -C\left[\frac{t}{\eta_m}+\frac{1}{G_m}\right] \quad (49)$$

There are now the three terms from the Kelvin body whose sum gives the displacement from the Kelvin model which can be added to the three terms from the Maxwell body to give the total radial displacement of the Burger body. Adding equations (40), (43), (44), (47), (48) and (49), we find

$$u_{r\ Burger} = \left[(A-C)\left(\frac{G_k+G_m}{G_kG_m}\right)+B\left(\frac{3K+4G_k}{6KG_k+2G_k^2}+\frac{K+G_m}{2G_mK}\right)\right]$$

$$+\left(\frac{C-A}{G_k}-B\left[\left(1+\frac{G_k}{3K}\right)\left(\frac{3K+4G_k}{6KG_k+2G_k^2}\right)-\frac{2}{3K}\right]\right)e^{-\frac{G_k}{\eta_k}t}$$

$$+B\left[\left(\frac{1}{3K}\left(\frac{3K+4G_k}{6K+2G_k}\right)-\frac{2}{3K}\right)e^{-\left(\frac{3K+G_k}{\eta_k}\right)t}-\frac{G_m}{K(6K+2G_m)}e^{-\left(\frac{3KG_m}{3K\eta_m+G_m\eta_m}\right)t}\right]$$

$$+\left(A+\frac{B}{2}-C\right)\frac{t}{\eta_m} \quad (50)$$

ROCK BOLT SUPPORT IN ELASTIC AND LINEAR VISCOELASTIC MEDIA

The displacement of the tunnel wall described by equation (50) can be counteracted with the use of rock bolts. Goodman (1989) uses the displacement predicted by the pressure of the dilatometer test in a Burger body to approximate the benefit of rock bolts.

The relative displacement of the tunnel after application of the rock support pressure of p_b can be determined by superimposing on the displacements predicted by equation (50) the displacements predicted by equation (51).

$$u_r(t) = \frac{p_ba^2}{2G_mr}+\frac{p_ba^2}{2G_kr}-\frac{p_ba^2}{2G_kr}e^{-\frac{G_k}{\eta_k}t}+\frac{p_ba^2}{2\eta_mr}t \quad (51)$$

In prereinforcement applications, such as with untensioned fully grouted spiling, the tension induced on the rock bolts by radial deformation must be resisted by the shear strength of the bond between the bolt and grout. A detailed discussion of field modeling and model studies of spiling reinforcement is given by Korbin and Brekke (1976) and Korbin and Brekke (1977). If we assume that the reinforcing member is insufficiently stiff to reduce the displacements of the tunnel, the shear stress distribution can be estimated as follows. Taking an infintesimal section of a grouted rock bolt as shown in Figure 6., one could write the summation of forces in the +x direction as

$$(\sigma_x+d\sigma_x)\pi b^2+2\pi b\tau_x dx = \pi b^2\sigma_x$$

rearranging $\frac{d\sigma_x}{dx} = -2\frac{\tau_x}{bE_s}$ ..... (52)

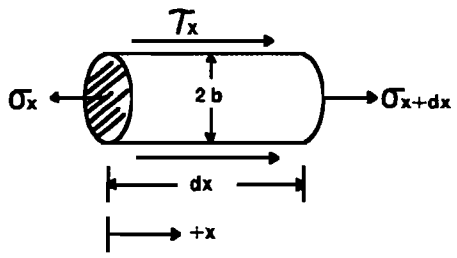

Figure 6. Infintesimal Bolt Section

For the bolt steel, the stress and strain are related by

$$\sigma_x = E_s\epsilon_x \quad \text{..... (53)}$$

Differentiating equation (53) and substituting $d\sigma_x/dx$ into equation (52), we obtain

$$\tau_x = -\frac{bE_s}{2}\frac{d\epsilon_x}{dx} \quad \text{..... (54)}$$

Assuming the strains are compatible in the viscoelastic medium, ϵ_x must be equal to ϵ_r where

$$\epsilon_r = \frac{-\partial u_r}{\partial_r} \quad \text{..... (55)}$$

One could also deduce that $d\epsilon_x/dx = \partial\epsilon_r/\partial r$ and therefore equation (54) becomes

$$\tau_x = -\frac{bE_s}{2}\frac{\partial\epsilon_r}{\partial r} \quad \text{..... (56)}$$

Differentiating equation (50) twice and substituting $-\partial\epsilon_r/\partial r$ into equation (56) we obtain

$$\tau_x = \frac{bE_s}{r^2}\left[(A-6C)\left(\frac{G_k+G_m}{G_kG_m}\right)+B\left(\frac{3K+4G_k}{6KG_k+2G_k^2}+\frac{K+G_m}{2G_mK}\right)\right]$$

$$+b\frac{E_s}{r^2}\left(\frac{6C-A}{G_k}-B\left[\left(1+\frac{G_k}{3K}\right)\left(\frac{3K+4G_k}{6KG_k+2G_k^2}\right)-\frac{2}{3K}\right]\right)e^{-\frac{G_k}{\eta_k}t}$$

$$+Bb\frac{E_s}{r^2}\left[\left(\frac{1}{3K}\left(\frac{3K+4G_k}{6K+2G_k}\right)-\frac{2}{3K}\right)e^{-\left(\frac{3K+G_k}{\eta_k}\right)t}-\frac{G_m}{K(6K+2G_m)}e^{-\left(\frac{3KG_m}{3K\eta_m+G_m\eta_m}\right)t}\right]$$

$$+b\frac{E_s}{r^2}\left(A+\frac{B}{2}-6C\right)\frac{t}{\eta_m} \quad \text{..... (57)}$$

The shear stress distribution predicted by equation (57) is not valid as long as there is significant plastic deformation taking place in which bonding is lost. Loss of bond proceeds from the wall where initially the shear stress

is maximum and migrates toward the anchor as stresses approach the anchor. Korbin (1979) describes the degradation of bond as load is transferred to the bolts. The shear stresses predicted by equation (57) in a linear viscoelastic medium compare favorably with the elastic case stress distributions of the hydrostatic load case presented by Korbin (1979) when time is at zero.

The bolt tensile stress can be estimated by taking the relative displacement between the head and anchor at each time step and dividing by the bolt length to determine the strain. The tensile stress is then the strain times the elastic modulus of the steel.

In the case of tensioned bolts, the shear stress distribution could be roughly approximated by differentiating equation (51) twice with respect to r and make successive substitutions into equations (55) and (56) to determine the shear stress contribution of the tensioning load. This shear stress would be subtracted from that determined by equation (57) to provide the net shear stress distribution on the bolt.

CONCRETE LINER SUPPORT IN A LINEAR VISCOELASTIC MEDIA

By the time a stiff concrete liner is placed against the tunnel wall, the instantaneous elastic displacement has taken place. It is therefore considered sufficient to consider the viscoelastic properties can be described as an incompressible ($\nu = 0.5$ and $K = \infty$) generalized Maxwell body shown in Figure 5(c). Furthermore the liner has a constrained boundary condition which negates the application of the Kirsch solution to determine the stresses.

Gnirk and Johnson (1964) presented the linear viscoelastic solution for a concrete lined shaft in a Burger material under the special case of hydrostatic loading or $p_0 = p_1 = p_2$. Goodman (1989) has presented the same solution in terms of the shear modulus, G, instead of the elastic modulus, E. In this special case of the biaxial stress field, the time-dependant constants of G_k, η_k and η_m describe the properties of the rock and the constants G_ℓ and ν_ℓ describe the properties of the liner. Considering a lined rock tunnel with an internal radius, a, and the liner-rock interface radius of b, the pressure developed at the interface is given as

$$p_b = p_0\left(1+C_1e^{r_1t}+D_1e^{r_2t}\right) \quad (58)$$

where C_1 and D_1 are given as

$$C_1 = \frac{\eta_m r_2}{G_k}\left(\frac{r_1(1+\eta_k/\eta_m)+G_k/\eta_m}{(r_1-r_2)}\right) \quad (59)$$

$$D_1 = \frac{\eta_m r_1}{G_k}\left(\frac{r_2(1+\eta_k/\eta_m)+G_k/\eta_m}{(r_2-r_1)}\right) \quad (60)$$

with r_1 and r_2 being the real roots of

$$\eta_k B_1 s^2+\left[G_k B_1+\left(1+\frac{\eta_k}{\eta_m}\right)\right]s+\frac{G_k}{\eta_m} = 0 \quad (61)$$

with B_1 being

$$B_1 = \frac{1}{G_1}\left(\frac{(1-2\nu_1)b^2+a^2}{b^2-a^2}\right) \quad (62)$$

For $a \le r \le b$, the stresses and displacements in the liner are

$$\sigma_r = p_b\frac{b^2}{b^2-a^2}\left(1-\frac{a^2}{r^2}\right) \quad (63)$$

$$\sigma_\theta = p_b\frac{b^2}{b^2-a^2}\left(1+\frac{a^2}{r^2}\right) \quad (64)$$

$$u_r = -\frac{b^2 r p_b (1-2\nu_1+a^2/r^2)}{2G_1(b^2-a^2)} \quad \ldots\ldots(65)$$

and for $r \geq b$, the stresses and displacements in the rock mass are

$$\sigma_r = p_0\left(1-\frac{b^2}{r^2}\right)+p_b\frac{b^2}{r^2} \quad \ldots\ldots(66)$$

$$\sigma_\theta = p_0\left(1+\frac{b^2}{r^2}\right)-p_b\frac{b^2}{r^2} \quad \ldots\ldots(67)$$

$$u_r = -\frac{b^2}{r}p_b\left(\frac{(1-2\nu_1)b^2+a^2}{2G_1(b^2-a^2)}\right) \quad \ldots\ldots(68)$$

In general terms the liner is considered stiff and the elastic constants remain constant with time. The liner reduces radial deformation over the unlined case. As the rock mass strains with time, radial stresses increase gradually on the rock side of the rock-liner interface at r=b, whereas the tangential stresses decreases. As time progresses, the radial and tangential stresses increase within the liner as load is transferred to the concrete. Eventually, if strain is not checked, the tangential stresses will approach the compressive strength of the liner and cracking will occur. Collapsible supports or wood chocks are useful in such cases to allow the rock to carry more of the load with minor straining to keep stresses below the concrete compressive strength.

For an unlined tunnel, the generalized maxwell body radial displacement is derived using the same procedure as used for equation (50) and given as

$$u_r = \left(A+\frac{B}{4}\left(2-\frac{a^2}{r^2}\right)\right)\frac{t}{\eta_m}+\left(\frac{A}{G_k}+\frac{B}{4G_k}\left(2-\frac{a^2}{r^2}\right)\right)\left[1-e-\frac{G_k}{\eta_k}t\right] \quad \ldots\ldots(69)$$

where the variables A and B are as previously defined in equation (36).

COMPUTER PROGRAM "SQEZBRGR"

Included in this presentation is the computer code listing for the GW-BASIC, MS-DOS based computer program called "SQEZBRGR". The program is self guiding and provides on-screen and printed report. The program has three options which include that for the unlined circular tunnel, concrete lined tunnel and the rock bolted unlined tunnel. The unlined option utilizes equation (50) to compute the radial displacement as a function of time in a Burger type material. The lined option provides the stresses and radial displacements in the liner and rock mass as described by equations (63)-(68). The rock bolt option provides the relative radial displacement by superimposing the Burger radial displacements, equation (50), with the displacements predicted by equation (51). This option also presents the shear stress distribution along the bolt as given by equation (57) including the benefit of tensioning where $p_b > 0$. The standard time intervals provided in the program are at 0 minutes, 20 minutes, 1 hour, 12 hours, 1 day, 2 days, 4 days, 1 week, 2 weeks, 4 weeks, 1 year and 10 years including user specified time. The program is activated by typing in "BASICA" after the DOS prompt and then LOAD "SQEZBRGR" while in GW-BASIC.

```
10 CLS
20 DIM T0(13), U3(13),U4(13),U5(13),P9(13),S4(13),S1(13),S2(13),S3(13)
30 DIM U7(13),U8(13),T4(13)
40 PRINT" PROGRAM >SQUEEZEBURGER< - CIRCULAR TUNNEL ANALYSIS IN BIAXIAL STRESS"
50 PRINT" FIELD IN A LINEAR VISCOELASTIC ROCK MEDIUM"
60 PRINT" J SCOTT LEECH, PE, 2/16/95"
70 PRINT "*****************************************************************"
80 PRINT "*  NO LIABILITY FOR WARRANTIES EXPRESSED OR IMPLIED, CONCERNING  *"
90 PRINT "*  COMPUTER PROGRAM ARE MADE OR ASSUMED BY THE AUTHOR OR THE U.S.*"
100 PRINT "* GOVERNMENT. THE USER IS ASSUMED TO BE FULLY RESPONSIBLE FOR ANY*"
```

```
110 PRINT "* CONCLUSIONS OR RESULTS DRAWN FROM ITS USE.                    *"
120 PRINT "*****************************************************************"
130 PRINT
140 INPUT"TYPE Y IF YOU UNDERSTAND THIS DISCLAIMER";W$
150 IF W$<>"Y" THEN 1380
160 PRINT
170 INPUT" ENTER OPTION: 1=UNLINED TUNNEL, 2=LINED TUNNEL, 3=BOLTED TUNNEL";O1
180 IF O1=2 THEN 230
190 INPUT"ENTER ROCK BOLT SUPPORT PRESSURE, pb (PSI)"; P5
200 INPUT"ENTER BOLT RADIUS (IN)";R2
210 INPUT"ENTER BOLT STEEL ELASTIC MODULUS";E1
220 GOTO 260
230 INPUT"ENTER LINER THICKNESS (IN)";T8
240 INPUT"ENTER ELASTIC MODULUS OF CONCRETE, Ec (PSI)"; E0
250 INPUT"ENTER POISSON'S RATIO OF CONCRETE";V0
260 INPUT"ENTER KELVIN VISCOSITY, nk (PSI-MIN)";N1
270 INPUT"ENTER MAXWELL VISCOSITY,nm (PSI-MIN)";N2
280 INPUT"ENTER P1 AND P2 (PSI,PSI)";P1,P2
290 INPUT"ENTER KELVIN SHEAR MODULUS Gk (PSI)";G1
300 INPUT"ENTER MAXWELL SHEAR MODULUS Gm (PSI)";G2
310 INPUT"ENTER TUNNEL RADIUS (FT)";A1
320 A1=A1*12
330 INPUT "ENTER POSITION RADIUS AND ANGLE FROM HORIZ. (FT, DEG)";R0,T9
340 R0=R0*12
350 T9=T9*3.141592654#/180
360 A0=(P1+P2)*A1^2/R0/4
370 B0=(P1-P2)*A1^2*COS(2*T9)/R0
380 C0=(P1-P2)*A1^4*COS(2*T9)/R0^3/4
390 T0(1)=0:T0(2)=20:T0(3)=60:T0(4)=720:T0(5)=1440:T0(6)=2880:T0(7)=5760
400 T0(8)=10080:T0(9)=20160:T0(10)=80640!:T0(11)=525600!:T0(12)=5256000!
410 INPUT"ENTER SPECIFIC TIME IN MINUTES";T0(13)
420 IF O1=2 THEN 740
430 INPUT"BULK MODULUS,K (PSI)";K1
440 B1=(3*K1+G1)/3/K1
450 B2=((3*K1)+(4*G1))/((6*K1)+(2*G1))
460 B3=2/K1/3
470 B4=(3*K1+G1)/N1
480 B5=(K1+G2)/2/G2/K1
490 B6=G2/K1/((6*K1)+(2*G2))
500 B7=3*K1*G2/((3*K1*N2)+(G2*N2))
510 B8=1/(2*N2)
520 Z$="BURGER BODY Ur(t) IN UNLINED TUNNEL"
530 IF O1=1 THEN 550
540 Z$="BURGER BODY Ur(t) IN ROCK BOLTED TUNNEL"
550 FOR I = 1 TO 13
560 C1=(1-EXP(-G1*T0(I)/N1))/G1
570 A2=(T0(I)/N2)+(1/G2)
580 A3=(1-EXP(-G1*T0(I)/N1))/G1
590 C2=(T0(I)/N2)+(1/G2)
600 U0=A0*(A2+A3)
610 U1=U0+B0*((-B1*B2/G1+B3)*EXP(-G1*T0(I)/N1)+((1/3/K1)*B2-B3)*
EXP(-B4*T0(I))+B2/G1)
620 U2=U1+B0*(B5-B6*EXP(-B7*T0(I))+B8*T0(I))
630 U3(I)=U2-C0*(C1+C2)
640 IF O1=1 THEN P5=0
650 U7(I)=P5*A1^2*((1/G2)+(1/G1)-(EXP(-G1*T0(I)/N1)/G1)+(T0(I)/N2))/2/R0
660 U8(I)=U3(I)-U7(I)
670 T1=A0*(A2+A3)
680T2=T1+B0*((-B1*B2/G1+B3)*EXP(-G1*T0(I)/N1)+((1/3/K1)*B2-B3)*
EXP(-B4*T0(I))+B2/G1)
690 T3=T2+B0*(B5-B6*EXP(-B7*T0(I))+B8*T0(I))
700 T4(I)=(T3-6*C0*(C1+C2)-U7(I))*R2*E1/R0^2
710 NEXT I
720 GOTO 970
```

```
730 IF O1<>2 THEN 970
740 Z$="Ur AND STRESSES IN A GENERALIZED INCOMPRESSIBLE MAXWELL BODY W/ LINER"
750 B9=T8+A1
760 P0=(P1+P2)/2
770 FOR I = 1 TO 13
780 G0=E0/2/(1+V0)
790 B1=((1-2*V0)*B9^2 + A1^2)/(B9^2-A1^2)/G0
800 R8=(-(G1*B1+1+N1/N2)+SQR((G1*B1+1+N1/N2)^2-(4*N1*B1*G1/N2)))/2/N1/B1
810 R9=(-(G1*B1+1+N1/N2)-SQR((G1*B1+1+N1/N2)^2-(4*N1*B1*G1/N2)))/2/N1/B1
820 C1=N2*R9*(R8*(1+(N1/N2))+(G1/N2))/G1/(R8-R9)
830 D1=N2*R8*(R9*(1+(N1/N2))+(G1/N2))/G1/(R9-R8)
840 P9(I)=P0*(1+C1*EXP(R8*T0(I))+D1*EXP(R9*T0(I)))
850 IF R0>B9 THEN 920
860 S1(I)=P9(I)*B9^2*(1-(A1/R0)^2)/(B9^2-A1^2)
870 S2(I)=P9(I)*B9^2*(1+(A1/R0)^2)/(B9^2-A1^2)
880 U4(I)=B9^2*R0*P9(I)*(1-2*V0+(A1/R0)^2)/2/G0/(B9^2-A1^2)
890 IF T0(I)=0 THEN U4(I)=0 AND  S1(I)=0
900 IF T0(I)=0 THEN S2(I)=0
910 GOTO 960
920 S1(I)=P0*(1-(B9/R0)^2)+P9(I)*(B9/R0)^2
930 S2(I)=P0*(1+(B9/R0)^2)-P9(I)*(B9/R0)^2
940 U4(I)=B9^2*P9(I)*((1-2*V0)*B9^2+A1^2)/2/G0/R0/(B9^2-A1^2)
950 IF T0(I)=0 THEN U4(I)=0 AND S1(I)=0
960 NEXT I
970 PRINT"INPUT PARAMETERS - COMPUTER PROGRAM >SQEZBRGR<"
980 LPRINT"INPUT PARAMETERS - COMPUTER PROGRAM >SQEZBRGR<"
990 IF O1 <>2 THEN 1040
1000 PRINT
1010 LPRINT
1020  PRINT"Ec=";E0;"  PSI    POISSON'S  RATIO  OF  CONCRETE=";V0;"      LINER
THICKNESS=";T8;" IN."
1030  LPRINT"Ec=";E0;"  PSI    POISSON'S  RATIO  OF  CONCRETE=";V0;"      LINER
THICKNESS=";T8;" IN."
1040 PRINT"nk=";N1;" PSI-MIN    nm=";N2;" PSI-MIN    P1=";P1;" PSI    P2=";P2;"
PSI"
1050 LPRINT"nk=";N1;" PSI-MIN    nm=";N2;" PSI-MIN    P1=";P1;" PSI    P2=";P2;"
PSI"
1060 PRINT"Gk=";G1;" PSI    Gm=";G2;" PSI"
1070 LPRINT"Gk=";G1;" PSI    Gm=";G2;" PSI"
1080 IF O1<>3 THEN 1130
1090 PRINT"ROCK SUPPORT PRESSURE, pb=";P5;"  BOLT RADIUS, b=";R2;"  E steel=";E1
1100 PRINT"BULK MODULUS, K=";K1;"  PSI"
1110 LPRINT"BULK MODULUS, K=";K1;"  PSI"
1120 LPRINT"ROCK SUPPORT PRESSURE, pb=";P5;"  BOLT RADIUS, b=";R2;"  E steel=";E1
1130 PRINT"TUNNEL RADIUS, A=";A1/12;" FT.    TARGET RADIUS, R =";R0/12;" FT."
1140 LPRINT"TUNNEL RADIUS, A=";A1/12;" FT.    TARGET RADIUS, R =";R0/12;" FT."
1150 PRINT"THETA=";T9*180/3.141592654#;" DEG"
1160 LPRINT"THETA=";T9*180/3.141592654#;" DEG"
1170 LPRINT
1180 PRINT Z$
1190 LPRINT Z$
1200 PRINT
1210 LPRINT
1220 IF O1=2 THEN 1300
1230 PRINT"TIME (MIN)     Ur (IN)        TAU X (PSI)"
1240 LPRINT"TIME (MIN)     Ur (IN)        TAU X (PSI)"
1250 FOR I = 1 TO 13
1255 IF O1=1 THEN T4(I)=0
1260 PRINT T0(I);TAB(14);U8(I);TAB(29);T4(I)
1270 LPRINT T0(I);TAB(14);U8(I);TAB(29);T4(I)
1280 NEXT I
1290 GOTO 1360
1300 PRINT"TIME (MIN)    Ur (IN)         SIGMAR (PSI)    SIGMATHETA (PSI)"
1310 LPRINT"TIME (MIN)    Ur (IN)         SIGMAR (PSI)    SIGMATHETA (PSI)"
```

```
1320 FOR I = 1 TO 13
1330 PRINT T0(I);TAB(14);U4(I);TAB(29);S1(I);TAB(44);S2(I)
1340 LPRINT T0(I);TAB(14);U4(I);TAB(29);S1(I);TAB(44);S2(I)
1350 NEXT I
1360 INPUT"TRY AGAIN WITH NEW R, THETA (Y/N)";T$
1370 IF T$="Y" THEN 330
1380 END
```

REFERENCES

Afrouz, A. and Harvey, J., "Rheology of Rocks Within the Soft to Medium Strength Range," Int. J. Rock Mech. Min. Sci. and Geomech. Abstr., Vol. 11, pp. 281-290. London: Pergamon Press, 1974.

Bland, D., The Theory of Linear Viscoelasticity, International Series of Monographs in Pure and Applied Mathemeatics, New York: Pergamon Press, 1960.

Churchill, R., Operational Mathematics. 2nd ed. New York: McGraw-Hill, 1958.

Cristescu, N., Rock Rheology. 1st ed. Dordrecht, The Netherlands: Kluwer Academic Publishers,
1989.

Farmer, I., "Stress Distribution along a Resin Grouted Rock Anchor," Int. J. Rock Mech. Min. Sci. and Geomech. Abstr., Vol. 12, pp. 347-351. London: Pergamon Press, 1975.

Gnirk, P. and Johnson, R., "The Deformational Behavior of a Circular Mine Shaft Situated in a Viscoelastic Medium Under Hydrostatic Stress," Proceedings of the 6th Symposium on Rock Mechanics, pp. 231-258. Rolla, MO: University of Missouri-Rolla, October 1964.

Goodman, R., Introduction to Rock Mechanics. 2nd ed. New York: John Wiley and Sons, 1989.

Jaeger, J. and Cook, C., Fundamentals of Rock Mechanics. 3rd ed. London: Chapman and Hall, 1979.

Korbin, G., "Prereinforcement and Reinforcement in Underground Openings - Performance and Design Considerations," Proceedings of Fjellsprengningsteknikk/Bergmekanikk/Geoteknikk 1978. Oslo, Norway: Tapir, 1979.

Korbin, G. and Brekke, T., "A Field Study of Spiling Reinforcement in Underground Openings," Technical Report MRD-1-77. Omaha, NE: U. S. Army Corps of Engineers Missouri River Division, June 1977.

Korbin, G. and Brekke, T., "Model Study of Tunnel Prereinforcement," Journal of the Geotechnical Engineering Division. New York: Proceedings of the American Society of Civil Engineers, September 1976.

Obert, L. and Duvall, W., Rock Mechanics and the Design of Structures in Rock. 1st ed. New York: John Wiley and Sons, 1967.

Park, R. G., Foundations of Structural Geology. 2nd ed. New York: Chapman and Hill, 1989.

Saada, A., Elasticity: Theory and Applications. New York: Pergamon Press, 1974.

Ugural, A., Stresses in Plates and Shells. 1st ed. New York: McGraw-Hill, 1981.

THE HOOVER SLIDES IN PROVO CANYON, UTAH

THOMAS S. LEE AND STEVE H. BRANDON

Parsons Brinckerhoff Quade & Douglas, Inc., San Francisco, California

ABSTRACT

Provo Canyon in Utah has a complex geologic history beginning as long as 300 to 500 million years ago. Continuing into the present, the Canyon has undergone uplift and faulting. The Hoover Slides are located in Provo Canyon and have been active for at least fifty years. They exist in a prehistoric landslide which covers a 1.6 kilometer long stretch of canyon along U.S. 189 beginning approximately 2.4 kilometers below the Deer Creek Dam. Exactly what caused the landslides has been a question for at least the last fifty years. However, it has previously been believed that the slides are caused by movements in the Manning Canyon shale - a black to brown shale with interbeds of sandstone, limestone, and quartzite.

The geology of Provo Canyon is generally composed of Pennsylvanian age rocks of the Oquirrh Formation, a cherty limestone and quartzite with shale and sandstone interbeds, and the Manning Canyon Shale Formation. These units are underlain by Mississippian age limestones of the Humbug and Great Blue Formations. Recent or Quaternary soil deposits, locally covering the rock units, include alluvial fans, river alluvium, colluvium or talus, river terraces, moraine and glacial outwash, and mudflows.

Faults of various types are commonly found in Provo Canyon. The Hoover Slides area is within a thrusted fault known as the Deer Creek thrust fault which is the highest of the major thrust faults in Provo Canyon. It is an especially prominent structural feature as the fault is relatively flat-lying and is rather close to surface in much of Provo Canyon. The Manning Canyon shale is the principal material upon which movements along the Deer Creek thrust fault occur.

Widening and realignment of US-189 from two to four lanes in Provo Canyon will require cuts and fills through a portion of the Hoover Slides. This area poses the most challenging geotechnical related issue along the existing as well as the newly proposed alignment. A geotechnical exploration program was conducted to assess the feasibility for the proposed roadway widening. Field work included borings, test pits, in situ testing, downhole geophysical testing, seismic refraction surveys, and instrumentation of inclinometers and observation wells. Additionally, geologic mapping was conducted to delineate the extent of the Hoover Slides area.

This paper will discuss the complex geology of the Hoover Slides and present postulated geologic chronology of the Hoover Slides area.

INTRODUCTION

U.S. Highway 189 (US-189), a principal arterial, is designated as a scenic byway on the official Utah Highway map. It passes through the Wasatch mountains east of Orem, Utah, connecting Utah Valley and Heber valley through Provo Canyon. Locally, it provides access from Utah valley to the recreational resources of Provo Canyon and beyond, and gives residents of Heber valley access to the Provo/Orem metropolitan area (Figure 1).

US-189 is a rural two-lane highway and was designed over 60 years ago, it no longer safely meets the private and commercial traffic needs of the region. Improvements to the highway are intended to eliminate existing hazardous driving conditions and to increase the capacity of the facility to safely accommodate projected traffic loads for the next 20 years.

In October 1993, Centennial Engineering Inc. (CEI) and Parsons Brinckerhoff (PB), a geotechnical consultant to CEI, were retained by the Utah Department of Transportation (UDOT) to proceed with the design phase of widening the US-189 (from two lanes to four lanes) for the section from the Wasatch County line near Wildwood to the Deer Creek State Park. In November 1993, Parsons Brinckerhoff began a geotechnical exploration program for the segment from Wildwood to Deer Creek State Park. The segment being designed includes about 9 kilometers of roadway with a series of cut and fill slopes, retaining walls, and rock cuts.

The geotechnical exploration accomplished to date includes (1) collection and review of existing information, UDOT geotechnical study reports, geologic mapping, and aerial photographs, (2) conducting site reconnaissance and detailed geologic mapping, (3) drilling boreholes and installing inclinometers, (4) digging test pits, (5) running seismic refraction survey lines, (6) monitoring inclinometers, (7) conducting downhole geophysics logging, (8) laboratory testing, (9) interviews/meetings with UDOT, CEI, and related agencies, and (10) interim synthesis of data.

HISTORY OF GROUND MOVEMENTS ON US-189

Many areas of Provo Canyon have long been recognized as hazardous. Mudslides, landslides, and snowslides have repeatedly blocked highway and railway service almost annually since their construction dated as far back as the early 1930's. For the last six decades, new construction works have been proposed in the Provo Canyon, many of which were planned outside the landslide areas. An example was construction of the Salt Lake Aqueduct in 1940's. In an early Salt Lake Aqueduct Investigation dated August 1938, a point was made on the advisability of locating the aqueduct in the river gravels to avoid possible disturbance of potential landslides along the roadway now called US-189 (Murdock, 1941).

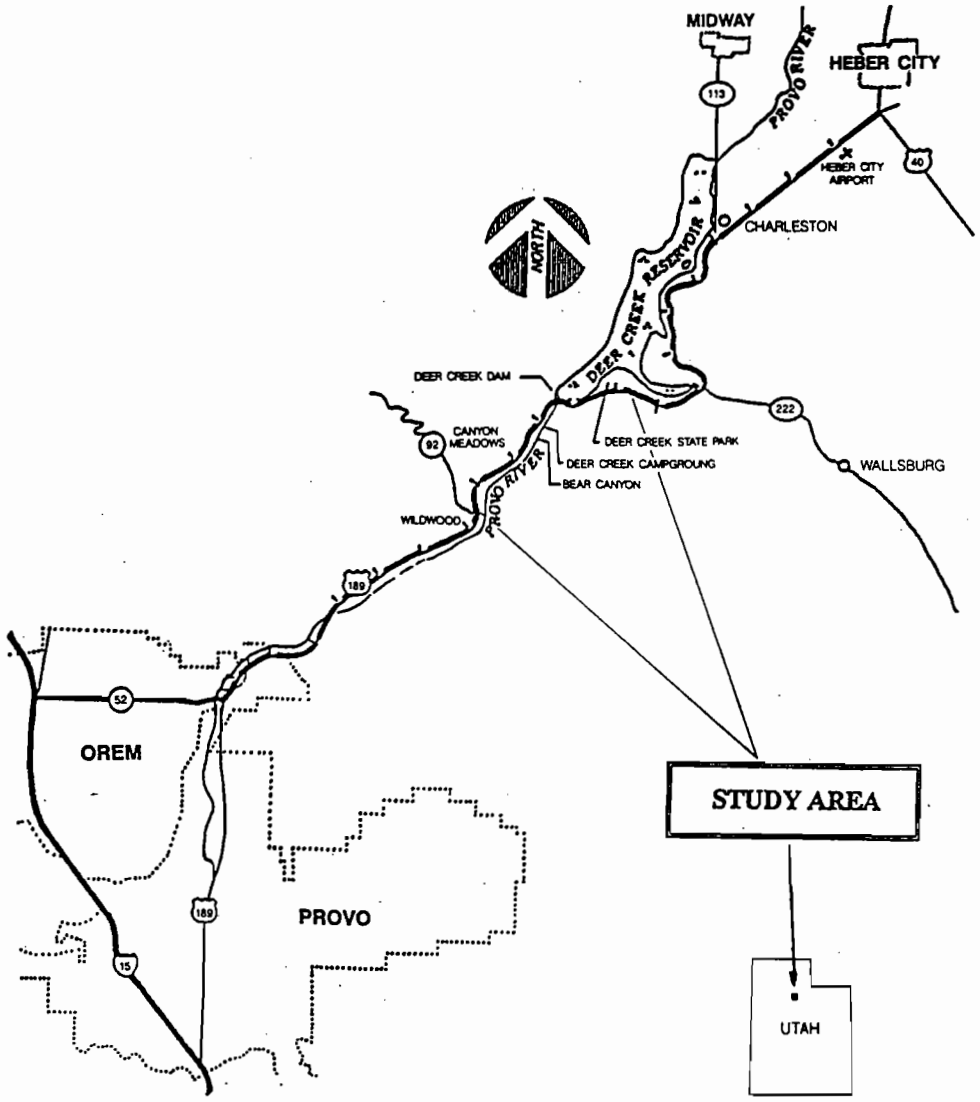

Figure 1 - Site Location Map

Records have shown that these landslides occurred in 1940's or earlier. Murdock (1941) in his geologic report on "Geological Features of Salt Lake Aqueduct" wrote that "The gaging house operated by the Bureau of Reclamation moved outward at the top toward the river so it had to be moved upstream. The railroad fill and track alignment shows a decided movement to the east...". Comparing with the current site plan, the

gaging house is roughly located about 1,680 to 1,830 meters south of the Deer Creek Dam along US-189. Murdock (1941) suggested that if sufficient data were available, all the slides could probably be attributed to a formation of black shale (called Manning Canyon shale) which underlies the limestone that outcrops throughout Provo Canyon.

The existing US-189 was previously widened with fill placed over the old rural roadway in 1959 and early 1960. Fill as much as 8-10 meters deep was once placed on the old roadway. The load induced by this fill triggered a big landslide in 1959. The location of this 1959 landslide is approximately 110 to 140 meters southeast of Station 21+200 of the preferred alignment (Note: all stations quoted hereinafter are referred to those of the preferred alignment proposed by Centennial Engineering, Inc.). Since then, the US-189 roadway in the Hoover Slides area has continued to suffer creep movements, resulting in cracking of roadway pavements and raveling of slopes which are repaired periodically.

REGIONAL GEOLOGY

US-189 is located in Wasatch County in north-central Utah. The study area is in the Colorado Plateau Physiographic Province and very near the eastern border of the Basin and Range Physiographic Province (Shannon & Wilson, 1989). The highway trends approximately north-south along the east and west banks of the Provo River in the Wasatch Mountains. The Wasatch Mountains were formed during faulting in the late Cretaceous period (about 70 to 140 million years ago), which included both regional uplift and large-scale thrusting. Modern day faulting in the Wasatch Range started in Miocene time (about 15 million years ago) and continues into the present (Delta, 1994).

Geologic mapping of Provo Canyon was originally done by Baker (1964) in a series of 1:24,000 scale U.S. Geological Survey maps (Figure 2). More recently, another U.S. Geologic Survey map at 1:125,000 scale by Bryant (1992) was published. The major structural feature presented in these maps is the Charleston-Deer Creek thrust faults. The Deer Creek thrust is the primary structure of interest in Upper Provo Canyon. The two geologic units along which thrusting occurred are the overriding Oquirrh Formation and the underlying Manning Canyon shale. The Manning Canyon shale served as the regional detachment for the nearly horizontal thrust movement (Baker, 1964). Erosion through the upper plate (Oquirrh Formation) of the Deer Creek thrust fault has exposed the Manning Canyon shale in some locations in Provo Canyon. One of these exposures in the project area is known as the Sulphur Springs Window. Most of the earthflows and slumps that have occurred in the project area are located within the Sulphur Springs Window.

Hydrogeology

Groundwater in the project area occurs in both alluvial and bedrock deposits. The groundwater levels fluctuate throughout the year, with the highest levels occurring in late spring in association with runoff of snowmelt. Unconsolidated alluvial deposits in the Provo River valley are major aquifers. They are recharged by infiltration of precipitation

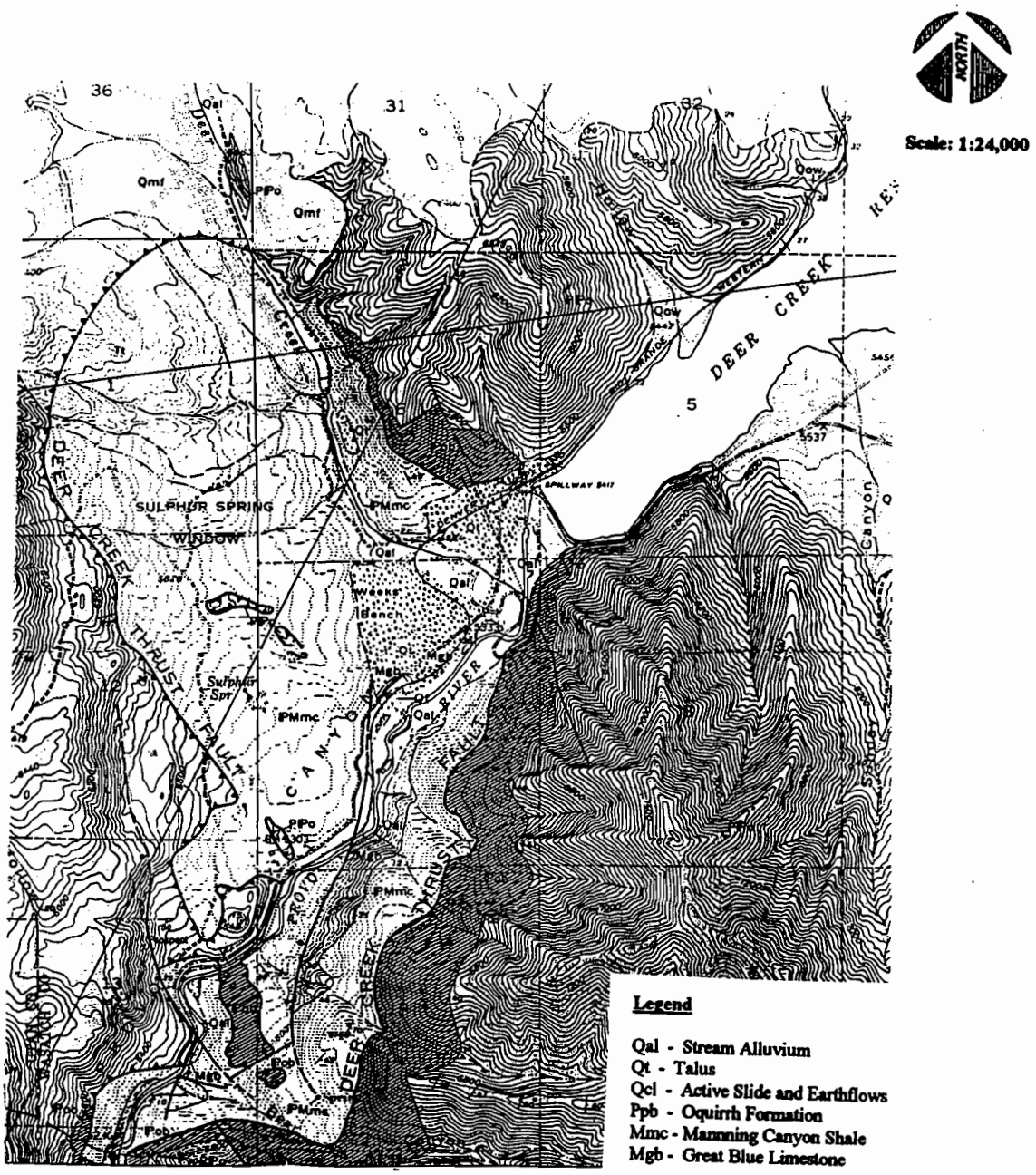

Figure 2 - Geologic Map (Baker, 1964)

as well as through discharge of underlying bedrock units. Water levels in the alluvial deposits in the project site are at or near ground surface. Groundwater in bedrock units is found in the Oquirrh and Manning Canyon Formations. Groundwater flow in the Oquirrh Formation is primarily by flow through discontinuities in the rock (secondary permeability). Groundwater occurrence in the Manning Canyon shale is evident by the

numerous springs, seeps, and swampy areas, particularly in the Sulphur Springs Window (Canyon Meadows) area. The Manning Canyon shale serves as an aquiclude to the infiltration of groundwater, causing the upper layers of the unit to become saturated. The highly disturbed state of the Manning Canyon shale in the project area, as a result of the Deer Creek Thrust fault, has provided locally variable subsurface conditions which result in numerous springs and seeps, many of which flow throughout the year. Groundwater emanating from the Manning Canyon shale is highly acidic due to the formation of sulfuric acid by leaching of pyrite out of the shale.

GEOLOGICAL INVESTIGATIONS

Desk Study

Aerial Photograph Interpretation

During the initial stages of the investigation, aerial photographs from Wildwood to Deer Creek State Park dating back to 1953 were reviewed to observe cultural changes and make preliminary geologic interpretations.

Of paramount importance in the aerial photograph interpretation was the identification of landslide areas to serve as a basis for future analysis. The central part of the preferred alignment is dominated by hummocky landslide areas, where several generations of landslides that ranged from small roadcut failures to large earthflows could be identified. Landslide morphologies vary widely, including large slide blocks of semi-intact bedrock to soil-like earthflows. Aerial photographs taken in 1953 and 1984 were compared to determine possible creep. No visible movements were observed on any large slides. A small rotational slump occurred sometime between 1962 and 1969 in a roadcut approximately 600 meters downstream from Horseshoe Bend. The road cut was made between 1959 and 1962 when US-189 was improved, and sometime between 1962 and 1969, a failure occurred in the roadcut.

Evidence of flow from the Sulphur Spring, located on the Hoover Slides area, was visible on all of the aerial photographs except for those taken in 1969. Possible explanations for the lack of flow include a dry year, piping of the spring for agricultural purposes, or perhaps lack of contrast on the photographs giving the appearance of no flow. Probably the most notable changes were observed between the 1969 and 1984 photographs, when roads and houses were constructed as part of a subdivision development in the Hoover Slides area known as Canyon Meadows.

Field Explorations

Borings and Geologic Mapping

The field exploration was accomplished in three phases. The first phase of field exploration was performed by UDOT and included a total of twenty four (24) borings varying from 12 meters to 46 meters. Of these 24 borings, 21 borings were drilled in the Canyon Meadows area, two (U-23 and U-24) on the east side of the Provo River, and one (U-19) on the upstream of Horseshoe Bend. The objectives of the exploration were to determine; (1) the subsurface conditions in the Canyon Meadows area, and (2) the movements experienced in the Canyon Meadows area.

The second phase of field exploration began in March 1994 when the preferred alignment was not yet determined. As such, it focused on; (1) field reconnaissance which included mapping and logging of geologic features along and adjacent to the existing US-189, and (2) delineation of the Hoover Slides.

The third phase of field exploration started when potential alignments had been laid out for evaluation. This included drilling of 20 borings of depths varying from 18 meters to 50 meters, digging eleven test pits, running seismic refraction survey lines, downhole geophysics logging, and laboratory testing. Both the second and third field explorations were carried out by Delta Geotechnical Consultants, Inc. of Salt Lake City. All of the boring locations and depths were selected by Parsons Brinckerhoff, Inc.

Seismic Refraction Survey

The purpose of this survey was to determine the approximate depths, profiles and seismic velocities of the bedrock underlying overburden soils in areas of interest. Four seismic survey lines were performed in the Horseshoe Bend, and a survey line was made in the Camp Ground. Each line segment employed 12 geophones, each spaced at 3 to 6 meter intervals. A hammer was used as the energy source at all locations

The results indicated that overburden soils encountered at the site consist of (1) highway embankment fill, (2) colluvial deposits derived by gravity and runoff from upslope areas, (3) alluvium, and (4) weathered bedrock. The normal fault identified in the Baker's USGS map was verified by the seismic line (Figure 2). Alluvial deposits as inferred from the seismic line survey are very shallow (i.e., only 2 to 4 meters in thickness).

Downhole Geophysics Logging

Two phases of downhole geophysics logging tests were carried out. The first phase consisted of conducting downhole geophysical logging on four existing PVC cased borings, two (PB-6 and U-19) in Horseshoe Bend and two (U-3 and U-21) on US-189 off

the Canyon Meadows area. The second phase included testing in three existing PVC-cased wells (PB-1, PB-3, PB-4) in Horseshoe Bend and one (PB-11) at the Canyon Meadows area.

The existing PVC-cased inclinometers were logged with gamma, induction, neutron, and 4-pi gamma-gamma density. Log plots were developed for interpreting the lithology, stratigraphy, and moisture content of the subsurface layers.

In summary, there was no major discrepancy between the geophysical log response and the geologic descriptions. High gamma values usually correspond to high apparent clay volumes. Major slippage features as identified by the downhole geophysics logging generally occur in saturated clay-rich (high gamma, low neutron, and low induction) zones or at the boundaries of these zones. However, not all zones that are clay-rich and apparently saturated have shown movements as indicated by the logging results. In addition, the logs at PB-6 support the presence of landslide debris encountered at the borehole where the inclinometer is located in clay poor (low gamma, high neutron, and high resistivity) lithologic units that appear to be carbonate rich. No slippage was identified from the logging of PB-6.

Instrumentation

Inclinometers

Inclinometers were installed upon completion of borings in Phase 1 and Phase 3 field explorations. The annular spacing between the inclinometer casing and the drilled hole was tremie backfilled with grout to the top of the hole. Initial readings in each inclinometer were taken a few days after the grout was set, and subsequent readings have been taken once every two weeks or longer depending on weather conditions. Of these fifteen inclinometers, seven are located in Horseshoe Bend, four in the Canyon Meadows area, and four elsewhere along the proposed alignment.

Readings to date indicate that movements, if any, generally occurred either at : (1) the fill below US-189, (2) the sheared and gouge zones at the contact between the Oquirrh formation and the Manning Canyon shale, or (3) the alluvial deposits deep below the Provo River, or a combination of (1) and (2) or (1) and (3) above (Figure 3).

Piezometers

An observation well was installed in the vicinity of each of the twenty two boreholes drilled in the first phase field exploration. These observation wells were drilled to depths varying from 6 to 22 meters, and are intended to monitor the fluctuation of the groundwater table. Based on the UDOT monitoring records coupled with our in situ water sampling from some of the observation wells, the groundwater fluctuates with time, with much higher level during the spring, dropping to a low level in the late summer.

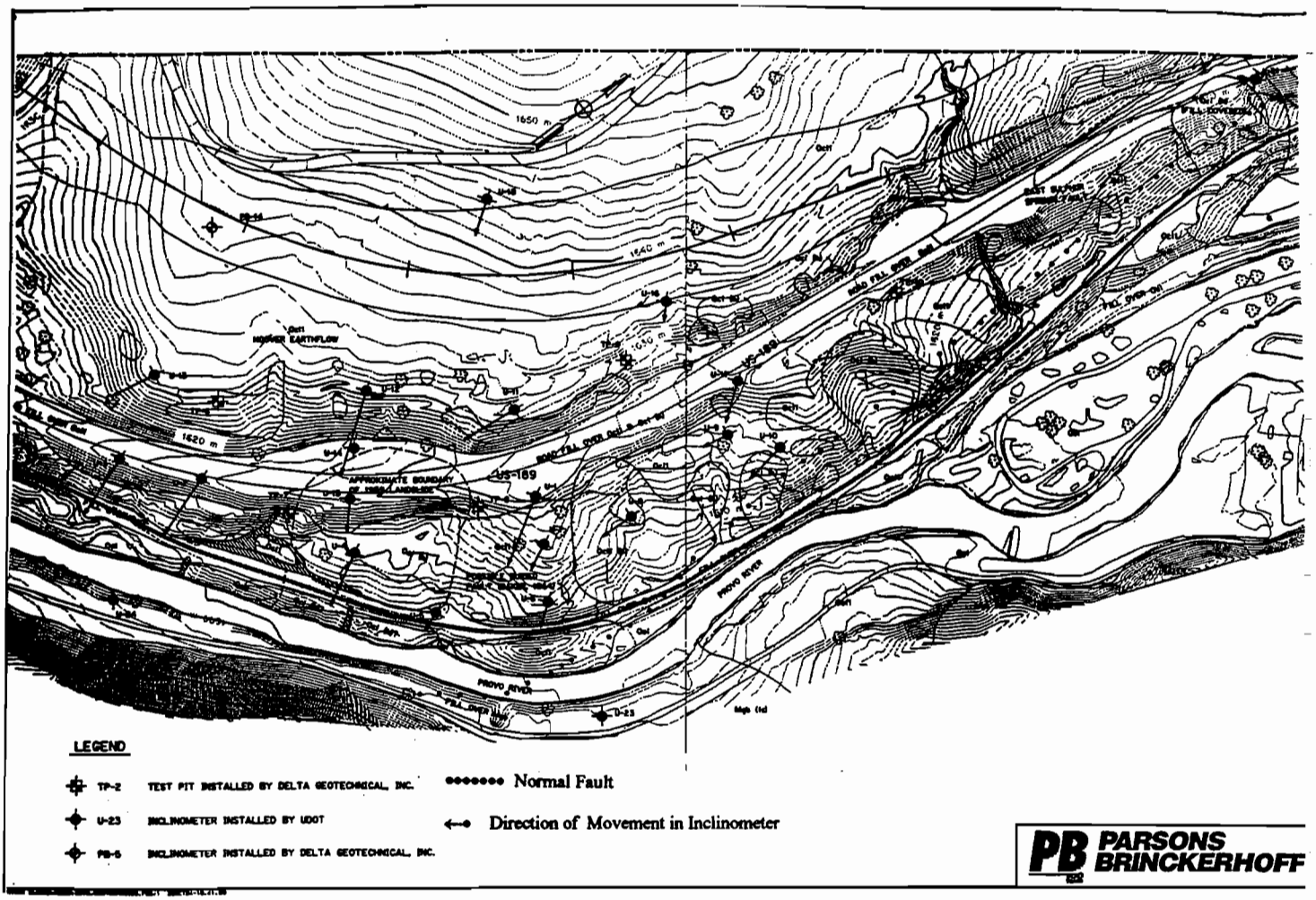

Figure 3 - Movement Directions as Recorded in the Canyon Meadows Area

Laboratory Testing

The laboratory testing comprised unit weight/moisture content, index properties, particle size distribution determinations, hydrometer, direct shear, unconfined compression, one-dimensional consolidation, slake durability, compaction, X-ray diffraction analysis, water chemistry, and soil chemical analysis. All tests were conducted in accordance with ASTM standards.

GEOLOGIC MAPPING

The geologic structures of the project site are quite complex, with several types of faults and folds. The dominant structure, the Deer Creek thrust fault, which has placed the Oquirrh Formation in thrust contact with the Manning Canyon shale, forms the boundary of the Sulphur Springs window. Generally, thrust faults place older rocks over younger rocks. However, in this case, the Manning Canyon shale (lower thrust plate) is older than the Bridal Veil Falls Member of the Oquirrh Formation (upper thrust plate).

Smaller, intraformational bedding-plane thrust faults, most likely associated with regional faulting, are exposed in the Bridal Veil Falls limestone and quartzarenite members of the Oquirrh Formation. The Manning Canyon shale and Great Blue limestone both contain folding, faulting, and shearing likely as a result of footwall deformation and regional compressional tectonism. A historic slump in a roadcut (approximately between Station 19+200 and Station 19+300) is centered over an intraformational thrust within the Manning Canyon shale, which gives evidence to the fact that geologic structures play an important role in geologic hazard assessment.

Several normal faults were mapped by previous investigators (Bryant, 1992; and Baker, 1964). Significant faults have been assigned names for ease of locating them during discussion. An example is the East Sulphur Springs Fault which was mapped by Baker as a north-trending, down to the west normal fault that juxtaposes Manning Canyon shale with Great Blue limestone just east of the Provo River (Figure 2, Baker Map). Another normal fault which was not mapped either by Baker or Bryant was found by field mapping and seismic refraction survey in Horseshoe Bend. This fault is possibly a high-angle fault which traverses Horseshoe Bend and is concealed beneath the Provo River channel. It is has been named the Horseshoe Bend Fault as shown in Figure 3. Evidence for this fault includes; (1) an outcrop of Great Blue Limestone on the inside of Horseshoe Bend that is stratigraphically higher than the landslide deposits of Manning Canyon shale across the river, and (2) borehole logs could not be correlated across the river, which suggests that a high-angle structure exists between the boreholes.

The Manning Canyon shale was overrun by the a thick sequence of the Oquirrh Formation, which resulted in significant folding and faulting in the underlying shale. Several types of folds include S- folds, upright and overturned anticlines and synclines, and recumbent synclines were mapped in roadcut exposures. Broad, open folding was noted in the Oquirrh Formation, most likely due to regional compressional stresses.

GEOLOGICAL INTERPRETATIONS OF LANDSLIDE AREAS

Three of the five landslides on existing US-189 are found near the Canyon Meadows development. They are underlain by the Manning Canyon Shale formation which consists of black to brown shale with interbedded slabby sandstone, thin beds of quartzite, and thin- to thick-bedded gray to black limestone. The shale weathers rapidly when exposed to the atmosphere and becomes highly plastic when wet. The weathering

process is accelerated by the presence of sulphur springs along the thrust fault zone, as a result of which the shales have been weathered to a soil consistency to a depth of 5 to over 20 meters in this area.

Based on data gathered during this study, literature review, and evaluation of the local geology and hydrogeology of the Hoover Slides area, a geologic chronology of the Hoover Slides areas has been postulated. It must be stressed that:

(1) this is NOT one landslide; it is several landslides,

(2) The geology and landslide mechanisms at this site are quite complex,

(3) Each landslide is unique and likely has different mechanisms at work,

(4) Two sliding planes have been identified from the inclinometers installed on US-189 in the Hoover Slides area (i.e., U-1, U-2, U-3, U-15, U-17, U-19, and U-21); one is in the fill, and the other is deep-seated in the contact between the landslide debris and intact Manning Canyon shale.

Postulated Geologic Chronology of the Hoover Slides Area

Canyon Meadows

The following postulated geologic chronology of the landslide movements at Canyon Meadows is presented based on our literature review, aerial photograph interpretation, borehole log data, seismic refraction survey, downhole geophysics, laboratory testing results, and geologic mapping:

1. Movement along the sub-horizontal Deer Creek thrust fault (Late Cretaceous) sheared the rocks along the contact between the Manning Canyon shale and the overlying Oquirrh Formation (limestone and sandstone). The regional thrust sheared and crushed the rock in both formations above and below the sliding plane. The predominant rock type involved in the sliding in this area is the Manning Canyon shale. As a result of either the regional thrusting or other tectonic activity related to the formation of the Wasatch Mountain range, the bedrock strata on the west side of the river dip approximately 10° to 20° to the east-southeast.

2. Normal faults contemporaneous with the regional thrust faults formed as a result of adjustments (relaxation) of the ground to the large scale shear movements. For the most part, the normal faults dip steeply, from approximately 70° to sub-vertical. One of the normal faults mapped by Baker (1964) is found in the Canyon Meadows slide area and is of particular interest. This fault (named as the East Sulphur Springs fault) trends nearly north-south with the down-thrown block on

the west side of the fault. A seismic refraction survey line was run that trends northwest-southeast near the toe of the slide and appears to confirm the existence of the normal fault. The presence of this normal fault brings older rock units of the Great Blue Limestone Formation into lateral contact with younger rocks of the Manning Canyon Shale along portions of the Provo River in the Canyon Meadows slide area.

3. After the normal faulting took place the Provo River continued downcutting. Historic records of the U. S. Bureau of Reclamation for the Deer Creek Reservoir (USBR, 1941), core logs and geologic mapping indicate the river has cut as much as 10 to 20 meters below its present level. It is postulated that during the downcutting, a particularly weak stratum within the Manning Canyon shale was exposed. It is likely that the weak layer has a relatively moderate dip, possibly as low as 10° to 15° to the east-southeast, and is composed of a very low strength plastic clay. The exposure of this layer is judged to have triggered the initial slides. The subsurface deposits in the Canyon Meadows area are a combination of slide debris related to the slides in the Manning Canyon shale as well as sheared limestone and sandstone of the overlying Oquirrh Formation. Deposits of the Oquirrh may be a result of; (1) undermined blocks that rafted downslope as a result of the slides in the shale, (2) remaining blocks of the historic thrust sheet, or (3) a combination of both.

4. The historic river channel has subsequently filled back in with a combination of slide debris and alluvial sediments transported from upstream. The sediments in the river channel likely are a transgressive series of deposits that vary both in lateral and vertical extent throughout the river channel.

5. The present-day slides within the Canyon Meadows are further exacerbated by the presence of high groundwater table, perched water tables, and artesian spring conditions. The groundwater has a high sulfur concentration due to leaching out of pyrite within the shale. This causes chemical weathering of the shales and acts to further weaken the landslide debris composed partly of Manning Canyon shale.

6. The data from inclinometers in the Canyon Meadows slide area reveal that the entire slide mass is creeping at a slow rate (about 3 to 30 mm per year), generally to the east-southeast (toward the river). The rate of ground movement increases dramatically near the west side of US-189 as a result of the sidehill roadcuts. The rate of movement on the downslope side of the highway is also much greater than the overall slide movement rate as a result of the increased load of the road and fill on the weak slide material as well as the close proximity to the river. The inclinometers indicate movement is deflected to the south-southeast in the northern part of the slide as a result of the presence of the Great Blue limestone acting as a buttress to movement of the slide material (Figure 4). In the southern portion of the slide area where the Manning Canyon shale is present at the bank of the river,

there is no buttress, and thus, the toe of the slide has continued to erode through time as there is little resistance to downslope movement.

Horseshoe Bend

The geology inferred from the site investigation is extremely complex because of localized faulting within the Horseshoe Bend area (Figure 4). The following proposed geologic chronology of the landslide movements at Horseshoe Bend is presented based on our borehole data, shallow seismic refraction survey data, laboratory testing results, downhole geophysics logging, and field mapping:

1. Movement along the sub-horizontal Deer Creek thrust (Late Cretaceous) fault sheared the rocks along the contact between the Manning Canyon shale and the overlying Oquirrh Formation (limestone and sandstone). The regional thrust sheared and crushed the rock in both formations above and below the near horizontal thrust plane. The rocks of the Oquirrh Formation present at Horseshoe Bend are located in close proximity to the plane of shearing, and as a result are highly sheared and fractured, resulting in a weak rock mass.

2. In the northern portion of Horseshoe Bend (west side of the river), the weak rock mass is resting on a plastic, sheared clay gouge surface that represents the top of the Manning Canyon shale. The weak Oquirrh Formation present at Horseshoe Bend is likely the result of landslide material that has slid downslope toward the Provo River. The Oquirrh Formation has a high secondary permeability due to the fractured and weathered state of the rocks that allows water to percolate easily down through the unit. When the groundwater reaches the top of the Manning Canyon shale, which is nearly impervious, it collects and saturates the shear plane zone as well as the top layers of the shale. Thus the strength of an already weak zone is further reduced by the uplift pressures created along the contact of the Oquirrh and Manning Canyon Formations. Pore pressures may also be building in the clayey shales below the sheared contact zone. The saturated state of the shear plane also results in further chemical weathering of the shale which reduces its shear strength as discussed above.

3. The southern portion of the Horseshoe Bend area has distinctly different subsurface conditions as evident in borings PB-1, PB-2, PB-5, and PB-7. After movement along the Deer Creek Thrust, a normal fault trending east-west is postulated to have formed between PB-2 and PB-3 with the downthrown side on the north (upstream) side of the fault. The upthrown block is composed of Great Blue limestone, which crops out on both sides of the Provo River and dips to the south-southeast. A normal fault with the Great Blue limestone on the upthrown side would explain the cause for the Horseshoe Bend feature. The river deflects sharply to the west due to the hard resistant limestone at this location.

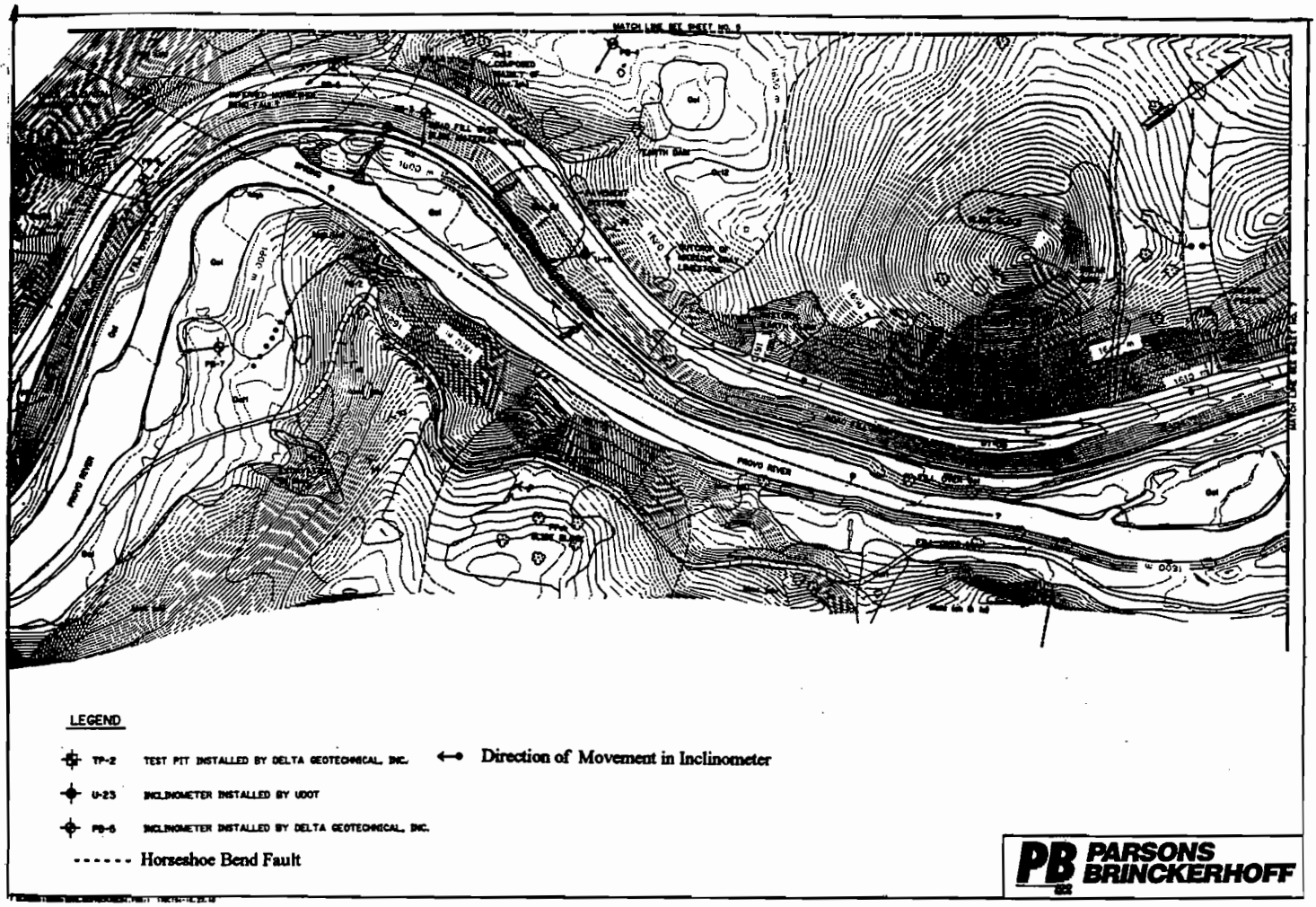

Figure 4 - Horseshoe Bend

The geologic conditions in the southern portion of Horseshoe Bend are very complex as exemplified in the presence of overturned bedding in a southbound roadcut on US-189 between borings PB-1 and PB-5. At this time no reliable explanation of the geologic structure of the southern portion of Horseshoe Bend has been conceived.

CONCLUSIONS

(1) Hoover slides are within a very complex geologic region which is heavily thrust faulted, resulting in intense fracturing of the rock. They are located on a site of a large prehistoric landslide in Canyon Meadows which is underlain by the Manning Canyon Shale formation consisting of black to brown shale with interbedded slabby limestone. The shale weathers rapidly when exposed to the atmosphere and acidic water, and loses its shear strength upon wetting.

(2) The Hoover Slides area consists of one deep-seated sliding plane that originated from the tectonic movements of the Deer Creek thrust fault and local faulting and numerous localized smaller landslides that resulted from fill placed as part of widening of the old rural highway.

(3) The active creep movements occur primarily where fills have been placed on top of a large block of landslide debris which was formed as a result of tectonic movements of the Deer Creek thrust fault and downcutting of the Provo River.

(4) The inclinometer readings provide a fairly consistent picture of the overall creep movements of the Hoover Slides. The directions of creep movements are due south to southeast towards the Provo River. The creep movements are of two types, the shallow one which occurs at the fill/landslide debris contact, and the deeper one is associated with the continual weathering and degradation of the Manning Canyon shale. The movements in the northern portion are directed to the south to southeast as a result of the Great Blue Limestone acting as a buttress to the slide.

(5) The inclinometer readings have indicated that there are essentially little to no movements on the east side of the Provo River. If there are movements, they are very small and are expected to be along sheared or gouge zones.

(6) The cracking of roadway pavement is believed to be ascribed to the continual creep movements of the underlying fill. The rate of movements is, however, not constant, being the highest during snow-melt in the spring when the groundwater table rises. The rate of movements recorded so far ranges from 10 to 40 mm per year which is considered to be of a small magnitude.

(7) A normal fault which is called by the writers as "The Horseshoe Bend fault" was found during our site reconnaissance. Such a normal fault is not mapped by the USGS map by Baker (1964).

ACKNOWLEDGMENTS

The geological mapping described was conducted by Delta Geotechnical Consultants, Inc. of Salt Lake City, Utah. Without their mapping, some of the faults and folds would not have been discovered. The writers wish to thank Messrs. Ed Keane and Randy Park of Utah Department of Transportation (UDOT), Messrs. Mike Robertson and Lance DeBernardi of Centennial Engineering Inc. (CEI), and Mr. Lee Abramson of Parsons Brinckerhoff Quade & Douglas, Inc. (PBQ&D) for their encouragement and support for writing this paper as well as for granting permission for its publication. However, any explicit and implicit statements made herein by the writers should not be inferred as the official or procedures of UDOT, CEI, and PBQ&D.

REFERENCES

Baker, A. A. (1964), Geology of the Aspen Grove quadrangle, Utah: U. S. Geologic Survey Map GQ-239, scale 1:24,000.

Bryant, B. (1992), Geologic and structure maps of the Salt Lake City 1° x 2° quadrangle, Utah and Wyoming: U.S. Geological Survey Map - I-1997, scale: 1:125,000.

Centennial Engineering Inc. (1994); Alignment Variations at Horseshoe Bend, US-189 Wildwood to Deer Creek State Park, April.

Colog, Inc. (1994a) Borehole Geophysical Logging on US highway 189, Upper Provo Canyon, Wasatch County, Utah, August 20, 1994.

Colog, Inc. (1994b) Borehole Geophysical Logging on US highway 189, Upper Provo Canyon, Wasatch County, Utah, November 2, 1994.

Delta Geotechnical Consultants, Inc. (1994), Technical Report - Geology US Highway - 189, Wildwood to Deer Creek State Park, Provo Canyon, Utah.

Howard Needles Tammen & Bergendoff (1989), Final Supplemental Environmental Impact Statement for the US Highway 189 from Utah Valley to Heber Valley, Utah and Wasatch Counties, Utah.

LGS & Associates, Inc., (1994), Seismic Refraction Investigations of the Hoover Slides Area, Provo Canyon, Utah, August 9.

Murdock, J. N. (1941), Geological Features of Salt Lake Aqueduct, Location - Provo Canyon Section, Provo River Project, Utah, U. S. Bureau of Reclamation.

Shannon & Wilson (1989), Final Engineering Geology Technical Report, US Highway 189, Utah Valley to Heber Valley, Utah and Wasatch Counties, Utah, pp.40.

INTENTIONAL BURIAL OF TWO ARCHAEOLOGICAL SITES BELOW A HIGHWAY IN MONTAGUE COUNTY, TEXAS: ANALYSIS OF DYNAMIC LOADING DURING CONSTRUCTION

Christopher C. Mathewson and Lloyd E. Morris
Center for Engineering Geosciences
Texas A&M University
College Station, TX 77843-3115

ABSTRACT

It has been proposed that archaeological sites can be protected through intentional burial below an engineered cover. Laboratory and controlled field tests have demonstrated that a properly designed site burial will provide a significant amount of site protection. Burial projects can be designed to alter the physical, biological and chemical conditions within the cultural horizon such that preservation of the site components is enhanced. Full-scale load tests carried out during the construction of FM-2953 in Montague County, Texas indicate that low-ground pressure equipment can be used to place cover materials. These tests further demonstrate that the impact of dynamic loading from vehicular traffic is effectively filtered out below about 5 ft (1.7 m) of cover. Construction specifications for the construction of the site burial included: Site clearing, Surface preparation, Geogrid, Limestone protection course and Fill and Road Section. These full-scale field tests demonstrated that it is both economically and environmentally sound to consider site burial as a technique to protect and preserve the Nations cultural heritage below highways and transportation routes.

ARCHAEOLOGICAL SITE PROTECTION THROUGH BURIAL

The objective of site preservation is to strike a delicate balance between the systematic data and artifact recovery and the long-term protection of artifacts that can be preserved in-situ (Moratto, 1977). Site excavation should be reduced to a minimum where long-term protection is feasible; and many cultural deposits should remain intact and be visually indistinguishable from the surrounding environment. When protected from natural or human destruction, archaeological data can be preserved for the future, to be studied and interpreted with fresh insights using the most up-to-date information and technology available. The concept of site protection through burial maintains the total archaeological resource in place.

Any definition of site protection and preservation should also have legal implications (Mathewson and Gonzalez, 1988; Mathewson, 1989a), which include:

- The goal of preservation is not to prevent change, but to reduce or shield a site from adverse human and natural impacts.
- Preservation involves what is technologically and financially feasible at present; i.e., "is it an achievable goal?"

- Preservation is limited to the length of time that the technique utilized will afford protection.

Because sites have been in place for hundreds or even thousands of years, we often assume that the site exists as a relatively constant entity. Whereas the excavator may choose to view a site as a fixed entity at the time of excavation, in fact, a site is located along a continuum of change over time. Therefore, preservation cannot be defined as non-change, but instead should be defined as "any action which reduces or eliminates detrimental changes resulting from site impacts." The goal then is that preservation activities should reduce the rate of change of the ongoing natural processes on the site matrix and contents (Mathewson and Gonzalez, 1988; Mathewson, 1989a).

Ample evidence exists to suggest that the burial of an archaeological site provides long-term protection and preservation of the archaeological materials. Archaeological investigations and excavations of burial mounds throughout the world have recovered numerous artifacts, materials, and skeletal remains. The successful preservation of these materials and remains in and below burial mounds indicates that engineered fills could provide a similar degree of protection to a site buried for preservation. The concern about burial as a site preservation technique is not that burial preserves a site, but that adverse physical, biological, and chemical conditions may be induced within the site upon burial.

Physical and Chemical Effects of Burial

To determine the physical and chemical effect burial has on the components and interrelationships of an archaeological site, a field and laboratory investigation of the natural alteration of buried soil profiles in Central Texas and in the Mississippi Valley was conducted (Gonzalez, 1989). Soils buried under constructed embankments, including four railroad berms, two river levees and one airfield apron, were compared to nearby unburied soils to evaluate changes within and between sites. Details of the investigation can be found in Gonzalez (1989) and Mathewson and others (1992).

The changes observed in the buried soils appear to have occurred shortly after burial, at least within the first 40 or so years. The amount of change observed appears to be controlled by site-specific geologic, climatic, hydrologic, and most importantly, geomorphic conditions. The changes in buried soils described herein may differ from changes observed in buried soils in drier or more humid geographic locations. Comments on the effects of burial on various soil properties are presented below:

- **Thickness**: Most of the buried soils analyzed have thicker soil profiles and thicker horizons than the unburied soils. These differences may reflect the pre-burial slope position of the soils, or in some cases, the result of increased moisture, with increased pedogenic development, of the buried soils. Burial also protects the buried soils from erosion.
- **Color**: Buried soil horizons have yellower hues, lower values, and lower chromas than unburied soils, although the change in chroma is not statistically significant. The differences in color are associated with gleying, and in some sites, with the preferential preservation of organic carbon in the buried soils. Preservation of organic carbon in saturated buried soils results in low chromas and neutral hues. Theoretically, unburied soils continually exposed to surficial, oxidizing processes would have redder hues,

higher values and higher chromas than adjacent buried soils. Given that the soils analyzed for this investigation have been buried for a maximum of 130 years, it is difficult to argue that the changes in color observed are the result of a decrease in leaching and weathering rates of the buried soils.

- **Gleying and Mottling**: Gleying and associated mottling are more common in buried soils. Buried soils were often wetter than the unburied soils. In areas of shallow ground water, the embankment may cause a rise in the ground-water table. The embankment may also limit the evapotranspiration rate of the buried soils, or it may trap runoff and precipitation along its sides with a resultant increase in moisture in the buried soils. Soils in a pre-burial toe-slope position would have thick, preferentially clay-rich horizons with a strong water retention capacity. These soils may have been mottled before burial.
- **Texture**: Burial has no noticeable effect on the texture of the buried soils. Any textural differences observed in the upper buried soil horizons appear to have resulted from a mechanical mixing of the fill and soil materials during construction of the embankments. Translocation of fines into the buried soil, with a resultant change in texture, is expected in sites where coarse-grained soils are covered with fine-grained fills. However, this condition was not evaluated in this study because none of the sites analyzed fully met these textural requirements.
- **Structure**: Buried soil horizons, particularly clay-rich horizons, show a coarsening of their structure as a result of burial. These differences in structure appear to be the result of increased vertical loading with depth, thus limiting the number of shear planes that develop in the soils. Buried soils also have six times as many structureless horizons as unburied soils. This condition is most prevalent in wet buried horizons. The lack of structure may result from increased pore water pressures or increased sodium cations in the soil solution essentially deflocculating the soil particles. It is also possible, however, that coring destroyed any evidence of structure in these wet horizons.
- **Calcium Carbonate**: Buried soils have less calcium carbonate concretions than unburied soils. Increased wetness of the buried soils may prevent calcium carbonate from precipitating into concretions or filaments. A resultant decrease in pH upon burial may also be responsible for this change.
- **Organic Carbon**: Saturated horizons preserve organic carbon. Because the preservation of humus depends on bonding between the organic fraction and the clay colloids, saturation does not guarantee the preservation of larger organic remains.

Effects of Compression

Very limited research has been carried out to determine the relationship between soil stress and damage to archaeological materials. In 1981, the California Department of Transportation (Caltrans) conducted a study on the effects of burial on an engineered archaeological site (Garfinkel et al., 1983). The results of burial of materials under 75 ft (26 m) of embankment fill for two years suggests that limited gross morphological changes do occur upon burial. The organic objects, including shells, bones, and charcoal sticks suffered the most damage by breaking or bending as the fill compacted.

Texas Eastern Gas Pipeline Company contracted with Battelle to carry out an analysis and laboratory testing of compaction-induced damages to archaeological materials. Concerns were expressed about the potential impacts of pipe-laying equipment on the Kauffman II site in Chester County, Pennsylvania. Olson and others (1988) carried out two different laboratory test programs. In the first test, modern pottery samples were buried in soil placed in a 24 in. (61 cm) diameter steel pipe and loaded using a MTS 130-kip universal tension-compression machine. The test pottery cracked at soil pressures ranging from 7.6 psi, for a straight sided pot filled with soil, to 15.6 psi, for a rounded pot that was filled with cotton to prevent soil entry. In the second test, manufactured and natural archaeological materials were placed in an excavated pit in a 48 in. (122 cm) diameter steel pipe and loaded using a MTS 1000-kip universal tension-compression machine. In this test, none of the archaeological materials were damaged. In fact, it was found that excavation of the materials caused more damage than the soil loading did (Olson, 1989; Skinner, 1989).

Laboratory experiments of compressive loading and artifact breakage were carried out using twenty different arrangements of archaeological materials placed in a sand box (Mathewson et al., 1992). The results of this testing program indicate that clay pots and ceramic sherds approximately 0.23 in. (6 mm) thick, and buried 9.8 in. (25 cm) below the surface, will fracture under a surface load of approximately 30 psi. General conclusions that can be drawn from these tests include:

- Thin walled pottery will fracture more readily than thick walled pottery.
- Pottery oriented horizontally will break more frequently than pottery standing vertically.
- Rapid loading tends to cause more damage than slow loading.
- Pottery in contact with more dense materials or in contact with other pottery are more susceptible to failure than isolated pottery.
- The controlling factor causing breakage appears to be related to total strain (displacement) rather than total stress (loading).
- Weaker, more brittle, charcoal sticks tend to fracture more readily than more ductile materials.

A field scale test of various protection techniques that would protect an archaeological site from construction equipment loading was carried out by Mathewson and others (1992) at the Texas Engineering Extension Service, Heavy Equipment Training School site in Brazos County, Texas. In this experiment, a series of twelve test pits, 3 ft (1 m) wide, 12 ft (4 m) long, and 3 ft (1 m) deep, were excavated and filled with test artifacts. The pits were organized in parallel pairs, with four pairs aligned along a construction road, one pit in each lane of traffic. This arrangement made it possible to place the test artifacts in two different types of backfill material - a fine sand and a silty loam.

An "archaeological site" was constructed in each test pit using 4-in. (10 cm) and 6-in. (15 cm) clay flower pots, 4-in. and 6-in. clay pot trays, artist charcoal sticks, 30-in. long glass rods and a 30-in. (76 cm) long strip of sheet metal. The flower pots were manufactured in the same production batch to minimize differences in the firing and treatment of the pots. Laboratory strength tests indicated that the flower pot sherds

behaved in a similar manner as aboriginal sherds. The placement of pots set the 6-in. pot as a "skull" located in the center of the arrangement, with two "burials" and two "cooking" arrangements in each corner.

The test artifacts were arranged in four replicate test arrangements and buried approximately 36 in. (91 cm), 24 in. (60 cm), and 12 in.(30 cm) below the ground surface. Each test arrangement was rotated 90 degrees between each successive cell, A through D. To facilitate post-excavation analyses of the damages caused by construction loading, each pot was color coded on both the outside and inside. The outside color identified the layer depth and the inside color identified the pot use. The artist charcoal sticks were also color coded using the layer color. Site burial was performed by a Texas Department of Highways Heavy Construction School using conventional construction techniques. All students in the school were experienced Highway Department heavy equipment operators.

A board road was constructed on-site from three crossed layers of 2 x 12 lumber. The 18-in. (46 cm) and 36-in. (92 cm) soil covers were placed using a front end loader to place the cover material without driving directly on the site. A motor grader with the blade extended to the side was used to spread the material. Once an access ramp was constructed, the cover was extended by placing new cover material from the end of the ramp. The cover material was a locally available clay. A motor grader was used to construct a clay road on top of the soil cover which was compacted by the traffic loads. The road was periodically maintained and low spots were refilled to keep the road at the desired grade. A total of 1300 vehicle axle passes were made across the road using loaded and unloaded scrapers, dozers, pick-up trucks, crew bus, rubber tired front end loaders, tractor backhoes, and motor graders.

Following the heavy equipment school, the test sites were excavated by experienced field archaeologists from the Department of Anthropology at Texas A&M University. Damage of each pot was classified for each test cell and averaged to obtain the damage for a specific burial depth, pot orientation, matrix type and protective method. Data from the laboratory analysis can be found in Mathewson and others (1992). The saturated artists charcoal sticks were generally found intact but deformed because the charcoal sticks became very ductile upon saturation. The glass rods buried at shallow depths in unprotected pits were generally found to be broken into as many as five pieces. Rods buried at greater depths in each pit and in the control pits were intact or broken into two pieces. The three-feet (1 m) depth layer was not excavated in the sand-filled pit protected by the board road because no breakage was detected in any of the test artifacts in the two-ft (66 cm) depth layer.

The full-scale field testing also indicates that the controlling factor in breakage is related to the total strain (displacement) rather than the total stress (load). In the field, stronger more brittle pottery tended to fracture more readily than the weaker, water-saturated charcoal sticks that were more ductile.

Compressive breakage of the test artifacts indicates that original depth of burial has a direct controlling effect on the amount of breakage caused by surface loading. The amount of damage to the test pots drops off rapidly with increasing depth of original burial, except in a few rare cases. For example, the average number of broken pieces of the 6-in. diameter "skull" pot in an unprotected site in a silty loam matrix at a one-foot

depth is 28.25, at a two-feet (66 cm) depth is 22.75 and at a three-feet (1 m) depth it is 12.50.

Breakage of the test artifacts appears to be related to both the size and orientation of the artifacts. The 6-in. pot lying on its side experienced more breakage than a similar 4-in. diameter pot. Pots lying on their side are more susceptible to breakage because the pot must carry the entire vertical load rather than transfer it to the matrix material. Pots set vertically, either open upward or inverted, are able to transfer the load to the underlying matrix material and thereby, experience less breakage. In the case of the covered pot, the pot transferred the load by penetrating the underlying matrix and therefore, reducing the total strain on the pot; however, both the pot and the capping lid fractured. The inverted 4 in. pot resting in a 6 in. tray tended to cause greater breakage to the underlying tray by punching a circular hole in the tray because it was not able to penetrate into the underlying matrix. The 4 in. diameter upright pot, filled with matrix material, experienced the least amount of breakage.

The amount of breakage in the more compressible silty loam matrix material was greater than in the less compressible fine sand matrix. Glass rods in the silty loam matrix always showed greater breakage than in the sand matrix, indicating greater differential movement within the silty loam. Compressibility of the matrix appears to be a significant factor in the amount of artifact breakage both in the test pits and in natural burial mounds. The relationship between burial depth and matrix material shows that the amount of breakage is greater in the silty loam than in the sand.

The maximum amount of pot breakage occurred in the unprotected site in all cases. The constructed board road, which spreads the vehicle load over a larger area and does not significantly load the site, provided the best protection against breakage caused by moving construction equipment. Some pot breakage was caused by the construction of the 36-in. thick protective cover. In some cases, greater damage was caused by the construction of the 36-in. control cover than was caused by the cover plus the vehicle loading. Artifact breakage in the sites protected by the 18-in. thick soil cover were generally greater than that in the 36 in. cover control sites and in the 36 in. protected sites.

The field experiments indicate that the breakage of archaeological materials is controlled by the interaction of the original burial depth, the orientation and interrelationship between artifacts, the compressive characteristics of the burial matrix, and the type of protective cover.

MONTAGUE COUNTY CONSTRUCTION LOADING

The Texas Department of Transportation (TXDoT) contracted with the Center for Engineering Geosciences at Texas A&M University to bury two archaeological sites below an engineered fill in Montague County, Texas. Archaeological significance testing was carried out by the Texas Department of Transportation (Price, 1992). The two sites, designated 41MU60 and 41MU62, are located in northeastern Montague County about 300 ft (100m) south of the Red River. The sites have been interpreted to be the remains of single occupations of unknown duration that date from the Late prehistoric II period. A radiocarbon data for site 41MU60 yielded date of AD 1310 +/- 90 while one for site 41MU62 yielded a date of AD 1380 +/- 60.

Site 41MU60 contains bone, shell, charcoal, granular lithics, ceramics, and features that are generally scattered and dispersed throughout the site. Stratigraphic relationships are generally poorly defined, with the upper horizon disturbed by recent human activities. The primary archaeological horizon exists between about 12 and 30 in. (30 -70 cm) below the ground surface. The upper horizon is a plow zone. Part of the site is situated within an agricultural field that has been plowed and the other part is situated below a non-agricultural area containing oaks, brush, and grasses.

The site is located on a nearly level bluff along the south side of the Red River. Bedrock in the area is Permian age mudstones and sandstones, containing some small pebbles, chert, and iron nodules. The soils formed on upland terraces and are generally loams to sandy loams (fine silty-sand to fine sandy-silt). These soils formed in a subhumid, warm-temperate, continental climate, in the southern edge of the Great Plains physiographic region of the United States. Rainfall and potential evapotranspiration are approximately equal. The area is near the southern limit of the grassland mollisols, and is characterized by grassland prairie with hardwoods, and tree lined riparian areas. Some calcium carbonate cementation and nodules are expected because the primary soil forming process in this region is calcification.

Site 41MU62 contains bone, shell, plants/ecofacts, granular lithics, ceramics, and features that are generally scattered and dispersed throughout the site. Stratigraphic relationships are generally poorly defined, with the upper horizon disturbed by recent human activities. The primary archaeological horizon lies between approximately 12 and 50 in. (30 - 125 cm) below the ground surface. Approximately one-half of the site is situated below a short-grass pasture while the other half is situated below a long-grass pasture. A portion of the site was exposed during the construction of a County Road that cuts into the ridge along the northern boundary. This area is known to "pot hunters", who dig for arrow heads and other archaeological components of the site.

The site is located on a low ridge about 10 to 20 ft (3-6m) above the Red River and Broadtree Creek floodplains. Bedrock in the area is Permian age mudstones and sandstones, containing some small pebbles, chert, and iron nodules. The soils formed on upland terraces affected by occasional river flooding and are generally clay-loams to clays (fine silty-clay to clay). These soils formed in a subhumid, warm-temperate, continental climate, in the southern edge of the Great Plains physiographic region of the United States. Rainfall and potential evapotranspiration are approximately equal, however, soil moisture is probably higher than the upland soils because of their higher clay content and lower relative elevation. The area is near the southern limit of the grassland mollisols. These upland/alluvial clay-soils may be mildly expansive in nature (vertisols). The area is characterized by grassland prairie with hardwoods, and tree lined riparian areas. Some calcium carbonate cementation and nodules are expected because the primary soil forming process in this region is calcification. Some soil mottling is expected because poor soil drainage allows anaerobic (reducing) conditions to develop. These anaerobic conditions may explain why plant remains and ecofacts were preserved in this site and not in Site 41MU60.

The design concept of the burial was controlled by the site decay matrix (Mathewson and Gonzalez, 1988; Mathewson, 1989b) which established the desired site conditions to preservation (Figure 1). The site components included bone materials, shell,

SITE CONDITIONS	SITE COMPONENTS: Animal Bones	Shell	Plants, Ecofacts	Charcoal	Crystalline Lithics	Granular Lithics	Ceramics	Features	Soil Attributes	Metals	Context	Isotopic Content
Acidic Environment	A	A	E	N	N	A	N	N	A	A	N	A
Basic Environment	E	E	A	N	N	E	N	N	A	A	N	N
Continuously Dry	E	E	E	E	N	E	N	N	N	E	N	E
Continuously Wet, Anaerobic	E	E	E	A	A	A	A	A	A	A	N	A
Continuously Wet, Aerobic	A	A	A	A	N	A	A	A	A	A	N	A
Cyclic Wet-Dry	A	A	A	A	A	A	A	A	A	A	N	A
Cyclic Freeze-Thaw	A	A	A	A	A	A	A	A	A	N	A	A
Freeze	A	A	A	A	N	A	A	N	E	N	A	E
Thaw	N	N	N	N	N	A	N	N	A	N	A	A
Compression	A	A	A	A	N	N	A	A	A	N	A	N
Movement	N	N	N	A	N	N	N	A	A	N	A	N
Microorganisms	A	N	A	A	N	N	N	N	N	A	A	A
Macroorganisms	A	A	A	A	N	A	N	A	A	N	A	N
Human Intrusion	A	A	A	A	A	A	N	A	A	A	A	A

Notes
E = Condition Enhances Preservation
A = Condition Accelerates Decay
N = Condition is Neutral or Has No Effect
Bold = Existing Site Characteristics

Figure 1. Archaeological site protection matrix for site 41MU60 in Montague County, Texas.

granular lithics, ceramics and features. The site was subjected to cyclic wet-dry and freeze-thaw events, human intrusion and burrowing by organisms.

The burial was designed to direct all surface water away from the site area, prevent ponding and concentration of surface water, reduce freeze-thaw and prevent human and animal intrusion into the site. A schematic section of the burial is shown in Figure 2. Preconstruction engineering analyses indicate that the geogrid and burial would greatly reduce the dynamic traffic loading on the site components (Figure 3). The project specifications for burial included:

- **Site clearing:** limited to spray with a herbicide to kill all vegetation on the site. Trees and large brush to be removed by hand methods. All stumps to be cut flush with the ground surface. Following removal of large vegetation, the site was to be burned in order to remove all remaining surface organic matter.
- **Surface preparation:** placement of sand (limestone screenings) to fill low spots to smooth the surface for construction vehicle traffic and prepare the surface for a geogrid. The screenings to be placed using a small, low ground-pressure dozer. Upon placement, screenings are to be compacted using a pneumatic or non-vibrating steel wheel roller.
- **Geogrid:** hand placed over the entire section to provide lateral strength to the base of the cover material and to mark the top of the original ground surface
- **Limestone protection course:** placed over the geogrid to a minimum thickness of 0.5 ft (15 cm) and compacted using a pneumatic roller. No equipment to be allowed to travel on top of the unprotected geogrid.
- **Fill and Road Section:** local material spread over the site to bring the site up to the design grade with the road surface placed on top.

Site Investigation and Instrumentation

Prior to the final design and implementation of the site burials, a series of field geotechnical tests were run at each site. A portable cone penetrometer, manufactured by Triggs Technology, was used to obtain profiles of soil strength versus depth. These soundings show that the shear strength of the near surface soils are adequate to support the proposed burial against significant deflections. Shelby tube samples were also collected using a TXDoT exploration rig. Samples from the Shelby tubes were tested to determine the consolidation characteristics of the soils.

Following the field investigation, each site was instrumented with three total pressure cells and one total settlement (vertical movement) monitor prior to the placement of any cover material. The sensors were placed on top of the cultural horizon and buried with native soil to detect loading conditions at this level and to provide some protection to the sensors. Vertical loads (pressure) were recorded following both a dynamic and static procedure. Dynamic loads were recorded at a rate of 100 readings/sec for a 5 sec burst in order to obtain the full range of dynamic loads as a test vehicle passed over a selected load cell. Dynamic load readings were made at selected times during the construction period while static loads read at the rate of 1 reading/10 min were monitored throughout the construction process.

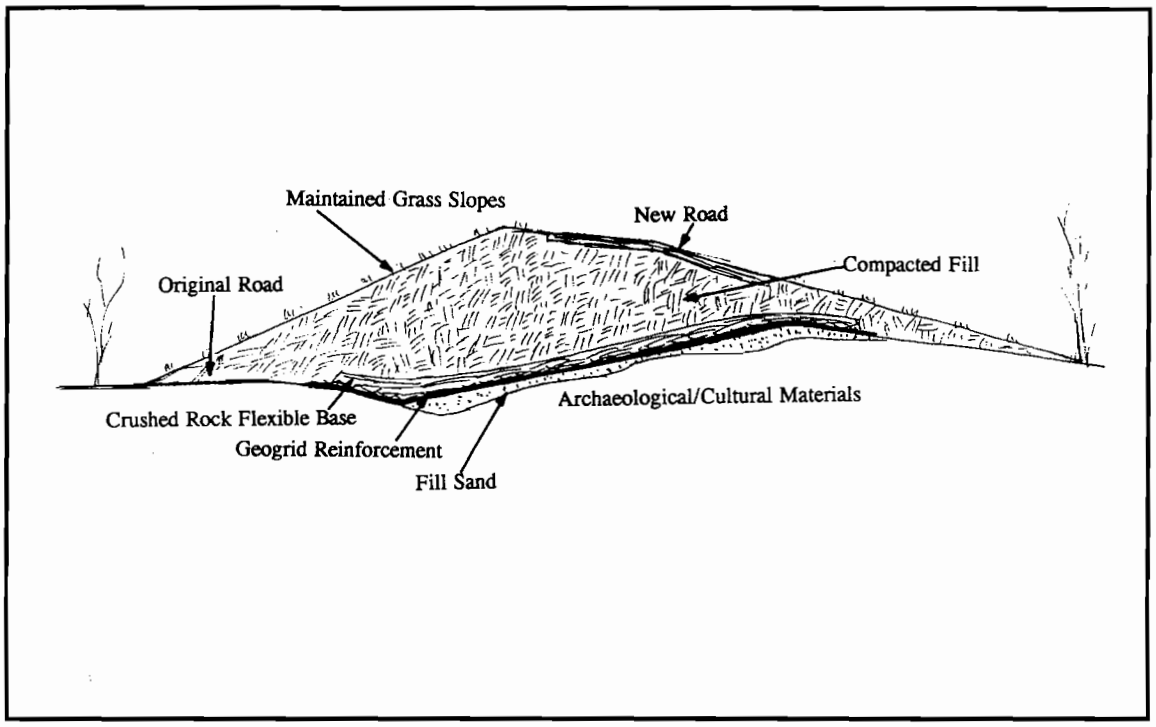

Figure 2. Schematic design of the Montague County, Texas site burial project below a new Farm to Market (FM) road.

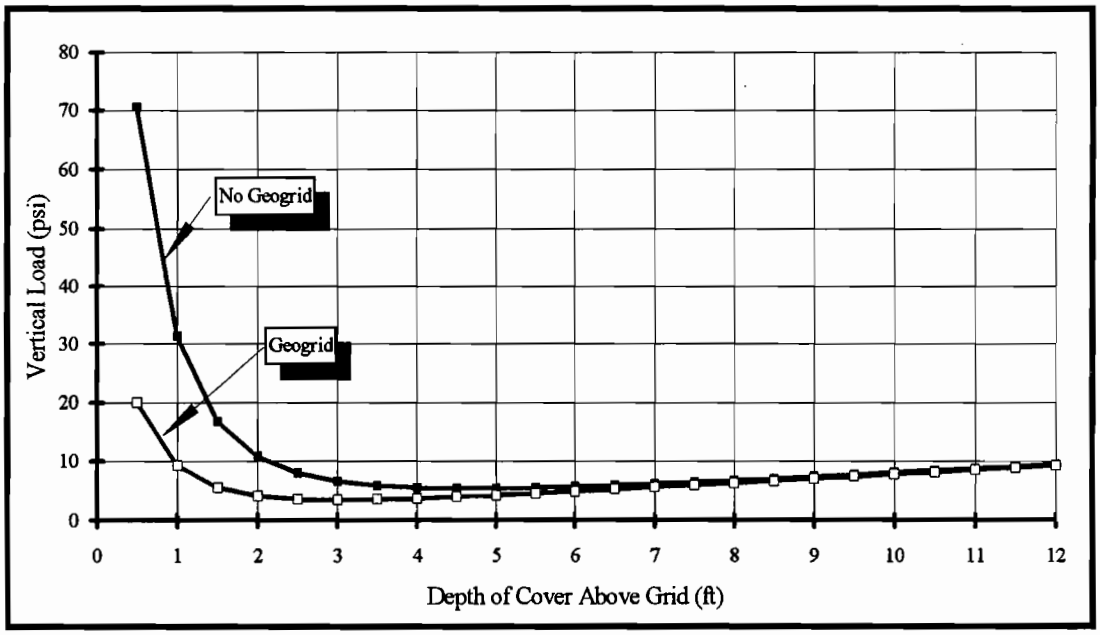

Figure 3. Calculated total load (dead + live) on cultural materials situated below an engineered fill showing the protection gained through the application of a geogrid placed directly on top of the site.

Land uses in the area indicate that the maximum historic loads that the site experienced are related to farm equipment used for pasture management, hay production and a family garden. The depth of the plow horizon was found to be approximately 0.5 ft (15 cm) below the existing ground surface.

A stomping man (Figure 4A) and standing horse and rider generated loads of about 5 to 7 psi at the top of the cultural horizon, 0.5 ft (15 cm) below the surface. At the same depth, a 1/2-ton pickup truck generated a maximum load of about 12 psi, while a John Deere 2950* farm tractor (Figure 4B) generated a load of about 16 psi. These data were used to establish the maximum historic load at 16 psi.

A CAT D4 LGP (Caterpillar D4 low-ground pressure) dozer (Figure 4C) was tested across the load cells to determine its suitability for moving the screenings onto the site. Maximum ground pressures on top of the cultural horizon were within the maximum historic loads. The contractor was authorized to use the LGP dozer for all on-site work with the stipulation that the dozer blade avoid excavating into the cultural horizon. However, loading tests in the laboratory demonstrated that rapid loading caused greater artifact breakage that slow loading. Because the vibratory character of the loading signal generated by the LGP dozer has the potential to cause breakage of artifacts the contractor was also instructed to operate the dozer at 1/2-speed while on the site to minimize the impact loads that cause artifact breakage.

Additional construction equipment can be allowed on the site as soon as the screenings have been placed and smoothed by the LGP dozer, however, speeds must be at a minimum to reduce impact loads on the site. A loaded IH S2500 water truck (Figure 4D) can be allowed on the site to maintain moisture content control necessary to obtain optimum density of the screenings. A CAT 140G motor grader (Figure 4E), 12-yard belly dump hauler (Figure 4F), Ingram 11-5400Q pneumatic roller (Figure 4G) and an Ingersol SD-100D steel wheel roller, not vibrating, (Figure 4HA) can be used over the screenings. The vibrating load generated by the Ingersol steel wheel roller is a "sharp impact" type of load that exceeded the allowable level and can cause significant artifact damage (Figure 4HB).

Once the limestone screenings had been placed and compacted, the geogrid was placed by hand. Because no equipment was allowed to drive directly on top of the geogrid, the D4 LGP dozer was used to push a locally obtained crushed limestone protection coarse over the grid. Once the fill thickness reached 3 ft (1 m), a CAT 815 pad foot compactor was used to compact the fill to TXDoT specifications. At shallower thicknesses, the pneumatic and steel wheel roller was used to obtain desired compaction of the fill. A CAT 973 track loader can be used to transport fill material if the existing fill exceeds 1.5 ft (50 cm) in thickness.

As the thickness of the fill section increases, the dynamic loading associated with passing traffic sharply decreases. Field monitoring supported the calculated load vs. fill thickness (Figure 4) relationship. For example, the dynamic load from the loaded water truck driving on top of the screenings (0.7 ft (21 cm) above the cultural horizon) was

*The use of manufacturer's name and model number is provided to assist in the selection of similar type equipment and does not reflect endorsement by TXDoT or TAMU.

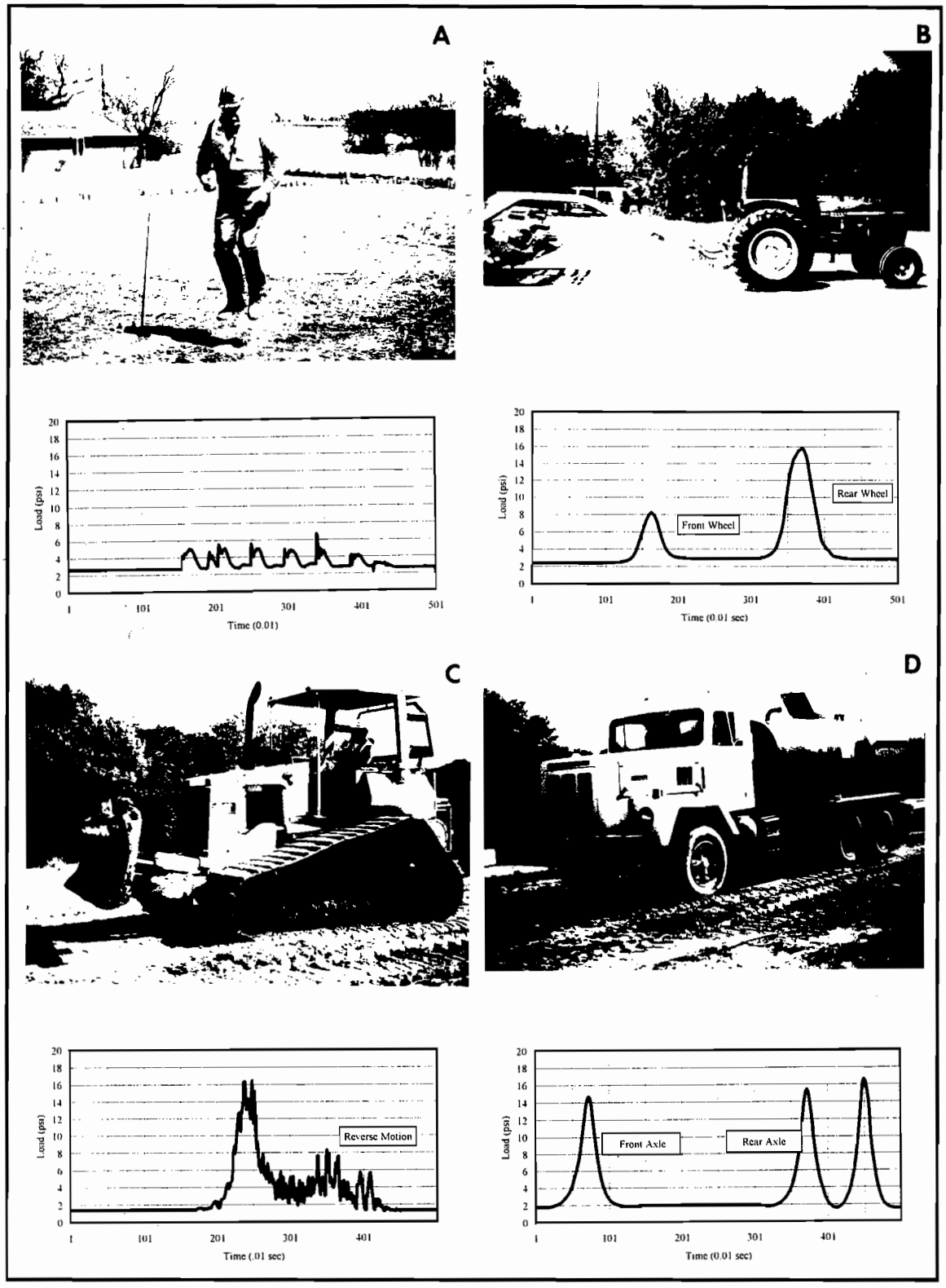

Figure 4. Dynamic loads generated by various sources operating about 0.5 ft above the load cell.

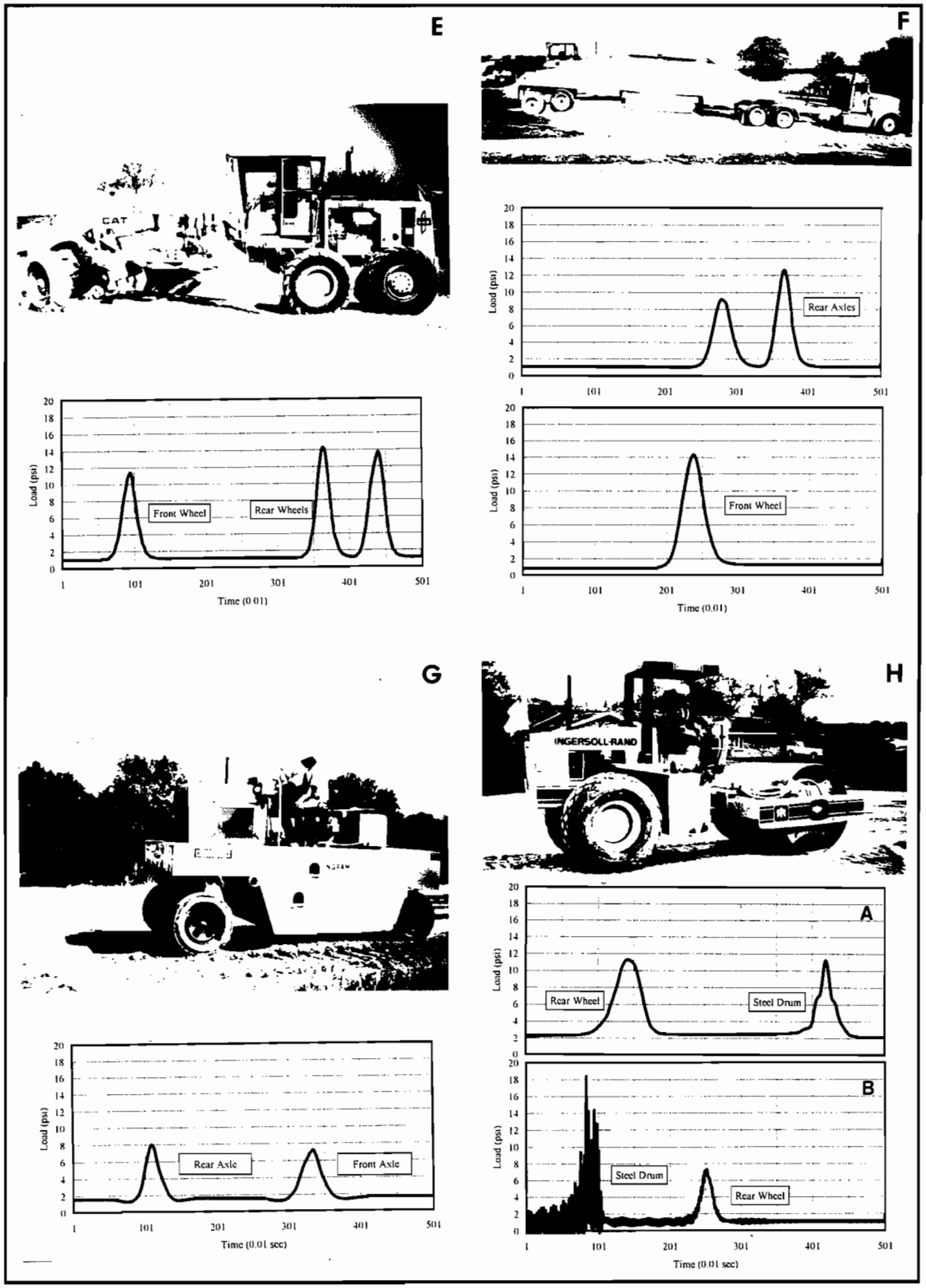

Figure 4 continued.

approximately 15 psi. The load of the water truck decreases to about 2 psi when the fill is about 3 ft (1 m) thick and to less than 1 psi at a fill thickness of 7 ft (2.3 m).

EFFECTS OF BURIAL ON A SITE

Archaeological sites are a complex system of geographic, stratigraphic, and ethnographic relationships that are over-printed with a mixture of different archaeological materials. Each site is, in turn, preserved within a unique physical, biological, and chemical environment. A change in the physical, biological, or chemical environment of a site induced through burial may result in the enhanced preservation or accelerated decay of the site components.

Burial can be used as an effective site preservation technique. However, burial will effect the site in both beneficial and deleterious ways, as follows:

- Burial will increase the vertical load on archaeological sites.
- Artifact breakage decreases as the depth of burial increases.
- Artifacts that are oriented in such a manner that they can transfer the compressive load to the matrix are less susceptible to breakage.
- Artifacts that are in contact with other artifacts are more susceptible to breakage.
- As the matrix material becomes more compressible, the amount of artifact breakage increases.
- Protective covers that minimize the amount of differential strain on the buried artifacts will provide greater protection than those that cause or allow the transfer of strain downward.
- Burial limits site erosion and reduces the rate of near-surface weathering of archaeological materials.
- Burial will reduce the impact of microorganisms and burrowing macroorganisms on archaeological sites.
- Burial will usually increase the moisture content of the soil matrix.
- Burial can induce a limited change in the pH of the soil matrix.
- Burial of a site limits the deleterious effects of freeze-thaw and wet-dry cycles, the two most damaging natural agents to archaeological sites.
- Burial of a site reduces the amount of vertical strain (displacement) related to construction equipment loading.
- Burial reduces the significance of dynamic loading from vehicular traffic.
- Burial projects can be constructed using conventional construction techniques and methods if care is exercised in equipment selection and operation.

ACKNOWLEDGEMENTS

This study was supported through an interagency agreement between the Texas Department of Transportation (TXDoT) in Austin, TX and the Center for Engineering Geosciences at Texas A&M University. The authors express their appreciation for the cooperation and assistance provided by Leiland L. Jett, P.E., and John Barton, P.E., Supervising Resident Engineers, Wichita Falls District of the TXDoT, Bowie Office; George Mayfield, Project Engineer and his supervisors and crew of Garey Construction,

Austin, TX.. We especially appreciate the interest and assistance provided by the project's neighbors Jennifer Gaston, Steve Paschall and Kevin Haralson.

REFERENCES

Garfinkel, A.P.; Lister, B.L.; and Boost, A., 1983, *Effects of High Embankment Construction on Archaeological Materials*: California Department of Highways, Construction Division, Sacramento, CA, 84 p.

Gonzalez, Tania, 1989, *Study of Soils Buried Under Embankments to Determine the Potential for Burial as a Preservation Technique for Archaeological Sites*: unpublished Master of Science thesis, Texas A&M University, College Station, TX, 331 p.

Mathewson, Christopher C., 1989a, Introduction to the Workshop and the Concept of a Site Decay Model: in Mathewson, C.C. (editor), *An Interdisciplinary Workshop on the Physical-Chemical-Biological Processes Affecting Archaeological Sites to Develop and Archaeological Site Decay Model*: Technical Report EL-89-1 for the U.S. Army Engineer Waterways Experiment Station, Vicksburg, MS, 238 p.

Mathewson, Christopher C., 1989b, Logic-Based Qualitative Site Decay Model for the Preservation of Archaeological Sites: in Mathewson, C.C. (editor), *An Interdisciplinary Workshop on the Physical-Chemical-Biological Processes Affecting Archaeological Sites to Develop an Archaeological Site Decay Model*: Technical Report EL-89-1 for the U.S. Army Corps of Engineer, Waterways Experiment Station, Vicksburg, MS, pp. 227-238.

Mathewson, Christopher C. and Gonzalez, Tania, 1988, Burial of Archaeological Sites for Protection and Preservation: in Proceedings, *24th Annual Symposium on Engineering Geology and Soils Engineering*: University of Idaho Press, Coeur d'Alene, ID, pp. 443-452.

Mathewson, Christopher C.; Gonzalez, Tania; and Eblen James S., 1992, *Burial as a Method of Archaeological Site Protection*, Contract Report EL-92-1: US Army Engineer Waterways Experiment Station, Vicksburg, MS, 125 p.

Moratto, J.C., 1977, Research Prospects: New Melones Archaeological Project: in Schiffer, M.B. and Gumerman, G.J. (editors), *Conservation Archaeology: A Guide for Cultural Resource Management Studies*: Academic Press, New York, NY, pp. 401-411.

Olson, R.J., 1989, *Soil-Structure Interaction Testing for Assessing the Impact of Pipe Lying Operations at the Kauffman II Archaeological Site*: unpublished report prepared for Texas Eastern Gas Pipeline Company by Battelle, Columbus Division, Columbus, OH, 35 p.

Olson, R.J.; Guerrieri, D.A.; and Jones, D.J., 1988, *The Impact of Pipe Lying Operations on the Kauffman II Archaeological Site*: unpublished report prepared for Texas Eastern Gas Pipeline Company by Battelle, Columbus Division, Columbus, OH, 24 p.

Price, Dennis G. R., 1992, *Archaeological Significance Testing at Sites 41MU60, 41MU61, 41MU62 and 41MU63 Montague County, Texas*: Texas Department of Transportation, Division of Highway Design, Austin, TX, 6 Sections.

Skinner, Shanne M., 1989, *Experimental Study to Assess the Effects of Compaction and Pressure on Artifacts in Archaeological Sites*: unpublished report prepared for Texas Eastern Gas Pipeline Company by Archaeological Services Consultants, Inc., Columbus, OH, 25 p.

TOMOGRAPHY APPLIED TO GEOTECHNICAL ENGINEERING PROBLEMS

by

Hector E. Marin, Ph.D.[1], Howard A. Spellman, Jr.[2] and Dean Alford[3]

Abstract

The inversion of boundary measurements to establish mechanical, electrical, chemical or thermal parameters within a media is an extremely powerful approach in the evaluation of geotechnical systems. While tomographic imaging offers unique capabilities in the evaluation of these systems, limitations must be recognized in their application and interpretation. A review of some fundamental aspects of geotomography is presented, followed by a brief discussion of two field cases in which the application of tomography could help the engineer define the magnitude and extent of the problem at hand. The cases presented are: (1) identification of the source(s) causing differential foundation settlement at an existing parabolic antenna in Spain, and (2) delineating limits and extent of dissolved phase groundwater contaminant at a transportation site in Las Vegas.

INTRODUCTION

Geotomography (tomography applied to geotechnical engineering) is most often based on wave propagation data, such as time, attenuation, or full-time series. Collected data from transmission (e.g., cross-hole) and reflection (e.g., from surface or from single borehole) may be used in tomographic inversion. Given an object, a "projection" is the manifestation of the object on an observation plane. Projections are composed of multiple-path integrals of the field of a specific parameter measured at boundaries of the unknown region. The basic goal of tomography is to reconstruct the object by inverting its projections, i.e., "back-projecting" boundary measurements onto the unknown space. Tomography is a special case of the more general problem of inverting measurements. The inversion of boundary measurements to determine the field of a chemical, electrical, thermal or mechanical parameter within the body is an extremely powerful approach in the study of geotechnical systems. The following discussion is an introduction to the fundamental aspects of tomographic inversion, to highlight issues related to its implementation in near-surface geotechnical applications. While emphasis is perhaps

[1]Senior staff engineer, Converse Consultants West, Pasadena, California.

[2]Consulting Geologist, 1236 Oakglen Avenue, Arcadia, California 91006.

[3]Project hydrogeologist, Converse Consultants Southwest, Las Vegas, Nevada.

placed on mechanical waves and the unique aspects of propagation in soil/fractured rock media, the same reconstruction algorithms are used if electromagnetic waves are applied to illuminate the unknown region, Santamarina (undated). The acoustic wave equation, as applied to cross-hole tomography, is presented by Pratt and Worthington (1990). The inversion of wave-based measurements involves input signals applied onto the boundary of the system under study and output signals which are recorded at other boundary locations. Field parameters like wave velocity within the unknown region can be obtained by subsequent forward simulations or by formal mathematical inversion. Often the solution is not unique, and strongly depends on assumptions made, such as constitutive behavior of the material or the model of energy propagation used.

PROPAGATION OF WAVES IN SOIL/FRACTURED ROCK MEDIA

Tomography is the coherent display of multiple planes or slices of a body. While computerized tomographic inversion, which started early in the 1970s, found immediate applications in the fields of medicine and geology, geotechnical tomography faces inherent restrictions which are not encountered in medical or laboratory applications. The limitations include wave propagation (diffraction, anisotropy, heterogeneity), equipment customization to every field situation, field dependency of transducer performance, and limited projection angles. In addition, there are unique applications of geotomography that require special considerations, namely, the use of tomography in monitoring evolution of geotechnical processes. Such processes involve variations in the state of stress near the failure surface of a sliding mass or the movement of contaminants across a porous media.

It is important to recognize that the performance of most geotechnical systems is often determined by the global variability of governing parameters rather than by the exact value of a parameter at a given point (e.g., failure, deformation, seepage, diffusion, etc.). Consequently, most field situations require the imaging of significant anomalies, clearly contrasting discontinuities of sizeable inclusions. The requirements of high resolution images for these inclusions can be somewhat relaxed.

Materials and geometrical characteristics of the medium affect wave propagation. Therefore, it is important to understand wave propagation and wave-material interaction to adequately invert measured data to interpret tomographic images. Some of the most relevant parameters affecting geotomography, as summarized by Santamarina (undated), are briefly discussed below.

Velocity: Characteristic parameters such as strength, stiffness, dilatancy and brittleness are conditioned by the state of stress within geomaterials. This is particularly the case in soils and fractured rock. From a wave propagation perspective, the state of stress affects velocity, attenuation, heterogeneity, and anisotropy. Several correlations have been proposed between the effective mean confining stress and (1) maximum shear modulus, (2) shear wave and (3) compressional velocities. However, laboratory experiments in the '70s and '80s showed that the propagation of P-waves depends primarily on the stress along the direction of propagation, and that the propagation of the S-waves is conditioned by the stresses on the polarization plane, i.e., the stress in the direction of propagation and the stress in the direction of particle motion.

Attenuation: In addition to geometric attenuation due to geometric characteristics of the medium, there are also internal energy losses within the material. Under isotropic conditions, the higher the stress the lower the attenuation. The strain level also affects attenuation, whereby the higher the amplitude of the perturbation, the higher the attenuation.

Vertical Heterogeneity: The stress-dependency of wave propagation in particulate media, and the geostatic state of stress combine to produce vertically heterogeneous profiles, where velocity increases and attenuation decreases with depth. Vertical heterogeneity modifies spherical wave fronts, elongating them towards increasing depth. When rays are drawn, normal to the wave fronts, ray bending is observed. This effect is particularly significant in horizontal shots (e.g., cross-hole) and when the ratio of the depth to the length of the ray is low.

Anisotropy: Mechanical anisotropy depends on the fabric of the material as characterized by a polar histogram of contact normals, and stress anisotropy which is manifested in polar diagrams of normal and tangential contact forces. Both anisotropy components affect wave propagation. Wave propagation in anisotropic media is complex: energy in shear waves splits, the ray direction is given by the direction of energy transport, the ray is not perpendicular to the wave front (quasi P- or S-waves), and the ray direction does not necessarily remain in the plane. Anisotropy alone does not lead to curved ray paths, however anisotropy couples with vertical heterogeneity to deviate rays from the simplest straight path condition. In a given set of data, such as cross-hole travel times, it is difficult to separate the effect of anisotropy from vertical heterogeneity. If inversion is implemented assuming isotropic cells, anisotropy will manifest itself by enhancing the rate of vertical heterogeneity. Anisotropy applies both to velocity and attenuation. Attenuation is highly affected by stress ratio.

Reflection and Refraction: At the interface between two materials with different impedance (material density times velocity) part of the energy is transmitted and part of the energy is reflected. Furthermore, if materials have shear rigidity, mode conversion takes place: incident P-waves are reflected and refracted as P- and S-waves; the same occurs with the S-wave component normal to the interface. Generalized Snell's Laws, Potts and Santamarina (1993), characterize the effect of interfaces, and are often used in combination with algebraic tomographic inversions.

Ray Assumption: Interaction of waves with inclusions depends primarily on the size of the inclusion with respect to the wavelength. The ray assumption applies when the inclusion is much, much larger than the wavelength. Specifically, ray tomography is applicable when the scale length of the anomaly is at least the radius of the first Fresnel zone; Cerveny and Soares (1992). As an extension of X-ray tomographic imaging in medical applications, the straight ray assumption has dominated the development of geotechnical tomography in the recent past. From optics, the straight ray approximation applies if (1) the travel length is much larger than the wavelength and (2) if the wavelength is significantly smaller than the size of the anomaly, and (3) if velocity changes are less than 20 to 30 percent.

Diffraction: When the size of inclusions is within the same order of magnitude as the wavelength, the ray approximation does not hold, and propagation must be considered from the point of view of the wave front and scattered energy. Diffraction degrades the quality of tomograms when the linear ray assumption is made: low velocity inclusions are imaged smaller than real size, while high-velocity anomalies are imaged larger. Low-velocity anomalies are more sensitive to diffraction than high-velocity ones, and their detection becomes difficult when the plane of receivers is located about twice the diameter of the inclusion away from it. Diffraction is significant in tomographic inversions in geotechnical engineering because sources of mechanical waves in soils produce signals with relative low-frequency content, Potts and Santamarina (1993).

Fresnel's Ellipse: The position of scatterers that affect wave arrival at the source is related to the wavelength. Indeed, waves scattered from diffractors within an ellipse, so that the travel distance (the sum of the distances from a point on the ellipse to both focal points) is smaller than the straight distance between focal points plus one-fourth or one-half of the wavelength, will arrive in phase with the direct wave travelling the straight path between focal points. This observation is relevant in selecting ray-tracing algorithms (often a thick ray assumption is used; Qin, Cai, and Schuster (1994)), and in selecting source and receiver configurations: transducers too close together do not necessarily add information content.

DISTRIBUTION OF INFORMATION CONTENT

A very simple case in which all boundaries of the unknown region are accessible is portrayed in Figure 1. The square region is discretized into four subregions or pixels, and two sources/receivers are located on each of the four boundaries. Assuming straight ray propagation, each pixel is defined by segments of several ray paths (lines between sources and receivers). However, the geometric distribution of sources and receivers results in uneven distribution of information content within each pixel, and therefore the unknown region. In geotechnical practice, access to all boundaries is usually limited, i.e., cross-hole or down-hole setups. Referring back to Figure 1, a cross-hole setup that includes the ground surface and two boreholes as boundaries (three instead of four boundaries) would show a reduction of information content for all four pixels, but particularly for the two next to the boundary (bottom) where sources/receivers are missing. Therefore, most applications will have areas within the region which may be overdetermined (abundant information) and areas which are underdetermined (lack of information). Different field setups will also have a wide range of information content for a given cross-section. In standard cross-hole tomographic measurements, the information content is highest at the center. Anomalies within this area have the highest probability of being detected. The distribution of information content very strongly affects the resulting images generated by inversion algorithms.

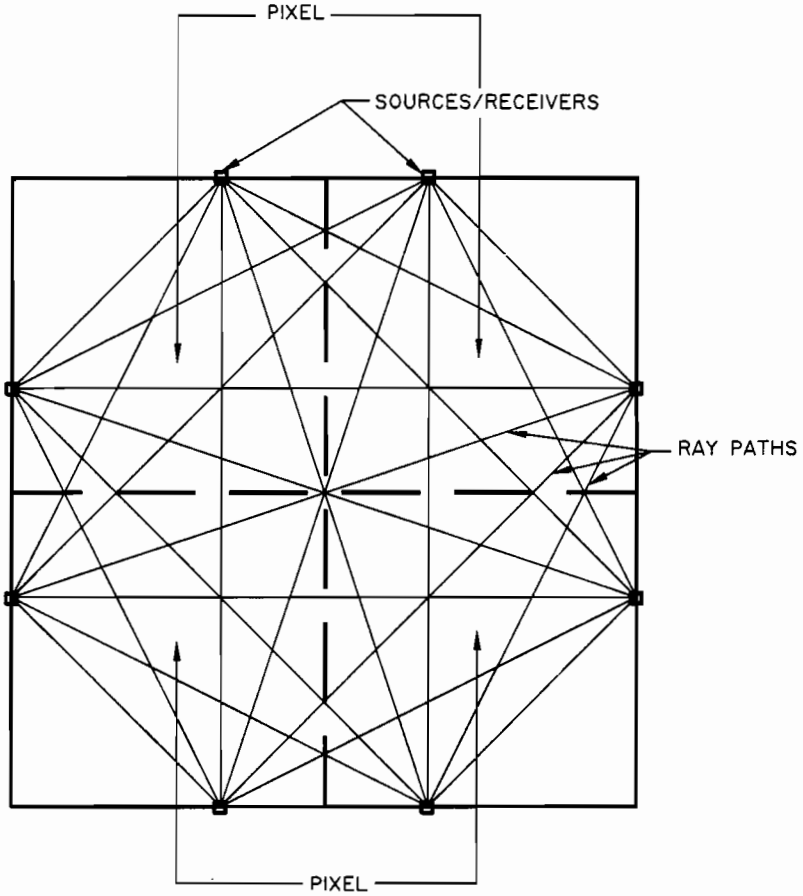

Figure 1. Discretization of space and information content.

Wave measurements based on travel times obtained by generating input signals applied onto the boundaries of the system being studied and collecting output signals which are recorded at other boundary locations, allow for field parameters like wave velocities within the unknown region to be obtained either by forward simulation or by formal mathematical inversion. Tomographic imaging based on wave propagation models will not necessarily produce a unique solution. Factors that may reduce the quality of inversions and increase the possibility of non-uniqueness of the solution include: (1) the model assumed for wave propagation, (2) the constitutive behavior of the material, (3) the wave-material interaction, and (4) errors in the data.

THEORETICAL DEVELOPMENTS IN TOMOGRAPHIC INVERSION

While several tomographic inversion techniques have been established already, new and more powerful approaches, coupled with smoothing and filtering techniques to enhance imagery, are still being developed today. Classical inversion approaches, including matrix-based methods, iterative algorithms, and transform methods, are described by Santamarina (undated). The range of validity for an analytical generalized inverse associated with one-dimensional vertical seismic profiles (VSP) or common depth

point (CDP) travel time equations is presented by Schuster, Johnson, and Trentman (1988). An iterative procedure involving two-dimensional velocity estimation followed by reflection point migration to model the velocity field and reflector locations from seismic reflection data is presented by Dyer and Worthington (1988). A wave equation travel time inversion procedure is presented by Luo and Schuster (1991). Cross-well imaging by seismic travel time and wave form inversion is presented by Zhou et al. (1993). The theory of a wave path eikonal travel time inversion is presented by Schuster and Quintus-Bosz (1993). A non-linear iterative inversion method to first arrival travel times from refraction seismic data, referred to as Turning Ray tomography, is presented by Qin, Cai, and Schuster (1994).

DISCUSSION

While tomography is a powerful approach in the study of geotechnical systems, the analyst must recognize the limitations involved when interpreting tomographic images. As presented earlier, geotomography, by nature, faces restrictions that include wave propagation, limited projection angles (accessibility), equipment customization to every field situation, and dependency of equipment performance in the field. An inadequate wave propagation model results in model error. For example, anisotropy, vertical heterogeneity, reflection, refraction, and diffraction deviate from the assumptions made for simple straight ray models. On the other hand, measurement errors add additional unwanted "noise". Under these conditions, the quality of the inversion degrades, and the probability of a non-unique solution increases (e.g., blurring of reconstructed images, size and location of inclusions and anomalies). Some mathematical algorithms used in geotomography do not converge to a unique solution as a result of data errors; Qin, Cai and Schuster (1994).

The geometric distribution of transducers results in uneven distribution of information content within the unknown region. While information from all possible directions is desirable, access limitations are usually the norm in geotechnical field applications. As a result, most problems will have regions which will be overdetermined (high concentration of data) and regions which will be undetermined (low concentration of data) by the information collected in the field. The distribution of information content strongly affects the resulting tomographic image.

It is emphasized that material and geometrical characteristics of the medium under analysis affect wave propagation. It is important to understand wave propagation and wave-material interaction to adequately invert measured data to interpret tomographic images. However, it should be kept in mind that most geotechnical processes are often determined by global variability of governing parameters as opposed to the exact value of a parameter at a given point (e.g., failure surface in a slope, loose or soft soil pockets under foundations, seepage through an earth dam, location and extent of underground spills). For this reason, most field situations require imaging of significant anomalies, for which the requirements of high resolution images can be somewhat relaxed.

POTENTIAL APPLICATION OF TOMOGRAPHY FOR THE SOLUTION OF GEOTECHNICAL ENGINEERING PROBLEMS

Example 1: This example presents a scenario where shallow subsurface tomography could be very useful in identifying the source(s) causing differential foundation settlement at an existing parabolic antenna located in the southern part of central Spain, west of the Sierra de Guadarrama. The materials which compose this region may be defined as granitic rocks which form a continuous batholithic mass extending throughout most of the area. Inclusions of metamorphic rocks are also found in the granitic rock.

The parabolic antenna rests on a steel frame structure supported by a concrete ring foundation. The ring foundation is approximately 21 meters in diameter and extends down to a depth of about 3 meters below existing grade. The total weight of the antenna structure is estimated at 2500 kips with a maximum moment of approximately 900 kip-feet and a maximum shear load of 160 kips. The water table is at the bottom of the foundation system, 3 meters below existing ground surface. Figure 2 shows the parabolic antenna. The purpose of the tomographic imaging techniques would be to (1) define pockets of loose or disturbed soils directly under the ring foundation supporting the antenna, (2) define the thickness and depth of decomposed rock materials underlying the soils, and (3) detect sizeable cracks and joints within the competent rock underneath. The ultimate goal would be to efficiently define areas where grout could be injected in order to reduce the potential for additional differential settlement of the foundation.

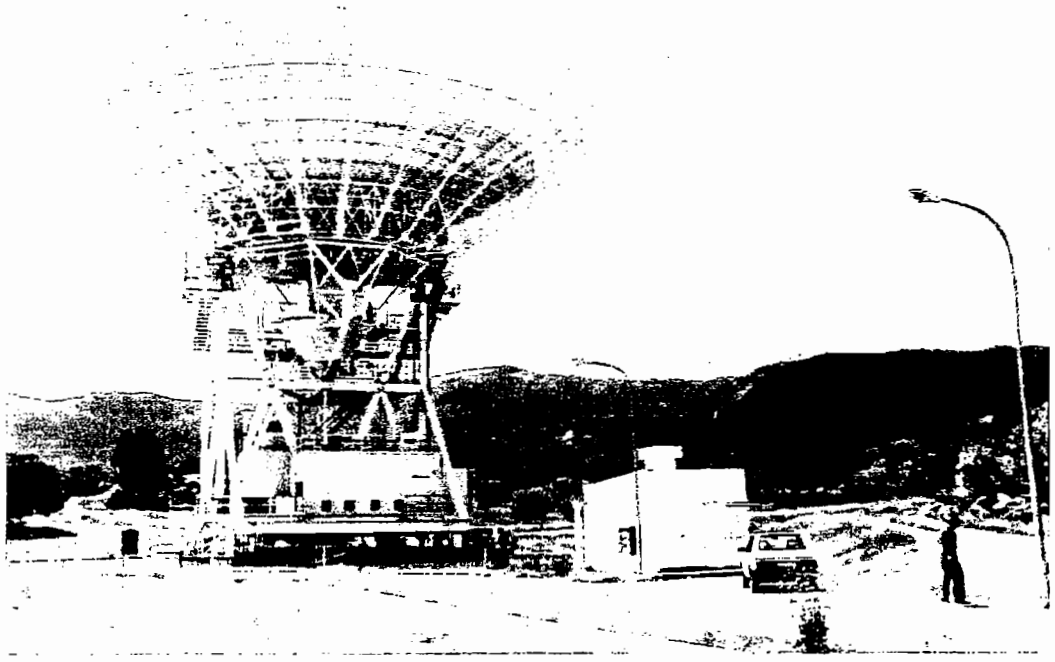

Figure 2. Parabolic antenna in Spain.

Gathering field information from the area within the ring foundation at the site would pose a difficult problem. Data for the tomographic inversion of the materials supporting the antenna foundation system would have to be collected at depths greater than 3 meters, under submerged conditions, and from areas that may exclude the interior of the ring foundation. However, cross-hole measurements underneath the foundation ring could be possible and meaningful if a polygon pattern approximating the centerline of the ring foundation is performed. The pattern is shown on Figure 3. The boreholes, which would be used to place the sources and the receivers at various depths would be located at the vertices of the selected polygon.

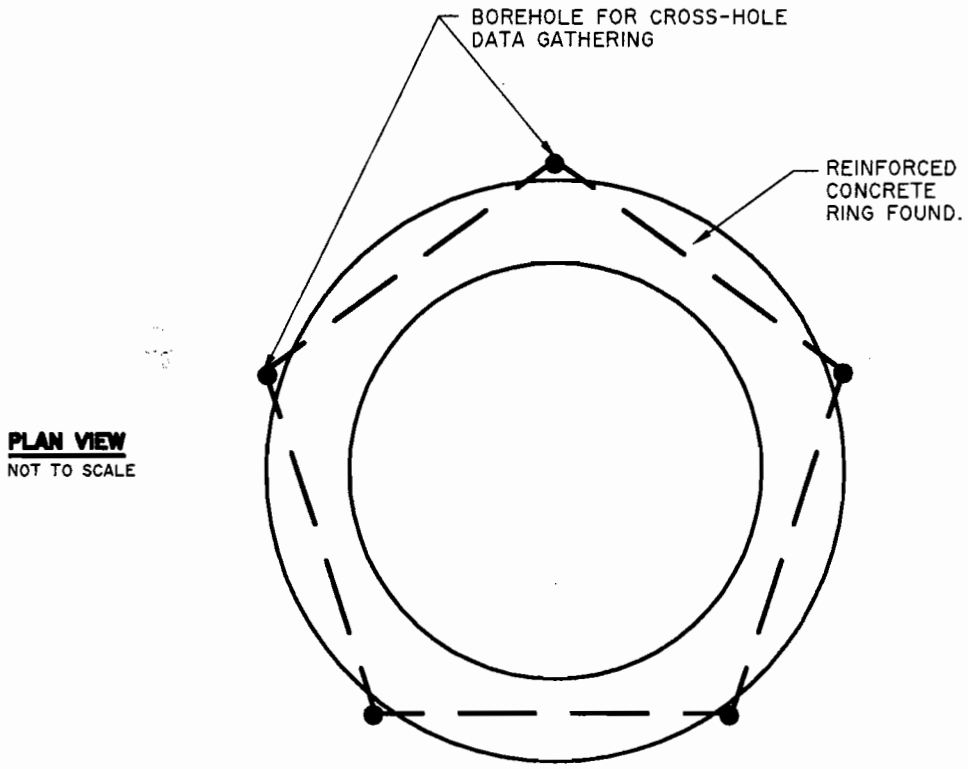

Figure 3. Polygon pattern for cross-hole data gathering.

Provided that pertinent and meaningful field data can be obtained for each side (vertical slice of the foundation materials) of the polygon described above, tomographic imagery would provide valuable qualitative information as to (1) the difference in relative densities of subsurface soils under the ring foundation, (2) the extent and limits of decomposed and competent granitic rocks, and (3) some of the significant fracture patterns within the rock mass. This information can then be evaluated and used for subsequent remedial recommendations to mitigate and even correct the differential settlement problem.

Example 2: This project consists of the delineation of the limits and extent of Volatile Organic Compound (VOC) and organic solvent contaminants in groundwater at the project site for subsequent soil and groundwater restoration. The project site is one of four fueling and maintenance facilities in the Las Vegas Valley. Over 150 school buses and several hundred additional vehicles use the facility. The project was initiated with the removal of six underground storage tanks (USTs) containing gasoline, diesel motor fuels, and lubricating oil (Figure 4). Upon removal of the USTs, extensive contamination of subsurface soils and groundwater were encountered.

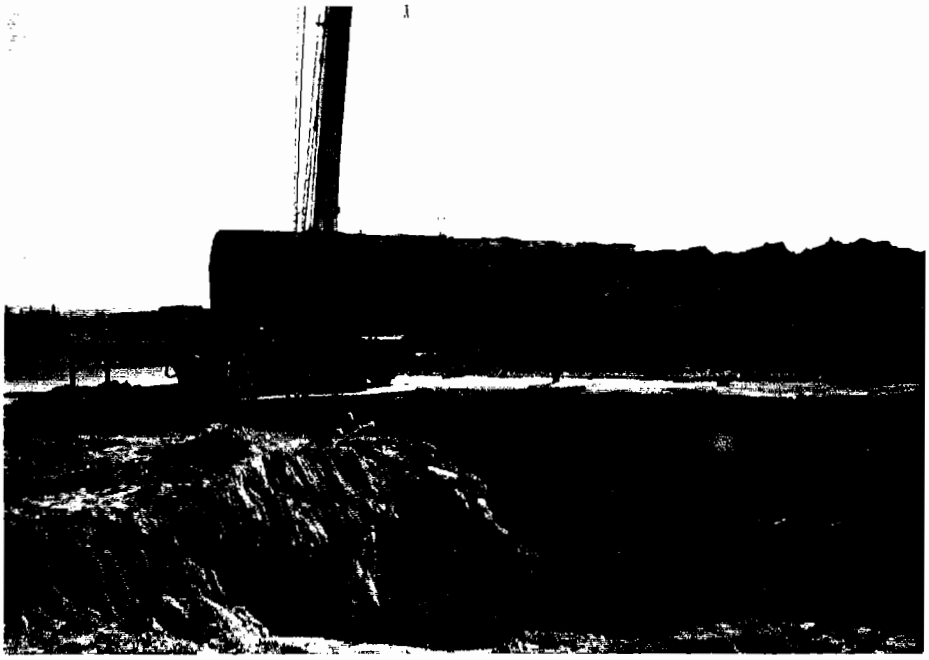

Figure 4. Underground contamination.

Site evaluation consisted of using several techniques, some of which could be used for tomographic inversion. Techniques included subsurface exploration via monitor well drilling, a soil gas survey, ground-penetrating radar, well sampling to evaluate chemical characteristics, aquifer testing, air injection (sparge) testing, and two-dimensional predictive numerical groundwater modeling.

The purpose of evaluation activities were two-fold. First, the limits and extent of subsurface contaminants in groundwater and soils required delineation for evaluation of threats to human health and the environment. Second, assessment of subsurface characteristics of impacted media were required such that a practical and effective approach to site restoration could be developed.

Two-dimensional modeling using FLOWPATH code and site-specific parameters estimated particle travel times, and allowed prediction of future contaminant migration over defined time frames. Potential impacts to adjacent sites and down-gradient

receptors were predicted from aquifer parameters and contaminant characteristics. Steady-state models allowed transient-state modeling to evaluate optimal placement of in-situ and ex-situ remedial systems.

Correlation of data acquired, defining specific and unique site parameters, allowed for the development of a two-dimensional model of subsurface contaminant distribution. The application of invertive tomographic techniques would provide a three-dimensional view of contaminant fields, allowing optimal design, selection and placement of treatment systems for site restoration.

Addition of geophysical techniques to further define site-specific characteristics could allow utilization of geotomographic techniques. Unknown regions within the tomographic "space" could be illuminated by reconstructive algorithms for propagation of contaminant particles in porous media defined from field evaluative techniques. Resistivity, ground-penetrating radar and cross-hole wave propagation data defined for a given area within the contaminant plume could be used to evaluate non-illuminated regions.

SUMMARY AND CONCLUSIONS

Tomography is a powerful approach and useful tool available to the engineer for the study of geotechnical systems. Geotomography based on measured travel times of mechanically-induced waves within a soil media is affected by heterogeneity, anisotropy, and diffraction, which in turn affect wave propagation. Data errors and the model assumed for wave propagation play a major role in the quality of inversions, and increase the non-uniqueness of a solution. Therefore, the nature of wave-material interaction must be recognized by the user when interpreting tomographic images.

Since geotechnical systems are often determined by global variability of governing parameters as opposed to exact values of the parameters at a given point, the requirements of high resolution images can be relaxed.

Finally, as discussed in the examples, the application of tomographic imaging could allow the user unique capabilities for the evaluation of mechanical and geochemical processes that exist or take place underground, provided that pertinent and meaningful field data is collected and an appropriate wave propagation model is used.

ACKNOWLEDGMENTS

The authors would like to thank Messrs. Anthony Riewe and Ben Salduda at the Jet Propulsion Laboratory in Pasadena, and to the Clark County School District in Las Vegas for allowing the presentation of the antenna site and the fueling station site as examples. The authors would also like to thank Dr. J. C. Santamarina at the University of Waterloo, and Dr. G. Schuster at the University of Utah for their valuable information and insight as to tomographic inversion applied to engineering problems.

REFERENCES

CERVENY, V., AND SOARES, J., 1992, Fresnel Volume Ray Tracing: Geophysics, 57, 902-915.

DYER, B.C., AND WORTHINGTON, M. H., 1988, Seismic Reflection Tomography: A Case Study; First Break, Vol. 6, No. 11, 354-366.

LUO, Y., AND SCHUSTER, G.T., 1991, Wave-equation Traveltime Inversion: Geophysics, Vol. 56, No. 5, 645-653.

POTTS, B.D., AND SANTAMARINA, J.C., 1993, Geotechnical Tomography: The Effects of Diffraction, ASTM Geotechnical Testing Journal, Vol. 16, No. 4, 510-517.

PRATT, G., AND WORTHINGTON, M., 1990, Inverse Theory Applied to Multisource Crosshole Tomography. Part 1: Acoustic Wave Equation Method: Geophys. Prosp. 38, 287-310.

QIN, F., CAI, W., AND SCHUSTER, G., 1994, Turning Ray Tomography, unpublished.

QUIN, F., LUO, Y., OLSEN, K. CAI, W. AND SCHUSTER, G., 1992, Finite-difference Solution of the Eikonal Equation: Geophysics, 57, 478-487.

SANTAMARINA, J.C., undated, Tomographic Inversion in Geotechnical Engineering, University of Waterloo, Ontario. Report submitted to the National Science Foundation.

SCHUSTER, G., JOHNSON, D.P., AND TRENTMAN, D.J., 1988, Numerical Verification and Extension of an Analytic Generalized Inverse for Common-depth-point and Vertical-seismic-profile Traveltime Equations: Geophysics, 53, 326-333.

SCHUSTER, G., AND QUINTUS-BOSZ, A., 1993, Wavepath Eikonal Traveltime Inversion: Theory, Geophysics, Vol. 58, No. 9, 1314-1323.

ZHOU, C., CAI, W., LUO, Y., SCHUSTER, G., AND HASSANZADEH, S., 1993, High-resolution Cross-well Imaging by Seismic Traveltime + Waveform Inversion: The Leading Edge, 988-991.

ABSTRACT

"CONSTRUCTION OF THE MEEKS CABIN DAM CUT OFF WALL"

31st Annual Geological & Geotechnical Symposium
Utah State University, Logan, Utah
March 30, 1995

Michael A. Pagano, P.E., President, Bauer of America
Beate Pasche, Project Manager, Bauer of America

The Meeks Cabin Dam was constructed in 1971 by the Bureau of Reclamation as an irrigation and flood control structure. The 170 foot high earth fill embankment spans 3200 feet across the valley on the upper reaches of the Black Fork River approximately 30 miles south of Ft. Bridger, Wyoming in the SW corner of the state. The crest elevation is at approximately 8700 feet. The structure was founded upon a moraine deposit formed by the glaciation of the Uinta Mountians to the South. These moraine deposits contain various layers of sand, gravel, cobbles, and boulders consisting of hard Quartzite with compressive strengths in excess of 40,000 psi. The moraine deposits below the dam embankment material are subclassified as an impermeable glacial till and permeable outwash materials.

Seepage through the outwash materials below the western abutment of the dam embankment had posed a serious threat to the stability of the dam itself. In order to ameliorate the potential risk, The Bureau of Reclamation, Upper Colorado Region, advertised in September 1992, a contract to construct a plastic concrete cut off wall through the dam embankment & moraine deposits. Bauer of America was awarded this project in July 1993.

The project scope included excavating a 36" wide trench 170 feet in depth, 825 feet in length through the West abutment of the dam. The excavated trench was to be backfilled with a plastic concrete material to form a low permeability barrier that would mitigate the seepage problem. The plastic concrete backfill material was chosen for its known and controllable permeability characteristics as well as its ability to remain flexible during movements such as imposed by a seismic event.

The project was particularly challenging for a number of reasons. First, the working platform at the dam crest and surrounding site was limited. Second, the remoteness of the site and the limited construction season (April through September) posed logistical problems, and finally the excavation itself was to be performed through extremely difficult soil conditions.

This last item represents the focus of our paper. Faced with the logistical problems and time constraints, Bauer of America with assistance from its parent company, proposed to utilize a Bauer BC 30 hydraulic trench cutter to perform the bulk of the excavation. The advantages of this technique for the project were that at the design depths, excavation would be more rapid, the excavation slurry and spoils would be more controlled in a closed system, and the use of end stops would be eliminated by the panelized construction.

The difficulties for this technique would be the excavation through the quartzite boulders, known to be as large as 42 inches. To address this situation Bauer developed special roller bit cutter wheels.

The performance of these wheels and the alternate trench excavation techniques that were utilized on this project are reviewed in detail as well as the overall execution of the work.

GEOTECHNICAL DESIGN FOR THE MITIGATION OF ENVIRONMENTAL IMPACTS IN PROVO CANYON, UTAH

Edward G. Keane, Utah Department of Transportation
Salt Lake City, Utah 84119-5998

ABSTRACT

U.S. Highway 189 is a principal artery that passes through the Wasatch Mountains southeast of Salt Lake City, Utah. The rural two lane highway connects Provo City and Utah Valley with the Heber Valley and its recreational resources which includes two world renowned destination ski areas, Deer Valley and Park City Resort. The ever-increasing traffic volumes on this facility, designed sixty-five years ago, required appropriate improvements to eliminate existing hazardous driving locations and provide a facility with the capacity to safely accommodate projected traffic. The "Tunnel Project" consists of a two-mile-long segment in a section between Vivian Park and the Sundance Ski Area turnoff called the "Narrows". This section is the narrowest in the canyon with rock walls close to the Provo River. The Provo River is designated as a Class I and Class II fishery offering some of the best fishing in the State of Utah. In short, this section of Provo Canyon is a very environmentally sensitive area that required extensive negotiations with Resource Agencies and citizen groups.

Utah DOT was "between a rock and a wet spot" that required flexibility in design concepts to fit the road in this section at a price that we could afford.

The terrain consists of a series of steep rock canyon ridges and cobble-filled talus valleys. The topography and geology required a combination of slope stabilization measures, retaining walls and rock cuts in addition to the tunnels. These geotechnical concepts and features were required to blend in with the canyon and be as unobtrusive as possible.

The measures to mitigate the impact and accepted by the public included the following. Exploratory drill rigs were helicoptered to hand assembled wooden platforms that were dismantled after use and the ground revegetated. Geogrid reinforced modular block walls were proposed adjacent to the river. The walls would not be protected by rip-rap nor will the contractor be allowed to place equipment out bound of the wall face to protect the riparian zone. The concrete will be colored to approximate the color of the native limestone. A talus slope will be removed entirely to expose the natural rock slope that is outside the right-of-way in lieu of a retaining wall at the right-of-way line. Soil nail walls will be constructed in locations where alluvium overlies the rock cuts. The wall faces will be cast in place with a random board finish to approximate the natural limestone rock face. The concrete will be colored and the slope of the wall face will be the same as the rock cut.

Rockfall characteristics for the proposed cut slopes were investigated using the Colorado Rockfall Simulation Program (CRSP). Results of the CRSP indicate that a 22 foot wide rockfall zone is adequate for the cut slopes along the proposed alignment. Twelve foot high temporary rock retaining fence will be placed during construction to minimize rock fall onto the highway. This was a major inconvenience to the motoring public on the adjacent project.

The major feature of this project will be the construction of 400 foot long parallel tunnels through a limestone ridge. Excavation will be by blasting methods. The tunnels will be separated by a rock pillar a minimum of 20 foot thick. Stabilization of the tunnel will rely on shotcrete and rock dowels with a final concrete lining with ceramic tiles.

Construction of this 30 million dollar contract is expected to begin in the fall of 1995.

CASE HISTORY OF A DESIGN-BUILD TIEDBACK WALL ON STATE ROUTE 91 BETWEEN BRIGHAM CITY AND MANTUA IN UTAH

John A. Franceski
Schnabel Foundation Company
8751 E. Hampden Avenue, Suite C-4
Denver, Colorado 80231

Claus J. Ludwig
Schnabel Foundation Company
3075 Citrus Circle, Suite 150
Walnut Creek, California 94593

ABSTRACT

For many years, Utah State Route 91, a two-lane road between Brigham City and Mantua, has been the scene of many serious accidents and delays. To eliminate these problems, the Utah Department of Transportation (UDOT) wanted to widen the road and improve its alignment. Since Box Elder Creek, a Class 3 (high priority) fishery ran adjacent to Route 91, extensive precautions would be necessary to minimize disturbance to the stream. In some areas large cuts and substantial fills were made to obtain the desired geometry. In other areas the limited right-of-way and steep hillsides required the construction of mechanically stabilized earth embankments and retaining walls in cuts.

The most difficult section required excavation into a steep talus slope on the south side of Box Elder Canyon. To prevent a massive over excavation into the hillside, the UDOT planned to construct a tiedback wall approximately 600 feet long and 40 feet high. However, the soil conditions at the location of the wall, predominantly cobbles and boulders, made the construction of conventional soldier pile tiedback walls too expensive, if not impossible. This paper focuses on the contracting method, design and construction of a tiedback wall built without soldier beams which proved to be a practical and economical solution for anchored wall construction in mountainous terrain.

CONTRACTING METHOD

The Utah Department Of Transportation (owner) and Centennial Engineering, Inc. (prime designer) recognized that the section of retaining wall known as R-278 presented numerous challenges. To build this section of the road at the desired alignment and grade required the construction of a retaining wall up to 40 feet in height. The excavation would be made into the existing hillside which extended for several hundred feet above the back of the proposed wall on a slope of approximately 45 degrees. A tiedback wall was the most practical and economical option—other wall systems were eliminated because they either required massive excavation up the hillside or a temporary earth retention system to construct a permanent retaining wall.

Historically, tiedback walls have been developed and constructed by Specialty Contractors. The prominent companies have developed an in-house geotechnical and structural engineering capability through the day-to-day design and construction of tiedback retaining walls. Through

this specialized engineering practice, many of these firms have developed innovations which have lowered cost and increased quality. However, many of these innovations have been patented, and are only available to owners through the design-build process. The advantages of the design-build contract extends further in that the engineers who design the tiedback wall systems will be the ones who are responsible for the construction and performance of the wall. This is a major factor in providing rapid and economical responses to design changes dictated by actual field conditions. This is important in underground work where it is unusual for geotechnical studies to be complete enough to precisely predict actual conditions.

Contracting for a design-build tieback wall follows a variety of formats in public works construction. The two most common procedures are to invite tieback Specialty Contractors to submit their designs to compete with each other or to invite them to compete with each other and a base design that is prepared by the agency or its consultants.

Following the first procedure, one of the approved designs submitted by a Specialty Contractor will be chosen at bid time. The quality of the system is controlled by the Owner, since complete detailed drawings have been submitted, reviewed and revised prior to acceptance as a contract document. The choice of which wall gets built is made at bid time and is based on the most economical system proposed between the competing Specialty Contractors. Each approved Contractor's design is allowed to be built only by that Contractor.

Following the second procedure, a base design which can be a tiedback wall or some other retaining wall system is also included in the contract documents. The base design can be bid by the General Contractors or other Specialty Contractors who have not chosen to submit their own designs. In this case, the Specialty Contractors' alternates compete on the basis of quality and price with the base design. Since the Specialty Contractors are not paid for their designs, the only costs to the Owner are those incurred to review the design submittals.

Variations of these contracting methods are used, however, these two provide the Owner with the optimum combination of quality and economy available through design-build contractor technology. Value engineering is typically an option to any of the contract designs, but time constraints and administrative procedures limit effective competition in many cases. Besides, with value engineering, the Owner realizes at best 50% of the savings that could have been captured with pre-bid design-build.

For this project, UDOT invited several specialty wall contractors to submit preliminary designs for a tiedback wall system. As a starting point, the contractors were given the following information: 1) Results of the geotechnical investigation and proposed earth pressure diagram; 2) Proposed wall alignment and grades; 3) Level of corrosion protection, as well as testing and acceptance criteria for the permanent tiebacks; and 4) Required architectural finish on the concrete facing. Other details such as drainage and construction tolerances were developed as the design phase proceeded. The agreement was that once approved by the owner and the prime designer, the speciality contractor's wall design would be included in the bid documents. Then, if one of the design-build tiedback walls was selected by the general contractor winning the contract, the specialty firm that submitted the design would construct the wall. After reviewing the preliminary retaining wall designs, two companies were selected to proceed with the preparation of complete sets of drawings to be included in the contract documents.

The detailed drawings, including substantiating calculations, were submitted and reviewed by Centennial Engineering, UDOT and FHWA. The drawings, with comments and requested changes, were returned to the contractors for revisions. Changes were made and the drawings resubmitted. This process was repeated several times until all parties included were satisfied with

the proposed designs. At bid time the general contractors would select the wall system that produced the most economical overall project.

SITE GEOLOGY

In general, the existing slope at the wall location ranged from 35 to 50 degrees. The face of the hill consisted of a boulder-cobble colluvium with a silty, clayey sand matrix. Several areas across the slope were covered with talus slides composed of quartzite cobbles and boulders.

The subsurface profile, as determined by a representative boring at this location, consisted of white-pink and greenish-grey quartzite and quartzitic sandstone cobbles and boulders, supported by a dark brown, clayey sand matrix above quartzite bedrock encountered 45 to 70 feet below the existing grade at the wall location. Boulders up to three feet in diameter were encountered in the boring. The amount of matrix appeared to vary.

This description, taken from the report of the subsurface investigation by Chem Northern, Inc., turned out to be very representative of the conditions encountered during excavation. The most significant features, with regard to construction of the wall, were the abundance of cobbles and boulders, and the matrix in which they were found. In some areas, the course material was completely surrounded by sand, gravel, silt and clay. At other locations along the wall alignment, the excavation exposed cobbles and boulders with interconnected voids that are best described in cubic feet of void space.

DESIGN

Based upon the soils report and a pre-design jobsite investigation, two major constraints impacted the type of wall to be built: 1) The use of soldier beams was eliminated from consideration due to the difficult subsurface conditions (i.e., boulders, cobbles, hard rock) which would have made installation of the soldier beams very expensive; and 2) In the absence of the soldier beams, the temporary stability of the excavated face became an even greater concern. As a result, the wall was designed to be on a batter no steeper than 1:3 (one horizontal to three vertical).

A typical section through the tiedback wall is shown in Figure 1. The primary elements of the wall are: permanent tiebacks, horizontal cast-in-place reinforced concrete wales; precast panels; cast-in-place reinforced concrete footing; connections from the precast panels to the wales; and, steel posts spanning from wale to wale. Shotcrete and soil nails were installed as required to provide temporary shoring during the excavation of the cut slope. A patent is pending on this system.

The tiedback wall was designed using a rectangular earth pressure diagram with a pressure of 30H psf (H=height of cut). The maximum pressure of 30H was determined by calculating the total force resulting from the recommended equivalent fluid pressure, provided by the geotechnical engineer (i.e., triangular pressure distribution) and converting the force to an equivalent rectangular pressure.

The tieback design force was calculated based on the 30H design pressure, the wale spacing of a 10-foot maximum and tieback spacing of a 10-foot maximum. The tiebacks were designed to resist the full earth pressure. The maximum tieback design load was 140 kips, which allowed the option of using bar tendons for all tiebacks. The tiebacks were tested to 133% of their design

load.

The reinforced concrete wale was designed as a continuous beam having a maximum span of 10 feet. The maximum wale size was 3 feet wide by 1.5 feet deep. The wale size and amount of flexural and shear reinforcement varied as a function of the height of cut.

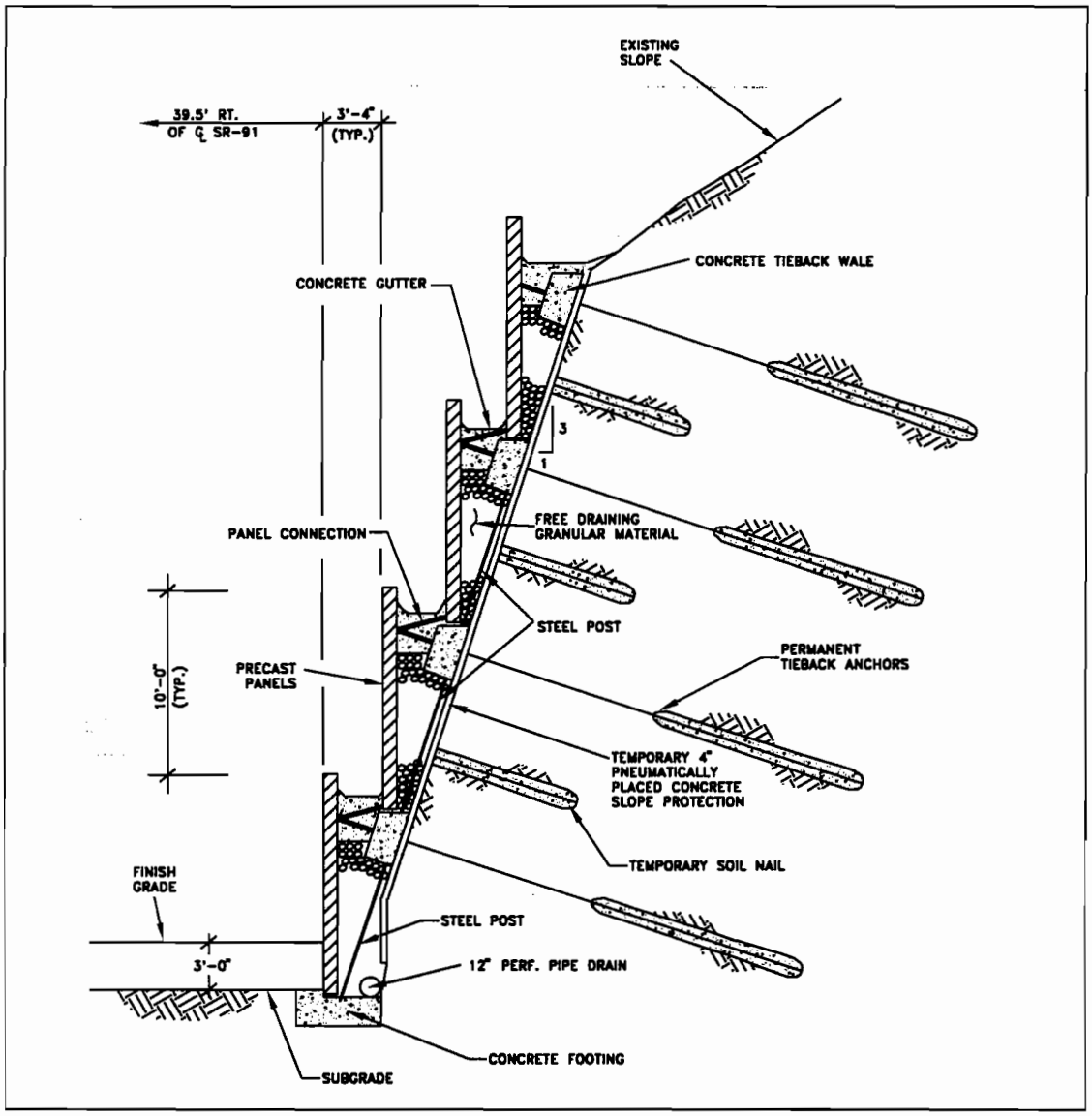

Figure 1 — Section Through Wall

The wale widths were designed so that the maximum soil bearing pressure would not exceed 7 ksf. The loads which contributed to the bearing pressure equations included the following: the tieback force; the self-weight of the precast panel; the 'strap' (i.e., connection of wale to precast panel at the top of each panel) force acting on the panel; the self-weight of the granular backfill above the wale; the self-weight of the wale; and, the forces in the steel tube posts.

The bearing pressure was checked for loading conditions occurring at three different stages of construction: 1) After the tiebacks were stressed against the reinforced concrete wale, but

before the tube posts and precast panels were installed; 2) After the tiebacks have been stressed against the wale, and after the tube posts and precast panels have been installed, but before any earth pressure acts on the panels; and 3) The final loading condition after the tiebacks have been stressed against the wale, after the tube posts and precast panels have been installed, and after the full earth pressure is acting on the panels.

The shear stress acting at the wale-shotcrete interface was checked for the loading condition acting before the tube posts and precast panels were installed. The tube posts were designed to support any loads acting to shear the wale along the wale-shotcrete interface. These posts also acted to counter the bearing pressures generated by the forces acting to 'torque' the wale.

The precast panels were designed for the greater pressure of 80% of 30H psf, or 1000 psf. The 80% factor is an effective arching factor which takes into account some degree of soil arching which will occur between the wales. The pressure was assumed to act over a height equal to the clear span from wale to wale.

The design of the connection between the cast-in-place wale and precast panel involved the use of embedded plates in both the precast panels and wales, steel strap plates welded to the embedded plates, reinforcing steel and a concrete closure pour (the top of which formed the gutter behind each panel). The steel strap plates, although designed as temporary, were designed to resist the full design earth pressure acting on the panels. These steel straps were welded to the plates embedded in the wale and panel. Hooked tensile bar reinforcement was placed parallel to the inclination of the tiebacks at the location of the embedded plates. The embedded plates were designed with headed stud anchors on each side of the plate. The studs protruding into the concrete closure effectively overlapped the tensile bar reinforcement, thereby providing the permanent connection. Besides acting as a gutter, the concrete closure pour also acts as a strut to transfer horizontal forces at the bottom of each panel to the top of the panel below.

The footing was designed to support vertical loads from the panel and backfill and the load in the tube post, as well as lateral loads from the full earth pressure acting on the bottom half of the lowest panel and the lateral thrust from the tube post embedded in the footing.

CONSTRUCTION DETAILS

The first step in constructing the tiedback wall was to build a bench from which the top row of tiebacks could be installed. Since the face of the wall was within 10 feet (plus or minus) horizontally of existing ground surface, and the drilling equipment required a 20-foot bench, additional soil was imported from on site to widen the bench. The next step was to make a cut for the proposed excavation line on a 1:3 batter. Immediately after making the excavation, prefabricated geocomposite vertical drains were placed at 5 feet on center. Next, welded wire fabric and a 4-inch nominal shotcrete facing was applied.

This step proved to be more difficult than had been anticipated. It was assumed at bid time that a 5-foot excavation at a 1:3 batter would be stable for the several hours between excavation and shotcreting. In many areas this was not the case and excavation lifts had to be reduced to 2.5 feet. Even the 2.5-foot lifts caved, requiring shotcrete as thick as 3 feet to establish the back face of the wall on line. Some areas were more stable than others; however, when totaled, the actual volume of shotcrete placed equaled an average 10-inch thickness—nearly 2.5 times the neat plan quantity.

After the shotcrete was placed and rough finished at the wale location, the tiebacks were in-

stalled. The open-graded cobble and boulder formation also caused excess grout takes at some anchor locations. The majority of the 183 tieback anchors had grout takes of 6 to 10 cubic feet of grout at 150 to 300 psi pressure. However, approximately 20 anchors required 40 to 100 cubic feet of grout in order to fill the hole and maintain pressure. All anchor holes required casing to prevent caving of the holes.

All anchors were tested with a center-hole hydraulic jack to a minimum of 133% of the design load. Only one anchor failed to successfully hold the test load—it was supplemented with an additional anchor.

Of particular note in the drilling was the excess bit wear encountered. While the drilling rates were approximately what had been anticipated (about 1-foot per minute), the bit life was extremely poor. Average percussion bit life was approximately 300 linear feet of drilling. Although the quartzite, sand, gravel, cobbles and boulders were not particularly hard or tough, they were extremely abrasive.

After the tiebacks were installed, but prior to testing, the reinforced concrete wales with the required embeds were cast around these tieback tendons. At each tieback location an additional sleeve was cast in the wale to allow drilling a supplemental or replacement anchor if the original one failed to hold the test load. When the concrete in the wales reached the 3000 psi design strength, the anchors were tested and locked off.

Photo 1 — Tiedback Wall System Prior to Precast Erection

The vertical distance between wales is 10 feet and after the anchors were locked off, a 5-foot cut was made where the ground would stand (less if not) and shotcrete placed. Because the distance between the bottom of the previous wale and the bench for the next anchor/wale level was 12 feet, short soil nails were installed midway between wale levels to stabilize the slope as

the excavation proceeded. The sequence of installation of shotcrete, soil nails, tieback anchors, and cast-in-place wales was repeated until wall subgrade was reached.

At wall subgrade a 48-inch by 18-inch continuous strip footing was cast to carry the vertical load of the wall system. The analysis of all the vertical forces imposed by the vertical component of tieback force, the weight of wale, precast and backfill (minus the resisting frictional force on the back of the wales), produced a net downward vertical force which was carried by columns or posts, as we call them. These posts were designed to carry the vertical load down from wale to wale and eventually into the footing. The posts were structural steel tubes welded to plates embedded in the wale. In order to protect the posts and plates from corrosion, they were encased in shotcrete after being welded in place.

After the footing was cast and reached design strength, erection of the precast facing panels was begun. Up to this point the temporary shotcrete and soil nails carried the earth pressure between successive wale levels. The final step in completing the load transfer from the earth to the wales was the erection of precast panels to span vertically between wales. The bottom row of 10-foot by 11-foot by 9-inch precast panels were placed on the footing and attached to the first wale by temporary erection straps welded between embedded plates in the back of the precast and similar plates cast in the wale. These plates also have shear studs which form part of the permanent wale to precast connection once the closure pour is made (see Figure 2).

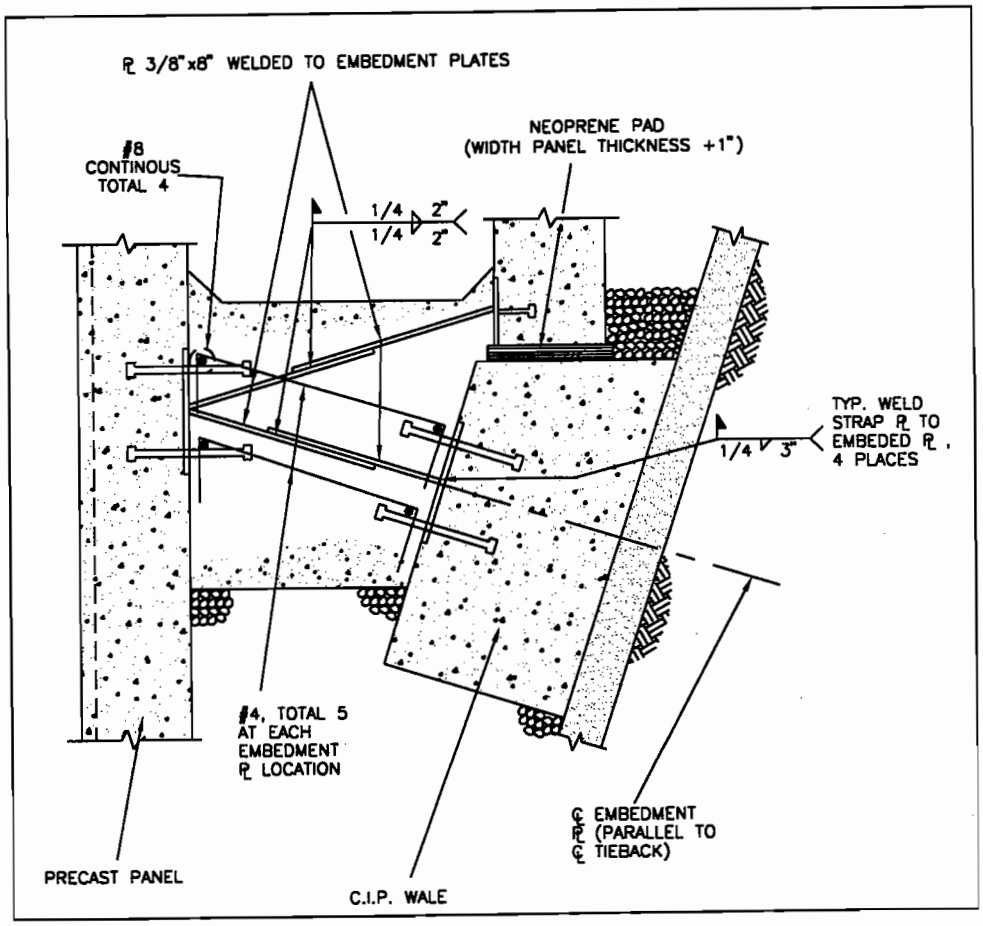

Figure 2 — Precast Panel-to-Wale Connection

After the bottom tier of precast panels were set, the space between the shotcrete face and the back of the precast was backfilled with 1.5-inch gravel. The gravel serves to transfer the earth pressure to the precast as the temporary shotcrete deteriorates over time. The gravel was placed to a level of 3 inches below the bottom of the embed plates. Next, the precast for the second level was set, bearing on the lowest wale level, and secured top and bottom with temporary weld plates.

The final step was to place the reinforcing steel and structural concrete which forms the permanent connection of the wales to precast. The hook bars and longitudinal reinforcing connect the shear studs on the wale to shear studs in the back of the precast. This closure pour also serves as a drainage ditch at the bottom of each tier of precast to carry surface water runoff away from the wall.

This same process was repeated at each precast tier from bottom to top until the wall was completed.

CONCLUSION

Photo 2 — Finished Tiedback Wall Constructed Without Solider Beams

The method of contracting gave the Owner the benefit of several Specialty Contractors' expertise in the design and construction of tiedback wall systems. As with most engineered structures, there is more than one approach that will satisfy the technical requirements of a particular project. Logically, the design and construction sequence that provides the owner the best value in terms of function, longevity, aesthetics, maintenance and cost is the one that should be selected. With anchored walls, many of the systems that maximize these values are proprietary and protected by patents and are available to the owner only through the design-build process. Additionally, the owner can control product quality and design through the review process, and ensure a competitive price through the process of competitive bidding.

The tiedback wall portion of the SR-91 Project was bid as a lump sum design-build project. The final cost for the wall was within one-half of a percent of the bid price. There were no claims for extras and the only change order was for the cost to seal the concrete on the precast facing, an item which was not addressed in the original contract.

FHWA Geotechnical Metrication Guidelines

Presentation by
John L. Walkinshaw P.E., G.E.

Abstract

Note: The attached paper is a condensed version of a soon to be published Federal Highway Administration (FHWA) Publication (No. FHWA-SA-95-035, March 1995) prepared by Chris Dumas and John L. Walkinshaw, Geotechnical Engineers in Washington D.C. and San Francisco, respectively. The complete version will be available through NTIS (703) 487-4650 or the FHWA Publication Center (703) 285-2144 in late April, early May.

The "Metric Conversion Act of 1975," as amended by the "Omnibus Trade and Competitiveness Act of 1988," establishes as the policy of the United States, "(1) the designation of the metric system of measurement as the preferred system of weights and measures for United States trade and commerce, and (2) the requirement that each Federal agency, by a date certain and to the extent economically feasible.... use the metric system of measurement in its procurements, grants, and business-related activities..."

This document was prepared as a guide to assist those preparing for the conversion to the International System of Units (Modern Metric or "SI") of any document dealing with geotechnical engineering.

The base model for this document is a paper prepared by the Subcommittee on Symbols, Units and Definitions of the International Society of Soil Mechanics and Foundation Engineering (ISSMFE). The paper was published in the Proceedings of the 1977 Tokyo conference. The authors of the present document (John Walkinshaw and Chris Dumas) have updated the list of Symbols, Units and Definitions to reflect changes that have transpired in the discipline since 1977. Where deemed necessary, changes have been made to reflect U.S. customary practice and comply with the American Society for Testing Materials Standard Practice for Use of the International System of Units (SI) ASTM E-380. Also incorporated are recommended symbols from the International Geosynthetic Society (IGS) of November 1993.

Document Content and Structure

This document compiles information on geotechnical engineering symbols, units, and definitions used by governments and professional societies throughout the world. This information has been compiled and modified by the authors [1] to reflect customary practice in the United States, and to comply with the American Society for Testing Materials (ASTM) Standard Practice for Use of the International System of Units (SI) ASTM E-380 [2].

The base model for this document is a paper prepared by the International Society of Soil Mechanics and Foundation Engineering (ISSMFE) subcommittee on Symbols, Units, and Definitions and presented at their 1977 conference in Tokyo [3]. This paper was updated to include changes in the discipline that have occurred since 1977 and the development of new emphasis areas such as geosynthetic materials and groundwater hydrology. Additions include the extensive information from the International Geosynthetic Society (IGS) publication on recommended symbols from the International Geosynthetic Society (IGS) of November 1993 [4] and the Canadian Foundation Manual [5].

The document structure follows a logical path designed to guide the reader to a clear understanding of the SI system and its proper use. The guidelines begin with a discussion about basic SI building blocks, and builds on this foundation in a logical progression that culminates with proper SI correspondence "grammar." It also covers a full range of geotechnical usages that include physical properties of soil, mechanical properties of soil, properties related to fluids, in-situ tests, practical problems, and properties related to geosynthetics.

As with the ISSMFE paper, each technical section is presented in column format which proceeds from left to right with a symbol, dimension, unit, and a symbol definition. The definitions are short and assumes the reader is familiar with Soil Mechanics.

Base Dimensions

L Length

T time

M Mass

| Dimensionless parameters

- for parameters that are defined in percentage, e.g., Liquid Limit $w_L = 45$.

In section *4.5.1 Rules for Writing Unit Symbols* of the ASTM Standard E-380; "Standard Practice for Use of the SI INTERNATIONAL SYSTEM of UNITS" it states that SI "Unit symbols should be printed in upright type regardless of the type style used in the surrounding text." As a consequence, the chosen dimension

abbreviations *L, T, M* are shown in italics to avoid confusion with the SI symbols L, T, M for liter (L), tera (T = 10^{12}) or mega (M = 10^{6}), respectively. Good practice requires that letter variables or abbreviations that might be confused with SI symbol or prefixes be written in *italic*.

Base Units

The SI system is composed of the seven base units[1]. Four of these seven units are commonly used in geotechnical engineering as presented below.

s **second (SI Base Unit)**

m **metre or meter (SI Base Unit).** In USA, "meter" spelling is preferred by government agencies over "metre" as shown in ASTM-E380.

- μm micrometer or micron = 10^{-6} m
- mm millimeter = 10^{-3} m
- km kilometer = 1000 m
- m^2 square meter
- m^3 cubic meter

kg **kilogram (SI Base Unit)** = 10^{3} g. For historical reasons, the kilogram is the only base unit with a prefix. This causes the other prefixes used with gram to be 1000 times too large relative to the base unit for mass.

- mg milligram = 10^{-3} g or 10^{-6} kg
- g gram = 10^{-3} kg
- Mg megagram = 10^{6} g or 1000 kg, commonly known as the metric ton. ASTM E 380 discourages the use of the term "metric ton" for engineering documents, and restricts it to commercial usage. FHWA and the American Association of State Highway Officials (AASHTO) agree that the metric ton (t), is acceptable for commercial use.

K **degree kelvin (SI Base Unit).** Thermodynamic temperature. Note the degree (°) symbol is **not** used with K.

---

[1] A complete list of SI base units and their relationship with derived units is located in Appendix A.

Derived Units

°C **degree Celsius.** Water freezes at 0°C (273.15 K) and boils at 100°C (373.15 K) at 101.325 kPa (standard atmosphere = 760 mm of mercury). The temperature interval 1-degree Celsius equals exactly the interval of 1-degree kelvin.

N **newton (force = *M*· a) = kg· m/s^2**

kN kilonewton = 10^3 N
MN Meganewton = 10^6 N

Pa **pascal (pressure = force/area) = N/m^2** In many countries, newton per square meter (N/m^2) is used for stress instead of pascal. However, the SI system and ASTM-E380 require the use of pascal.

kPa kilopascal = kN/m^2
MPa megapascal = MN/m^2

J **joule (work = Force·distance) = N· m**

° **degree (angle)** or temperature when used with **°C**

Prefixes for Units

The SI prefixes commonly used in geotechnical engineering are presented below. These prefixes follow the engineering guidelines established in ASTM E 380 whereby only multiples of 1000 are accepted. Larger or smaller prefixes can be found in Table 5 of ASTM E 380.

G giga = 10^9

M mega = 10^6

k kilo = 10^3

\- unity = 1.0

m milli = 10^{-3}

μ micro = 10^{-6}

General Definitions

VARIABLE SYMBOL	BASE UNIT DIMENSIONS	SI UNIT SYMBOL	VARIABLE DEFINITION
L^2,l	L	m	length
B,b	L	m	width (breadth), diameter
H,h	L	m	height and thickness
D,z	L	m	depth
D,d	L	m	diameter
A^2	L^2	m^2	area
V^2	L^3	m^3	volume
t	T	s	time
v	LT^{-1}	m/s	velocity
a	LT^{-2}	m/s^2	acceleration
g^2	LT^{-2}	m/s^2	acceleration due to gravity (g = 9.81 m/s^2)
m^2	M	kg	mass
ρ	ML^{-3}	kg/m^3	mass density
γ	$ML^{-2}T^{-2}$	kN/m^3	unit weight
F	|	-	factor of safety
π	|	-	3.1416
e	|	-	2.7183
θ	°	°	degrees
x,y	L	m	planar coordinates
r	L	m	polar coordinates
$\dot{\epsilon}$	|	-,%	linear strain rate
Δ	L	mm	settlement

[2] To avoid confusion with base units, derived units, and prefixes, these symbols should be presented in italics.

Sign Conventions

|	denotes a dimensionless variable
-	denotes SI unit for variables which are defined in percentage, but do not require the % unit symbol, e.g., Liquid Limit $w_L = 45$
′	A "prime" applies to effective stress, e.g., σ'
¯	A "bar" above a symbol relates to average property, e.g., $\bar{\rho}$. The ISSMFE Subcommittee on Symbols recommends avoiding the use of a "bar" to denote effective stress.
•	A "dot" above a symbol denotes the first derivative with respect to time, space, e.g., $\dot{\epsilon}$. A multiple number of dots may be used to represent 2nd, 3rd etc number of derivations.
δ, Δ	Prefix denotes an increment or a change.

Density and Unit Weights

VARIABLE SYMBOL	BASE UNIT DIMENSIONS	SI UNIT SYMBOL	VARIABLE DEFINITION
ρ_s	ML^{-3}	kg/m^3	Mass[3] density of solid particles. Ratio between mass and volume of solid particles.
γ_s	$ML^{-2}T^{-2}$	kN/m^3	Unit weight of solid particles. Ratio between weight and volume of solid particles. In measurement systems based on "absolute units" ($F=M\cdot a$), unit weight $\gamma_s = \rho_s \cdot 9.81$ m/s [6].
ρ	ML^{-3}	kg/m^3	Mass density of soil. Ratio between total mass and total volume of soil.
γ	$ML^{-2}T^{-2}$	kN/m^3	Unit weight of soil $\gamma = \rho \cdot g$. Ratio between total weight and total volume of soil.
ρ_d	ML^{-3}	kg/m^3	Mass density of dry soil. Ratio between mass of solid particles and total volume of soil.
γ_d	$ML^{-2}T^{-2}$	kN/m^3	Unit weight of dry soil. Ratio between weight of solid particles and volume of soil $\gamma_d = \rho_d \cdot g$.
ρ_{sat}	ML^{-3}	kg/m^3	Mass density of saturated soil. Ratio between total mass and total volume of completely saturated soil.
γ_{sat}	$ML^{-2}T^{-2}$	kN/m^3	Unit weight of saturated soil. Ratio between total weight and total volume of completely saturated soil $\gamma_{sat}=\rho_{sat} \cdot g$.
ρ'	ML^{-3}	kg/m^3	Mass density of submerged soil. Difference between mass density of soil and mass density of water.

[3] Since the geotechnical community within the U.S. is accustomed to using unit weight and density interchangeably, the authors suggest the term "Mass" accompany "Density" during the transition to SI. It is otherwise redundant.

VARIABLE SYMBOL	BASE UNIT DIMENSIONS	SI UNIT SYMBOL	VARIABLE DEFINITION
γ'	$ML^{-2}T^{-2}$	kN/m^3	Unit weight of submerged soil. Difference between unit weight of soil and unit weight of water ($\gamma' = \gamma - \gamma_w$). Note: If submerged soil is saturated and a pore pressure gradient exists, the equation becomes $\gamma' = \gamma_{sat} - \gamma_w$ (1-i), with i = pore water gradient.
G_s	|	-	Specific gravity. Ratio between mass density of solid and water, ρ/ρ_w .
e	|	-	Void ratio. Ratio between volume of voids and volume of solid particles.
e_0	|	-	In-place void ratio. Ratio between volume of voids and volume of solid particles found in an "undisturbed" sample. Initial void ratio before application of new stress on sample.
n	|	-, %	Total porosity. Ratio between volume of voids and total volume of soil.
w	|	-, %	Water content. Ratio between weight of pore water and weight of solid particles (often expressed in percentage). Note: Some disciplines express water content as a ratio of volumes.
S_r	|	-, %	Degree of saturation. Ratio between volume of pore water and volume of voids.

Physical Properties Related To Fluids

VARIABLE SYMBOL	BASE UNIT DIMENSIONS	SI UNIT SYMBOL	VARIABLE DEFINITION
ρ_w	ML^{-3}	kg/m^3	Mass density of water (equal to 1000 kg/m^3 at 4 °C).
γ_w	$ML^{-2}T^{-2}$	kN/m^3	Unit weight of water (equal to 9.81 kN/m^3). For many applications, it is adequate to use γ_w = 10 kN/m^3 , (less than 2% error).
η	$ML^{-1}T^{-1}$	kPa · s	Absolute or dynamic viscosity of a liquid.

Flow Properties

VARIABLE SYMBOL	BASE UNIT DIMENSIONS	SI UNIT SYMBOL	VARIABLE DEFINITION
h	L	m	Hydraulic head or potential. Sum of pressure height (h_p) and geometrical height (h_z) above a given datum elevation.
h_z	L	m	Elevation head. Distance above a given datum elevation.
h_p	L	m	Pressure head. Pore water pressure in a porous medium divided by the unit weight of water.
h_v	L	m	Velocity head.
Q (or V)[4]	L^3	m^3	Quantity or volume of fluid

[4] Variable before parentheses is typically used in geotechical literature; variable in parentheses is typically used in groundwater literature.

VARIABLE SYMBOL	BASE UNIT DIMENSIONS	SI UNIT SYMBOL	VARIABLE DEFINITION
q (or Q)[4]	L^3T^{-1}	m^3/s	Rate of discharge. Volume of water seeping through a given area per unit of time.
v (or q)[4]	LT^{-1}	m/s	Discharge velocity.
v_s (or v)[4]	LT^{-1}	m/s	Seepage velocity.
i, ∇h	|	-	Hydraulic gradient. Loss of hydraulic head per unit length in direction of flow.
K (or k)	LT^{-1}	m/s	Hydraulic conductivity or coefficient of permeability. Ratio between discharge velocity and corresponding hydraulic gradient (v/i).
k (or K)	L^2	m^2	Intrinsic permeability.
k_u (or K_u)[4]	LT^{-1}	m/s	Unsaturated hydraulic conductivity.
k_r (or K_r)[4]	|	-	Relative permeability (k_u /k).
Θ_w	|	-	Volumetric water content.
Θ_a	|	-	Volumetric air content.
j	$ML^{-2}T^{-2}$	kN/m^3	Seepage force. The force due to flow with which the seeping water acts upon the soil particles in a unit volume of soil ($j = i \cdot \gamma_w$).

Mass Transport Properties[7]

VARIABLE SYMBOL	BASE UNIT DIMENSIONS	SI UNIT SYMBOL	VARIABLE DEFINITION
J	M/L^2	kg/m^2 /s	Solute mass flux.
D^*	L^2/T	m^2/s	Effective soil diffusion coefficient.
D_m	L^2/T	m^2/s	Mechanical dispersion coefficient.
D_o	L^2/T	m^2/s	Aqueous or free-solution diffusion coefficient.
D (or D_h)[5]	L^2/T	m^2/s	Hydrodynamic dispersion coefficient.
K_d	L^3/M	m^3/kg	Distribution coefficient.
K_p	L^3/M	m^3/kg	Partition coefficient.
R_d	|	-	Retardation factor.
T	|	-	Dimensionless time ($v_s \cdot$ t/L) or pore volumes of flow.
n_e	|	-	Effective porosity.
c	M/L^3	mg/L	Solute concentration in pore water.
c_s	M/M	mg/kg	Adsorbed solute concentration expressed in terms of mass of the soild phase (soil).
c'_s	M/L^3	mg/L	Adsorbed solute concentration expressed in terms of volume of pore water in the medium (soil).
c_a	M/L^3	mg/L	Solute concentration in air.
τ	|	-	Tortuosity factor.
τ_a	|	-	Apparent tortuosity factor.

[5] Variable before parentheses is typically used in geotechical literature; variable in parentheses is typically used in groundwater literature.

Standard Penetration Test

Item	English Unit	SI Unit
SOIL SAMPLER DIMENSIONS	inches	mm
SAMPLING INTERVALS	feet	m
N	blows/ft	blows/0.30 m

The SI unit of blows/0.30 m is used for N because of its close approximation to 1-foot for which most historical correlations are based. An accuracy of two significant figures was selected for N because it represent a realistic maximum visual accuracy of 1 cm.

Static Probing

VARIABLE SYMBOL	BASE UNIT DIMENSIONS	SI UNIT SYMBOL	VARIABLE DEFINITION
q_c	$ML^{-1}T^{-2}$	kPa	Static point resistance (or cone resistance). Average pressure acting on the conical point in the standard static penetration test.
f_s	$ML^{-1}T^{-2}$	kPa	Local side friction. Average unit side friction acting on the friction sleeve in the standard static cone penetration test.

Pile Driving

ITEM	EXISTING UNIT	SI UNIT
RESISTANCE AND CAPACITY	tons	kN
FRICTION & STRESS	lbs/ft^2	kPa
SURFACE AREAS	ft^2	m^2
HAMMER MASS	lbs	kg
HAMMER ENERGY	ft · lbs	joules (N · m)
BLOW COUNT	blows/ft	blows/0.25 m
PENETRATION	in/blow	mm/blow
REFUSAL CRITERIA	blows/in	blows/25 mm
GRAVITY	ft/s^2	m/s^2
COATING THICKNESS	Mils	μ m

FHWA Modified GATES Dynamic Pile Driving Formula

$$R = (6 \times \sqrt{E} \times \log 10N) - 445$$

where,

R = **Ultimate** Pile Capacity in kilonewtons

E = Manufacturer's rated energy in Joules for the stroke observed in the field. Do not use Ram Mass times the drop height.

Log = Log to the base 10

N = Number of blows for 25 mm of pile penetration

The use of the FHWA modified GATES formula should be restricted to piles with ultimate capacities of less than 2600 kN.

The SI units of blows/0.25 m for blow count, blows/25 mm for refusal criteria, and blows/25 mm for the GATES formula N value were selected for the following reasons:

1. **Practicality in field use.** In the field it is easy to physically and visually divide the pile into 4 equal sections per meter (0.25 m sections). An SI blow count unit of blows/0.30 m, as used in other codes, would require a physically and visually awkward division of 3 equal sections per meter (0.33 m sections).

2. **Simplicity and consistency.** Calculation of "N" for the GATES ultimate capacity formula is simply done by dividing the blow count (blows/0.25 m) by 10 to obtain required SI unit of blows/ 25 mm. This is superior to both the English unit of blows/inch and an SI unit of blows/0.30 both of which would require cumbersome conversions with calculators.

3. **Easier conversion to metric units.** Conversion will be easier for field personnel because 25 mm is easily discerned with the eye and is approximately equal in magnitude to the customary english unit of 1-inch. An SI unit of blows/0.30 m would require a cumbersome conversion to provide similar magnitudes.

Slopes

VARIABLE SYMBOL	BASE UNIT DIMENSIONS	SI UNIT SYMBOL	VARIABLE DEFINITION
H	L	m	Vertical height of slope.
β	|	°	Backslope angle or angle of slope to a horizontal plane.
$\bar{\tau}$	$ML^{-1}T^{-2}$	kPa	Average shear strength mobilized along sliding surface.
R	|	-	Residual factor. Defined as: $R = \frac{\tau_f - \bar{\tau}}{\tau_f - \tau_R}$
r_u	|	-	Pore pressure ratio. Ratio between the in-situ pore pressure and the total overburden pressure: $u/\gamma \cdot z$.
D	L	m	Depth below toe of slope to hard stratum.

REFERENCES

[1] "List of Symbols, Units and Definitions," Volume 3 (pp. 156-169) of the Proceedings of the Ninth International Conference on Soil Mechanics and Foundation Engineering held in Tokyo, 1977, reprinted with permission from the Japanese Society of Soil Mechanics and Foundation Engineering (March 11, 1994).

[2] "Standard Practice for Use of the International System of Units (SI), (The Modernized Metric System)" ASTM E-380-93, American Society for Testing Materials, Philadelphia, PA 19103.

[3] "Recommended Mathematical and Graphical Symbols" Pamphlet of the International Geotextile Society, Easley, SC 29642, November 1993.

[4] "Canadian Foundation Manual"

[5] J.L.Walkinshaw, P.E., G.E. — FHWA Regional Geotechnical Engineer San Francisco, CA

Christopher Dumas, P.E. — FHWA Geotechnical Engineer Bridge Division Washington, D.C.

[6] Submitted by Dr. Shackelford, Colorado State University. For information on a book by Shackelford, Daniel, and Benson, call 303-491-6081/5048.

[7] "SI Units for Geotechnical Engineering" Discussion by Richard S. Ladd, ASCE Journal, Volume III, Number 4, April 1985

APPENDIX B
METRIC PILE SIZES

Pipe Piles

Typical pipe pile sizes are presented below in both english and SI units. This information was obtained from Section 3.2 "Large Diameter Double Submerged Arc Welded (DSAW) Pipe" of IPSCO Inc, Regina Saskatchewan, Canada (306) 924-7700. To determine the cross sectional area of the pipe in mm^2, divide the linear mass of the pipe in kg/m by the density of the section material (0.00785 g/mm^3 for steel).
For example:

A steel pipe pile with an outer diameter of 1067 mm and a wall thickness of 6.4 mm has a linear mass of 167.39 kg/m. The sectional area is
$[(167.39\ kg/m) \cdot (1000\ g/kg) \cdot (1\ m/1000\ mm)]/(0.00785\ g/mm^3) =$
$(167.39\ kg/m)/(0.00785) = 21324\ mm^2.$
The same answer may be found by multiplying the average circumference by the wall thickness
$[(1067-3.2) \cdot \pi] \cdot (6.4) = 21324.6\ mm^2.$

PIPE PILE DIAMETER	WALL THICKNESS							
	0.250 in.	6.4 mm	0.375 in.	9.5 mm	0.500 in.	12.7 mm	0.625 in.	15.9 mm
16 in. 406.4 mm	42.05	63.13	62.58	92.98	82.87	123.30	102.63	153.11
18 in. 457.0 mm	47.39	71.12	70.59	104.84	93.45	139.15	115.98	172.95
24 in. 610.0 mm	63.41	95.26	94.62	140.68	125.49	187.06	156.03	232.94
30 in. 762.0 mm	79.43	119.24	118.65	176.29	157.53	234.67	196.08	292.54
36 in. 914.0 mm	95.45	143.24	142.68	211.9	189.57	282.27	236.13	352.14
42 in. 1067.0 mm	111.47	167.39	166.71	247.74	221.61	330.19	276.18	412.13
48 in. 1219.0 mm	127.49	191.38	190.74	283.35	253.65	377.79	316.23	471.73
54 in. 1372.0 mm	143.51	215.52	214.77	319.19	285.69	425.71	356.28	531.72
60 in. 1524.0 mm	159.53	239.51	238.80	354.80	317.73	473.71	396.33	591.32
72 in. 1829.0 mm	191.27	287.65	286.86	426.25	381.81	568.83	476.43	710.91

METRIC H-PILES
SURFACE & BOX PERIMETERS & AREAS
W/D RATIOS

Designation		Surface Perimeter	W/D Ratio	Surface Perimeter	W/D Ratio	Box Perimeter	W/D Ratio	Box Perimeter	W/D Ratio	Surface Areas & Box Areas Per Meter Of Length			
mm x kg/m	in. x lbs./ft.	mm		mm		mm		mm		m^2/m	m^2/m	m^2/m	m^2/m
HP360 x 174	HP14 x 117	1775	0.098	2153	0.081	1100	0.158	1478	0.118	1.77	2.15	1.10	1.48
HP360 x 152	HP14 x 102	1764	0.086	2140	0.071	1088	0.140	1464	0.104	1.76	2.14	1.09	1.46
HP360 x 132	HP14 x 89	1749	0.075	2122	0.062	1075	0.123	1448	0.091	1.75	2.12	1.08	1.45
HP360 x 108	HP14 x 73	1736	0.062	2106	0.051	1062	0.102	1432	0.075	1.74	2.11	1.06	1.43
HP310 x 125	HP12 x 84	1493	0.084	1805	0.069	936	0.134	1248	0.100	1.49	1.81	0.94	1.25
HP310 x 110	HP12 x 74	1483	0.074	1793	0.061	926	0.119	1236	0.089	1.48	1.79	0.93	1.24
HP310 x 93	HP12 x 63	1472	0.063	1780	0.052	914	0.102	1222	0.076	1.47	1.78	0.91	1.22
HP310 x 79	HP12 x 53	1462	0.054	1768	0.045	904	0.087	1210	0.065	1.46	1.77	0.90	1.21
HP250 x 85	HP10 x 57	1231	0.069	1491	0.057	768	0.111	1028	0.083	1.23	1.49	0.77	1.03
HP250 x 62	HP10 x 42	1211	0.051	1467	0.042	748	0.083	1004	0.062	1.21	1.47	0.75	1.00
HP200 x 53	HP8 x 36	983	0.054	1190	0.045	615	0.086	822	0.064	0.98	1.19	0.62	0.82

SUBSURFACE INVESTIGATION OF POSSIBLE KARST CONDITIONS AT THE JEWFISH CREEK BRIDGE REPLACEMENT, KEY LARGO, FLORIDA

By: Richard C. Benson, P.G. and Lynn Yuhr,
Technos, Inc., Miami, FL, 33142,
and
Barry C. Berkovitz, P.E.,
Federal Highway Administration, Atlanta, GA, 30367

ABSTRACT

The purpose of this investigation was to evaluate the possible presence of significant karst (old sinkholes or cavities) within the area of a proposed 7,500-foot bridge over Lake Surprise and Jewfish Creek, just north of Key Largo, Florida. Five independent sets of data indicate anomalous geologic conditions between Lake Surprise and Jewfish Creek, over a distance of about 1,800 feet, and include:

- A large microgravity anomaly;
- Three boreholes near the center of the gravity anomaly which contain 45% of the total fluid loss noted among 34 boreholes;
- Subbottom profiling data (seismic reflection) which indicate possible dissolution-enlarged joints;
- A major photo lineament indicating the possible presence of joints and fractures; and
- Extensive road maintenance within the immediate area of concern.

In addition, the presence of a large 2,000 foot diameter paleocollapse sinkhole, located in the area by USGS, indicates that larger deeper cave systems can and do exist in the Florida Keys.

The subbottom data, lineaments, borehole fluid loss, and the DOT maintenance records each by themselves could be dismissed as irrelevant. However, the coincidence of these independent sets of data with a large gravity anomaly clearly focus attention on the area as an area of unusual geologic conditions, with a strong possibility of significant karst. This case-history outlines the approach used to identify karst and assess its impact upon the proposed bridge design.

CASE HISTORY

Background

A new bridge will be constructed across Jewfish Creek on US-1 just northwest of Key Largo (Figure 1). The bridge will extend about 7,500 feet from northwest of the present Jewfish Creek bridge, southeast over Lake Surprise to Key Largo. Lake Surprise is a circular lake with US-1 passing though its center for about 3,500 feet. Drilled shaft foundations will be placed parallel to US-1 over Jewfish Creek and through the center of Lake Surprise.

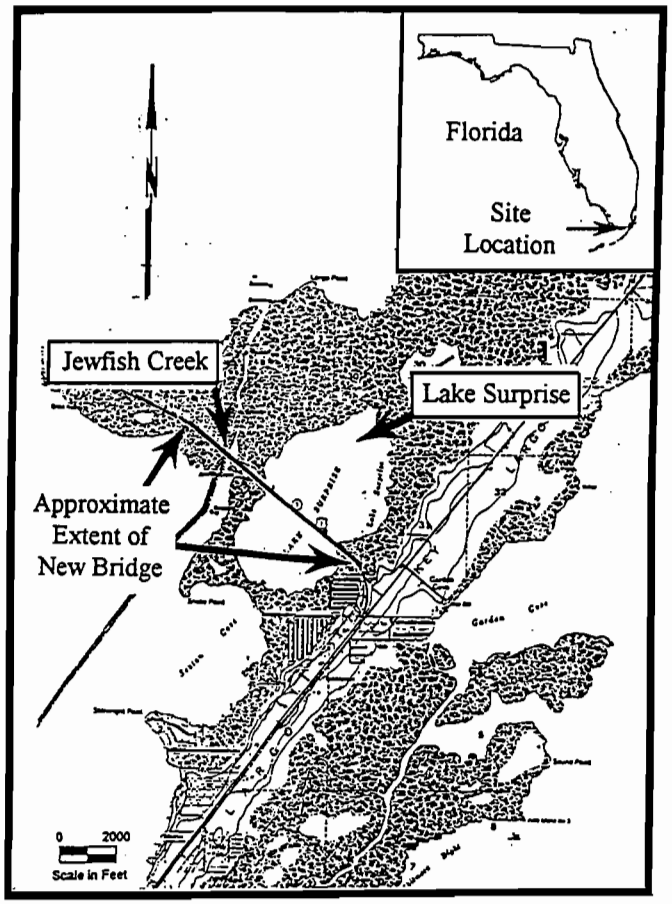

Figure 1: Site location map

Data from 34 borings along the bridge right-of-way (14 are within Lake Surprise) indicate the presence of localized zones (Law Engineering, 1994) of loose material. These may be an indication of infilled dissolution cavities. In addition, there were numerous zones where loss of drilling fluids occurred within the cemented limestone and sandstone, possibly indicating very porous zones or cavities.

In addition, Lake Surprise is one of at least five (5) "circular" lakes which occur in a northeast to southwest alignment (Figure 2). This northeast to southwest alignment is prevalent throughout Florida. Such alignments often indicate the presence of an underground cave system where the lakes are associated with collapse or subsidence sinkholes. Therefore, Lake Surprise was suspected of being a sinkhole lake.

The United States Geological Survey (Shinn, et al., 1994) indicated that a large (2,000 feet diameter) paleokarst sinkhole collapse filled with unconsolidated materials was found among the reefs of Key Largo, 5 miles to the southeast of Lake Surprise (Figure 3).

These conditions prompted concern for the presence of karst features (sinkholes and cavities) within the area of bridge construction. The following five tasks were carried out to evaluate the possible presence of significant karst (old sinkholes or cavities) within the area of bridge construction at Jewfish Creek and over Lake Surprise.

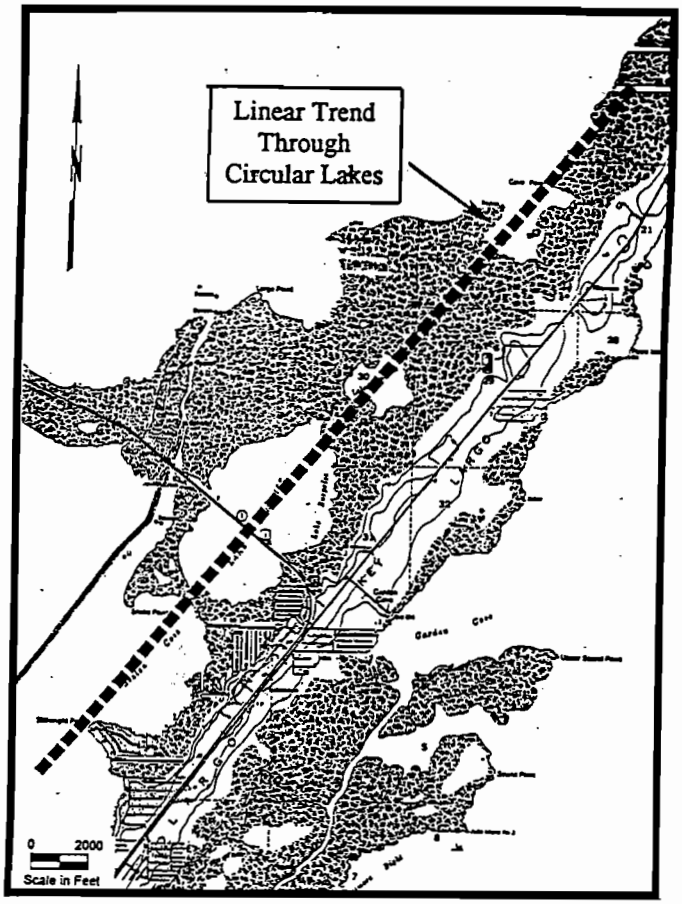

Figure 2: Lineament through Lake Surprise

- a review of karst literature for South Florida;
- an aerial photo interpretation;
- a review of drill logs;
- a subbottom (seismic reflection) profile within Lake Surprise along the bridge alignment and surrounding areas (field measurements); and
- a microgravity survey parallel to the bridge alignment along US-1 (field measurements).

Continuous subbottom profile data and closely spaced (25 feet) microgravity measurements provided the high data densities needed to locate karst conditions (Benson and Yuhr, 1993; Yuhr, et al., 1993).

Critical to this study are the questions:

- Can the bridge as designed, be stable for at least 100 years in the given geologic environment?
- Can additional geophysical and geotechnical investigation fully identify unstable geology, such that bridge decks can be placed or lengthened to safely span the critical geologic conditions?

Results

Geology

The sequence of rocks from the surface downward in the Upper Florida Keys is shown in Figure 4. The rock underlying the site consists of the Key Largo Limestone.

The Key Largo Limestone is a coralline reef rock ranging from hard and dense to soft and cavernous. The spaces between and around the coral heads are filled with limestone debris, cemented carbonate sands and uncemented carbonate sands. Near the center of Key Largo (near Lake Surprise) the Key Largo Limestone is estimated to be about 70 feet thick (Parker, et al., 1955).

The Caloosahatchee formation is mostly eroded and exists as discontinuous patches. It consists of sandy marls, clay, silt, sand, and shell beds. The formation yields some water but generally has low permeability.

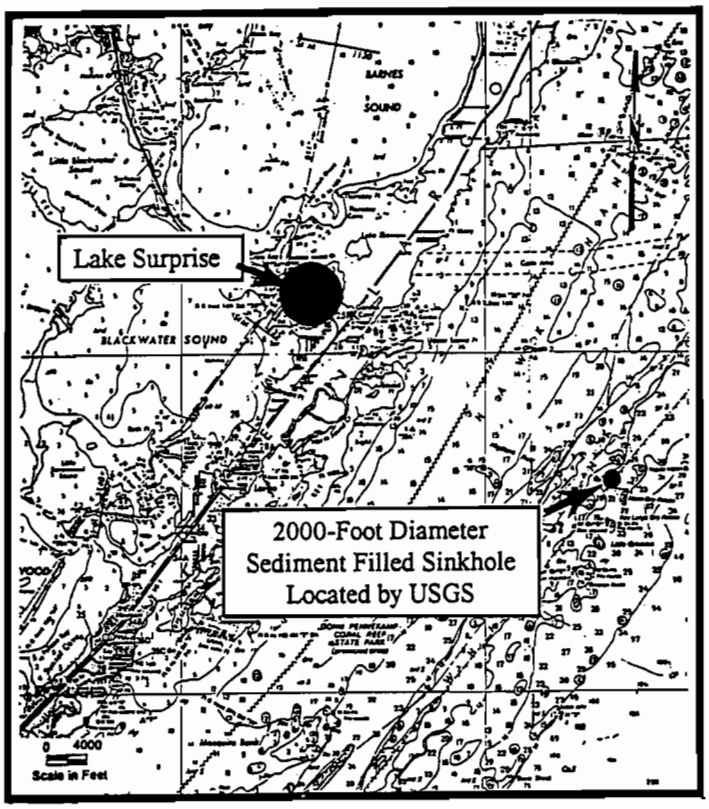

Figure 3: Location of a large paleokarst collapse sinkhole off Key Largo

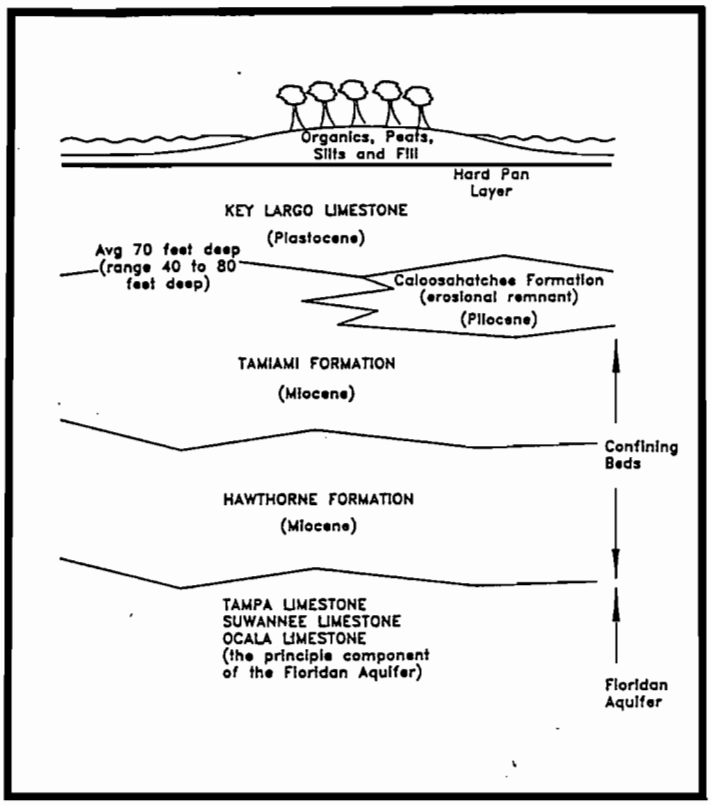

Figure 4: Generalized geologic section

The Tamiami formation is a creamy-white limestone and greenish gray clay and calcareous marl locally hardened to limestone, silty and shelly sands, and shell marl. A major part of the formation is of low to very low permeability.

The Hawthorn formation consists of sandy, phosphatic marl, interbedded with clay, shell marl, silt and sand.

The Tamiami and the Hawthorn formations comprise the major part of the Floridan aquiclude which is underlain by the Floridan Aquifer.

The bridge piers will be founded on cast-in-place drilled shafts which will extend to depths of 70 to 90 feet, slightly into Caloosahatchee/Tamiami formations.

This region of South Florida is commonly riddled with solution holes, large voids, and interconnecting cavity systems. Topographic features in the area (i.e. circular and ellipsoid lakes, sounds, and bays) suggest the possibility of dolines (depressions in the rock surface) and sinkholes. The circular lakes as shown in Figure 2 are common in the Florida Bay area. But are referred to as mangrove lakes and are thought to be a function of mangrove growth and evolution and not due to karst. Large surficial karst features or deeper caves have not been recorded in South Florida and in the Florida Keys as they frequently occur in Central Florida. This is because most karst features in South Florida are old, likely inactive, and probably infilled. Therefore, they are not easily visible as they are in Central Florida. While no large sinkholes collapses or other significant karst features are reported in the literature for South Florida, the existence of off-shore springs have been noted over 100 years and large cavities, encountered in deep foundations for buildings, have been noted over the past 30 years.

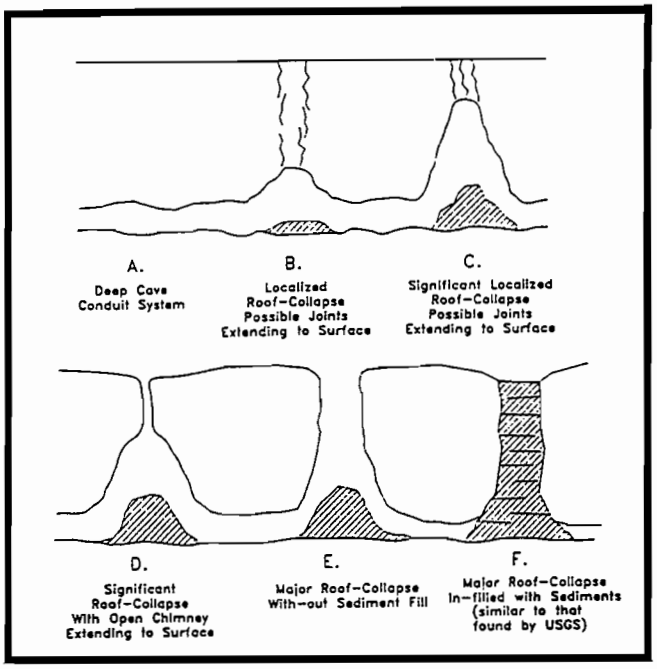

Figure 5: Possible karst models

In addition, open water-filled caves and sinkholes are found in similar geologic environments such as the numerous blue holes on Andros Island in the Bahamas and large collapsed caves on Grand Bahama Island. The largest known blue hole is located off Belize in the Caribbean and is about 1,000 feet in diameter and 460 feet deep. All of these karst features are at elevations similar to that of the Florida Keys. The proximity of a large sinkhole only 5 miles from Lake Surprise clearly implies the potential presence of other caves in the area (since large cave systems which cause collapse sinkholes do not exist as a single localized void in the limestone). Given the fact that

Shinn, et al., (1994) finds sediments to a depth of 179 feet and the sinkhole has a very large diameter, implies that the cave system, which caused this sinkhole, had to be a few hundred feet deep or more and likely has its origin in the underlying carbonate Floridan Aquifer.

Possible Karst Models

Simplified conceptual geologic models of possible caves or paleokarst collapse conditions are shown in Figure 5. Associated with any cave system are dissolution-enlarged conduits along joints and or bedding planes (Figure 5a). If deep enough such conduits would have no impact upon the bridge design. At locations of weakness in overlying rock, which usually occur at the intersections of joints, roof degradation will begin to occur (Figure 5b). Degradation of roof rock can continue to approach the surface (Figure 5c).

In some cases, a pipe or chimney will develop through the overlying rock to the surface (Figure 5d). This type of sinkhole is common in the sinkhole lakes of Central Florida. In some cases, roof collapse will continue until a large portion of the roof has given way (Figure 5e) leaving an open or water-filled cave. These are typical of the many blue holes in the Bahamas and the large 1,000 foot diameter sink off Belize in the Caribbean. The closest similar sinkhole in Florida is warm salt springs in Sarasota County 180 miles northwest of Lake Surprise (Ferguson, 1947). In some cases, open sinkholes can be filled by sediments such as in Figure 5f. Such is the case for the sinkhole found by USGS 5 miles southeast of Lake Surprise on the reef off of Key Largo. It is likely that most of the sinkholes in this area which were open to the surface (Figure 5e) are filled with sediment similar to the one located by USGS. This is probably why collapse sinkholes are not readily identified in southern Florida. However, it is possible that portions of old cave systems (Figures 5a, 5b, 5c and 5d) may not be completely sediment-filled.

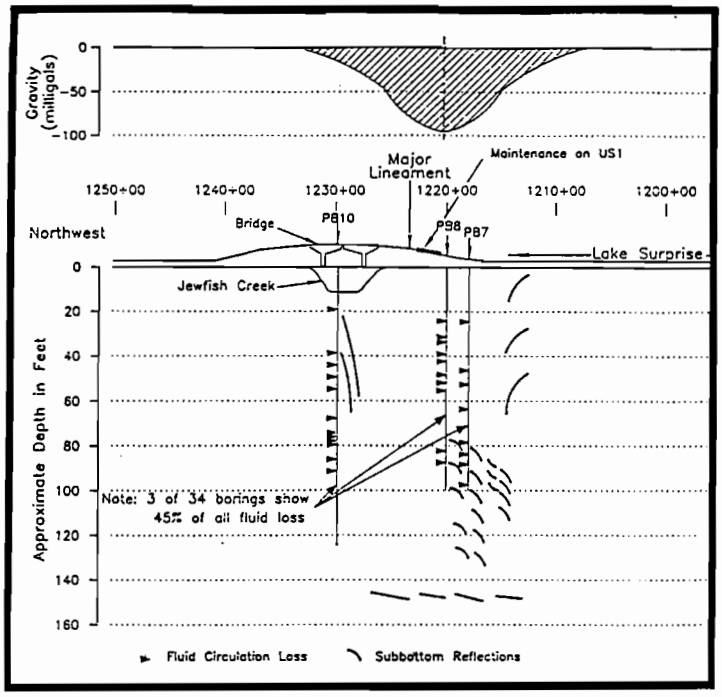

Figure 6: Cross-section showing location of gravity subbottom, and borehole anomalies with photo lineament

Indication of Possible Karst Conditions

Five independent sets of data encountered anomalous conditions just northwest of Lake Surprise and extending to Jewfish Creek. The location and the anomalous conditions are shown in cross section (Figure 6).

- A large microgravity anomaly centered between Lake Surprise and Jewfish Creek clearly indicates a mass deficiency. This anomalous area occurs along the new bridge alignment and is centered about 950 feet southeast of the crest of the existing draw bridge. This large gravity anomaly has been confirmed by additional measurements which have also resulted in direct evidence that the anomaly extends at least 250 feet to the southwest of US-1.
- Boring data indicates a concentration of fluid loss in three boreholes near the center of the gravity anomaly. These fluid losses represent 45% of the total fluid loss noted in the 34 boreholes;
- Subbottom profiling data indicates variable geologic conditions in this area. These can either be interpreted as local zones of cementation within the complex geologic conditions, or as cemented strata either side of dissolution-enlarged joints or chimneys associated with a deeper cavity;
- An aerial photo lineament analysis reveals a major lineament through this area indicating the possible presence of joints and fractures;
- FDOT has carried out extensive road maintenance in the southbound lane of US-1 which is within the immediate area of concern and indicates possible soil piping activity.

Assessment of the Gravity Anomaly

Since the cause of a gravity anomaly cannot be attributed to any unique geologic condition or set of geologic conditions based upon the field data alone, we must estimate possible solutions based upon:

- rules of thumb;
- forward gravity models of simple geologic and karst geometries; and
- the use of geologic conditions that are reasonable for the geologic setting.

The simplest possible cause of the gravity anomaly would be a localized increase in depth to rock with organics or loose sediments above rock. However, since deepening of rock is not indicated by the boring data (10 boreholes within the gravity anomaly) , it is reasonable to conclude that this is not the cause and that deeper geologic conditions must be the cause.

Assuming the gravity anomaly is caused by a large cave that can be approximated by a sphere, we can calculate the maximum depth of such a sphere by using a half width rule. For this anomaly (a half width of about 435 feet x 1.3 results in a maximum depth of 565 feet). Then, by forward modelling (using both, a large water-filled and sediment-filled cave), we can estimate the radius of this sphere. The gravity models indicate that a large cave centered from about 500 to 565 feet below surface with radius of 140 to 200 feet and a mass deficit ranging from 426,000 to 1,240,00 cubic yards of rock will fit the field data. A conceptual geologic model of this sphere is shown to approximate scale in Figure 7.

The presence of such a deeper cave system are further supported by the fact that a large 2,000 foot diameter filled paleocollapse sinkhole recently located by USGS indicates:

- that larger cave systems have existed in the Florida Keys; and

- that the cause of such a large palleocollapse would likely be deep-seated. Since coastal cave development by dissolution occurs at or somewhat below the water table, the maximum depth of such a cave system is related to a combination of lower sea levels, up to 400 feet lower than present, and land subsidence of up to 200 feet. Therefore, caves with depths of 500 to 600 feet below present sea level are consistent with previous sea levels and subsidence data, as well as the depth of other known cave systems, such as the large bluehole off of Belize which is 450 feet deep, and the bluehole on Long Island in the southern Bahamas which is at least 650 feet deep.

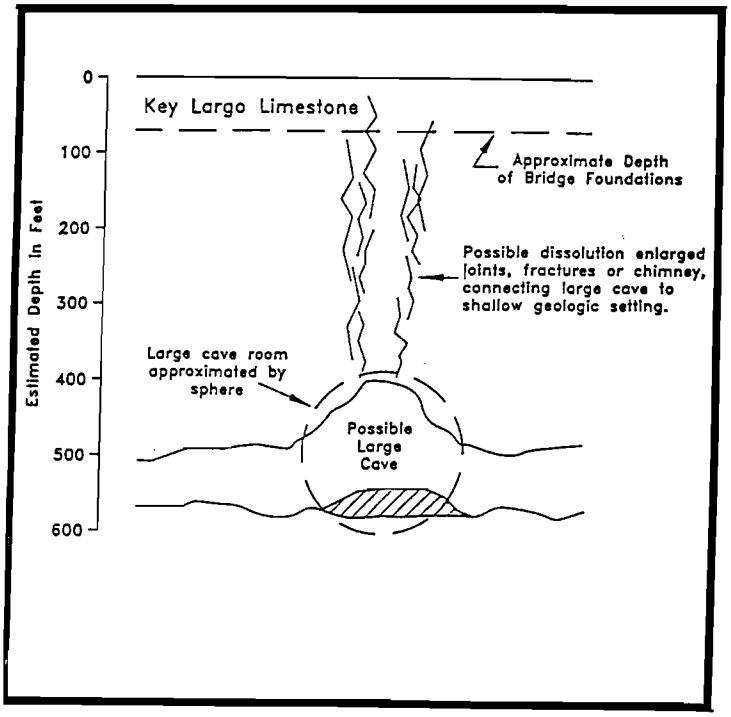

Figure 7: Conceptual model showing maximum depth and size of cavity (one possible model fit to the field data).

Significance of Karst Findings

Over Lake Surprise there are no significant anomalies in the 14 borings, in the gravity data along US-1 or in six subbottom profile lines through the lake. Based upon this data, the results of this investigation indicate that Lake Surprise is probably not a large filled paleokarst collapse sinkhole similar to that found by USGS, but may be related to the possible karst conditions between Lake Surprise and Jewfish Creek.

The subbottom data, lineaments, borehole fluid loss, and the DOT maintenance records of US-1 between Lake Surprise and Jewfish Creek, each by themselves, could be dismissed as irrelevant. However, the coincidence of these independent sets of data with a large gravity anomaly clearly focus attention on the area between Jewfish Creek and Lake Surprise as an area of unusual geologic conditions, and when combined are a strong indication of possible karst.

A deep-seated cave system by itself may not be a problem, if the thickness of overlying rock between the base of the drilled shafts foundation (about 80 to 100 feet deep) and the roof of the cave is sufficiently thick and stable (minimum thickness based upon the gravity models are calculated at 240 to 264 feet). However, the differential conditions associated with fluid loss in the borings and subbottom data, indicate the possibility of dissolution-enlarged joints, fractures, and chimneys at depths of about 75 to 200 feet.

Such features may contain loose soil and rock and may be associated with piping of loose soil and rock downward into a deeper cavity. Furthermore, these features appear to occur at depths of about 75 to 200 feet which includes the depths at which bridge foundations will be

located. These features may undermine the stability of the bridge foundation, leading to weak and unstable zones of soil and rock at the base of cast in-place bridge foundations. Longer spans between foundations may be required to bridge over the critical geologic conditions.

The chemical dissolution of the limestone is a very slow process in the range of one inch per thousand years. Dissolution of deeper cave systems probably ceased as sea level rose and the cave systems were totally saturated by sea water. Exceptions might exist in the zone of mixing between fresh and sea-water, which can accelerate dissolution (Ford, 1994), and near injection wells where stable chemical conditions of ground water may be altered. In any case, dissolution by itself does not represent a serious problem over hundreds of years. The two items of concern are:

- a large cave room which has enlarged upward significantly and which is not infilled with soil and rock debris. In such cases, roof breakdown due to stress and erosion can proceed at a much greater rate than dissolution; and
- the piping of soil through voids into a cave and the placement of piles in or near weak zones of piping can be a significant problem.

While some of the anomalous geologic conditions identified by this work can be explained by geologic depositional and geomorphic sequences not related to karst, the coincidence of these data is a strong indication of potential karst problems. It is therefore imperative that special attention be focused at the locations of the drilled shaft bridge foundations in the 1,800 feet area between Jewfish Creek and Lake Surprise.

References

Benson, R. and L. Yuhr, 1993. Spatial sampling considerations and their applications to characterizing fractured rock and karst system. 4th Multidisciplinary Conf. on Sinkholes and the Engineering and Environmental Impact of Karst. Panama City, FL.

Ferguson, G. E., C. W. Lingham, S. K. Love and R. O. Vernon, 1947. Springs of Florida. Dpt. of Conservation, Florida Geological Survey, Geological Bull. No. 31, Tallahassee, Florida.

Ford, D. C. and P. W. Williams, 1994. Karst geomorphology and hydrology. Chapman & Hall, New York.

Law Engineering and Environmental Services., 1994. Report of geotechnical exploration, Jewfish Creek Bridge Replacement, Volumes I and II.

Parker, G. G., G. E. Ferguson and S. K. Love, 1955. Water resources of southeastern Florida. USGS Geological Survey Water- Supply paper 1255.

Shinn, E. A., C. D. Reich, S. D. Locker and A. C. Hine, 1994. A giant sediment trap in the Florida Keys. US Geological Survey Center for Coastal Geology, St. Petersburg, FL.

Yuhr, L., R. Benson, and D. Butler, 1993. Characterization of karst features using electromagnetics and microgravity: a strategic approach. Paper presented at SAGEEP'93, San Diego, California, April 18-22.

DETERMINATION OF PERTINENT ENGINEERING AND EXPLORATION PARAMETERS THROUGH DECOMPOSITION AND INVERSION OF ELASTIC REFLECTION DATA

Alvin K. Benson

Department of Geology and Geophysics, Brigham Young University, Provo, UT 84602

Abstract

The elastic wave displacement equation is transformed into pressure-stress coordinates, where the Born approximation of the Lippman-Schwinger equation in the Fourier-transform domain is employed to decompose the observed fields into their scattered components: P-P, P-S, S-P, and S-S. Triple Fourier transforms of the scattered elastic wave data are linear combinations of the double Fourier transforms of the relative changes in the medium properties. Angular-dependent reflection coefficients for each of the scattering modes are constructed, and an inversion algorithm is outlined. Inversion of the observed elastic wave fields is accomplished in a manner similar to the acoustic problem (Clayton and Stolt, 1981). Density, bulk modulus, and shear modulus variations in an elastic earth can be recovered by utilizing the angular-dependent information present in the observed wave fields. Examples illustrate these points.

Transforming the elastic wave data back to displacement coordinates and assuming a compressional source, an analysis of recorded amplitudes yields some practical answers about converted-wave data. Significant amounts of P→S data should typically be generated by compressional sources, with significant contributions at smaller angles. However, signal-to-noise calculations suggest that more sweeps and more geophone channels at longer offsets will typically be necessary to get P-S sections of comparable quality to P-P sections.

Introduction

Seismic inversion algorithms range from traveltime inversion (Dines and Lytle, 1979; Paulsson et al., 1985; Ivansson, 1985; Bishop et al., 1985; Lines, 1988; Justice et al., 1989, Luo and Schuster, 1991; and many others) to Born inversion (Clayton and Stolt, 1981; Weglein, 1982; Keys and Weglein, 1983; Bleistein and Gray, 1985; Carrion and Foster, 1985; Wenzel and Menges, 1989; and others) to full-wave inversion (Johnson and Tracy, 1983; Tarantola, 1987; and others). Traveltime inversion typically uses ray tracing to compute both the traveltimes and the perturbations of traveltimes with respect to velocity. Although computationally efficient, traveltime inversion can fail when the earth's velocity variations are characterized by the same wavelength as in the source wavelet. However, a conjugate gradient optimization algorithm can sometimes determine a correct velocity model fairly quickly, and successful inversion can result even when the starting model is far from the actual model.

Full-wave inversion overcomes limitations imposed by the high-frequency restrictions in traveltime inversion and the weak scattering approximation of Born methods by perturbing the velocity model until the synthetic seismograms match the observed seismograms. The synthetic

seismograms are usually computed by a finite-difference solution to the wave equation, and few approximations are necessary. However, the procedure can fail because the normed difference between the observed and synthetic seismograms can be highly nonlinear with respect to the velocity models.

To bridge the gap between the extremes of traveltime and full-wave inversion, linearized Born inversion and other amplitude methods have been employed. These intermediate methods can be highly successful for some data sets, but not typically for data with strong impedance contrasts. Other intermediate methods include surface-wave inversion (Wattrus, 1989) and diffraction tomography (Lo et al., 1988). This paper will concentrate on linearized decomposition and inversion of seismic data using the elastic wave equation.

Elastic Wave Equation

Clayton and Stolt (1981) applied the Born approximation to the acoustic wave equation and related the reflectivity function to variations in the density and bulk modulus of the medium. A similar approach is implemented in this paper for the elastic wave equation, leading to four reflectivity functions that depend on variations in three medium parameters — the density, the bulk modulus, and the shear modulus. The beginning point of this particular derivation is the two-dimensional elastic displacement equation (Ewing et al., 1957), which is written here in matrix form:

$$\mathrm{LU}=\left[\rho\omega^2\begin{bmatrix}1 & 0\\ 0 & 1\end{bmatrix}+\begin{bmatrix}\partial_x K\partial_x+\partial_z\mu\partial_z & \partial_x(K-2\mu)\partial_z+\partial_z\mu\partial_x\\ \partial_z(K-2\mu)\partial_x+\partial_x\mu\partial_z & \partial_x\mu\partial_x+\partial_z K\partial_z\end{bmatrix}\right]\begin{bmatrix}U_x\\ U_z\end{bmatrix}=0, \tag{1}$$

where U = displacement,
ρ = density,
K = bulk modulus,
μ = shear modulus,
ω = frequency.

The spatial and temporal dependence of operators, such as L, will be suppressed until later.

If the density, bulk modulus, and shear modulus are all constant background values, i.e., $\rho=\rho_r$, $K=K_r$, and $\mu=\mu_r$, then the operator L in equation (1) becomes

$$\mathrm{L}_r=\left[\rho\omega^2\begin{bmatrix}1 & 0\\ 0 & 1\end{bmatrix}+\begin{bmatrix}K_r\partial_x^2+\mu_r\partial_z^2 & (K_r-\mu_r)\partial_x\partial_z\\ (K_r-\mu_r)\partial_x\partial_z & \mu_r\partial_x^2+K_r\partial_z^2\end{bmatrix}\right]. \tag{2}$$

It is convenient to rewrite L_r in diagonalized form by using the operator

$$\mathrm{H}=\begin{bmatrix}\partial_x & \partial_z\\ -\partial_z & \partial_x\end{bmatrix}. \tag{3}$$

Then

$$L_r = H^{-1} \begin{pmatrix} K_r L_P & 0 \\ 0 & \mu_r L_S \end{pmatrix} H, \tag{4}$$

where

$$L_P = (\rho \omega^2 / K_r) + \nabla^2, \tag{5a}$$

$$L_S = (\rho \omega^2 / \mu_r) + \nabla^2, \tag{5b}$$

and H^{-1} is the inverse operator of H.

The Green's operator associated with the wave operator L_r is formally defined as (Taylor, 1972, p.129)

$$G_r \equiv -L_r^{-1}. \tag{6}$$

Likewise, if we define $G_P \equiv -L_P^{-1}$ and $G_S \equiv -L_S^{-1}$, then

$$G_r = H^{-1} \begin{pmatrix} G_P/K_r & 0 \\ 0 & G_S/\mu_r \end{pmatrix} H. \tag{7}$$

The latter equation can be rewritten as

$$\begin{pmatrix} G_P & 0 \\ 0 & G_S \end{pmatrix} = \begin{pmatrix} K_r & 0 \\ 0 & \mu_r \end{pmatrix} H G_r H^{-1}, \tag{8}$$

which expresses G_r in the pressure-stress (P-S) coordinate system (vs. displacement coordinates).

The Scattering Equations — Born Approximation

To relate G (the Green's operator for L in equation (1)) and G_r, we will employ the simple identity

$$A = B + B(B^{-1} - A^{-1})A$$

and associate G with A and G_r with B. Consequently, if we define $V = L - L_r$, then

$$G = G_r + G_r V G, \tag{9}$$

which is the Lippmann - Schwinger equation for G, and V corresponds to the scattering potential. Equation (9) is valid for any choice of G_r that satisfies the same external boundary conditions as G. Formally solving equation (9) for G,

$$G = (1 - G_r V)^{-1} G_r. \tag{10}$$

Keeping the first two terms of the Born series expansion of equation (10) yields the Born approximation to the Lippmann - Schwinger equation:

$$G \approx G_r + G_r V G_r. \tag{11}$$

If L_r is close enough to L that G_r reasonably models the direct wave between the source and receiver, then $G_r V G_r$ should model simple reflections, and the discarded higher terms should involve multiple reflections only.

For elastic waves, the scattering potential V is the difference between the wave operators L (equations 1) and L_r (equation 2):

$$V = L - L_r = \left[\rho_r a_1 \omega^2 \begin{pmatrix} 1 & 0 \\ 0 & 1 \end{pmatrix} + \begin{pmatrix} K_r \partial_x a_2 \partial_x + \mu_r \partial_z a_3 \partial_z & K_r \partial_x a_2 \partial_z + \mu_r (\partial_z a_3 \partial_x - 2 \partial_x a_3 \partial_z) \\ K_r \partial_z a_2 \partial_x + \mu_r (\partial_x a_3 \partial_z - 2 \partial_z a_3 \partial_x) & \mu_r \partial_x a_3 \partial_x + K_r \partial_z a_2 \partial_z \end{pmatrix} \right], \tag{12}$$

where

$$a_1 = [(\rho / \rho_r) - 1], \tag{13a}$$

$$a_2 = [(K / K_r) - 1], \tag{13b}$$

$$a_3 = [(\mu / \mu_r) - 1], \tag{13c}$$

and a_1 represents the variations in density, a_2 represents the spatial variations in bulk modulus, and a_3 represents the variations in shear modulus relative to the reference shear modulus. Note that these perturbation parameters a_i are defined slightly differently in this paper than in Clayton and Stolt (1981) and Stolt and Weglein (1985).

It is convenient to define the data scattered wave field D as the impulse response G minus the direct wave arrival G_r (Clayton and Stolt, 1981). Using equation (7) and the Born approximation in equation (11), the relationship between the data field and the scattering potential is

$$\begin{aligned} D &= (G - G_r) S(\omega) = G_r V G_r S(\omega) \\ &= H^{-1} \begin{pmatrix} G_P / K_r & 0 \\ 0 & G_S / \mu_r \end{pmatrix} H V H^{-1} \begin{pmatrix} G_P / K_r & 0 \\ 0 & G_S / \mu_r \end{pmatrix} H S(\omega), \end{aligned} \tag{14}$$

where $S(\omega)$ is the Fourier transform of the source time function.

Elastic Wave Components of Reflectivity

If the source generates both compressional and shear waves, then the observed data field would generally consist of four types of scattered waves: (a) P→P primary scattering (D_{PP}), (b) S→P converted scattering (D_{SP}), (c) P→S converted scattering (D_{PS}), and (d) S→S primary scattering (D_{SS}). Performing the same transformation on the data as was applied to the Green's functions (equation (8)), and using equations (3), (4), (12), and (14), the data can be represented in the pressure - stress (P-S) domain as

$$\begin{bmatrix} D_{PP} & D_{SP} \\ D_{PS} & D_{SS} \end{bmatrix} = \begin{bmatrix} K_r & 0 \\ 0 & \mu_r \end{bmatrix} HDH^{-1}S(\omega)$$

$$= \begin{bmatrix} G_P & 0 \\ 0 & G_S \end{bmatrix} HVH^{-1} \begin{bmatrix} G_P/K_r & 0 \\ 0 & G_S/\mu_r \end{bmatrix} S(\omega) \qquad (15)$$

$$= \begin{bmatrix} G_P & 0 \\ 0 & G_S \end{bmatrix} \left[\begin{bmatrix} K_r a_2 & 0 \\ 0 & \mu_r a_3 \end{bmatrix} \nabla^2 + H \begin{bmatrix} \omega^2 a_1 \rho_r & 2\mu_r(\partial_z a_3 \partial_x - \partial_x a_3 \partial_z) \\ 2\mu_r(\partial_x a_3 \partial_z - \partial_z a_3 \partial_x)) & \omega^2 a_1 \rho_r \end{bmatrix} H^{-1} \right] \begin{bmatrix} G_P/K_r & 0 \\ 0 & G_S/\mu_r \end{bmatrix} S(\omega). \qquad (16)$$

Since in the space - frequency domain there is an implied convolutional integral over space at every matrix multiplication, equation (16) is actually an integral equation (Clayton and Stolt, 1981). In addition, since most of the operators are differential operators, most of the integrals are simple, but at least one spatial integral will remain.

In the following, we will take the earth to be two - dimensional (2-D), although relatively straightforward extensions can be made to 3-D (see Clayton and Stolt, 1981 and Stolt and Benson, 1986). In the 2-D problem, the recorded data D is a function of the receiver location x_g, the source location x_s, and the frequency. Because the convolution over the spatial variable x becomes a simple multiplication in the Fourier domain, and the derivatives with respect to x become constants ik_x, the simplest expression of equation (16) is in the (k_x, z, ω) domain. Using WKBJ Green's operators and notation similar to Clayton and Stolt (1981), equation (16) becomes

$$\begin{bmatrix} D_{PP}(k_g, z_g \mid k_s, z_s; \omega) & D_{SP}(k_g, z_g \mid k_s, z_s; \omega) \\ D_{PS}(k_g, z_g \mid k_s, z_s; \omega) & D_{SS}(k_g, z_g \mid k_s, z_s; \omega) \end{bmatrix} = -(1/4) \int dz \begin{bmatrix} \left(e^{i\nu_s \mid t - z_s \mid}\right)/\nu_g & 0 \\ 0 & \left(e^{i\eta_s \mid t - z_s \mid}\right)/\eta_g \end{bmatrix}$$

$$\cdot \left[\begin{bmatrix} K_r a_2 & 0 \\ 0 & \mu_r a_3 \end{bmatrix} \left(\partial_z^2 - k_s^2\right) + H \begin{bmatrix} \omega^2 a_1 \rho_r & 2i\mu_r(\partial_z a_3 k_s - k_g a_3 \partial_z) \\ 2i\mu_r(k_g a_3 \partial_z - \partial_z a_3 k_s)) & \omega^2 a_1 \rho_r \end{bmatrix} H^{-1} \right]$$

$$\cdot \begin{bmatrix} \left(e^{i\nu_s \mid t - z_s \mid}\right)/(k_r \nu_s) & 0 \\ 0 & \left(e^{i\eta_s \mid t - z_s \mid}\right)/(\mu_r \eta_s) \end{bmatrix} S(\omega), \qquad (17)$$

where k_g and k_s are the wavenumbers corresponding to the Fourier transforms of x_g and x_s, respectively, and

$$\nu_g = (\omega/\alpha_r)\sqrt{1-(k_g^2\alpha_r^2/\omega^2)}, \tag{18a}$$

$$\eta_g = (\omega/\beta_r)\sqrt{1-(k_g^2\beta_r^2/\omega^2)}, \tag{18b}$$

$$\nu_s = (\omega/\alpha_r)\sqrt{1-(k_s^2\alpha_r^2/\omega^2)}, \tag{18c}$$

$$\eta_s = (\omega/\beta_r)\sqrt{1-(k_s^2\beta_r^2/\omega^2)}, \tag{18d}$$

and

$$\alpha_r^2 = (K_r/\rho_r), \tag{19a}$$

$$\beta_r^2 = (\mu_r/\rho_r). \tag{19b}$$

As can be seen from equation (19a), α_r is the reference (background) compressional wave velocity, and from (19b), β_r is the reference (background) shear wave velocity.

Let's consider the case for surface reflection data. The observations of the wave field response are made on the horizontal surface ($z_s=z_g=0$). We will not consider the presence of a free surface, and so we will stop the medium above the datum from scattering by assuming that $a_1(x,z)=a_2(x,z)=a_3(x,z)=0$ for $z<0$. Under these conditions, the absolute value signs in the exponentials in equation (17) disappear, and the evaluation of the derivatives is simplified. Applying the derivatives to the left of a_1 , a_2 and a_3 to the exponentials on their left through integration by parts, we obtain the following expressions for the elastic wave components:

$$D_{PP}(k_g,k_s,\omega)=\int dz\left(e^{i(\nu_g+\nu_s)z}/(4\nu_g\nu_s)\right)$$
$$\left[a_2(\omega/\alpha_2)^2+a_1(\nu_g\nu_s-k_gk_s)-2a_3(\beta_r/\omega)^2(k_g\nu_s+\nu_gk_s)^2\right]S(\omega), \tag{20}$$

$$D_{PS}(k_g,k_s,\omega)=-\int dz\beta_r^2\left(e^{i(\eta_g+\nu_s)z}/(4\alpha_r^2\eta_g\nu_s)\right)$$
$$\left[a_1(\eta_gk_s+k_g\nu_s)+2a_3(\beta_r/\omega)^2(\eta_g\nu_s-k_gk_s)(\eta_gk_s+k_g\nu_s)\right]S(\omega), \tag{21}$$

$$D_{SP}(k_g,k_s,\omega)=\int dz\alpha_r^2\left(e^{i(\nu_g+\eta_s)z}/(4\beta_r^2\ \nu_g\eta_s)\right)$$
$$\left[a_1(k_g\eta_s+\nu_gk_s)+2a_3(\beta_r/\omega)^2(\nu_g\eta_s-k_gk_s)(k_g\eta_s+\nu_gk_s)\right]S(\omega), \tag{22}$$

and

$$D_{SS}(k_g,k_s,\omega)=\int dz\left(e^{i(\eta_g+\eta_s)z}/(4\eta_g\eta_s)\right)$$
$$\left[a_1(\eta_g\eta_s-k_gk_s)+a_3\left((\omega/\beta_r)^2-2(\beta_r/\omega)^2(k_g\eta_s+\eta_gk_s)^2\right)\right]S(\omega). \tag{23}$$

Strictly speaking, the expressions in equations (20) thru (23) are only valid at a particular frequency ω for k_g and k_s sufficiently small in magnitude that the arguments of all the square roots in ν_g, η_g, ν_s, and η_s (equations (18a) thru (18d)) are positive. If one or more of these square roots are negative, we are in the evanescent region, and equation (17) is still valid as long as proper care of the signs is taken (Stolt and Benson, 1986). In the limit of small a_1, a_2 and a_3, the expressions in equations (20) thru (23) become exact, and

$$a_1 \approx \ln(\rho/\rho_r),\ a_2 \approx \ln(K/K_r),\ \text{and}\ a_3 \approx \ln(\mu/\mu_r). \tag{24}$$

Apart from the exponentials, the only z-dependence in the integrals in equations (20) thru (23) is the perturbation parameters a_1, a_2 and a_3. Consequently, these four integrals can be represented as linear combinations of Fourier transforms of a_1, a_2 and a_3. Letting $\bar{a_i}(k_x,k_z)$ represent the double Fourier transform of $a_i(x,z)$, equations (20) through (23) become

$$D_{PP}(k_g,k_s,\omega)=(1/4\nu_g\nu_s)\left[(\omega/\alpha_r)^2\bar{a_2}(k_g-k_s,\nu_g+\nu_s)+(\nu_g\nu_s-k_gk_s)\bar{a_1}(k_g-k_s,\nu_g+\nu_s)\right.$$
$$\left.-2(\beta_r/\omega)^2(k_g\nu_s+\nu_gk_s)^2\bar{a_3}(k_g-k_s,\nu_g+\nu_s)\right]S(\omega), \tag{25}$$

$$D_{PS}(k_g,k_s,\omega)=(-1/4\eta_g\nu_s)(\beta_r/\alpha_r)^2(\eta_g\nu_s+k_g\nu_s)\left[\bar{a_1}(k_g-k_s,\eta_g+\nu_s)\right.$$
$$\left.+2(\beta_r/\omega)^2(\eta_g\nu_s-k_gk_s)\bar{a_3}(k_g-k_s,\eta_g+\nu_s)\right]S(\omega), \tag{26}$$

$$D_{SP}(k_g,k_s,\omega)=(1/4\nu_g\eta_s)(\alpha_r/\beta_r)^2(\nu_gk_s+k_g\eta_s)\left[\bar{a_1}(k_g-k_s,\nu_g+\eta_s)\right.$$
$$\left.+2(\beta_r/\omega)^2(\nu_g\eta_s-k_gk_s)\bar{a_3}(k_g-k_s,\nu_g+\eta_s)\right]S(\omega), \tag{27}$$

and

$$D_{SS}(k_g,k_s,\omega)=(1/4\eta_g\eta_s)\left[(\eta_g\eta_s-k_gk_s)\bar{a_1}(k_g-k_s,\eta_g+\eta_s)\right.$$
$$\left.+((\omega/\beta_r)^2-2(\beta_r/\omega)^2)(k_g\eta_s+\eta_gk_s)^2\bar{a_3}(k_g-k_s,\eta_g+\eta_s)\right]S(\omega). \tag{28}$$

The P-P reflections (equation (25)) respond to changes in all three medium parameters, and the shear modulus contribution to this mode is negative, corresponding to the loss of energy due to mode conversion to P-S waves. On the other hand, the converted-wave data (P-S and S-P) and the S-S data respond to changes in shear modulus and density, but not to changes in bulk modulus.

Linearized Inversion

To invert equations (25) through (28), the first step is to deconvolve the source $S(\omega)$, and thus define

$$D'(k_g,k_s,\omega) = \frac{D(k_g,k_s,\omega)}{S(\omega)}. \tag{29}$$

As pointed out by Clayton and Stolt (1981), to avoid instabilities due to $S(\omega)$ being band-limited, we simply set D' to zero outside the frequency band width of $S(\omega)$. This means we will only be able to resolve the variations in a_1, a_2 and a_3 within this passband. The inverse problem for equations (25) through (28) then becomes

$$D'(k_g,k_s,\omega) = \sum_{i=1}^{3} A_i(k_g,k_s,\omega)\bar{a_i}(k_g-k_s,k_z), \tag{30}$$

where

$$k_z = \nu_g + \nu_s, \tag{31a}$$

$$A_1 = (1/4\nu_g\nu_s)(\nu_g\nu_s - k_g k_s), \tag{31b}$$

$$A_2 = (1/4\nu_g\nu_s)(\omega/\alpha_r)^2, \tag{31c}$$

and

$$A_3 = (-1/2\nu_g\nu_s)(\beta_r/\omega)^2(k_g\nu_s + \nu_g k_s) \tag{31d}$$

for equation (25);

$$k_z = \eta_g + \nu_s, \tag{32a}$$

$$A_1 = (-1/4\eta_g\nu_s)(\beta_r/\alpha_r)^2(\eta_g k_s + k_g\nu_s), \tag{32b}$$

and

$$A_2 = 0, \tag{32c}$$

$$A_3 = (-1/2\eta_g\nu_s)(\beta_r/\omega)^2(\beta_r/\alpha_r)^2(\eta_g k_s + k_g\nu_s)(\eta_g\nu_s - k_g k_s) \tag{32d}$$

for equation (26);

$$k_z = \nu_g + \eta_s, \tag{33a}$$

$$A_1 = (1/4\nu_g\eta_s)(\alpha_r/\beta_r)^2(\nu_g k_s + k_g\eta_s), \tag{33b}$$

$$A_2 = 0, \tag{33c}$$

and

$$A_3 = (1/2\nu_g\eta_s)(\alpha_r/\omega)^2(\nu_g k_s + k_g\eta_s)(\nu_g\eta_s - k_g k_s) \tag{33d}$$

for equation (27);

$$k_z = \eta_g + \eta_s, \tag{34a}$$

$$A_1 = (1/4\eta_g\eta_s)(\eta_g\nu_s - k_g k_s), \tag{34b}$$

$$A_2 = 0, \tag{34c}$$

and

$$A_3 = (1/4\eta_g\eta_s)\left[(\omega/\beta_r)^2 - 2(\beta_r/\omega)^2\right](k_g\eta_s + \eta_g k_s)^2 \tag{34d}$$

for equation (28).

The slight differences between the A_i for P-P scattering in equations (31b) through (31d) and those of Stolt and Weglein (1985) are due to the slightly different definition of our a_i (equations (13a) through (13c)) and that we are presently in pressure - stress coordinates vs. displacement coordinates. Equations for the other modes of scattering are not discussed by Stolt and Weglein (1985). From equation (30), the a_i can be reconstructed as weighted averages of $D'(k_g,k_s,\omega)$ determined at different offsets by using a least-squares formulation similar to that described by Clayton and Stolt (1981).

Angular-Dependent Reflection Coefficients

The coefficients in equations (25) thru (28) can be cast in a more physically understandable form by defining the following angles:

$$k_g = (\omega/\alpha_r)\sin(\phi_{Pg}) = (\omega/\beta_r)\sin(\phi_{Sg}), \tag{35a}$$

and

$$k_s = (\omega/\alpha_r)\sin(\phi_{Ps}) = (\omega/\beta_r)\sin(\phi_{Ss}). \tag{35b}$$

Then, the expressions for ν_g, η_g, ν_s, and η_s in equations (18a) thru (18d) become

$$\nu_g = (\omega/\alpha_r)\cos(\phi_{Pg}), \tag{36a}$$

$$\eta_g = (\omega/\beta_r)\cos(\phi_{Sg}), \tag{36b}$$

$$\nu_s = (\omega/\alpha_r)\cos(\phi_{Ps}), \tag{36c}$$

and

$$\eta_s = (\omega/\beta_r)\cos(\phi_{Ss}). \tag{36d}$$

Since the Fourier transforms $x_g \rightarrow k_g$ and $x_s \rightarrow k_s$ decompose the data into plane wave components, it is rather easy to interpret the angles defined in equations (36a) thru (36d) (see Figure 1):

ϕ_{Ps} is the angle between the incident compressional plane wave and the vertical;
ϕ_{Ss} is the angle between the incident shear plane wave and the vertical;
ϕ_{Pg} is the angle between the reflected compressional plane wave and the vertical;
ϕ_{Sg} is the angle between the reflected shear plane wave and the vertical.

Using these angles, another set of physically significant angles can be defined as follows:

$$\theta_{PP} = (\phi_{Pg} + \phi_{Ps})/2, \tag{37a}$$

$$\theta_{SP} = (\phi_{Pg} + \phi_{Ss})/2, \tag{37b}$$

$$\theta_{PS} = (\phi_{Ps} + \phi_{Sg})/2, \tag{37c}$$

$$\theta_{SS} = (\phi_{Ss} + \phi_{Sg})/2. \tag{37d}$$

These angles represent the half-angles between the incident and reflected waves (Figure 1). If the reflection is from a flat interface, θ_{PP} is the angle of incidence (and reflection) to that interface for a compressional wave, and θ_{SS} is the angle of incidence (and reflection) to that interface for a shear wave. For the converted modes, θ_{PS} and θ_{SP} are averages of the incident and reflected angles.

With the angles defined in equations (37a) thru (37d), the coefficients in equations (25) thru (28) become

$$\nu_g\nu_s - k_g k_s = (\omega/\alpha_r)^2\cos(2\theta_{PP}), \tag{38a}$$

$$k_g\nu_s + \nu_g k_s = (\omega/\alpha_r)^2\sin(2\theta_{PP}), \tag{38b}$$

$$\eta_g k_s + k_g\nu_s = (\omega^2/\alpha_r\beta_r)\sin(2\theta_{PS}), \tag{38c}$$

$$\eta_g\nu_s - k_g k_s = (\omega^2/\alpha_r\beta_r)\cos(2\theta_{PS}), \tag{38d}$$

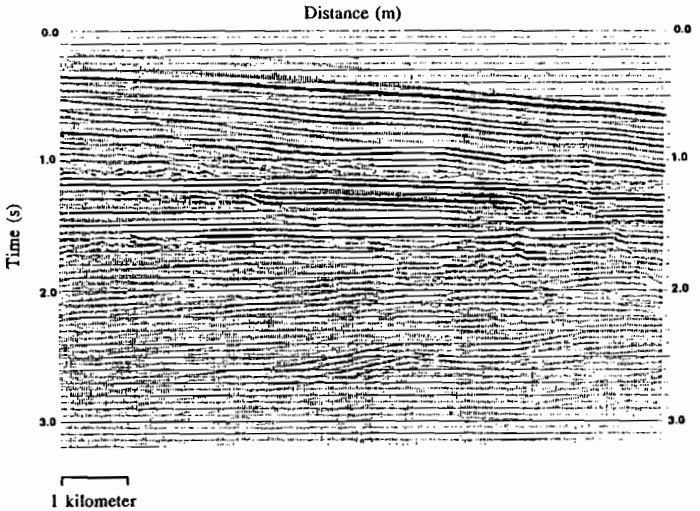

Figure 3 F-k prestack migration of the Gulf of Mexico data used to produce Figure 2 (after Stolt and Benson, 1986).

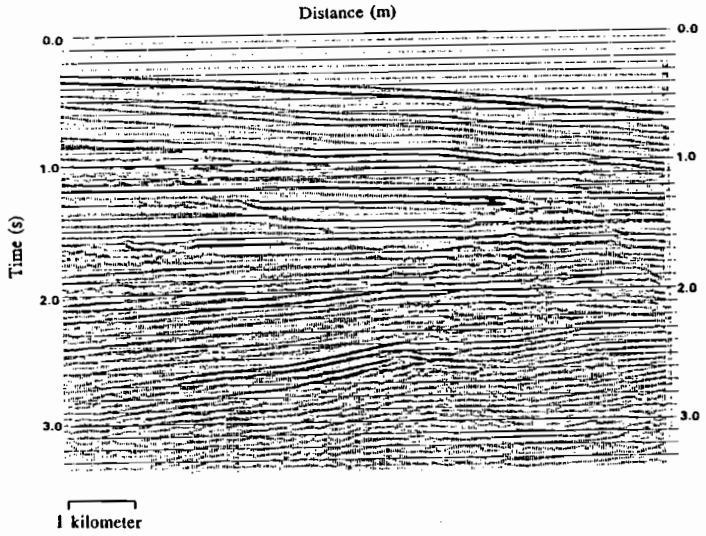

Figure 4 Elastic wave migration/inversion of prestacked data used to produce Figure 2. This section shows the relative changes in bulk modulus.

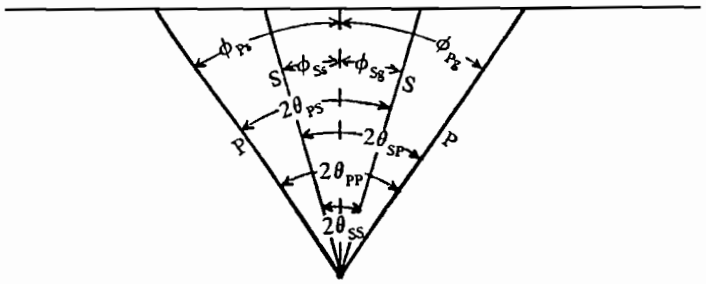

Figure 1 Geometrical relationships of incident and reflected angles (ϕ) and half angles (θ) for compressional and shear waves (equations (35a) and (35b) and (37a) thru (37d)).

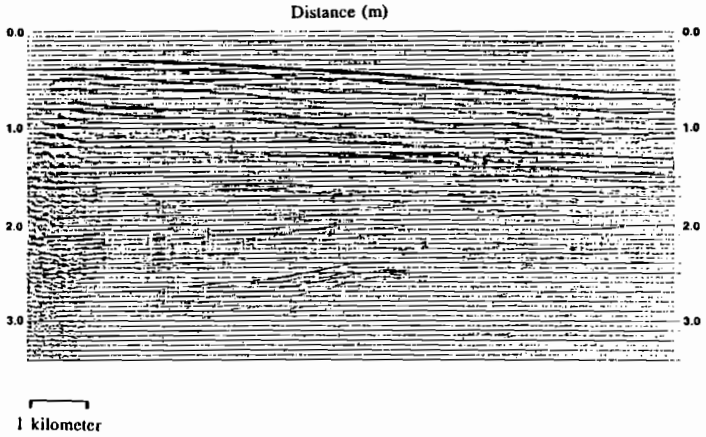

Figure 2 CMP stacked section (P-P data) from the Gulf of Mexico (after Stolt and Benson, 1986).

$$\nu_g k_s + k_g \eta_s = (\omega^2/\alpha_r\beta_r)\sin(2\theta_{SP}), \tag{38e}$$

$$\nu_g \eta_s - k_g k_s = (\omega^2/\alpha_r\beta_r)\cos(2\theta_{SP}), \tag{38f}$$

$$\eta_g \eta_s - k_g k_s = (\omega/\beta_r)^2\cos(2\theta_{SS}), \tag{38g}$$

and

$$k_g \eta_s + \eta_g k_s = (\omega/\beta_r)^2\sin(2\theta_{SS}). \tag{38h}$$

Therefore, using equations (35a), (35b), (36a) thru (36d), and (38a) thru (38h), equations (25) through (28) can be written as follows:

$$D_{PP}(k_g,k_s,\omega) = \{1/(4\cos(\phi_{Pg})\cos(\phi_{Ps}))\}[\cos(2\theta_{PP})\bar{a_1}(k_g-k_s,\nu_g+\nu_s) + \bar{a_2}(k_g-k_s,\nu_g+\nu_s) - 2(\beta_r\sin(2\theta_{PP})/\alpha_r)^2\bar{a_3}(k_g-k_s,\nu_g+\nu_s)]S(\omega), \tag{39}$$

$$D_{PS}(k_g,k_s,\omega) = \{-\beta_r^2\sin(2\theta_{PS})/(4\alpha_r^2\cos(\phi_{Sg})\cos(\phi_{Ps}))\}[\bar{a_1}(k_g-k_s,\eta_g+\nu_s) + (2\beta_r\cos(2\theta_{PS})/\alpha_r)\bar{a_3}(k_g-k_s,\eta_g+\nu_s)]S(\omega), \tag{40}$$

$$D_{SP}(k_g,k_s,\omega) = \{\alpha_r^2\sin(2\theta_{SP})/(4\beta_r^2\cos(\phi_{Pg})\cos(\phi_{Ss}))\}[\bar{a_1}(k_g-k_s,\nu_g+\eta_s) + (2\beta_r\cos(2\theta_{SP})/\alpha_r)\bar{a_3}(k_g-k_s,\nu_g+\eta_s)]S(\omega), \tag{41}$$

and

$$D_{SS}(k_g,k_s,\omega) = \{1/(4\cos(\phi_{Sg})\cos(\phi_{Ss}))\}[\cos(2\theta_{SS})\bar{a_1}(k_g-k_s,\eta_g+\eta_s) + \cos(4\theta_{SS})\bar{a_3}(k_g-k_s,\eta_g+\eta_s)]S(\omega). \tag{42}$$

Thus, the triple Fourier transforms of the scattered elastic wave data are linear combinations of the double Fourier transforms of the relative changes in the medium properties expressed through a_1, a_2 and a_3. As previously mentioned, in the limit of small a_1, a_2 and a_3, these three perturbation parameters can be expressed by equation (24), and in this limit, equations (20) thru (23) and (39) thru (42) become exact. The converted-wave (P-S) reflection amplitude increases with the sine of the angle between the converted wave and the incident P-wave (equation (40)), whereas the contribution from the shear modulus to the P-P wave changes as the square of the sine of the corresponding angle (equation (39)). Consequently, converted-wave amplitudes will become significant at smaller angles than shear modulus contributions to the P-P wave.

The integrated, angular-dependent reflection coefficients $R(\mathbf{x},\theta)$ for each of the scattering modes can now be easily extracted from equations (39) through (42):

$$R_{PP}(x,\theta) = \cos(2\theta_{PP})a_1(x) + a_2(x) - 2(\beta_r/\alpha_r)^2\sin^2(2\theta_{PP})a_3(x), \quad (43)$$

$$R_{PS}(x,\theta) = (\beta_r/\alpha_r)^2\sin(2\theta_{PS})a_1(x) + (\beta_r/\alpha_r)^3\sin(4\theta_{PS})a_3(x), \quad (44)$$

$$R_{SP}(x,\theta) = (\alpha_r/\beta_r)^2\sin(2\theta_{SP})a_1(x) + (\alpha_r/\beta_r)\sin(4\theta_{SP})a_3(x), \quad (45)$$

and

$$R_{SS}(x,\theta) = \cos(2\theta_{SS})a_1(x) + \cos(4\theta_{SS})a_3(x), \quad (46)$$

where the angles are defined in equations (37a) thru (37d) (see Figure 1), and **x** is the reflection point between the incident and reflected rays. Although not explicit in equations (43) thru (46), R depends upon source and receiver coordinates x_s and x_g through the angular dependence θ. The filtered P-P reflection coefficient, $R_{PP}(\mathbf{x},\theta)$, in equation (43) is identical with that of Stolt and Weglein (1985).

Examples

The above inversion algorithm was applied to a set of P-P data from the Gulf of Mexico, where some well control existed. Figures 2 thru 4, respectively, show a CMP stacked section, a f-k prestack migrated section, and a prestack migrated/inverted section (based upon equations (30) thru (31d)). The latter figure shows relative changes in bulk modulus. The migrated sections (Figure 3 and 4) show the same geological structure, but they have obvious amplitude differences since the f-k prestack migration didn't attempt to maintain relative amplitudes, while the inversion algorithm did.

For a second example, the inversion algorithm was applied to a set of data from another area in the Gulf of Mexico where good well control existed. Part of a relative-amplitude P-P stacked section is shown in Figure 5, and according to equations (25) thru (28) (or (39) thru (42)), this section is actually a superposition of the relative changes in bulk modulus, shear modulus, and density. The amplitudes are plotted with positive amplitudes appearing dark and negative amplitudes light. Based upon equations (30) thru (31d), the prestack data were inverted to form the three sections shown in Figures 6 thru 8: (a) relative changes in bulk modulus (Figure 6); (b) relative changes in shear modulus (Figure 7); and (c) relative changes in density (Figure 8).

The large negative amplitudes in bulk modulus (Figure 6) along the horizon near 1.5 seconds are indicative of encountering a shale/gas sand boundary. Since, there are larger relative amplitudes at location #2 than at location #1, this indicates that the gas saturation is greater at location #2, which is in agreement with existing well log data. On the other hand, the shear modulus response (Figure 7) along this same horizon is positive, which would be expected since

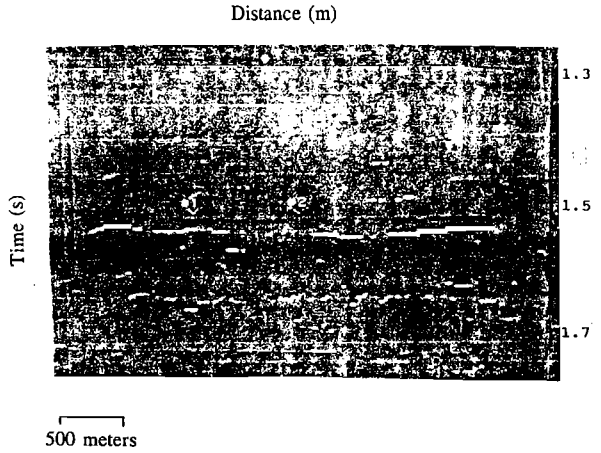

Figure 7 Variable density display of relative changes in shear modulus produced by elastic wave inversion of the prestacked data used in Figure 5 example (based upon equations (30) thru (31d)).

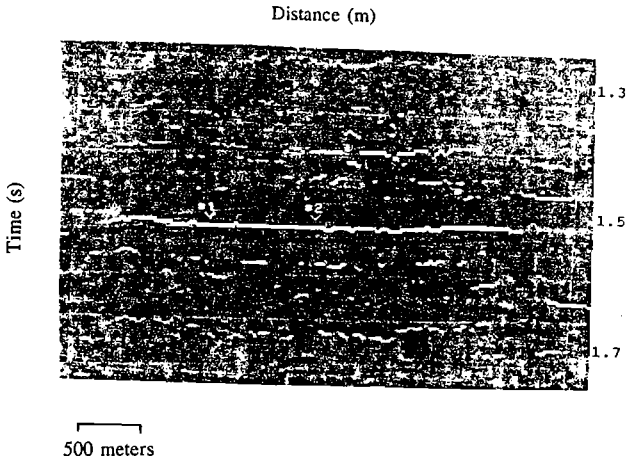

Figure 5 Variable density display of a relative amplitude stacked section (P-P data) from the Gulf of Mexico (courtesy Conoco, Inc.).

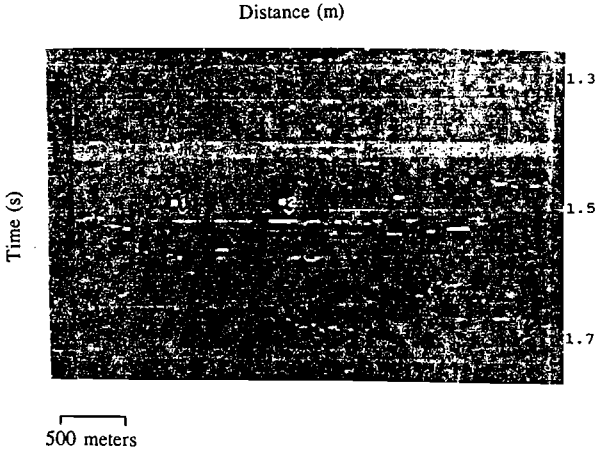

Figure 8 Variable density display of relative changes in density produced by elastic wave inversion of the prestacked data used in Figure 5 example (based upon equations (30) thru (31d)).

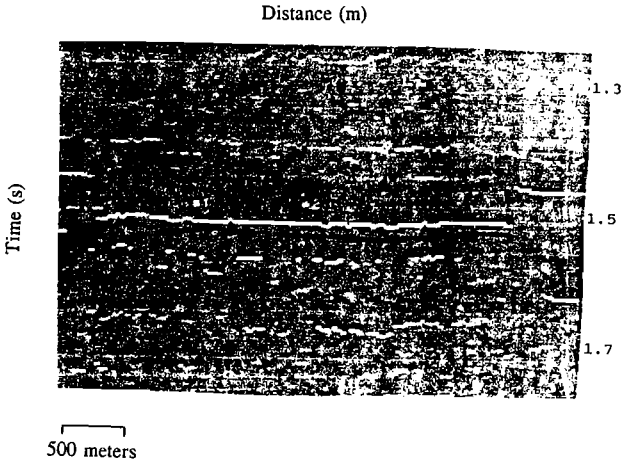

Figure 6 Variable density display of relative changes in bulk modulus produced by elastic wave inversion of the prestacked data used in Figure 5 example (based upon equations (30) thru (31d)).

sandstones are typically more rigid than unconsolidated shales in this area of the Gulf of Mexico. The larger positive response at location #1 compared to that at location #2 suggests that the sandstone near location #1 is more rigid than the sandstone near location #2, and this is again confirmed by well log data. Finally, from the relative change in density (Figure 8), one of the largest lateral density contrasts appears between the location of lower gas saturation (#1) and the location of higher gas saturation (#2).

In summary, the relative change in bulk modulus should be a qualitative indicator of gas sands, the relative change in shear modulus should contain at least qualitative information about the "firmness" or "softness" of the reservoir rock, and the relative change in density should help delineate regions of high gas concentration (Stolt and Benson, 1986). However, caution must always be used in interpreting these elastic parameter changes, since magnitude and sign will depend on the particular reservoir, the surrounding rock, the depth of burial, etc. Thus, some well control in the area is necessary.

Converted-Wave Data — Some Practical Answers

The proper expressions for data recorded at the surface as pressure and shear stress are equations (39) thru (42). The vector comprised of the components D_{PP} and D_{PS} denotes the data generated by an impulsive pressure source, while the vector formed from D_{SP} and D_{SS} is that due to an impulsive shear source. Assuming that the source is purely compressional, the relative amplitudes of D_{PS} and D_{PP} yield the relative strength of the converted waves.

From the transformation in equation (4),

$$\begin{pmatrix} D_{PP} \\ D_{PS} \end{pmatrix} = \begin{pmatrix} K_r & 0 \\ 0 & \mu_r \end{pmatrix} H \begin{pmatrix} U_x \\ U_z \end{pmatrix}, \tag{47}$$

where U_i are the displacement coordinates in equation (1). For data recorded as displacements, the inverse to equation (47) must be employed:

$$\begin{pmatrix} U_x \\ U_z \end{pmatrix} = H^{-1} \begin{pmatrix} 1/K_r & 0 \\ 0 & 1/\mu_r \end{pmatrix} \begin{pmatrix} D_{PP} \\ D_{PS} \end{pmatrix} = \frac{i}{\rho_r \omega^2} \begin{pmatrix} k_g D_{PP} + \eta_g D_{PS} \\ -\nu_g D_{PP} + k_g D_{PS} \end{pmatrix}. \tag{48}$$

If the direction of travel becomes vertical at the surface due to refraction, then from equation (35a) $k_g = 0$, and

$$U_x = (i/\rho_r \omega \beta_r) D_{PS}, \tag{49a}$$

$$U_z = (-i/\rho_r \omega \alpha_r) D_{PP}. \tag{49b}$$

For horizontal and vertical geophones of equal sensitivity, and considering a typical case

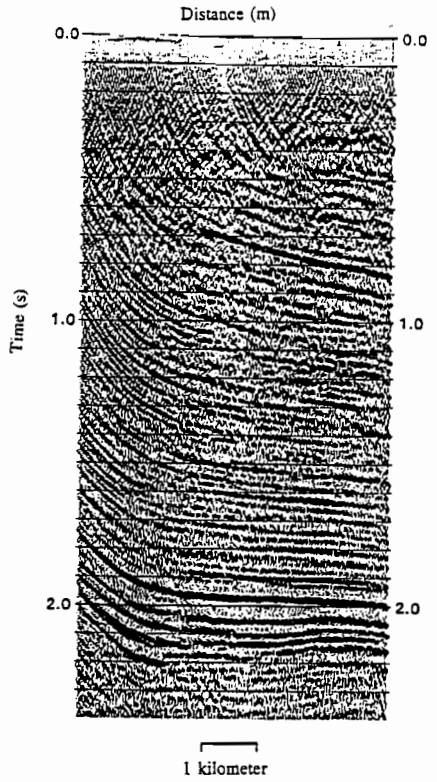

Figure 9 P-P stacked section from southern Oklahoma (courtesy Conoco, Inc.).

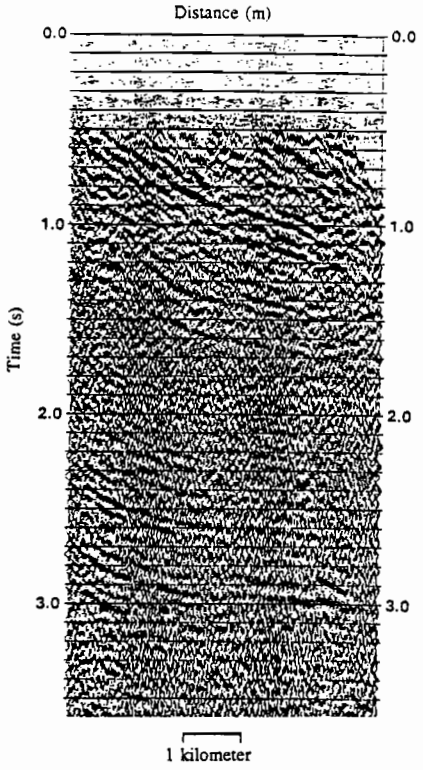

Figure 10 P-S stacked section from southern Oklahoma (courtesy Conoco, Inc.).

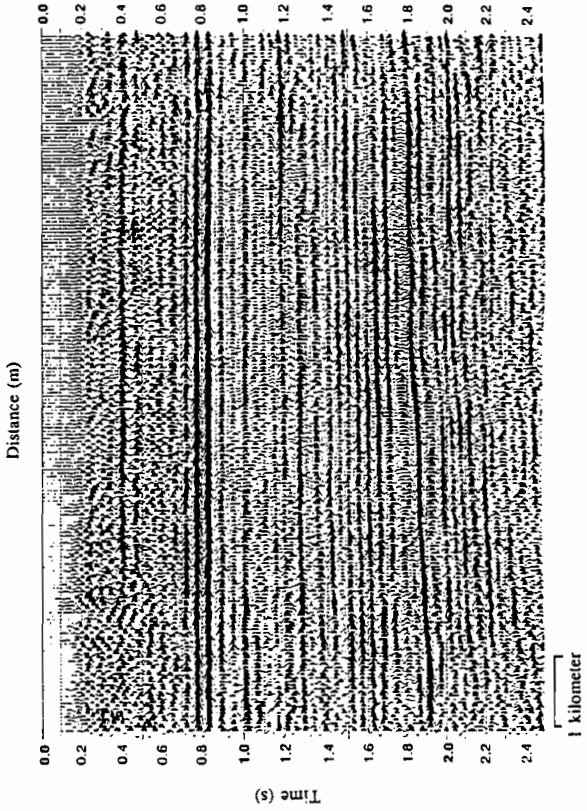

Figure 11 P-P stacked section from western Oklahoma (courtesy Conoco, Inc.).

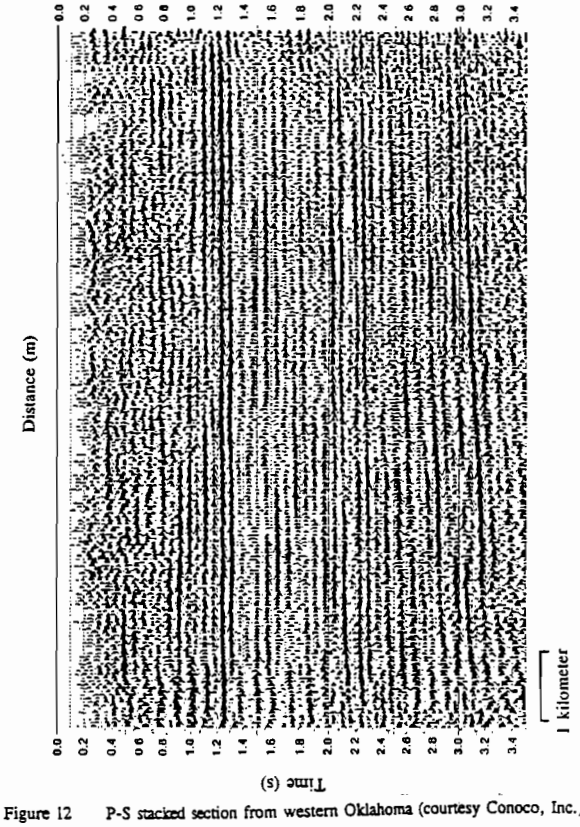

Figure 12 P-S stacked section from western Oklahoma (courtesy Conoco, Inc.).

of $a_2 \approx a_3$ and $\alpha \approx 2\beta$, the relative sizes of P-S and P-P reflections will be

$$r = \frac{|u_x|_{typical}}{|u_z|_{typical}} \approx \frac{\beta_r}{\alpha_r} \sin(2\theta_{PS}) \approx (1/2)\sin(2\theta_{PS}) . \qquad (50)$$

For an angle of incidence of $\approx 15°$, $\sin(2\theta_{PS}) \approx ½$, and $r \approx ¼$. If the incident angle is $\approx 30°$ then $r \approx (\sqrt{3}/4) \approx 0.4$. Thus, for typical reflection data, the amplitude in the horizontal channel will be about 0.25 to 0.4 of the amplitude in the vertical channel. Furthermore, if both channels have comparable noise levels, the vertical channel will have a signal-to-noise ratio about 5 to 16 times greater than the horizontal channel. Due to this low SNR for the P-S waves, a significantly higher field effort will be necessary to produce a P-S section of comparable quality to the P-P section.

A P-P stacked section (Figure 9) was produced from the vertical-array data collected by a P-wave vibrator in southern Oklahoma. The corresponding P-S stacked section constructed from the long-offset field files taken from the horizontal-array data is shown in Figure 10. Although the SNR is marginal, some correlations can be made between the sections, and β/α ratios estimated.

Using more and longer sweeps and more geophone channels at longer offsets, P-P data and P-S data were also collected from a P-wave vibrator experiment at a site in western Oklahoma. The P-P stacked section is shown in Figure 11 and the P-S stacked section in Figure 12. As can be seen, the P-S section is of comparable quality to the P-P section, which is largely due to the increased field effort, but is also a function of the geology of the area. These data illustrate that significant amounts of converted (P-S) data can be generated by compressional sources. Good correlations can be made between the events in these two sections, as well as good estimates of β/α ratios.

Conclusions

Elastic wave data have been decomposed into their primary reflection components, P-P, P-S, S-P, and S-S, and the integrated, angular-dependent reflection coefficients determined for each mode by using a linearized approximation. A general prescription to invert any of these data components to recover relative variations in the medium parameters can be summarized as follows:

(1) Fourier transform the data from x_g, x_s, and t to k_g, k_s, and ω (equation (17));
(2) Downward continue the data to depth z with appropriate Green's operators. Update background parameters and angles (equations (37a) thru (37d)) in each layer. For variable background, numerically construct the WKBJ Green's operators;
(3) Image the data by summing over ω. Steps (2) and (3) would effect a prestack migration of the data;
(4) Change to a new independent variable k_z appropriate for each scattering mode (equations (31a), (32a), (33a), (34a)) and form a set of linear equations like (30) for each mode,

with the A's given in equations (31b) thru (31d), (32b) thru (32d), (33b) thru (33d), and (34b) thru (34d). Solve for the perturbations a_i (equations (13a) thru (13c)) using a least-squares solution over available offsets (or available angles) in the data;

(5) Construct the angular-dependent reflection coefficients (equations (43) thru (46));

(6) Inverse Fourier transform over k_g-k_s and k_z to yield a spatial map of the local reflectivity as a function of the angle of incidence.

Using this algorithm for a three-parameter inversion of P-P data, the following three migrated/inverted sections would result from the input data: (1) relative changes in density, (2) relative changes in bulk modulus, and (3) relative changes in shear modulus. This was illustrated with data from the Gulf of Mexico. Mapping the relative variations of these subsurface parameters provides vital information for engineering and exploration decisions.

Considering compressional sources, the following conclusions about reflection data recorded as displacements can be drawn from equations (39) thru (49):

(1) Compressional sources should generally generate significant amounts of converted (P-S) wave data.

(2) The converted (P-S) wave data (and also S-P data) respond to changes in shear modulus and density, but not to changes in bulk modulus.

(3) The P-P reflections respond to changes in all three parameters, and the shear modulus contribution to this mode is negative, which corresponds to the loss of energy due to mode conversion to P-S waves.

(4) For typical reflections, which are well within the limits of the linearized approximation, the converted (P-S) wave data is equally sensitive to increases and decreases in shear modulus.

(5) The converted-wave reflection amplitude increases with the sine of the angle between the converted wave and the incident P-wave, whereas the contribution from the shear modulus to the P-P wave increases as the square of the sine of this angle. Consequently, the converted-wave amplitudes will become significant at smaller angles than the shear modulus contribution to the P-P wave. However, as noted from equation (50), the signal-to-noise ratio for the converted waves will typically be smaller than that for P-P waves. This indicates that a significantly higher effort would usually be necessary to produce a good quality P-S section than needs to be made to produce a comparable P-P section, including (a) more, and probably longer, sweeps and (b) more geophone channels at longer offsets.

References

Bishop, T., Bube, K., Cutler, R., Langan, R., Love, P., Resnick, J., Shuey, R., Spindler, D., and Wyld, H., 1985, Tomographic determination of velocity and depth in laterally varying media: Geophysics, **50**, 903-923.

Bleistein, N., and Gray, S., 1985, An extension of the Born inversion method to a depth dependent reference profile: Geophys. Prosp., **33**, 999-1022.

Carrion, P., and Foster, D., 1985, Inversion of seismic data using precritical reflection and refraction data: Geophysics, **50**, 759-765.

Clayton, R., and Stolt, R., 1981, A Born WKBJ inversion method for acoustic reflection data: Geophysics, **46**, 1559-1567.

Dines, K., and Lytle, R., 1979, Computerized geophysical tomography: Proc. IEEE, **67**, 1065-1072.

Ewing, W.M., Jardetzky, W.S., and Press, F., 1957, **Elastic Wave in Layered Media**: McGraw-Hill Book Co.

Ivansson, S., 1985, A study of methods for tomographic velocity estimation in the presence of low-velocity zones: Geophysics, **50**, 969-988.

Johnson, S., and Tracy, M.L., 1983, Inverse scattering solutions by a sinc basis, multiple source, moment method; part 1, Theory; Ultrasonic Imaging 5, 361-375.

Justice, J., Vassiliou, A., Singh, S., Logel, J., Hansen, P., Hall, B., Hutt, P., and Solankil, J., 1989, Acoustic tomography fro enhancing oil recovery: The Leading Edge, **8**, 12-19.

Keys, R., and Weglein, A., 1983, Generalized linear inversion and the first Born theory: J. Math. Phys., **24**, 1444-1449.

Lines, L., 1988, Inversion of geophysical data: Soc. Expl. Geophys., Reprint series no. 9.

Lo, T., Toksöz, N., Shao-hui, X., and Wu, R., 1988, Ultrasonic tests of geophysical tomographic reconstruction: Geophysics, **53**, 947-956.

Luo, Y., and Schuster, G.T., 1991, Wave-equation traveltime inversion: Geophysics **56**, 645-653.

Paulsson, B., Cook, N., and McEvilly, T., 1985, Elastic wave velocities and attenuation in an underground repository of nuclear waste: Geophysics **50**, 551-570.

Stolt, R.H., 1978, Migration by Fourier transform: Geophysics **43**, 23-48.

Stolt, R.H., and Weglein A.B., 1985, Migration and inversion of seismic data: Geophysics, **50**, 2458-2472.

Stolt, R.H., and Benson, A.K., 1986, **Seismic Migration: Theory and Practice**: Geophysical Press.

Tarantola, A., 1987, **Inverse problem theory**: Elsevier Sci. Publ.

Taylor, J.R., 1972, **Scattering Theory**: John Wiley and Sons, Inc.

Wattrus, N., 1989, Inversion of ground roll dispersion for near-surface shear-wave velocity variations: Presented at the 59th Ann. Internat. Mtg., Soc. Expl. Geophys., Expanded Abstracts, 946-948.

Weglein, A., 1982, Multidimensional seismic analysis: Migration and inversion: Geoexpl., **20**, 47-60.

Wentzel, F., and Menges, D., 1989, A comparison between Born inversion and frequency-wavenumber migration: geophysics, **54**, 1006-1011.

PEAK UNDRAINED RESISTANCE OF LOOSE SANDS

G. Norris, R. Madhu, M. Ashour, and R. Valceschini

Department of Civil Engineering
University of Nevada, Reno
Reno, NV 89557

R. Ledbetter
U.S. Army Engineers
Waterways Experiment Station
Vicksburg, MS 39180

ABSTRACT

The peak undrained resistance ($\sigma_{d,upeak}$) of a loose sand during liquefaction under monotonic loading does not necessarily occur at or near the Mohr Coulomb failure envelope. Instead, it occurs as that combination or product of a decreasing effective confining pressure ($\bar{\sigma}_3$) and an increasing stress level (i.e., deviatoric stress, σ_d, divided by drained failure stress, σ_{df}, at that confining pressure, $\bar{\sigma}_3$). The condition where this product is a maximum occurs at a particular point on a plot of deviator stress (σ_d) or stress level (SL) versus volumetric strain during shear (ϵ_v) as assessed from drained triaxial tests on loose sands.

A method is presented whereby a single drained test with volume change measurements can be used to assess this undrained peak. This is a refinement of the effective stress method involving the use of drained triaxial tests for liquefaction analysis presented at the 29th Symposium.

INTRODUCTION

At one time, it was believed that the undrained peak strength of sand occurred corresponding to the fully mobilized drained or effective stress friction angle at the resultant critical confining pressure, $\bar{\sigma}_{3crit}$ (Seed and Lee, 1967). It was argued that the critical confining pressure for the void ratio of consolidation, e_c, could be determined as that value of $\bar{\sigma}_3$ from a series of drained tests that yielded a volume change or volumetric strain at failure due to shear loading , ϵ_{vf}, equal to zero (see Fig. 1).

However, as shown by different investigators since Seed and Lee (1967), the peak undrained strength of loose sands that experience complete or limited liquefaction under monotonic loading occurs at the top of the effective stress path at a corresponding deviator stress, σ_d, that is only a small portion (or stress level) of the fully mobilized drained strength, σ_{df}, at the associated confining pressure, $\bar{\sigma}_{3,upeak}$ (less than σ_{3c}, the consolidation

pressure of the undrained test). See, for example, Figs. 2, 3, and 4.

These figures show the undrained stress-strain curves and effective stress paths for triaxial tests (three each) on a subrounded Nevada sand (void ratios, e_c, of 0.82 and 0.94 for Series 1 and 2 respectively) and a subangular Ione sand ($e_c \cong 0.91$). The open circles represent the predicted undrained response as assessed from drained tests with volume change measurements (see Norris et al., 1993). Figure 5 depicts the superposed rebounded drained (i.e., effective stress) stress-strain curves for Series 1 from which one can see that the peak undrained resistance, $\sigma_{d,upeak}$, occurs at a stress level, SL ($= \sigma_{d,upeak}/\sigma_{df}$), well below the drained or effective stress failure (σ_{df}) for the associated confining pressure ($\bar{\sigma}_{3,upeak}$). Only beyond the post peak minimum for the limited liquefaction in Series 1 tests on Nevada sand and the tests on Ione sand does the material reach the Mohr Coulomb failure envelope (see Figs. 2 and 4). For the complete liquefaction that occurs in the Series 2 tests on Nevada sand, the effective stress failure condition is reached only at the residual strength condition (Fig. 3). Therefore, the undrained peak resistance is not strictly an effective stress failure condition. Note also from Fig. 5 that the "strain softening" of the undrained stress strain curve is an artifact of the drop in position of the points on the drained or effective stress stress-strain curves.

Figure 6 shows the collection of rebounded drained stress-strain curves for Nevada Series 1 tests (Fig. 5), each normalized by its drained strength (σ_{df}) so that the vertical axis is a scale of the stress level , SL ($= \sigma_d/\sigma_{df}$). If, for the following discussion, one considers that, instead of the spread seen in Fig. 6, a single SL versus drained axial strain (ϵ_1) curve results (see Fig. 7a), then the corresponding peak undrained resistance of Fig. 7c can be characterized as the maximum of the product of an increasing stress level (SL) times a decreasing confining pressure ($\bar{\sigma}_3$) with increasing axial strain (ϵ_1) times a constant [$\tan^2(45 + \phi/2)-1$]. In other words,

$$\sigma_d = SL\ \sigma_{d_f} \tag{1}$$

where

$$\sigma_{d_f} = \bar{\sigma}_3 \left[\tan^2\left(45 + \frac{\phi}{2}\right) - 1 \right] \tag{2}$$

so that

$$\sigma_d = SL\ \bar{\sigma}_3 \left[\tan^2\left(45 + \frac{\phi}{2}\right) - 1 \right] \qquad (3a)$$

or

$$\sigma_d = SL\ \bar{\sigma}_3 A \quad ; \quad A = \left[\tan^2\left(45 + \frac{\phi}{2}\right) - 1 \right] \qquad (3b)$$

As shown in Fig. 5b, where the dilatancy ratio $(d\epsilon_v/d\epsilon_1)_f$ is the same for all of the rebounded tests, the same drained friction angle, ϕ, results provided the constant volume friction angle, ϕ_{cv}, doesn't change with decreasing pressure. Therefore, σ_d of Eq. 3 varies with SL and $\bar{\sigma}_3$ for a constant ϕ (and, therefore, a constant value of A).

It is that condition where the product of $\bar{\sigma}_3$ and SL equals a maximum that yields the peak undrained resistance. This is the subject of this paper.

METHODS OF ANALYSIS

As shown by Norris et al. (1995), there are four possible approaches to assessing the peak resistance from consolidated rebounded drained tests. One approach is to undertake a multitude of drained tests with the hope of choosing the rebounded confining pressure, $\bar{\sigma}_3$, that corresponds to the peak condition, i.e., $\bar{\sigma}_{3,upeak}$. In that instance, the construction procedure demonstrated via Fig. 5 for Series 1 (as explained by Norris et al., 1993) and the other series (see Norris et al., 1995) will yield a direct assessment or an extrapolation of the peak undrained resistance. Of course, the excessive testing of such an approach is undesirable.

Alternatively, one can put equations to the drained stress-strain-volume change curves (e.g., Fig. 5) and, separately, the isotropic expansion ($\epsilon_{v,iso}$ vs. $\bar{\sigma}_3$) response shown schematically in Fig. 8b (where Fig. 8 is the basis for the effective stress evaluation of undrained behavior described by Norris et al., 1993) and Fig. 9 for Series 1 tests. (Note, for instance, from Fig. 9 that $\epsilon_{v,iso}$ for a drop in $\bar{\sigma}_3$ from the consolidation pressure σ_{3c} = 400 kPa to a rebounded $\bar{\sigma}_3$ of, say, 100 kPa is 1.14-0.77 or 0.37%.) Then, the systematic evaluation of $\epsilon_{v,iso}$, ϵ_1, SL, and σ_d for an assumed rebounded $\bar{\sigma}_3$ (= σ_{3c} - Δu_d, where Δu_d represents the porewater pressure buildup due to shear loading) would lead to an evaluation of σ_d with ϵ_1 from which the maximum value of σ_d would be ascertained by inspection.

Of course, with the governing drained equations established, one might differentiate to try to assess the maximum σ_d explicitly

as a function of the parameters used to characterize the drained response.

The success of Methods 2 and 3 are dependent upon one's ability to accurately formulate the drained (i.e., effective stress) response. Norris et al. (1995) provide such an analysis but have found that, because of the changing shape of the SL vs. ϵ_1 curve (Fig. 6) with an increasing overconsolidation ratio ($\sigma_{3c}/\bar{\sigma}_3$), such analytical methods are only moderately successful (i.e., they predict $\sigma_{d,upeak}$ to within 5 to 20%). Instead, the authors propose a mixed analytical-graphical method (a fourth method) that is as successful, easier to undertake, and, at the same time, informative.

MIXED ANALYTICAL-GRAPHICAL METHOD

Given σ_d as a function of the changing values of SL and $\bar{\sigma}_3$ in Eq. 3b,

$$\frac{\partial \sigma_d}{\partial \epsilon_1} = \frac{\partial SL}{\partial \epsilon_{v,shear}} \frac{\partial \epsilon_v}{\partial \epsilon_1} \bar{\sigma}_3 \, A$$

$$+ \frac{\partial \bar{\sigma}_3}{\partial \epsilon_{v,iso}} \frac{\partial \epsilon_v}{\partial \epsilon_1} SL \, A$$

Equating the above to zero and given that $\epsilon_{v,iso} = \epsilon_{v,shear}$ in undrained loading (see Fig. 8 and/or refer to Norris et al., 1993), one has that

$$\bar{\sigma}_3 \frac{\partial SL}{\partial \epsilon_v} = -SL \frac{\partial \bar{\sigma}_3}{\partial \epsilon_v} \tag{4}$$

On the other hand, the isotropic rebound or swell, $\epsilon_{v,iso}$, resulting from the reduction in confining pressure from σ_{3c} to $\bar{\sigma}_3$ in Fig. 8b or Fig. 9 can be expressed as

$$\epsilon_{v,iso} = C_{\epsilon r} \ln \frac{\sigma_{3c}}{\bar{\sigma}_3} \tag{5}$$

(Note that Eq. 5 is for isotropic rather than k_o response and $C_{\epsilon r}$ is related to the $\log_e$ or ln rather than the $\log_{10}$ variation.) From Eq. 5,

$$\frac{\partial \epsilon_v}{\partial \bar{\sigma}_3} = -\frac{C_{\epsilon r}}{\bar{\sigma}_3} \tag{6}$$

Substituting (6) into (4) yields

$$\bar{\sigma}_3 \frac{\partial SL}{\partial \epsilon_v} = -SL \left[\frac{-\bar{\sigma}_3}{C_{\epsilon r}}\right]$$

or

$$SL \frac{\partial \epsilon_v}{\partial SL} = C_{\epsilon r} \tag{7}$$

If, instead of σ_d or SL vs. ϵ_1, one plots SL vs. ϵ_v (from drained shear), a curve of the form shown in Fig. 10 results. Note that, from 0 to a point A, SL vs. ϵ_v can be expressed as

$$SL = m_A \epsilon_v \tag{8}$$

while, for the straight line portion beyond B,

$$SL = SL_o + m_B \epsilon_v \tag{9}$$

If one differentiates Eqs. 8 and 9, then

$$\frac{\partial SL}{\partial \epsilon_v} = m_A \qquad \textit{between 0 and A} \tag{10a}$$

and

$$\frac{\partial SL}{\partial \epsilon_v} = m_B \qquad \textit{beyond B} \tag{10b}$$

If one substitutes the reciprocal of Eq. 10 into 7, the peak undrained strength occurs where

$$SL \frac{1}{m} = C_{\epsilon r} \tag{11}$$

However, if one evaluates SL times (1/m) at points A and B, one finds that

$$SL_A \frac{1}{m_A} < C_{\epsilon r}$$

$$SL_B \frac{1}{m_B} \gg C_{\epsilon r}$$

Using a secant slope between points A and B, m_{BA}, at A

$$SL_A \frac{1}{m_{AB}} > C_{\epsilon r}$$

Therefore, Eq. 11 is satisfied at point A as the curve rolls over and the slope quickly changes from m_A to a value greater than m_{AB}.

Note that Eq. 7 or 11 says that, where the stress level times the rate of change of volumetric strain with stress level just equals $C_{\epsilon r}$ (i.e., the volumetric expansion per natural log change in confining pressure from σ_{3c}), one has the undrained peak strength. This is a verbal statement of the condition of the undrained peak resistance.

While the foregoing assumes a single SL vs. ϵ_v curve, as with the SL vs. ϵ_1 curves (Fig. 6), a family of SL vs. ϵ_v curves result (see Fig. 11). However, imagine that, in undrained response, the effective stress (ES) behavior is characterized by a path that traverses the drained SL vs. ϵ_v curves as shown by the dashed line in Fig. 11. Therefore, there will be a particular point A from the many curves through which the dashed ES path passes that is the undrained peak point condition. It is a matter of finding that point A and the associated $\bar{\sigma}_3$ value where the ϵ_v at A equals $\epsilon_{v,iso}$ which yields the same $\bar{\sigma}_3$ from the isotropic rebound curve. To find this point and the corresponding peak undrained resistance, perform the following operation.

Procedure

1. For each SL vs. ϵ_v curve at a given $\bar{\sigma}_3$ during shear (i.e., $\bar{\sigma}_{3,shear}$), establish point A.

2. Note the value of $\epsilon_{v,shear}$ at point A. Taking $\epsilon_{v,iso}$ as equal to this value of $\epsilon_{v,shear}$, establish the corresponding $\bar{\sigma}_3$ from the isotropic rebound curve (for instance, Fig. 9 for Series 1 drained tests). Call this $\bar{\sigma}_{3,iso}$.

3. Plot the $\bar{\sigma}_{3,iso}$ vs. $\bar{\sigma}_{3,shear}$ coordinate as shown in Fig. 12.

4. Repeat Steps 1 through 3 for tests at other $\bar{\sigma}_3$ values.

5. From this plot, establish the $\bar{\sigma}_3$ value where the data would cross the 1:1 line. This is $\bar{\sigma}_{3,upeak}$ where $\epsilon_{v,iso} = \epsilon_{v,shear}$ of a point A where Eq. 7 (and 11) is satisfied.

6. With the value of $\bar{\sigma}_{3,upeak}$ established, return to the collection of SL vs. ϵ_v curves of the type shown in Fig. 11 and for the associated $\epsilon_{v,iso}$, enter at $\epsilon_{v,shear} = \epsilon_{v,iso}$, and establish or interpolate the position of point A for the imagined $\bar{\sigma}_{3,upeak}$ curve. Note the SL_A of this point.

7. Calculate $\sigma_{d,upeak}$ as the product of $\bar{\sigma}_{3,upeak}$ from Step 5, SL_A from Step 6, and $[\tan^2 (45 + \phi/2) - 1]$ as per Eq. 3b.

Table 1 provides a comparison between the measured (i.e., observed) peak undrained response (see Figs. 2a, 3a, and 4a) and the calculated values via Method 4. The magnitude of the error is less than 10%.

Unfortunately, Methods 1-4 require a great number of drained rebounded tests. However, in the course of performing the Method 4 analysis, a simplification was noted, one that might limit the number of required tests to a single good test. The simplification that serves as the basis for a modified Method 4 is that the value of ϵ_v of point A from a series of rebounded drained tests (i.e., ϵ_v along the line of "A" points in Fig. 11) is proportional to the confining pressure, $\bar{\sigma}_3$. Accordingly, to assess the peak undrained resistance, follow the steps outline below.

Procedure Based on a Single Rebounded Drained Test

1. Select a rebounded confining pressure, $\bar{\sigma}_3$, at which to test, i.e., $\bar{\sigma}_3 \cong \frac{1}{2}\ \sigma_{3c}$.

2. Establish $\epsilon_{v,shear}$ at point A from the corresponding SL vs. ϵ_v plot from this test.

3. Take $\epsilon_{v,iso}$ equal to ϵ_v at A, and establish $\bar{\sigma}_{3,iso}$ from the corresponding isotropic rebound curve or from Eq. 5 based on $C_{\epsilon r}$ for the rebounded pressure.

4. Compare the $\bar{\sigma}_{3,iso}$ from Step 3 with the test pressure, $\bar{\sigma}_{3,shear}$. If the two values match, say, to within 1%, go to Step 9.

5. If the values do not match, assume a new value of $\bar{\sigma}_3$ (i.e., $\bar{\sigma}_{3,2}$) between the test and calculated values.

6. Determine $\epsilon_{v,shear}$ at Point A (or $\epsilon_{v,2}$) of the new pressure, $\bar{\sigma}_{3,2}$, based on ϵ_v at A of the test pressure (i.e., $\epsilon_{v,1}$ at $\bar{\sigma}_3$ from the test or $\bar{\sigma}_{3,1}$) as

$$\epsilon_{v,2} = \overline{\sigma}_{3,2}\frac{\epsilon_{v,1}}{\overline{\sigma}_{3,1}}$$

7. Calculate $\overline{\sigma}_3$ from Eq. 5 using $\epsilon_{v,iso} = \epsilon_{v,2}$ from Step 6, and compare it to the value of $\overline{\sigma}_3$ assumed in Step 5.

8. Repeat Steps 5, 6, and 7 until convergence occurs.

9. After convergence with respect to $\overline{\sigma}_3$, calculate $\sigma_{d,upeak}$ based on Eq. 3 using SL_A from point A in Step 2 and ϕ from the test.

Example

The following example is presented using the results from Series 2. The SL vs. $\epsilon_{v,shear}$ curve at $\overline{\sigma}_3 = \frac{1}{2}\sigma_{3c} = 200$ kPa is presented in Fig. 13.

1. Assume $\overline{\sigma}_3 = \frac{1}{2}\overline{\sigma}_{3c} = 200$ kPa.

2. $\epsilon_{v,A} = 0.25\%$ (from Fig. 13).

3. $C_{\epsilon r} = 0.346\%$ as noted from the isotropic rebound response of the test.

$$\overline{\sigma}_3 = (400)\, e^{-\left(\frac{0.25}{0.346}\right)} = 194\ kPa$$

4. $\overline{\sigma}_3$ calculated in Step 3 does not equal the $\overline{\sigma}_3$ assumed in Step 1.

5. Assume $\overline{\sigma}_3 = 197$ kPa.

6.

$$\epsilon_{v,A} = .25\left(\frac{197}{200}\right) = 0.246\%$$

$$\overline{\sigma}_3 = (400)e^{-\left(\frac{0.246}{0.346}\right)} = 196\ kPa$$

Therefore, say that $\overline{\sigma}_3$ at $\overline{\sigma}_{d,upeak} = 196$ kPa.

7. $SL_A = 0.30$ (from Fig. 13) and $\phi = 31°$.

8.

$$\sigma_{d,upeak} = (0.30)(196)\left[\tan^2\left(45 + \frac{31}{2}\right) - 1\right] = 125\ kPa$$

Table 1 presents a summary of the simplified Method 4 determinations of $\sigma_{d,upeak}$ for the series of tests performed. As can be judged, the method provides values as good as Method 4.

DISCUSSION

This paper has dealt with the prospect of accurately assessing the monotonic undrained peak resistance, $\sigma_{d,upeak}$, of a loose sand from drained tests. Four separate methods were investigated, though only one method was presented here for discussion. As noted, the modified fourth method yields values that are in as good agreement as Method 4 though it requires only a single (good) rebounded drained test at $\bar{\sigma}_3 \cong \frac{1}{2}\sigma_{3c}$.

It should be pointed out that the undrained peak of these loose sands occurs at a stress level of between 30% and 55% of the drained strength at $\bar{\sigma}_{3,upeak}$. This is why the peak of the effective stress path for such liquefiable soils is so far removed from the strength envelope.

REFERENCES

Seed, H.B. and Lee, K.L., "Undrained Strength Characteristics of Cohesionless Soils," *Journal of Soil Mechanics and Foundation Division*, ASCE, Vol. 93, No. SM6, 1967, pp. 333-360.

Norris, G.M., Zafir, Z., and Siddharthan, R., "Liquefaction and Residual Strength of Loose Sands from Drained Triaxial Tests," *Proceedings 29th Engineering Geology and Geotechnical Engineering Symposium*, March 1993, pp. 301-315.

Norris, G.M., Madhu, R., Valceschini, R., and Ashour, M., "Liquefaction and Residual Strength of Loose Sands from Drained Triaxial Tests," Report 2, Civil Engineering Department, Report No. CCEER-95-2, University of Nevada, Reno, February 1995.

Table 1. Comparison of Measured and Calculated Undrained Peak Resistance			
Series	Measured	Method 4	Method 4 (single test)
Nevada, Series 1	214	208	200
Nevada, Series 2	127	135	125
Ione	350	360	353

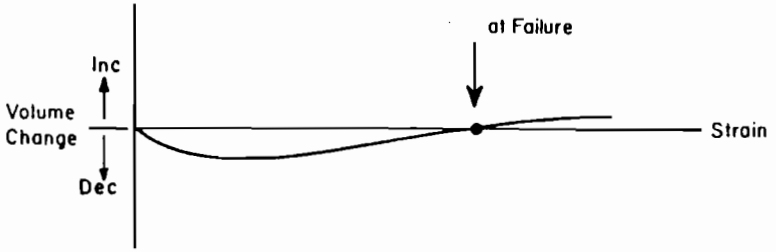

Fig. 1. Test yielding critical confining pressure after Seed and Lee (1967).

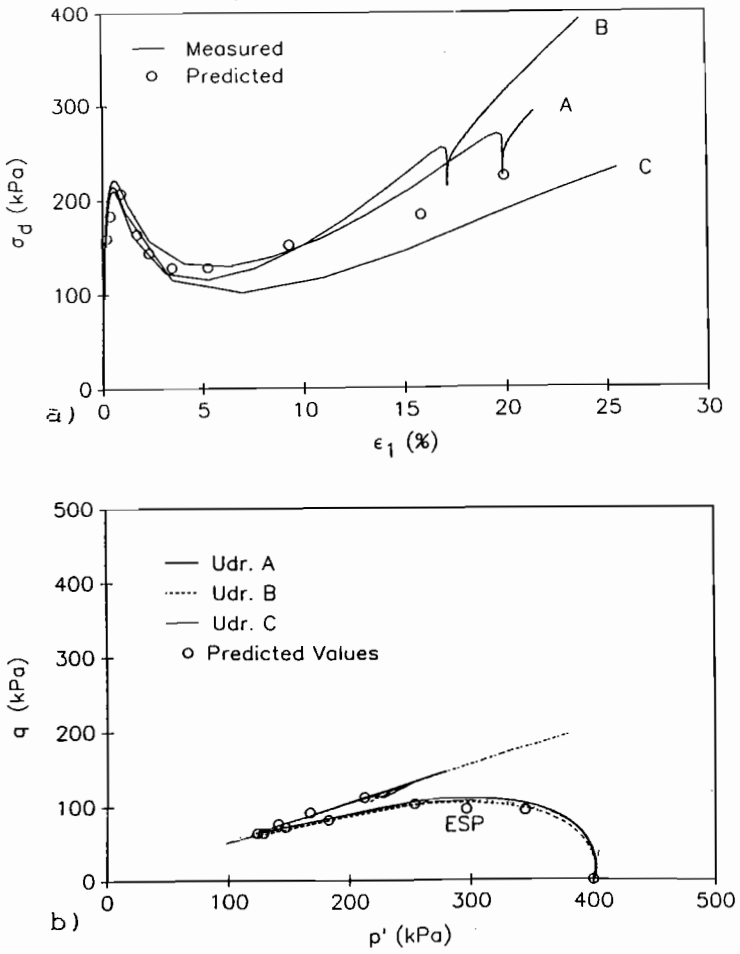

Fig. 2. Undrained a) stress-strain curve and b) effective stress path, Nevada sand, $e_c \cong 0.82$, σ_{3c} = 400 kPa (Series 1).

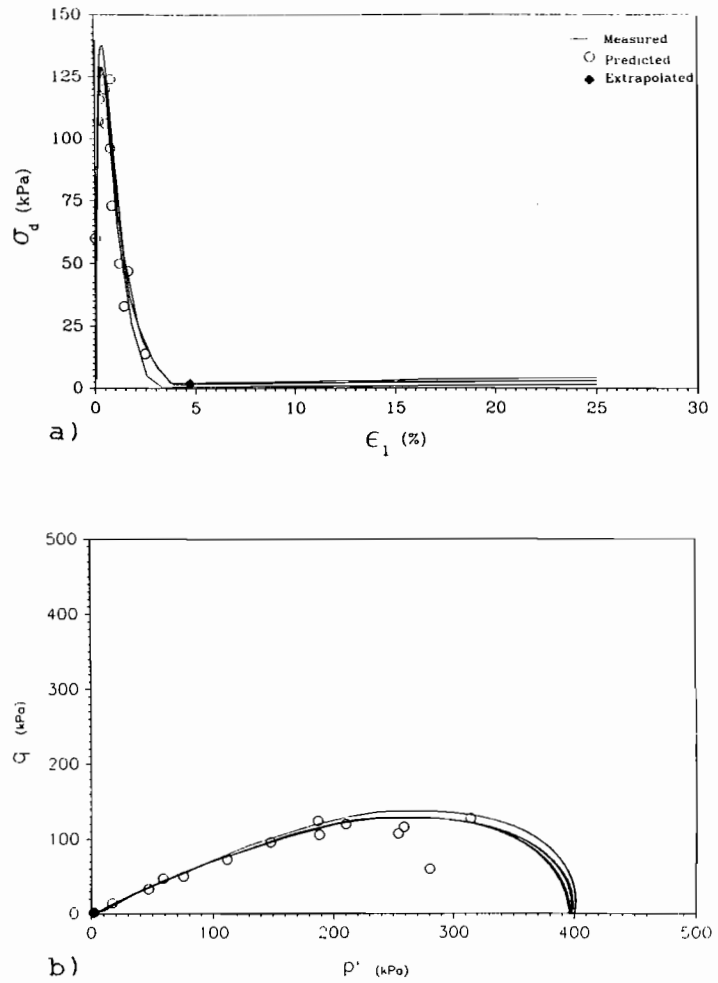

Fig. 3. Undrained a) stress-strain curve and b) effective stress path, Nevada sand, $e_c \cong 0.94$, σ_{3c} = 400 kPa (Series 2).

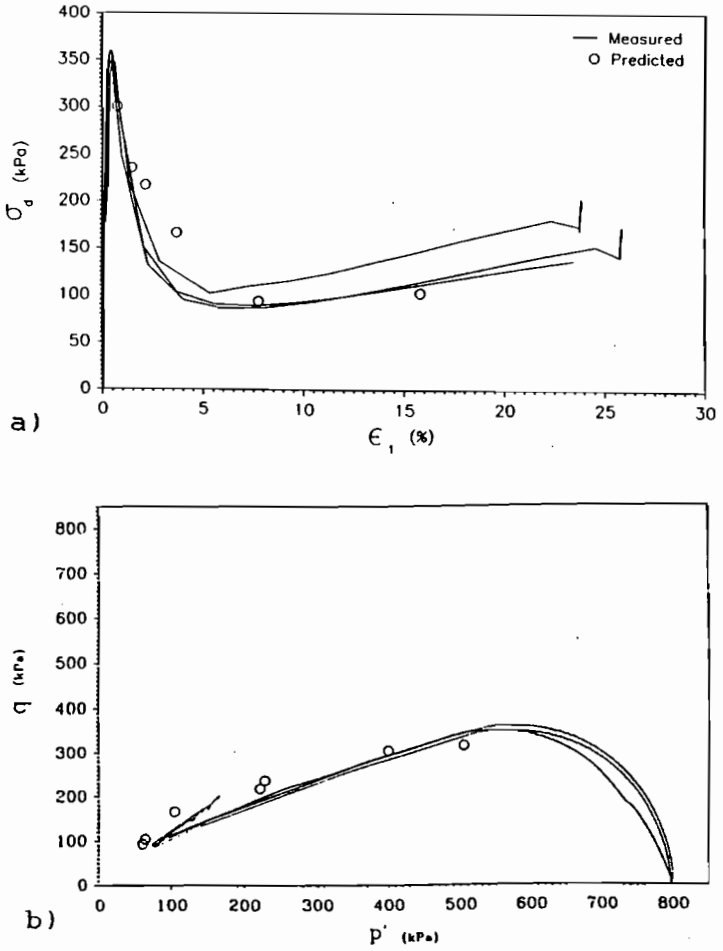

Fig. 4. Undrained a) stress-strain curve and b) effective stress path, Ione sand, $e_c \cong 0.91$, $\sigma_{3c} = 800$ kPa.

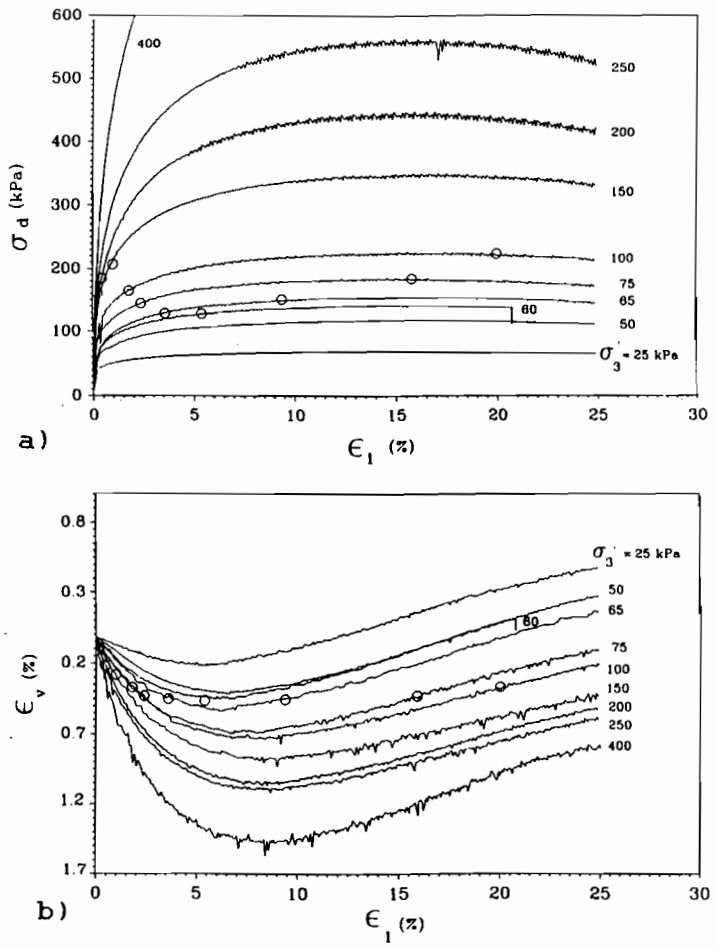

Fig. 5. Drained a) stress-strain and b) volume change response during shear, Series 1.

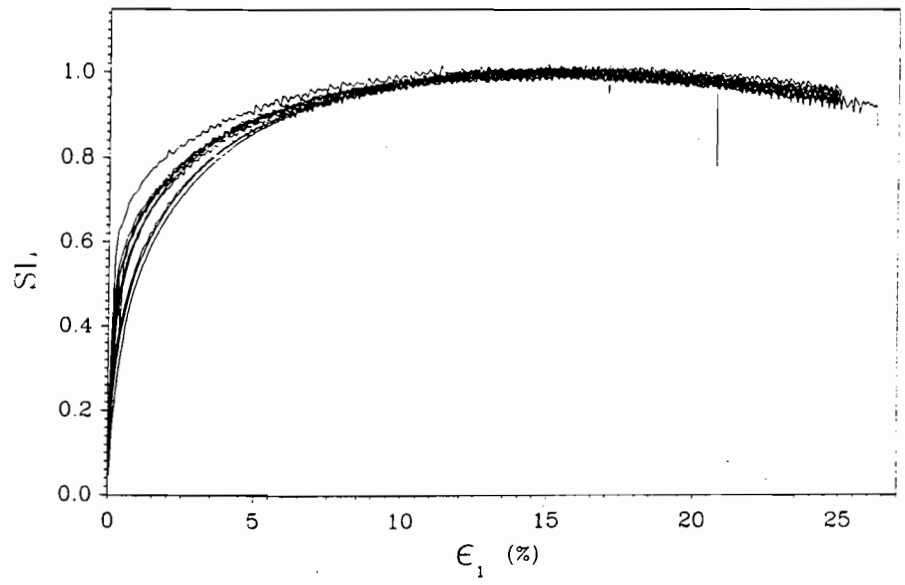

Fig. 6. SL vs. ϵ_1 curves, Series 1.

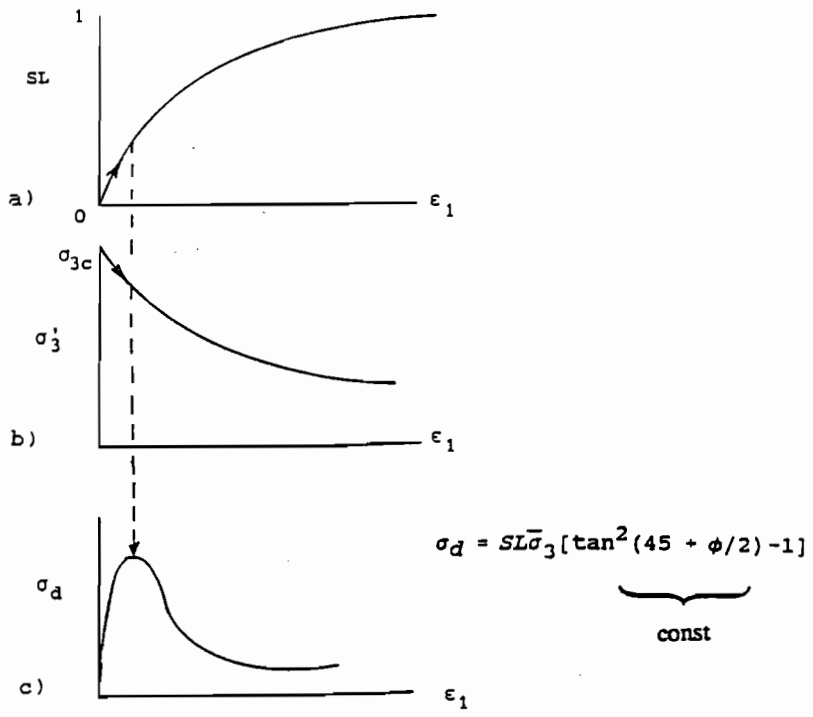

Fig. 7. Form of the relationship of a) increasing stress level (SL), b) decreasing confining pressure ($\bar{\sigma}_3$) that leads to c) the undrained peak resistance.

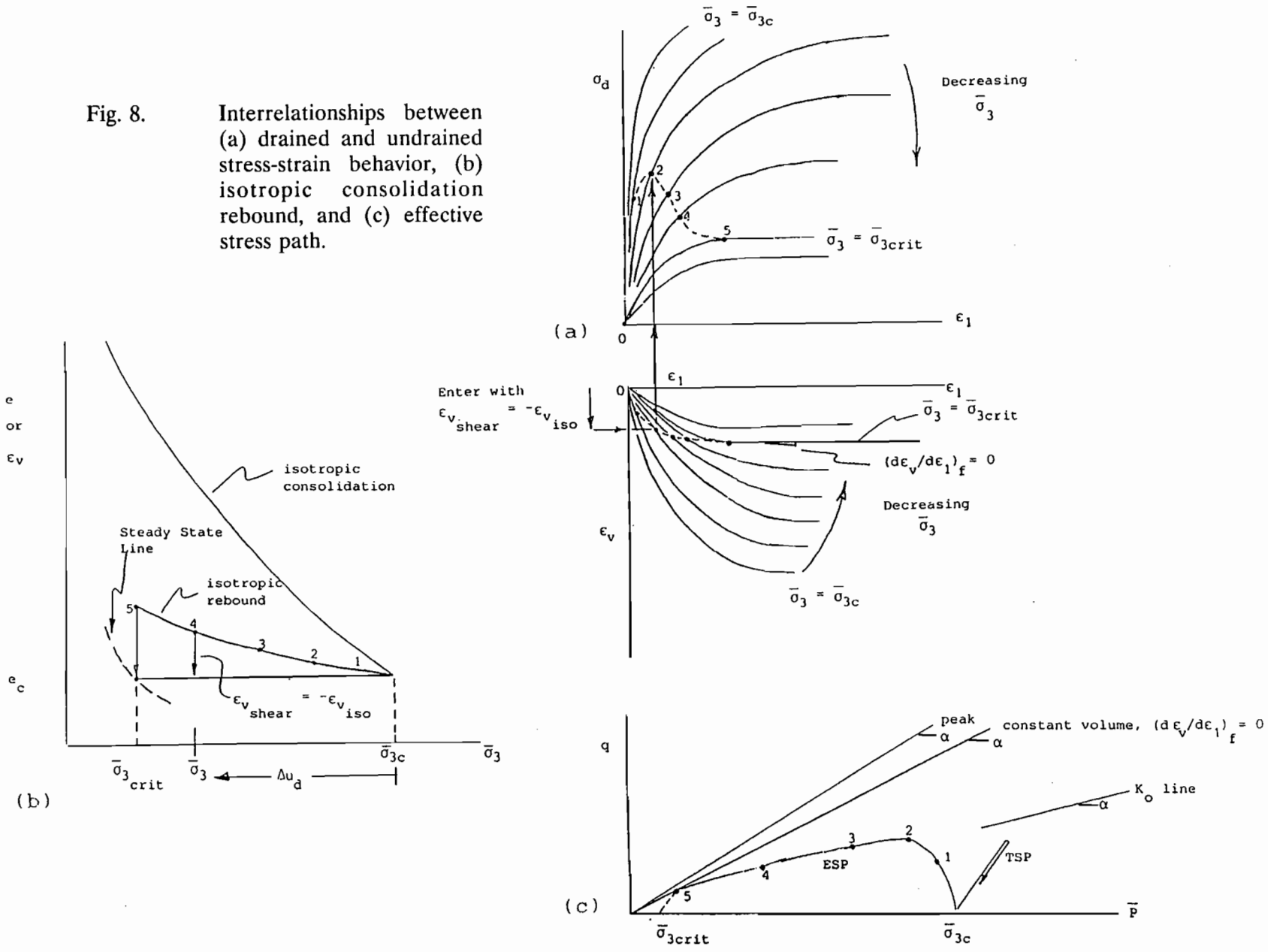

Fig. 8. Interrelationships between (a) drained and undrained stress-strain behavior, (b) isotropic consolidation rebound, and (c) effective stress path.

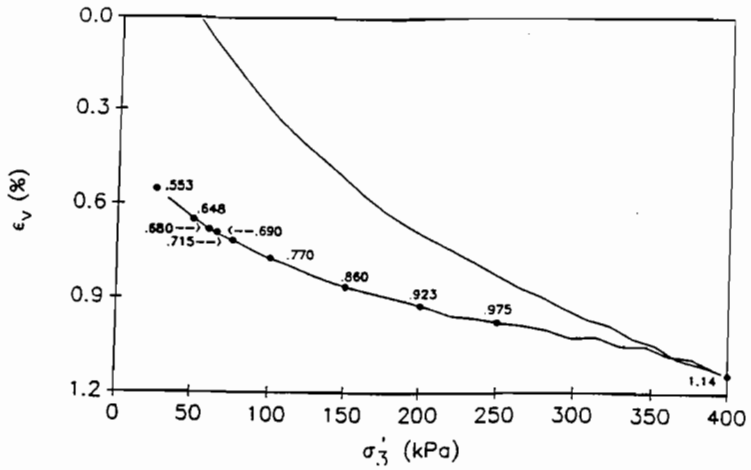

Fig. 9. Isotropic consolidation and rebound response, Series 1.

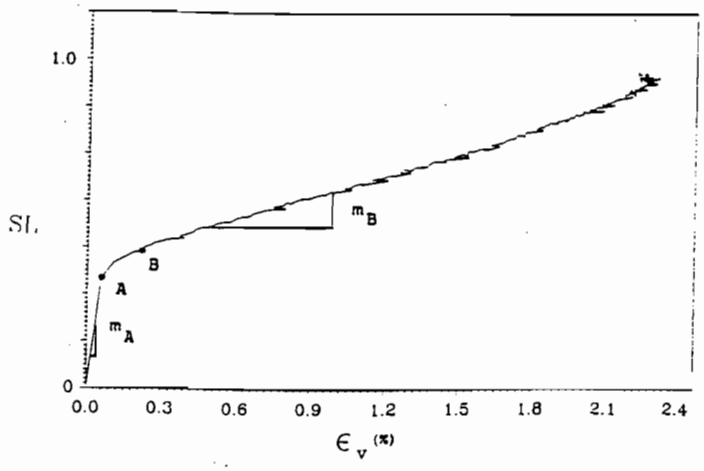

Fig. 10. Form of SL vs. ϵ_v curve.

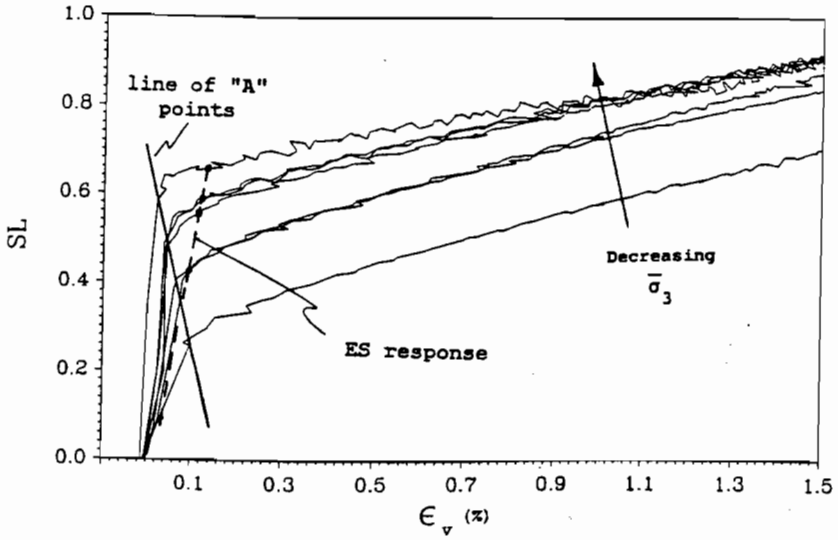

Fig. 11. Family of drained rebounded SL vs. ϵ_v curves.

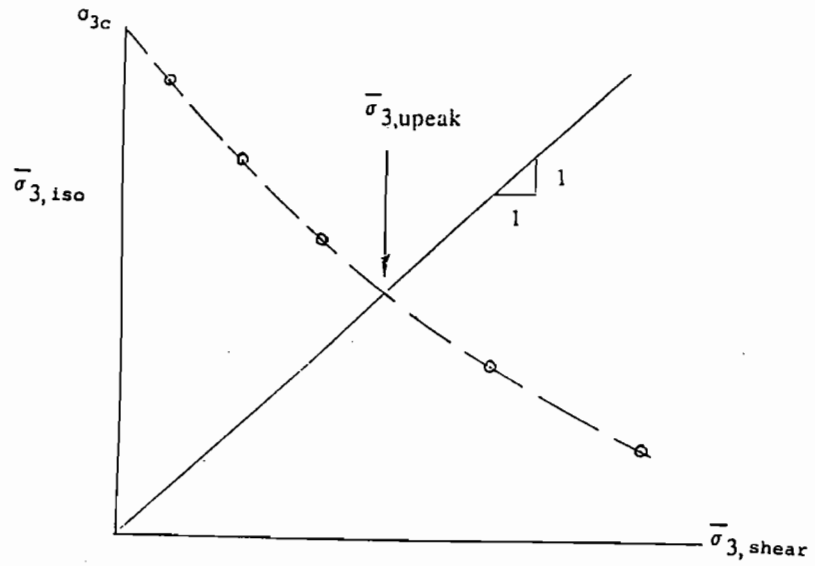

Fig. 12. Evaluating $\bar{\sigma}_{3,upeak}$ for Method 4.

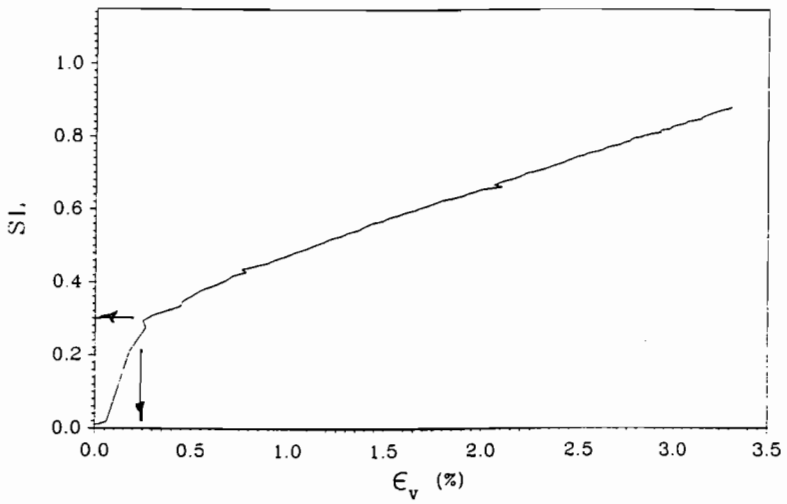

Fig. 13. SL vs. ϵ_v curve for test at $\bar{\sigma}_3 = \frac{1}{2}\sigma_{3c}$ (= 200 kPa), Series 2.

HYPERBOLIC MODEL PARAMETERS OF UNSATURATED NORTHWEST AGRICULTURAL SOILS

Mitchell F. Schaub and James H. Hardcastle
Department of Civil Engineering, University of Idaho, Moscow, Idaho

John E. Hammel
Division of Soil Science, University of Idaho, Moscow, Idaho

ABSTRACT

Compaction of near-surface agricultural soils below the depth of tillage by heavy farm machinery reduces soil permeability, crop root penetration, root density and overall soil productivity. Factors affecting compaction include soil composition, soil water content (or suction) and the stresses induced in the subsoil by the surface wheel loads. Previous studies of stress distributions in agricultural soils have modeled the soils as either homogenous or vertically layered, linear elastic media. In order to provide nonlinear, stress-dependent soil modulus values consistent with low confining stresses for use in finite element stress and strain analyses, 70 drained triaxial compression tests were performed on 7 agriculturally important soils from the Pacific Northwest. This paper presents the results of the tests and describes their interpretation within the framework of the Duncan and Chang (1970) hyperbolic model of soil stress-strain behavior. Difficulties encountered in fitting the hyperbolic model to the response of undisturbed, unsaturated natural soils are discussed. The effects on stress-strain behavior of seasonal changes in subsoil water content are compared in terms of a "suction modulus number" and a "suction modulus exponent." These parameters are analogous to the Janbu (1963) modulus number and modulus exponent used to characterize the conventional confining stress dependency exhibited by soils. The results of the study also have application in settlement analyses of foundations on soils subject to post-construction increases in subgrade water content.

INTRODUCTION

Compaction of soils by heavy farm machinery wheel loads is a concern in long-term soil and crop management. Compaction beneath the tillage zone (approximately 18 inches deep) decreases soil permeability, decreases root penetration and density and causes a subsequent reduction in plant access to moisture and nutrients.

The factors which affect the compaction of agricultural soils include soil composition, soil moisture content (or matric suction), confining stress, and the stresses induced in the soil by the applied wheel loads. Previous studies of stress distributions in agricultural soils at low confining stresses have modeled the soils as either homogenous or vertically layered continua with linear elastic moduli of elasticity and Poisson's ratios. A more realistic constitutive model should include consideration of the nonlinear, stress-dependent stress-strain behavior as a function of moisture content (or suction).

To account for nonlinearity of the stress-strain behavior, the Duncan and Chang (1970) hyperbolic model was selected and triaxial compression tests were performed on seven Northwest agricultural soils. This model was selected because of its use in a number of available finite element programs capable of predicting stress-strain behavior for a variety of load and soil conditions. This paper presents the results of tests and the hyperbolic model parameters obtained. The influence of variations in soil suction on the stress-strain behavior is also presented. The application of the results to settlement predictions for foundations and pavements on soils which undergo post-construction increases in moisture content is briefly discussed.

PARAMETERS OF THE HYPERBOLIC MODEL

The use of the hyperbolic model to represent nonlinear stress-dependent stress-strain behavior of soils requires nine parameters derived from the triaxial test data. Included in these parameters are dimensionless modulus numbers and exponents which relate how the model changes as a function of the confining stress

Based on the work by Kondner (1963), the nonlinearity of the stress-strain curve can be modeled using a hyperbola with the equation:

$$(\sigma_1 - \sigma_3) = \frac{\varepsilon}{1/E_i + \frac{\varepsilon}{(\sigma_1 - \sigma_3)_{ult}}} \qquad (1)$$

where $(\sigma_1 - \sigma_3)$ is the deviator stress, ε is the axial strain, E_i is the initial stress-dependent tangent modulus, and $(\sigma_1 - \sigma_3)_{ult}$ is the asymptotic value of the deviator stress.

To obtain a best-fit hyperbola from the results of triaxial compression tests, it is convenient to transform the equation into the slope-intercept form of a straight line as follows:

$$\frac{\varepsilon}{(\sigma_1 - \sigma_3)} = \frac{1}{E_i} + \frac{\varepsilon}{(\sigma_1 - \sigma_3)_{ult}} \qquad (2)$$

The intercept on the $\varepsilon / (\sigma_1 - \sigma_3)$ ordinate is $1 / E_i$ and the slope of the straight line is the asymptote of the hyperbola, $(\sigma_1 - \sigma_3)_{ult}$. The best-fit hyperbola is obtained by plotting the values of $\varepsilon / (\sigma_1 - \sigma_3)$ vs ε from the triaxial test stress-strain data. Duncan and Chang (1970) recommend that the best-fit hyperbola be obtained by plotting the values of deviator stress and axial strain corresponding to 70 and 95 percent of the maximum deviator stress observed in the triaxial test.

The experimental maximum (failure) deviator stress $(\sigma_1 - \sigma_3)_f$ is related to the asymptote of the hyperbola by a failure ratio factor, R_f, as follows:

$$(\sigma_1 - \sigma_3)_f = R_f (\sigma_1 - \sigma_3)_{ult} \qquad (3)$$

The relation of $(\sigma_1 - \sigma_3)_f$ to σ_3 is defined using the Mohr-Coulomb strength equation :

$$\left(\sigma_1 - \sigma_3\right)_f = \frac{2c\cos\phi + 2\sigma_3 \sin\phi}{(1-\sin\phi)} \qquad (4)$$

where c is the cohesion intercept and ϕ is the angle of internal friction. To account for a nonlinear (curved) Mohr-Coulomb failure envelope, Duncan et al. (1980) introduced the following relationship:

$$\phi = \phi_o - \Delta\phi \ \log_{10}\left(\frac{\sigma_3}{p_a}\right) \qquad (5)$$

where ϕ_0 is the value of ϕ when the confining pressure is equal to atmospheric pressure, and $\Delta\phi$ is the reduction in ϕ for a ten fold increase in σ_3.

The hyperbolic model accounts for the stress-dependency of the initial tangent modulus using the Janbu (1963) relationship

$$E_i = K\ p_a \left(\frac{\sigma_3}{p_a}\right)^n \qquad (6)$$

where K is termed the modulus number, n is the modulus exponent, σ_3 is the confining stress and p_a is atmospheric pressure in any desired system of units.

Confining stress also has an effect on the volumetric strain behavior of a given soil. In a conventional triaxial test the volumetric or bulk modulus is defined by

$$B = \frac{\left(\sigma_1 - \sigma_3\right)}{3\varepsilon_v} \qquad (7)$$

where $(\sigma_1 - \sigma_3)$ is the deviator stress and ε_v is volumetric strain. The initial value of the bulk modulus at small strains can be related to the confining stress in the following equation:

$$B = K_b p_a \left(\frac{\sigma_3}{p_a}\right)^m \qquad (8)$$

where K_b is defined as the bulk modulus number, m is the bulk modulus exponent and p_a is atmospheric pressure expressed in the same units as σ_3 and B.

By differentiating Eq. 1 with respect to axial strain and substituting Eqs. 3, 4, 5 and 6, the expression for the stress and strain-dependent tangent modulus is obtained as

$$E_t = \left[1 - \frac{R_f(1-\sin\phi)(\sigma_1-\sigma_3)}{2c\cos\phi + 2\sigma_3\sin\phi}\right]^2 Kp_a\left(\frac{\sigma_3}{p_a}\right)^n \qquad (9)$$

This equation is used to calculate the value of the tangent modulus for any conditions of confining stress and deviator stress provided the values of K, n, c, ϕ, and R_f are known.

Due to the inelastic behavior of a soil, the stress strain curve during unloading and reloading is steeper than the stress-strain curve during primary loading. The unloading-reloading modulus (E_{ur}) is related to the confining pressure by the equation

$$E_{ur} = K_{ur} p_a \left(\frac{\sigma_3}{p_a}\right)^n \qquad (10)$$

where K_{ur} is the unloading-reloading modulus number and is always larger than the value of K for primary loading. The value of the exponent n is similar to the value for primary loading and is usually assumed to be the same. The parameters used in defining the best fit hyperbolic model are summarized in Table 1.

Parameter	Name	Function
K, K_{ur}	Modulus number	Relate E_i and E_{ur} to σ_3
n	Modulus exponent	Relate E_i and E_{ur} to σ_3
ϕ, $\Delta\phi$	Friction angle parameters	Relate $(\sigma_1-\sigma_3)_f$ to σ_3
c	Cohesion intercept	Relate $(\sigma_1-\sigma_3)_f$ to σ_3
K_b	Bulk modulus number	Relates B to σ_3
R_f	Failure ratio	Relates $(\sigma_1-\sigma_3)_{ult}$ to $(\sigma_1-\sigma_3)_f$
m	Bulk modulus exponent	Relates B to σ_3

TABLE 1. The hyperbolic parameters and their function in the hyperbolic model.

SOILS AND TEST CONDITIONS

Triaxial stress tests were completed on intact samples of seven agriculturally important soils found in the Pacific Northwest. Samples for each location were collected from a depth of 18 inches in areas which had not been previously disturbed by heavy wheel traffic or tillage. The names, locations, and physical properties of the soils used in this study are given in Table 2.

Ten samples were obtained at each location. Samples were obtained by hand carving to minimize structural disturbance. Using a process similar to the pressure plate extraction technique (Klute, 1986), two samples were equilibrated with matric suction values of 4.4, 7.3 and 43.5 psi. Four samples were equilibrated with matric suctions of 14.5 psi. Samples were allowed to equilibrate at each suction value for a minimum of 30

days prior to testing. The relationships between matric suction and volumetric water content are shown in Figure 1. Additional details of sample conditioning are in Salire et al. (1994).

Soil Series	Location	Clay %	Silt %	Sand %	LL %	PI	Group Name	Group Symbol
Declo	Aberdeen, ID	17	66	17	27.8	4.1	Silt with Sand	ML
Naff	Genesee, ID	27	58	15	37.7	12.5	Silt with Sand	ML
Larkin	Moscow, ID	25	65	10	36.0	16.9	Lean Clay	CL
Mission	Sandpoint, ID	27	68	5	33.5	9.2	Silt	ML
Palouse	Moscow, ID	24	64	12	35.8	19.4	Lean Clay	CL
Owyhee	Parma, ID	23	56	21	29.6	5.7	Silt with Sand	ML
Walla Walla	Pendleton, OR	14	69	17	27.8	4.1	Silt with Sand	ML

TABLE 2. Physical properties and locations of Northwest agricultural soil samples.

Triaxial compression tests were performed at confining stresses of 3 and 5 psi for each matric suction value. The tests were completed in two phases, with samples at matric suctions of 4.4, 7.3 and 14.5 psi in Phase One and samples at matric suctions of 14.5 and 43.5 psi in Phase Two. Phase Two testing occurred approximately 12 months after Phase One. Samples were stored in air-tight containers at a temperature of 40 degrees Fahrenheit prior to testing. Phases were conducted by two different operators using the same equipment.

Prior to placement in the triaxial cell, each sample was trimmed to an approximate length to diameter ratio of 2:1 and enclosed in a flexible rubber membrane. The cell was filled with de-aired water and a cell pressure applied. Each sample was allowed to equilibrate under the confining stress while the volume changes in both the sample and the cell fluid were monitored. Axial deformations were measured with a dial gauge. Axial loads were measured with a proving ring. The confining pressure was monitored with a pressure transducer. Corrections were made to account for expansions in the triaxial cell and connecting lines due to the confining pressure. A total of 70 triaxial tests were completed.

FITTING THE HYPERBOLIC MODEL

Typical results of stress-strain curves at confining stresses of 3 and 5 psi and a low matric suction value are shown in Figure 2. Results of tests completed at higher matric suction values and a confining stress of 5 psi are shown in Figure 3.

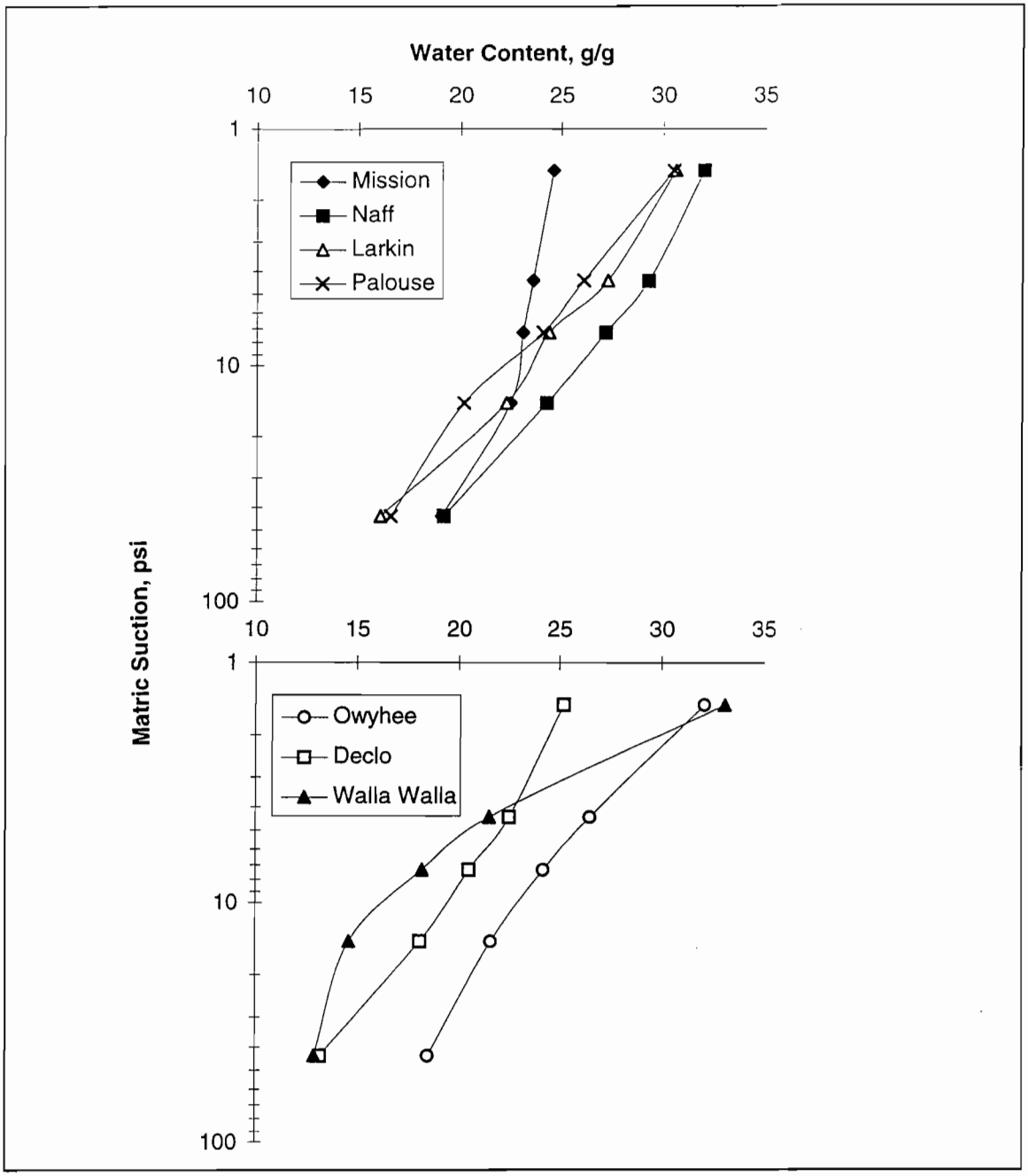

Figure 1. Water content-suction relationships.

The stress-strain curves at low matric suctions are characteristic of soft or loose soils. They exhibit low initial tangent moduli and a maximum deviator stress reached asymptotically at larger axial strains. The response curves at higher matric suctions generally are more like dense or brittle soils with a higher initial tangent modulus and a peak deviator strength reached at low strains. The stress-strain curves completed at suctions of 14.5 and 43.5 psi show an initial increase in the tangent modulus followed by a decrease. Duncan et al. (1980) suggest shifting the stress-strain curves so that the

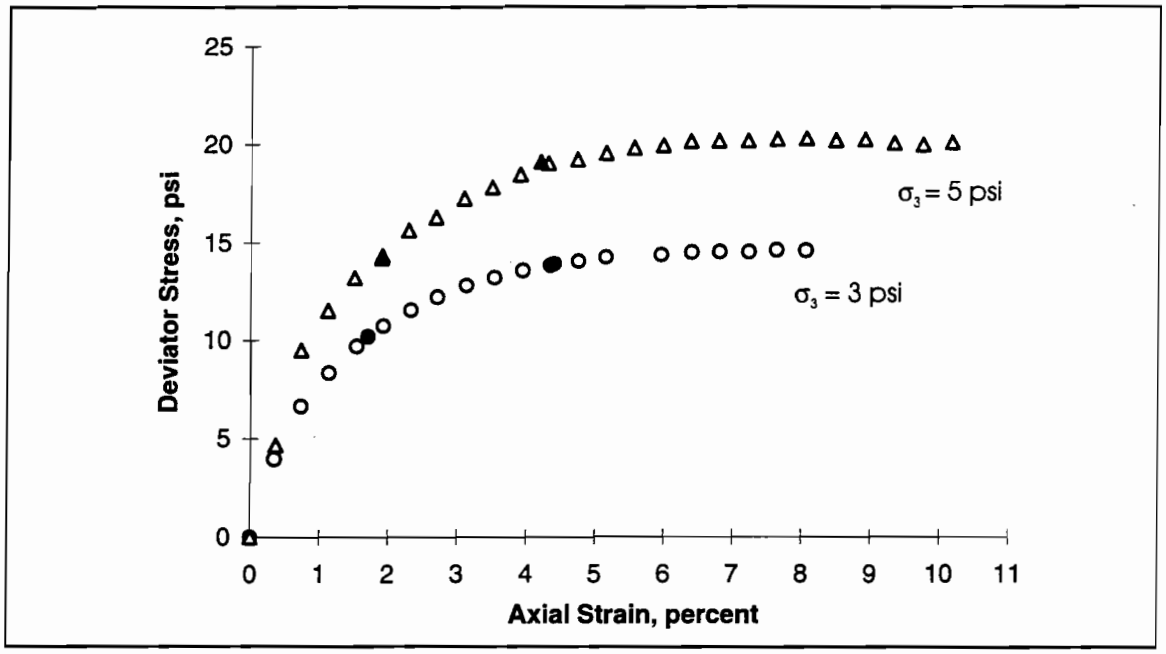

Figure 2. Stress-strain curve for Declo soil at 4.4 psi suction. Solid symbols denote values of 70 and 95 percent of the maximum deviator stress.

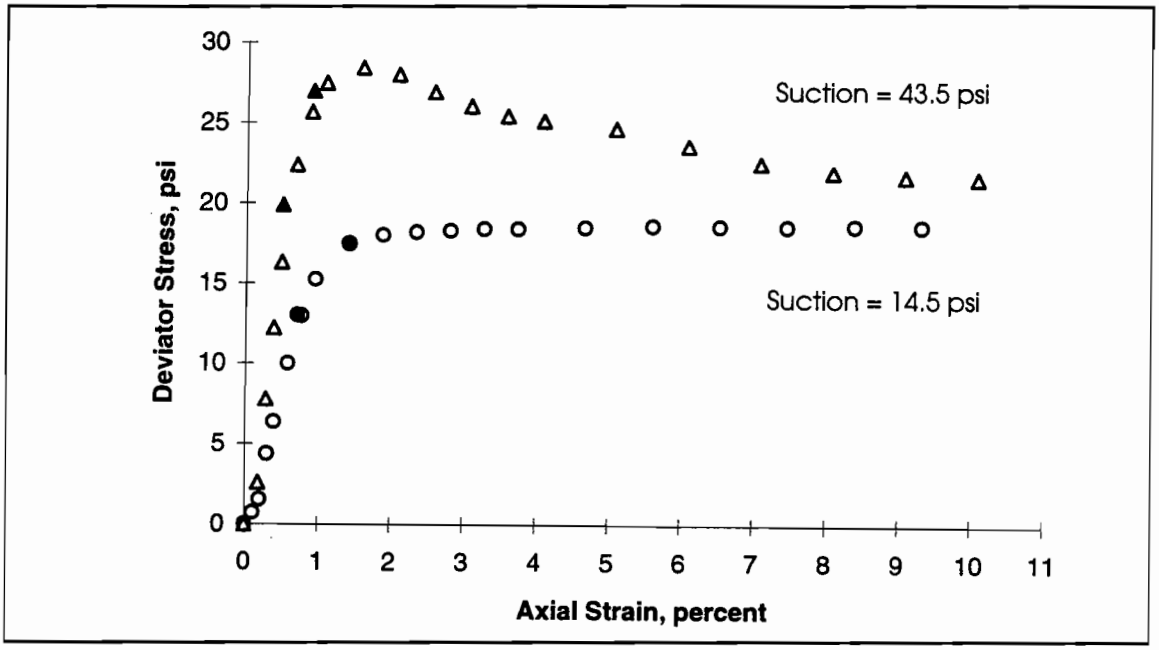

Figure 3. Stress-strain curve for Walla-Walla soil at 5 psi confining stress. Solid symbols denote values of 70 and 95 percent of the maximum deviator stress.

tangent to the stress-strain curve just above the inflection point passes through the origin. This was done for the stress-strain curves of the samples at 14.5 and 43.5 psi suction prior to the determination of the best-fit hyperbola.

The hyperbolic model parameters were determined from drained triaxial tests using the methods suggested by Duncan et al. (1980). The initial tangent modulus and ultimate strength of the best-fit hyperbola were obtained by plotting the test values of $\varepsilon / (\sigma_1 - \sigma_3)$ vs ε at 70 and 95 percent of the maximum deviator stress for each triaxial test as shown in Figure 4. Typical test data and the resulting best-fit hyperbolas are shown in Figure 5.

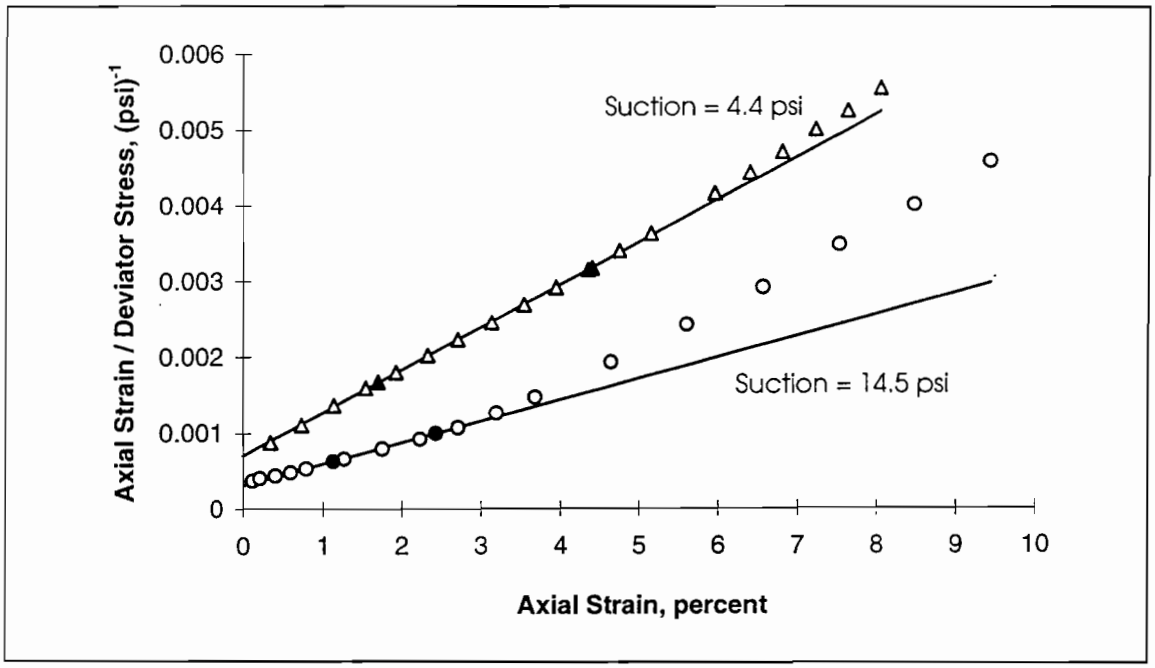

Figure 4. Transformed stress-strain curve for Declo soil at 3 psi confining stress.

STRESS DEPENDENCY ANALYSIS

The stress-dependent modulus number K and modulus exponent n were determined using the initial tangent modulus obtained from the best-fit hyperbolas. The parameters K and n are defined as the y-intercept and the slope of the plots of (E_i/p_a) vs (σ_3/p_a) as shown in Figure 6.

The relationship between the bulk (or volumetric) modulus and the confining stress was determined by plotting the normalized bulk modulus, B/p_a, against the normalized pressure, σ_3/p_a. Duncan et al. (1980) suggest using the value of the volumetric strain at a deviator stress equal to 70 percent of the peak stress in the determination of B. The values of K_b and m are defined as the y-intercept and the slope of the line in the same manner as K and n are defined for the initial tangent modulus of elasticity.

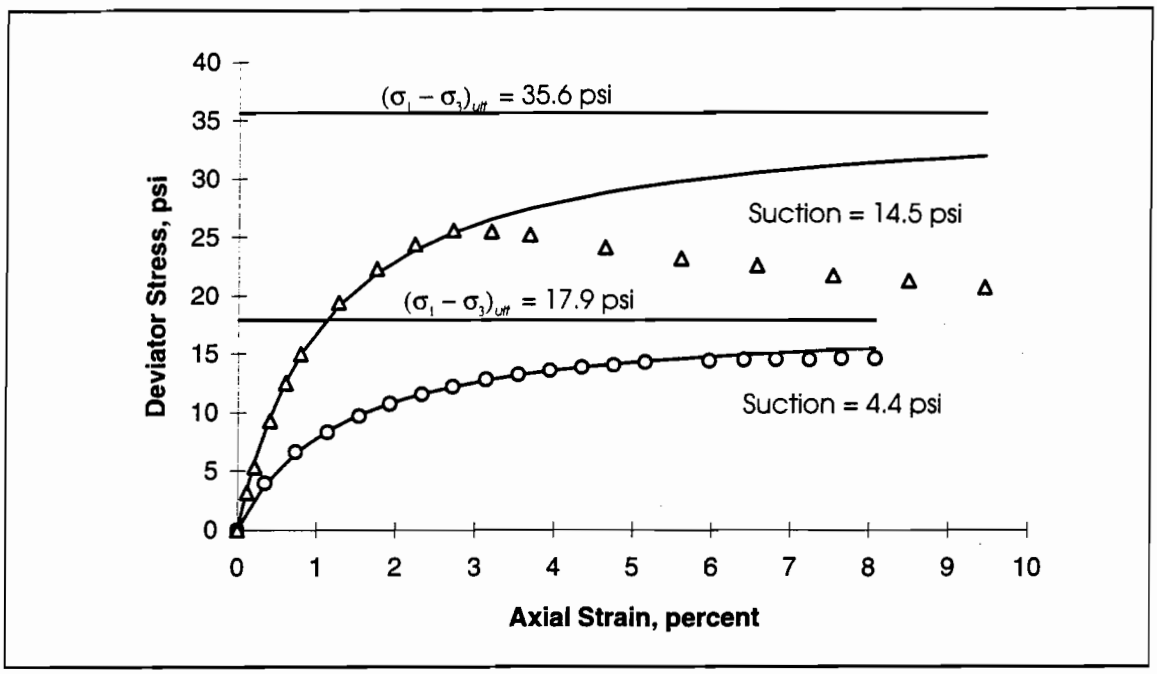

Figure 5. Experimental stress-strain curves and corresponding best fit hyperbolas for Declo soil at 3 psi confining stress.

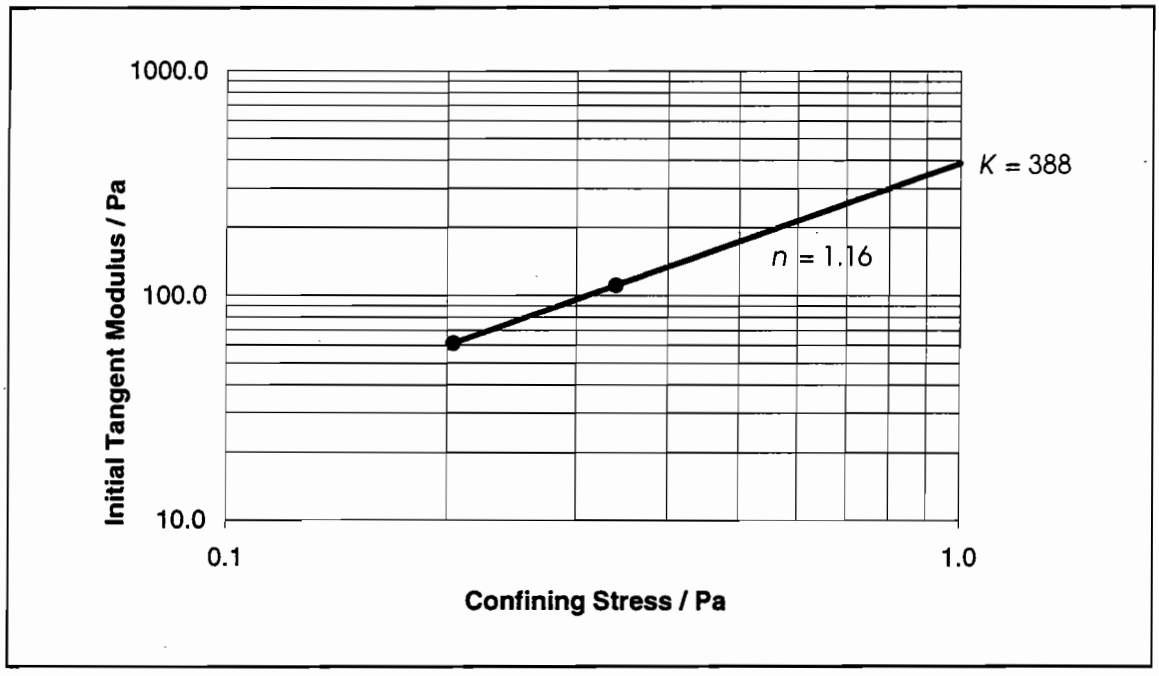

Figure 6. Relationship of confining stress and initial tangent modulus for Naff soil at 4.4 psi suction.

The values of the unloading-reloading modulus, K_{ur}, and exponent, n, are determined in the same manner as K and n. In the absence of unloading-reloading tests, Duncan et al. (1980) suggest using values of K_{ur} / K of 1.2 for dense soils and 3 for loose soils. The modulus exponent n for reloading is taken as equal to the modulus exponent n for primary loading. All the hyperbolic parameters determined from the triaxial tests are in Table 3.

The influence of suction-induced confining stresses on the initial tangent modulus of the agricultural soils was examined using a "suction modulus number" K' and a "suction modulus exponent" n'. These parameters are analogous to the Janbu (1963) modulus number K and exponent n used to describe the conventional confining stress-dependency of the initial tangent modulus. Values of K' and n' are determined by plotting the normalized initial tangent modulus values at a given confining stress against the corresponding normalized suction as shown in Figure 7 for the Palouse soil. Values of K' and n' for all the tests are listed in Table 4.

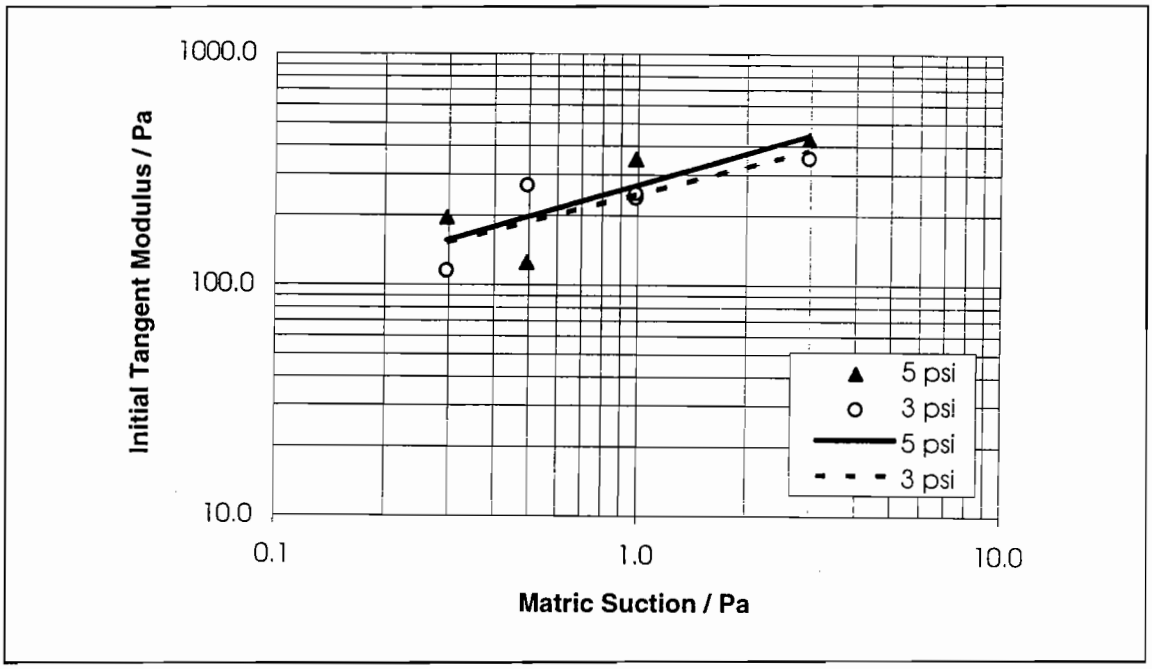

Figure 7. Relationship of matric suction and tangent modulus of Palouse soil at confining stress of 3 and 5 psi.

CONCLUSIONS

Among the objectives of this study was the development of stress-strain parameters applicable at low confining stresses. Comparisons of these low-stress moduli with those reported for similar soil types at more usual (higher) engineering stress levels was also of interest. While direct comparisons were made difficult by the fact that the water contents and suctions of the silty soils described in the literature are unknown and the water contents of the soils in this study were varied over a wide range, comparisons based on average values from Table 3 and K and n values of 16 and .95 reported by

Table 3. Summary of Hyperbolic Model Parameters based on Confining Stress

Matric Suction = 4.4 psi

Soil Series	ϕ	c psi	R_f	K	n	K_b	m
Declo	32.5	2	.75	127	.17	38	.07
Naff	28.0	3	.82	388	1.16	199	1.20
Larkin	32.5	3	1.36	337	.67	93	.44
Mission	34.0	2.5	.92	73	-.15	12	-1.34
Palouse	32.5	3	1.11	594	1.03	88	.34
Owyhee	30.0	2	.88	139	.04	52	.13
Walla Walla	32.0	2	1.70	45	-.83	8	-1.36

Matric Suction = 7.3 psi

Soil Series	ϕ	c psi	R_f	K	n	K_b	m
Declo	32.5	3	.68	73	-.33	23	-.32
Naff	28.0	3.5	.99	424	.81	249	1.06
Larkin	32.5	4	1.82	5720	.42	120	.74
Mission	34.0	3	.92	24	-1.2	61	-..03
Palouse	32.5	6	1.53	25	-1.51	89	.09
Owyhee	30.0	3	.96	772	1.34	70	.18
Walla Walla	32.0	5	1.51	772	-1.05	45	-.33

Matric Suction = 14.5 psi

Soil Series	ϕ	c psi	R_f	K	n	K_b	m
Declo	32.5	4	.49	155	-.22	77	.22
Naff	28.0	4	.72	132	-.28	54	-.39
Larkin	32.5	5	.88	206	-.21	41	-.35
Mission	34.0	3.5	.70	583	.09	569	.53
Palouse	32.5	9	1.55	375	-.42	160	.48
Owyhee	30.0	4	.94	787	.07	86	-.37
Walla Walla	32.0	4	1.00	899	.92	118	.41

Matric Suction = 43.5 psi

Soil Series	ϕ	c psi	R_f	K	n	K_b	m
Declo	32.5	5	.44	174	-.33	23	-.75
Naff	28.0	10.5	.39	233	-.16	31	-.86
Larkin	32.5	6	.55	516	.40	178	.69
Mission	34.0	4	.22	846	.13	60	-1.07
Palouse	32.5	13	1.23	632	.36	28	-.99
Owyhee	30.0	5	.24	116	-1.0	5	-2.50
Walla Walla	32.0	5	.60	574	.16	254	.55

Boscardin et al. (1990) and values of 200 and 1.07, respectively, reported by Duncan et al. (1980) showed that the near-surface agricultural soils generally had larger modulus numbers (K) and smaller modulus exponents (n) than the engineering soils. Although the insitu dry unit weights of the engineering soils were quite variable, they typically were five to ten percent lower than the reported dry unit weights of the engineering soils. Because K represents the normalized initial tangent modulus at relatively low confining stresses (one atmosphere), it appears that the higher suctions no doubt experienced by the near-surface agricultural soils during their existence are at least as effective in producing a stiff soil structure as is conventional confining stress or compaction. The generally smaller average modulus exponents of the agricultural soils indicate that they are also not as sensitive to changes in confining stress as are the engineering soils referred to above. This may also reflect the effectiveness of high suction values in producing a soil structure whose behavior is more like a "solid" material and less like a material consisting of particles.

Table 4. Summary of Hyperbolic Model Parameters based on Soil Suction.

Confining Stress	3 psi		5 psi	
Soil Series	K'	n'	K'	n'
Declo	186	.51	167	.42
Naff	175	.68	188	.35
Larkin	183	.40	267	.32
Mission	272	.85	251	1.00
Palouse	247	.40	271	.46
Owyhee	261	.77	261	.43
Walla Walla	79	.33	276	.63

It was expected that at high water contents (low suctions), the soil moduli would be more sensitive to conventional confining stresses then at low water contents (high suctions). No such increased stress-dependency was observed. Because the suction modulus exponent, n', averaged for the two confining stresses used (3 and 5 psi) were larger than the conventional modulus exponent n averaged for each soil over the four suction levels used (4.4, 7.3, 14.5, 43.5 psi), it was concluded that at the low stress levels of interest in the agricultural soil compaction problem the changes in suction, i.e., water content, are more significant with respect to the soil stress-strain characteristics than are equivalent changes in conventional confining stresses.

Efforts to establish relationships between the soil types as characterized by liquid limits, plasticity indices, and the Unified Soil Classification System class and the initial tangent modulus parameters were not very successful. No clear relationships existed between soil modulus number, modulus exponent, and soil types. A qualitative dependence of the suction modulus number, K', (the initial tangent modulus of elasticity corresponding to a suction of one atmosphere) on the "colloidalness" of the agricultural soils is suggested by the data in Tables 2 and 4. These data show that the largest values of K' generally correspond to the soils having the highest plasticities.

To examine the effect of post-construction increases in moisture content, a finite element analysis was completed on a soil model represented by the stress-dependent hyperbolic model, using the FEADAM84 program (Duncan et al., 1984). A 1.5 ft. wide spread footing with a contact pressure of 100 kPa (approximately 1 ton per square foot) was applied to a wet soil (low suction) and a dry soil (high suction). These soils were modeled using average K and n values of 300 and .6 for wet soils respectively, and K and n values of 600 and .26 for dry soils. The results indicate a settlement of 0.5 inch for the soil at low suctions and settlements of 0.07 inch for the same soil at high suction. This analysis indicates that post-construction increases in moisture content are an important consideration in the evaluation of settlement potential in these unsaturated, near-surface Northwest agricultural soils.

REFERENCES

Boscardin, M.D., E.T. Selig, R.S. Lin, and G.R. Yang. 1990. Hyperbolic parameters for compacted soils. Journal of the Geotechnical Engineering Division, ASCE, Vol. 116, No. 1., pp. 88-104.

Duncan, J.M. and C.Y. Chang. 1970. Nonlinear analysis of stress and strain in soils. Journal of Soil Mechanics and Foundations Division, ASCE,Vol 96,No. SM5,pp. 1629-1653.

Duncan, J.M., R.B. Seed, K.S. Wong, and Y. Ozawa. 1984. Feadam84: A computer program for finite element analysis of dams. Geotechnical Engineering Research Report No. SU/GT/84-03, Department of Civil Engineering, Stanford University, Palo Alto, California. 56 p.

Duncan, J.M., P. Byrne, K.S. Wong, and P. Mabry. 1980. Strength, stress-strain and bulk modulus parameters for finite element analysis of stresses and movements in soil masses. Report No. UCB/GT/80-01, Department of Civil Engineering, University of California , Berkely, California. 70 p.

Janbu, N. 1963. Soil compressibility as determined by oedometer and triaxial test. Proceedings of the European Conference on Soil Mechanics and Foundation Engineering, Weisbaden, Germany. Vol. 1, pp. 19-25.

Klute, A. 1986. Water retention: laboratory methods. In A. Klute (editor), Methods of Soil Analysis, Part 1. Physical and Minerological Properties. Agronomy Monograph No. 9, 2nd Edition, American Society of Agronomy, Madison, pp. 635-662.

Kondner, R.L. 1963. Hyperbolic stress-strain response: Cohesive soils. Journal of Soil Mechanics and Foundations Division, ASCE. Vol. 89, No. SMI p. 115-143.

Salire, E.V., J.E. Hammel, and J.H. Hardcastle. 1994. Comparison of intact subsoils under short-duration loading. Soil and Tillage Research, Vol. 31, pp 235-248.

Statnamic Load Testing of Bridge Pier Foundations in North America

Matthew Janes, P.Eng.[1]

Introduction

Statnamic load testing is becoming widely accepted as a method to quickly and economically determine the load deflection behaviour and ultimate static resistance of high capacity deep foundations. The quasi static test method uses gas pressure to temporarily load the foundation. During testing, load and displacement are measured directly to produce a load deflection curve for the foundation. A simplified method of analyzing the field measurements permits an accurate derivation of static load deflection response. Depending upon the shaft and soil conditions the derived static response is often very similar to the measured Statnamic response. Recent programs sponsored by the Federal and State Highways Departments in the United States have used Statnamic load testing as part of an overall quality assurance program for new bridge structures. Four bridge structures in the design phase or now under construction have used the Statnamic load test method to establish shaft resistance and geotechnical design parameters.

The Statnamic load test method is introduced through a discussion of case histories of several projects involving vertical tests in of 14 to 30 MN (1500 to 3400 tons) and lateral pier tests of up to 0.6 MN (68 tons). A discussion of the method, theory and interpretation of test results is included.

Statnamic Method

Theory

During conventional static load testing a shaft under goes compression as a whole in unison with the soil. The pile soil system acts as a rigid body, with the shaft compression stresses distributed in equilibrium throughout the shaft. In contrast a pile hammer blow will load only a small portion of the shaft and soil at any moment. It loads the shaft with a compressive stress pulse which propagates down the shaft as a stress wave traveling at the speed of sound (5000 m/s in steel). The stress wave will travel down the shaft, failing the shaft-soil interface as it propagates to the toe of the shaft. This will require approximately 3 milliseconds for a 30 meter shaft (100 ft). The Statnamic load test method loads the shaft and soil using a compressive load lasting up to 120 milliseconds. This duration of loading is longer than the natural period of even a very long flexible shaft. The result is the stress wave effects are minimised and the shaft is compressed as a rigid body, similar to that of the conventional static load test. When the shaft is loaded slowly as a rigid body the soil and shaft have time to act together with the shaft transferring load to the soil as it would under static loading. In addition, when the peak load is applied to the top of the shaft the toe of the shaft is under peak loading as well. It should be noted that the shaft does under go translation during the period of loading and thus shaft velocities and accelerations are present. These dynamic effects can influence the shaft behaviour in very soft soils.

Apparatus

The Statnamic load test consists essentially, of a compressed air jack. Compressed air forces apart the piston and cylinder with the piston acting downward onto the foundation and the cylinder acting upward against a reaction. The reaction in the case of Statnamic load testing is not an immovable mass (as in the case of a kentledge load test) but the inertial resistance of a small mass. By reacting against a small mass for a short period of time adequate load may be applied to the foundation for a long enough duration to slowly fail the shaft and soil.

---

[1] M. C. Janes Dynamic Engineering Services, Vancouver, B.C., Canada: Consultant to the Berminghammer Foundation Equipment Co. Ltd., Hamilton, Ontario, Canada.

The Statnamic test method uses solid fuel burned within a pressure chamber consisting of a piston and cylinder. As the gas pressure increases, an upward force is exerted on a reaction mass while an equal and opposite force pushes downward on the foundation. The reaction mass is accelerated to 20 g so a mass of only 5% of the peak load produced is required. Loading increases linearly to a maximum over a period of 80 to 100 milliseconds followed by a controlled venting of the gas pressure to unload. During the test (100 to120 milliseconds) 2,000 load and displacement readings are measured directly by a built-in load cell and laser sensor. Foundation acceleration and velocity are less than 1 g and 1 m/s respectively.

Soil Condition Effects

The long period loading of the Statnamic load test method is effective in transferring a load condition to the pile at a rate which allows the shaft and soil to react in unison, similar to that of static load conditions. The question of soil visco elasticity effects remains for geotechnical engineers in their evaluation of the Statnamic load test information. Soil visco elasticity, or the degree of strain rate dependency of soil engineering properties is a concern for geotechnical engineering design under any conditions. A measure of the visco elastic properties of a soil may be made directly using a dynamic triaxial test or, more crudely, a consolidation test. The cause of visco elastic soil behaviour is the time dependent compression of voids within the soil matrix. Small pores in the soil trap gas and water which under short period loading will not disperse and in fact may pressurize and carry some load. Under static loading the pore gas or water may be squeezed out of the compressed soil, reducing the 'excess pore pressures'. Excess pore pressures are both confinement and strain magnitude dependent. Confinement is highly influenced by pore volume and path tortuousity. Very soft clays or loose silt soils tend to have high pore volume (high void ratio) combined with low permeability (high flow path tortuousity). High strain magnitudes in these soils will induce high excess pore pressures through large deformation of the voids. It is recognized that soft clayey soils and loose silts are difficult soils to characterize and engineer foundations in. They are poor soils for load bearing, are highly compressible and are avoided or removed for most engineering works. The long period loading of the Statnamic load test method is too short to allow the pore gas and water to be squeezed out of the soil matrix. However, many soils including: rock, dense cohesionless soils and well graded or stiff cohesive soils exhibit very low visco elastic effects. During static loading they exhibit very little settlement under sustained load increments or peak loading. The low levels of consolidation do not influence the static shaft stiffness and thus they have little influence upon Statnamic loading results.

Pile foundations are generally constructed through weaker overburden or loose fill soils into competent cohesionless soils, stiff to hard clayey soils or rock. These bearing soils are not significantly effected by excess pore pressures during loading and provide little consolidation during sustained static loading. Piles and drilled shafts may be developed economically to very high loads. The Statnamic load test method provides results which closely resemble the static load test results and are easily interpreted to provide accurate static load displacement estimates. When weak highly visco elastic soil conditions exist and the proposed structure is light or inexpensive often a low capacity skin friction pile will be the most economical foundation solution. In these cases Statnamic load testing may not be the best tool for quality assurance or investigation of foundation load deflection behaviour. Invariably these low capacity shafts may be economically load tested using a simple reaction beam system on neighbouring production piles. As the proposed structure increases in weight and expense, higher capacity foundation elements penetrating to deeper, higher bearing soils (less subject to visco elastic behaviour) become economical. Static load testing becomes increasingly more expensive as the required peak load increases and alternative load deflection investigation techniques become economical. In these cases the Statnamic method becomes an economical tool which may be used in soils appropriate for the application of short period loading.

Interpretation of Statnamic Load Test Results

The Statnamic load test method produces shaft top load, top deflection and top acceleration data. Statnamic provides a load-displacement curve for the shaft in a manner identical to the load-displacement curve produced for a static load test.

The Statnamic load-displacement curve can be divided into 5 distinct stages. Figure 1 below shows a worse case scenario for Statnamic because of strong dynamic components present in the measurement results. In stage 1, the Statnamic reaction mass is placed on the pile top. The load displacement behaviour is fully static. The measured load and displacement at the end of stage 1 are F_{stat} and u_{stat} and the spring stiffness k_1 is calculated from:

$$k_1 = F_{stat}/u_{stat}$$

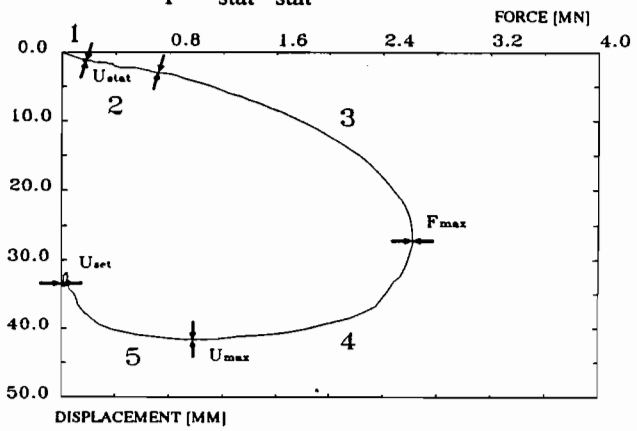

Figure 1 5 Stages in STAT*NAMIC* test

In stage 2, the reaction mass is launched and Statnamic loading starts. The soil resistance is elastic; inertia and damping forces acting on the pile are very low. In stage 3, the static soil resistance reaches ultimate strength and yields at a value F_{uy}. Velocity induced damping and inertia increase more progressively. At the end of this stage, the maximum Statnamic load is reached. In stage 4, the Statnamic load decreases, however, due to the inertia of the pile, there is still an increasing displacement. The soil is yielding with value F_{uy}. Pile velocity reduces to zero and changes sign. At the end of this stage, at time t_{umax}, the displacement reaches a maximum value u_{max} and the velocity becomes zero. Because velocity is zero, the damping forces are zero and the Statnamic load minus the inertia force equals the static soil resistance at this point.

$$F_u(t_{umax}) = F_{stn}(t_{umax}) - m{\cdot}a(t_{umax})$$

This force can be seen as an under limit of the maximum static resistance delivered by soil during loading. When the pile has been loaded to failure, the ultimate capacity F_{uy} is considered to be equal to $F_u(t_{umax})$ for Statnamic.

$$F_{uy} = F_u(t_{umax})$$

In stage 5, the unloading force $F_u(t)$ of the static soil resistance overcomes the other opposing forces and pushes the pile upwards. At the end of this stage, the final settlement of the pile is observed.

Dynamic effect is due to the inertia and damping of the shaft and soil. By measuring the acceleration and estimating the shaft mass a description of the contribution of inertia may be subtracted from the Statnamic result. Similarly integrating the acceleration signal and differentiating the displacement signal produces an accurate description of shaft velocity which is then multiplied by a damping constant to describe the contribution of shaft and soil damping. Damping contributes to the consumption of applied energy through radiation of stress waves out into the soil (geometric damping) and non linear soil deformation (hysteretic damping). Through an empirical study using comparative static and Statnamic load testing at numerous sites and in a full range of soils conditions a range of damping parameters has been established. Many soils show little contribution to the test results due to inertia and damping. The effects are dependent upon the soil and the velocity developed in the shaft. Significantly overloading the shaft causes higher damping effects which may complicate the results. similarly in very weak soils where deflection and shaft velocities may be high evaluation of the Statnamic results becomes more complicated. Often a load velocity plot is used to assist in predicting the onset of soil elasto plastic behaviour and of fully plastic

(soil failure) behaviour. The Statnamic load test method produces results very similar to the static load test method. The onset of shaft failure is determined using the increase in shaft deflection with increasing load. When the shaft displaces by greater and greater amounts for a given load increment, the shaft is recognized as showing elasto plastic or fully plastic soil behaviour. Similarly for Statnamic the shaft shows elasto plastic or fully plastic soil behaviour with the onset of an increasing rate of shaft displacement with increasing load. This increasing rate of displacement is often easily recognized in a load velocity plot where the haft velocity (load displacement rate with time) is plotted against the applied load. Since the shaft displaces directly with increasing load a linear load velocity plot occurs under the elastic portion of the loading. As plastic soil behaviour occurs the rate of shaft displacement increases and an increasing load velocity trait emerges. Dramatic breaking increases in this curve may be witnessed when plunging failure of the shaft occurs.

Unloading point method

The measured values of load and displacement versus time and load versus displacement for a 5 MN test (760 mm diameter, 13.8 m long drilled shaft in stiff clay) are shown in Figure 2 below. Characteristic of Statnamic load testing for any foundation, the maximum displacement lags the maximum applied load—here, maximum displacement of 5.7 mm at 98 ms follows maximum load of 4.48 MN at 90 ms. Net settlement is 1.77 mm. The "unloading point" (point of inflection between loading and unloading) occurs at maximum displacement and zero velocity. Pile accelerations range from a maximum of .5g during loading to a maximum of -1.5g at the unloading point. Velocity and acceleration versus time, calculated from the measured displacement, are shown in Figure 3.

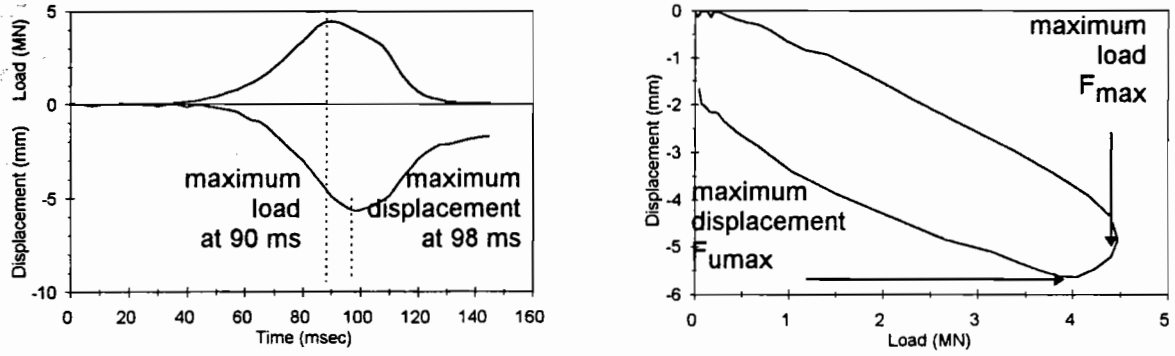

Figure 2 a) Load-Displacement Curve. **b)** Measured Statnamic Signals.

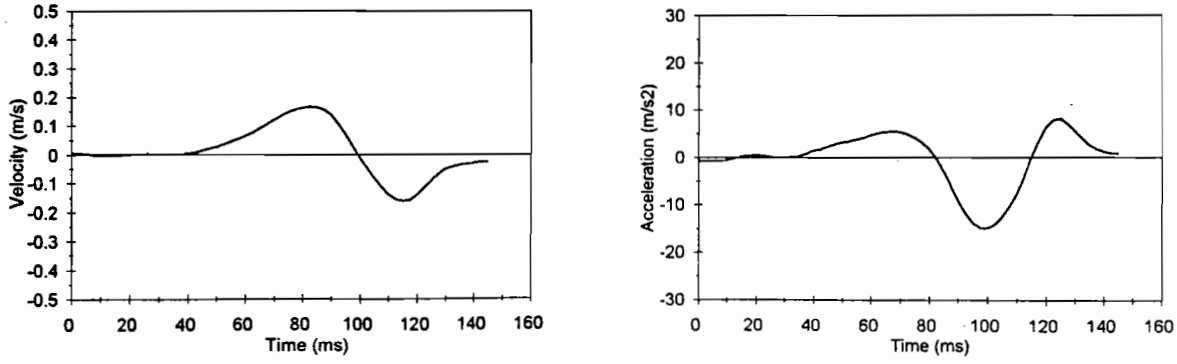

Figure 3 a) Calculated Velocity. **b)**Calculated Acceleration.

Due to the relatively long duration of Statnamic loading, pile/soil behaviour is not controlled by a stress wave travelling down the pile as in a dynamic load test. Instead, the pile is under constant compression

during Statnamic loading, comparable to a static load test, and can be modelled as a mass on which the following forces act:

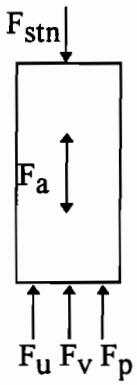

1. Statnamic Force (F_{stn})
2. Inertial Force (F_a)
3. Soil Resistance ($F_{soil} = F_u + F_v + F_p$)

Soil resistance is comprised of
static soil resistance F_u,
damping forces from soil F_v,
and pore water pressure resistance F_p.

Figure 4. Pile Forces

For equilibrium, the following equation is valid:

$$F_{stn}(t) = F_{soil}(t) + F_a(t) \quad [1]$$

where: $$F_{soil}(t) = F_u(t) + F_v(t) + F_p(t) \quad [2]$$

and

$F_{stn}(t)$	= Statnamic load (measured)		
$F_{soil}(t)$	= soil resistance		
$F_u(t)$	= k·u(t)	(static soil resistance)	[3]
$F_v(t)$	= C·v(t)	(damping force from soil)	[4]
$F_p(t)$	= P·v(t)	(pore pressure resistance)	[5]
$F_a(t)$	= m·a(t)	(pile inertial force)	[6]
k	= spring stiffness (N/m)		
C	= damping factor (Ns/m)		
P	= pore water pressure damping (Ns/m)		
m	= pile mass (kg)		
u(t)	= measured displacement (m)		
v(t)	= du/dt = velocity (m/s)		
a(t)	= d^2u/dt^2 = acceleration (m/s^2)		

(For the purposes of this study, it is assumed that pore water pressure resistance is included as part of the damping force from soil. Limited field observations have shown that pore water pressure resistance is less than 5%. Tests have also shown that inertial forces are minimal since pile accelerations are typically on the order of 1g.)

Thus, from [1] and [2]:

$$F_{stn}(t) = F_u(t) + F_v(t) \quad [7]$$

or $$F_u(t) = F_{stn}(t) - C \cdot v(t) \quad [8]$$

where the damping coefficient, C, is calculated from [8] at the unloading point (UP) and at the maximum applied load (F_{max}):

at UP: velocity = 0, $F_u(t)$ is a maximum (F_{umax}) $\therefore F_{umax} = F_{stn}(UP)$ [9]

at F_{max}: $F_u(t)$ is a maximum (F_{umax}) $\therefore F_{umax} = F_{max} - C \cdot v(F_{max})$ [10]

Thus, from [9] and [10]:

$$C = \frac{F_{max} - F_{umax}}{v(F_{max})} \qquad [11]$$

From $F_u(t)$ and u(t), a load-displacement curve can be drawn representing the static soil resistance as a function of displacement. The resultant curve passes through the "ultimate capacity" point, F_{umax}. The portion of the original Statnamic load-displacement curve to the right of $F_u(t)$ depicts the rate effects due to velocity. (Note: At the unloading point, velocity equals zero and, thus, the force due to damping is zero.)

A good measure of the rate effects present in a Statnamic test is the percentage of the force due to damping included in F_{max} (or the percentage difference between F_{max} and F_{umax}). In the above case, 9.8% of the maximum applied Statnamic load is the result of rate effects due to velocity.

Although the Unloading-Point model provides a readily available measure of the force due to damping at the maximum applied load, it assumes linear damping over the entire loading region and negligible inertial effects. Since comparisons between static and Statnamic tests have shown that damping is very low in the elastic region, linear damping under-predicts static capacity in this region. Furthermore, results have shown that the stress-strain relationship of the pile during unloading provides valuable insight into the next static loading cycle and, thus, the true static equivalent for a Statnamic test.

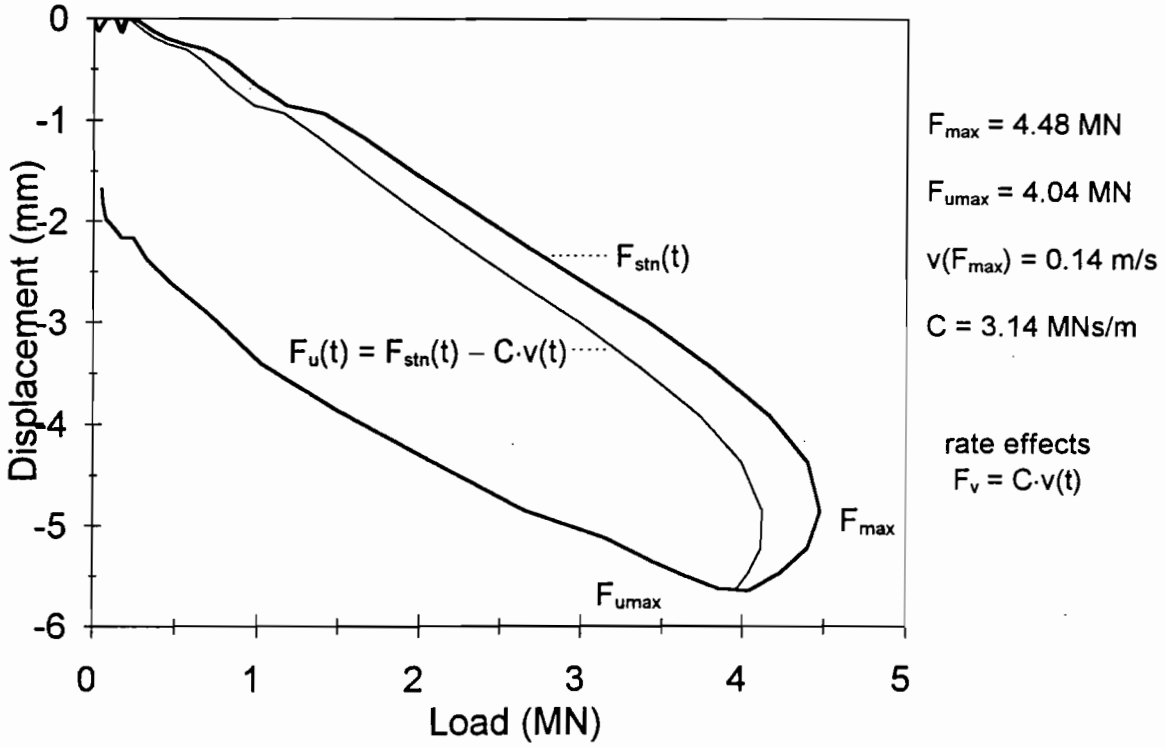

Figure 5. $F_{stn}(t)$ and $F_u(t)$ versus u(t)

Statnamic Load testing: Case Histories

Statnamic load testing was redcently conducted on high capacity drilled shafts to 3400 Tons (30 MN) at several DOT bridge pier test facilities in the United States. Tests were conducted vertically and laterally on strain instrumented shafts and in some cases testing was completed over water. A total of 15 load tests were performed on four projects in North Carolina and Florida, and over 20 tests have been conducted or

are scheduled throughout the Pacific Rim.. Instrumented shaft test results provide shaft load distribution with depth and shaft shear transfer stress throughout the soil stratum. Shaft end bearing and ultimate end bearing stress values were provided. Lateral load test results were correlated with static results and provided useful dynamic response and damping data. Dynamic response and soil damping parameters may be used to more accurately predict shaft response to dynamic excitation such as earthquake or ship impact loading. Testing provided valuable geotechnical parameters permitting design evaluation and foundation redesign which resulted in value engineered savings of over 6 million dollars on one project alone. On another project Statnamic load testing is providing load test data and confirmation of geotechnical parameters permitting a lowering of conventional safety factors and a potential cost savings of 6 to 8 million dollars.

North Carolina DOT

New Bern, NC

Site Location and Soils Conditions

The Neuse River foundation testing site is located immediately south of the confluence of the Trent and Neuse Rivers at New Bern, North Carolina. The site lies in a triangular depression between earth fill structures supporting US 70 to the south, an on ramp to the east, and a local road to the west. The natural geography is dominated by mature river formations and designated wetland foreshores. The site elevation is 1.6 m (5.2 ft).

The site soils consist of typical mature river delta formations overlying calcified sandstone bedrock referred to locally as marl. The overburden soils consist of layered deposits of soft saturated clayey silts overlying thick deposits of dense fine occasionally silty sand. The overall depth of overburden remains fairly constant across the site. At the location of the 1.22 m (48 inch) diameter shaft, the marl bedrock is encountered at an elevation of -5.5 m (-18 ft). Similarly, at the location of the 0.61 m (24 inch) diameter shaft, the marl bedrock is encountered at an elevation of -5.2 m (-17 ft). In this region of North Carolina, the marl bedrock extends to depths beyond elevation -100 m (-330 ft). The marl bedrock is considered highly porous, fissured, and subject to localized formation of significant cavities. The highly variable rock quality is known to produce vast changes in both rock and formation integrity over very short distances.
Bore holes were developed at the test facility and across the Neuse River at the proposed bridge pier locations. Augured boring results taken during April of 1994 reveal sand layers extending to beneath the founding elevation of the drilled shafts. North Carolina Department of Transportation (NC DOT) personnel advised the bore hole logs provided—numbers DS-1 (Station 1+340, offset -40) and B-12 (Station 1+607, offset 195) were located within the area of the test shafts. Subsequently, NC DOT personnel indicated the augured borings had been superseded by corings taken at the site on September 16, 1994. In addition to the augured bore hole and coring work, the drilled shaft production records provide an indication of stratigraphy through observation of the drill cuttings and auger penetration.

Augured bore hole results indicated soft top soil layers of clayey silt soils layered with and giving way to tan fine sands with depth. The water table resides at or above elevation 0 m with surface runoff collecting and lingering at the shaft location for long periods. At elevation -5.5 m (-18 ft), the cuttings abruptly change to gray, fossiliferous, calcareous fine to coarse sand with indurated layers. Of particular interest is the abrupt change in SPT blow count per 300 mm (1 ft). Within the upper stratigraphy, blow counts were on the order of 5 blows per 300 mm. At and below elevation -5.5 m, the blow counts abruptly increase to the high 30's with layers at 75 to 100 blows per 300 mm, indicating dense to very dense conditions. This trend continues to the end of boring at elevation -31.4 m (-103 ft). Coring B-4, located at the test shaft site (Station 1+344, offset 55), showed stratigraphy below 5.5 m (18 ft), consisting of mixed layering of fossiliferous limestone and sands. From -5.5 m (-18 ft), the coring revealed gray fossiliferous limestone and sand layers to an elevation of -9.6 m (-31 ft). At this elevation, tan dense very fine sand is encountered with fossiliferous limestone layering starting at elevation -12.65 m (-41 ft) through to -17.2 m (-56 ft). At elevation -17.2 m (-56.4 ft), tan calcareous cemented sand gives way to unweathered gray

moldic limestone to the end of the coring at elevation -22.7 m (-74 ft). The correlation appears high between increased SPT blow counts and rock layering indicated by corings. Finally, the drilled shaft production record confirms the coring report with layered sand and cavitated hard limestone layers below an elevation of -5.3 m (-17.5 ft). Layered fossiliferous limestone layers with fine sand were encountered to the founding elevation on a hard rock layer at elevation -25.5 m (-83.6 ft). Overall reports on geotechnical conditions by all three methods are considered consistent.

Pile Foundations

Two drilled shaft foundations were developed at the New Bern, North Carolina test site as part of the preliminary design program for the proposed US 70 Neuse River Bridge. The shafts are 1.22 m (48 inch) diameter and 0.61 m (24 inch) diameter reinforced concrete drilled piers. Figure 1 provides a plan and cross section representation of the 1.22 m diameter design and a section of the 0.61 m diameter design. The shafts were developed under mud using a drilling table and auger. Permanent casings were used for each shaft. A typical shaft cross section for the NC and FL projects is provided at the end of the paper.

Proposed Statnamic Load Test Program

A series of graduated axial compressive Statnamic load tests were planned for the 1.22 m diameter shaft. The initial loading was planned for 11 MN (1240 tons) with subsequent tests at 22 MN (1480 tons) and 30 MN (3375 tons) or until shaft failure occurred. The 0.61 m diameter shaft was to be loaded to failure under axial compression followed by a series of lateral Statnamic loading events. As part of the Statnamic load test program, the drilled shafts were instrumented with ten (10) foil type strain gauges. The 1.22 m diameter shaft was core drilled to an elevation of -24.25 m (-79.5 ft) and a strain instrumented pipe grouted into place. Initial pier information indicated a maximum elevation of -21.3 m (-70 ft) would be obtained by the coring and thus insufficient cable was supplied for the mounted strain gauges. As a result, a dummy section of pipe was placed below the instrumented section to provide a lowest strain gauge monitoring point of -22.1 m (-72.5 ft). The 0.61 m diameter shaft was cored in two locations. Cores were taken within the reinforcing cage and slightly to the north of the east-west centre line of the shaft. Strain gauges were grouted in place at equal elevations within each core hole. The west coring is centered 125 mm (5 inches) off the north-south centre line of the shaft and the east coring is centered 160 mm (6.5 inches) off the north-south centre line. This orientation was used to maximize the potential for obtaining bending moment data within the shaft under lateral Statnamic loading conditions.

Statnamic Testing

Two axial compression Statnamic load tests were conducted on the 1.22 m (48 inch) diameter shaft. The first Statnamic load test was conducted on September 30, 1994 to an ultimate loading of 11.7 MN (1,316 tons). The second Statnamic load test was conducted on October 3, 1994 to an ultimate loading of 21.1 MN (2,375 tons). A single axial compression Statnamic load test was performed on the 0.61 m (24 inch) diameter shaft. The test was performed on October 5, 1994 to an ultimate loading of 6.97 MN (784 tons).

The two Statnamic load tests performed on the 1.22 m diameter shaft may be represented as two cycled load tests. Figure 6 provides the load-displacement curves for Statnamic load tests 1 and 2 with the results of test 2 offset by the net displacement of test 1. The results demonstrate the effect of the initial test, including shaft set and shaft residual compression, upon the second failure test performed on the shaft. The response of the shaft to an initial failure loading would be best described by the envelope encompassed by both tests. The estimated static load response described on the graph is generated using velocity and acceleration dependent correction for dynamic effects. The unloading point method provides damping constants of 1.36 MN·s/m and 3.97 MN·s/m for tests 1 and 2 respectively. These damping constants are considered appropriate for the low visco-elastic soils and rock encountered at the site. The predicted static load-displacement curve shows elastic pile soil behaviour up to a loading of 11 MN (1240 tons). Beyond a loading of 11 MN, the predicted static curve shows an increased rate of displacement with increasing loading, reflecting the onset of plastic soil behaviour within the pile soil system. At a displacement of -14 mm (-0.55 inch), which corresponds to the Davisson's offset criterion, a loading of 12 MN (1350 tons) is achieved. A high confidence is maintained in the static response depicted. This

conclusion is based upon the agreement between results portrayed by the load-velocity graph, the shaft end condition as described above, the strain gauge results, and the shape of the predicted static curve.

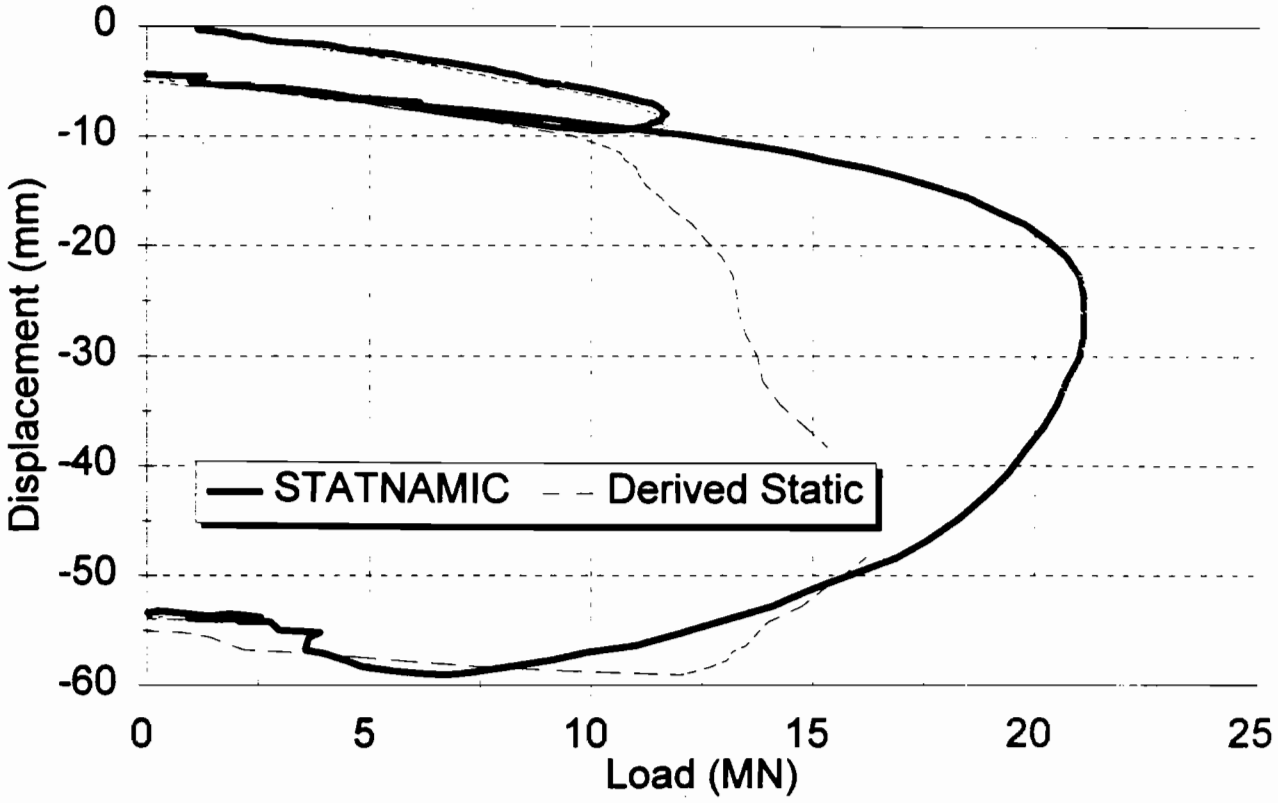

Figure 6 Tests 1 and 2, 1.22 m Diameter Shaft Statnamic and Derived Static Prediction.

The accompanying figures 7 and 8 provide the shaft load time history and distribution of shaft load with depth for the second Statnamic load test on the 1.22 m diameter shaft. Some apparent release occurs prior to achieving peak Statnamic load for the test. This may be due to rock layer failure or inter-bedding conditions in this region of the shaft. It is suggested that average frictional values or values of shaft friction prior to the break in the event curve be used to calculate geotechnical design parameters. Note that shaft mobilization occurring at a top load of 12.25 MN would indicate failure of shaft shear and end bearing values at a time corresponding to the break in the shaft load-time histories. Drawing a line through the shaft load-time traces at the break point on the appropriate slope (proportional to the wave speed of stress along the pile shaft) would provide apparent shaft loads at the moment of predicted failures. The data shows the top sleeved section of the pile above the rock to have shear stress transfer on the order 80 kN/m^2 (1.7 kips/ft^2). It is believed this result is an over-estimate of shear transfer and that some other condition, perhaps a high stress transfer at the overburden rock interface or cross section area discontinuity, contributes to this anomaly. Subsequent instrumentation, gauges 7 and 8, show little shear transfer with a major discontinuity occurring at gauge level 6. Averaging the shaft response between strain gauges 8 through 10 provides an estimate of shaft shear transfer of 60 kN/m^2 (1.35 kips/ft^2). Averaging the response of gauges 5 through 8 provides an estimate of shear transfer of 95 kN/m^2 (2.0 kips/ft^2) for the cased pile in the upper rock section. The lower non-cased section of the pile averages a shear transfer of 186 kN/m^2 (3.9 kips/ft^2).

Figure 7 Test 2, 1.22 m Diameter Shaft Load Time History, New Bern, NC.

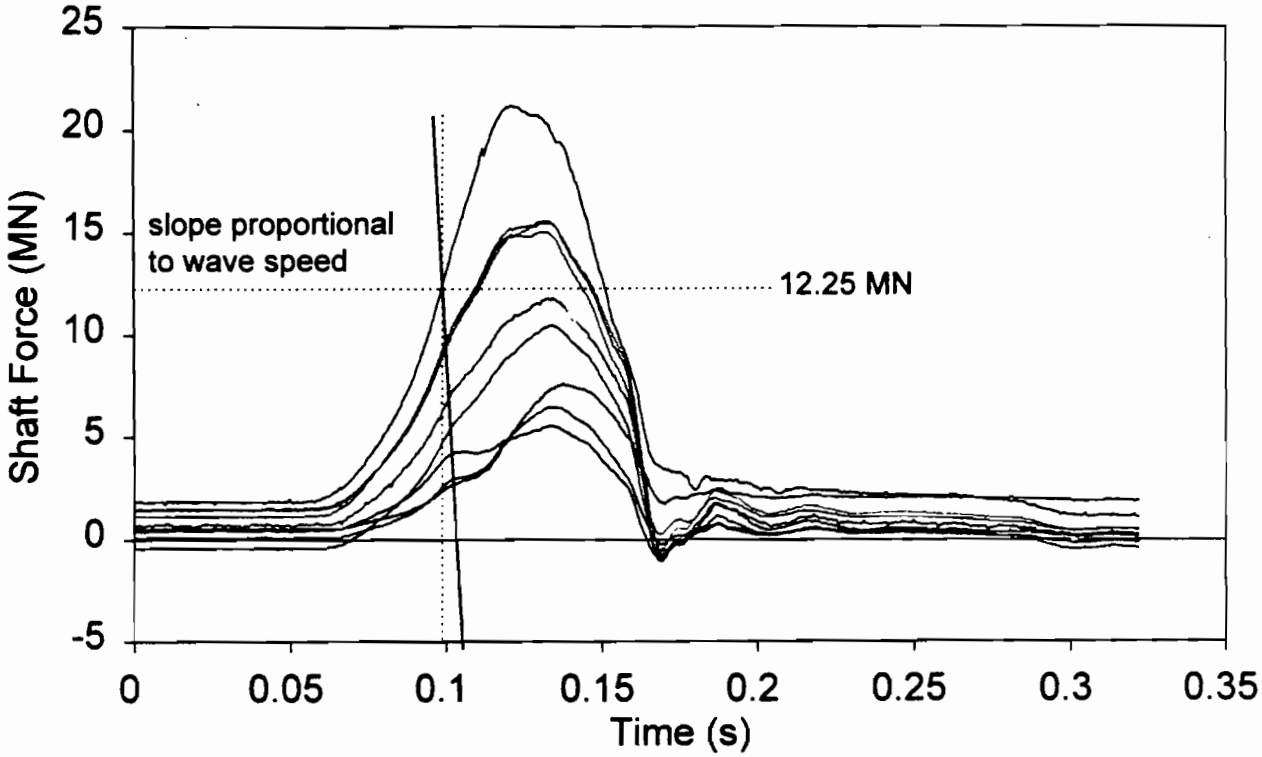

Figure 8 Test 2, 1.22 m Diameter Shaft Peak and Plastic Shaft Loads, New Bern, NC.

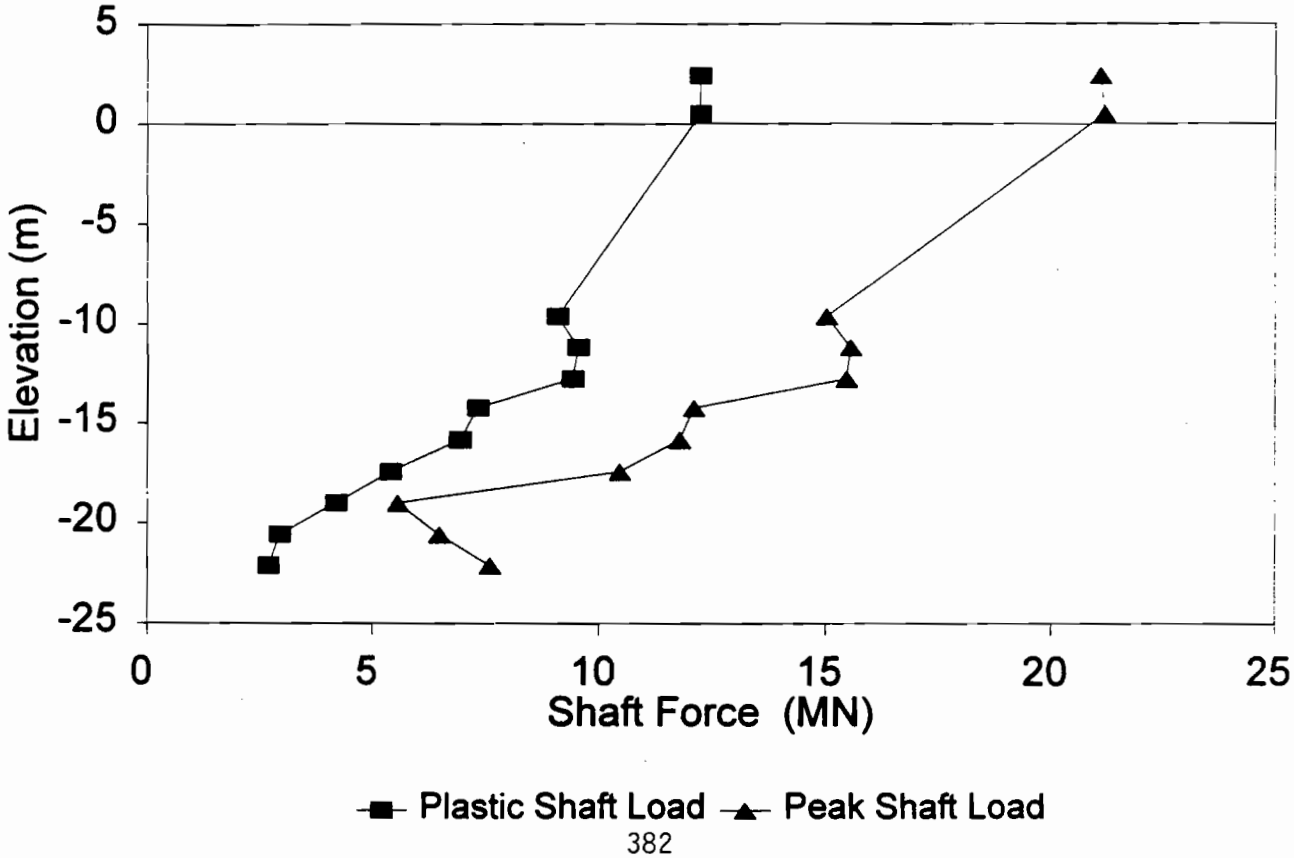

New River, Jacksonville, NC

Site Location and Soils Conditions

The New River foundation testing site is located immediately north of the New River at the Kiwi maneuvers area of Camp Johnson. The Camp Johnson base area is located within the Camp Lejeune Marine Corps base in Jacksonville, North Carolina. The site lies high on the north river bank in a cleared area approximately 200 m north west of the planned bridge structure. The natural geography is dominated by mature river flood plain formations. The site ground elevation is designated 309.15 m (1014 ft).

The site soils consist of mature river delta formations. The overburden soils consist of layered deposits of fine sands over medium to dense gray green fine sands. The soils strata is dominated by an ancient river bend formation consisting of a layer of calcified course sand with indurated layers. The overall depth of soils investigation is 37.8 m (124 ft) and terminates in a gray green silt formation at elevation 273 m (895 ft). The upper medium dense sands have SPT blow counts per 300 mm (1 ft) varying from 10 to 20 blows and extend to the water table at an elevation of 305.3 m (1001.5 ft). A very weak, wet, gray silty clay layer with SPT blow counts of 1 to 3 lies below the surface sand. The silty clay gives way with depth to a gray sand which lies directly above the calcified course sand. The calcified river bend sand strata occurs between an elevation of 296 m and 299 m (970 to 980 ft) or a depth of 10.15 to 13.15 m (34 to 44 ft). The calcified sand layer, with SPT blow counts of 30 to 69, forms a hard, brittle mantle within the sand layers. Beneath the calcified sand layer, gray green fine sands, with SPT blow counts of 30 to 40 extend to an elevation of 274.7 m (901 ft). The investigation terminates 1.3 m further in a dense clayey silt.

Pile Foundations

Two drilled shaft foundations were developed at the Camp Johnson test site. The shafts are 1.22 m (50 inch) diameter and 0.61 m (24 inch) diameter reinforced concrete drilled piers. The shafts were developed under mud using a Kelly bar type drilling table and auger. Permanent casings were used for each shaft. As part of the Statnamic load test program, the 1.22 m diameter drilled shaft was instrumented with fourteen (14) foil type strain gauges.

Statnamic Testing

Two axial compression Statnamic load tests were conducted on the 1.22 m diameter shaft. The first Statnamic load test was conducted on December 22, 1994 to an ultimate loading of 11.9 MN (1,340 tons). The second Statnamic load test was conducted on January 7, 1995 to an ultimate loading of 22.8 MN (2,565 tons). Three lateral Statnamic lateral load tests were performed on the 0.61 m (24 inch) diameter shaft on January 6, 1995 to an ultimate loading of 0.35, 0.47 and 0.59 MN (39, 53, and 66 tons respectively).

The two Statnamic load tests performed on the 1.22 m diameter shaft may be represented as two cycled load tests. Figure 9 provides the load-displacement curves for Statnamic load tests 1 and 2 with the results of test 2 offset by the net displacement of test 1. Note the dashed lines represent the offset Statnamic derived static response. The results demonstrate the effect of the initial test, including shaft set and shaft residual compression, upon the second failure test performed on the shaft. The response of the shaft to an initial failure loading would be best described by the envelope encompassed by both tests. The estimated static load response described on the graph is generated using velocity and acceleration dependent correction for dynamic effects. The damping constants used are 3.5 MN·s/m and 6.9 MN·s/m for tests 1 and 2 respectively. A 3.5 MN damping constant is considered appropriate for the low to moderate visco-elastic sandy soils encountered at the Jacksonville, North Carolina site. The 6.9 MN·s/m damping constant used for the second test is considered high for the site soils but is not unreasonable considering the large deformations and high velocities experienced during the second Statnamic load test. The predicted static load-displacement curve shows elastic pile soil behaviour up to a loading of 11 MN (1240 tons). Beyond a loading of 11 MN, the predicted static curve shows an increased rate of

displacement with increasing loading, reflecting the onset of plastic soil behaviour within the pile soil system. At a displacement of -21.5 mm (-0.85 inch), which corresponds to the Davisson's offset criterion, a loading of 14.5 MN (1630 tons) is achieved. The derived static load-displacement is based upon the agreement between results portrayed by the results from Statnamic load tests 1 and 2, load-velocity graph results, the shaft end condition as described above, the strain gauge results, and the shape of the predicted static curve.

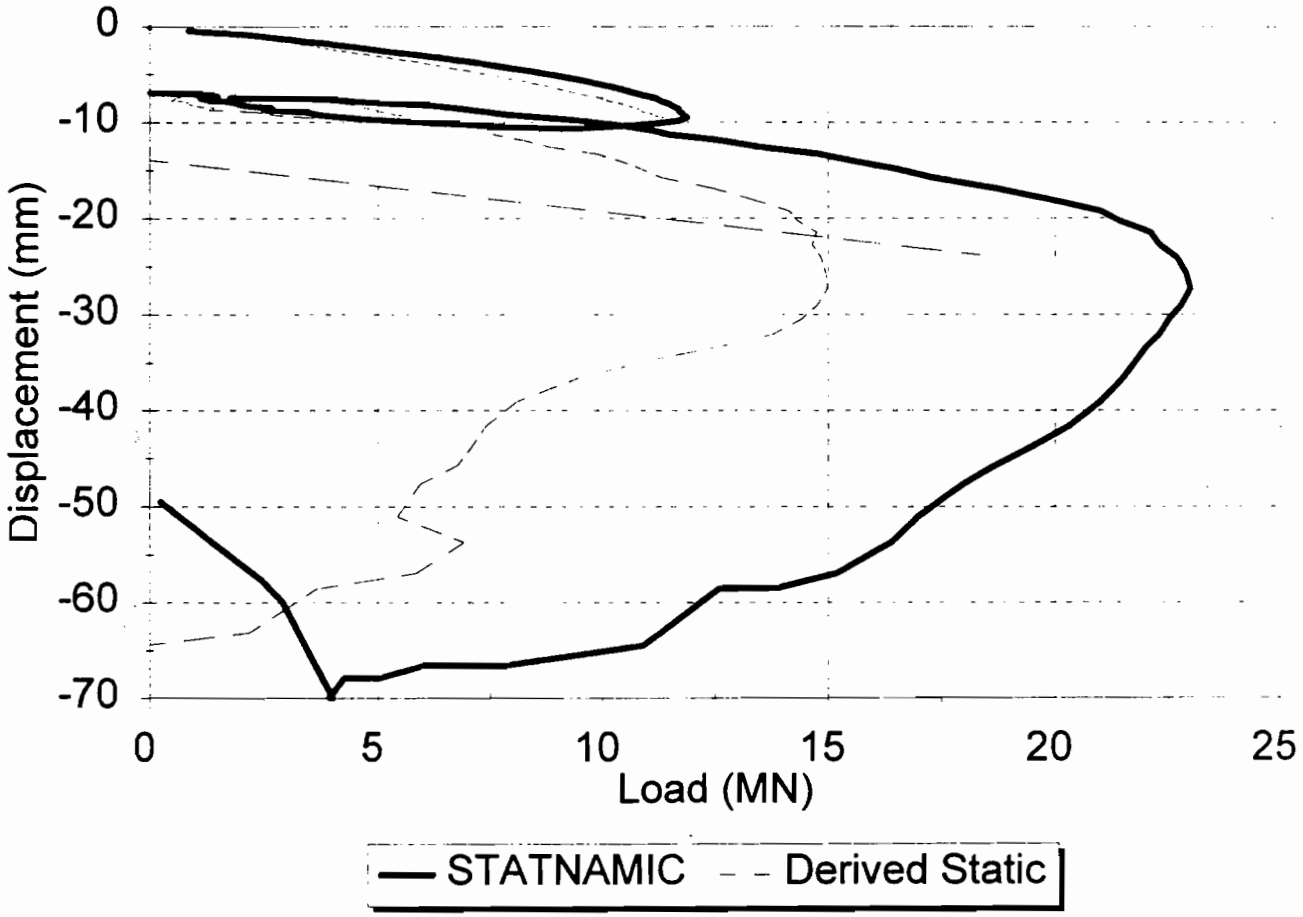

Figure 9 Tests 1 and 2, 1.22 m Diameter Shaft Statnamic and Derived Static Prediction.

Statnamic and Static Lateral Load Testing

Three Statnamic lateral load tests were performed at increasing load increments of 0.35, 0.47, and 0.59 MN (78.7, 105.6 and 132.7 kips respectively). Loading was performed in the west to east direction, which is the opposite direction to the previous static lateral load test. The west to east direction of loading was selected to minimize the effects of previous lateral loading. It is well established in geotechnical literature that lateral shaft resistance is largely developed by the passive or compressive soil wedge in front of a loaded shaft as opposed to the trailing or tensile wedge behind a loaded shaft. By Statnamically loading the shaft in the opposite direction to the previous static lateral load test, the least disturbed static trailing wedge became the passive wedge for the Statnamic load. A schematic of the Statnamic lateral load test set up is provided in figure 10 below.

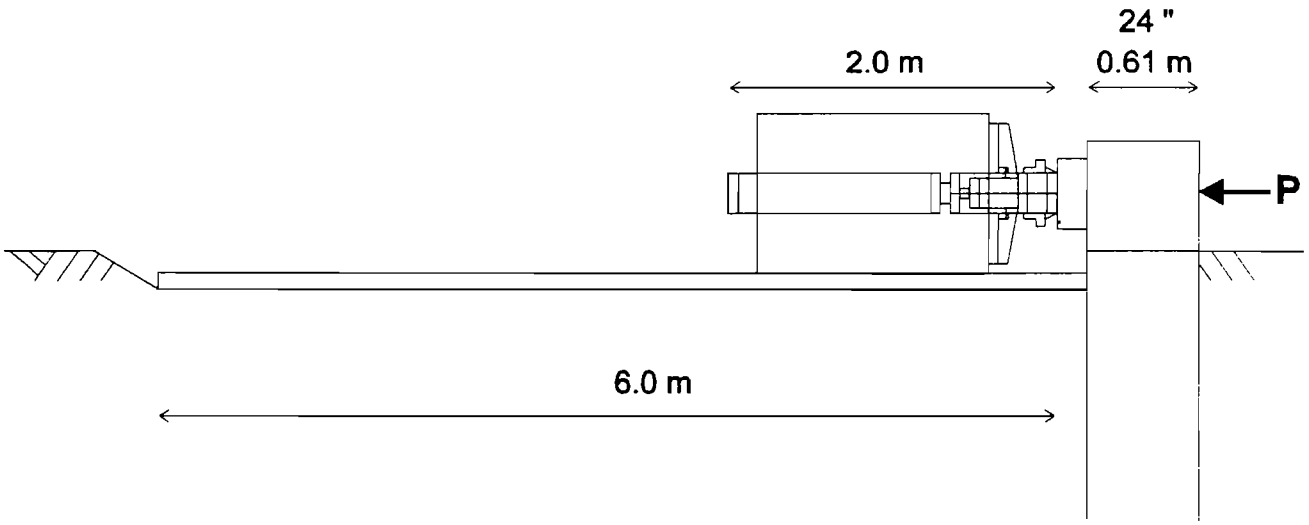

Figure 10. Statnamic lateral load test set up.

Figure 11 provides a comparison of the static load test result for the 0.61 m diameter shaft along with the two recorded Statnamic results and the Statnamic derived prediction of static lateral load-displacement. Note that the Statnamic results appear stiffer than the static result. This is expected for a Statnamic test where dynamic shaft response (inertia and damping) will result in apparent higher shaft stiffness. The static load test result provides a linear shaft response to a loading of 0.2 MN. The stiffness to this point is 0.063 m/MN. Beyond the 0.2 MN loading, the shaft begins to show elasto plastic response with a stiffness at 0.445 MN of 0.087 m/MN. Statnamic lateral load test results provide an elastic stiffness at a load of 0.2 MN of 0.055 m/MN and an elasto plastic stiffness at 0.445 MN of 0.089 m/MN.

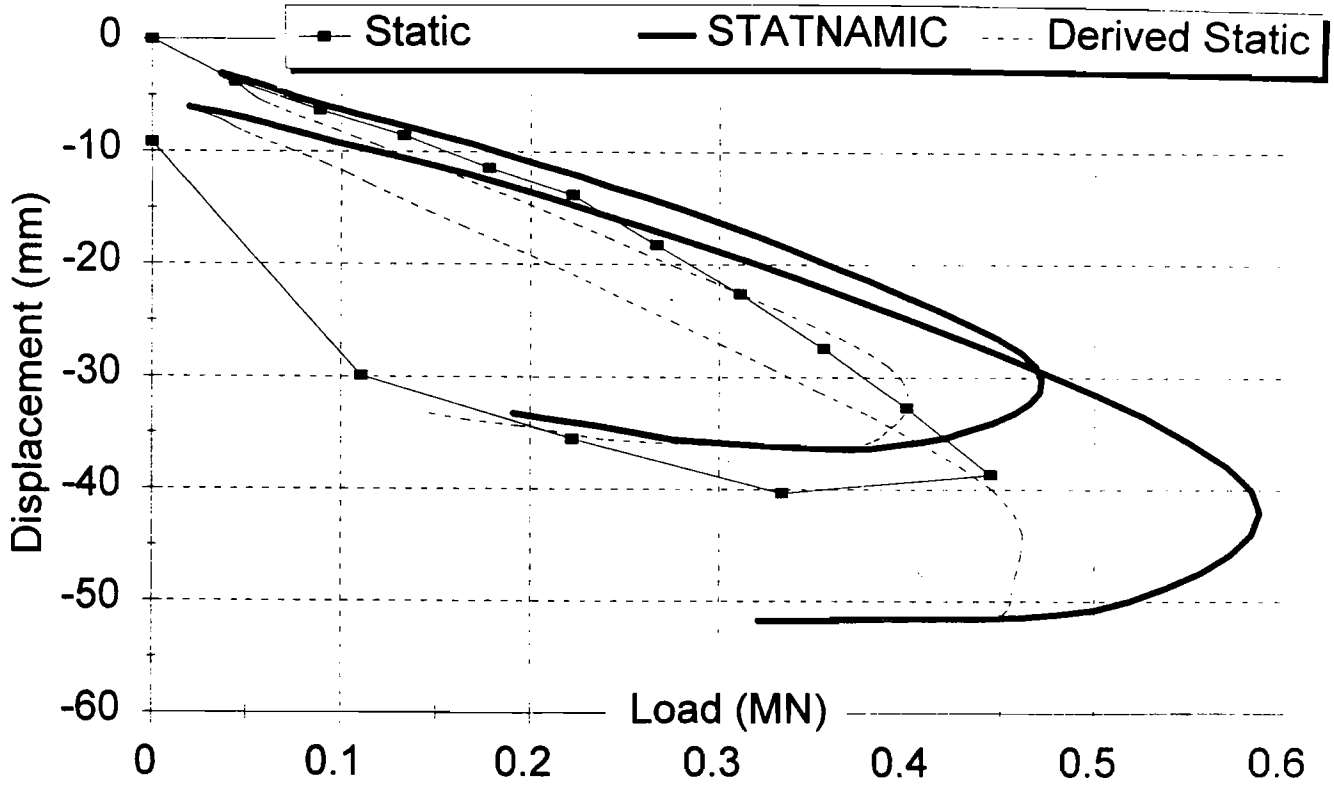

The application of conventional Statnamic prediction theory to lateral loading may not be justified. The Statnamic theory is based on application of a load of a much longer period than the natural period of the shaft. In the lateral condition, Statnamic may not provide a substantially longer period load and satisfy

this premise. As may be seen in Figure 12 the natural period of this foundation in bending is 0.079 seconds and the period of Statnamic loading is 0.1 seconds with a lower period load release. Thus, the loading portion of the Statnamic excitation may provide a duration which permits some investigation of the prediction theory. The figure shows that the offset Statnamic derived prediction curves provide an adequate representation of static response. The overall Statnamic predicted response used for this analysis is that described by the outer envelope of the curves provided. The Statnamic predicted stiffness at 0.2 MN is 0.0725 m/MN (as compared to 0.065 m/MN for the static curve). The predicted stiffness at 0.4 MN is 0.0875 m/MN (as compared to 0.084 m/MN for the static curve). Beyond a load of 0.4 MN through to the ultimate static prediction of 0.46 MN, the prediction appears good. It should be noted that while the predicted response for this load case is encouraging, other correlations for Statnamic predicted lateral load response have not been as good.

The acceleration time history trace shown in figure 12 below provides the rebound or oscillation of the shaft immediately after loading. The oscillation occurs at the natural period of the foundation in bending which may be calculated for one complete cycle as 0.079 sec. This oscillation is quickly reduced or decayed by the presence of the soil. The rate of decay of shaft motion describes the dissipation of shaft energy into the soil, also known as damping. The magnitude of damping may be calculated by the rate of decay of the motion. A simple method to determine system damping based upon free damped vibration assumptions (including system linearity) is made using a decay function envelope. The method indicates a heavy damped simple system with soil damping through hysteretic and geometric damping on the order of 20%. Using this value of damping when calculating the resistance of foundations to earthquake or ship impact loading will more accurately describe foundation behaviour. High system damping contributes significantly to overall system resistance to these types of random excitation.

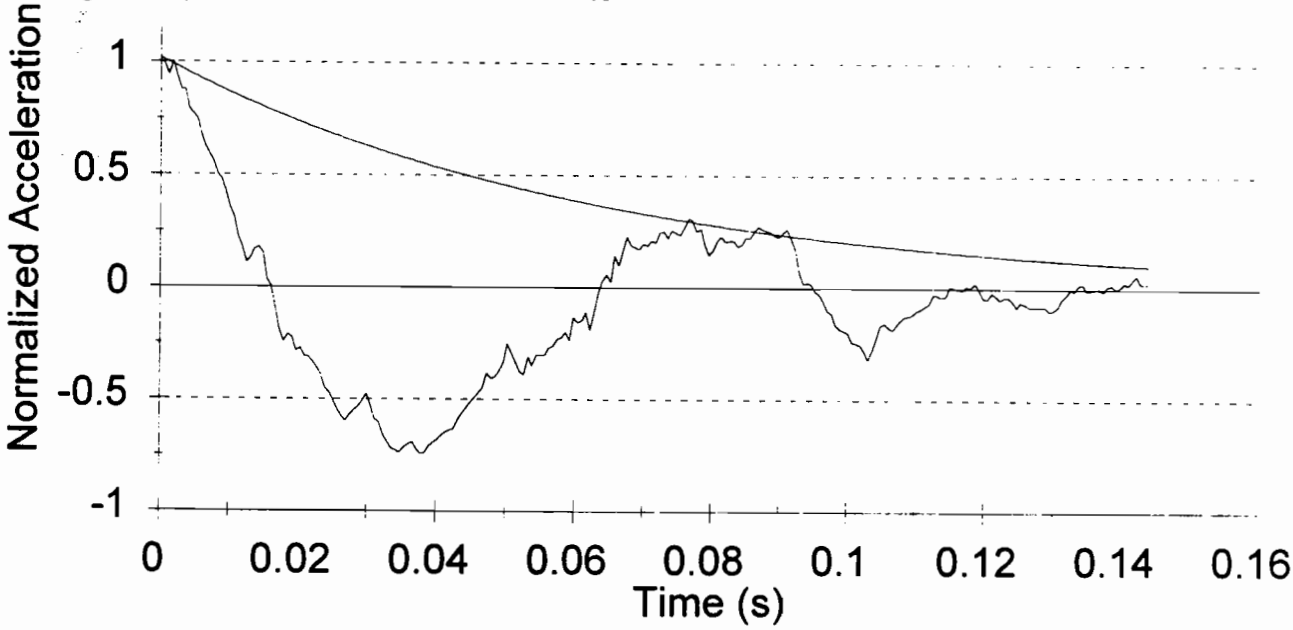

Figure 12 Acceleration History Statnamic Lateral Load Test 3.

Florida DOT

Tampa, Florida

A total of three high capacity Statnamic load tests were conducted at the Gandy Bridge in Tampa Florida. The test program involved the testing of 6 shaft at three locations across the 4 km site. Shafts were developed in pairs according to the construction methodology specified for the production shafts. At each location one shaft was tested using the Statnamic load test method and one test using an Osterberg load

cell.. The results of the testing were compared to evaluate both the shafts and the respective testing methods. An accompanying paper in this volume describes in detail the site, soils and comparative load test results for this test program. As a result a brief description and a single comparative load test curve for all three shafts are presented in this paper.

A comparative load displacement plot is provided in figure 13 showing Statnamic load displacement for all three shafts. In addition a static derived load displacement comparison is provided. The plots show the relative difference in stiffness between the shafts. The elastic compression of the shafts dominates the response up to loads of about 15 MN. Beyond loads of 15 MN the rock socket and end bearing at each shaft location begin to show their differences. The shaft at pier 91 shows a large reduction in stiffness at 19 MN, while the shafts at pier 52 and 26 show little or only gradual relaxation at higher loading. The results reflect clearly the rock socket and end bearing effects at each shaft location.

The load displacement traces and corresponding load velocity traces show 3 distinct shapes. Pier 91 shaft # 3 is a long shaft (21.5 m) with 15 m of free length and a 6.5 m rock socket. The test results shows characteristic mobilization of a shaft under Statnamic loading including: hysterisis in the load displacement plot dominated by large displacements at peak loading, high shaft velocity and a distended peak on the load velocity plot. In softer soils shaft mobilization would include a breaking increase in velocity on the load velocity plot. This would not be expected when testing shafts socketed into competent rock. Pier 52 shaft # 3 is a shaft of 16.7 m length with 10 m free length and 6.7 m of rock socket. The very tight load displacement curve with low hysterisis, rounded load velocity trace with peak velocity tapering off before peak load and very low net displacements indicate a highly elastic response. The linearity of the response also indicates the shaft has not exceeded its ultimate skin friction in the rock socket and is achieving only a fraction of the potential end bearing resistance. Pier 26 shaft # 2 is a short shaft only 10.2 m long with 5.2 m of free length and a 5 m rock socket. Rounding of the load displacement trace with moderate hysterisis, a high peak velocity relative to shaft stiffness and peak velocity occurring near peak load with some distention on the load velocity plot indicate the shaft is approaching plastic response. The gradual change in stiffness through the build up of load indicates a coinciding increase in both shaft friction and end bearing resistance. This response is quite different from the shaft at Pier 91 # 3 where there was a distinct break in the curve. The break indicated in the Pier 91 # 3 trace reveals higher quality rock in the socket than in end bearing rock at this location. Weaker end bearing rock would require large deformations before achieving full strength and ultimately yield. Thus as the rock socket shear transfer load reached a peak, further shaft displacement is required in order to mobilize the end bearing. For the shaft at Pier 26 # 2 the high quality of both socket and end bearing rock permitted a coinciding increase in end bearing mobilization under lower shaft displacements. The shaft at Pier 52 # 3 resides in socket and end bearing rock of such high quality that the load developed by Statnamic did not mobilize the shaft much beyond the rock socket shear capacity. The static derived and measured shaft stiffness are equal to or higher than the theoretical elastic stiffness of the shaft up to a significant load. This indicates the shaft is not fully compressed and is shedding the majority of load in rock socket shear transfer.

Conclusion

Statnamic load testing has been successfully used at over 15 Federal and State Department of Transportation test sites throughout the United States over the past 5 years. The results have proven the Statnamic load test method will provide good quality load displacement information and static failure load predictions in a variety of foundation and soil conditions. The application of the Statnamic method requires informed geotechnical engineering consideration. Statnamic, like many of the tools available to geotechnical engineers, requires evaluation of the site and soil condition at each site under consideration. Load testing in highly visco elastic soils will provide results which require more complicated interpretation and evaluation. Over all the Statnamic load test is a highly economical test method for high capacity foundations.

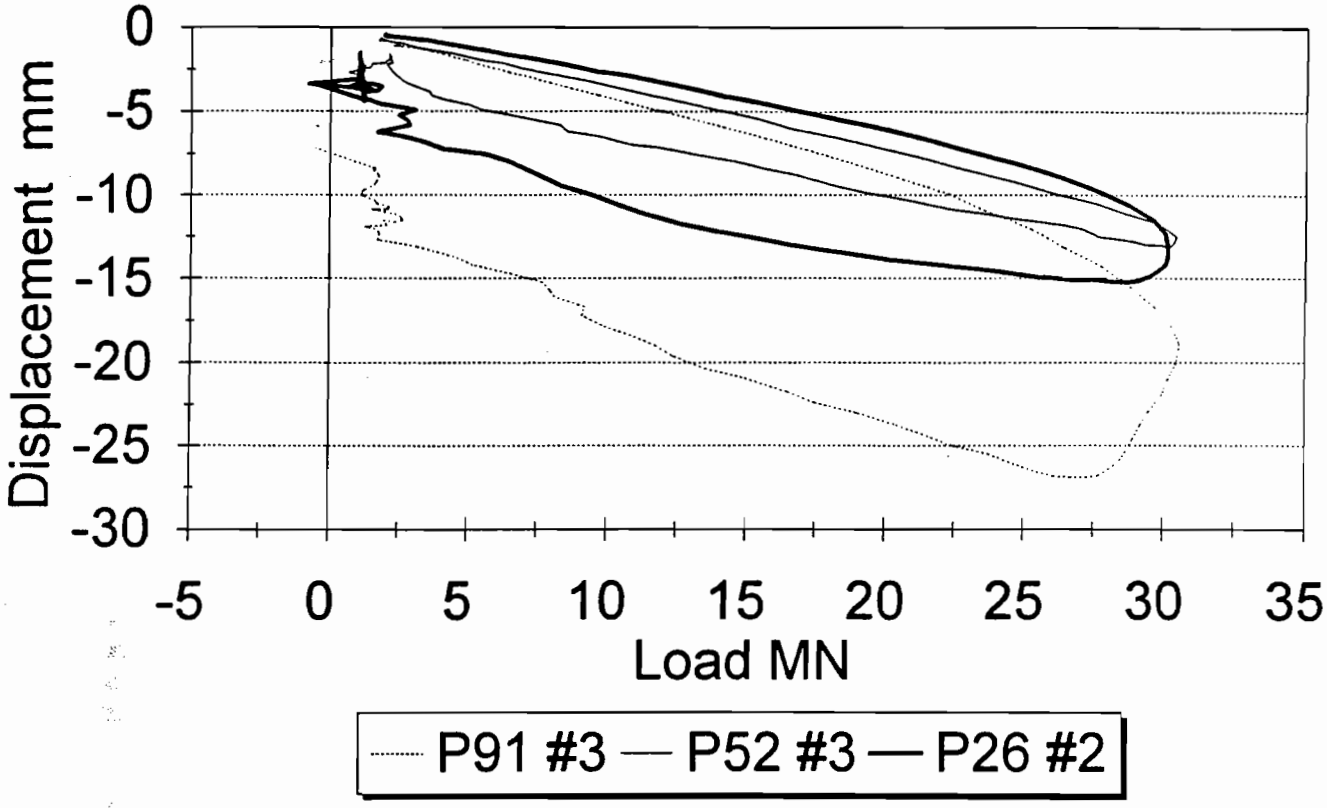

Figure 13 Comparison of Statnamic and Static Lateral Load Test Results Gandy Bridge, Tampa, Florida.

04-OCT-1994 12:21
/usr2/emily/harry/anotti.dgn
harry

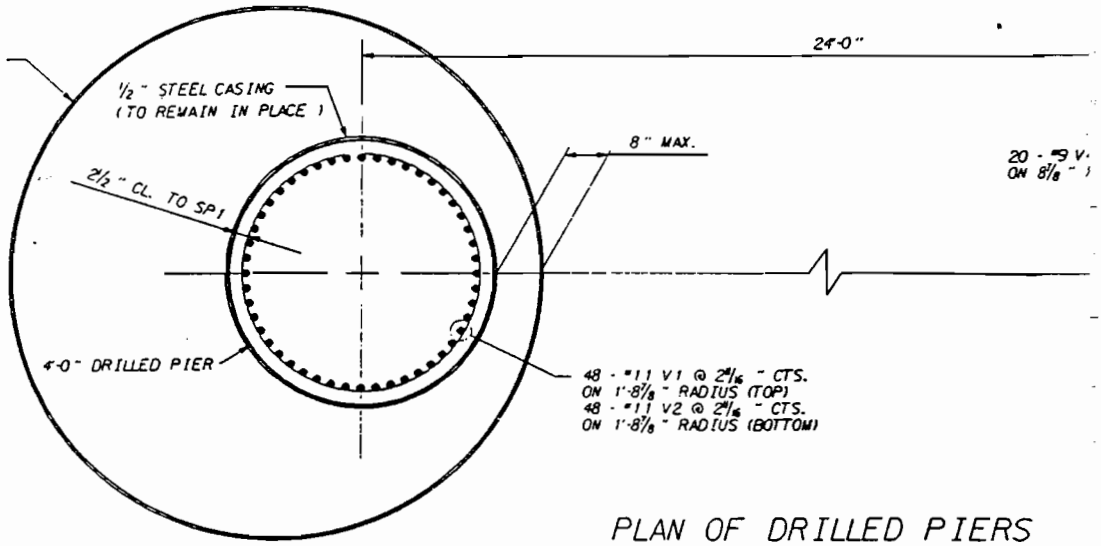

PLAN OF DRILLED PIERS

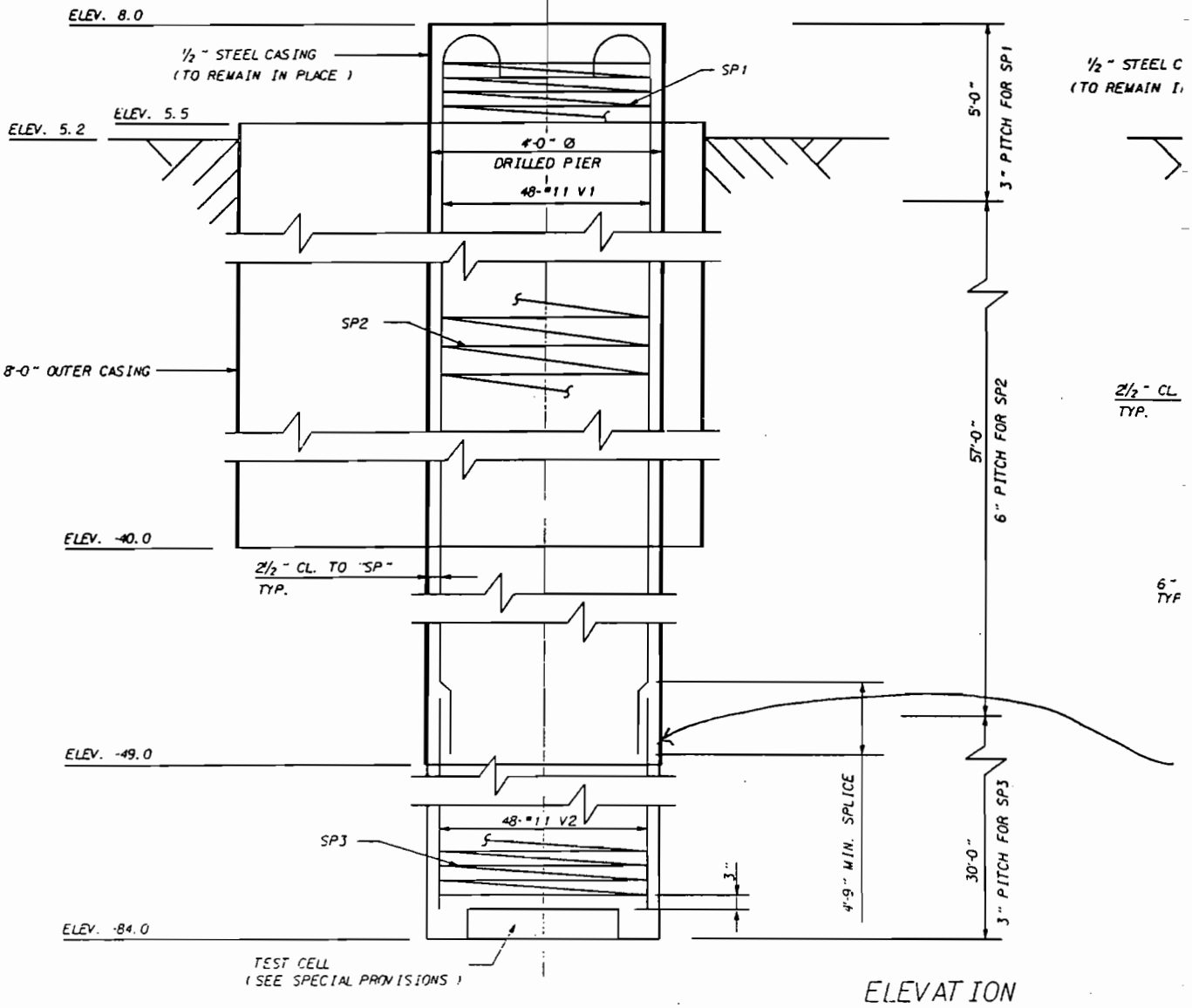

ELEVATION

DRAWN BY : H. A. LUCAS DATE : 5/4/94
CHECKED BY : _____ DATE : _____

22

A COMPARISON OF STATNAMIC AND OSTERBERG FIELD TESTS IN FLORIDA LIMESTONE

William F. Knight[1], Theresa N. Puckett[2], Keith D. Bennett[3], Donald T. Robertson[4], and Lawrence D. Spears[5]

ABSTRACT

The results of four Statnamic and five Osterberg tests performed in Florida limestone have been compared. Three of the Statnamic tests were conducted at the Westbound Gandy Bridge Replacement Project and one was performed at the Victory Bridge Project, to verify design parameters. This paper first introduces the difficulties of foundation design in Florida limestone and discusses the purposes of performing load tests. Results of the Statnamic tests are compared to the results of the Osterberg load tests based on shear strength.

LOAD TESTS IN FLORIDA LIMESTONE

Limestone in Florida has presented numerous installation problems for both driven and cast-in-place piles. It is characterized by its karstic activity, erratic surface elevation and highly variable strength. Most Florida limestones used for foundation support are relatively young (less than 2 million years old). Many Geologists outside Florida characterize the limestone as "soft". Some do not even recognize it as a "limestone". Because of this variability and "softness", Florida limestones are generally easy to drill. Therefore, geotechnical designers in this state try to take advantage of this softness. Since the limestone can be drilled, skin friction becomes a major component of drilled shaft capacity. Because the strength is so variable, it is not generally attempted to maximize end bearing. Therefore, a test that can fully mobilize skin friction and end bearing was needed. The Statnamic load test can mobilize these higher capacity piles in side friction and end bearing, as a unit, and can be reused for other test piles on site as well.

[1] William F. Knight, District 3 Geotechnical Engineer, Florida Department of Transportation, Chipley, Florida
[2] Theresa N. Puckett, District 1 Geotechnical Engineer, Florida Department of Transportation, Bartow, Florida
[3] Keith D. Bennett, Senior Geotechnical Engineer, Williams Earth Sciences, Inc., Largo, Florida
[4] Donald T. Robertson, Senior Geotechnical Engineer, Williams Earth Sciences, Inc., Largo, Florida
[5] Lawrence D. Spears, Project Engineer, Williams Earth Sciences, Inc., Largo, Florida

The load test programs were developed for six major purposes: 1) verify axial design capacities and tip elevations; 2) verify lateral load design capacities; 3) ensure that the contractor has properly sized equipment and can install the shafts in accordance with the specifications; 4) evaluate the design methodology; 5) evaluate the use of small scale anchor pull-out tests (Gandy only); 6) compare results of the embedded Osterberg load cell test method versus the externally applied Statnamic test method. The focus of this paper is on Item 6, which compares the use of an innovative test procedure, the Statnamic test, to the Osterberg test results which has a greater database within the state of Florida.

When introduced, the Osterberg load cell became the preferred method for performing static load tests in Florida since it can be performed without a reaction system. However, the entire shaft cannot be failed without a reaction system and an external jack. Because of it's location in the shaft, the Osterberg load cell fails in either skin friction or end bearing.

Statnamic load testing is an innovative method which is capable of loading high capacity piles to failure in both skin and end bearing simultaneously. It is a nondestructive low-velocity dynamic test that has been used successfully world-wide on large and small piles. Repeatable, reusable and mobile, this test furnishes data immediately following the test with the use of user friendly software. Test programs outside Florida and on smaller loads have shown that the predicted static response from the Statnamic test is nearly identical to static load test results. It is interesting to note that the 30 MN device was originally conceived for these two projects. Although the test operates dynamically, the rate of loading is slow enough to allow the soil and pile to act as a rigid body, similar to a static test. Statnamic test methodology is not discussed in this paper, but has been presented elsewhere in these proceedings.

OVERVIEW OF INSTALLATION PROCEDURES

Drilled shafts at both the Westbound Gandy and Victory Bridges were installed using "wet-hole" construction techniques. In both cases, the shafts were drilled with clean water, without the introduction of a pre-mix slurry. The shafts were installed in accordance with the Florida Department of Transportation's Supplemental Specification 455 for Drilled Shaft Construction.

CASE HISTORY 1: WESTBOUND GANDY BRIDGE TEST SITE

Six 48-inch diameter test shafts were installed to the approximate tip elevation given in the plans. The test locations were chosen to: 1) provide a site with as little overburden as practical and 2) provide coverage of the expected limestone condition across Tampa Bay. In selecting the sites, it was attempted to test "good" limestone, "average" limestone, and "poor" limestone. The locations chosen were Pier 26, 52, and 91. Each shaft was installed as a permanent shaft location, therefore, all shafts needed to be left in an undamaged condition for the completed structure. The Westbound Gandy Bridge is located on Tampa Bay, as illustrated in Figure 1. The approximate locations configuration of and a typical bent is illustrated in Figure 2.

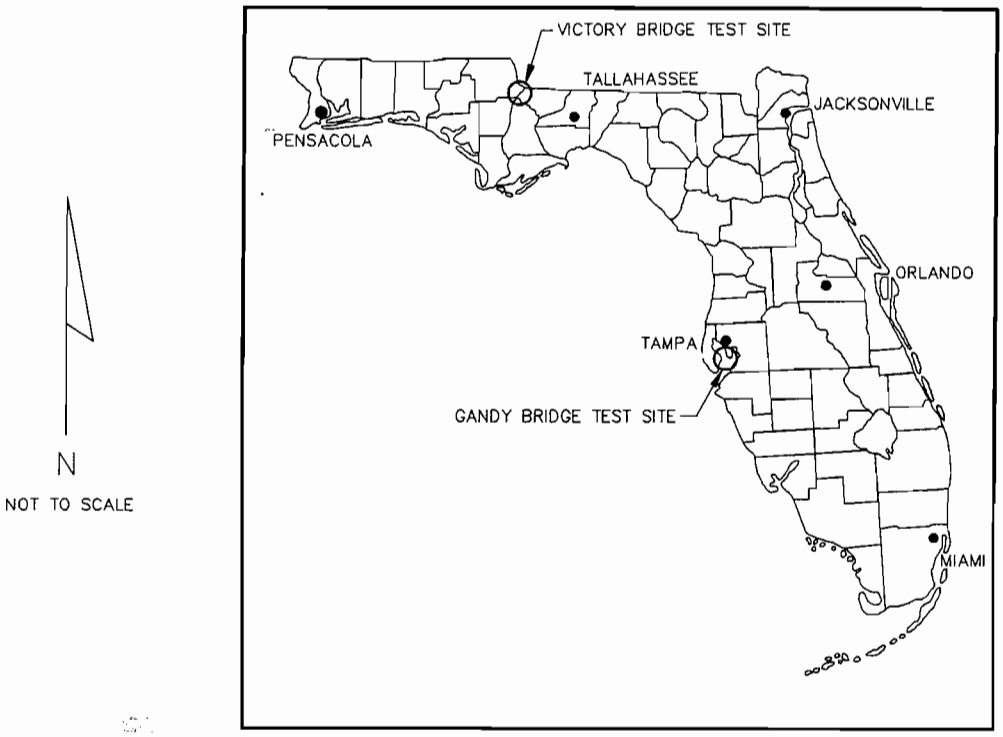

Figure 1. Test Site Location Plan.

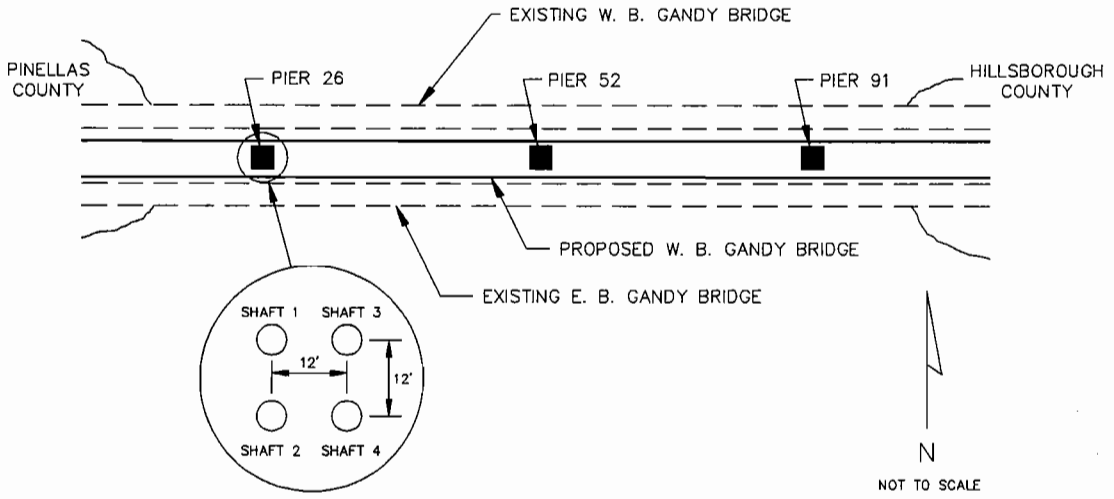

Figure 2. Test Locations for Westbound Gandy Bridge Site.

Based on the geotechnical exploration, the design called for a minimum of 12 feet of competent limestone socket to carry the 542-ton design load. The elevation of the top of the limestone formation varied considerably from one end of the project to the other, having as little as 2 feet of loose shelly fine sands on the west end of the bridge and up to 35 feet of similar material at the east end.

A single 32-inch, 3000-ton capacity Osterberg load cell was installed at three of the six test shafts. The cells were welded to the bottom of the reinforcement cages and were placed near the bottom of the shaft. Six levels of vibrating wire strain gauges were used for each test. Generally, the levels of the strain gauges were evenly distributed from just above the top of the load cell to the scour elevation (top of limestone formation). Three strain gauges were placed at each level for a total of 18 strain gauges per shaft. Tell-tales were placed at the bottom and top of the load cell, and at levels corresponding to those of vibrating wire strain gauges.

The 30 MN (3400 ton) Statnamic tests were performed on shafts adjacent (12 feet north) to the Osterberg test shafts. A load cell placed on top of the shafts was used to measure load and a laser device was used to measure deflection. The tests generally took 3 days to setup, however, the actual firing sequence was completed in milliseconds. Figure 3 shows the Statnamic test just after firing at Pier 52.

CASE HISTORY 2: VICTORY BRIDGE TEST SITE

At the Victory Bridge Test Site, three test locations were selected. These locations were chosen to verify design assumptions and possibly reduce the design shaft lengths at this site. At Test Sites 1 and 3, the load test program consisted of one Statnamic load test, two Osterberg load cell tests and one lateral load test. The site was configured as shown in Figure 4. The Osterberg cells were positioned with the hope that the shaft with the Osterberg cell at the tip (Shaft 1) would fail in end bearing and the shaft with the Osterberg cell in the middle (Shaft 2) would fail in skin friction. Both Osterberg cell shafts were located in permanent shaft locations. The Statnamic test shaft was positioned between the two permanent shafts and had a planned rock socket of 8 feet. At Test Site 2, a Statnamic test was planned to confirm the results from Sites 1 and 3. Unfortunately, only the Statnamic test at Site 3 was performed. The Osterberg cell tests and the lateral load tests were performed under the direction of Schmertmann and Crapps, Inc. for the Florida Department of Transportation, District Three. The Statnamic testing was performed by The Berminghammer Corporation Limited.

The design for the Victory Bridge called for a minimum 16-foot rock socket to carry a design load of 590 tons, however, the desire was that through the use of the load test program the rock socket length could be reduced to 8 feet. The actual in-place rock socket length was 9.5 feet. The planned elevation for the Osterberg cell located in Shaft 1, Bent 19 was 20.8 feet, which was the bottom of the shaft. The actual in-place rock socket length was 12.4 feet.The planned elevation for the Osterberg cell located in Shaft 2, Bent 19 was 20.8 feet, however, the planned tip elevation was 5.8 feet. The in-place rock socket length was 9.5 feet. Both Osterberg cell test shafts had three levels of strain gauges with three gauges at each level for a total of nine gauges per shaft. Tell-tales were also placed at the top and bottom of the Osterberg cell and above the top level of strain gauges.

The Statnamic test was performed on Test Shaft Nº 5. Three levels of strain gauges were positioned like those in the Osterberg cell shafts.

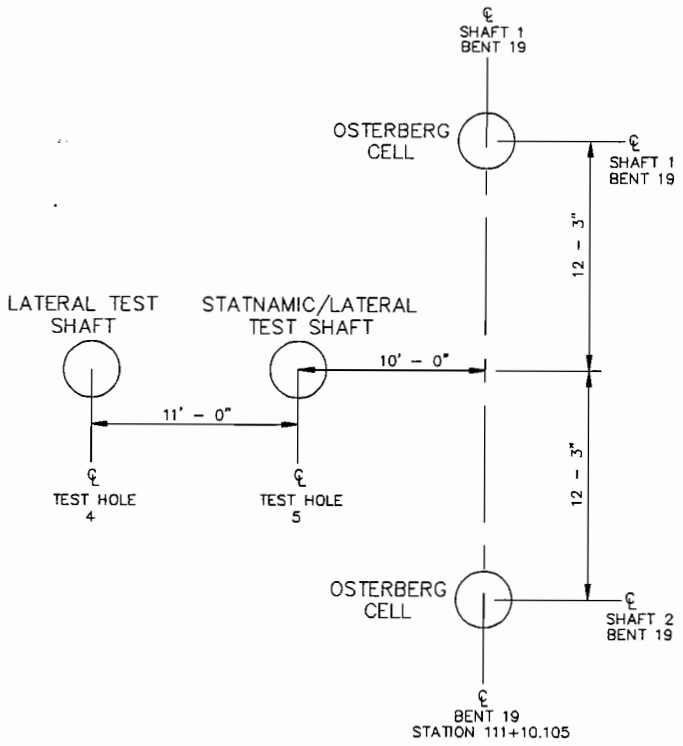

Figure 4. Test Shaft Configuration at Bent 19, Victory Bridge Site.

LOAD TESTS AND RESULTS

For comparison purposes, the Osterberg and Statnamic load test data plots have been normalized by converting applied load into applied shear strength. This was accomplished by dividing the applied load by the effective surface area of the rock socket.

Westbound Gandy Bridge Test Site

Pier 26

At Pier 26, the shaft failed in side friction at a maximum load of 700 tons with a corresponding movement of 1.0 inches at the top of the Osterberg load cell (Figure 5). From the plot of elevation versus load transfer from the vibrating wire strain gauge data (Figure 6), an interesting irregularity is seen at elevation 16.7 feet. At loads of 433 tons and above, the strain gauges at this level recorded no further increase, indicating failure at this elevation. The test was terminated to prevent further damage to the shaft. The effective rock socket length for this shaft was computed to be 3.9 feet, taken as the length from the top of the Osterberg cell to the anomaly seen in the strain gauge data. The equivalent shear strength was 14.3 tsf.

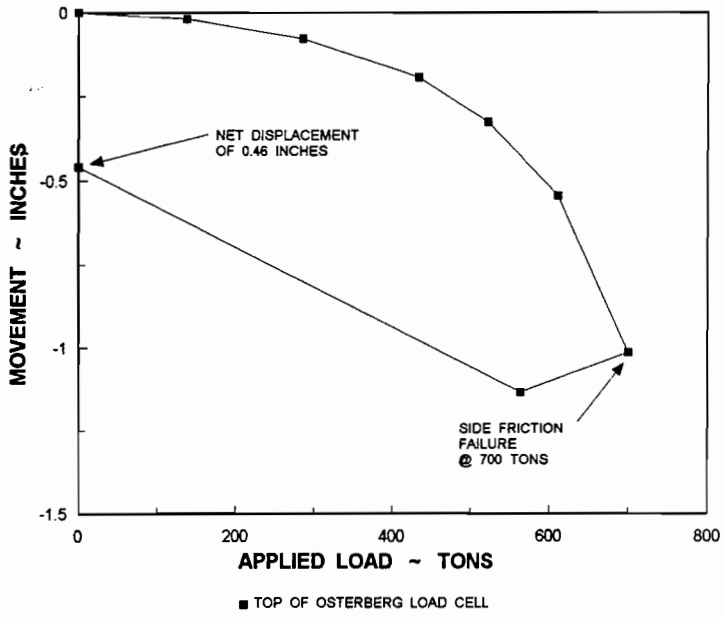

Figure 5. Movement Versus Load for Osterberg Load Test at Westbound Gandy Site, Pier 26.

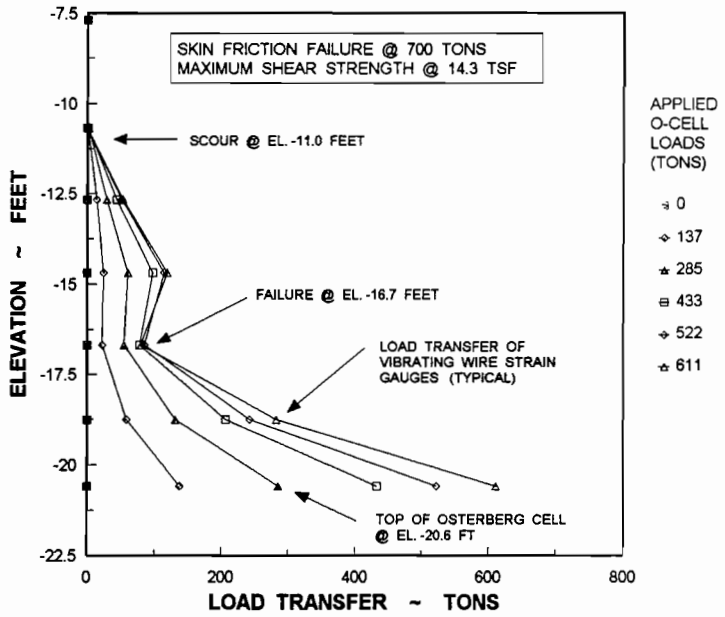

Figure 6. Vibrating Wire Strain Gauge Versus Elevation Plot for Osterberg Load Test at Westbound Gandy Bridge Site, Pier 26.

The displacement versus load plot (Figure 7) shows a peak Statnamic load of 3375 tons with a corresponding peak displacement of 0.53 inches. At 1350 tons, the plot shows the change in shaft stiffness which depicts a change from side friction due to load transfer to the rock socket to mostly end bearing resistance from 1350 tons to the peak loading. The corresponding displacement at 1350 tons was 0.2 inches. The net displacement of the shaft was 0.16 inches. The shaft was not fully mobilized by the application of 3375 tons. The effective rock socket length for this shaft was computed to be 8.0 feet, taken as the length from the bottom of the shaft at elevation -24.7 feet to the anomaly found during the Osterberg test at elevation -16.7 feet. The resulting shear strength was 13.4 tsf.

From the plot of movement versus shear strength (Figure 8), good agreement is evident from the point of application of the loads to about 6 tsf. Then, the movement from the Osterberg load test begins to increase to failure. The Statnamic data however continues in an elasto-plastic manner to the peak load, which did not fully mobilize the shaft in end bearing. The rebound curve from the Statnamic plot shows a slight change in curvature at about the same load (13.4 tsf) where the estimated ultimate skin friction occurs. In general, the correlation of the two plots show good agreement for skin friction, suggesting that the Statnamic test method provides a reasonable means of estimating ultimate skin friction. However, a larger applied load would have been necessary to fully mobilize the shaft in end bearing.

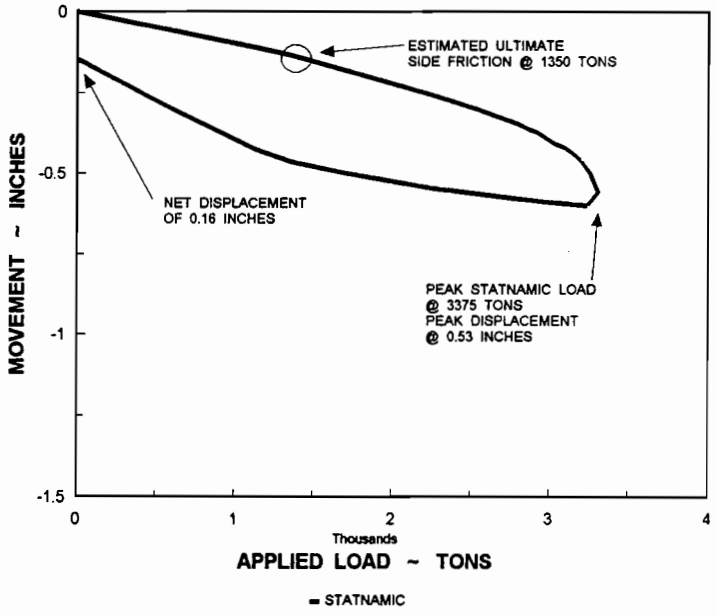

Figure 7. Displacement Versus Load for Statnamic Test at Westbound Gandy Bridge Site, Pier 26.

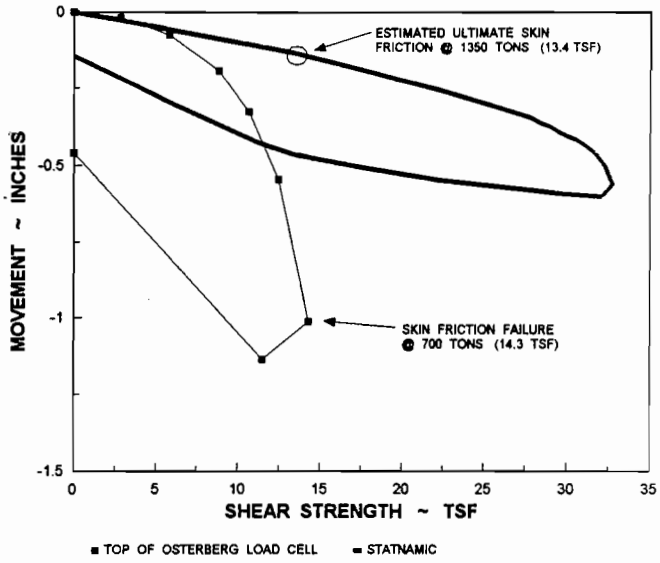

Figure 8. Shear Strength Comparison at Westbound Gandy Bridge Site, Pier 26.

Pier 52

At Pier 52, the shaft failed in end bearing at an applied Osterberg cell load of 2614 tons (Figure 9). The tell-tale data from the top of the shaft suggests the movement to be relatively linear at the end of the test. Therefore, we anticipate the ultimate skin friction to be higher. With an effective rock socket length of 21.7 feet, the computed shear transfer was 9.6 tsf. The strain gauge data (not shown) for this test showed evenly distributed load transfer to the rock socket in a parabolic fashion.

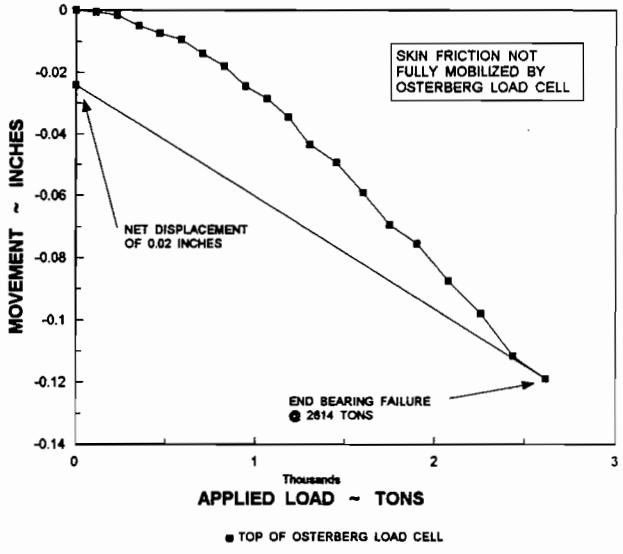

Figure 9. Movement Versus Load for Osterberg Load Test at Westbound Gandy Bridge Site, Pier 52.

A peak Statnamic load of 3450 tons was applied with a corresponding peak deflection of 0.52 inches. The plot (Figure 10) shows linear response of the shaft to increasing load, followed by limited displacement of the shaft under peak loading and linear rebound. The plot demonstrates typical behavior of a very stiff shaft which has not been fully mobilized under Statnamic loading. The rebound of the shaft resulted in a net displacement of 0.01 inches. This represents only 1/500 of the shaft diameter. In summary, the shaft responded purely elastically to the application of a 3450-ton peak load with no indication of shaft or soil plasticity. The effective rock socket length for this test was computed to be 22.3 feet. This was the length from the bottom of the shaft to the bottom of the casing at elevation -24 feet. The resulting shear strength is 12.2 tsf.

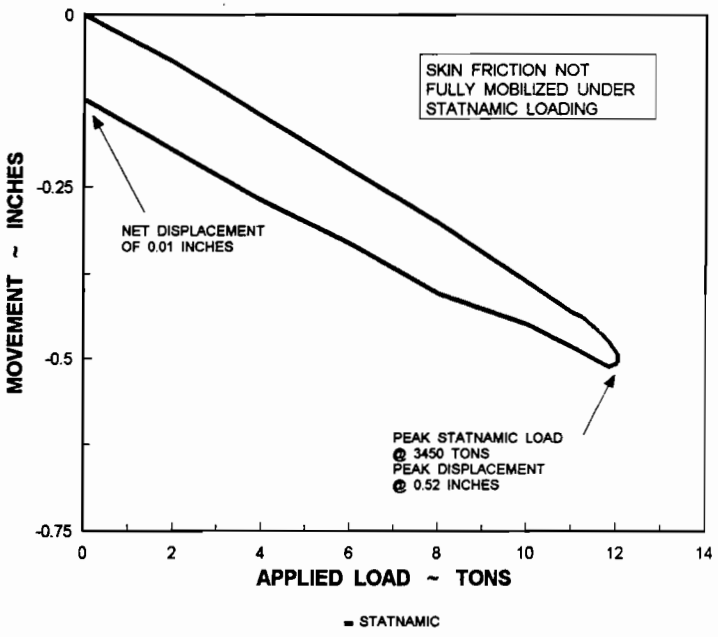

Figure 10. Displacement Versus Load for Statnamic Test at Westbound Gandy Bridge Site, Pier 52.

Figure 11 shows the comparison of shear strengths at Pier 52 for the Osterberg and Statnamic load tests. From the plot, we see that the Osterberg curve is stiffer than the Statnamic curve, indicating perhaps a more competent shaft. The net displacement of the Statnamic test is much greater than that of the Osterberg test. Neither test was able to fully mobilize skin friction, however, the loads at failure were over five times the design load of 542 tons.

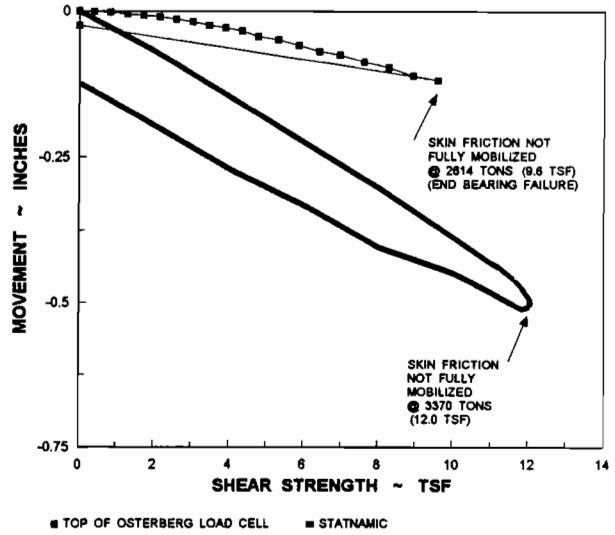

Figure 11. Shear Strength Comparison at Westbound Gandy Bridge Site, Pier 52.

Pier 91

At Pier 91, the maximum stroke of the load cell of 5 inches was expended prior to failing the shaft. The maximum load applied during the test was 1474 tons prior to failure (Figure 12), with a corresponding average bottom cell movement of 2.4 inches. The tell-tales and strain gauges indicated that the cell was tilting during the test. The effective rock socket for this shaft was 10.6 feet. Due to a 6-foot layer of soft clayey soil encountered during drilling, 6.0 feet was subtracted from the actual rock socket. The resulting shear strength was 11.1 tsf.

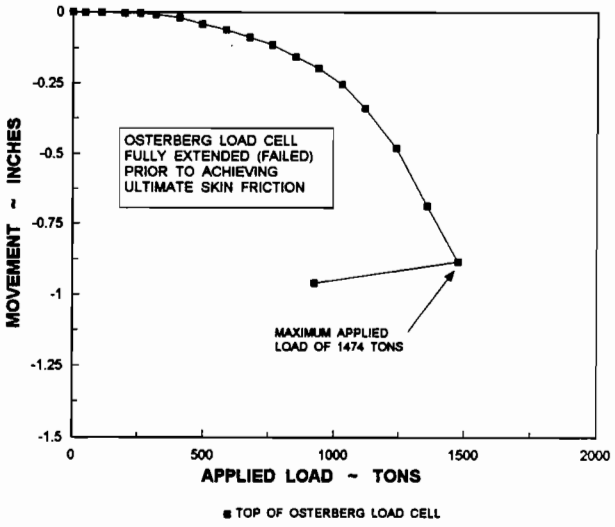

Figure 12. Movement Versus Load for Osterberg Load Test at Westbound Gandy Bridge Site, Pier 91.

At Pier 91, The displacement versus load plot (Figure 13) shows a peak Statnamic load of 3436 tons with a corresponding peak displacement of 0.74 inches. The plot shows relatively linear load response to 2135 tons then becomes elasto-plastic to about 2700 tons. Then the shaft yields to the peak displacement of 1.1 inches. The rebound of the shaft is linear with a net displacement of 0.3 inches. This plot shows typical behavior of a fully mobilized rock socketed shaft. The effective rock socket length of 15.1 feet was taken from the bottom of the shaft at elevation -61.6 feet to the bottom of the casing at elevation -40.5 feet, minus 6.0 feet to account for a soft clayey soil layer. The resulting shear strength was 11.3 tsf.

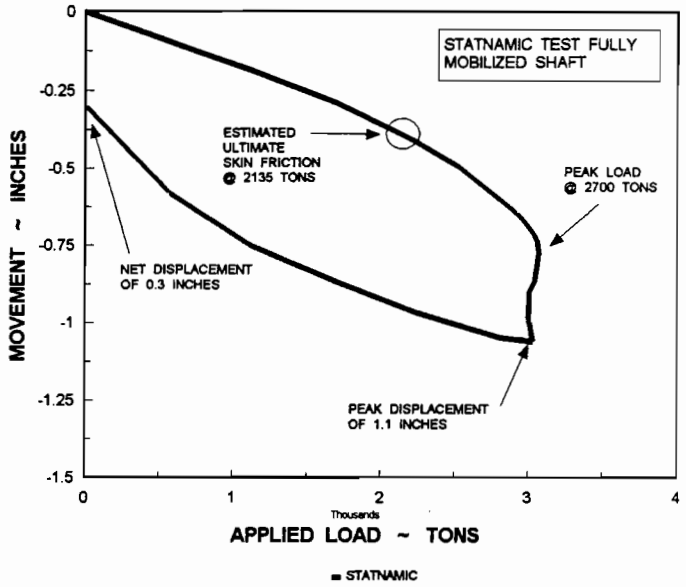

Figure 13. Displacement Versus Load for Statnamic Test at Westbound Gandy Bridge Site, Pier 91.

The Osterberg and Statnamic load test comparison plot (Figure 14) shows relatively good agreement in skin friction to about 7.5 tsf, where the Osterberg plot begins to plunge to 11.1 tsf, where the shaft failed in end bearing. However, the shape of the curve exhibits signs of failure. The estimated ultimate skin friction failure of 11.2 tsf for the Statnamic test compares extremely well. This test location was the only one of the three to fully mobilize both skin and end bearing for the Statnamic test, as evidenced by the shape of the curve at peak loading and the significant net displacement of 0.3 inches.

Victory Bridge Test Site

At Shaft 1, the Osterberg test shaft failed in skin friction at an applied load of 1537 tons with a corresponding movement of 0.24 inches. It was hoped however, that this test shaft would fail in end bearing, with the load cell placed at the bottom of the shaft. Based on the shape of the curve, it appears that failure occurred suddenly, with little warning. The reload curve illustrates that the rock does not regain strength upon reloading. For the initial loading, the net

displacement was 1.8 inches. The computed rock socket length for Shaft 1 was 12.4 feet, resulting in an ultimate side shear strength at 9.9 tsf.

At Shaft 2, the test shaft failed in skin friction above the load cell, as anticipated, at an applied load of 930 tons with a corresponding movement of 0.48 inches. The failure curve shows evidence of residual strength of approximately 550 tons. With a computed effective rock socket length of 9.5 feet, the ultimate side shear strength was 7.8 tsf.

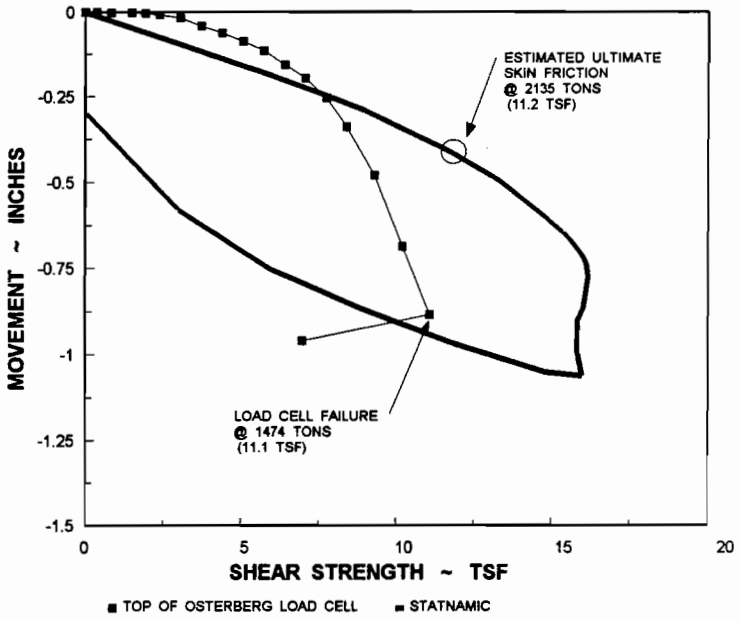

Figure 14. Shear Strength Comparison at Westbound Gandy Bridge Site, Pier 91.

A peak Statnamic static load of 3485 tons was applied with a corresponding peak displacement of 0.54 inches. The plot (Figure 16) shows linear response of the shaft to about 1530 tons, followed by limited displacement of the shaft under peak loading and linear rebound. The plot demonstrates typical behavior of a very stiff shaft which has not been fully mobilized under Statnamic loading. The rebound of the shaft resulted in a net displacement of 0.16 inches. There is no indication of shaft or soil plasticity. The effective rock socket length for this test was computed to be 9.5 feet, taken as the length from the bottom of the shaft to the bottom of the casing at elevation +25.5 feet. The resulting side friction shear strength is 12.8 tsf.

Figure 17 shows the comparison of shear strengths for the two Osterberg tests and Statnamic load tests. The curves compare reasonably well during initial loading to about 7 tsf. Then both of the Osterberg plots plunge rather quickly to failure. The estimated ultimate skin friction from the Statnamic test is considerably higher than it's counterparts. This is due to much stronger rock at this location, as evidenced in the lateral load test and Standard Penetration Test N-values. Further indication of the rock quality is seen in the net displacement, where the Osterberg test is significantly greater than that of the Statnamic test, even though the Statnamic test applied more load.

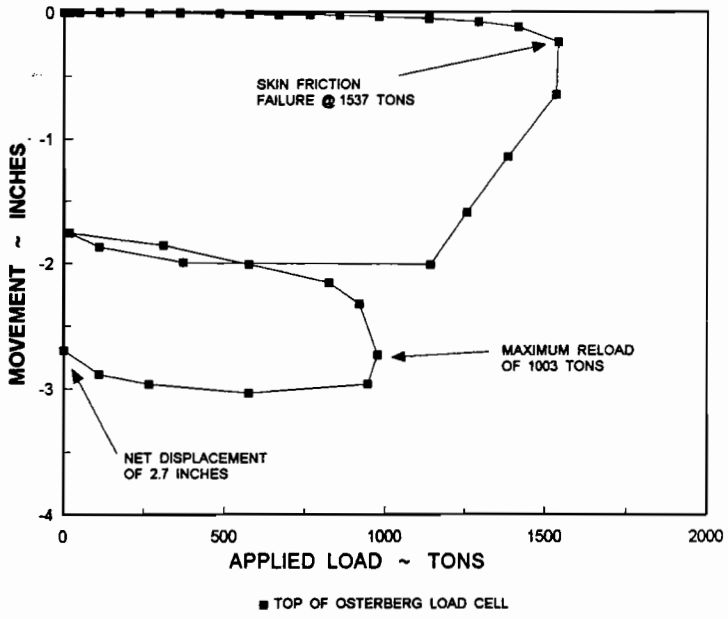

Figure 15. Movement Versus Load for Osterberg Load Test at Victory Site, Bent 3, Shaft 1.

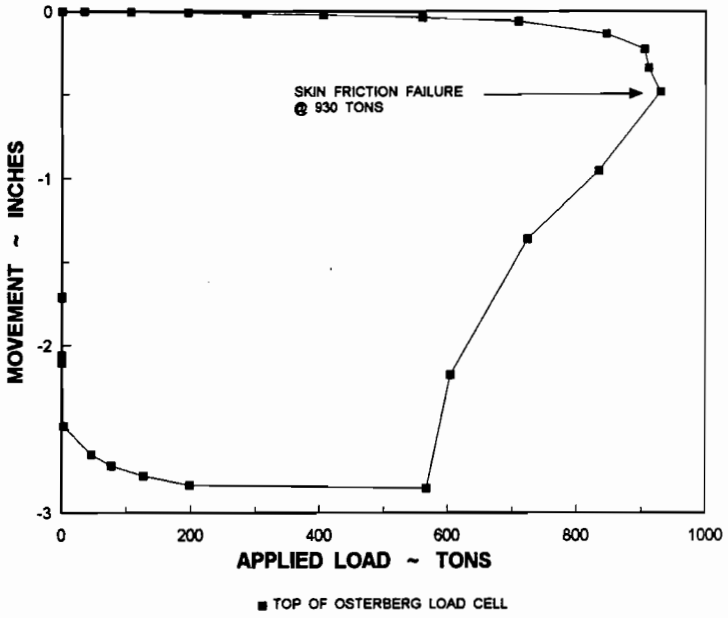

Figure 16. Movement Versus Load for Osterberg Load Test at Victory Site, Bent 3, Shaft 2.

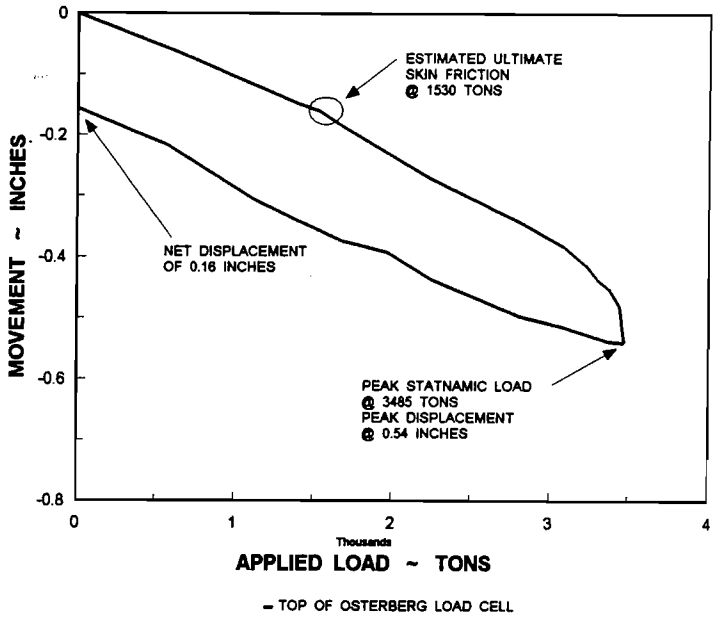

Figure 17. Displacement Versus Load for Statnamic Test at Victory Site, Bent 3.

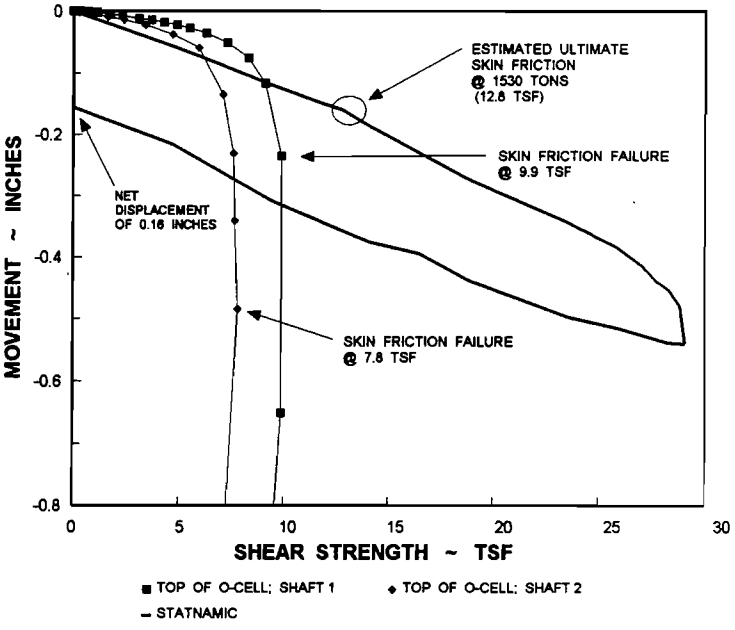

Figure 18. Shear Strength Comparison at Victory Site, Bent 3.

CONCLUSION

The Osterberg and Statnamic Load Tests both provide excellent methods for testing of drilled shafts, however, they are only tools which must be properly implemented to provide useful data. The experience gained from both projects in Florida indicates these test methods have advantages and disadvantages which must be considered.

The Osterberg load test provides the following advantages when compared to a standard static load test and the Statnamic Load Test:

1) Requires no external frame and is constructed in conjunction with the shaft.

2) Multiple load cells placed at the base of the shaft can be used to test shaft to capacities above 90 MN.

3) Load cells placed at different levels in the shaft can be used to test both end bearing and skin friction, separately.

4) Ability to reload test shafts to obtain residual side shear strength.

Advantages of the Statnamic Test when compared to the Osterberg Cell and static load test include:

1) The ability to test constructed shafts for capacity verification without the use of internal instrumentation.

2) The Statnamic Test can be performed to capacities of up to 30 MN and has the potential for higher capacities.

3) The Statnamic Test device can be reused.

4) The Statnamic Test has little or not effect on the integrity of the shaft (non-destructive).

FAILURE OF DRILLED PIER FOUNDATION IN COLLAPSIBLE SOILS

James E. Nordquist, P.E., Applied Geotechnical Engineering Consultants, Inc., Midvale, Utah

ABSTRACT: A small, single story structure supported on drilled piers was investigated after experiencing up to 6 inches of differential settlement.

Subsurface investigation revealed that moisture sensitive soil extends below the foundation of the building. Field and laboratory tests indicated that the soils had become moist to a depth of at least 55 feet (35' below the bottom of the piers).

This case study reviews the geotechnical aspects of the site along with the provisions presented in the original geotechnical report and the design and construction details that attempted to prevent unacceptable settlements of the structure.

(A copy of the paper maybe obtained from the author.)

INTERPRETATION OF PILE LOAD TEST RESULTS FOR THE UTAH DEPARTMENT OF TRANSPORTATION

Andrew L. Palmer, Staff Engineer
Converse Consultants Southwest, Las Vegas, Nevada

Loren R. Anderson and Joseph A. Caliendo
Utah State University, Logan, Utah

ABSTRACT

The purpose of this paper is to interpret pile load test data for several instrumented piles to determine the load transfer characteristics of driven piles in soft soils. Piles develop resistance to axial loads through side friction and end bearing. The rate that resistance develops is dependent upon soil type, pile type, and movement of the pile with respect to the soil. This paper addresses load transfer for driven pipe piles in deep lacustrine deposits along the Wasatch Front area of Utah. The piles used in this study were installed for the support of highway structures in the Salt lake City area. The information used in this study was obtained from the Utah Department of Transportation. Suggestions for pile capacity prediction are included as part of this study.

INTRODUCTION

The Utah Department of Transportation (UDOT) has completed a test program for deep foundations in lacustrine deposits along the Wasatch Front (UDOT Project Number I-215-9(78)22). This paper presents a portion of that study addressing the load transfer mechanisms of driven piles in fine-grained soils.

Information provided by UDOT included: raw strain gage data, pile load test data, soil boring logs for four sites, laboratory test data for two sites, and construction plans and drawings for the pile load test program containing general and site specific information. The Federal Highway Administration published a report that contains pile driving records for the piles installed as part of the pile load testing program.

Two pipe piles, designated as long and short, were tested at each of four sites. The lengths of the piles varied from approximately 55 to 127 feet. The eight test piles have an outside diameter of 12.75 inches and a wall thickness of 0.375 inches. The piles were driven with a steel plate welded on the bottom. Steel-reinforced concrete was placed inside the pile after driving. The steel reinforcement cage was instrumented with vibrating wire strain gages to detect internal strain during loading.

This paper will address the following:

1. The load distribution along the length of the pile including the end bearing capacity.
2. The stress-strain relationship of the pile-soil system, in particular the strain required to mobilize the maximum shaft resistance at a specific point.
3. The relationship between shaft resistance and the Standard Penetration Test blowcounts.
4. Design values for pile capacity predictions in fine-grained lacustrine deposits along the Wasatch Front.

SITE DESCRIPTION

Four bridge sites were selected for pile load tests. Two piles at each of the four sites were tested. The individual piles will be referred to by their site number and whether they are long or short. For example, the longer of the two piles at site 1 will be called pile 1-L. Likewise, pile 3-S refers to the shorter of the two piles at site 3. The test piles, located in the Salt Lake Valley, were driven in deep lake bed deposits from ancient Lake Bonneville. The deposits are mostly low strength, fine-grained silts and clays. Sites 1 and 2 are in the vicinity of the 40th West and I-80 interchange. Sites 3 and 4 are near the I-80 and West-side belt route interchange. Table 1 lists the structure number and a brief description of the location of each site.

Table 1. Site identification

Site#	Structure #	Location
1	C-628	North bound 40th West over I-80
2	C-637	"M" ramp over I-80
3	C-688	West-side I-215 over 5th South
4	C-460	West-side I-215 over Indiana Ave.

Subsurface investigations were done at three of the four sites. Subsurface exploration results from a nearby project were substituted for site 4. The boring logs include Standard Penetration Test (SPT) results and soil classification of the soil profile.

PILE INFORMATION

The eight piles are 12-inch diameter, closed-end pipe piles. The piles varied in length from 57 feet to 129 feet. Embedment length and total length are given in table 2. Reinforced concrete was placed in the piles a few days after driving. The vertical reinforcing steel was instrumented with Sinco (Slope Indicator Company) model No. 52621 vibrating wire strain gages and No. 52622 pickup sensors. The strain gages were placed 1-foot from the bottom of the pile and at 10-foot intervals up to the surface as shown in figure 1. Two strain gages were placed diametrically opposite one another at each level. By averaging the data collected at each level, the effects of bending can be eliminated.

Table 2. Lengths of piles

Pile #	Embedment length	Total length
1-L	102	104
1-S	55	57
2-L	81	83
2-S	71	73
3-L	127	129
3-S	119	121
4-L	103	105
4-S	67	69

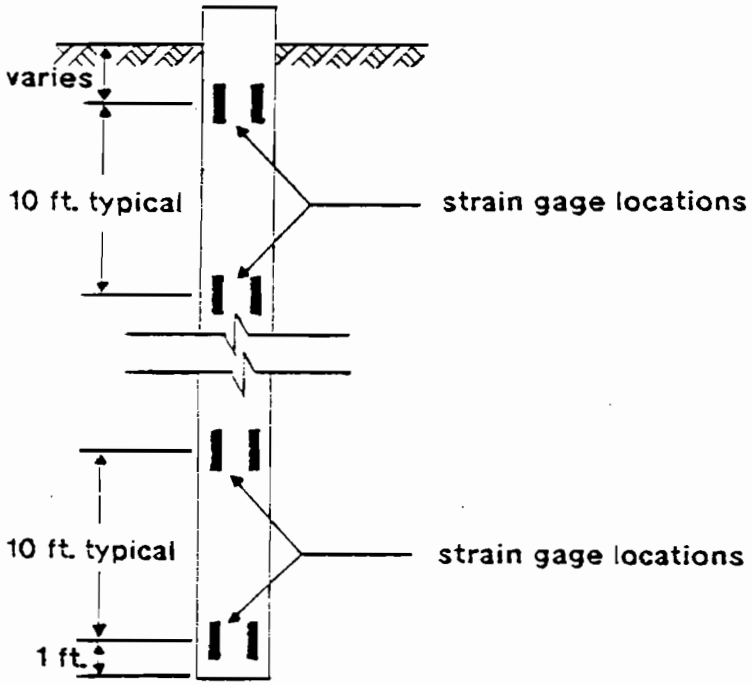

Figure 1. Typical placement of strain gages.

Pile 4-L, which should have had 11 levels of strain gages, had only 10 levels. It is assumed that the missing strain gages would have been two feet below the ground surface. To compensate for the missing strain gage data, the strain vs. depth was plotted and the line was extrapolated to where the strain gages should have been placed. The extrapolated strain at that point was used to determine the stress-strain relationship for the pile.

PILE LOAD TESTS

Load tests were conducted approximately 30 days after concrete was placed. Slight variations to the Texas Quick Load Test method include the following items. The load was applied in 25 ton increments instead of the 5- to 10-ton increments that are recommended. The time interval between loads was 3 minutes instead of the recommended two and a half minutes.

Pile load tests were conducted according to the Texas Quick Load Test method (Butler and Hoy, 1976). Test loads were applied by jacking against a reaction beam anchored to two 14-inch diameter pipe piles that were driven on either side of the test piles.

The piles were loaded to apparent failure and then the load was maintained for 6 minutes with readings taken after 3 and 6 minutes. The load was then released and readings were taken at 3 and 6 minutes after release. Deflection of the top of the pile was measured at each load increment by using dial gages that were read accurately to the nearest 0.001 inch. Two dial gages were placed diametrically opposite one another on separate reference beams to eliminate the effects of bending during testing. The two readings were averaged to get the deflection at each load increment. Interpretation of the load test was done by Bret Dixon (Dixon et al., 1992). The ultimate load for each pile was interpreted using three different methods. The methods used were: double tangent method (Butler and Hoy, 1976), Terzaghi's method (Terzaghi, 1942) and Davisson's method (Fellenius, 1975). The results from the pile load test interpretation are contained in table 3.

Table 3. Pile load test interpretation results in tons (Bret Dixon, unpublished thesis)

Pile	Interpretation method:		
Number	Davisson's	Double tangent	Terzaghi's
1-L	505	490	482
1-S	200	199	218
2-L	372	358	368
2-S	244	240	255
3-L	525	534	463
3-S	465	460	405
4-L	592	574	524
4-S	246	240	254

In addition to reading the dial gages, readings were taken from each strain gage for each load increment. The strain gage data was collected using a Slope Indicator Company Model No. 52630 data logger and printed on thermal paper for permanent record. There were a few cases where one of the two strain gages at a particular level failed to give good data. When this happened, the reading for the good strain gage was used as the average of the two readings. In only one case did both strain gages at a particular level fail to provide valid results. In that instance the average strain was estimated by a straight line interpolation between the strain gages directly above and below the failed strain gages. Except for these

minor changes, the strain gage data were left in their raw state to allow comparison of manipulated data to the raw data.

INTERPRETATION OF LOAD TEST RESULTS

Stress Strain Relationship

The first task of analysis was to determine the stress-strain relationship for the composite piles. An attempt was made to determine the modulus of elasticity for the piles theoretically. The equivalent modulus of a composite pile should be equal to the sum of the modulus of elasticity of steel multiplied by the area of the steel and the modulus of elasticity of concrete multiplied by the area of concrete divided by the total area of the pile. A relationship that applied to all of the piles could not be found, presumably due to the variability of the modulus of elasticity for concrete. An experimental approach to finding the elastic modulus was also tried with better results.

The strain from the top level of strain gages was plotted versus the load applied to the pile during the load test as shown in figure 2. For analysis, the strain in the top strain gages was assumed to be due to the total applied load at the top of the pile, i.e., shaft resistance between the surface of the ground and the top strain gages was negligible. The slope of the load vs. strain plot represents the modulus of elasticity multiplied by the cross-sectional area of the pile. The load-strain plot was quite linear and the slope was found using the linear regression function within Quattro-Pro. The standard deviations ranged from 0.5% to 2.1% with an average of 1.4% of the modulus of elasticity. The lowest R^2 value was 0.95; all others were greater than 0.98 and half of the total were at least 0.99. The composite modulus of elasticity was found to vary from 5,489 ksi to 7,040 ksi; the average composite modulus of elasticity was 6,369 ksi with a standard deviation of 49 ksi. This range of values is reasonable given the variability of concrete, which makes up a major portion of the pile.

Load Distribution

The load at depth was determined by multiplying the strain at a particular depth by the modulus of elasticity and the area of the pile. The end bearing in the pile was calculated using data from the bottom strain gages, which were placed 1 foot from the bottom of the pile (Keane, 1991). The load distribution for each pile was determined at each load increment. The distribution of load over the length of the pile for each loading increment is contained in appendix D. Graphical representations of the load distribution for each pile at selected load intervals are included in figure 3. Values for the average deflection and unit skin friction were calculated for points midway between strain gage levels.

The movement of the pile was calculated for points midway between the strain gage levels. The movement at a point between the first and second strain gage levels, is equal to the movement at the top of the pile, minus the strain of the top strain gage, multiplied by the distance from the mid-point between the first and second strain gage levels. The next point where movement was calculated was halfway between the second and third strain gage levels. Movement at this point is equal to the calculated movement at the point as described above, minus the strain of the second level of strain gages multiplied by the sum of half the distances

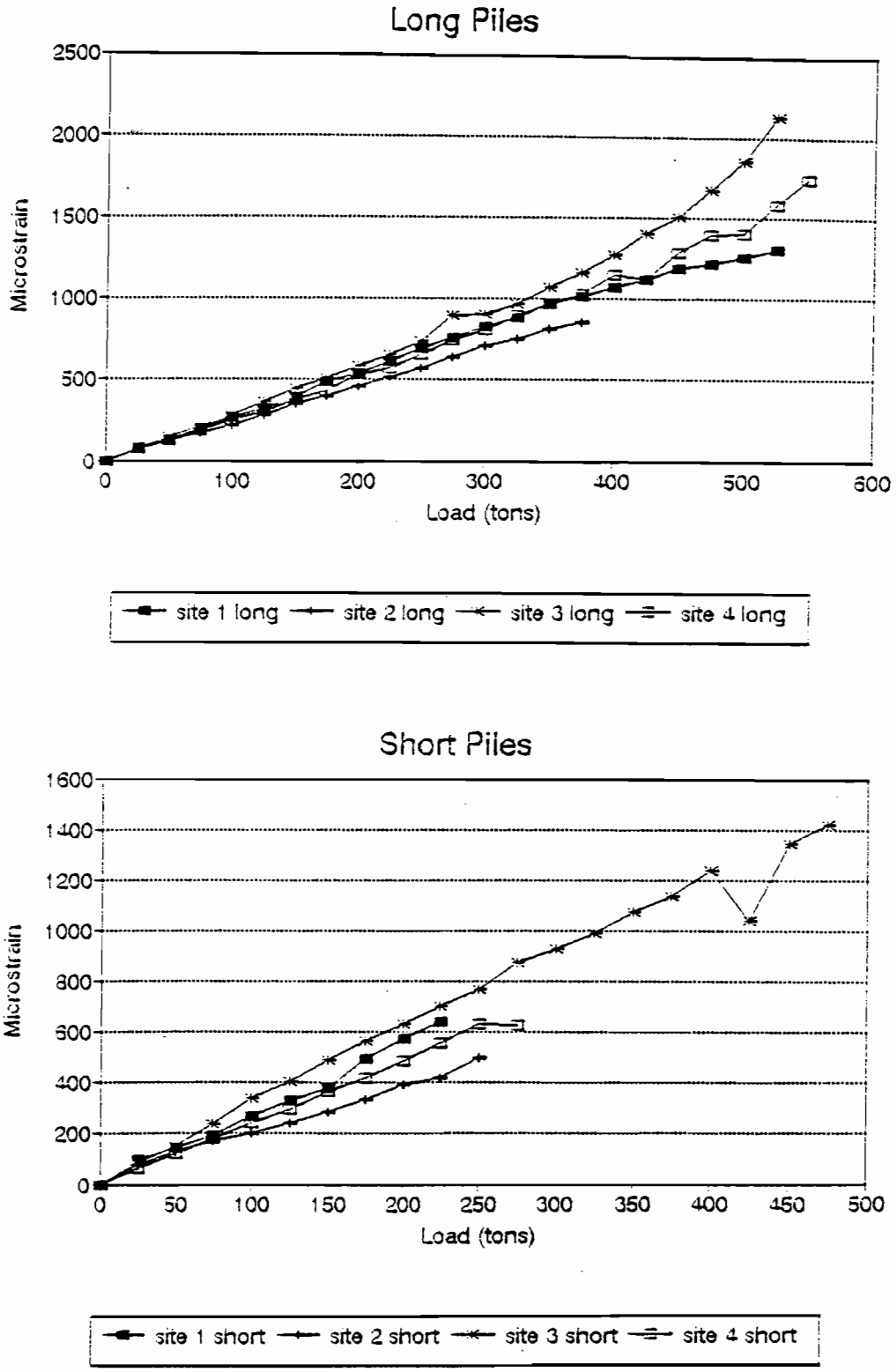

Figure 2. Stress vs. strain plots for top levels of strain gages.

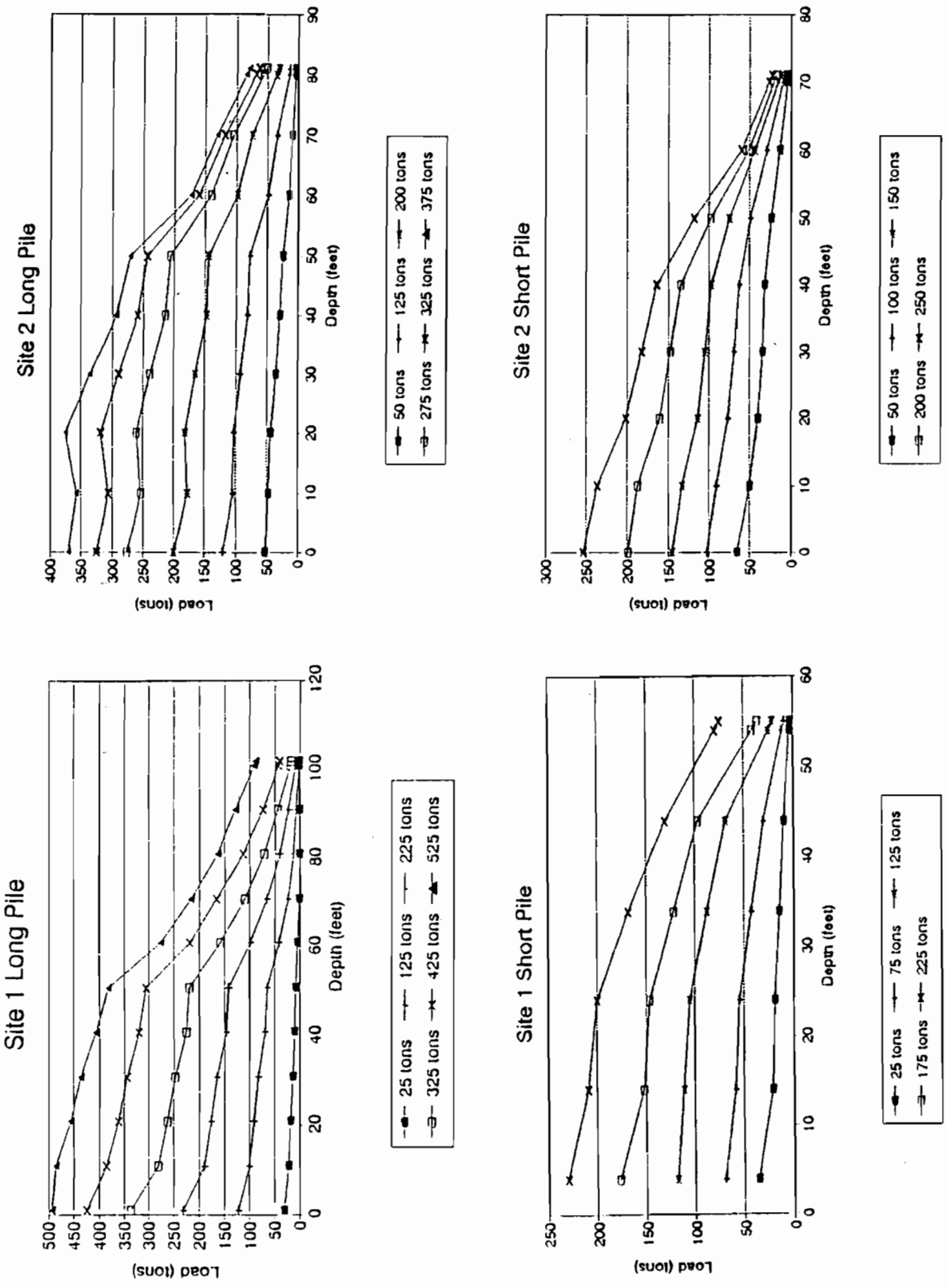

Figure 3. Load distribution curves.

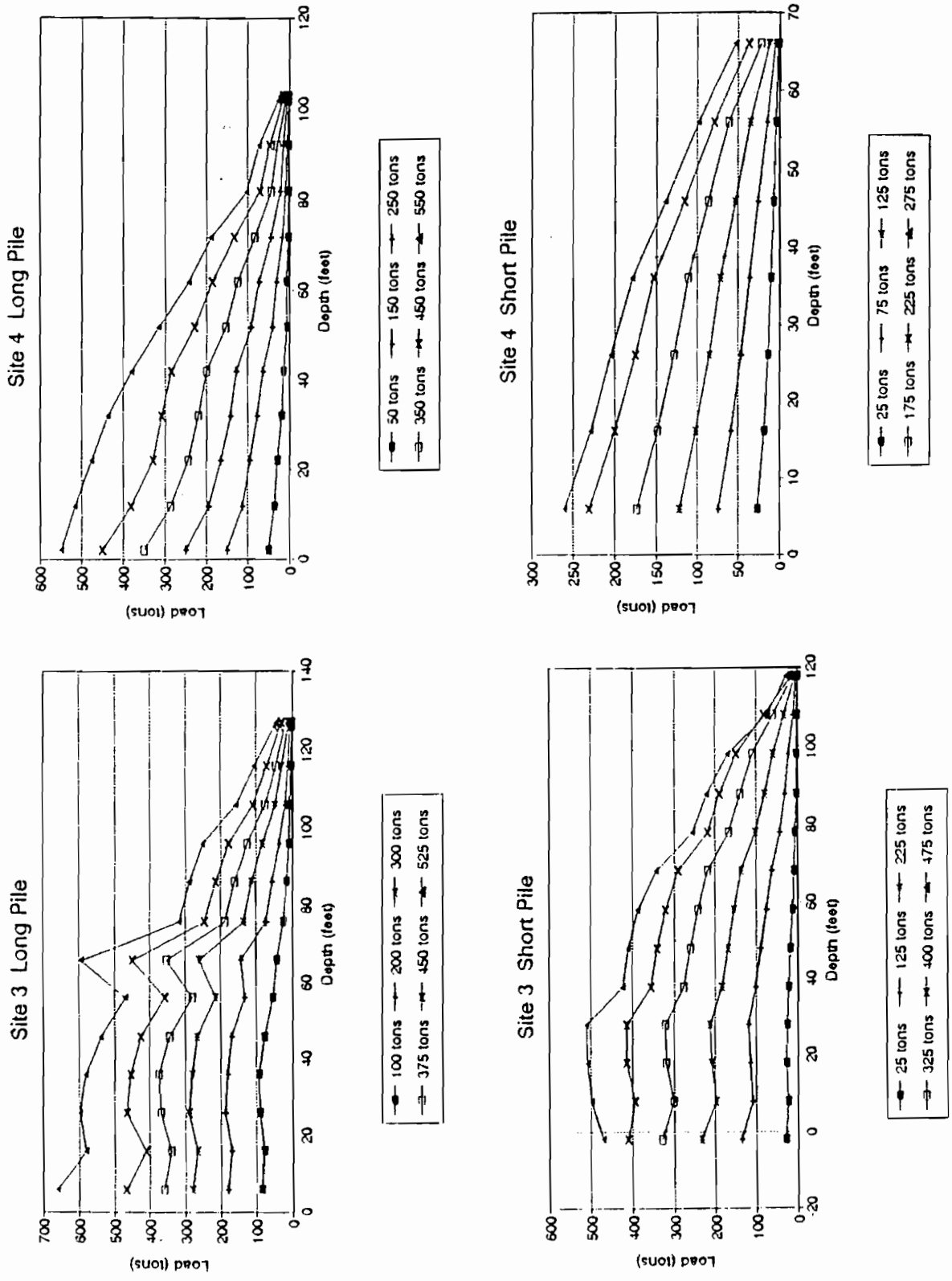

Figure 3. Continued

between adjacent strain gage levels. This procedure was repeated down to the bottom of the pile.

The average unit skin friction was determined for the points where movement was calculated. The average friction was calculated simply by dividing the change in load by the surface area over which the change occurs. The area is found by multiplying the distance between strain gage levels and the circumference of the pile. The change in load is simply the load at the upper strain gage level minus the load at the lower strain gage level for any given interval. The movement and unit friction were calculated for each point at each loading increment. Selected samples of friction vs. movement plots are shown in figure 4 to show the development of side friction with relative movement of the pile. In general, friction vs. movement plots indicate that the maximum unit friction at a point is mobilized at approximately 1/4 to 1/2 inch of relative movement.

For some of the piles, the load vs. depth plot had a significant discontinuity in load at the top strain gage. In one case, Pile 2-S, the strain, and therefore the calculated, load was lower at the top than it was at the second layer of strain gages. The increased load could only be caused by negative skin friction due to a settling soil mass around the pile. But since all data were taken during the pile load test, settlement could not have taken place as fast as the pile deflection. In several other cases the load increased dramatically at the top level of strain gages. The discontinuities that show an increased load at the top could indicate that the top layer, which is a stiffer, overconsolidated layer, causes much more friction on the pile than the soft soils deeper in the profile. Another possible explanation for the higher apparent load at the top strain gage level is that the reinforced concrete is deforming more than the steel pipe casing. This could happen if the majority of the load is applied to the reinforced concrete when the distance from the top of the pile to the first level of strain gages is insufficient for the friction between the steel pipe and the concrete to effectively bond the two components into a single composite member.

An effort has been made to smooth three such discontinuities, including piles 2-S, 3-L and 3-S. In the case of pile 2-S, the soil above the top strain gage level should not settle in a way that could cause negative skin friction. Furthermore, during the pile load test, the pile is being forced down relative to the soil, thereby causing positive skin friction at all points along the pile. The strain at the top of pile 2-S has been increased by a factor of 1.3 to smooth the load vs. depth plot. At site 3, the upper 34 feet of the piles are encased in a pipe to prevent negative skin friction due to settlement of a constructed fill. Since the piles are encased, there should be no friction acting on the upper 34 feet. The strains at the top level of strain gages have been adjusted to be consistent with the strains at the second and third levels of strain gages for both piles at site 3.

Values of end bearing were calculated by determining the load at the lowest strain gage level in each pile and subtracting the side resistance in the bottom 2 feet of the pile. Maximum end bearing values measured in the piles ranged from approximately 20 to 70 tons. The movement required to mobilize the maximum end bearing ranged from 0.15 to 0.5 inches of calculated movement at the pile tip. These movements at the pile tip correspond to movements of 0.5 to 1.25 inches at the top of the pile. The values of movement required to mobilize the maximum end bearing are relatively small. The low values may be a result of

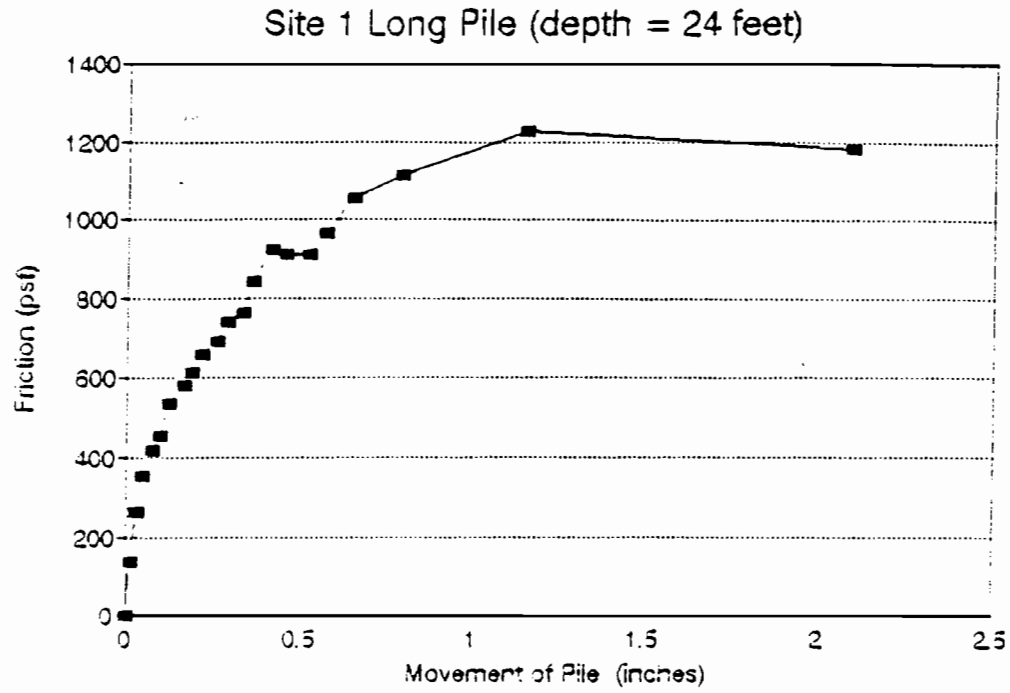

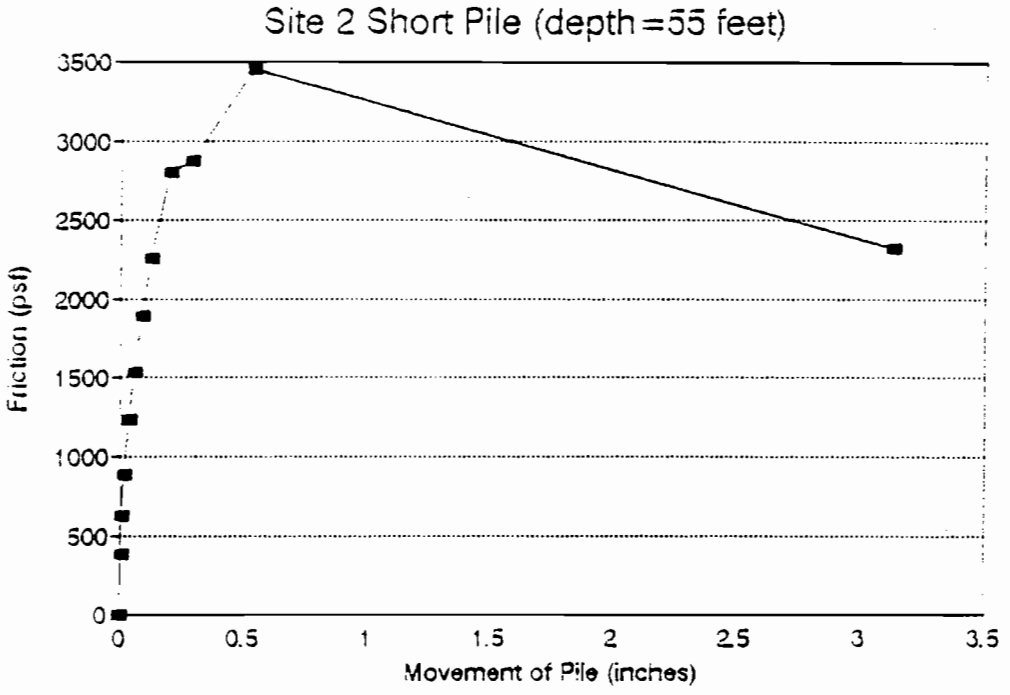

Figure 4. Friction vs. movement plots at selected locations and depths.

resistance that built up during pile driving when the tip of the pile was driven down, creating a zone of stiffer consistency soil directly beneath the pile tip. Test piles Long 3 and Long 4 had negligible apparent movement at the pile tip. Because the movements were negligible, error induced in reading and or calculating caused the end bearing vs. movement plot to include very small negative movements. The values of end bearing determined in this study appear to be greater than typical soft clay soils could provide.

PREDICTION OF LOADS BY STATIC METHODS

The load-carrying capacity of the test piles is of interest to many who would like to use data from geotechnical investigations to predict the capacity of piles to be constructed in similar soil conditions. The majority of the pile load-carrying capacity is derived from frictional resistance along the pile shaft. Since end-bearing capacity plays a secondary role in total load-carrying capacity, the end bearing was subtracted from total load while working backwards to find a functional relationship between the pile load test results and the conditions encountered during a geotechnical investigation.

Laboratory data from two pile sites were provided by UDOT. The data available pertained to sites 1 and 3. Lab data for sites 2 and 4 were not included as part of the information package from UDOT. A majority of the soils encountered at the four sites consisted of fine-grained clays and silts. Methods of predicting pile capacity in clay soils include the α, β, and λ methods.

α-Method

Values of friction derived from the α-method of prediction did not match values measured during the pile load test. The predicted friction is a function of the undrained cohesion of the soil. Limited undrained cohesion values were available for use in predicting. The predicted values of friction are compared with the measured values in table 4.

Table 4. Comparison of calculated and measured values of skin friction

Test Site #	Depth (ft)	AASHTO Soil Classification	C_u (tsf)	q_u (tsf)	α	f_{calc} (tsf)	f_{observ} (tsf)
1	12	A-7-6(11)	.075	.15	1	.075	.86
1	22	A-6(10)	.04	.08	1	.04	.55
1	37	A-4(4)	.35	.70	.7	.24	.85
1	42	A-7-6(16)	.46	.93	.55	.25	.88
3	42	A-7-6(12)	.14	.29	1	.14	.34
3	82	A-4(8)	.35	.70	.7	.25	.78

β-Method

The β-method, similar to methods used for granular soils, utilizes the lateral earth pressure coefficient, k, and the remolded friction angle, ϕ_R, to predict the frictional resistance.

Lab data available for the pile load test project were inconsistent with values of ϕ ranging from 3° to 34° for the same soil classification. A summary of soil classification and shear strength based on boring logs and laboratory data is presented in table 5. With the significant variation in ϕ_R and the resulting difference in k, a suitable relationship between lab data and measured values could not be established.

Table 5. Summary of shear strength for different soil types

Test Site #	Depth (ft)	AASHTO Soil Classification	ϕ (degrees)	Cohesion (tsf)
1	17	A-7-6(11)	10.5	0.15
1	38	A-4(4)	0	0.35
1	92	A-4(8)	28.5	0.75
2	47	A-4(8)	9.0	0.53
2	51	A-3	38	0
2	58	A-4(8)	3.0	0.6
2	67	A-4(5)	8.0	0.4
2	92	A-4(8)	31	0.25
2	107	A-7-6(12)	18.5	0.29
2	112	A-4(8)	34	0.30
2	122	A-4(8)	32	0.52

λ-Method

The λ-method allows for more flexibility than the other predicting formulas. The equation for the λ-method is as follows:

$$f_{av} = \lambda\left(\overline{\sigma}_v{}' + 2c_u\right).$$

Weighted average values of c_u were calculated and used to estimate the pile capacity. Consistent results were obtained from three of four sites with the λ-method. Values of λ for the test piles are given in table 6.

A weighted undrained cohesion value (c_u) of 0.25 tsf was used for all of the pile sites. This value was estimated by selecting an average value of the undrained cohesion as determined in the laboratory testing program. Low values of λ at site 3 could be a result of the surcharge load caused by approximately 34 feet of fill material placed above the native ground surface. The piles at site 3 were cased for the upper 34 feet to reduce the risk of negative skin friction should the fill material settle around the pile. The higher values of $\overline{\sigma}_v{}'$ may be the difference of the values of λ (0.38 and 0.40 tsf). Values of λ for the other sites ranged from 0.62 to 0.79 with an average of 0.69 tsf and a standard deviation of ±0.06 tsf.

Table 6. Values of λ for test piles

Pile	Embedment Length	λ
1-L	55	0.68
1-S	101	0.79
2-L	81	0.67
2-S	71	0.62
3-L	127	0.38
3-S	119	0.40
4-L	103	0.73
4-S	67	0.65

RESULTS AND CONCLUSIONS

Instrumentation

Results from pile load tests indicate that the strain gage instrumentation performed adequately. Load distribution behaved as expected. Given the margin of error and the potential sources of error, the overall results were fairly consistent. With this project it seems that because of the large number of people and different organizations involved, some important information was either not obtained during construction or lost at some time thereafter. For example, the actual locations of the top strain gages were not included in the information package provided by UDOT. For future instrumentation projects, accurate records of strain gage locations should be kept. The most effective location for the top strain gages would be at the ground surface so that the total load on the pile would be "felt" by the uppermost level of strain gages. Care should also be taken when constructing composite piles so that there is adequate bonding between steel and concrete. If either the concrete or the steel undergoes more compression than the other, the material that compresses more will carry more than its share of the load, giving skewed results. This could be detected near the top of the pile by instrumenting both the reinforcing steel and the pipe pile. It may also be of interest to include an embedment-type strain gage in the concrete near the strain gages attached to steel.

Load Distribution

The load distribution results are presented in figure 3 entitled Load Distribution Curves. In addition to the load vs. depth plots, plots were prepared to show the development of frictional resistance and end-bearing for each pile. The load vs. movement plots show the total load vs. movement (at top of pile) along with friction vs. movement and end bearing vs. movement. As shown in figure 5, the end bearing pressure is a relatively small portion of the total resistance. The end bearing, which takes greater movement to mobilize, is even less at design loads which can be carried easily by side friction. The maximum friction at any given point generally occurred at pile movements of 0.1 to 1.0 inches with respect to the adjacent soils. The maximum friction occurred at an average movement of 0.35 inches. The piles experienced a maximum end-bearing pressure at movements of 0.15 to 0.5 inchesof calculated

movement at the tip. It should be noted that the movements at the top of the piles (as shown in figure 5) were considerably higher than the calculated movement at depth. The maximum end bearing may not have been reached in some of the piles because of the high friction load compared to end bearing. It appeared that the movement required to mobilize the maximum end bearing would generally range from 0.5 to 1.25 inches at the top of the pile.

Pile Capacity Prediction

Variation in strength characteristics of the many layers in the soil profile made prediction of capacity on a layer-by-layer basis difficult. The λ-method, which makes use of an empirical value for the entire pile length, gave consistent results for piles where there was no significant surcharge pressure. Values for λ ranged from 0.62 to 0.79 with an average of 0.69. Using a value of 0.65 for piles in similar soil conditions and having similar dimensions should give reasonable values for pile capacity prediction. End-bearing capacity prediction was not addressed in this paper due to the minor contribution to the total load. For most of the piles, the maximum end-bearing capacity was not developed.

LITERATURE CITED

Butler, H.D. and H.E. Hoy. 1976. The Texas quick load method for foundation load testing. User's Manual. U.S. Department of Transportation Report no. FHWA-IP-77-8. 54 p.

Dixon, B.G., L.R. Anderson, R. Rahmen, and E. Keane. 1992. Estimation of ultimate capacity of piles in the Utah region by dynamic methods. Proceedings, 28th Symposium on Engineering Geology and Geotechnical Engineering, April 1-3, 1992, Boise, Idaho. pp. 458-472

Fellenius, B.H. 1975. Test loading of piles and new proof testing procedure. Journal of the Geotechnical Engineering Division, ASCE, 101(GT-9):855-869.

Keane, E. 1991. Chief Geotechnical Engineer, Utah Department of Transportation. Written communication, June 4.

Poulos, H.G. and E.H. Davis. 1980. Pile foundation analysis and design. John Wiley and Sons, New York. 397 p.

Prakash, S. and H. D. Sharma. 1990. Pile foundations in engineering practice. John Wiley and Sons, New York. 734 p.

Terzaghi, K. 1942. Discussion of the progress report of the committee on the bearing value of pile foundation. Journal of the Geotechnical Engineering Division, ASCE, 68:311-323.

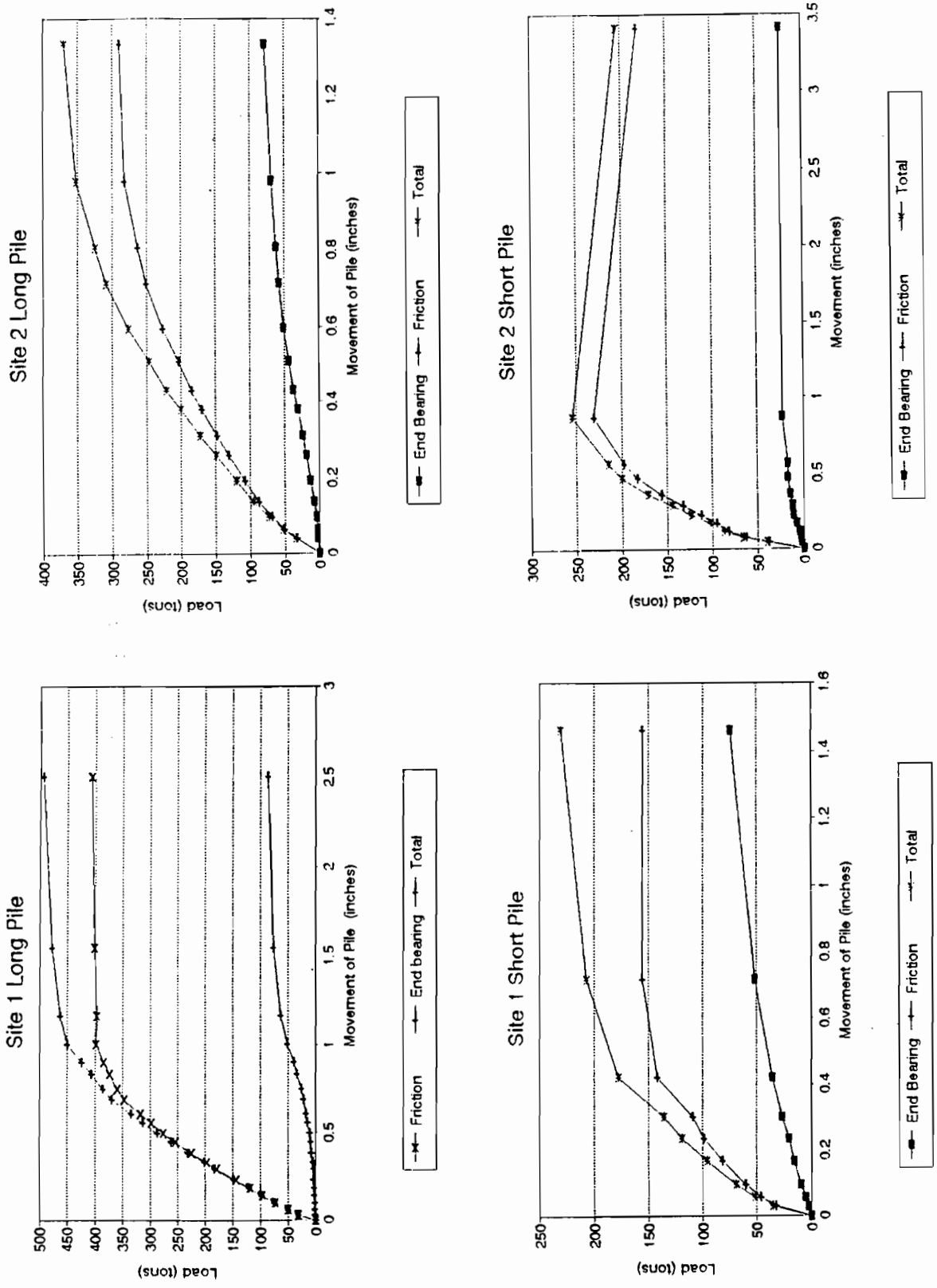

Figure 5. Loads vs. movement.

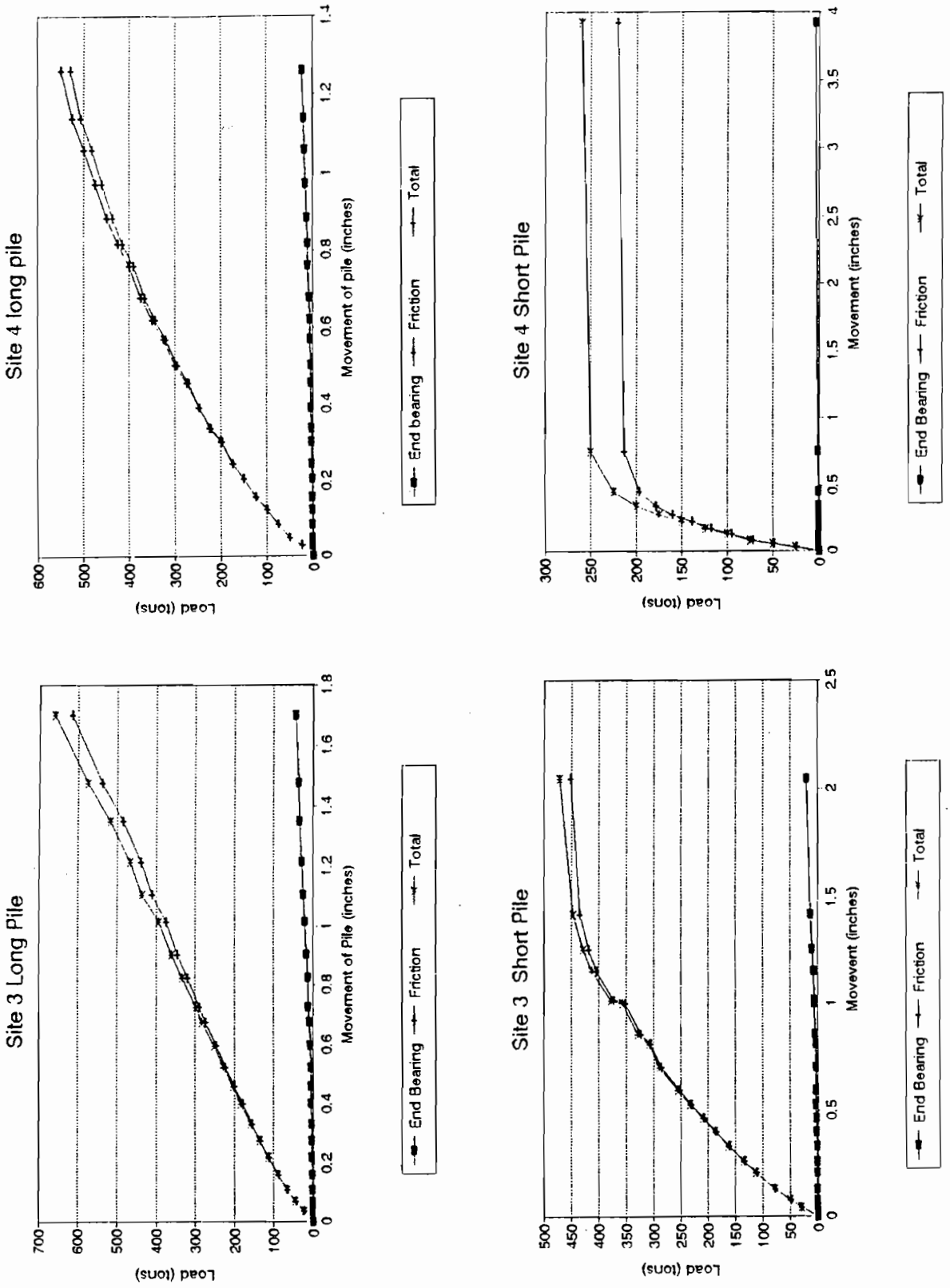

Figure 5. Continued

APPLICATIONS OF GEOPHYSICAL METHODS TO HELP MAP GROUND-WATER CONTAMINATION--A CASE STUDY

Alvin K. Benson, Kelly L. Payne, and Melissa A. Stubben
Department of Geology, Brigham Young University, Provo, UT 84602

ABSTRACT

Geophysical methods can be helpful in mapping areas of contaminated soil and ground wtaer. Electrical resistivity and very low frequency electromagnetic induction surveys were carried out at a site of shallow hydrocarbon contamination in Utah County, Utah. Previously installed monitoring wells facilitated analysis of water chemistry to enhance interpretation of the geophysical data. The electrical resistivity and very low frequency electromagnetic data correlate well and were used to help map the contaminant plume which was delineated as an area of high apparent and interval resistivities.

INTRODUCTION

Electrical resistivity (ER) and electromagnetic induction (EM) surveys are sensitive to ground-water quality and hydrocarbons in a porous medium (Telford and others, 1990; Benson, 1991). Benson (1991) points out that hydrocarbon plumes may be delineated as resistivity highs since hydrocarbons have high resistivities relative to water, or as resistivity lows if inorganic compounds are added to contaminated ground water to stimulate biorememdiation, thus increasing the total dissolved solids in the water. Also, if biodegradation of the hydrocarbons is taking place, resistivity values may be lower where this is occurring, since biodegradation also tends to increase the amount of dissolved solids in the ground water. Studies by Foster and others (1987) and Benson and others (1991) report low resistivities over hydrocarbon-contaminant plumes.

Most studies have used contoured apparent resistivity data at a given depth to model plumes of hydrocarbon contamination, but we will use interval resistivities obtained by iterative computer modeling of the apparent resistivity data. Since the apparent resistivity values collected in the field are affected by the thickness and fluid content of each of the subsurface layers, interval resistivities should provide a much more accurate picture of resistivity as a function of depth.

SITE INFORMATION

Data were collected from a site in central Utah Valley, Utah County, Utah in a parking lot on the northeast corner of the intersection of 1230 N. 200 W., Provo, Utah. Utah Valley is an alluvial basin along the west side of the Wasatch Front (figure 1). The shallow subsurface geology of the study site consists of unconsolidated to semiconsolidated alluvial deposits of gravel, sand, silt and clay (Gates and Freethey, 1989). According to the Utah County Soil Survey, the surface soils are Sunset loan and Keigley silty-clay loam. These soils are

moderately permeable (5.64×10^{-4} to 1.76×10^{-3} cm/s).

Monitoring wells (MW), which had been previously installed at the site, facilitated analyses of water chemistry and ground-water flow direction to enable correlation between geophysical data, hydrologic conditions, and water chemistry. A service station to the north of, and upgradient from, the study site reported a leak from an underground gasoline tank in February, 1990. Gasoline has contaminated the ground water as far south as MW-3 and MW-4 (figure 2) and was also found to be leaking into the stream running along the east edge of the gas station and study site. Ground water has been pumped from several wells and is being treated on-site to remove contaminants (J.D. Keith, Brigham Young University, Personal Communication, 1993). This has arrested further migration of the contaminant plume.

Water levels in the monitoring wells were measured in May, 1993, and the elevation of the water level in each well was determined relative to a chosen datum. The depth to water in each well is summarized in table 1. The surface of the water table was contoured, and the gradient calculated to be 9.9 centimeters per 100 meters (0.33 ft/328 ft). This gradient indicates a flow direction approximately southwest toward Utah Lake (figure 1), which is in good agreement with local and regional topography.

Table 1. *Depths to water in monitoring wells for study site.*

Monitoring Well	Date	Depth to Water (m)
MW-1	05-06-93	1.90
	10-15-93	1.29
MW-2	05-06-93	1.73
	10-22-93	1.58
MW-3	05-06-93	1.47
	10-15-93	1.58

WATER CHEMISTRY

Water samples were collected from MW-1, MW-3, and MW-4 on 15 October 1993 and from MW-2 on 22 October. Samples from each well were analyzed at BYU for anion concentrations using an ion chromatograph and for cation concentrations using an atomic absorption spectrometer. Using a gas chromatograph, ground waters from MW-1 and MW-3 were analyzed for total petroleum hydrocarbons (TPH) and benzene, toluene, ethylbenzene, and xylene (BTEX constituents) by Richard Laboratories in Pleasant Grove, Utah.

Results of the water analyses are summarized in tables 2 and 3. MW-3 and MW-4 encounter the contaminant plume, while MW-1 had no detectable TPH or BTEX, and MW-2 had no detectable product odor. From the direction of ground-water flow, contamination might be expected in all of the monitoring wells. However, the fact that contamination is not present in MW-1 and MW-2 indicates that pumping began soon enough at the site to prevent the contaminant(s) from migrating extensively, and/or perhaps the shallow subsurface layers have

a low hydraulic conductivity, which has slowed the movement of the contaminant(s) through the soils.

Table 2. *Dissolved solids analysis results for ground-water samples collected from study site. Concentrations are in mg/L.*

Monitoring Well	F^-	Cl^-	NO^{3-}	$SO4^{2-}$	$HC0^{3-}$	Na^+	K^+	Ca^{2+}	Mg^{2+}	TDS
MW-1	0.1	49	1.9	69	375	34	4.4	116	25	675
MW-2	0.3	40	1.0	68	384	26	3.8	119	26	668
MW-3	0.4	44	0.4	45	743	36	16.5	119	46	1121
MW-4	0.7	46	0.5	54	889	49	16.0	199	53	1307

Table 3. *BTEX and TPH analysis results for ground-water samples collected from study site. Concentrations are in mg/L.*

Monitoring Well	Benzene	Toluene	Ethylbenzene	Xylene	TPH
MW-1	<5.0	<5.0	<5.0	<5.0	<500
MW-3	2850	344	414	4432	13258

ELECTRICAL RESISTIVITY RESULTS

Thirty-two electrical resistivity soundings were made between 6 October and 13 October 1993. The locations of these soundings are shown in figure 2. To obtain maximum coverage, electrode arrays were set up going both north-south and east-west, and in several instances, the array crossed the stream. Some of the soundings were repeated on 3 December 1993 to assure reproducibility and accuracy of the data.

The apparent resistivity data at electrode spacings (a-spacings) of four and eight meters (figures 3 and 4, respectively) were plotted and contoured. These a-spacings were chosen because the water table is at approximately 1.3 to 1.6 meters (4.3 to 5.3 ft) deep, and the depth of penetration is typically about half of the a-spacing. A four meter a-spacing should represent the apparent resistivity of a plane near the water table, while an eight meter a-spacing should represent the apparent resistivity of a plane within the saturated sediments below the water table.

Both apparent resistivity plots (figures 3 and 4) show a resistivity high near MW-3, where contamination levels are high, and decreasing values to the south where the contamination

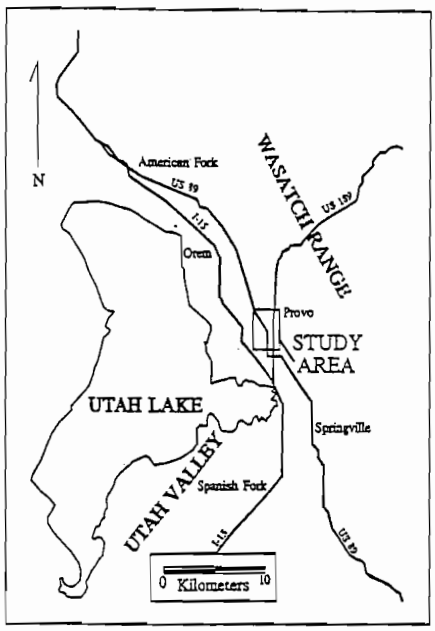

Figure 1. *Index map of the Utah Valley (modified from U.S. Geological Survey, 1 x 2 degree topographic map of Salt Lake City, Utah, 1970).*

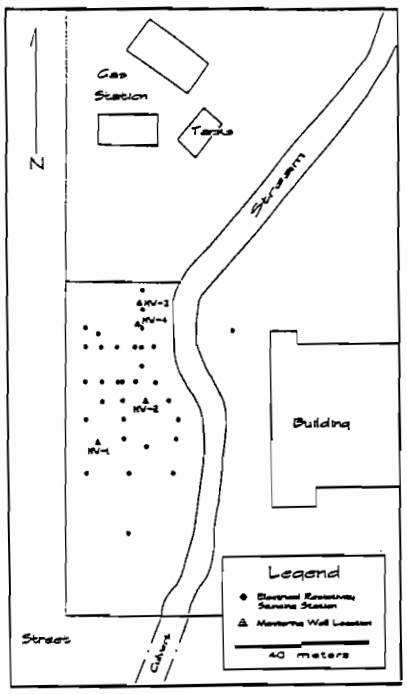

Figure 2. *Case study site location in Provo, Utah. Map shows position of monitoring wells (MW) and resistivity sounding locations.*

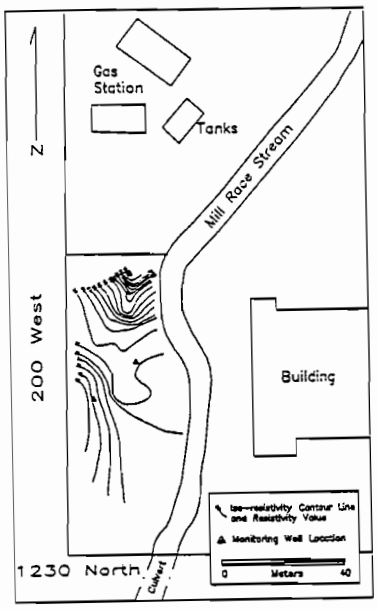

Figure 3. *Study site apparent resistivity contour map for an a-spacing of 4 m (13 ft). Contour interval is 4 Ohm-m.*

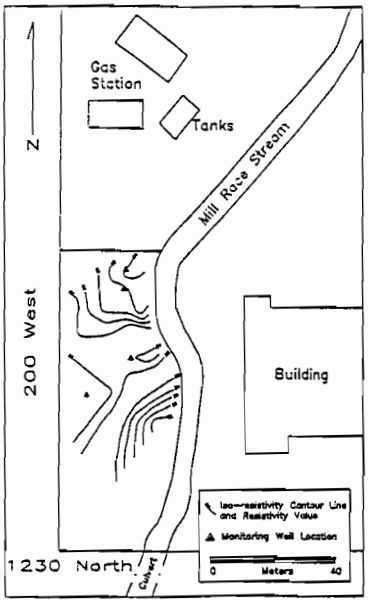

Figure 4. *Study site apparent resistivity contour map for an a-spacing of 8 m (26 ft). Contour interval is 4 Ohm-m.*

is below detection limits. At the four meter a-spacing, apparent resistivities range from 75 Ohm-m near MW-3 to 24 Ohm-m near MW-1. At the eight meter a-spacing, apparent resistivities range from 55 Ohm-m near MW-3 to 21 Ohm-m near MW-1. This drop in apparent resistivity values is less dramatic than for the four meter a-spacing, probably due to the fact that gasoline is less dense than water and tends to float on the water table, so the effect of the contamination is less pronounced below the surface of the water table. For both a-spacings, the contaminant plume appears to be outlined by a "nose-shaped" pattern of high apparent resistivities in the area where contamination levels are highest.

The apparent resistivity data were modeled using the BOSSIX modeling program (Interpex, 1988) to obtain interval resistivities which were plotted and contoured for different a-spacings. The contour map for the four meter a-spacing (figure 5) represents the resistivity values at a depth near the water table. It shows a resistivity high in the northern part of the study area where contaminant levels are high. These values decrease to the south where contaminant levels drop below detectable limits. Resistivity values range from 36 Ohm-m near MW-3 to less than 10 Ohm-m near MW-1. The contaminant plume appears to be outlined by a geometrically-shaped "nose" of high resistivity values corresponding to the area of high contamination as determined from the water chemistry analyses.

The areas of high resistivity also correspond to a higher concentration of dissolved solids (table 3) which should decrease the resistivity of the water table. At this site, however, the resistivity appears to be primarily controlled by the gasoline floating on the water table, and/or the gasoline constituents wetting the soils above the water table, rather than by the dissolved solids in the contaminated water. This effect may be further enhanced by clays at the site which can trap the gasoline, not allowing it to readily escaped. At some other sites in Utah and Arizona, where the amount of dissolved solids increases relative to the amount of residual hydrocarbons (due to degradation of hydrocarbons), ground-water contamination has been mapped as a resistivity low (Benson and others, 1991; Benson 1992).

VLF SURVEY RESULTS

VLF data were collected on 29 November and 3 December 1993. Nine VLF traverses were made at the study site (figure 6). These data were filtered, using a Karous-Hjelt (1983) filter, processed, and plotted at a selected depth near the water table (figure 7).

Interpretation of these traverses indicate a resistivity high (less positive values) over the contaminant plume, which correlates well with the ER data. The magnitude of the resistivity of the subsurface materials decreases going south from the gas station, or away from he contaminated area. VLF traverses 1 and 3 (figures 7a and 7b) cross the contaminant Plume. These figures show the contaminant plume as a resistivity high surrounded on both sides by materials of lower resisitivity. In figure 7a, the resistivity high begins about 5 meters (16.4 ft) from the west edge of the study area and extends to about 26 meters (85.3 ft) from the west edge. Figure 7b shows a resistivity high beginning about 7 meters (23 ft) from the west edge of the study area and extending to about 16 meters (52.5 ft) from the west edge. Thus, the contaminant plume is narrowing laterally, as well as decreasing in intensity. Traverses 4 through 9 also show the same decreasing pattern of contamination toward the south.

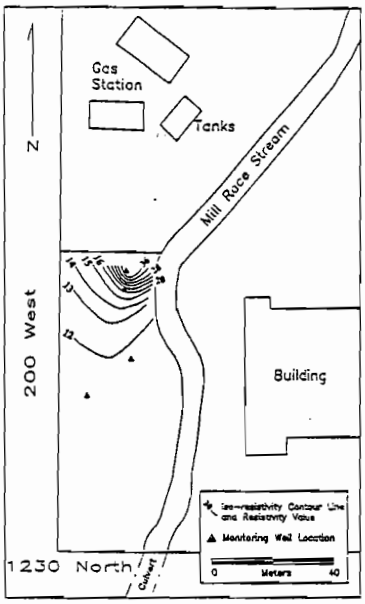

Figure 5. *Study site interval resistivity contour map at a depth of 1.6 m (5.3 ft). Contour interval is 4 Ohm-m to the north and 1 Ohm-m to the south.*

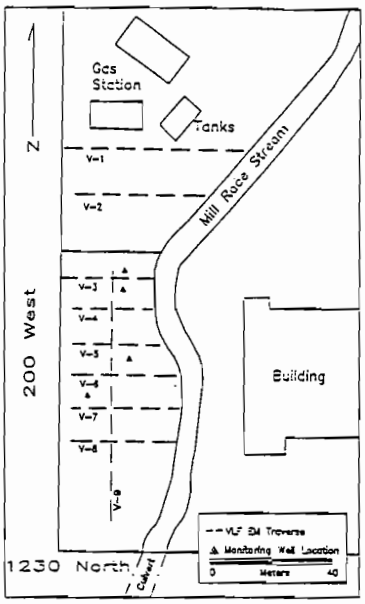

Figure 6. *VLF EM traverse locations for study site. Higher values on the vertical axis correspond to lower resistivities.*

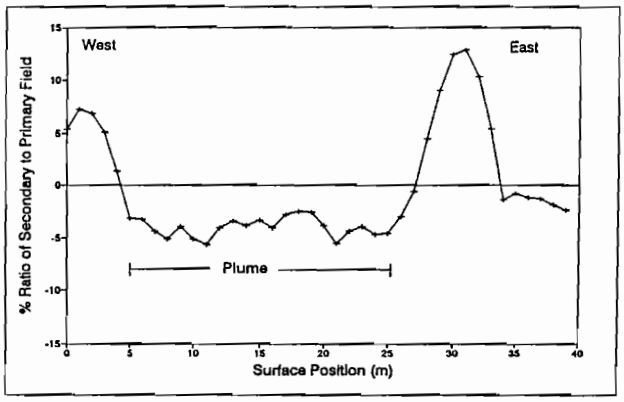

Figure 7a. *VLF EM data filtered and plotted at a depth of 1 meter (3.3 ft) for traverse V-1.*

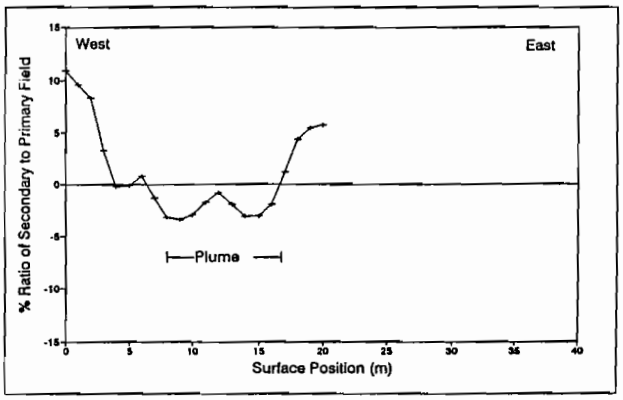

Figure 7b. *VLF EM data filtered and plotted at a depth of 1 meter (3.3 ft) for traverse V-3.*

CONCLUSIONS

Electrical resistivity (ER) and very low frequency electromagnetic induction (VLF) surveys were successfully combined to help outline a contaminant plume produced by gasoline leaking from an underground storage tank. Good correlation exists between the geophysical surveys and hydrocarbon contamination in strategically located wells, and the geophysical data has effectively extended the horizontal extent of the borehole data. Both geophysical methods identified the contaminant plume by high resistivity values, even though there were higher total dissolved solids (TDS) concentrations in the contaminated ground water as compared to the cleaner ground water. The resistivity of the hydrocarbons in the soils and those floating on the water table appears to be the dominating factor at this site. Interpretations of the filtered VLF data correlate well with the interpreted interval ER data. These geophysical methods show promise for application at sites of hydrocarbon contamination to help identify the source(s) of contamination, help strategically locate monitoring wells, and help monitor clean-up activities.

REFERENCES CITED

Benson, A.K. 1992, Integrating seismic, resistivity, and ground penetrating radar to delineate the water table and ground-water contamination: in Water-Rock Interaction, v.1, Low Temperature Environments, Kharaka, Y.K., and Maest, A.S., eds.: Rotterdam, Netherlands, Balkema, p. 361-365.

Benson, A.K., Frederickson, C., and Mustoe, N.B., 1991, Ground-penetrating radar, electrical resistivity, soil and water quality studies integrated to determine the source(s) and geometry of hydrocarbon contamination at a site in north-central Arizona: Proceedings of the 27th Symposium on Engineering Geology and Geotechnical Engineering, p. 38.1-38-13.

Benson, R.C. 1991, Remote sensing and geoghysial methods for evaluation of subsurface conditions: in Practical Handbook of Ground-water Monitoring, Nielsen, D.M., ed., Chelsea, MI, Lewis Publishers, p. 143-194.

Foster, A.R., Veatch, M.D., and Baird, S.L., 1987, Hazardous Waste Geophysics: Geophysics, The Leading Edge, v. 6, p. 8-13.

Gates, J.S., and Freethey, G.W., 1989, The relation of the geohydrologic setting to the potential for ground-water contamination in Utah: in Geology and Hydrology of Hazardous Waste, Mining-waste, and Repository Sites in Utah, Cordy, G.E., ed.: Salt Lake City, UT, Utah Geological Association, p. 11-28.

Interpex Limited, 1988, BOSSIX User's Manual: Golden, Colorado, Interpex Limited.

Karous, M., and Hjelt, S.E., 1983, Linear-filtering of VLF dip-angle measurements: Geophysical Prospecting, v. 31, p. 782-894.

Telford, W.M., Geldart, L.P., and Sheriff, R.A., 1990, Applied Geophysics, 2nd edition: New York, NY, Cambridge University Press, 770 p.

GRAVITY-DEFINED SUBSURFACE STRUCTURE AND GEOMETRY OF THE LOWER PORTNEUF RIVER AQUIFER

T.V. Reid
Idaho State University (208-236-3365)
J.A. Welhan
Idaho Geological Survey (208-236-4254)
(Both at Department of Geology, Idaho State University, Campus Box 8072, Pocatello, ID 83209)
J.R. Pelton
Center for Geophysical Investigations of the Shallow Subsurface (208-385-3640)
(Department of Geology, Boise State University, Boise, ID 83725)

ABSTRACT

A gravity survey was undertaken in the lower Portneuf River valley (LPRV) to help establish the hydrogeologic boundaries of the shallow alluvial aquifer from which the City of Pocatello produces all its municipal water. This study was initiated, following the discovery of trichloroethylene contamination up-gradient of the municipal well field, to provide additional subsurface constraints for remediation efforts. Located in northwest Bannock County, southeastern Idaho, the northwest trending LPRV is bounded by the Bannock Range to the west, the Northern Portneuf Range to the east, and is believed to lie in a half-graben structural basin bounded by a west-dipping normal fault along its eastern margin. The modern valley's axis is oriented obliquely to the regional Basin and Range structural grain. Two objectives comprise the gravity survey: to help define the subsurface geometry of the sedimentary basin-fill; and to refine the current structural models of the LPRV and its Cenozoic history.

The gravity survey was designed as a longitudinal profile and a series of transverse profiles over a portion of the valley 6 miles (9.3 km) long and approximately 1 mile (1.6 km) wide. The longitudinal profile parallels the valley's axis with transverse profiles at 3/4 mile (1.2 km) intervals, normal to the valley's axis. Transverse gravity stations were spaced 200 feet (61 m) apart, the approximate depth to the expected first density contrast, whereas gravity stations along the valley's axis were spaced at 1/4 mile (0.4 km) intervals. Most of the data was collected and reduced during the summer of 1994, with additional data collection planned during the upcoming field season.

The data will be modeled using GRAVCAD, a two dimensional, graphical software package developed by Gradient Geology and Geophysics. The objectives of modeling are to: define (a) the subsurface bedrock topography responsible for the 10 milligal variation observed along the valley's axis which indicates the regional southward deepening of the bedrock; and (b) define the subsurface topography of the partially indurated Tertiary sediments overlying bedrock which is believed responsible for the 0.3 to 1.2 milligal variations observed in the transverse profiles. This information will be integrated with surface geologic information, seismic data, and well log information to define the effective lateral and basal boundaries of the LPRV aquifer, and to further explain the Cenozoic structural evolution of the region.

Preliminary results suggest that, geometrically, the subsurface sedimentary basin is a slightly asymmetric, longitudinal trough shallowing abruptly at both ends. Subsurface

topography generally seems subdued. At present, the extent of the gravity survey is inadequate to define the eastern graben margin, but future work is intended to clarify this aspect.

INTRODUCTION

Pocatello is located in a narrow alluvial valley in extreme northwest Bannock County, southeastern Idaho. The northwest trending valley opens onto the Snake River Plain to the north, and merges with the Marsh Creek Valley to the southwest, spatially separated from the latter by a narrow, incised bedrock feature known as the Portneuf Gap (Fig. 1). The Portneuf River flows northward through the valley from which the lower Portneuf River valley (LPRV) derives its name.

The city of Pocatello produces 100% of its municipal water from the shallow, strip-aquifer beneath the LPRV. Trichloroethylene (TCE) contamination, introduced from source (s?) up-gradient of the municipal well field, forced closure of two wells in 1993, and several other wells more recently. Because the contaminant plume potentially jeopardizes the entire well field, a sense of urgency has been placed on physically characterizing the aquifer. The gravity survey in progress, and discussed in this paper, is one of the principal components focused on this characterization.

Scope and Objectives

The scope of the gravity project covers an area of the LPRV from Red Hill to the Portneuf Gap (Fig. 1), approximately 1 mile (1.6 km) wide by 6 miles (9.3 km) long. The area of this study is restricted to the southern portion of the Pocatello aquifer because of the inadequacy of available subsurface control data for the adjacent northern aquifer. Two primary objectives comprise the gravity survey: (1) to define the subsurface geometry and geology of the sedimentary basin enclosing the southern aquifer; and (2) to refine the current structural models of the LPRV and its Cenozoic history.

Geologic Setting

The contemporary LPRV reflects a complex structural development history through Cenozoic time. The valley is bounded to the southwest by the Bannock Range, and to the northeast by the Northern Portneuf Range. East dipping late Proterozoic and Cambrian rocks comprise both valley bounding ranges. These strata were uplifted and thrust eastward during the Jurassic to Paleocene Sevier Orogeny (Burgel et al., 1987; Armstrong and Oriel, 1965), and subsequently dissected along north-northwest trending, west dipping normal faults related to Neogene Basin and Range extension. The resultant structures are serial horst blocks and sediment filled, half or full grabens (Link et al., 1985) characteristic of the Basin and Range province. A half-graben structure, fault bounded along its eastern margin, is thought to define the present day LPRV. Synorogenic detritus shed off the Bannock and Portneuf Ranges, and thick sequences of volcaniclastics constituting the Tertiary Salt Lake Group largely filled the ancestral valley. Progressive removal of the basin fill sediments during the Pliocene by fluvial down-cutting processes followed in response to base level changes associated with Snake River Plain volcanic and drainage change events (Ore, 1982).

A second episode of basin backfilling apparently occurred during the Pleistocene partially

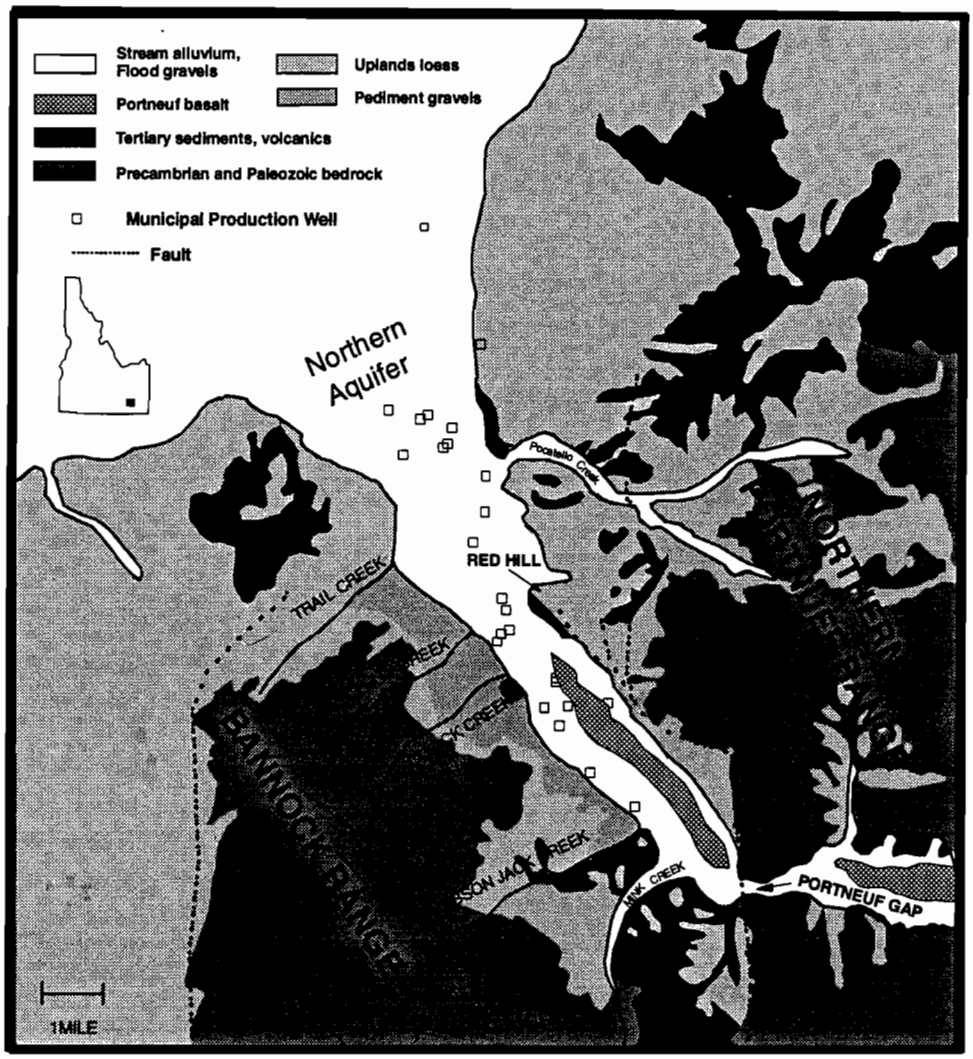

Figure 1: Generalized surface geology of the Lower Portneuf River Valley; condensed from Trimble (1976) and Rodgers (unpublished data).

filling the valley with locally derived material into which new valleys were re-cut giving rise to the benches flanking the modern LPRV. These second generation sediments were dissected to levels somewhat below the present day floodplain surface, and the resultant valleys received fluvial sediments which are overlain and/or intercalated by lacustrine clays from ancient American Falls Lake.

Two other major events complete the Cenozoic structural evolution of the LPRV, and the development of the modern aquifer. Prior to 600 ka, the ancestral Portneuf River is thought to have flowed along the modern valley's eastern margin providing a channel into which the middle Pleistocene Portneuf Basalt flowed from the Gem Valley. Emplacement of the channel-confined basalt displaced the Portneuf River's meander plain westward where continued cutting and filling set the stage for the Bonneville Flood event. About 15,000 years ago, pluvial Lake Bonneville overtopped its threshold at Red Rock Pass at the southern edge of the Marsh Valley catastrophically discharging some 1150 cubic miles of water northward through the LPRV, and debouching onto the Snake River Plain (O'Conner, 1990). This event truncated the fanglomerate benches flanking the Bannock Range, scoured the Portneuf Basalt, and stripped much of the pre-existing valley fill along the valley's bottom. Additionally, waning floodwaters emplaced a thick package of clean, well-sorted coarse gravels (Michaud Gravels (?)) and sands on the valley floor, which together with the overlying, post-Bonneville fluvial gravels constitute the most productive portion of the municipal aquifer (Welhan et al., 1995). The aquifer gravels are presently mantled by a few 10's of feet of post-flood river silt and loess.

Figure 1 shows a generalized surface geologic map of the various rock units in the lower Portneuf River Valley. The Tertiary basin filling sediments appear to be moderately well indurated over a large area of the LPRV (Welhan et al., 1995), and are discontinuously juxtaposed to bedrock and flood gravels, for example at the mouth of Mink Creek. Based well data and on the valley evolution model discussed above, it appears this relationship is replicated in the subsurface. That is, the vertical stratigraphic succession is Proterozoic bedrock base overlain by Tertiary cemented gravels grading upward into poorly indurated volcaniclastics, sands and clays, with Michaud Gravels, or their equivalent, on top. This succession serves as the postulate dictating the design of the gravity survey, and constraining the modeling process.

APPROACH AND METHODS

Survey Design

The gravity survey was designed as a series of profiles: a longitudinal profile, coinciding with the modern valley's axis, and a series of transverse profiles at 3/4 mile (1.2 km) intervals, normal to the longitudinal line (Fig. 2). Individual gravity stations were spaced about 1/4 mile (0.4 km) apart along the axis profile, whereas the transverse profiles employed a 200 foot (61 m) spacing. A 200 foot spacing was chosen because that is the approximate depth to the first density contrast expected at the cemented Tertiary to aquifer gravel interface, and to provide higher resolution of the residual gravity variations. The bedrock/Tertiary density interface lies much deeper and is believed responsible for the regional gravity trend which declines sharply from Red Hill to the Portneuf Gap. Figure 2 shows the design of the survey, and the gravity profiles that were completed during the 1994 field season. Notice that the transverse profiles--denoted RRP, BP, etc.--are located where some well control is available as marked by heavy filled squares. Profiles A-A' and B-B' shown in Figure 2 will be the foci of the results section of this paper.

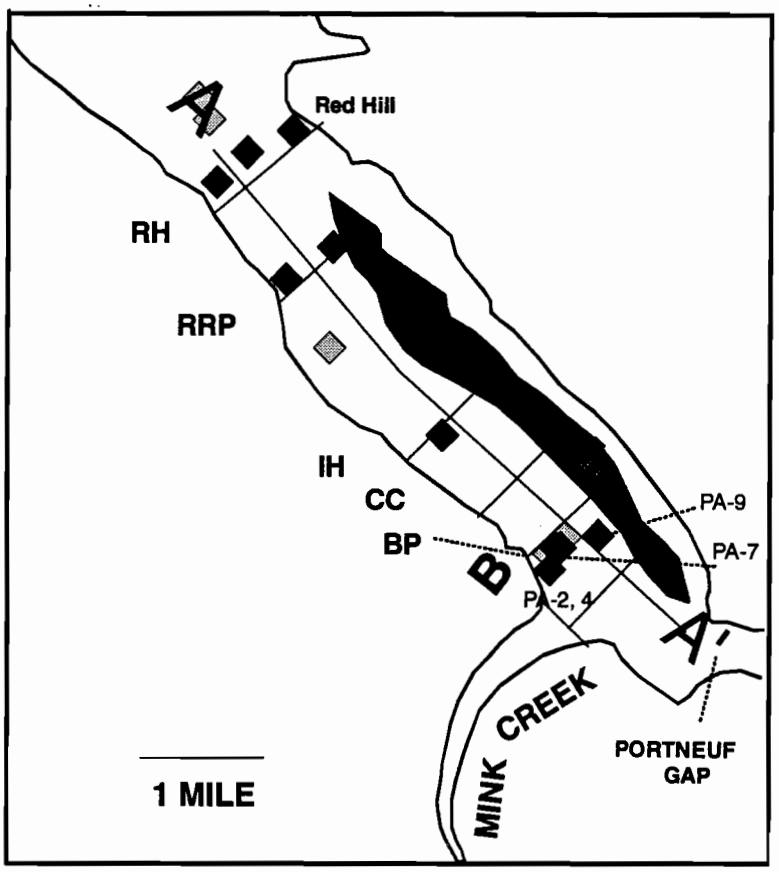

Figure 2: Locations of gravity survey traverses across the southern aquifer. Solid lines identified by initials identify individual traverses. Profiles A-A' and B-B' are illustrated in succeeding figures. Also shown are locations of some of the municipal and monitoring wells (filled squares) used to provide lithologic control in gravity-based interpretations of subsurface geology.

Gravity Data Corrections

To establish the true relative gravity variations between different stations, all field data were corrected to remove effects which are unrelated to local subsurface geology. The necessary corrections included: daily gravimeter drift and tidal corrections; latitude corrections; free-air corrections; Bouguer corrections; and terrain corrections (Sharma, 1986). Drift and tidal corrections were determined from field data as described below, and were applied to the raw field gravity readings. Latitude corrections were calculated and applied with respect to the midpoint of longitudinal profile, assuming a constant gradient over that north-south distance. Free-air, Bouguer, and terrain corrections were all calculated with respect to a common sea level datum.

Terrain corrections were performed using the Hammer (1939) graphical method. Three transparent templates were constructed to be overlain on topographic maps of different scales. Near-field terrain corrections (zones B through E of Hammer) employed 1:2400 high resolution maps contoured at 2 foot intervals which were provided by the City of Pocatello. Intermediate-field corrections (zones G through I) were determined from 1:24,000, 7.5", 40 foot contour interval maps, and far-field corrections (zones J through M) used 1:62,500, 15", 50 foot contour interval maps. Because the local topographic relief is extreme, all gravity stations were corrected for terrain variations within a 13 mile (22 km) radius of their respective locations. Additionally, it was found that the variability of far-field corrections across profiles normal to the valley axis was insignificant, whereas, the terrain correction values along the valley axis profile changed markedly. Therefore, a calibration curve was constructed from the actual far-field correction values derived from longitudinal profile stations, and applied to transverse stations as interpolated from the calibration curve.

Elevation Surveying

Elevation control is critical to gravity surveying. To preserve the gravimeter's accuracy, the elevation of each station must be known to 0.1 feet. This project used the trigonometric profile leveling method in which slope distance was electronically measured, and elevation was calculated as a function of the sighting angle and distance. Equipment utilized included a self-level-correcting digital theodolite, an electronic distance measuring instrument (EDMI), and a microwave triple reflector.

Individual gravity stations were located along a profile, and staked at desired intervals. The theodolite was then set up at an arbitrary point on the profile line, precisely leveled, the EDMI and reflector height set equal, and the EDMI calibrated to atmospheric operating conditions. A backsight was shot to a benchmark yielding the elevation of the setup point, and a series of foresights were made as the reflector was moved to succeeding stake locations up to a sighting distance of 600 to 1000 feet (183-305 m). At each station location the slope distance and sighting angle were recorded. The theodolite was then moved forward along the profile line and a backsight shot to the last location occupied by the reflector, and another series of foresights executed. Closure was achieved by concluding the profile survey with a foresight to another benchmark. All benchmarks used were recently recovered and adjusted to a 1989 datum. Any profile not meeting the 0.1 foot closure requirement was re-surveyed until closure was attained.

Mathematically, station elevations were calculated in the following manner. Using a zenith theodolite the elevation difference (V) for inclined sights between two points, (i.e, between the instrument and the reflector) is equal to the product of the slope distance (S) and the

sine and cosine of the zenith angle (Z); V = S sin Z cos Z. All backsight values were subtracted from the elevation of the backsighted object, and all foresight values were added to the elevation of the theodolite setup point.

Gravity Surveying

Once station locations and elevations were established, gravity measurements commenced. A Worden gravimeter, Model W-2 was used in this project. The gravity meter's sensitivity and levels were checked for accuracy as prescribed by the manufacturer's documentation each day before actual field operation. In the field, an arbitrary base station was chosen at a convenient point along the profile being measured. The relative gravity value was measured at this base station first, last, and at no more than 2 hour intervals. These base station measurements yield the rate of drift, i.e., milligals/unit time, for the time interval that was required to measure the complete profile. The drift corrections were then applied based on the time elapsed between the first base station measurement and the respective gravity station measurement.

At each individual station location, the base plate was placed securely on the ground, the gravimeter was placed on the plate and precisely leveled using the base plate for stabilization. A series of 5 readings were made and recorded to yield an average value in dial units which was subsequently converted to a gravity value. The gravimeter was then moved to the next station location, and the procedure repeated until all stations in the profile had been measured. Drift and diurnal oscillations were calculated from the field data, and their effects removed in the data reduction process as described above. Only relative gravity values were produced by data reduction, and used in modeling and interpretation.

Modeling

All field data will be modeled using GRAVCAD, a two dimensional, graphical software package developed by Gradient Geology and Geophysics, but to date only two gravity profiles have been completed. Lithologic information from well logs was used to constrain a models' geologic parameters (depth and density contrasts) and subsurface interpretations along the 2-D profiles. The objectives of modeling were: (a) to define the subsurface bedrock topography responsible for the high amplitude variation observed along the valley's axis; and (b) to define the subsurface geometry and topography of the partially indurated basin-filling sediments overlying bedrock which are believed responsible for the low amplitude variations observed in the transverse profiles. This information will be integrated with surface geologic information, seismic data, and well log information to define the effective lateral and basal boundaries of the LPRV aquifer, and to further explain the Cenozoic structural evolution of the region.

Field Calibration

Calibration of the gravity model interpretations to subsurface geologic conditions incorporated surface geologic and structural interpretations, seismic refraction data, and well control, but relied most heavily on the latter. A total of 10 new monitoring wells were drilled across the LPRV aquifer in 1994 as part of the City of Pocatello's remediation of the TEE contamination problem. Three of these wells intersected Tertiary sediments, and a fourth

terminated in basalt. As a test case for calibration of the cemented gravel-unconsolidated gravel interface, profile B-B' (Fig. 2) was intentionally located closely coincident with this line of monitoring wells. Calibration to bedrock depths was provided by two wells along profile RRP (Fig. 2).

RESULTS

The valley axis profile (Fig. 3-a) shows a 10 milligal gravity low that is flanked by steep gradients (approximately 5 mgal/mile or 3 mgal/km) to the northwest and southeast. This anomaly is interpreted to represent a substantial deepening of Proterozoic bedrock between Red Hill and Mink Creek, and a concomitant increase in the thickness of the valley filling sediments. The abrupt increase in depth of the bedrock southeast of Red Hill may be a result of faulting, whereas the shallowing of the bedrock near the Portneuf Gap is possibly related to the oblique trend of the valley axis profile relative to the regional structural grain.

In contrast, the transverse profiles indicate relatively uniform gravitational fields normal to the valley's axis, at least over short distances. For example, the primary feature in profile B-B' (Fig. 4-a) is a gravity low of 1 milligal amplitude with superimposed small residual anomalies. The interpretation of the transverse profiles is complicated by the possible superposition of bedrock effects (associated with the valley margins) on steeply dipping, relatively shallow density contrasts within the valley fill sediments, such as between the aquifer gravels and the underlying Tertiary cemented gravels. In this paper, it is shown that a reasonable density contrast and geometry describing the two gravels can account for the observed gravity low, and that subsurface basalt bodies can account for the small residual anomalies. However, more reliable interpretation of the transverse profiles depends on increasing their length relative to the valley width so that bedrock effects can be more fully evaluated.

INTERPRETATION

Interpretation of the data has been facilitated by modeling. Modeling is an attempt to replicate the configuration of the observed anomaly curve by manipulating variable subsurface geometry and geologic conditions using computer graphics. As geologic and geometric parameters are modified, an anomaly curve is computer generated which reflects the theoretical values that would be observed for a given set of conditions. The given set of conditions is termed a model.

In the interpretations discussed below, the Tertiary section and the aquifer gravels were modeled with an average density of 2.1 and 2.0 gm/cm^3, respectively. The assumed Tertiary sediment density is at the low end of values measured in hand specimens collected during drilling, which showed a range of 2.0 - 2.4 gm/cm^3. The density of aquifer gravels is based on measurements of grab samples collected in a gravel pit in the central part of the southern valley. Bedrock and basalt bulk densities were assumed to be 2.65 gm/cm^3 and 3.00 gm/cm^3, respectively.

Axial Profile A-A'

Minimum depth to bedrock used to constrain the gravity interpretation of Profile A-A' model is 110 feet (Welhan et al., 1995) at traverse RRP (Figs. 2 and 3b). A density contrast of -

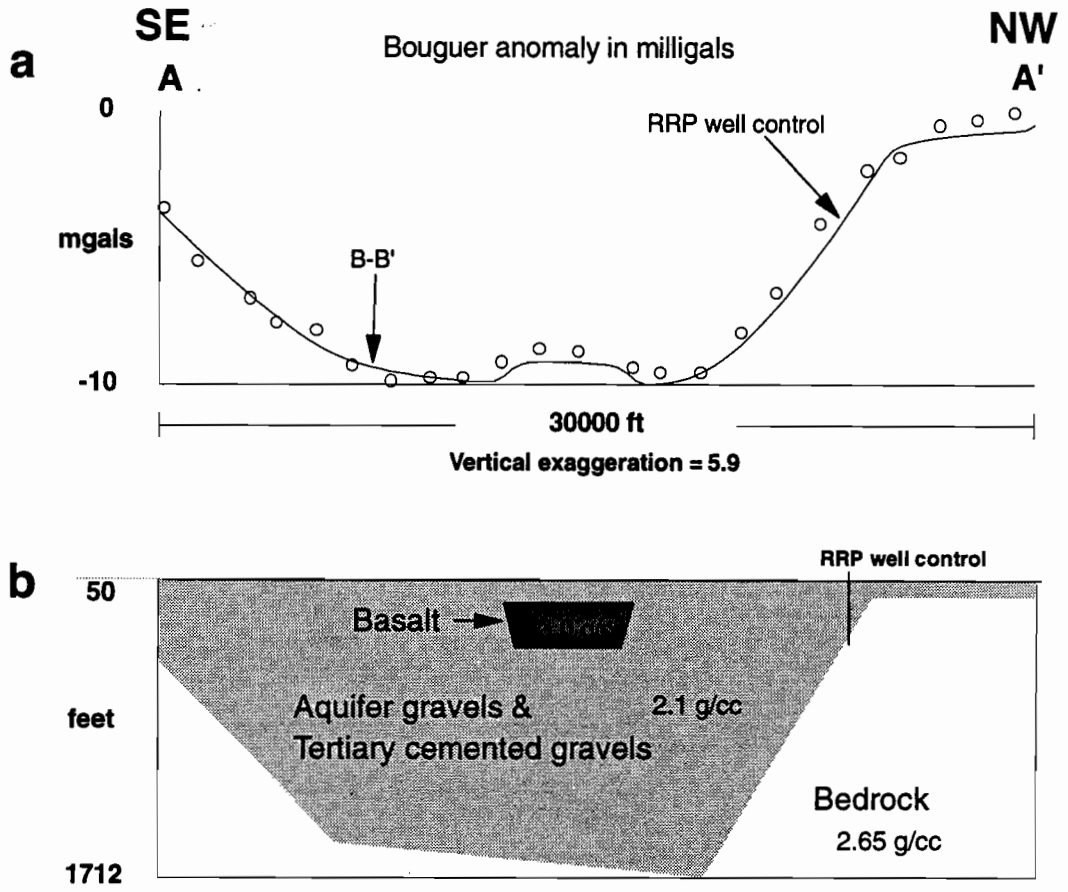

Figure 3: (a) Gravity anomaly along profile A-A' showing field measurements (circles) and model calculations (solid curve); (b) model of the subsurface geometric and lithologic characteristics of the Tertiary-bedrock interface. Note the midsection gravity low flanked by steep gradients to the northwest and southeast.

0.55 between bedrock and basin filling sediments was used in this preliminary model. The bedrock topography illustrated in Figure 3-b shows two significant features. First, the graben appears to be fairly deep; maximum depth to bedrock in the model is about 1700 feet (518 m). For a density contrast of -0.3, more than 3000 feet of basin relief would be required. This range is consistent with structural geologic interpretations of the LPRV graben (D. Rodgers, pers. comm., 1993).

Secondly, the local gravity high in the central part of the profile can be modeled only by a relatively near-surface, high-density body. The small polygon in the upper portion of the sedimentary section of Figure 3-b is intended to represent a basalt boulder-filled channel, deposited during the Bonneville flood. Such an interpretation, although speculative, would be consistent with Trimble's (1976) observation that flood-deposited basalt boulders progressively increase in diameter from the widest to the narrowest portion of the flood channel, and that basalt boulders larger than 10 feet in diameter should be expected south of Red Hill. Additional evidence of such a feature is considered in the interpretation of profile B-B', below. The modeled anomaly shows a reasonable correlation to the field data, however, future modeling and data acquisition will doubtless improve the fit.

Transverse Profile B-B'

Superimposed on the regional gravity trend are short wavelength, low amplitude residual anomalies seen in the transverse profiles. The observed variations range from 0.1 to about 1.2 milligals in magnitude. Figures 4 and 5, showing the modeled profile B-B', and a geologic cross section, respectively, illustrate one example. Data for the geologic cross-section (Fig. 5) is from CH^2M-Hill (1994). Wells PA-3 and -7 coincide precisely with the gravity line, whereas PA-2 and -4 are spatially displaced a few 10's of feet, and PA-9 is located about 300 feet (91 m) south of the profile (see Fig. 2). The aquifer gravels were initially modeled as a distinct unit relative to the Tertiary cemented gravels based on a density contrast of -0.1 gm/cm^3. This density contrast produced a geologically improbable model. Therefore, to produce a more reasonable model, Figure 4-b employs a density contrast of -0.33 gm/cm^3. Additionally, basalt elements were incorporated in the model.

Notice that the gross aquifer geometries illustrated in Figures 4-b and 5 are similar, including lateral boundary attitudes. The gravity model's western boundary is constrained by previously mentioned well data, however, the eastern Tertiary boundary is more conjectural. Maximum aquifer gravel thickness in the model is about 300 feet (91 m); a thickness consistent paleo fluvial base level indications. The large basalt element (lower left, Fig. 4-b) has the aspects of either a relatively thin flow or a large boulder-filled channel, and was integrated into the model to account for the moderate upward inflection near the west end of profile B-B'. Supporting this interpretation is the fact that PA-7 bottomed in basalt at 170 feet (52 m), although its aspects remain speculative. The small rectangular element (upper center, Fig. 4-b) perhaps represents a basalt block from the Portneuf Basalt flow which is located a few hundred feet to the east. This element was introduced to account for what is essentially a one point anomaly on the gravity profile. Whatever is responsible for the sharp inflection in Figure 4-b, it can only be accounted for by a shallow, high density feature. More detailed gravity data are needed in the vicinity of the anomaly to resolve its origin.

Although preliminary modeling of B-B' has produced a geologically reasonable model, only an approximate fit to field data has been attained. It must be re-emphasized that currently

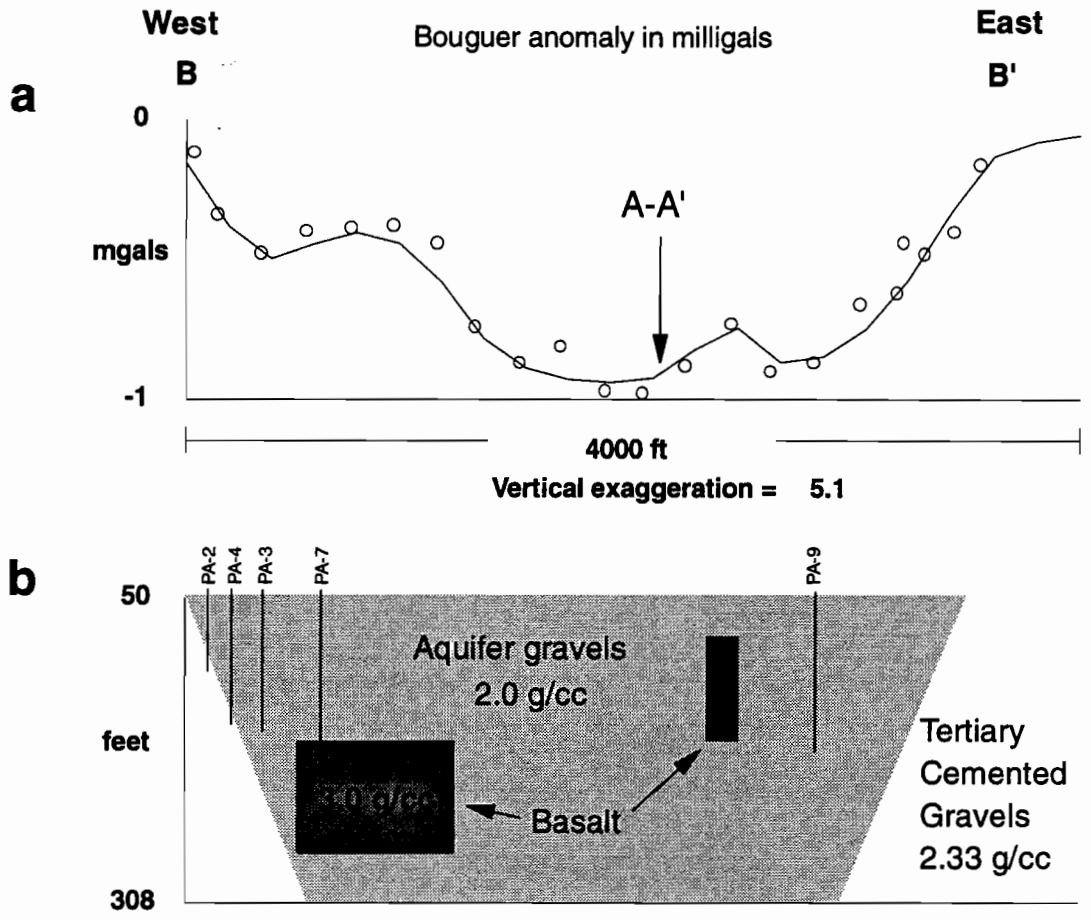

Figure 4: (a) Gravity anomaly along profile B-B' showing field measurements (circles) and model calculations (solid curve); (b) model of the subsurface geometric and lithologic features of the aquifer gravel to Tertiary cemented gravel interface. Note the broad 1 milligal low across the profile with superimposed smaller amplitude variations.

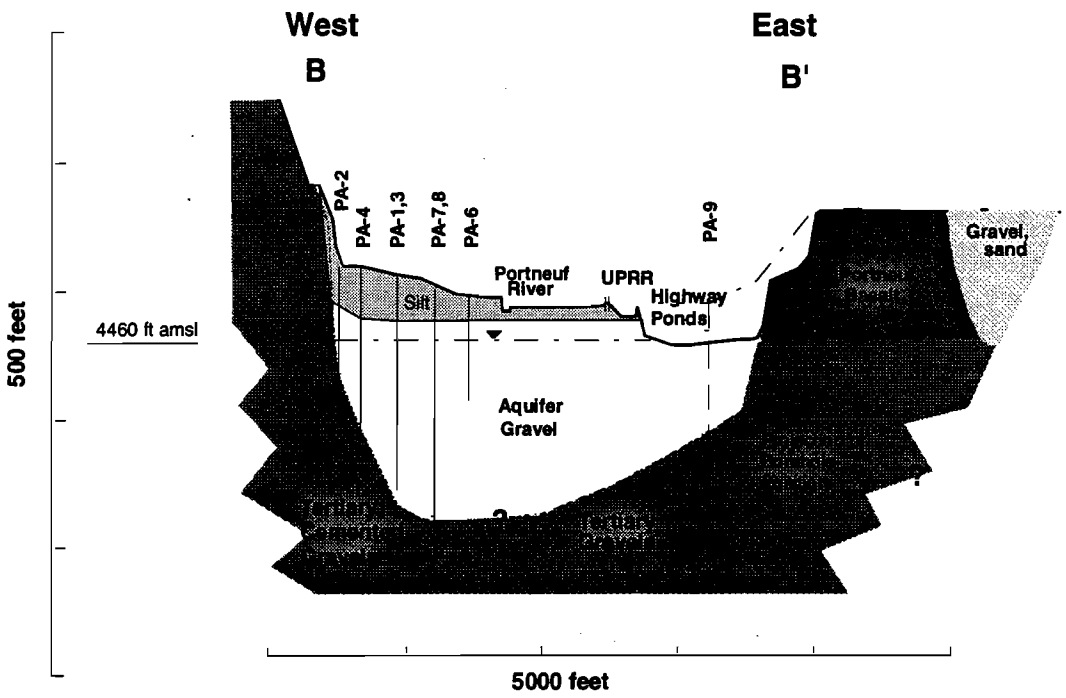

Figure 5: Conceptual geologic cross-section along profile B-B' developed from CH^2M-Hill drilling data. Note that the the aquifer gravels thin moderately eastward, and that gross geometry is similar to the gravity model illustrated in Figure 4-b.

modeling is in its infancy, which compels further modeling and refinements.

CONCLUSIONS

Two of the gravity survey's profiles have been modeled in 2-D producing reasonably satisfactory results. To a first approximation, the subsurface sedimentary basin seems shaped as a slightly asymmetric trough shallowing at both ends longitudinally. In cross-sectional profile, one model indicates that the aquifer gravel/cemented gravel interface may lie at least 300 feet (91 m) below the surface. Tertiary topography seems generally subdued, whereas bedrock topography is characterized by two features: a deep, southward deepening graben basement; and an undetermined, high-density element along the valley's axial midsection. But clearly additional work needs to be done to present a complete physical characterization of the subsurface geometric and lithologic relationships. In particular, the assumptions inherent in 2-D modeling of the valley axis need to be evaluated in the context of the actual structural attitude of the graben relative to the model profiles. Subsequent modeling will employ 2 1/2-D and 3-D approaches to evaluate these questions.

Supplementary data acquisition is planned for the upcoming field season to extend the survey southeastward into the Portneuf Gap, and to the valley margin east of the Portneuf Basalt. Unresolved at this point is the attitude and location of the graben-bounding fault, and its implications for the eastern valley margin and basin-fill thickness. Future work will attempt to clarify these relationships.

ACKNOWLEDGEMENTS

This research project has received generous funding from the City of Pocatello, and the Idaho Water Resource Research Institute.

REFERENCES

Armstrong, F.C., and Oriel, S.S.,1965, Tectonic development of Idaho-Wyoming thrustbelt: American Association of Petroleum Geologists Bulletin, v. 49, pp. 1847-1886.

Burgel, W.D., Rodgers, D.W., and Link, P.K., 1987, Mesozoic and Cenozoic structures of the Pocatello region, southeastern Idaho; *in* W.R. Miller ed., The Thrustbelt Revisited, Wyoming Geological Association, 38th Field Conference Guidebook, pp. 91-100.

CH2M-Hill, 1994, Hydrogeology and assessment of TEE contamination in the southern portion of the Pocatello aquifer- Phase I Aquifer Management Plan; 100 pp.

Hammer, S., 1939, Terrain corrections for gravimeter stations, Geophysics, vol. 4, p. 184-194.

Link, P.K., LeFebre, G.B, Pogue, K.R., and Burgel, W.D., 1985, Structural geology between the Putnam thrust and the Snake River Plain, southeastern Idaho, *in* Kerns, G.J., and Kerns, R.L. Jr., eds., Orogenic Patterns and Stratigraphy of North-Central Utah and Southeastern Idaho: Utah Geological Association Publication 14, pp. 97-117.

O'Conner, J.M., 1990, Hydrology, hydraulics, and sediment transport of Pleistocene Lake Bonneville flooding on the Snake River, Idaho, [PhD dissertation], University of Arizona, 192 pp.

Ore, H.T., 1982, Tertiary and Quaternary evolution of the landscape in the Pocatello, Idaho area; Northwest Geology 11, pp. 31-36.

Sharma, P.V., 1986, Geophysical methods in geology, 2nd edition: New York, New York, Elsevier Science Publishing Co. Inc., p. 91-154.

Trimble, D.E., 1976, Geology of the Michaud and Pocatello quadrangles, Bannock and Power counties, Idaho; U.S. Geological Survey Bulletin, 1400, 88 p.

Welhan, J., Meehan, C., and Reid, T., 1995, Hydrogeology of the lower Portneuf River valley aquifer: a geologic and hydrogeologic model and implications for wellhead protection strategies, 131 pp.